

Effect of Semiconductor Laser Noise on Coherent Optical OFDM Systems

Zaid Sami Abd-Alghany Al-Aubaidy

MSc in Communication Engineering

Supervisor: Professor Arthur J. Lowery

A thesis submitted for the degree of

Doctor of Philosophy

Department of Electrical and Computer Systems Engineering
Monash University, Melbourne, Australia

2012

Copyright Notices

Notice 1

Under the Copyright Act 1968, this thesis must be used only under the normal conditions of scholarly fair dealing. In particular no results or conclusions should be extracted from it, nor should it be copied or closely paraphrased in whole or in part without the written consent of the author. Proper written acknowledgement should be made for any assistance obtained from this thesis.

Notice 2

I certify that I have made all reasonable efforts to secure copyright permissions for third-party content included in this thesis and have not knowingly added copyright content to my work without the owner's permission.

Corrections

Corrections of Professor M. Nazarathy

Language and Style Corrections

<i>Page No. / Section No. / Paragraph details</i>	<i>Note / Mistake</i>	<i>Corrected to / Modified to</i>
p.4 / S. 2.1 / the 1 st row	... is demonstrated	... is performed
p.7 / S. 2.3 / the 5 th row in the 1 st bullet	... can operates	... can operate
p.8 / S. 2.4 / the 8 th row	... DSP potential	... DSP complexity
p.9 / S. 2.5 / the bottom	... which usually accomplished	... which is usually accomplished
p.14 / S. 3.2.2.2 / the 3 rd row before equation (3.4-a)	... of a service channels	... of service channels
p.21 / S. 3.3.1 / the 2 nd row	... which results optimum performance	... which results in optimum performance
p.22 / S. 3.3.1 / the 1 st row before equation (3.16)	... the impulse response	... the frequency response
p.25 / S. 3.3.2.1 / the 5 th row in point No. 6	inside-band, outside-band	in-band, out-of-band
p.47 / S. 4.2.1 / the 5 th row after Fig. 4.2a	... as shown In Fig. 4.2	... as shown in Fig. 4.2
p.48 / S. 4.2.2 / the 3 rd and 4 th rows after equation (4.2)	... both formes are used without prior notice	... both formes are used interchangeably
p.57 / S. 4.2.3.2.2 / the 1 st and 2 nd rows	... is the algebraic sum	... is the sum
p.82 / S. 4.4 / the 12 th row	... which results compact	... which results in compact
p.82 / S. 4.4 / the 4 th rows before the end	... which are concerning with extraction	... which are concerning extraction
p.84 / S. 5.2.2 / the 7 th rows before the end	... in conjugation with MATLAB [®]	... in conjunction with MATLAB [®]
p.126 / S. 7.2.1 / the 1 st row after equation (7.2)	... is a complex Gaussian	... is a complex circular Gaussian
p.126 / S. 7.2.1 / the 2 nd row before S. 7.2.2	A discrete expression	A distinct expression
p.126 / S. 7.2.2.2 / the 1 st row	The 2 nd term in (7.3) is $y_{m,s}[\ell]$, which is calculated from (7.2) when $k = m$ and yields	The 2 nd term in (7.3) is $y_{m,s}[\ell]$, which is calculated from (7.2) by retaining the term with $k = m$ in the summation
p.133 / S. 7.2.2.3 / the 1 st row before Fig. 7.7	... be add	... be added

Corrections

p.144 / S. 7.3.2.1 / the 1 st bullet	... is a slow phase shifts	... is a slow phase shift
p.144 / S. 7.3.2.1 / the 2 nd bullet	... since it determine	... since it determines
p.145 / S. 7.3.2.2 / the 5 th rows before 1 st bullet	... let B_C is expressed by	... let B_C be expressed by
p.147 / S. 7.3.2.3 / the 1 st row	... is obtain	... is obtained
p.147 / S. 7.3.2.3 / the 3 rd row after equation (7.32)	... of powerful	... of high level
p.147 / S. 7.3.2.3 / the bottom	... which is typically has a zero-mean	... which has typically a zero-mean
p.148 / S. 7.3.2.3 / the 2 nd row	... are vanished	... vanish
p.148 / S. 7.3.2.3 / the 9 th row	... on symbol bases after the FFT is performed as in the conventional OFDM.	... on symbol-by-symbol bases after the FFT is performed as in conventional OFDM.
p.149 / S. 7.3.2.4 / the 1 st row before S. 7.3.3	... per frequency smaple.	... per frequency sample.
p.149 / S. 7.3.2.4 / the 1 st row before S. 7.3.3	Wiener-Khenchen theorm	Wiener-Khenchen-theorem
p.153 / S. 7.3.3.2.1 / the 1 st and 2 nd rows	... are usually have poor steepness	... have usually poor steepness
p.153 / S. 7.3.3.2.2	7.3.3.2.2 Effect of Δ_N when only the white FN is effective	7.3.3.2.2 Effect of Δ_N when only the white FN is in effect
p.158 / S. 7.3.4 / the 1 st row before S. 7.3.5	... used to describe the colour noise	... used to describe coloured noise
p.176 / S. 7.3.8	7.3.8 Maximum usable linewidth	7.3.8 Linewidth tolerance
p.184 / S. 8.1 / the 5 th row	... is involved,	... is attained,
p.184 / S. 8.1 / 4 th rows before S. 8.2	... has yet been adopted the real optical	... has yet been adopted in the real optical
p.187 / S. 8.2.2 / 6 th rows before the end	... is biased at π	... is biased at $\pi/2$
p.189 / S. 8.2.2 / the 16 th row in the 4 th point	... and then up-converted using an RF IQ-modulator	... and then up-convert it using an RF IQ-modulator
p.190 / S. 8.2.2 / the 3 rd row in the 5 th point	... are similar of using	... are similar to use
p.190 / S. 8.2.3.1 / the 3 th before the end	...via manual tuning of	... via scanning procedure
p.211 / S. 9.2 / the 1 st row	As any other work,	As in any other work,
p.211 / S. 9.2 / the 4 th point	In-depth analysis of the ICI's PDF	In-depth analysis of the ICI's PDF and second-order statistics

p. = page number, S. = Section number

Corrections

Technical Notes and author's action

- **Meaning of “~” in equation (7.1)?** Details in the text (p.126 / S. 7.2.1 / the 1st row).
- **Reason of proposing the side-pilot?** The side-pilot is adopted by the author to solve technical difficulties of the high required IF frequency and high BPF steepness when central-pilot is used. Details in the text (p.142 / S. 7.3.1 / the 7th row after Fig. 7.11).
- **About the Reduced Guard Interval (RGI)-OFDM.** Added with the 3rd point in the future work (S. 9.2).
- **Effect of the CD on the received PN and IN on the conventional CO-OFDM?** Since PA-FFL or RF/Optical PLL are not used in the conventional CO-OFDM, no correlation between the RF-LO-SCL's PN and the received distorted PN exist, and hence only additional phase shift term is added to all SCs with a slight differences between them due to CD. Details in (p.129 / S. 7.2.2.2.1 / the 6th row before bottom).
- **About equation (7.25d).** Perfect clock synchronization is assumed as given in the text (p.143 / S. 7.3.2.1 / the 1st and 2nd rows).
- **Why the IN is ignored in equation (7.33)?** IN effect due to the SC under-test has negligible effect (p. 132 / S. 7.2.2.2.3), while the IN due to other SCs is counted in the ICI calculation in equation (7.35).
- **About linearization of equation (7.33).** The linearization is possible due to PN subtraction with low long-term variance (a reviewer note). 1st row after equation (7.33) is changed according to this note.
- **P.167 / S. 7.3.5.3 / 1st bullet:** “the performance with the PA-FFL is inhomogeneous” is added.
- **About the TrS's overhead.** Detailed discussion about this issue is in the text (p.27 / S. 3.2.2.1 / the 4th row after equation (3.26) up to the 7th row).
- **About the disadvantageous of Shieh proposal (p.208 / S. 8.3).** Another point is added “PN is enhanced due to the use of low sampling rate” according to the reviewer suggestion.
- **Reference [98]** is replaced by: [98] M. Nazarathy, W.V. Sorin, D.M. Baney, and S.A. Newton, "Spectral analysis of optical mixing measurements," *J. of Lightwave Technol.*, vol.7, no.7, pp.1083-1096, Jul 1989. This reference is more thorough than the previous one.

Corrections

Corrections of Dr. S. Savory

Language and Style Corrections

<i>Page No. / Section No. / Paragraph details</i>	<i>Note / Mistake</i>	<i>Corrected to / Modified to</i>
p.17 / S. 3.2.3.1 / the 1 st row	CD is a time distortion	CD is a temporal distortion
p.18 / S. 3.2.3.2 / the 1 st row	PMD is a time-variant random process	PMD is a time-varying random process
p.103 / S. 6.2 / the 2 nd row before equation (6.11)	... Wiener-Khintchine theorem	... Wiener-Khintchin theorem
p.108 / S. 6.3.1	6.3.1 Approximate analysis of the beat-note PSD in the DSH test	6.3.1 Approximate analysis of the beat-frequency PSD in the DSH test
p.136 / S. 7.2.3.2 / the 8 th row	... Weiner process	... Wiener process
p.149 / S. 7.3.2.4 / the 1 st row before S. 7.3.3	... Wiener-Khenchen theorem,	... Wiener-Khinchin theorem,

p. = page number, S. = Section number

Declaration

This thesis contains no material which has been accepted for the award of any other degree or diploma at any university or equivalent institution and that, to the best of my knowledge and belief, this thesis contains no material previously published or written by another person, except where due reference is made in the text of the thesis.

Summary

Orthogonal frequency division multiplexing (OFDM) is a modulation/multiplexing method that has many advantages when it is employed in optical fiber communications. However, the OFDM signal is very sensitive to semiconductor laser's phase noise that requires either to use a very stable semiconductor laser with a narrow linewidth, or to equalize the phase noise effect before or after demodulation. This thesis presents an in-depth analysis of the long-haul coherent optical OFDM (CO-OFDM) link with pilot-aided feedforward loop (PA-FFL), which is used for pre-demodulation phase noise compensation. The thesis examines effect of large semiconductor laser noise on the OFDM's performance yielding a new homodyne OFDM design, and showing the feasibility of this technique comparing with the conventional coherent OFDM system.

فلا أقسم بالخنس (15) الجوار الكنس (16).

So verily, I swear by those which are the most silent and hidden (slinkers) (15) the runners the sweepers (sinkers) (16).

القران الكريم سورة التكمير.

Quran, Al-Takweer.

Acknowledgements

I am deeply grateful to my supervisor Prof. Arthur J. Lowery for his guidance, helpful suggestions, patience, and encouragement and to Prof. Chris Davis for his wise suggestions at the difficult times.

I am also appreciated to the staff of the “Department of Electrical and Computer Systems Engineering of Monash University” for making the place friendly and productive, with special thanks to Roslyn Rimington, Maria Scalzo, and Jane Moodie for their support. I’m so grateful to Prof. Moshe Nazarathy for his valuable and thorough corrections and to Dr. Seb Savory for his notes.

Special thank goes to my sponsor “Ministry of Higher Education and Scientific Research of Iraq” for giving me the opportunity of completing my PhD research.

All thanks go to me brother Auday for his indescribable generosity and support, my father Prof. Sami Al-Aubaidy, and my dearest and kindest mother, who I will be always indebted to them. I am so grateful to my wonderful wife Salwa and my children for their understanding, endless support, and patience. Finally, many thanks go to my younger brothers for their continuous encouragements and support.

Table of Contents

1	Introduction	1
2	CO-OFDM System: General Review	4
2.1	Introduction	4
2.2	Background	4
2.2.1	Optical fiber communications	4
2.2.2	OFDM Systems	5
2.2.2.1	Radio frequency (RF) OFDM Systems	5
2.2.2.2	Optical OFDM Systems	5
2.3	SCLs' phase noise reduction techniques	7
2.4	Feedforward loop (FFL)	8
2.5	CO-OFDM design considerations	9
3	Main Considerations and Components in CO-OFDM Design	11
3.1	Introduction	11
3.2	Optical Channel	11
3.2.1	Types of single mode optical fibers	11
3.2.2	Optical link power analysis	12
3.2.2.1	Optical amplifier	12
3.2.2.2	Optical signal-to-noise ratio (OSNR)	14
3.2.2.3	Optical link budget	14
3.2.3	Optical channel response	16
3.2.3.1	Chromatic dispersion (CD)	17
3.2.3.2	Polarization mode dispersion (PMD)	18
3.2.3.3	Overall optical channel response	20
3.3	OFDM system	20
3.3.1	Continuous baseband model of OFDM link	20
3.3.2	Baseband DSP-based OFDM link	23
3.3.2.1	Baseband DSP-based OFDM transmitter	24
3.3.2.2	Baseband DSP-based OFDM receiver	27
3.3.3	DAC/ADC	29
3.3.4	Anti-Aliasing filtering	30
3.3.5	Discrete representation of baseband OFDM link	32

3.3.6	Ideal performance of OFDM links	34
3.3.6.1	Sources of penalties in OFDM links	37
3.4	Optical up and down conversion in CO-OFDM system	40
3.4.1	Optical up-converter	40
3.4.2	Optical down-converter	42
3.4.3	OSNR and SNR_b	44
3.5	Conclusions	45
4	Characteristics and Measurement	46
	Methods of Semiconductor Laser	
4.1	Introduction	46
4.2	Characteristics of SCLs	46
4.2.1	Lasing condition and basic characteristics	46
4.2.2	Main results from rate equations	48
4.2.3	PSD of a single-mode SCL	50
4.2.3.1	PSD in OD when only the white FN is counted and $ H_c(f) ^2 = 1$	51
4.2.3.2	PSD in OD when the IN is ignored and $ H_c(f) ^2 = 1$	52
4.2.3.2.1	Numerical calculations	55
4.2.3.2.2	Mixed-field linewidth	57
4.2.3.3	PSD in OD when all parameters are counted	58
4.3	Measurement methods of SCLs	60
4.3.1	RIN Measurements	60
4.3.2	FN Measurements	62
4.3.2.1	FN measurements using direct method	62
4.3.2.2	FN measurements using heterodyne setup	63
4.3.2.2.1	RF frequency discriminator	65
4.3.2.2.2	Phase-locked loop (PLL)	65
4.3.3	Delayed self-heterodyne (DSH) test	67
4.3.3.1	Beat-note PSD when only white FN is counted and $ H_c(f) ^2 = 1$..	70
4.3.3.2	Flicker FN contribution on the beat-note PSD	70
4.3.3.3	Numerical computations	71
4.3.3.4	Main calculation results	75
4.3.4	Time-Domain Frequency Stability Measurements	77
4.4	Conclusions	82
5	Semiconductor Laser Simulator Model	83
5.1	Introduction	83

5.2	Construction of SCL functional model	83
5.2.1	Design constraints	83
5.2.2	Model analysis	84
5.2.3	Model implementation	87
5.3	Model validation	92
5.3.1	FN monitoring	93
5.3.2	Time domain monitoring	94
5.3.3	Simulation results of DSH test	96
5.4	Conclusions	99
6	Exact Analysis of Semiconductor Laser Field along an Optical Fiber	100
6.1	Introduction	100
6.2	PSD of dispersive field components	101
6.3	Analysis of DSH test of SCL's field along dispersive fiber	107
6.3.1	Approximate analysis of the beat-frequency PSD in the DSH test	108
6.3.2	Exact analysis of the beat-note PSD in the DSH test	109
6.3.3	Comparison with previous work	112
6.3.4	Exact analytical solution	114
6.4	PN and IN PSDs and variances	118
6.5	Conclusions	123
7	Effect of SCL Noise on OFDM System Performance with/without PA-FFL	124
7.1	Introduction	124
7.2	Effect of SCL noise on CO-OFDM performance	124
7.2.1	Modeling	124
7.2.2	Analysis of $y_m[\ell]$ terms	126
7.2.2.1	The channel noise term $y_{m,n}[\ell]$	126
7.2.2.2	The useful term $y_{m,s}[\ell]$	126
7.2.2.2.1	Phase shift due to channel response	127
7.2.2.2.2	$\eta_{\phi,m}[\ell]$	127
7.2.2.2.2.1	Statistical description of $ \eta_{\phi,m}[\ell] $	128
7.2.2.2.2.2	Statistical description of $\arg\{\eta_{\phi,m}[\ell]\}$	131
7.2.2.2.3	$\eta_{\alpha,m}[\ell]$	132
7.2.2.3	The ICI term $y_{m,ICI}[\ell]$	133
7.2.3	Performance estimation	134

7.2.3.1	Preliminary Analysis	134
7.2.3.2	Simulation results and calculation	136
7.3	OFDM system with pilot-aided feedforward loop	141
7.3.1	Modeling of OFDM link with PA-FFL	141
7.3.2	Analysis of OFDM link with PA-FFL	143
7.3.2.1	Preliminary Analysis	143
7.3.2.2	The modified noise term $\dot{y}_{m,n}[\ell]$	145
7.3.2.3	The modified useful-signal term $\dot{y}_{m,s}[\ell]$	147
7.3.2.4	The modified ICI term $\dot{y}_{m,ICI}[\ell]$	148
7.3.3	Effect of time-distorted SCL noise on an individual SC in PA-FFL ...	149
7.3.3.1	Long-term phase error	149
7.3.3.2	Analysis of spectral components of a pilot-SC in PA-FFL	152
7.3.3.2.1	BPF selection	152
7.3.3.2.2	Effect of Δ_N when only the white FN is in effect	153
7.3.3.2.3	Effect of CD when only the white FN is effective	154
7.3.3.2.4	Effect of CD when only the RIN is counted	155
7.3.3.2.5	PSD of a pilot-SC in PA-FFL when all parameters are counted	156
7.3.4	Analytical equations of OFDM link with PA-FFL	156
7.3.5	The modified colored noise variances estimation	158
7.3.5.1	The modified ICI variance	159
7.3.5.1.1	The modified ICI term in back-to-back setup for a special case	159
7.3.5.1.2	The modified ICI term when only the IN is ignored	160
7.3.5.1.3	The modified ICI term when only the IN is counted	164
7.3.5.2	Long-term phase error variance	166
7.3.5.3	Results discussion	167
7.3.6	Performance Analysis	167
7.3.6.1	The modified SNR_b equation	167
7.3.6.2	Optimal pilot-to-signal power ratio (PSPR)	168
7.3.6.3	BER estimation when all the color noise components are GRVs	169
7.3.7	Performance calculations	170
7.3.7.1	Calculation procedure	170
7.3.7.2	Calculation example	171
7.3.8	Linewidth tolerance	176
7.3.9	Optimal side pilot-tone insertion conditions	180
7.4	Conclusions	182

8	Design of an Optimal 100Gbps Homodyne CO-OFDM System	184
8.1	Introduction	184
8.2	Optimal 100Gbps homodyne CO-OFDM design	184
8.2.1	Preliminary design parameters	184
8.2.2	System Description	187
8.2.3	System Analysis	190
8.2.3.1	Frequency and phase analysis in the auxiliary circuit	190
8.2.3.2	Propagation delay condition	192
8.2.3.3	Polarization diversity analysis	193
8.2.3.3.1	Polarization diversity analysis of the main detection block	193
8.2.3.3.2	Polarization diversity analysis of the auxiliary circuit	194
8.2.3.4	Overall channel response estimation	195
8.2.3.5	Optimal operating conditions of the IQ optical modulators	196
8.2.3.5.1	Driver amplifiers' nonlinearity	196
8.2.3.5.2	Nonlinearity of the IQ optical modulator	198
8.2.3.5.3	Design calculation	199
8.2.3.5.4	Automatic bias control (ABC) design	200
8.2.4	Performance analysis and final design parameters	202
8.3	Comparison with other CO-OFDM proposals	206
8.4	Conclusions	208
9	Conclusions and Future Work	209
9.1	Conclusions	209
9.2	Future Work	211
	Appendices	212
Appendix-A	Derivation of Some Equations	212
Appendix-B	BER of Different M-QAM Mapping in Presence of Gaussian Phase Noise	224
Appendix-C	I/Q Imbalance Analysis and the Proposed Training Symbol	231
Appendix-D	Nonlinearity Effect due to the Driver Amplifiers and the IQ Optical Modulators	235
	Bibliography	245

Abbreviations

AA	Anti-Aliasing
ABC	Automatic Biasing Controller
ACF	Auto-Correlation Function
ADC	Analog to Digital Convertor
AFC	Automatic Frequency Controller
AGC	Automatic Gain Controller
AOM	Acoustic Optical Modulator
APC	Automatic Polarization Controller
APS	Automatic Phase shifter
ASE	Amplified Spontaneous Emission
AWGN	Additive White Gaussian Noise
BB	Baseband
BBS	Back-to-Back Setup
BC	Beam Combiner
BD	Balanced Detector
BER	Bit Error-Rate
BPF	Band-Pass Filter
BS	Beam Splitter
BW	Bandwidth
CD	Chromatic Dispersion
CFO	Carrier Frequency Offset
CO-OFDM	Coherent Optical OFDM
CP	Cyclic Prefix
CPE	Common Phase Error
DA	Driver Amplifier
DAB	European Digital Audio Broadcasting
DAC	Digital to Analog Convertor
DBM	Double-Balanced Mixer
DC	Direct Current (0Hz-frequency component)
DCF	Dispersion Compensation Fiber
DDO-OFDM	Direct-Detection Optical OFDM
DGD	Differential Group Delay
DS	Double-Sided
DSF	Dispersion Shifted Fiber
DSH	Delayed Self-Heterodyne Test
DSP	Digital Signal Processing
DVB	European Digital Video Broadcasting
ECL	External Cavity Laser
EDFA	Erbium-Doped Fiber Amplifier
FD	Frequency Domain
FDM	Frequency Division Multiplexing
FEC	Forward Error Correction

FFL	Feed-Forward Loop
<i>FFT</i>	Fast Fourier Transform
FIR	Finite Impulse Response
FN	Frequency Noise
FPGA	Field Programmable Gate Array
FrV	Frequency Vector
FWHM	Full Width Half Maximum
<i>FT</i>	Fourier Transform
GRV	Gaussian Random Variable
GVD	Group Velocity Dispersion
I/P	Input
ICI	Inter-Carrier Interference
IF	Intermediate Frequency
<i>IFFT</i>	Inverse Fast Fourier Transform
<i>IFT</i>	Inverse Fourier Transform
IMP	Inter-modulation Product
IN	Intensity Noise
IRF	Image-Rejection Filter
ISI	Inter-Symbol Interference
LF	Loop Filter
LO	Local Oscillator
LPF	Low-Pass Filter
LUT	Laser Under Test
MZM	Mach-Zehnder Intensity Modulator
NCG	Net Coding Gain
O/P	Output
OD	Optical Domain
OFDM	Orthogonal Frequency Division Multiplexing
OFS	Optical Frequency Shifter
OOK	On-Off keying
OPM	Optical Power Meter
OSA	Optical Spectrum Analyzer
OSNR	Optical Signal-to-Noise power ratio
PA-FFL	Pilot-Aided Feed-Forward Loop
PBC	Polarization Beam-Combiner
PBS	Polarization Beam-Splitter
PC	Polarization Controller
PD	Photo Diode
PDF	Probability Density Function
PLL	Phase-Locked Loop
PMD	Polarization Mode Dispersion
PMF	Polarization Maintaining Fiber
PMF	Polarization-Maintained Fiber
PN	Phase Noise
Pol-Mux	Polarization Multiplexing
PoM	Power Meter

PSPR	Pilot-to-Signal Power Ratio
PSPs	Principal States of Polarization
QAM	Quadrature Amplitude Modulation
QPSK	Quaternary Phase-Shift Keying
RBW	Resolution Bandwidth
RF	Radio Frequency
RIN	Relative Intensity Noise
RV	Random Variable
RX	Receiver
SA	Spectrum Analyzer
SC	Subcarrier
SCL	Semiconductor Laser
SCM	Single Carrier Modulation
SER	Symbol Error-Rate
SNR	Signal-to-Noise power ratio
SOP	State of Polarization
SS	Single-Sided
SSMF	Standard Single-Mode Fiber
TD	Time Domain
TF	Transfer Function
TIA	Trans-Impedance Amplifier
TiV	Time Vector
TrS	Training Symbol
TX	Transmitter
UWB	Ultra Wideband
VCO	Voltage-Controlled Oscillator
WDM	Wavelength Division Multiplexing
ZOH	Zero-Order Hold
bps	Bits-per-second
Sps	Samples-per-second

Chapter 1

Introduction

The continuous growth of internet traffic, cell phone services, and TV broadcasting is expected to reach an enormous value of more than 1000-Tbps (Tera bits per second) globally in the core optical networks by 2030 [1]. This increasing demand has imposed many technical challenges in front of telecommunication engineers, such as the limited bandwidth (**BW**) of the already installed optical fibers, power consumption of the developed systems, and cost. Several 100-Gbps (Giga bps) per wavelength systems have been proposed recently to meet this goal using the standard single-mode fiber (**SSMF**), which is the most deployed fiber type. In the ITU wavelength division multiplexing (**WDM**) grid, 50-GHz is allocated per channel, which requires high density modulation and/or polarization multiplexing (**Pol-Mux**) to be employed. However, the maximum reach becomes limited for a system with high density modulation due to the relatively large required optical signal-to-noise ratio **OSNR**, while the complexity is at least doubled when Pol-Mux is employed. On the other hand, the SSMF is highly dispersive at the lowest attenuation optical window (1.55- μm), which limits maximum distance in single carrier modulation (**SCM**) and the conventional ON-OFF keying (**OOK**), and dispersion compensation fibers (**DCF**) must be used periodically along the link [2].

One of the promising candidates that: can achieve 100-Gbps and beyond per wavelength, does not require DCF, and fulfills all the future design goals is optical orthogonal frequency division multiplexing (**OFDM**). The OFDM signal exhibits many advantages such as the low inter-symbol interference (**ISI**) due to the relatively long symbol duration, compact dense spectrum, and uses the cyclic prefix, which allows zero-ISI to be achieved [3]. Besides, channel response, I/Q imbalance, and polarization fluctuations can all be corrected using digital signal processing (**DSP**) [3]. However, some issues are still challenging such as: the semiconductor laser's (**SCL**)'s noise, the channel's and components' nonlinearity, and the availability of power-efficient high speed and high quantization resolution digital-to-analog convertors (**DAC**)s and analog-to-digital convertors (**ADC**)s. Many satisfactory results in the development and standardization of optical OFDM system have been published since 2005 by different research groups

around the world [4]-[7]. Although no standard optical OFDM has yet been adopted; however, 100-Gbps has been proven to be possible using both direct detection optical OFDM (**DDO-OFDM**) and coherent optical OFDM (**CO-OFDM**) [8]-[10]. Recently, another line of research that depends on optical implementation of the fast Fourier transform processor using photonic techniques is active [11]. However, the photonic technologies are not mature as radio frequency (**RF**) ones, and hence a practical all-optical OFDM system might not be standardized in the near future. In CO-OFDM, the laser's noise and particularly phase noise (**PN**) represents the main challenge, since it distorts orthogonality between the OFDM's overlapped subcarriers. One direct solution is to use highly stable narrow-linewidth lasers in the transmitter and receiver. However, such lasers are expensive and less reliable in long-term operation and harsh environment [12]. While cheap SCLs are reliable, and can efficiently be integrated with optical systems but at the expense of a relatively broad linewidth.

This work fills some gaps in the previous important works of optical OFDM in the literature and focus on the SCL's noise. The main effort is dedicated for an in-depth study of the effect of SCL noise on system's performance when pilot-aided feedforward loop (**PA-FFL**) is employed, and optimal homodyne CO-OFDM design when commercially available SCL is used. The adopted strategy in this study is by modeling, mathematical derivations and analysis, numerical calculations, real-time simulation, and design. The main author's contributions are:

- a derivation of exact SCL's field in the dispersive channel, which results an exact SCL's noise model in CO-OFDM, which can also be used for DDO-OFDM,
- an exact penalty estimation due to SCLs' noise with/without a PA-FFL technique,
- an accurate Simulink[®] functional model of a SCL, and
- an optimal 100-Gbps homodyne CO-OFDM design proposal with bandwidth efficiency (**BW_{eff}**) of more than 4-bps/Hz per polarization and up to 500-km assuming commercially available SCLs are used.

In this study, three major issues must be analyzed and cited adequately, which are: the OFDM system design (RF and optical), the SCL's noise and its interaction with the optical channel, and the FFL analysis and possible structures. This thesis is organized as follows. In **Chapter 2**, a general literature review and technical gaps in CO-OFDM

design is given. In **Chapter 3**, a review of optical channel characteristics and transfer function, baseband OFDM signal design, and performance of ideal CO-OFDM systems are given aiming to establish the necessary foundations for the next chapters. In **Chapter 4**, a review of SCL noise theory and measurement methods is presented taking the engineering point of view and the effective parameters into account. Based on the analyses and results of this chapter, modeling of a reliable and accurate functional model of SCLs can be achieved, and the exact dispersive field can be derived. In **Chapter 5**, a Simulink[®] model of SCL is constructed and validated depending on the analyses of Chapter 4, and reliable references in the literature. This model will be used in the simulation of different CO-OFDM structures and measurement setups. In **Chapter 6**, an exact analyses and derivations of SCL's field in the dispersive channel is conducted and examined for validity. A generalized expression of the beat-note power spectral density is obtained, which can be exploited in many applications such as the exact penalty estimation of CO-OFDM systems with PA-FFL, in DDO-OFDM, and in RF-over-Fiber. In **Chapter 7**, a performance analysis of CO-OFDM systems in the presence of relatively large SCLs' noise with/without PA-FFL is discussed. The conventional CO-OFDM without PA-FFL is examined first aiming to show the feasibility of using the PA-FFL block. Then the PA-FFL is introduced and discussed thoroughly aiming to determine the effective design parameters such as: optimal pilot-to-signal power ratio, optimal pilot's frequency index, and optimal compensation BW. Other parameters such as: the power distribution over OFDM's subcarriers, bit-error-rate over the OFDM's subcarriers, and the best practical compensation filter's prototype are also analyzed. In **Chapter 8**, a new 100-Gbps homodyne CO-OFDM system is introduced, analyzed, and discussed. The main advantage of this new design is that all the effective impairments and design difficulties such as: the SCLs noise, polarization diversity structure, driver amplifiers' specifications for the lowest nonlinearity, IQ optical modulators' nonlinearity and optimal driving powers, I/Q imbalance, channel response and synchronization are considered relying on the DSP as well as the analog circuitry. Besides, a new training symbol is introduced to facilitate extraction and equalization of the polarization diversity matrix, the I/Q imbalance matrix, and the channel response matrix in a single computation. In **Chapter 9**, conclusions and future work are discussed.

Chapter 2

CO-OFDM Systems: General Review

2.1 Introduction

In this chapter, a review of development of CO-OFDM systems is performed focusing on the recent challenging design problems. After a short historical review of optical communication systems, the following items are discussed next: semiconductor's (SCL)'s linewidth reduction techniques, the feedforward loop (FFL) technique for noise reduction and response equalization, and main CO-OFDM design constraints. Finally, a list of the main research gaps in CO-OFDM system design is given.

2.2 Background

2.2.1 Optical fiber communications

The use of optical fiber as a communication channel was first proposed in 1966 by C. Kao when he proved that the high attenuation in existing glass was due to impurities, which could be significantly removed [13]. The next important step was in 1970, when a successful development of fiber with loss of about 20-dB/km was published [14]. In the mid of 1970's, the first 45-Mbps ON/OFF keying link with repeater spacing of 10-km was successfully achieved. Manufacturing of the single-mode fiber allowed the development of an optical system with up to 1.7-Gbps, and 50-km repeater spacing at the 1.3- μm window in the late 1980s [14]. Third-generation optical systems operated at the lowest attenuation window (1.55 μm) with 0.2-dB/km and, by using dispersion-shifted fiber to overcome pulse spreading, 2.5-Gbps with 100-km repeater spacing became possible [14]. The fourth huge step forward was when the Erbium-doped fiber amplifier (EDFA) invented, which significantly reduces number of repeaters and made the wavelength division multiplexing (WDM) economic, which multiplies data capacity [14]. This new development in the early 1990's allowed fast growth of system capacity of up to 10Tbps by 2001. Recently, data-rates of 26Tbps over 50km [11], 32.5Tbps over 227km [15], 69.1Tbps over 240km [16], and 101.7Tbps over 165km [17] become possible using all-optical OFDM and WDM.

2.2.2 OFDM Systems

2.2.2.1 Radio frequency (RF) OFDM Systems

The birth of OFDM was in 1966 when R. Chang proposed theoretically a bandwidth-efficient frequency division multiplexing (**FDM**) method without inter-carrier interference (**ICI**) [18]. Five years later, a huge step in OFDM theory was achieved, when Weinstein and Elbert suggested to use fast Fourier transform (**FFT**) and its inverse (**IFFT**) to implement the BB OFDM link without need for the bulk elements (oscillators, filters, modulators, etc), which would highly simplifies the implementation [19]. The next breakthrough was in 1980, when the cyclic prefix (**CP**) is introduced which allows signals detection without introducing ISI, as well as facilitating symbol's timing and synchronization without causing any spectral spreading [20]. At that time, the digital signal processing (**DSP**) complex computations and DAC/ADC sampling frequency requirements were hard to fulfill, however, the adoption of OFDM in wireless applications was revived by the work of Cimini in 1985 [21]. The last, but not the least, important conceptual step was in 1997, when Schmidl and Cox introduced an efficient method for OFDM synchronization, channel estimation, and wideband I/Q imbalance estimation using a training symbol [22]. Apart from theory, the OFDM development in wideband communication has witnessed many achievements such as the European digital audio broadcasting (**DAB**) from 1987-1995, the European digital video broadcasting (**DVB**) since 1993, the European wireless local area network (**WLAN**) standard HiperLAN started since 1995, HiperLAN/2 was defined in 1999, the (Wi-Fi; IEEE 802.11 a/g) standard, asymmetric digital subscriber lines (**ADSL**; ITU G.992.1), and other standards and systems which are expected to merge in the near future [23]. Finally OFDM may even be standardized in the 4th generation (**4G**) wireless communication, and in the most of ultra wideband (**UWB**) communication systems [23].

2.2.2.2 Optical OFDM Systems

Optical and RF OFDM systems are similar in all of their blocks except the up/down convertors, which adapt the signal with the transmission channel. The large allocated bandwidth (**BW**) (50/100-GHz) per channel in the WDM grid, the two available orthogonal polarizations, and the free-of-interference, multi-path, and fading make the

optical channels very attractive domain to reach 100-Gbps and higher. Many proposals of direct-detection optical OFDM (**DDO-OFDM**) [4], [7], and coherent optical OFDM (**CO-OFDM**) [5], [6], have been simulated and experimentally tested. These efforts have yielded eventually some promising structures, and shown clearly the possibility of reaching 100-Gbps with reasonable complexity and cost [8]-[10]. Besides, several real-time experiments have been conducted since 2009 until recently focusing mainly on realization of the transmitter [24], [25], [26]. In DDO-OFDM proposals, one of the challenging problems is the signal \times signal term or the inter-modulation product (**IMP**), which occurs when the OFDM signal with an assistant pilot-tone is directly detected by a photo-diode (**PD**), or by a balanced-detector (**BD**) [27]. In the most practical DDO-OFDM proposal [28], a side carrier is combined with the single side-band (**SSB**)-modulated OFDM signal, and used to assist detection. Due to the IMP, a guard frequency band, which is equal (or slightly lower) the whole OFDM optical BW, must be introduced between the pilot-tone and one of the frequency edges of the OFDM signal. Besides, the pilot-tone's power should equal (or slightly lower) the OFDM signal power for optimal performance, which reduces both BW efficiency (**BW_{eff}**) and the bit-error-rate (**BER**) [28]. Furthermore, DDO-OFDM is more susceptible to channel nonlinearity, which limits maximum reach [29]. However, DDO-OFDM is more cost-effective and less affected (for short distances) by the SCL's phase noise (**PN**) than CO-OFDM. Although no standard DDO-OFDM or final design has yet been chosen, the detection process contains effective cross-noise terms that cannot be reduced without additional cost [30]. For instance, Lowery has proven that performance of the DDO-OFDM can be improved by about 2-dB, when the pilot-tone is extracted optically and amplified by 10-dB more than the OFDM signal [30]. Accordingly, the author expects that the DDO-OFDM can be developed for the future metropolitan area connections, since a simple, high-modulation density, and cost-effective design can be achieved efficiently. For instance, the simple setup presented by Schmidt *et al.* in their first experiment can be adopted for this purpose, when an externally inserted pilot-tone is used (which is used in their next experiments) [28], [8]. While CO-OFDM is indeed the future long-haul candidate since it can approach the ideal OFDM system performance with minimal aggregate penalties, and the transmission distance becomes only limited by the amplified

spontaneous-emission (**ASE**) noise limit; however, cost of the system increases considerably [9], [10]. More details of CO-OFDM will be discussed in the next sections.

2.3 SCLs' phase noise reduction techniques

Generally, SCL's PN can be reduced using the following techniques:

- By increasing the injection current to reduce the spontaneous emission noise [31]. In this technique, the IN decreases, relaxation oscillation frequency increases and its peak decreases, and no additional components are required. However, under high output optical power condition, the carrier density in the cavity becomes non-uniform which causes linewidth re-broadening [31]. Hence the laser can operate at the minimum-linewidth power and no further reduction in **PN** is possible.
- By developing SCL structures with higher threshold carrier density to reduce both the linewidth enhancement factor and population inversion factor, which are proportional to linewidth broadening such as in quantum well SCL. Linewidths of sub-MHz have been obtained using this method [1].
- By using an external cavity (low-loss optical resonator) to increase photon life-time, which significantly reduces PN. External-Cavity Lasers (**ECL**)s with linewidths in the tens of kHz range has become commercially available; however, the SCL becomes susceptible to mechanical vibrations which restrict its applications especially in harsh environments [1].
- By using RF/optical feedback and feedforward loops. In the these techniques, RF/optical frequency discriminator is used to extract the laser's FN, which is converted to electrical domain, and then back either to the laser's driving port or to an external optical modulator via a loop filter [32], [33]. An optical phase locked-loop (**OPLL**) can be used for flicker FN cancellation and drift correction due to the unavoidable optical propagation delay [32], [34], while the FFL is suitable for white FN reduction, and its performance is limited by time delay change due to temperature fluctuations, when it is implemented using analog circuitry [35]. Linewidths of tens of Hz has been experimentally achieved by this technique [1].

2.4 Feedforward loop (FFL)

The FFL technique is used in a broad range of applications in the RF and optical systems for noise compensation and response-equalization due to its wide-compensated BW and relative simplicity over other techniques [36], [37], [38], [39]. This technique was first employed in RF OFDM by Robertson and Kaiser to compensate the local oscillator's (LO)'s PN using DSP computations [40]. It was used first in CO-OFDM by Jansen *et al.* to mitigate the SCLs' PN before the \mathcal{FFT} is applied in the receiver (RX) [6]. Their results showed that effect of the SCL's PN can be effectively reduced using this technique; however, a high DSP complexity was required in the implementation [6]. Besides, filter's group delay (GD) equalization, and the differential time-delay between the pilot-tone and the modulated-subcarriers (SC)s are not considered in their work. In DDO-OFDM, FFL is indirectly employed, since the carrier, which is essential in the detection process and acts as a reference phase phasor, is mixed with signal [28]. It is employed in this thesis for phase noise (PN) compensation, which significantly improve the CO-OFDM performance when commercial SCL is used.

Many distinct features can be observed when the FFL is used for SCLs' PN compensation in optical systems such as:

- An uneven **BER** distribution over the SCs, which is first noticed by Schmidt *et al.* [28], while Peng has demonstrated this effect in more details by introducing the chromatic dispersion's differential delay, and both works are in DDO-OFDM [41]. A similar effect occurs in single-carrier modulation (SCM), where maximum allowable SCLs' linewidth depends on the signal's BW or data-rate and the distance [42].
- Gaussian frequency noise (FN) remains Gaussian FN when the FFL is used [38].
- Phase noise to intensity noise (PN-to-IN) phenomenon, which occurs when the SCL's field in optical domain or its corresponding beat-note signal in RF/electrical domain experiences either a bandpass filtering [43], [44], or a time-delay distortion [45]-[47].

An exact model of the CO-OFDM system when the FFL is employed is required to yield the exact penalty estimation, which is one of the aims of this thesis.

2.5 CO-OFDM design considerations

Proposals for ultra-high speed (100-Gbps and higher) CO-OFDM systems must take into account some design considerations such as:

1. The RF BW of the modulating signal and the detected signal should not be larger than the operating BW of the commercially available optical and RF components (amplifiers, mixers, modulators, detectors, etc). This requires the designer to adopt one or more of the following solutions:
 - Use of high-density-modulation (high constellation levels) to increase number of bits per symbol (m). Usually M-QAM is employed since it results the optimal performance in additive-white-Gaussian-noise (AWGN) channel compared to other constellation schemes [48]. However, maximum reach for a given BER declines as m increases in a system dominated by the ASE noise [49].
 - Use of frequency division multiplexing (FDM) and/or Pol-Mux [1].
 - Use of homodyne detection which occupies only half the minimal required RF BW of heterodyne detection [50]. However, the complexity and cost increase considerably since a special optical structure is required [1].
2. The state-of-polarization (SOP) of the receiver's LO SCL (RX-LO-SCL) and the received signal must be aligned to obtain the highest mixing power. Many solutions are available such as:
 - Use of automatic polarization controller (APC) [1], which aligns SOP of the RX-LO-SCL with the received signal according to an algorithm, which depends on the detected power [1]. However, the APC is usually a bulky device that cannot be easily integrated with the system. Besides, in a long-haul OFDM link with an ultra-wideband (UWB) signal, the polarization mode dispersion (PMD) is a challenging issue since the SOP is not the same for all spectral components, and hence the APC becomes less efficient.
 - Use of a polarization diversity structure which ensures steady mixing level between the RX-LO-SCL and the received signal at the expense of doubling the complexity and cost [1], [51], [52]. However, the polarization matrix (Jones matrix) must be estimated continuously to equalize the PMD, which is usually accomplished by DSP.

3. SCL's PN, since the high stability laser is expensive and might not be reliable in the harsh environments [12]. Some of PN reduction techniques are listed in Section 2.4.
4. The DAC at the transmitter (**TX**) and the ADC at RX, have limited sampling rate (F_s) and effective number of quantization bits per sample (q_b). The only solution here is by partitioning the input (**I/P**) data-rate into many subchannels, such that each subchannel is set to have an OFDM's baseband (**BB**) BW lower than maximum F_s of the DAC or lower than the Nyquist rate, and then the FDM and/or Pol-Mux can be employed next. However, as higher m is, as higher the required q_b , and hence low level constellation is more efficiently sampled for a limited value of q_b [53].
5. Reasonable cost is expected. The efficient design should contain the minimal number of optical components, since the opto-electronic components are expensive and less flexible than the RF components. However, RF components in millimeter-wave bands are not cheap, and hence RF BW higher than 10GHz should be avoided [5].
6. Avoiding critical and sensitive components. Opto-electronic devices are usually susceptible to environmental fluctuations and hence continuous adjustments are required, especially in the IQ modulators.
7. Depending on software-based DSP rather than optical hardware. The beauty of OFDM is clearly shown in this point, because software is easily modified; however, due to the limited F_s and q_b , analog components are still required.
8. Some other practical considerations must also be considered such as the SCL's frequency drift, I/Q imbalance in the TX and RX, drivers amplifiers' nonlinearity, IQ optical modulator's nonlinearity, and components' frequency responses.

Hence, a realistic design is one which fulfills all the design considerations with the available technologies. However, not all the listed design considerations can be completely met, and a trade-off is essential provided that the received signal's envelope is maintained at a specific level without nulls. Therefore, more practical designs are required to be developed since the proposed systems in the literature cannot completely fulfill all the challenging points. Hence a new homodyne CO-OFDM design is presented in this study, which adopts pilot-aided FFL (PA-FFL) technique for SCLs' PN reduction, and takes all the aforementioned design considerations into account.

Chapter 3

Main Considerations and Components in CO-OFDM Design

3.1 Introduction

This chapter is dedicated to discuss main design considerations and components in CO-OFDM link focusing on the optical channel, OFDM system design, and coherent regime. The necessary design foundations that will be used in Chapter 8 are established here. The main goals of this chapter are to:

1. state the exact transfer function (TF) of optical channel,
2. obtain an optimal design of OFDM signal in optical channel,
3. investigate realization of CO-OFDM link, and
4. analyze the performance of a CO-OFDM system in an ideal case.

3.2 Optical channel

3.2.1 Types of single-mode optical fibers

There are many types of single-mode fibers used in optical telecommunication; some were characterized by the International Telecommunications Union (ITU), and some have not been characterized yet.

1- Standard single-mode fiber (SSMF)

This is the most widely deployed and supported fiber category in the world today. It is under ITU-T G.652 standard with the following key specifications [54]:

Cutoff wavelength 1260nm, maximum attenuation less than 0.4dB/km at wavelength (λ_0) of 1310nm, and less than 0.35dB/km at 1550nm, chromatic dispersion coefficient (\mathbf{D}) at $\lambda_0 = 1550\text{nm}$, less than 20ps/nm/km, and $\mathbf{D} \leq 3.5\text{ps/nm/km}$ in the optical window [1285-1330]nm, and maximum polarization mode dispersion coefficient less than 0.5ps/ $\sqrt{\text{km}}$. Typical values at $\lambda_0 = 1550\text{nm}$ are; attenuation 0.2dB/km, $\mathbf{D} = 17\text{ps/nm/km}$, and maximum polarization mode dispersion coefficient 0.2ps/ $\sqrt{\text{km}}$.

2- Dispersion shifted fiber (DSF)

This fiber is designed to reduce the chromatic dispersion at the 1550nm window with $\mathbf{D} \approx 0$ at [1525-1575]nm following the ITU-T G.653 standard with recommended \mathbf{D} of

less than 3.5ps/nm/km [54]. However, it has many drawbacks, such as higher polarization mode dispersion than SSMF, and a high nonlinearity coefficient making it less useful especially in the wavelength division multiplexing (**WDM**) [54].

3- Non-zero dispersion shifted fiber (NZDSF)

This fiber category is designed to compromise between low dispersion and low nonlinearity and following the ITU-T G.655 standard. However, the cutoff wavelength is around 1310nm, which limits the application of such category [54].

4- Dispersion compensating fiber (DCF)

This fiber category is designed with high negative **D** to equalize the dispersion effect in the SSMF at regular intervals using relatively short length per interval.

5- Polarization maintaining fiber (PMF)

This fiber category is designed to maintain linear polarization even when external stresses are applied. The most popular type is the PANDA fiber which has a compatible aperture to that of SSMF, and hence minimum splice loss is ensured [54].

3.2.2 Optical link power analysis

The long-haul optical link shown in Fig. 3.1 consists of many spans each with an in-line optical amplifier to compensate fiber attenuation. The link budget calculation depends on optical amplifiers specifications, fiber loss, other losses and total distance.

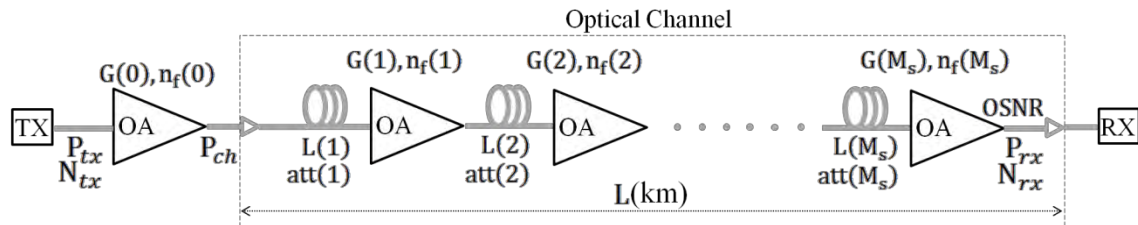


Fig. 3.1: Long-haul optical link consisting of M_s spans. Where L is the total distance of the link, $L(i)$, $\text{att}(i)$, $G(i)$, and $n_f(i)$ are fiber's length, fiber's attenuation, amplifier's gain and noise figure of the i -th span respectively. Note that neither WDM multiplexer / demultiplexer are shown nor the other transmitters and receivers, focusing only on single channel transmission. **RX** is the receiver, and **TX** is the transmitter.

3.2.2.1 Optical amplifier

An optical amplifier amplifies the optical signal directly without converting it into an electrical signal and usually without pre-knowledge of the signal's modulation or multiplexing. An important advantage of using optical amplifiers is that when the gain of

one of the amplifiers reduces in the link, the signal flow does not stop, which provides a significant level of system resilience [55]. From the many available types of optical amplifiers, the Erbium-doped fiber amplifier (**EDFA**) is the most attractive one for the following reasons [55]:

- Low distortion (the EDFA is highly linear device since it saturates very slowly due to its very long time constant)
- Low noise ($3\text{dB} \leq \mathbf{n}_F \leq 7\text{dB}$)
- Significantly lower cost than repeater
- Minimal polarization sensitivity
- Reliable (Very long time before failure)
- Very high gain (30dB)
- High output power (30dBm)
- Very broad bandwidth
- Low insertion loss.

The first advantage is particularly important in optical OFDM systems since linear amplification is essential to avoid inter-modulation distortion between the wavelength division multiplexing (**WDM**) channels [23]. Besides, when the EDFA is saturated, only its gain is reduced and no cross-talk occurs, which is exploited to run it at saturation in long-haul transmission for optimum design [55]. The optical amplifier is characterized by its power gain (**G**), noise figure (\mathbf{n}_F), output (**O/P**) power, saturated O/P power, saturated input (**I/P**) power, gain at saturated power, and other parameters [55]. However, only small signal gain is considered here, since the launch power per OFDM channel is already lower than that of the single-carrier counterpart [56]. The \mathbf{n}_F is measured based on shot noise quantum limit of a photo diode (**PD**), by measuring the electrical signal-to-noise ratio (**SNR**) at amplifier's I/P, and amplifier's O/P [57]. Thus the \mathbf{n}_F is defined as

$$\mathbf{n}_F \approx \frac{\text{SNR}_{\text{I/P}}}{\text{SNR}_{\text{O/P}}} = 2n_{sp} \frac{G-1}{G} \geq 2 \quad (3.1)$$

where n_{sp} is the spontaneous emission factor of optical amplifier. Typical values are $2 \leq \mathbf{n}_F \leq 5$ corresponding to $3\text{dB} \leq \mathbf{n}_F \leq 7\text{dB}$. Besides, the generated amplified spontaneous emission (**ASE**) noise is expressed by its double-sided (**DS**) PSD as [57]

$$\mathbf{S}_{\text{ASE}}(\mathbf{v}) = h\nu_0 \cdot (G-1) \cdot \mathbf{n}_F \quad (3.2)$$

where h is Plank's constant ($\approx 6.626 \times 10^{-34}$ W·s/Hz), ν_0 is the optical frequency ($\approx 193.5\text{THz}$). Note that the ASE noise is unpolarized white complex noise, and hence it

has a flat power spectral density (**PSD**), and half of this noise can be removed when tight polarization control is employed.

3.2.2.2 Optical signal-to-noise ratio (**OSNR**)

The received **OSNR** is an important figure of estimating the performance of any optical communication system, since it is related to the average **SNR** per bit (**SNR_b**) at the RX provided that exact definition of **OSNR** is used. The **OSNR** is defined as [55]

$$\text{OSNR} = \frac{P_{rx}|_{B_g}}{N_{rx}|_{B_{ref}}} \quad (3.3)$$

The definition in (3.3) states that, **OSNR** is the ratio of the received modulated-signal power per channel (**P_{rx}**) encompassed by the WDM filter with a bandwidth (**B_g**) defined by the optical grid frequency allocation (e.g. 50GHz), to the received accumulated ASE noise power (**N_{rx}**) measured by an optical spectrum analyzer (**OSA**) with resolution bandwidth (**RBW**) of (**B_{ref}**) (0.1nm or 12.5GHz at 1.55μm). The confusion occurs when the signal itself consists of a multiplexing of more than one subchannel and especially when pilot signal is used. The simplest technique of calculating the **OSNR** by definition is by measuring the overall received power per channel using optical power meter (**OPM**), and interpolating the measured noise floor of service channels (channels that are not occupied in the grid) separately using OSA with RBW of 0.1nm, or an OPM with a tuned filter [58]. This procedure can be summarized as

Measuring total optical power within B_g bandwidth (BW)	$P_{tot} _{B_g} = P_{rx} _{B_g} + N_{rx} _{B_g}$	(3.4-a)
---	--	---------

Measuring (interpolating) noise floor of service channel(s) within B_{ref} BW	$N_{rx} _{B_{ref}}$	(3.4-b)
--	---------------------	---------

Calculate OSNR by dividing (3.4-a) by (3.4-b)	$\text{OSNR} = \frac{P_{tot} _{B_g}}{N_{rx} _{B_{ref}}} - \frac{B_g}{B_{ref}}$	(3.4-c)
--	--	---------

3.2.2.3 Optical link budget

Referring to Fig. 3.1 and from the aforementioned discussion assuming only SSMF is used, then **P_{rx}|_{B_g}** and **N_{rx}|_{B_{ref}}** are expressed as

$$P_{rx}|_{B_g} = P_{ch} \cdot \left\{ \frac{G(1)G(2)G(3) \cdots G(M_s)}{\text{att}(1)\text{att}(2)\text{att}(3) \cdots \text{att}(M_s)} \right\} \quad (3.5-a)$$

$$\begin{aligned} N_{rx}|_{B_{ref}} \approx & \left\{ N_{tx}|_{B_{ref}} G(0) + h\nu_0 B_{ref} n_F(0) \{G(0) - 1\} \right\} \\ & \cdot \left(\frac{G(1)G(2)G(3) \cdots G(M_s)}{\text{att}(1)\text{att}(2)\text{att}(3) \cdots \text{att}(M_s)} \right) + h\nu_0 B_{ref} \\ & \cdot \left\{ n_F(1) \{G(1) - 1\} \cdot \left(\frac{G(2)G(3) \cdots G(M_s)}{\text{att}(2)\text{att}(3) \cdots \text{att}(M_s)} \right) \right. \\ & + n_F(2) \{G(2) - 1\} \cdot \left(\frac{G(3) \cdots G(M_s)}{\text{att}(3) \cdots \text{att}(M_s)} \right) + \cdots \\ & \left. \cdot + n_F(M_s) \{G(M_s) - 1\} \right\} \end{aligned} \quad (3.5-b)$$

where $\mathbf{P}_{ch} = G(0) \cdot P_{tx}|_{B_g}$ is launch power per channel, $\mathbf{N}_{tx}|_{B_{ref}}$ is due to the laser's intensity noise (**IN**), optical modulator nonlinearity, and other factors which can be ignored here and calculated as external penalties. The attenuation of the **i-th** span is calculated in linear scale and in decibels as follows [55]

$$\text{att}(i) = \exp(\alpha_f \cdot L(i)) \cdot \zeta_s \quad (3.6-a)$$

$$\text{att}(i)_{\text{dB}} = \widetilde{\alpha}_F \cdot L(i) + \alpha_S \cdot N_{splice} + \alpha_C \cdot N_{con} + \widetilde{\zeta}_s \quad (3.6-b)$$

where $\exp(\)$ is the exponential function, α_f is fiber's attenuation coefficient (0.046Nepers/km for SSMF), $L(i)$ is length of the **i-th** span in (km), ζ_s is total installation loss in linear scale of the **i-th** span, $\widetilde{\alpha}_F$ is fiber's attenuation coefficient in (dB) (0.2dB/km for SSMF), α_S in (dB) is average loss per splice, \mathbf{N}_{splice} is the total number of splices in the **i-th** span, α_C in (dB) is average loss per connector, \mathbf{N}_{con} is the total number of connectors in the **i-th** span, and $\widetilde{\zeta}_s$ in (dB) is additional expected loss due to bending and other factors. In practice, all amplifiers and spans are designed to be identical; besides, the amplifier's gain is chosen just to compensate fiber loss in every span. Thus, $\mathbf{G}(\mathbf{0}) = G(1) = G(2) = \cdots = G(M_s) = \mathbf{G}$, $\mathbf{n}_F(\mathbf{0}) = n_F(1) = n_F(2) = \cdots = n_F(M_s) = \mathbf{n}_F$, $\mathbf{att}(\mathbf{1}) = \text{att}(2) = \cdots = \text{att}(M_s) = \mathbf{att}$, $\mathbf{L}(i) = L_\ell$, and $\mathbf{G} \approx \text{att}$. In this case (3.5) becomes

$$P_{rx}|_{B_g} = P_{ch} \quad (3.6-a)$$

$$N_{rx}|_{B_{ref}} \approx h\nu_0 B_{ref} \cdot n_F \cdot (G - 1) \cdot (M_s + 1) \quad (3.6-b)$$

Although (3.6) might not reflect the exact practical situation, it is however, a useful generalization for the first step of link budget calculation. Thus the **OSNR** becomes

$$\text{OSNR}_{\text{dB}} \approx 58 + P_{ch,\text{dBm}} - n_{F,\text{dB}} - 10 \cdot \log(G - 1) - 10 \cdot \log(M_s + 1) \quad (3.7)$$

where $\log(\)$ is the base-10 logarithm. Note that (3.7) is a design equation, however, the effect of **G**, **L_ℓ**, and **M_s** in the **OSNR** calculation is tackled by reconsidering (3.6) as

$$\text{OSNR} \approx K \cdot \left\{ \frac{P_{ch}}{(L/L_\ell + 1) \cdot (\exp(\alpha_f L_\ell) \cdot \zeta_s - 1)} \right\} \quad (3.8)$$

where $K = 1/(h\nu_0 B_{ref} n_F)$, which is assumed to be constant, $G \approx \text{att}$, and $M_s = L/L_\ell$ are used in (3.8) derivation. The term between brackets in (3.8) is calculated versus **L_ℓ** as shown in Fig. 3.2, assuming $P_{ch} = 0\text{dBm}$, $n_{F,\text{dB}} = 6\text{dB}$, $L = [300, 1000, 3000, 10000]$ km, and all splices and connectors loss are ignored ($\zeta_s = 1$). Note that in Fig. 3.2, increasing $P_{ch,\text{dBm}}$, and decreasing $n_{F,\text{dB}}$ results linear increase in **OSNR_{dB}**. Therefore for a given **L**, the **OSNR** can be practically increased either by increasing P_{ch} or decreasing **L_ℓ**. However, as P_{ch} increases, the penalty due to fiber's nonlinearity increases also, and hence there is some optimal P_{ch} that should be chosen, which depends on the modulation/multiplexing scheme [56]. Besides, as number of optical amplifiers increase (by decreasing **L_ℓ**) the cost significantly increases, and hence the typical value of **L_ℓ** is between 50km to 100km [55].

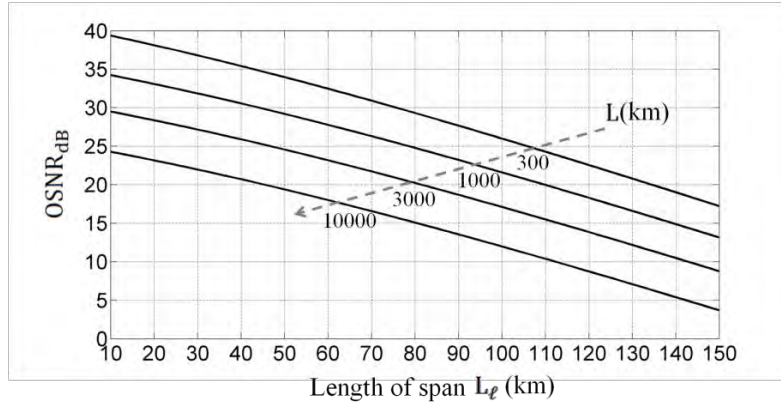


Fig. 3.2: **OSNR** versus span length for different reaches. Here all optical amplifiers and spans are identical with $P_{ch} = 0\text{dBm}$, $n_{F,\text{dB}} = 6\text{dB}$, **G** value equals span loss, and all other installation losses are ignored.

3.2.3 Optical channel response

The optical channel exhibits a number of linear and nonlinear impairments that distort not only the modulated-signal, but the spectral components of the optical carriers itself. The

linear impairments such as channel response, optical and radio frequency (**RF**) components response, and optical sources' noise will be discussed next. The nonlinear impairments such as four-wave mixing (**FWM**), self-phase modulation (**SPM**), and cross-phase modulation (**XPM**) can be mitigated using many pre-detection or post-detection techniques, or simply by reducing P_{ch} [59], [60]. However, most of these techniques require high speed digital signal processing (**DSP**), which imposes off-line (computer based and not a real-time calculations) treatments due to the lack of commercially available, low power, and high speed digital-to-analog (**DAC**), and analog-to-digital (**ADC**) convertors with an adequate resolution. On the other hand, by reducing P_{ch} , then L is also reduced, however, long reach is one of the goals of long-haul transmission. Thus the simplest choice is by calculating the optimal P_{ch} and adding a suitable power margin. As mentioned before, the nonlinear response of optical channel is not considered in this work, and hence it will be omitted from now on.

3.2.3.1 Chromatic dispersion (CD)

CD is a temporal distortion that causes different arrival times of frequency components of the modulated-signal [55]. This distortion gained importance in early systems due to pulse spreading in the conventional on-off keying (**OOK**), which limits high speed transmission due to the induced inter-symbol interference (**ISI**). The OOK and double-side-band (**DSB**) single-carrier modulation (**SCM**) are severely impaired by CD, and the transmission distance becomes limited [3]. Channel response due to the CD is [55]

$$H_{CD}(f, L) = \exp(-j\pi f^2 \beta_D(L)) \quad (3.9-b)$$

where $\{f = \nu - \nu_0\}$ is the baseband (**BB**) frequency or frequency with respect to optical carrier, $\beta_D(L)$ in (s/Hz) is the group velocity delay (**GVD**) as a function with total distance, and L is in (km). Note that (3.9) is applied with respect to the optical carrier and to whatever chosen state-of-polarization (**SOP**) at RX. Here f is related to $\Delta\lambda$ as,

$f = c/\lambda_0 - c/(\lambda_0 + \Delta\lambda) \approx c\Delta\lambda/\lambda_0^2$, or $\Delta\lambda \approx f \cdot \lambda_0^2/c$, and for the 1.55 μm window ($\lambda_0 = 1.55 \times 10^{-6}$ m), then $\Delta\lambda \approx 8 \times 10^{-12}f$ (nm), where c is the light speed (3×10^8 m/s).

Therefore $\beta_D(L)$ is calculated as

$$\beta_D(L) \approx D \cdot (\lambda_0^2/c) \cdot L \cdot 10^{-15} \quad \begin{array}{l} \text{(s/Hz), where } \mathbf{D} \text{ is substituted in} \\ \text{(ps/nm/km), } \lambda_0 \text{ in } (\mu\text{m}), \text{ and } \mathbf{c} \text{ in (m/s).} \end{array} \quad (3.10-a)$$

$$\beta_D(L) \approx (1.4 \times 10^{-22}) \cdot L \quad (\text{s/Hz}) \text{ for } \{\lambda_0 = 1.55\mu\text{m}, \mathbf{D} = 17.5\text{ps/nm/km}\}. \quad (3.10\text{-b})$$

Here $\beta_D(L) = 2\pi \cdot \beta_z \cdot L$, where β_z is the common definition of the GVD [45].

3.2.3.2 Polarization mode dispersion (PMD)

PMD is a time-varying random process that can only be considered as stochastic process for short lengths of fiber, and hence it cannot be predicted in general [61]. This phenomenon occurs due to core eccentricity or the imperfection in core's circular shape. Many factors enhance this effect such as manufacturing accuracy, mechanical vibrations and stresses, bends, and installation environment. Theoretically the SSMF is a cylindrical wave guide that passes only single transverse mode with two possible orthogonal polarizations, and rejects all other modes. A slight imperfection in the circular shape (fiber birefringence) changes the propagation velocity of the two orthogonal polarizations and results a slight differential time-delay between them [61]. This phenomenon can be examined either in time domain (**TD**), or in frequency domain (**FD**). In TD, PMD is characterized by measuring the differential group delay (**DGD**) between the two polarization eigenstates or the principal states of polarization (**PSPs**), which are SOP with maximum and minimum propagation time of a transmitted pulse [62]. The DGD is a random process that usually fits a Maxwellian distribution; however, it is not always the case, since uncertainty may occur depending on the link complexity and measurement accuracy [63]. The mean DGD is defined as

$$\overline{\tau_{\text{DGD}}}(L) = \tau_{\text{PMD}} \cdot \sqrt{L} \quad (3.11)$$

where τ_{PMD} is the PMD coefficient in (ps/ $\sqrt{\text{km}}$). However, Maxwellian probability density function (**PDF**) has high peak-to-average ratio (**PAR**), and hence a margin has to be introduced in the system design [63]. While in FD, PMD causes polarization rotation on the Poincaré sphere, which is proportional to the frequency separation between the highest and lowest frequencies in the band [64]. Based on Poole and Wagner's important study, the SOP of an optical signal is maintained over the fiber if the launch SOP is linear and identical to one of the PSPs; otherwise the launch SOP is resolved into the two PSPs and the received SOP is generally elliptical [61]. However, due to the time-variant statistical nature of this phenomenon, the PSPs can have any SOP at a specific time slot.

We will translate this into a mathematical model as follows. The TX has its own reference SOP identified by a polarization beam-splitter (**PBS**) and/or a polarization beam-combiner (**PBC**) SOPs given by \vec{x} , and \vec{y} , while at a specific time slot, the PSPs are denoted at TX as \vec{u}_{st} , and \vec{u}_{ft} and at RX as \vec{u}_{sr} , and \vec{u}_{fr} as shown in Fig. 3.3a. Where “s” stands for “slow”, and “f” stands for “fast”.

If the TX optical signal is aligned with \vec{x} , then the launched field is expressed as:

$\vec{E}_{t1}(\mathbf{t}) = V_{t1}(\mathbf{t})\vec{x}$, which can be resolved with respect to $[\vec{u}_{st}, \vec{u}_{ft}]$ and yields

$\vec{E}_{t1}(\mathbf{t}) = V_{t1}(\mathbf{t}) \cdot \cos(\theta_i)\vec{u}_{st} + V_{t1}(\mathbf{t}) \cdot \sin(\theta_i)\vec{u}_{ft}$, and arrived at RX as

$\vec{E}_{r1}(\mathbf{t}) = V_{rs1}(\mathbf{t} - \Delta\tau/2) \cdot \cos(\theta_i)\vec{u}_{sr} + V_{rf1}(\mathbf{t} + \Delta\tau/2) \cdot \sin(\theta_i)\vec{u}_{fr}$.

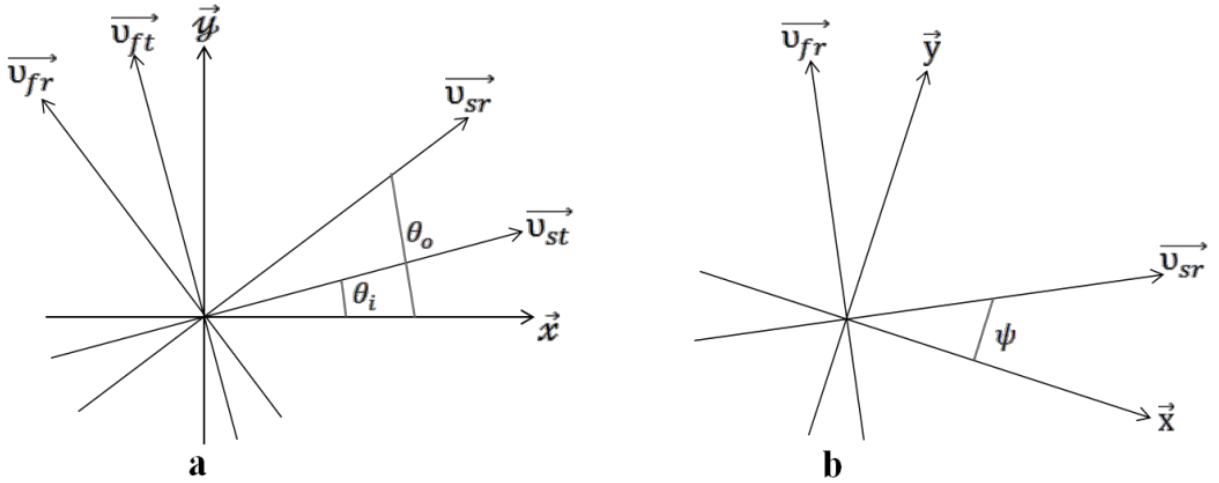


Fig. 3.3: PSPs at a specific time-slot with respect to TX references in (a), and with respect to RX references in (b). Here $[\vec{x}, \vec{y}]$ is PBS/C reference SOP vector at TX, and $[\vec{x}, \vec{y}]$ is at RX.

Where $V_{t1}(\mathbf{t})$ is the modulated-signal (real or complex), $\Delta\tau$ is $\tau_{\text{DGD}}(\mathbf{L})$ at a specific time-slot, $V_{rs1}(\mathbf{t})$, and $V_{rf1}(\mathbf{t})$ are the received modulated-signal components along the slow and fast PSPs respectively. Note that in practice, the mean value of DGD $\overline{\tau_{\text{DGD}}}(\mathbf{L})$ is used rather than $\tau_{\text{DGD}}(\mathbf{L})$ since it is consistent and countable. It is less feasible to write the received field with respect to TX reference vector $[\vec{x}, \vec{y}]$ because of the unpredictable nature of polarization fluctuation; however, it is required from channel modeling point of view. First let $V_{rs1}(\mathbf{t}) = \alpha_s V_{r1}(\mathbf{t})$, and $V_{rf1}(\mathbf{t}) = \alpha_f V_{r1}(\mathbf{t})$, where α_s , and α_f are the net linear loss/gain correspond to the slow and fast PSP respectively. Referring to Fig. 3.3a, the received field can be written as

$$\begin{aligned} \vec{\mathbf{E}}_{r1}(\mathbf{t}) = & \left\{ \alpha_s V_{r1}(t - \Delta\tau/2) \cdot \cos(\theta_i) \cdot \cos(\theta_o) - \alpha_f V_{r1}(t + \Delta\tau/2) \cdot \sin(\theta_i) \cdot \sin(\theta_o) \right\} \vec{\mathbf{x}} \\ & + \left\{ \alpha_s V_{r1}(t - \Delta\tau/2) \cdot \cos(\theta_i) \cdot \sin(\theta_o) + \alpha_f V_{r1}(t + \Delta\tau/2) \cdot \sin(\theta_i) \cdot \cos(\theta_o) \right\} \vec{\mathbf{y}} \end{aligned}$$

Note that $\vec{\mathbf{E}}_{t1}(\mathbf{t})$ is assumed to be aligned with $\vec{\mathbf{x}}$, however, it can be at any SOP, thus the generalized impulse response of the channel due to SOP fluctuations is expressed as

$$\begin{aligned} \mathbf{M}(\mathbf{f}, \mathbf{L})|_{[\vec{\mathbf{x}}, \vec{\mathbf{y}}]} \\ = \begin{bmatrix} \cos(\theta_i) & -\sin(\theta_i) \\ \sin(\theta_i) & \cos(\theta_i) \end{bmatrix} \begin{bmatrix} e^{-j\omega\tau_{\text{DGD}}(\mathbf{L})/2} & 0 \\ 0 & e^{j\omega\tau_{\text{DGD}}(\mathbf{L})/2} \end{bmatrix} \begin{bmatrix} \cos(\theta_o) & \sin(\theta_o) \\ -\sin(\theta_o) & \cos(\theta_o) \end{bmatrix} \end{aligned} \quad (3.12)$$

where $\mathbf{M}(\mathbf{f}, \mathbf{L})|_{[\vec{\mathbf{x}}, \vec{\mathbf{y}}]}$ is Jones matrix with respect to TX reference SOP $[\vec{\mathbf{x}}, \vec{\mathbf{y}}]$, and $\omega = 2\pi f$. Note that θ_i , and θ_o are assumed to be constants for a short observation time (\mathbf{T}_{OBS}). $\mathbf{M}(\mathbf{f}, \mathbf{L})|_{[\vec{\mathbf{x}}, \vec{\mathbf{y}}]}$ is not useful in practice since $[\vec{\mathbf{x}}, \vec{\mathbf{y}}]$ cannot be exactly determined to the RX (there is universal polarization), and the RX itself might have its own reference SOP vector $[\vec{\mathbf{x}}, \vec{\mathbf{y}}]$. Therefore it is more feasible to refer to Fig. 3.3b when polarization diversity structure is the issue, where the description is with respect to RX's reference SOP vector $[\vec{\mathbf{x}}, \vec{\mathbf{y}}]$.

3.2.3.3 Overall optical channel response

We can express the overall impulse response of the optical channel with respect to the TX's reference SOP vector $[\vec{\mathbf{x}}, \vec{\mathbf{y}}]$, by using (3.9b), and (3.12), however, the mean propagation delay \mathbf{T}_o , and an arbitrary phase ϕ_o might also be introduced. Accordingly, in relatively short \mathbf{T}_{OBS} , the overall channel response is given by

$$\mathbf{H}_{ch}(\mathbf{f}, \mathbf{L})|_{[\vec{\mathbf{x}}, \vec{\mathbf{y}}]} = \mathbf{M}(\mathbf{f}, \mathbf{L})|_{[\vec{\mathbf{x}}, \vec{\mathbf{y}}]} \cdot \mathbf{H}_{CD}(\mathbf{f}, \mathbf{L}) \cdot \exp(j\phi_o - j\omega\mathbf{T}_o) \quad (3.13)$$

3.3 OFDM system

3.3.1 Continuous baseband model of OFDM link

The ideal continuous model of BB OFDM system is shown in Fig. 3.4, which can be described as follows.

1. The TX consists of summation of \mathbf{N} frequency-separated and independently-modulated subcarriers (SC)s. Each SC has its own frequency index $\mathbf{k} \in [1, 2, \dots, \mathbf{N}]$, where the frequency separation between the SCs is an integer-multiple of the symbol-rate per

SC. Besides, each I/P symbol is mapped using complex mapping scheme such as M-QAM modulation, which results in optimum performance in a Gaussian noise channel, and is defined by $\mathbf{M} = 2^m$ [48], where \mathbf{M} is total number of constellation points, and m is number of the In-phase or quadrature-of-phase levels (I or Q levels). Therefore the I/P vector is $\mathbf{X}_\ell = [x_{1,\ell}, x_{2,\ell}, \dots, x_{k,\ell}, \dots, x_{N,\ell}]^T$, which is a complex vector that changes in every symbol's time period (T_s), with symbol's index identified by ℓ , where $\ell \in [0, 1, \dots, \infty]$.

2. The channel is assumed here as an additive-white-Gaussian-noise (AWGN) channel.
3. The transmitter consists of N correlation-detection branches with different down-conversion frequencies. These frequencies are the complex-conjugates of the TX ones. The O/P complex vector is $\mathbf{Y}_\ell = [y_{1,\ell}, y_{2,\ell}, \dots, y_{k,\ell}, \dots, y_{N,\ell}]^T$, which also changes periodically.

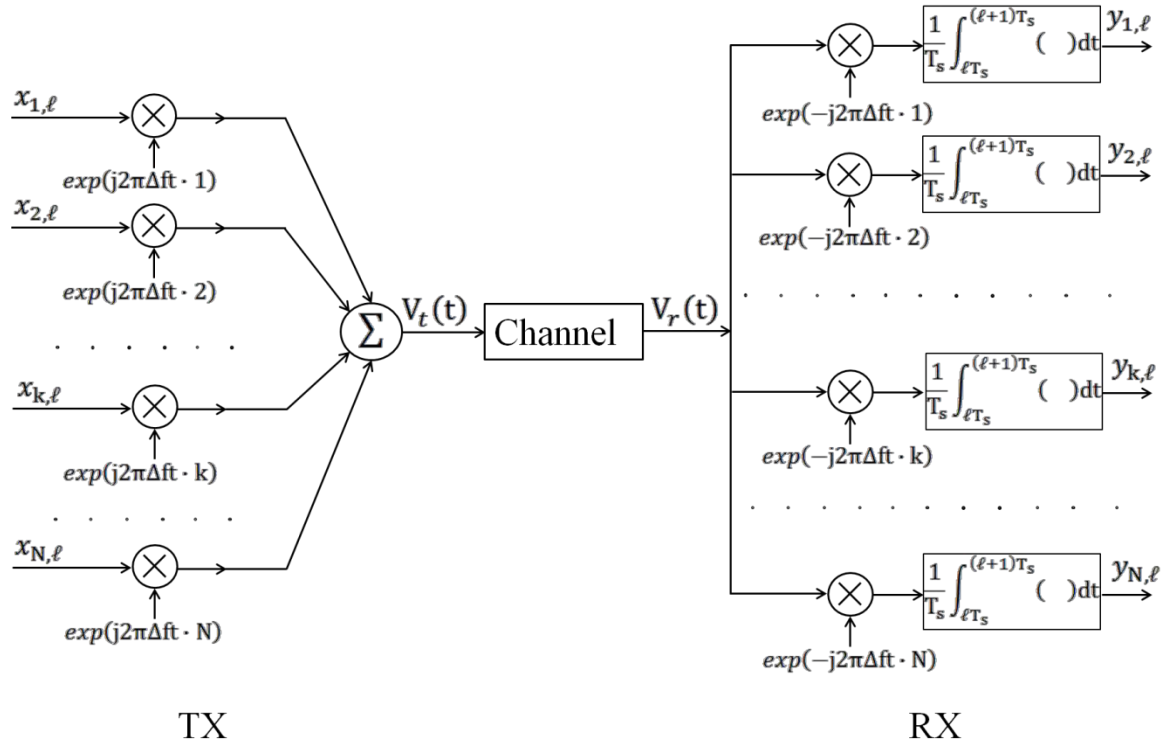


Fig. 3.4: Ideal BB continuous model of OFDM link in Gaussian channel.

The system is summarized mathematically as follows.

$$V_t(t) = \sum_{k=1}^N x_{k,\ell} \cdot \exp(j2\pi k \Delta f t) \quad (3.14-a)$$

$$V_r(t) = \sum_{k=1}^N x_{k,\ell} \cdot \exp(j2\pi k\Delta ft) + n(t) \quad (3.14-b)$$

$$y_{m,\ell} = \frac{1}{T_s} \int_{\ell T_s}^{(\ell+1)T_s} \left(\sum_{k=1}^N x_{k,\ell} \cdot \exp(j2\pi k\Delta ft) + n(t) \right) \cdot \exp(-j2\pi m\Delta ft) dt \quad (3.14-c)$$

where $\Delta f = 1/T_s$.

Now by calculating (3.14-c), assuming $\ell = 0$ for simplicity, yields

$$\begin{aligned} y_{m,0} &= \frac{1}{T_s} \int_0^{T_s} x_{m,0} dt \\ &\quad + \frac{1}{T_s} \int_0^{T_s} \sum_{\substack{k=1 \\ k \neq m}}^N x_{k,0} \cdot \exp(j2\pi(k-m)\Delta ft) dt + \frac{1}{T_s} \int_0^{T_s} n(t) \exp(-j2\pi m\Delta ft) dt \end{aligned}$$

For complex AWGN, the $\exp(-j2\pi m\Delta ft)$ factor has no effect and can be removed, while the 2nd right-hand term, which represents overall cross-talk, is then given by

$$\frac{1}{T_s} \int_0^{T_s} x_{k,0} \cdot \exp(j2\pi(k-m)\Delta ft) dt = 0 \quad \begin{array}{l} \text{If and only if} \\ \mathbf{k} \neq \mathbf{m}, \text{ and} \\ \Delta \mathbf{f} = \mathbf{1}/T_s \text{ are satisfied} \end{array} \quad (3.15)$$

Therefore the orthogonality condition in (3.15) is maintained as long as all SCs complete exactly an integer number of cycles every T_s , which is also the condition that the OFDM is based on. Accordingly, $\mathbf{y}_{m,0} = x_{m,0} + \widetilde{\mathbf{n}}_{m,0}$, where $\widetilde{\mathbf{n}}_{m,0}$ is the noise term. The noise term of all SCs is identical since the correlator's TF is the same, and $\mathbf{n}(\mathbf{t})$ has a white PSD. The frequency response (TF) of the correlator can easily be obtained as

$$H_c(f) = \text{sinc}(fT_s) \quad (3.16)$$

Hence the noise variance is given by

$$\sigma_n^2 = \int_{-\infty}^{\infty} S_n(f) \text{sinc}^2(fT_s) df = S_n/T_s \quad (3.17)$$

where $\mathbf{S}_n(\mathbf{f}) = S_n$ is the DS-PSD of the received noise. Note that noise BW per SC (\mathbf{BW}_n) is $\mathbf{BW}_n = 1/T_s$. Then the \mathbf{m} -th O/P at the ℓ -th OFDM symbol, and its corresponding powers are respectively is given by

$$y_{m,\ell} = x_{m,\ell} + \widetilde{\mathbf{n}}_{m,\ell} \quad (3.18-a)$$

$$\langle P_{m,O/P} \rangle = \langle x_{m,\ell} \cdot x_{m,\ell}^* \rangle + S_n/T_s \quad (3.18-b)$$

where $\langle \cdot \rangle$ denotes an infinite averaging with ℓ , and $*$ stands for complex conjugate. If the received power per SC $\langle \mathbf{x}_{m,\ell} \cdot \mathbf{x}_{m,\ell}^* \rangle$ is assumed to be equal for all the SCs, then $\langle \mathbf{x}_{m,\ell} \cdot \mathbf{x}_{m,\ell}^* \rangle = P_{rx}/N$, where P_{rx} is the received OFDM signal power. In this case the DS-PSD of the OFDM signal is given by

$$S(f) = \frac{P_{rx} \cdot T_s}{N} \sum_{k=1}^N \text{sinc}^2((f - k\Delta f)T_s) \quad (3.19)$$

Despite the cross-talk between adjacent SCs, orthogonality is maintained since (3.15) is valid. Therefore the first two nulls BW can be easily calculated as

$$BW_{nn} = N/T_s \quad (3.20)$$

However, many BW definitions are introduced later, and even the BW_{nn} is slightly different when a guard band is used. An important figure that judges a system's efficiency is the BW efficiency, which is defined as

$$BW_{eff} = R_b/BW \quad (3.21)$$

where BW is the total BW occupied by all components of the signal in the channel, and R_b is the aggregate bit rate (bps). For instance, in this model, $R_b = m \cdot N/T_s = m \cdot BW_{nn}$, hence $BW_{eff} = m$, which is twice as good as SCM under the same conditions, and it is one of the main advantages of the OFDM. However, this is an ideal case, and BW_{eff} cannot be higher than m in any OFDM proposal. The performance of the OFDM signal, in this ideal continuous model, is identical to that of SCM, which can be easily proven as follows

$$SNR_b = SNR/m \quad \text{In general} \quad (3.22-a)$$

$$SNR_b = \frac{P_{rx} \cdot T_s}{S_n \cdot N \cdot m} = \frac{P_{rx}/BW_{nn}}{S_n \cdot m} = \frac{P_{rx}}{BW_n \cdot m} \quad \text{In ideal BB OFDM} \quad (3.22-b)$$

Here (3.22-b) is identical to the SCM one, and hence the **BER** can be estimated using the **BER** equations given in Appendix-B.

3.3.2 Baseband DSP-based OFDM link

DSP is used to realize all the necessary computations of the BB OFDM at TX, and RX with important advantages of flexibility (programmable), reliability (low environmental sensitivity), repeatability, and adaptability with modifications.

3.3.2.1 Baseband DSP-based OFDM Transmitter

According to the extensive studies in the literature, the BB OFDM TX shown in Fig. 3.5 is configured based on these studies [65], [66], [67], [24]. Therefore the discrete OFDM TX model will be referred to Fig. 3.5, and hence it is analyzed as follows.

- 1- The I/P binary data with bit-rate of \mathbf{R}_b in (bps) is first buffered to maintain time continuity with buffer's size of \mathbf{N}_{Bf} . Pre-coding might be necessary according to the operating protocol; however, the protocol rate will be calculated separately here [6].
- 2- The buffer releases data bits with rate of $\widehat{\mathbf{R}}_b$ which is higher than \mathbf{R}_b , and becomes idle during training symbol (TrS) insertion period.
- 3- The released data is encoded using forward error correction (FEC) encoder to improve BER at RX with O/P coded-data rate of \mathbf{R}_c . For instance, RS(255, 239) corrects I/P BER from 1.4×10^{-4} up to 10^{-13} with redundancy of 6.69% and O/P code rate of $\alpha_{FEC} = 0.9373$ ($\mathbf{R}_c = \widehat{\mathbf{R}}_b / \alpha_{FEC}$) [68]. Doubling the redundancy such as when {RS(239, 223) + RS(255, 239)} is used, decreases the I/P BER limit to about 6×10^{-2} . However, some delay is introduced (latency), and such an overhead is too much. The coding penalty is

$$PEN_{FEC} = 1/\alpha_{FEC} \quad (3.23)$$

This penalty is calculated with overall coding gain to get net coding gain NCG [68].

- 4- The coded stream is mapped using BB complex mapper (BBCM). Usually M-QAM is adopted for its superior performance over other constellations in Gaussian channel. Hence, the O/P complex-symbol rate is $\mathbf{R}_s = R_c/m = \widehat{\mathbf{R}}_b / (m \cdot \alpha_{FEC})$ in (sym/s).

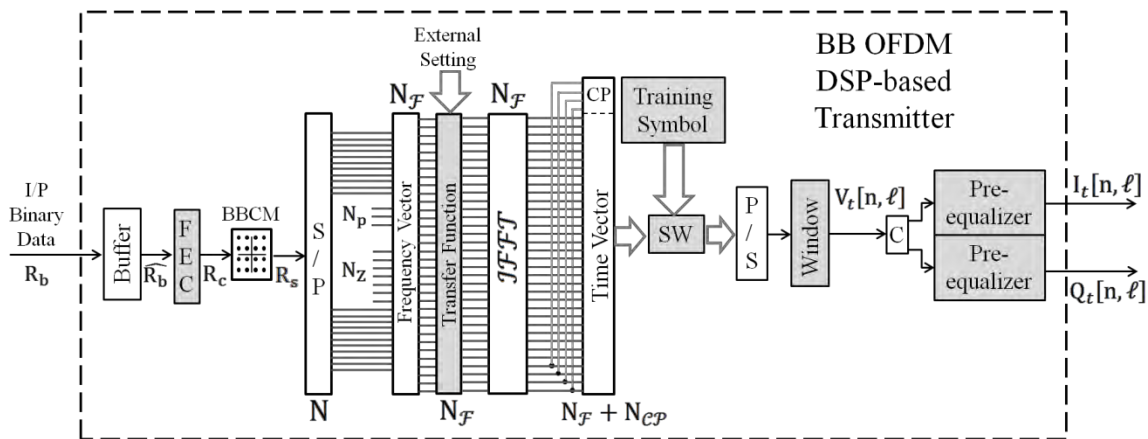


Fig. 3.5: DSP-based BB OFDM TX. The gray-colored blocks are not essential in the OFDM functions; however, they are used to enhance the performance.

- 5- The serial complex vector is converted into \mathbf{N} parallel tributaries using (**S/P**) convertor with $\mathbf{1}:\mathbf{N}$ conversion ratio. As soon as all cells of the S/P convertor are filled, the content is sent to a frequency vector (**FrV**).
- 6- The size of the FrV is $\mathbf{N}_{\mathcal{F}}$, which is the size of **IFFT** processor. This vector plays a vital role in the OFDM signal design since it determines the location of modulated, zero, and pilot SCs in the band. Here $\mathbf{N}_{\mathcal{F}} = \mathbf{N} + \mathbf{N}_{\mathbf{Z}} + \mathbf{N}_{\mathbf{p}} = \mathbf{N} + \mathbf{N}_{\mathbf{ZI}} + \mathbf{N}_{\mathbf{ZO}} + \mathbf{N}_{\mathbf{p}}$, where $\mathbf{N}_{\mathbf{p}}$, $\mathbf{N}_{\mathbf{Z}}$, $\mathbf{N}_{\mathbf{ZI}}$, and $\mathbf{N}_{\mathbf{ZO}}$ are respectively the total number of pilot-SCs, overall zero-SCs, in-band zero-SCs, and out-of-band zero-SCs. The pilot-SCs are required (especially in an RF channel) for channel estimation and correction, while zero-SCs are required to allow oversampling and facilitate anti-aliasing (**AA**) filtering [69]. Note that $\mathbf{N}_{\mathbf{ZI}}$ is identified for any zero-SC that is encompassed by non-zero-SCs. Hence the oversampling ratio is defined as,

$$\gamma_s = \mathbf{N}_{\mathcal{F}} / (\mathbf{N} + \mathbf{N}_{\mathbf{ZI}} + \mathbf{N}_{\mathbf{p}}) = 1 + \mathbf{N}_{\mathbf{ZO}} / (\mathbf{N}_{\mathcal{F}} - \mathbf{N}_{\mathbf{ZO}}) \quad (3.24)$$

- 7- A TF $\mathbf{W}[\mathbf{k}]$ maybe applied at the FrV for equalization purposes to: equalize DAC's TF, compensate some channel impairments (CD, nonlinearity, etc), and others [6], [70]. This TF is more suitable for pre-transmission phase-correction since amplitude correction is limited due to limited dynamic response of the DAC [70].
- 8- The **IFFT** computation is performed to the FrV or the modified one and the O/P complex time-samples vector is sent to a time vector (**TiV**).
- 9- The CP is inserted in the TiV by copying the last $\mathbf{N}_{\mathbf{CP}}$ samples of **IFFT** O/P and pasting them at the beginning of the TiV, such that the copy of the last **IFFT** sample is pasted just before the first **IFFT** sample. When $\mathbf{N}_{\mathbf{CP}}$ is wider than the estimated ISI, then no effect occurs on the effective window since the ISI only distorts the guard band between successive symbols, and hence zero-ISI can be achieved. Besides, the correlation between the first and last part of the symbol can be exploited for timing and synchronization using a circular correlator [48]. The TiV length equals the OFDM symbol's length and given by $\mathbf{N}_{\mathbf{sy}} = \mathbf{N}_{\mathcal{F}} + \mathbf{N}_{\mathbf{CP}}$.
- 10- In Fig. 3.5a, the selector switch (**SW**) allows the complex TiV to pass by default, and then after a number of successive TiV ($\mathbf{M}_{\mathbf{dt}}$) is sent, the SW changes the state and releases the pre-calculated TrS-TiV. Although the TrS might be generated periodically

at FrV and the SW is not required in this case. However, since the TrS has a fixed TiV, then it can be calculated, stored, and used periodically. Thus the SW is placed for illustration purposes only. The TrS constitutes of either one or two OFDM symbols, and hence $\mathbf{M}_{\text{tr}} = 1$ or 2 [71].

11- The parallel-to-serial (**P/S**) convertor with a conversion ratio of $\mathbf{N}_{\mathcal{F}} + \mathbf{N}_{\mathcal{CP}}$: $\mathbf{1}$ releases the complex time-samples, which is expressed by $\mathbf{V}_t[\mathbf{n}, \boldsymbol{\ell}]$.

Where $\mathbf{n} = [-N_{\mathcal{CP}}, -N_{\mathcal{CP}} + 1, \dots, -1, 0, 1, \dots, N_{\mathcal{F}} - 1]$ is time-samples index, and $\boldsymbol{\ell}$ is OFDM's symbol's index.

12- A window function might be applied to reduce side-lobes in the O/P PSD. The **C** block converts the complex TiV into its real and imaginary components, which is again introduced for illustration purposes. The I/Q imbalance of RF front-end and DACs can be corrected via pre-transmission equalization blocks, which perform fast convolution between $\mathbf{V}_t[\mathbf{n}, \boldsymbol{\ell}]$ and some time-vector obtained from measuring the differential response between the I and Q front-ends [70]. However, the window function and pre-equalization process are hard to implement due to the high number of complex computations at high sampling rates as well as the latency involved [24]. It is more feasible to use the rectangular window (no window is applied), and perform I/Q imbalance correction at the RX.

13- Therefore $\mathbf{V}_t[\mathbf{n}, \boldsymbol{\ell}]$ is the discrete representation of $\mathbf{V}_t(\mathbf{t})$ given in Section (3.3.2) with time resolution of $\mathbf{T}_{\text{sa}} = 1/F_S$, and frequency resolution of $\Delta\mathbf{f} = F_S/N_{\mathcal{F}}$, which is the frequency separation between the SCs, where \mathbf{F}_S is sampling frequency.

Data flow continuity has to be maintained and in order to insure this, let \mathbf{M}_{fr} be number of OFDM symbols per frame, and \mathbf{T}_{fr} is the corresponding time per frame. Hence from the aforementioned discussions, $\mathbf{M}_{\text{fr}} = M_{\text{dt}} + M_{\text{tr}}$, and $\mathbf{T}_{\text{fr}} = (N_{\mathcal{F}} + N_{\mathcal{CP}}) \cdot (M_{\text{dt}} + M_{\text{tr}}) \cdot T_{\text{sa}}$. However, total number of the transmitted data-bits during \mathbf{T}_{fr} is calculated as $\mathbf{N}_{\text{bits}} = N \cdot m \cdot M_{\text{dt}} \cdot \alpha_{\text{FEC}}$. Thus the maximum I/P data rate is calculated as $\mathbf{R}_b = N_{\text{bits}}/T_{\text{fr}}$, which is given by

$$\mathbf{R}_b = F_S \cdot m \cdot \alpha_{\text{FEC}} \cdot \left(\frac{N}{N_{\mathcal{F}}}\right) \cdot \left(\frac{M_{\text{dt}}}{M_{\text{dt}} + M_{\text{tr}}}\right) \cdot \left(\frac{N_{\mathcal{F}}}{N_{\mathcal{F}} + N_{\mathcal{CP}}}\right) \quad (3.25)$$

On the other hand, the transmitted power can be separated into two parts, one is the overall modulated-SCs' power, and one is reserved for the overhead (CP, TrS, and pilot-

SCs). Now since only the former part is used in **BER** calculations, then there is a power penalty due to the overhead which can be easily calculated as

$$\text{PEN}_{\text{oh}} = \left(1 + \frac{M_{\text{tr}}}{M_{\text{dt}}}\right) \cdot \left(1 + \frac{N_{\text{CP}}}{N_{\mathcal{F}}}\right) \cdot \left(1 + \frac{\sum_{r=1}^{N_{\text{p}}} P_{\text{p}}[r]}{\sum_{k=1}^N P_{\text{SC}}[k]}\right) \quad (3.26)$$

where $\mathbf{P}_{\text{SC}}[\mathbf{k}]$, and $\mathbf{P}_{\text{p}}[\mathbf{r}]$ are the mean power of k -th modulated-SC and r -th pilot-SC over ℓ . Note that FEC penalty is calculated separately with NCG. Note also that low $\mathbf{N}/\mathbf{N}_{\mathcal{F}}$ ratio does not result any penalty, however, it reduces sampling efficiency, and higher \mathbf{F}_{S} is required for a given \mathbf{R}_{b} , which should be avoided. From (3.26), as the insertion period of the TrS increases, or as \mathbf{M}_{dt} increases, PEN_{oh} decreases. However, this factor depends on channel stability and how fast it varies with time (for instance PMD is the challenging parameter in optical channel), which can only be estimated experimentally [6]. Besides, adopting TrS of one symbol is highly recommended for the same reason. In addition to that, higher $\mathbf{N}_{\mathcal{F}}$, and lower \mathbf{N}_{CP} results lower PEN_{oh} , however, high $\mathbf{N}_{\mathcal{F}}$ results technological difficulties in the implementation, and makes the signal more sensitive to PN. While in the conventional OFDM link, \mathbf{N}_{CP} value depends on channel response, and hence trade-off between power penalty and ISI penalty leads to the optimum value of \mathbf{N}_{CP} [72]. In (3.26), the ratio of total pilot-SCs power to total modulated-SCs power is known as pilot-to-signal power ratio (**PSPR**), which is required to be as minimum as possible for low PEN_{oh} .

3.3.2.2 Baseband DSP-based OFDM receiver

The BB OFDM RX shown in Fig. 3.6 is configured based on the extensive studies in the literature, which can be analyzed briefly as follows [65]-[67]. After the signal's detection, down-conversion (for heterodyne receiver), and sampling by I/Q ADCs, the real and imaginary time-samples tributaries are $\mathbf{I}_r[\mathbf{n}, \ell]$, and $\mathbf{Q}_r[\mathbf{n}, \ell]$, are converted into a single complex time-samples $\mathbf{V}_r[\mathbf{n}, \ell]$ in the DSP RX. Here \mathbf{n} , and ℓ are local indices that depends on RX sampling clock and is generally independent of the TX's \mathbf{n} , and ℓ vectors. Using synchronization techniques (TrS, or CP with circular correlator and blind frequency estimation), the \mathcal{FFT} window, and the carrier frequency offset (**CFO**) are estimated [67]. Hence a TiV with size of $\mathbf{N}_{\text{sy}} = \mathbf{N}_{\mathcal{F}} + \mathbf{N}_{\text{CP}}$ is generated, and the CP samples are discarded. The \mathcal{FFT} computation is applied at the useful part of the TiV, and

a FrV of length $\mathbf{N}_{\mathcal{F}}$ is generated again. Due to the TX's front-end, channel impairments, RX's front-end, and RX sampling clock frequency and phase shift, extensive equalization is required. After fine time and frequency synchronization is achieved, and channel equalization is done, de-mapping is performed only at the \mathbf{N} modulated-SCs. Then the \mathbf{N} parallel branches is converted into serial coded-data stream, which is decoded by FEC decoder, and hence binary data is released with rate of $\mathbf{R}_{\mathbf{b}}$ which is denoted as $\widetilde{\mathbf{R}}_{\mathbf{b}}$. Note that a buffer is required for data rate conversion to maintain time continuity when TrS is used, just as the case in TX. Obviously, stringent synchronization conditions are required to be fulfilled in the OFDM DSP RX whether direct detection or coherent detection is employed in the front-end, which is one of OFDM's disadvantages. The DSP TX and RX can be implemented using field programmable gate array (FPGA). Quantization noise of the FPGA is negligible since high resolution can be easily obtained [24], [73]. The maximum clock frequency in the FPGA is $\Delta\mathbf{f} \cdot \mathbf{q}_{bf}$, which is much lower than the required $\mathbf{F}_{\mathbf{S}}$. Where \mathbf{q}_{bf} is the effective number of quantization bits that is required to realize the real and imaginary parts of the complex TiV. The serial version of the complex TiV is realized by DAC/ADC and here is the bottleneck. Although we have represented the P/S block as part of the DSP TX, however, at **GSps** (Giga samples per second) applications, this cannot be implemented by FPGA. Besides, the O/P time-samples cannot practically be a chain of delta functions.

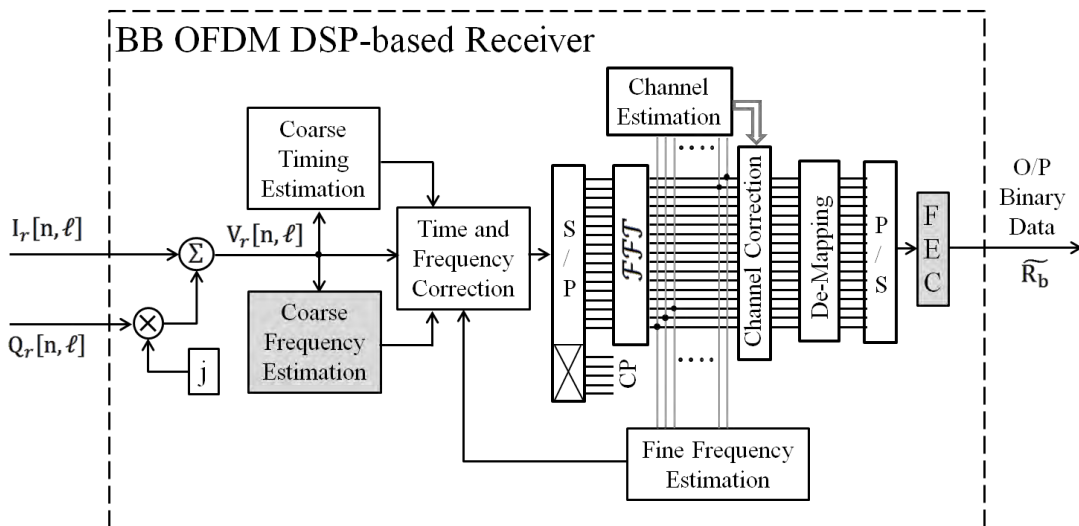


Fig. 3.6: DSP-based BB OFDM RX. The gray colored blocks are not essential in the OFDM functions; however, they are used to enhance the performance.

3.3.3 DAC/ADC

Two DACs and two ADCs are required in the BB realization of the complex TiV. In TX for instance, the real and imaginary components of TiV are converted into serial stream of time-samples with sample-width equals the time resolution or $\mathbf{T}_{sa} = 1/F_S$ [70]. The DAC performs zero-order hold (**ZOH**) TF, which its unnormalized version is given by

$$|H_{DAC}(f)| = (1/F_S) \cdot \text{sinc}(f/F_S) \quad (3.27)$$

Thus pre/post-equalization is necessary to ensure that all SCs have the same power. Since the I and Q DACs are assumed to have the same amplitude response, then the TF $\mathbf{W}[\mathbf{k}]$ in the DSP TX can be employed to flatten the I, and Q spectrum simultaneously, which is the easiest technique [70]. However, differential group delay between the two DACs cannot be corrected by $\mathbf{W}[\mathbf{k}]$, and a delay-line might be used for this purpose when the pre-equalization using fast convolution is unattainable. The key specifications of the DAC are the maximum \mathbf{F}_S , the effective number of quantization bits \mathbf{q}_b , and the dynamic range (maximum positive and negative voltage with respect to \mathbf{R}_L , which is usually 50Ω). From (3.25), it is obvious that a high \mathbf{R}_b requires a high \mathbf{F}_S with an adequate \mathbf{q}_b for low quantization noise; however, this represents a technological challenge for real-time applications, and partitioning the I/P data rate, and frequency division multiplexing (**FDM**) structure is still the choice. Usually clipping is performed on the TiV before the DAC to improve sampling efficiency due to the high PAR of OFDM signal [74]. However, the clipping process enhances nonlinear penalty and spreads the spectrum, and hence a trade-off between optimum clipping ratio and nonlinear penalty is required. Studies showed that for **BER** of 10^{-3} and at optimum clipping ratio, $\mathbf{q}_b = 5$ bits for QPSK, and $\mathbf{q}_b = 7$ bits for 16-QAM are adequate for lower than 0.5dB penalty due to the quantization noise of both the DAC and the ADC [74], [53]. In brief, the quantization noise, which can be modeled as AWGN, is not significant in a link dominated by the ASE noise when the minimum \mathbf{q}_b is fulfilled [23]. However, in most of these studies the AA-filtering is not taken into consideration. That is when group delay of the AA low pass filter (**LPF**) is not constant (for instance, Bessel-type LPF has a constant group delay), then the continuous-time OFDM signal after the AA-filter exhibits overshoots that again increases the PAR [75]. A LPF must also be used before the ADC at RX to reject the

unwanted signals that may exist in the same FD and overcoming sampling cross-talk (spectrum folding) [70].

3.3.4 Anti-Aliasing filtering

The AA-LPF is required after DACs to reject sampling harmonics that might interfere with other sub-channels of the transmitted signal, or other channels in the grid. As discussed earlier, oversampling (by zero-SCs insertion) facilitates the AA-filtering by providing enough frequency-gap for reasonable order of filter to highly attenuate the aliasing spectra (by more than 20dB) [69]. Although a Bessel-LPF has a flat group delay over the passband, which results minimal phase distortion, and so maintains low PAR when clipping is performed, it has poor steepness [75]. A better choice is the Chebyshev type II, or the Butterworth filter for their high steepness and flat passband response. In the filter design, signal to aliasing-noise power ratio (**SANR**) after the LPF must be much higher than the operating SNR especially if sub-channel multiplexing is adopted. The oversampling ratio γ_s determines the required filter's steepness in the transition band (between the passband and stopband), and for a stable filtering, γ_s should not be less than 1.175 [75]. In Table 3.1, a summary is given for the minimum required order of Chebyshev type II AA-LPF for different m in M-QAM mapping, **BER** $< 10^{-3}$, passband attenuation of less than 0.1dB, and **SANR** is 20dB higher than the operating **SNR**. In order to ensure free-of-aliasing sampling, F_s has to be higher than twice the effective BB BW of the signal (Nyquist rate) [69]. As the OFDM signal $\mathbf{V}_t(\mathbf{t})$ is a band-limited signal with limited single-sided (**SS**) BW, then the ideal sampled version of $\mathbf{V}_t(\mathbf{t})$ is given by

$$V_{t,\delta}(t) = V_t(t) \cdot \sum_{r=-\infty}^{\infty} \delta(t - r \cdot T_{sa}) \quad , \text{ which its } \mathcal{FT} \text{ is given by [48]}$$

$$V_{t,\delta}(f) = F_s \sum_{u=-\infty}^{\infty} V_t(f - u \cdot F_s) \quad , \text{ and by applying DAC's TF in (3.27) yields}$$

$$V_{t,s}(f) = \text{sinc}(f/F_s) \cdot \sum_{u=-\infty}^{\infty} V_t(f - u \cdot F_s)$$

Hence the single-sided (**SS**) PSD of the samples-signal is calculated as

$$\mathbf{S}_{t,s}(\mathbf{f}) = \langle V_{t,s}(f) V_{t,s}^*(f) \rangle = \text{sinc}^2(f/F_s) \sum_{u=-\infty}^{\infty} S_t(f - u \cdot F_s) \quad \dots\dots \quad f \geq 0 \quad (3.28)$$

where $\mathbf{S}_t(\mathbf{f})$ is the SS-PSD of the OFDM signal. Usually $\mathbf{I}_t[\mathbf{n}, \ell]$, and $\mathbf{Q}_t[\mathbf{n}, \ell]$ have identical SS-PSD to $\mathbf{S}_t(\mathbf{f})$ with only 3-dB lower.

Table 3.1

Anti-Aliasing LPF requirements for different M-QAM and different γ_s , $\mathbf{BER} < 10^{-3}$, passband attenuation is less than 0.1dB, \mathbf{SANR} is 20dB higher than the operating \mathbf{SNR} , assuming Chebyshev type II prototype.

Mapping	m	γ_s	Minimum order	SANR (dB)
QPSK	2	2.000	3	30
		1.538	4	
		1.334	5	
		1.175	6	
8-QAM	3	2.000	3	34
		1.538	4	
		1.334	5	
		1.175	7	
16-QAM	4	2.000	3	37
		1.538	4	
		1.334	5	
		1.175	7	
32-QAM	5	2.000	3	40
		1.538	4	
		1.334	6	
		1.175	8	

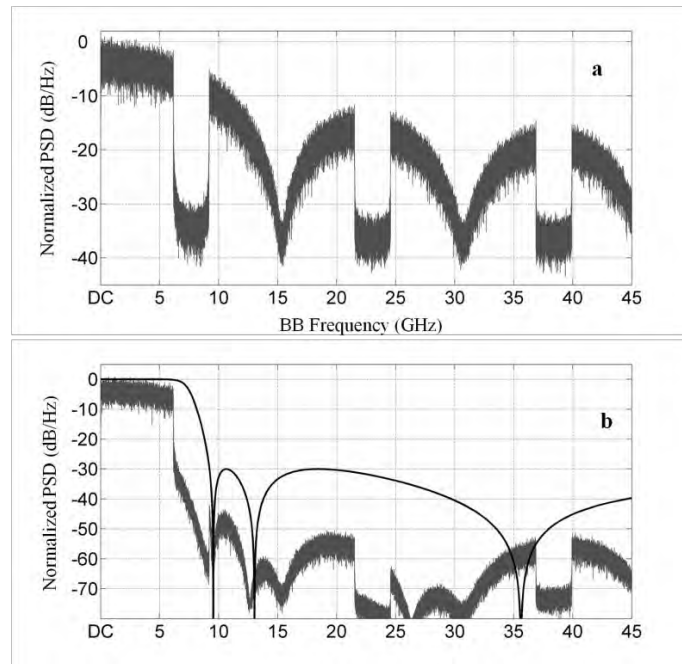


Fig. 3.7: Simulation of before and after AA-filtering (parameters are given in the text). After DAC SS-PSD of either non-equalized I, or Q tributaries of OFDM signal is shown in (a), which can also be calculated from (3.28). While the same signal after the AA-LPF of is shown in (b). The solid-black curve in (b) is the AA-LPF frequency response.

For example, DAC and AA-LPF specifications are required to be determined for the following OFDM transmitter's parameters (an extreme case), $\mathbf{R}_b = 55.22\text{Gbps}$, $N_{\mathcal{F}} = 1024$, $N_{\mathcal{CP}} = 16$, $N = 808$, $N_p = 0$, $N_{\mathbf{ZI}} = 0$, $N_{\mathbf{ZO}} = (1024 - 808) = 216$, $m = 5$ (32-QAM), $M_{\text{dt}} = 64$, $M_{\text{tr}} = 2$, $\alpha_{\text{FEC}} = 0.93725$ for RS(255, 239). Then from (3.24), (3.25), and (3.26) yields, $F_s \approx 15.64\text{GSps}$, $\gamma_s \approx 1.267$, $\text{PEN}_{\text{oh}} \approx 0.2\text{dB}$, and $q_b > 7\text{bits}$. From Table 3.1, the minimal required order that satisfies all the given conditions that are involved in this filter design is $\{7\}$, and the results of this example are shown in Fig. 3.7.

3.3.5 Discrete representation of baseband OFDM link

From the previous discussions, the frequency vector (\mathbf{FrV}) can be set as required to form the frequency spectra of the OFDM signal. Adding pilot-SCs, introducing diversity of the modulated-SCs to combat frequency-selective fading (in RF channel), and controlling SCs amplitude and phase, can all be easily implemented by controlling \mathbf{FrV} , which shows the beauty of OFDM. Besides, the upper and the lower sideband SCs can be modulated with different and independent mapping, which is an efficient technique to halve the required sampling frequency. Using this setting of \mathbf{FrV} , both the positive and negative frequency SCs are interfered in the BB FD, however, since the I and Q tributaries are separately sampled, then the interfered I and Q can be completely recovered at RX. For the ideally-sampled OFDM signal, the discrete representation of \mathbf{TiV} can be expressed as

$$V_t[n, \ell] = \sum_{\ell} \sum_{\substack{k=-N/2 \\ k \neq 0}}^{N/2} c[k, \ell] \cdot W[k] \cdot \exp\left(j2\pi \frac{k}{N_{\mathcal{F}}} n\right) \quad (3.29)$$

where $\mathbf{n} = [-N_{\mathcal{CP}}, -N_{\mathcal{CP}} + 1, \dots, -1, 0, 1, 2, \dots, N_{\mathcal{F}} - N_{\mathcal{CP}}, N_{\mathcal{F}} - N_{\mathcal{CP}} + 1, \dots, N_{\mathcal{F}} - 1]$,

$\mathbf{c}[\mathbf{k}, \ell]$ is the complex mapping of the \mathbf{k} -th SC at the ℓ -th OFDM symbol.

Noting that, $\exp(2\pi(N_{\mathcal{F}} + x) \cdot k/N_{\mathcal{F}}) = \exp(2\pi x \cdot k/N_{\mathcal{F}})$.

The indexing of the \mathbf{FrV} results single-side-band (SSB) modulation for the positive and the negative frequencies. The positive vector index is $[1, 2, \dots, N/2]$, and the negative one is $[N_a, N_a + 1, \dots, N_{\mathcal{F}}]$, where $N_a = N/2 + N_{\mathbf{ZO}} + 1$, and the DC-SC is set to zero (one of the $N_{\mathbf{ZI}}$ SCs). The positive and negative SCs are uncorrelated since they are mapped with different data. The real and imaginary O/P tributaries can then be written as

$$I_t[n, \ell] = \sum_{\ell} \sum_{\substack{k=-N/2 \\ k \neq 0}}^{N/2} r[k, \ell] \cdot \cos\left(2\pi \frac{k}{N_{\mathcal{F}}} n\right) - g[k, \ell] \cdot \sin\left(2\pi \frac{k}{N_{\mathcal{F}}} n\right) \quad (3.30-a)$$

$$Q_t[n, \ell] = \sum_{\ell} \sum_{\substack{k=-N/2 \\ k \neq 0}}^{N/2} g[k, \ell] \cdot \cos\left(2\pi \frac{k}{N_{\mathcal{F}}} n\right) + r[k, \ell] \cdot \sin\left(2\pi \frac{k}{N_{\mathcal{F}}} n\right) \quad (3.30-b)$$

where $\mathbf{r}[\mathbf{k}, \ell] = \Re\{c[\mathbf{k}, \ell] \cdot \mathbf{W}[\mathbf{k}]\}$, and $\mathbf{g}[\mathbf{k}, \ell] = \Im\{c[\mathbf{k}, \ell] \cdot \mathbf{W}[\mathbf{k}]\}$.

Here the functions $\Re\{\cdot\}$, and $\Im\{\cdot\}$ stand for the real and imaginary parts respectively.

Obviously when no pre-equalization is required, $\mathbf{W}[\mathbf{k}] = \mathbf{1}$ for all values of \mathbf{k} . Note that (3.30) can be rewritten as follows

$$I_t[n, \ell] = \sum_{\ell} \sum_{k=1}^{N/2} \{r[k^+, \ell] + r[k^-, \ell]\} \cdot \cos\left(2\pi \frac{k}{N_{\mathcal{F}}} n\right) - \{g[k^+, \ell] - g[k^-, \ell]\} \cdot \sin\left(2\pi \frac{k}{N_{\mathcal{F}}} n\right) \quad (3.31-a)$$

$$Q_t[n, \ell] = \sum_{\ell} \sum_{k=1}^{N/2} \{g[k^+, \ell] + g[k^-, \ell]\} \cdot \cos\left(2\pi \frac{k}{N_{\mathcal{F}}} n\right) + \{r[k^+, \ell] - r[k^-, \ell]\} \cdot \sin\left(2\pi \frac{k}{N_{\mathcal{F}}} n\right) \quad (3.31-b)$$

Thus the signal can be recovered even when the positive (denoted by \mathbf{k}^+) and negative (denoted by \mathbf{k}^-) subcarriers interfere in the BB domain. When only AWGN is introduced in the channel, then after timing and synchronization is performed at RX, the received signal has the same discrete time vector \mathbf{n} and can be expressed as

$$\mathbf{V}_r[n, \ell] = \left\{ \sum_{\ell} \sum_{\substack{k=-N/2 \\ k \neq 0}}^{N/2} c[k, \ell] \mathbf{W}[k] \exp\left(j2\pi \frac{k}{N_{\mathcal{F}}} n\right) \right\} + n[n, \ell]$$

where $\mathbf{n}[\mathbf{n}, \ell]$ is the sampled version of the received noise. Now when the CP is removed and the \mathcal{FFT} is applied, then the \mathbf{m} -th O/P SC is given by

$$\mathbf{y}_m[\ell] = \frac{1}{N_{\mathcal{F}}} \sum_{n=0}^{N_{\mathcal{F}}-1} \sum_{\substack{k=-N/2 \\ k \neq 0}}^{N/2} c[k, \ell] \mathbf{W}[k] \cdot e^{(j2\pi \frac{k-m}{N_{\mathcal{F}}} n)} + \frac{1}{N_{\mathcal{F}}} \sum_{n=0}^{N_{\mathcal{F}}-1} n[n, \ell] \cdot e^{(-j2\pi \frac{m}{N_{\mathcal{F}}} n)}$$

$$\mathbf{y}_m[\ell] = c[m, \ell] \mathbf{W}[m] + y_n[m, \ell]$$

where $\mathbf{n}[\mathbf{n}, \ell]$, and $\mathbf{y}_n[\mathbf{m}, \ell]$ are assumed to be complex Gaussian random variables (**GRV**)s with zero-mean. Note that the scaling factor ($\mathbf{1}/N_{\mathcal{F}}$) is used in the RX side here

to compare the discrete model with the continuous one given in Section 3.3.2. The noise variance per SC is calculated by averaging FD noise samples over large number of OFDM symbols and hence

$$\begin{aligned}\sigma_n^2[\mathbf{m}] &= \langle y_n[\mathbf{m}, \ell] \cdot y_n^*[\mathbf{m}, \ell] \rangle_\ell = \frac{1}{N_{\mathcal{F}}^2} E \left\{ \sum_{n_1=0}^{N_{\mathcal{F}}-1} \sum_{n_2=0}^{N_{\mathcal{F}}-1} n[n_1, \ell] n^*[n_2, \ell] e^{j2\pi \frac{\mathbf{m}}{N_{\mathcal{F}}} (n_2 - n_1)} \right\}_\ell \\ &= \frac{1}{N_{\mathcal{F}}^2} E \left\{ \sum_{n_1=0}^{N_{\mathcal{F}}-1} \sum_{n_2=0}^{N_{\mathcal{F}}-1} \sum_{k_1=-N_{\mathcal{F}}/2}^{N_{\mathcal{F}}/2-1} \sum_{k_2=-N_{\mathcal{F}}/2}^{N_{\mathcal{F}}/2-1} \hat{n}[k_1, \ell] \hat{n}^*[k_2, \ell] e^{j2\pi \frac{\mathbf{m}}{N_{\mathcal{F}}} \{n_1(k_1 - \mathbf{m}) - n_2(k_2 - \mathbf{m})\}} \right\}_\ell\end{aligned}$$

Only when $\mathbf{k}_1 = \mathbf{k}_2 = \mathbf{m}$, time-independent non-zero terms are obtained, hence $\sigma_n^2[\mathbf{m}] = \langle \hat{n}[\mathbf{m}, \ell] \hat{n}^*[\mathbf{m}, \ell] \rangle_\ell$. Therefore $\sigma_n^2[\mathbf{m}]$ equals the I/P noise power encompassed by a noise BW of $\mathbf{F}_S/N_{\mathcal{F}}$ at frequency index \mathbf{m} , with time-samples averaging window.

Accordingly, when the I/P noise is band-unlimited (white), the variance is

$$\sigma_n^2[\mathbf{m}] = \langle \hat{n}[\mathbf{m}, \ell] \hat{n}^*[\mathbf{m}, \ell] \rangle_\ell = \frac{\langle |n[n_o, \ell]|^2 \rangle_\ell}{N_{\mathcal{F}}}$$

where $n[\mathbf{n}, \ell] = \sum_{k=-N_{\mathcal{F}}/2}^{N_{\mathcal{F}}/2-1} \hat{n}[k, \ell] \cdot e^{j2\pi \frac{\mathbf{k}}{N_{\mathcal{F}}} \mathbf{n}}$, $\mathbf{E}\{ \}$ stands for the expectation,

and \mathbf{n}_o is any selected index of noise samples in TD.

3.3.6 Ideal performance of OFDM links

In addition to the previously discussed BB-TX/RX units, the OFDM system also requires up/down-convertors, and signal management just like any other communication system. Signal management includes all the analogue functions that aim to improve signal quality (amplification and filtering), multiplexing/demultiplexing (when sub-channel multiplexing is employed), equalization (to compensate some impairments like PN for instance), and interfacing between the BB unit and the up/down conversion unit (to flatten some TFs, and control the power level). Depending on the structure of the RF-frontends, the I and Q signals might be delivered/extracted in parallel, or delivered/extracted using only single signal (the I and Q tributaries are modulated using an RF IQ modulator) to/from the up/down convertor. The up/down convertor identifies the operating frequency band, whether it is an RF or an optical-OFDM, whether it is

coherent (local oscillator (LO) is essential) or direct detection system (LO is not required), and other features.

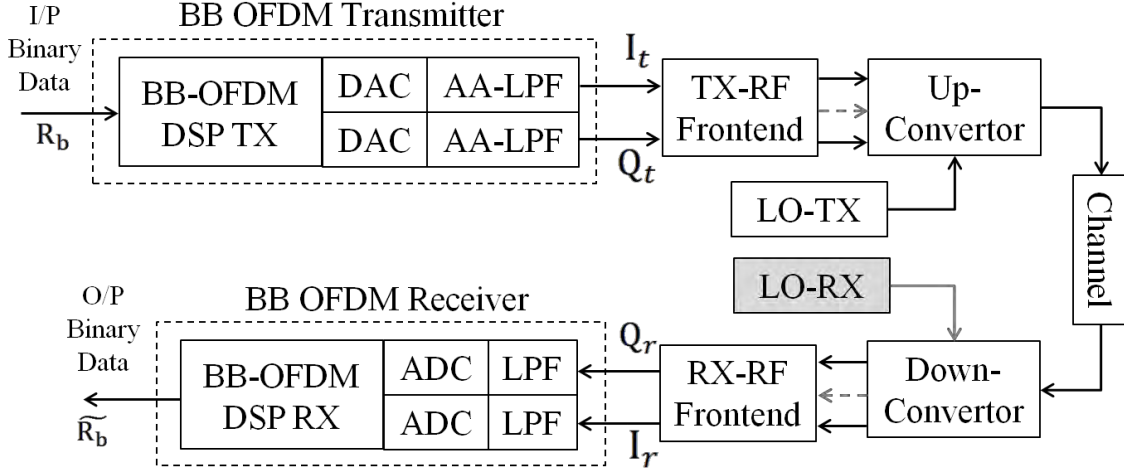


Fig. 3.8: General block diagram of the OFDM link. The gray-colored arrows indicate that one or two lines are possible in the structure, while the gray-colored LO-RX indicates that the use of this block depends on detection method.

The \mathbf{I}_t , \mathbf{Q}_t , \mathbf{I}_r , and \mathbf{Q}_r are the continuous-time version of $\mathbf{I}_t[\mathbf{n}, \ell]$, $\mathbf{Q}_t[\mathbf{n}, \ell]$, $\mathbf{I}_r[\mathbf{n}, \ell]$, and $\mathbf{Q}_r[\mathbf{n}, \ell]$ respectively. From (3.27), and (3.31), then \mathbf{I}_t , \mathbf{Q}_t can be written as follows

$$\begin{aligned} I_t(t) = g_I \sum_{\ell} \Pi_{\ell}(t) \sum_{k=1}^{N/2} |H_{AA,I}[k]| \cdot \text{sinc}(k/N_{\mathcal{F}}) \\ \cdot (r_{1k} \cos(\omega_k t - \vartheta_{1k}) - g_{1k} \sin(\omega_k t - \vartheta_{1k})) \end{aligned} \quad (3.32\text{-a})$$

$$\begin{aligned} Q_t(t) = g_Q \sum_{\ell} \Pi_{\ell}(t) \sum_{k=1}^{N/2} |H_{AA,Q}[k]| \cdot \text{sinc}(k/N_{\mathcal{F}}) \\ \cdot (g_{2k} \cos(\omega_k t - \vartheta_{2k}) + r_{2k} \sin(\omega_k t - \vartheta_{2k})) \end{aligned} \quad (3.32\text{-b})$$

where $\Pi_{\ell}(t) = \begin{cases} 1, & -T_g + \ell T_s \leq t \leq T_{\mathcal{F}} + \ell T_s \\ 0, & \text{elsewhere,} \end{cases}$

$\mathbf{T}_g = N_{CP} T_{sa}$ is the guard-band time duration,

$\mathbf{T}_s = (N_{\mathcal{F}} + N_{CP}) T_{sa}$ is the OFDM's symbol time period,

$\mathbf{T}_{\mathcal{F}} = N_{\mathcal{F}} T_{sa}$ is the \mathcal{FFT} 's time period,

$\omega_k = 2\pi k \Delta f$,

g_I , and g_Q are the net voltage gain/attenuation of I, and Q branches respectively,

$|\mathbf{H}_{AA,I}[k]|$, and $|\mathbf{H}_{AA,Q}[k]|$ are amplitude frequency-response of the AA-LPF of I, and Q branches respectively,

$\boldsymbol{\vartheta}_{1\mathbf{k}}$, and $\boldsymbol{\vartheta}_{2\mathbf{k}}$ are overall phase response of the AA-LPF and DAC of I, and Q branches respectively,

$$\mathbf{r}_{1,\mathbf{k}} = r[k^+, \ell] + r[k^-, \ell], \quad \mathbf{g}_{1,\mathbf{k}} = g[k^+, \ell] - g[k^-, \ell],$$

$$\mathbf{g}_{2,\mathbf{k}} = g[k^+, \ell] + g[k^-, \ell], \quad \mathbf{r}_{2,\mathbf{k}} = r[k^+, \ell] - r[k^-, \ell].$$

Similar equations can be obtained for \mathbf{I}_r , and \mathbf{Q}_r . The I/Q imbalance between the two tributaries can be corrected by measuring the differential scattering parameters, and the differential time delay between the two arms using network analyzer, and high speed oscilloscope. The measured FD vector is converted into a discrete-FD TF, which can be then converted into a discrete-TD TF. Pre-equalization can be achieved by applying fast convolution between $\mathbf{I}_t[\mathbf{n}, \ell]$, and $\mathbf{Q}_t[\mathbf{n}, \ell]$ with the calculated imbalance TD-vector [70]. However, this method is to some extent static, since the reading of the imbalance TD-vector is taken once. Besides, fast convolution at multiple Giga-Sps (**GSps**) is difficult as mentioned before. The best solution is to flatten both the $\mathbf{I}_t(\mathbf{t})$, and $\mathbf{Q}_t(\mathbf{t})$ amplitude responses benefiting from DSP computations via the $\mathbf{W}[\mathbf{k}]$ TF, and using analog techniques (delay line, gain adjustment, etc) in the initial setting to correct the amplitude and phase differences. Although I/Q imbalance at TX can be corrected together with RX I/Q imbalance at the RX DSP unit, since complex modulation in RF/optical domain depends on the orthogonality between the I and Q tributaries, then an amplitude and a phase imbalance of less than 0.5dB, and 2° are respectively recommended over the whole BB BW [76]. Usually driver amplifiers (**DA**) are used in the RF frontends to deliver/receive both $\mathbf{I}(\mathbf{t})$, and $\mathbf{Q}(\mathbf{t})$ at optimal power levels for transmission and detection. This amplifier pair has to be a matched-pair to ensure minimal I/Q imbalance contribution over the BB BW, and it should have a high 1dB compression point (**P_{1dB}**) for minimal nonlinearity at the TX. It is common practice to express the continuous time signal in complex form, and the I/Q imbalance matrix is applied later. That is

$$V_t(\mathbf{t}) = g \sum_{\ell} \Pi_{\ell}(\mathbf{t}) \sum_{\mathbf{k}=1}^{N/2} \mathbf{H}_T[\mathbf{k}] \hat{\mathbf{c}}[\mathbf{k}, \ell] \exp(j\omega_{\mathbf{k}}\mathbf{t}) \quad (3.33)$$

where $\mathbf{H}_T[\mathbf{k}]$ is the common overall TF (equals for both I and Q arms), which includes the DAC, AA-LPF, DA, and other components TFs, $\hat{\mathbf{c}}[\mathbf{k}, \ell] = c[\mathbf{k}, \ell]W[\mathbf{k}]$, and g is the common voltage-gain of the two arms. In the RF frontend, sub-channel multiplexing or

FDM structure might be adopted basically to avoid using high F_s DAC/ADC, which is the bottleneck in OFDM system design. In this case many definitions of BW are useful to be introduced and as follows.

$$BW_{nn} = (N + N_{ZI} + N_p - 1)/T_{\mathcal{F}} + \nu/T_s \quad \text{Which is the null-to-null BW of the main lobe per sub-channel} \quad (3.34-a)$$

$$BW_{20dB} = (1 + \epsilon_{BW}) \cdot BW_{nn} \quad \text{Outside this BW, the OFDM PSD is lower than the main lobe PSD by 20dB} \quad (3.34-b)$$

$$BW_{BB} = BW_{nn}/2 \quad \text{Which is BB BW of either I, or Q tributaries} \quad (3.34-c)$$

$$BW_{nT} = N/T_{\mathcal{F}} \quad \text{Which is the total noise BW} \quad (3.34-d)$$

$$BW_T = \left\{ \frac{BW_{nn}[1] + BW_{nn}[M_{Sch}] + BW_{20dB}[1] + BW_{20dB}[M_{Sch}]}{2} + \sum_{r=2}^{M_{Sch}-1} BW_{nn}[r] + \sum_{i=1}^{M_{Sch}-1} BW_G[i] \right\} \quad (3.34-e)$$

Which is the total occupied BW when sub-channel multiplexing is employed.

where $\nu \approx \begin{cases} 2, & \text{when the SCs at band edges are both modulated} \\ 1, & \text{when the SCs at band edges are a modulated-SC and a pilot-SC} \\ 0, & \text{when the SCs at band edges are both pilots,} \end{cases}$

ϵ_{BW} is the side-lobes coefficient, which can be reduced when window is applied,

M_{Sch} is total number of sub-channels, and

$BW_G[i]$ is the i -th frequency gap in the sub-channel multiplexing.

3.3.6.1 Sources of penalties in OFDM links

Although many sources of penalties might have to be equalized, mitigated, or tolerated in OFDM link, however, most of them are quasi-static that can be estimated using a TrS. Besides, in OFDM system, it is important to distinguish between $\mathbf{SNR}_b[\mathbf{k}]$, which is \mathbf{SNR}_b per SC's index, and the mean \mathbf{SNR}_b of OFDM signal as whole. Besides, we have also to distinguish between the delivered $\mathbf{SNR}_b[\mathbf{k}]$ and the required $\mathbf{SNR}_b[\mathbf{k}]$. That is

$$\text{SNR}_{\mathbf{b},\text{req}}[\mathbf{k}] = \text{SNR}_{\mathbf{b}}\{\text{BER}, m\} \cdot \prod_{r=1}^{M_{pen}} \text{PEN}_r[\mathbf{k}] \quad (3.35\text{-a})$$

$$\text{SNR}_{\mathbf{b},\text{del}}[\mathbf{k}] = P_{\text{SC}}[\mathbf{k}] / \sigma_n^2[\mathbf{k}] \quad (3.35\text{-b})$$

where $\text{SNR}_{\mathbf{b}}\{\mathbf{BER}, m\}$ is the theoretical required $\text{SNR}_{\mathbf{b}}$ for a given \mathbf{BER} and m , \prod is a multiplication function, M_{pen} is number of counted penalties, $\text{PEN}_r[\mathbf{k}]$ is the r -th penalty of the \mathbf{k} -th frequency index, “req”, and “del” stand for “required”, and “delivered” respectively. When the channel noise is AWGN, then $\sigma_n^2[\mathbf{k}]$ is constant for all SCs, or $\sigma_n^2[\mathbf{k}] = \sigma_n^2$. Not all penalties are \mathbf{k} -independent as it will be discussed next, and hence (3.35-a) has to be calculated for all SCs. When the difference between maximum and minimum $\text{SNR}_{\mathbf{b},\text{req}}[\mathbf{k}]$ is small or when $\Delta\text{SNR}_{\mathbf{b},\text{req}} \leq \epsilon_{\text{snr}}$ is satisfied, then the average I/P- $\text{SNR}_{\mathbf{b}}$ can be defined, where ϵ_{snr} is any arbitrary tolerance (1dB seems reasonable). However, when $\Delta\text{SNR}_{\mathbf{b},\text{req}} > \epsilon_{\text{snr}}$, then the average I/P- $\text{SNR}_{\mathbf{b}}$ is not a useful definition, and in that case the received signal’s quality is judged by its PSD as well as average I/P- $\text{SNR}_{\mathbf{b}}$. This is valid for multiple or adaptive constellation OFDM signal, where $\text{SNR}_{\mathbf{b}}$ is not evenly distributed over the whole spectrum [77]. However, if a high $\Delta\text{SNR}_{\mathbf{b},\text{req}}$ results from \mathbf{k} -dependent penalties, then a higher I/P- $\text{SNR}_{\mathbf{b}}$ might not be useful for equalization, since some penalties are correlated to the signal’s strength. In general, equalization using $\mathbf{W}[\mathbf{k}]$, analog techniques, or at the RX-DSP is essential to satisfy $\Delta\text{SNR}_{\mathbf{b},\text{req}} \leq \epsilon_{\text{snr}}$ condition for a single mapping OFDM signal. The I/P- $\text{SNR}_{\mathbf{b}}$ can then be used for comparison purposes with other systems, such as M-QAM SCM, or direct sequence spread spectrum (DSSS) systems. Sources of penalties in OFDM system are summarized below

- Overhead penalty, which is independent of \mathbf{k} , or $\text{PEN}_{\text{oh}}[\mathbf{k}] = \text{PEN}_{\text{oh}}$ per sub-channel. This penalty is a static one and depends on design’s parameters as discussed previously.
- Detection method penalty, which can be considered as independent of \mathbf{k} . This penalty depends on the down-convertor’s structure and whether direct detection or coherent detection is employed.
- I/Q imbalance penalty, which depends of \mathbf{k} . The I/Q imbalance occurs wherever two or more branches are used to describe a signal due to the components mismatch. Hence this effect is an accumulation of all TX and RX imbalances, which may severely

degrade the performance. However, it is a quasi-static effect that can be fully estimated and corrected using a TrS. Still I/Q penalty is expected whatever the correction method is, due to channel noise spreading in the correction process [78]-[79].

- Synchronization penalty, which is generally independent of \mathbf{k} . It includes CFO, \mathcal{FFT} window timing, and RX sampling clock offset penalties. Theoretically, all these offsets can be corrected continuously without any penalty since sources of the offsets are controllable (at RX). However, a trade-off between low synchronization penalty and low-complexity of the correction method is required. Besides, Δf has to be chosen much higher than the residual value of CFO to minimize this penalty, which also requires to be optimized with \mathbf{N}_{CP} .
- Reference clock jitter (PN), which depends on \mathbf{k} . This penalty is not significant in the recent technologies since high stability reference clocks (20MHz with 0.1ppm) are commercially available [67]. PN of the reference clock spreads over the SCs with integer-multiples of its original value, and hence the higher the \mathbf{k} , the higher the jitter.
- Quantization noise penalty, which is generally independent of \mathbf{k} . The quantization noise is usually modeled as AWGN, which is added to channel noise. Hence, as long as minimum q_b for a given m is used, then this penalty is marginal.
- Components' nonlinearity, which is dependent of \mathbf{k} . This penalty is an accumulation of driver amplifiers', up/down convertors', and other components' nonlinearity, which decreases as \mathbf{k} increases [80]. Usually this penalty is a function of the I/P power that derived these active components, and hence trade-off is made between the required O/P power and the worst case penalty.
- Channel response penalty, which is generally dependent of \mathbf{k} . The main to choose OFDM in the RF channel is to combat frequency-selective fading and multi-path problems, which are time-variant variables [69]. However, the optical channel is considered as quasi-static channel, in which only the slow PMD component is the time-variant variable [61]. Since the guard-band is introduced, no ISI occurs; however, correction is still required to correct CD's and PMD's induced phase shift per SC.
- LO noise penalty, which is independent of \mathbf{k} when no attempt of noise compensation is done. Although PN and intensity noise (**IN**) are presented in every source; however, PN is by far more significant and requires special attention. The main goal of this work is

to extensively analyze and compensate this impairment in multi-GSps optical OFDM system when the available semiconductor lasers (**SCL**)s are used in the system.

Note that fiber nonlinearity [59] is excluded from this summary. As soon as all these penalties are estimated, then the performance can be estimated too. For instance in the M-QAM mapping when PN is ignored, then from Appendix-B, the **BER** per SC is given by

$$\text{BER}[k] \approx \frac{1}{2} \text{erfc} \left\{ \sqrt{\text{SNR}_b[k]} \right\} \quad \dots\dots\dots \text{QPSK} \quad (3.36\text{-a})$$

$$\text{BER}[k] \approx \frac{3}{8} \text{erfc} \left\{ \sqrt{2 \cdot \text{SNR}_b[k]/5} \right\} \quad \dots\dots\dots 16\text{-QAM} \quad (3.36\text{-b})$$

where $\text{erfc}\{ \}$ is the complementary error function [81], and $\text{SNR}_b[\mathbf{k}]$ is obtained from (3.35-a). These two constellations are chosen because the gray coding is possible in both of them, and they represent good references of low and high modulation density.

3.4 Optical up and down conversion in CO-OFDM system

3.4.1 Optical up-converter

The up-converter is aimed to function as a SSB modulator at the transmission frequency. From all the proposed optical modulators, Mach-Zehnder intensity modulator (**MZM**) is proven to be the most efficient and controllable device [50]. The transfer characteristics (**TC**) and power ratio of zero-chirp x-cut MZM are respectively given by [50]

$$\frac{E_{O/P}}{E_{I/P}} = \frac{-1}{\sqrt{\text{att}_M}} \cdot \cos \left(\frac{\pi}{2} \cdot \frac{v_s}{v_\pi} \right) \quad (3.37\text{-a})$$

$$\frac{P_{O/P}}{P_{I/P}} = \frac{1}{\text{att}_M} \cdot \cos^2 \left(\frac{\pi}{2} \cdot \frac{v_s}{v_\pi} \right) \quad (3.37\text{-b})$$

where $E_{O/P}$ is the MZM's O/P optical field strength, $E_{I/P}$ is the MZM's I/P optical field strength, att_M is optical power attenuation of the MZM in linear scale, v_s is driving signal's voltage in RF domain, v_π is the MZM's switching voltage, $P_{O/P}$, and $P_{I/P}$ are O/P and I/P optical powers respectively. Biasing is usually used to shift up the driving signal level to improve modulation efficiency either by a bias-tee or separately depending on the available MZM. For instance, the optimum bias for OOK is at the quadrature point or $v_B = v_\pi/2$, where v_B is the biasing voltage. It is proven that optimal v_B for OFDM is

at the null point [82], or $v_B = v_\pi$, since the lowest 3rd order IMP result due to the relatively broad linear range at this operating point. Besides, at this v_B , the optical carrier is highly attenuated and the MZM functions as suppressed-carrier DSB-modulator. As an example, the TC when $v_B = 0$, and $v_B = v_\pi$ of an MZM with $v_\pi = 5$ volt, and $att_M = 3$ dB is shown in Fig. 3.9.

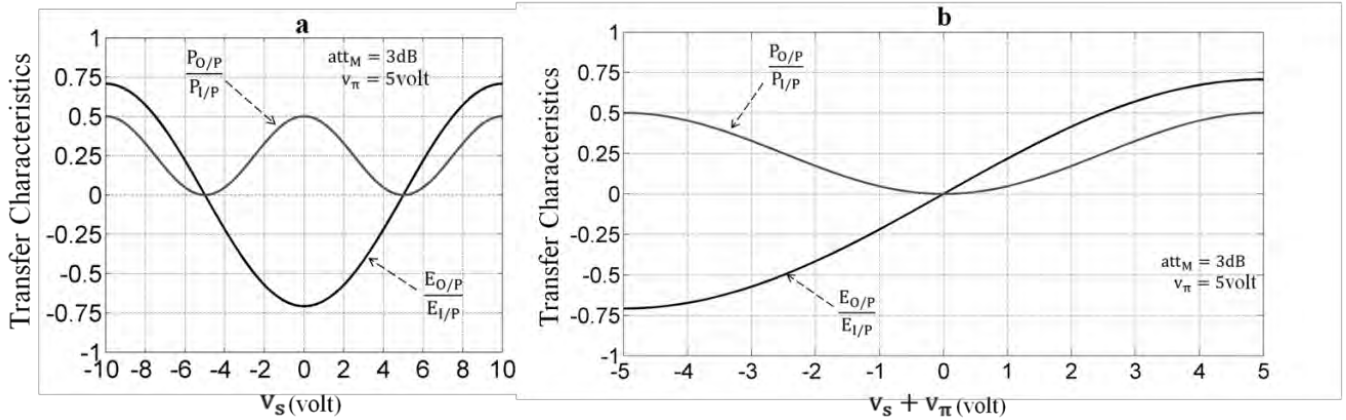
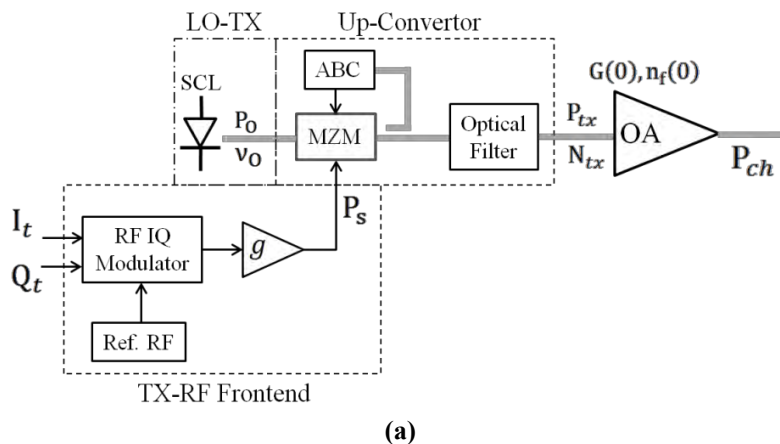


Fig. 3.9: TC of the MZM in the given example. The unbiased TC is shown in (a), and the biased TC with $v_B = v_\pi$ is shown in (b).

Thus, by substituting $v_s + v_\pi$ in v_s term of (3.37) yields

$$\frac{E_{O/P}}{E_{I/P}} = \frac{1}{\sqrt{att_M}} \cdot \sin\left(\frac{\pi}{2} \cdot \frac{v_s}{v_\pi}\right) \quad , \text{ and} \quad \frac{P_{O/P}}{P_{I/P}} = \frac{1}{att_M} \cdot \sin^2\left(\frac{\pi}{2} \cdot \frac{v_s}{v_\pi}\right) \quad (3.38)$$

Expansion of the sine function results a series of odd order IMP which cause nonlinearity penalty due to the optical modulator. Following the RF techniques, a SSB modulator can be constructed either by using one DSB-modulator with a bandpass filter (**BPF**) to bypass the required sideband and reject the other one, or two DSB modulators with 90° phase shifter [48].



(a)

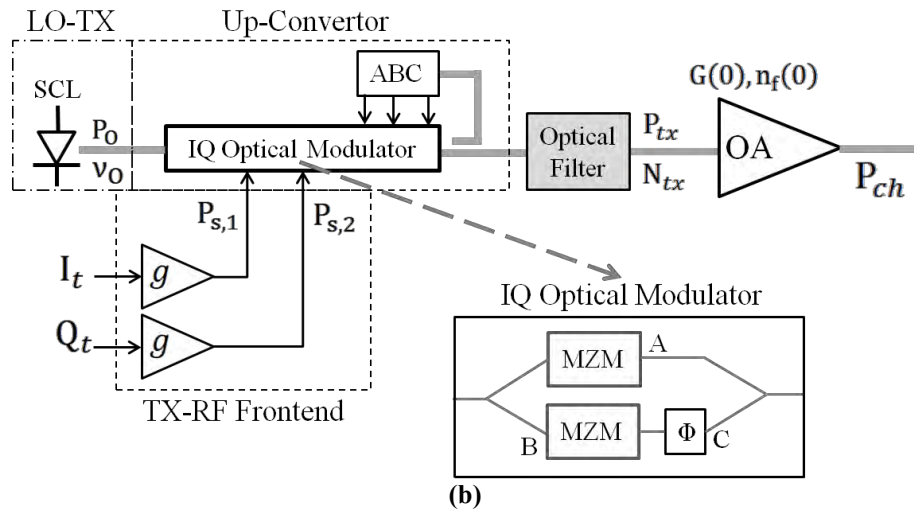


Fig. 3.10: Possible optical OFDM transmitter configurations. One MZM configuration is shown in (a), where the optical BPF is essential, and two MZMs with phase shifter is shown in (b), where the BPF can be removed. The A, B, and C are the biasing arms of the two MZMs and the phase shifter respectively.

Since the null-biased MZM is considered as a DSB modulator, the SSB implementation of optical modulator seems to be straightforward. However, \mathbf{v}_{π} , and \mathbf{att}_M are not precisely constant due to temperature fluctuations and vibrations, hence an automatic biasing circuit (ABC) is essential in long-term operation. Two possible configurations are illustrated in Fig. 3.10. The IQ optical modulator requires three biasing voltages, two for the two MZMs, and one for the optical phase shifter. The IQ modulator is commercially available either with external biasing as in Fig. 3.10b, or with the signal port via bias-tee. Note that the single MZM configuration is to some extent less complicated than the optical IQ configuration; however, it requires an UWB IQ-RF modulator, which is difficult to have a flat response over the entire band.

3.4.2 Optical down-converter

Two distinct down-conversion structures are commonly used in the receiver, which are the heterodyne and homodyne [36]. In heterodyne down-conversion configuration, the optical signal is first down converted into the intermediate frequency (IF) at a frequency of (\mathbf{f}_{IF}) and then it is demodulated as shown in Fig 3.11a. The advantages here is that a fair complexity of the optical down-conversion is required (single PD can be used instead of the balanced-detector (BD)), and can result the same performance of the homodyne detection when image-rejection optical filter is used. However, two critical issues have to

be taken into consideration such as the large IF BW, which impose state-of-the-art technologies in microwave frequencies to be used, the RF-IQ demodulator that covers the entire \mathbf{BW}_{nn} with minimal phase and amplitude errors might not be available.

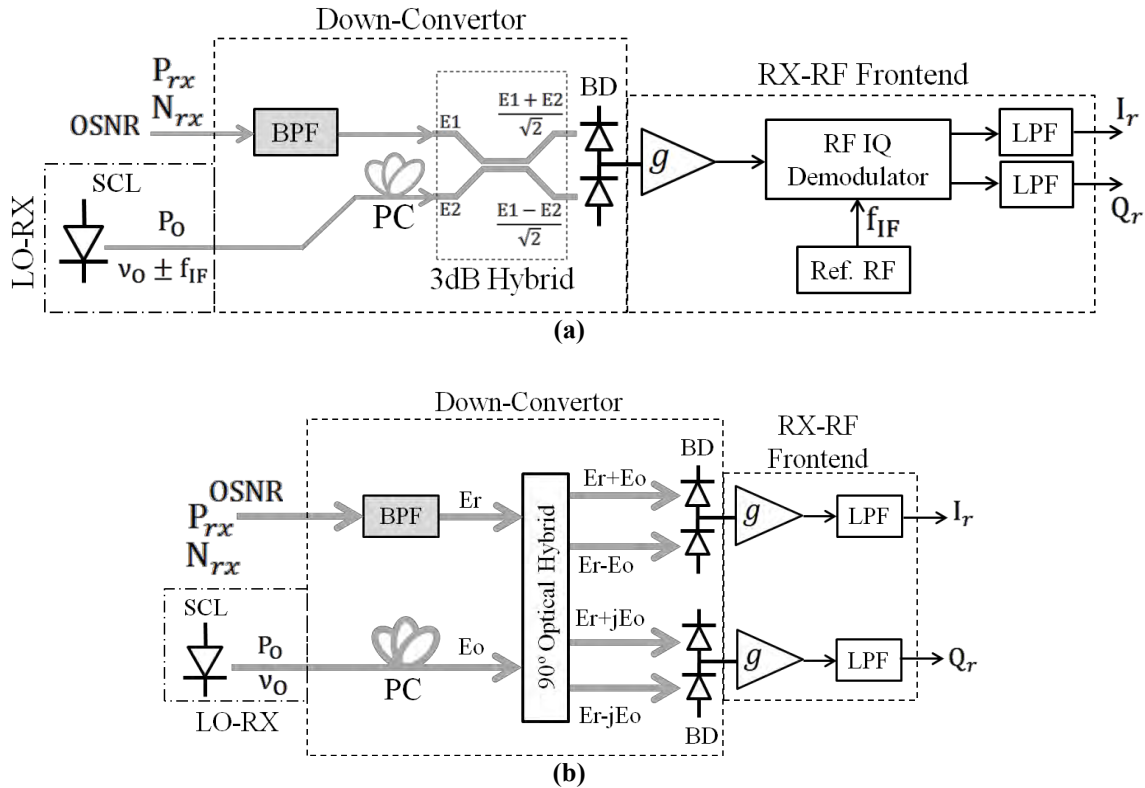


Fig. 3.11: Possible optical OFDM receiver configurations. Heterodyne detection (down-conversion) is shown in (a) with balanced-detector (BD), and Homodyne detection in (b). The BPF is not essential in both configurations.

The case becomes even more difficult when the ADC is used to directly sampled the IF frequency, due to the high F_s involved. While the main advantage of the homodyne detection, also called zero-IF detection, is that no IF frequency is required and the optical signal is directly down-converted into the BB frequency as shown in Fig. 3.11b. The critical component here is the 90° optical hybrid; however, many recently available products are less sensitive to environmental conditions. In both the heterodyne and homodyne structures, polarization control or polarization diversity (not illustrated in Fig. 3.11) is very important for long-term operation, which represents a real challenging problem for reliable coherent optical system. Note that in the conventional optical coherent DSB- SCM receiver, the SCL-LO has to be in phase locking with the incoming signal’s carrier, otherwise, the detected signal exhibits a fading effect. However, in SSB-

SCM and in OFDM, no such effect occurs, which highly simplifies receiver's design. When the received signal is not tightly filtered in optical domain, then the image noise in heterodyne detection reduces \mathbf{SNR}_b by 3-dB compared to that of homodyne detection. A new homodyne design will be discussed thoroughly in Chapter 8.

3.4.3 OSNR and \mathbf{SNR}_b

The definition of \mathbf{OSNR} in (3.3) does not give any details about $\mathbf{SNR}_b[\mathbf{k}]$, and only the average $\mathbf{SNR}_b[\mathbf{k}]$ can be calculated. This evokes two \mathbf{OSNR} definitions to be used here: first is the delivered one or (\mathbf{OSNR}_d), and second is the required one or (\mathbf{OSNR}_r). The \mathbf{OSNR}_r is based on calculation of $\mathbf{SNR}_{b,req}[\mathbf{k}]$ expressed by (3.35-a), while the \mathbf{OSNR}_d is based on link budget calculation expressed by (3.7), and results $\mathbf{SNR}_{b,del}[\mathbf{k}]$ given in (3.35-b). Since a generalized \mathbf{OSNR}_r expression might not be possible due to the variety of OFDM's signal configurations and mapping, only one important case is analyzed here, and a special case will be discussed in Chapter 8. In this common case, m is assumed to be equal for all the modulated-SCs, and the condition of $\Delta\mathbf{SNR}_{b,req} \leq \epsilon_{SNR}$ is fulfilled. Now since all \mathbf{k} -independent penalties are included in $\mathbf{SNR}_{b,req}$ expression given by (3.35-a), then, the received signal power \mathbf{P}_{rx} is assumed to be the overall modulated-signal power. Now since only \mathbf{BW}_{nT} is counted in \mathbf{SNR}_b calculation, then \mathbf{BW}_{nT} is compared with \mathbf{B}_{ref} . Besides, the ASE noise in (3.3) is of the two orthogonal polarizations, and hence when polarization control is employed at the receiver, half of the received ASE noise is rejected. Hence, noise power per SC is calculated as

$$\sigma_n^2 = \frac{N_{rx}|_{B_{ref}}}{B_{ref}} \cdot \frac{\mathbf{BW}_{nT}}{N} \cdot \frac{1}{\delta_{pol}} \quad (3.39)$$

From the above assumption we have $\mathbf{P}_{SC}[\mathbf{k}] = P_{SC} = P_{rx}/N$, and since

$$\mathbf{SNR}_b = \frac{P_{SC}/m}{\sigma_n^2}, \text{ and } \mathbf{SNR}_{b,req} = \left\{ \frac{P_{rx}/N}{m} \right\} / \left\{ \frac{N_{rx}|_{B_{ref}}}{B_{ref}} \cdot \frac{\mathbf{BW}_{nT}}{N} \cdot \frac{1}{\delta_{pol}} \right\}, \text{ hence}$$

$$\mathbf{OSNR}_r = \mathbf{SNR}_{b,req} \cdot \left(\frac{\mathbf{BW}_{nT}}{B_{ref}} \right) \cdot \frac{m}{\delta_{pol}} \quad (3.40)$$

where $\delta_{pol} = \begin{cases} 1, & \text{in polarization multiplexing (Pol-Mux)} \\ 2, & \text{in single polarization transmission, and tight polarization control.} \end{cases}$

For example, suppose an OFDM system with single polarization 16-QAM, $N_{\mathcal{F}} = 256$, $N_{\mathcal{CP}} = 16$, $N = 180$, $N_p = 4$, $F_S = 10\text{GHz}$, $M_{dt} = 64$, $M_{tr} = 2$, $\alpha_{\text{FEC}} = 0.9373$, pilot-SC power is 1.5 times the modulated-SC's power, the targeted $\text{BER} = 10^{-3}$, and only PEN_{oh} is counted. Thus $m = 4$, $\delta_{\text{pol}} = 2$, $B_{\text{ref}} = \underline{12.5\text{GHz}}$, $\text{BW}_{nT} = N/T_{\mathcal{F}} = N \cdot F_S/N_{\mathcal{F}} \approx \underline{7\text{GHz}}$, $\text{PEN}_{\text{oh}} = (1 + M_{tr}/M_{dt})(1 + N_{\mathcal{CP}}/N_{\mathcal{F}}) \left(1 + \sum_{r=1}^{N_p} P_p[r]/\sum_{k=1}^N P_{\text{SC}}[k]\right) \approx \underline{1.132}$. The only left term is $\text{SNR}_{\text{b}}\{\text{BER}, m\}$ in (3.35-a). Thus from (3.36-b), we get $10^{-3} \approx (3/8) \cdot \text{erfc}\{\sqrt{2 \cdot \text{SNR}_{\text{b}}/5}\}$, which yields $\text{SNR}_{\text{b}}\{10^{-3}, 4\} \approx \underline{11.2}$ (10.5dB). Therefore $\text{SNR}_{\text{b,req}} = \text{SNR}_{\text{b}}\{10^{-3}, 4\} \cdot \text{PEN}_{\text{oh}} = 11.2 \times 1.132 = \underline{12.678}$. From (3.40) yields $\text{OSNR}_{\text{r}} \approx \underline{14.2}$ (11.52dB). The maximum I/P bit-rate in this example can be determined from (3.25), thus $R_{\text{b}} \approx 24\text{Gbps}$. By making $\text{OSNR}_{\text{r}} = \text{OSNR}_{\text{d}}$ which is calculated from (3.7), the maximum reach for a given launch power can be estimated. By assuming the EDFA's noise figure of $n_{\text{F,dB}} = 6\text{dB}$, total attenuation per span is $\text{att}_{\text{dB}} = 20\text{dB}$ for 80km span, and EDFA's gain G equals span's loss, then from (3.7), the maximum number of spans M_{s} is $M_{\text{s}} \approx 10$ for $P_{\text{ch,dBm}} = -10\text{dBm}$, which corresponds to maximum reach of 800km, and $M_{\text{s}} \approx 34$ for $P_{\text{ch,dBm}} = -5\text{dBm}$, which corresponds to maximum reach of 2720km. Generally these results are to some extent optimistic since PEN_{oh} is usually higher than the given value since for instance $N_{\mathcal{CP}}$ is set to be higher as distance increases, the other penalties are not counted, ideal detection is assumed, and relatively low data-rate is used.

3.5 Conclusions

In this chapter, discussion of OFDM system considerations and components has been given to establish the necessary foundations for CO-OFDM design in Chapter 8. The main results of this chapter are the overall optical channel response expressed by (3.13), a detailed analysis of PMD phenomenon, the OSNR_{d} expressed by (3.4), (3.5), and (3.7), the mean OSNR_{r} expressed by (3.35-a), and (3.40), maximum R_{b} expressed by (3.25), overhead penalty PEN_{oh} expressed by (3.26), DAC/ADC requirements and equalization techniques, Anti-Aliasing filtering requirements, RF frontend requirements, and up/down conversion possible structures for CO-OFDM.

Chapter 4

Characteristics and Measurement Methods of Semiconductor Laser

4.1 Introduction

In this chapter, generalized characteristics of the semiconductor laser (SCL) are investigated to develop Simulink[®] functional model that will be used throughout this work. The analyses and measurement methods introduced here are essential in the construction and validation of SCL's functional model. The main goals of this chapter are

- To obtain the exact power spectral density (PSD) of SCL field in optical domain (OD) and in the delayed self-heterodyne (DSH) test.
- To investigate effect of the flicker frequency noise (FN) in relatively short delay.
- To estimate the beat-note center frequency fluctuations when the measurement time is much longer than a reference chosen time.

Fulfilling these goals will facilitates performance estimation of OFDM system in the next chapters.

4.2 Characteristics of SCLs

4.2.1 Lasing condition and basic characteristics

The basic structure of Fabry-Perot SCL is shown in Fig. 4.1a. The P-N junction produces charge pairs at the barrier of the active region spontaneously and by current injection.

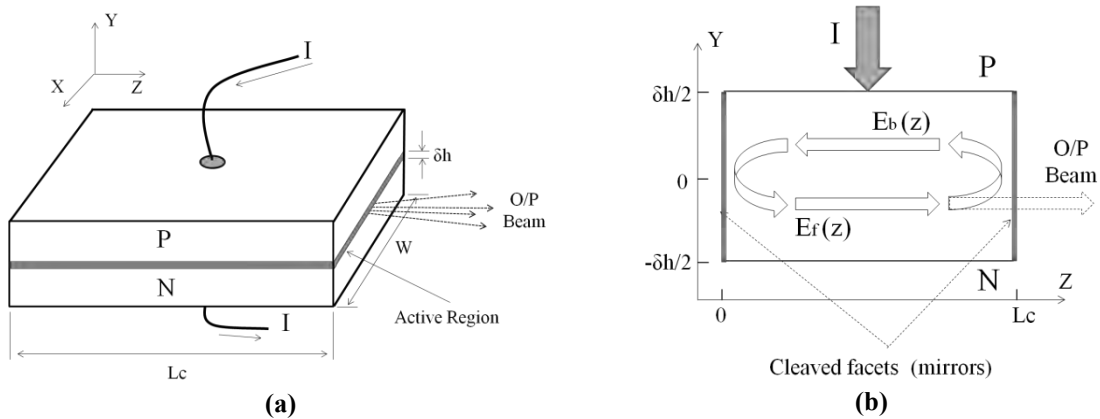


Fig. 4.1: Fabry-Perot SCL basic structure in (a), and the cavity model in (b). Where L_c is cavity length, $E_f(z)$ and $E_b(z)$ are the forward and backward (reflected) field respectively.

The active region effectively confines the charge pairs (due to its small thickness $\delta h = 0.1\text{-}0.2\mu\text{m}$) and forces the recombination process to take place within it as well as it serves as a waveguide for the generated light [31]. The oscillation is started when the round trip intensity of the generated light equals its initial intensity at a specific point in the Z-axis [83], which is the case when the optical gain equals the total loss of the cavity as illustrated in Fig 4.1b. Referring to [31], the oscillation condition and possible mode frequencies are given by

$$g_{\text{th}} = \alpha_{\text{att}} + \frac{1}{Lc} \ln\left(\frac{1}{r_1 \cdot r_2}\right) \quad (4.1\text{-a})$$

$$f_0 = m_d \cdot \frac{c}{2n_r Lc} \quad (4.1\text{-b})$$

where m_d is an integer, c is the light speed (3×10^8 m/s), n_r (≈ 3.5) is the refractive index of the cavity, r_1 and r_2 are the front and back facets' reflectivities (≈ 0.55), α_{att} is total cavity loss, g_{th} is the threshold gain, and $\ln(\)$ is the natural logarithm.

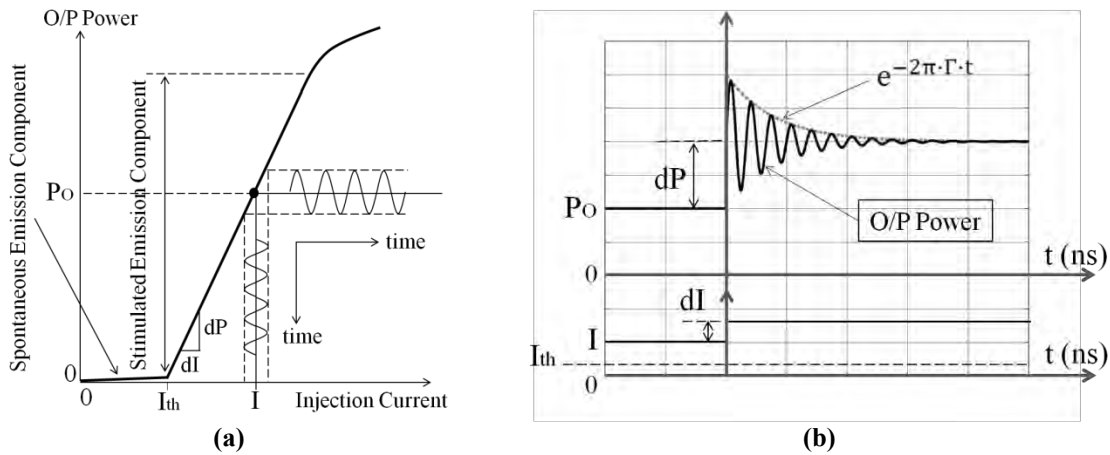


Fig. 4.2: Transfer characteristics of the SCL in (a), and the transient response of a unit step in (b).

The mode spacing is about 100-200GHz for $Lc = 200\text{-}400\mu\text{m}$, and hence tens of modes are expected to be produced for the typical gain-bandwidth of InGaAsP of 12THz unless frequency selective loss is introduced into the cavity such as in distributed-feedback laser [31]. The transfer characteristic of SCL exhibits three distinct regions which are the spontaneous emission, stimulated emission, and saturation region as shown in Fig. 4.2a [31]. The modulation characteristics of the SCL are measured by superimposing the modulating signal with a constant injection current via the driving circuit as in Fig. 4.2 [31]. In the step response, laser field exhibits a damped oscillation with oscillation

frequency of \mathbf{F}_R and damping factor of $2\pi\Gamma$ in (rad/s) as shown in Fig. 4.2-b. The use of the SCL for direct intensity modulation (**IM**) with bandwidth (**BW**) up to $1.2 \times \mathbf{F}_R$ was attractive in earlier works, however, the injected current also induces frequency modulation (**FM**) or chirp, and the driving circuit has usually a limited response making the use of external optical modulator more practical [84].

4.2.2 Main results from rate equations

Solutions of the rate equation (Appendix-A9) are thoroughly discussed in [31], [85], [86], and hence only the main results are demonstrated here, focusing on well above-threshold operating condition. The output (**O/P**) field of SCL can be expressed as

$$E(t) = \sqrt{P_0} \cdot \exp(j2\pi\nu_0 t + j\phi_n(t) + \alpha_n(t)) \quad (4.2)$$

where \mathbf{P}_0 is O/P power, ν_0 is the optical frequency ($\approx 193.5\text{THz}$), $\phi_n(t)$ and $\alpha_n(t)$ are the phase noise (**PN**) and normalized intensity noise (**IN**) terms in time domain (**TD**) respectively, and $\exp(\)$ or $e^{(\)}$ is the exponential function and both forms are used interchangeably. Here $\phi_n(t) = \int_{-\infty}^t \omega_n(\lambda) d\lambda$, where $\omega_n(t)$ is the FN in (rad/s). This can be written in frequency domain (**FD**) by using integration property of the Fourier transform (\mathcal{FT}) [87]. Then the single-sided (**SS**) PSD of the PN in (rad^2/Hz) is $\mathbf{S}_{\phi_n,SS}(f) = S_{\omega_n}(f)/(2\pi f)^2$, or

$$S_{\phi_n,SS}(f) = S_{fn}(f)/f^2 \quad (4.3)$$

where $\mathbf{S}_{\omega_n}(f)$ and $\mathbf{S}_{fn}(f)$ are FN SS-PSD in $((\text{rad/s})^2/\text{Hz})$, and (Hz^2/Hz) respectively. SCL's FN, just like radio-frequency (**RF**) oscillators, follows the power law noise process ($1/f^X$) having a white ($X = 0$), a flicker ($X \approx 1$), and a random-walk components ($X \approx 2$) due to the spontaneous emission, driving circuit noise, temperature fluctuations, and mechanical vibrations [88].

According to Henry's model, the white FN is generated from two uncorrelated real Gaussian random noise sources due to the spontaneous emission [89]. The IN component fluctuates laser's amplitude, which in turn, causes phase fluctuation (PN is enhanced), and hence the instantaneous white FN in (rad/s) is given by [90]

$$\omega_{nW}(t) = d\phi_{nW}(t)/dt = \left(N_f(t) - \alpha \cdot N_i(t) * h_c(t) \right) / \sqrt{P_0} \quad (4.4)$$

where $*$ stands for convolution, $\Phi_{nW}(\mathbf{t})$ is PN component due to the white FN only, α is linewidth enhancement factor, $\mathbf{N}_f(\mathbf{t})$ and $\mathbf{N}_i(\mathbf{t})$ are independent real Gaussian random variables (**GRV**) with zero-means and equal variances, and $\mathbf{h}_c(\mathbf{t})$ is the impulse response of the cavity transfer function (**TF**), which describes injection current to O/P power ratio versus frequency. Note that the SCL's linewidth is broader than that predicted by Schawlow-Townes by a factor of $(1 + \alpha^2)$ which is linewidth broadening factor and results directly from the variance of (4.4) [89]. Thus the overall SCL's FN SS-PSD in (Hz^2/Hz) can be written as follows [88]

$$\begin{aligned} S_{fn}(f) &= h_W \left\{ \frac{1}{1 + \alpha^2} + \frac{\alpha^2}{1 + \alpha^2} |H_c(f)|^2 \right\} + \frac{h_F}{f} + \frac{h_R}{f^2} \\ &= \frac{\delta f}{\pi} \left\{ \frac{1}{1 + \alpha^2} + \frac{\alpha^2}{1 + \alpha^2} |H_c(f)|^2 + \frac{f_C}{f} + \frac{f_C \cdot f_{rw}}{f^2} \right\} \end{aligned} \quad (4.5)$$

where h_W , h_F , and h_R are white, flicker, and random-walk coefficients in (Hz), (Hz^2), and (Hz^3) respectively, and $H_c(f)$ is the cavity TF which is given by [31]

$$H_c(f) = \frac{F_R^2}{F_R^2 - f^2 - j2\Gamma f} \quad (4.6)$$

On the other hand the IN is characterized by $\mathbf{RIN}_L(f)$ which is the normalized SS-PSD of photo-current when laser field is directly detected by a photo diode (**PD**). From (4.2), and by ignoring shot and thermal currents, then the photo-current is

$$i_{PC}(t) = \mathcal{R} \cdot (E(t)E^*(t)) = \mathcal{R}P_O(1 + 2\alpha_n(t) + \alpha_n^2(t)) \quad (4.7)$$

where \mathcal{R} is the PD's responsivity in (mA/mW), and $*$ symbol is used for complex conjugation. If the DC and $\alpha_n^2(t)$ terms are ignored, then the auto-correlation function (**ACF**) of (4.7) is $\mathbf{R}_{i_{PC}}(\tau) = \langle i_{PC}(t)i_{PC}^*(t - \tau) \rangle = 4(\mathcal{R}P_O)^2 \cdot \langle \alpha_n(t)\alpha_n^*(t - \tau) \rangle$, where $\langle \ \rangle$ denotes to an infinite time averaging.

Let $\mathcal{S}\{X(t)\}$ denotes the PSD of any TD function $\mathbf{X}(t)$ which its \mathcal{FT} is bounded. Then from **Wiener-Khintchin theorem**, $\mathcal{S}\{X(t)\} = \mathcal{FT}\{\langle X(t) \cdot X^*(t - \tau) \rangle\}$, and hence from (4.7), $\mathcal{S}\{2\mathcal{R}P_O\alpha_n(t)\} = 4(\mathcal{R}P_O)^2 \cdot \mathcal{FT}\{\langle \alpha_n(t) \cdot \alpha_n^*(t - \tau) \rangle\}$, which is the measured PSD. As $\mathcal{FT}\{\langle \alpha_n(t)\alpha_n^*(t - \tau) \rangle\} = \mathcal{S}\{\alpha_n(t)\}$, then from the relative intensity noise (**RIN**) definition [85], the double-sided (**DS**) PSD of the IN in OD is

$$S_{IN}(f) = P_O S_{\alpha_n}(f) = P_O (\mathbf{RIN}_L(f)/8) \quad (4.8)$$

where $\mathbf{S}_{\alpha_n}(\mathbf{f}) = \mathcal{S}\{\alpha_n(t)\}$ is the normalized DS-PSD of the IN, $\mathbf{RIN}_L(\mathbf{f})$ is the SCL's measured RIN after removing shot and thermal RINs and could be fitted with the following expression [31], [91], [92]

$$\mathbf{RIN}_L(\mathbf{f}) \approx \mathbf{RIN}_L(0) \cdot \left\{ \mathbf{K}_o \frac{f^2 + \mathbf{K}_z^2}{(\mathbf{F}_R^2 - f^2)^2 + 4\Gamma^2 f^2} \right\} = \mathbf{RIN}_L(0) \cdot |\mathbf{A}_c(\mathbf{f})|^2 \quad (4.9)$$

where $\mathbf{RIN}_L(0)$ is the low frequency RIN, \mathbf{K}_z is RIN fitting coefficient, and $\mathbf{K}_o = (\mathbf{F}_R^2/\mathbf{K}_z)^2$. Here we have introduced $\mathbf{A}_c(\mathbf{f})$ as the RIN TF.

4.2.3 PSD of a single-mode SCL

PSD of the optical field is derived directly from (4.2) taking into account that white FN is correlated with $\alpha_n(\mathbf{t})$ since both are driven by the same noise source $\mathbf{N}_i(\mathbf{t})$. Thus the ACF in the OD of (4.2) is

$$\mathbf{R}_E(\boldsymbol{\tau}) = \langle E(t)E^*(t - \tau) \rangle = \mathbf{P}_o \cdot e^{j2\pi\nu_o\tau} \cdot \langle e^{(\alpha_n(t) + \alpha_n(t-\tau) + j\phi_n(t) - j\phi_n(t-\tau))} \rangle$$

Now since $\{e^{j2\pi\nu_o\tau}\}$ term is only a frequency shift in the FD [87], and \mathbf{P}_o is an amplitude shift, then we define the normalized base-band (**BB**) ACF as

$$R_{EN}(\boldsymbol{\tau}) = \langle \exp(\sum \alpha_n(t, \tau) + j\Delta\phi_n(t)) \rangle \quad (4.10)$$

where $\sum \alpha_n(\mathbf{t}, \boldsymbol{\tau}) = \{\alpha_n(t) + \alpha_n(t - \tau)\}$, and $\Delta\phi_n(\mathbf{t}) = \{\phi_n(t) - \phi_n(t - \tau)\}$. A very useful expression (derived by the author) that can be applied for any complex GRV is

$$\langle \exp(x_1(t) \pm jx_2(t)) \rangle = \exp(\langle |x_1(t)|^2 \rangle / 2 - \langle |x_2(t)|^2 \rangle / 2 \pm j\langle x_1(t)x_2^*(t) \rangle) \quad (4.11)$$

where both $\mathbf{x}_1(\mathbf{t})$, and $\mathbf{x}_2(\mathbf{t})$ are real GRVs with zero-means and finite variances. Notice that the sign of the cross term depends on the initial sign of the imaginary part, and hence positive and negative signs are expected in practice. Since both $\alpha_n(\mathbf{t})$ and $\phi_n(\mathbf{t})$ are real signals, then using Fourier transform property of real signals [87] yields

$$\alpha_n(t) = \int_0^\infty \{\alpha_n(f)e^{j2\pi ft} + \alpha_n^*(f)e^{-j2\pi ft}\} df \quad (4.12-a)$$

$$\phi_n(t) = \int_0^\infty \{\phi_n(f)e^{j2\pi ft} + \phi_n^*(f)e^{-j2\pi ft}\} df \quad (4.12-b)$$

Therefore,

$$\sum \alpha_n(\mathbf{t}, \boldsymbol{\tau}) = \int_0^\infty \{\alpha_n(f)e^{j2\pi ft} \cdot (1 + e^{-j2\pi f\tau}) + \alpha_n^*(f)e^{-j2\pi ft} \cdot (1 + e^{j2\pi f\tau})\} df, \text{ and}$$

$$\Delta\phi_n(\mathbf{t}, \boldsymbol{\tau}) = \int_0^\infty \{\phi_n(f)e^{j2\pi ft} \cdot (1 - e^{-j2\pi f\tau}) + \phi_n^*(f)e^{-j2\pi ft} \cdot (1 - e^{j2\pi f\tau})\} df.$$

Now by applying (4.11) in (4.10) and by substituting $\mathbf{x}_1(\mathbf{t}) = \sum \alpha_n(\mathbf{t}, \tau)$, and $\mathbf{x}_2(\mathbf{t}) = \Delta\phi_n(\mathbf{t}, \tau)$, yields

$$R_{\text{EN}}(\tau) = \exp\left(4 \int_0^\infty \{S_{\alpha_n}(f) \cos^2(\pi f \tau) - S_{\phi_n}(f) \sin^2(\pi f \tau) \pm S_{X_g}(f) \sin(2\pi f \tau)\} df\right) \quad (4.13)$$

where $\mathbf{S}_{X_g}(\mathbf{f}) = \{\langle \alpha_n(f) \phi_n^*(f) \rangle - \langle \alpha_n^*(f) \phi_n(f) \rangle\} / 2$

$$= \sqrt{\frac{\text{RIN}_L(0) \cdot \delta f \cdot \alpha^2}{16\pi \cdot (1 + \alpha^2)}} \cdot \left(j \frac{|\mathbf{H}_c(f)|^2}{f}\right),$$

which is the imaginary part of the cross noise PSD derived in the Appendix-A1 as (A1.8), and $\mathbf{S}_{\phi_n}(\mathbf{f})$ is the DS-PSD of $\phi_n(\mathbf{t})$. The sign of the cross term in (4.13) is identical to the imaginary part's sign in (4.10). The imaginary part in the ACF causes asymmetry in the PSD's ground floor or uneven relaxation oscillation peaks [93]. Although no exact analytical solution is possible for (4.13), it can be well approximated benefiting from the domination of PN component [89]. Let $\mathbf{S}_{\text{EN}}(\mathbf{f}) = \mathcal{FT}\{R_{\text{EN}}(\tau)\}$ be the normalized BB-DS-PSD of SCL field which is calculated from (4.5),(4.6), (4.8), (4.9), and (4.13), then the following assumptions will be examined.

4.2.3.1 PSD in OD when only the white FN is counted and $|\mathbf{H}_c(f)|^2 = 1$

If only the white FN is counted and the relaxation oscillation is ignored ($|\mathbf{H}_c(f)|^2 = 1$), then the ACF and the BB-DS-PSD are derived in Appendix-A2 and given as

$$\mathcal{L}_W(\mathbf{f}) = S_{\text{EN}}(f) = \mathcal{FT}\{R_{\text{EN},W}(\tau)\} = \frac{\delta f}{2\pi} \cdot \frac{1}{(\delta f/2)^2 + f^2} \quad (4.14-b)$$

$$R_{\text{EN},W}(\tau) = R_{\text{EN}}(\tau) = \exp(-\pi \delta f |\tau|) \quad (4.14-b)$$

This is the Lorentzian line-shape, where the full-width half-maximum (FWHM) linewidth is calculated by putting $\mathcal{L}_W(\mathbf{f}_{3\text{dB}}) = \mathcal{L}_W(0)/2$, and hence $\delta \mathbf{f}_{\text{total}} = 2f_{3\text{dB}}$, therefore $\delta \mathbf{f}_{\text{total}} = \delta f$. Now since $\mathbf{R}_E(\tau) = \langle E(t)E^*(t - \tau) \rangle = P_0 \cdot e^{j2\pi\nu_0\tau} \cdot R_{\text{EN},W}(\tau)$, and by using frequency shift property of \mathcal{FT} [87], then the DS-PSD in OD is

$$S_E(f) = \mathcal{S}\{E(t)\} = P_0 \cdot \mathcal{L}_W(\nu - \nu_0) \quad (4.15)$$

where ν is the optical frequency. Note that we use f to indicate the BB frequency as $\{f = \nu - \nu_0\}$, as well as for beat-note frequency, RF frequency and intermediate frequency (**IF**). From Appendix-A2, the differential PN for any given time-delay ΔT is

$$S_{\Delta\phi_n}(f, \Delta T) = 2\pi\delta f(\Delta T)^2 \cdot \text{sinc}^2(f \cdot \Delta T) \quad (4.16)$$

assuming the observation time (\mathbf{T}_{OBS}) tends to infinity.

4.2.3.2 PSD in OD when the IN is ignored and $|\mathbf{H}_c(f)|^2 = 1$

Kikuchi and Okoshi first observed linewidth broadening due to the flicker FN leading to the definition of linewidth residual in high power laser [94]. While the first approximation of non-Lorentzian linewidth was given by O'Mahoney as [95]

$$\delta f_{\text{total}} \approx \delta f \cdot \sqrt{1 + \frac{4.72 \cdot f_c}{\pi\delta f} \cdot \ln\left(\frac{F_u}{F_l}\right)} \quad (4.17)$$

where F_u , F_l are the upper and lower cutoff frequencies of optical discriminator which is used to measure FN. In (4.17), lower frequency components of FN are rejected due to the limited scan time corresponds to F_l , hence δf_{total} is limited by F_l . Extensive efforts have been made to describe the flicker FN phenomenon and its significance in linewidth broadening especially in the delayed self-heterodyne (**DSH**) test [96], [97], [98]. These studies conclude that SCL's line-shape fits Voigt profile which has no analytical solution, however, it is usually closer to either Lorentzian or Gaussian curve depending on δf , f_c , and \mathbf{T}_{OBS} values, and thus approximation is possible [96].

The instantaneous frequency of the SCL can be written as

$$\nu(\mathbf{t}) = \nu_0 + f_{\text{nrw}}(\mathbf{t}) + f_{\text{nF}}(\mathbf{t}) + f_{\text{nW}}(\mathbf{t}) \quad (4.18)$$

where $f_{\text{nrw}}(\mathbf{t})$, $f_{\text{nF}}(\mathbf{t})$, and $f_{\text{nW}}(\mathbf{t})$ are due to white, flicker, and random-walk FN respectively. $f_{\text{nW}}(\mathbf{t})$ and is considered as a real additive white Gaussian noise (**AWGN**) term which determines SCL's natural linewidth. $f_{\text{nrw}}(\mathbf{t})$ can be modeled as an integration of a white FN source, and results a slow and yet effective frequency fluctuations that determine long-term stability (in hours). While $f_{\text{nF}}(\mathbf{t})$ does not have a simple model since it is generated from a white source with logarithmic-time memory (integration with a logarithmic time step) [99]. From the analysis in Appendix-A3, it is clear that for limited

\mathbf{T}_{OBS} , the low frequency components of the FN are attenuated and hence the flicker noise process is stationary. We also define a \mathbf{T}_{OBS} TF as $\mathbf{H}_{\text{OBS}}(\mathbf{f}) = \{1 - \text{sinc}(\mathbf{f} \cdot \mathbf{T}_{\text{OBS}})\}$ which has a high-pass filter (**HPF**) response. However, to avoid analysis difficulties, the aforementioned TF is replaced by the following TF

$$|\mathbf{H}_{\text{OBS}}(\mathbf{f})|^2 = \begin{cases} \mathbf{T}_{\text{OBS}} \cdot \mathbf{f} & \text{for } 0 \leq \mathbf{f} < 1/\mathbf{T}_{\text{OBS}} \\ 1 & \text{for } \mathbf{f} \geq 1/\mathbf{T}_{\text{OBS}} \end{cases} \quad (4.19)$$

Although \mathcal{FT} of the flicker FN for limited \mathbf{T}_{OBS} exists, which indicates a stationary process, different phase combinations of the flicker's frequency components produce different mean frequency-shift during the measurement time, and different phase variances per sample. Besides, this phase variance depends also on time instant at which measurement is conducted. Let $\boldsymbol{\tau}$ be an arbitrary time-delay such that $[0 \leq \boldsymbol{\tau} \leq \mathbf{T}_{\text{OBS}}]$, then we define

$$\Delta\phi_{\text{nF}}(\mathbf{t}, \boldsymbol{\tau}, \mathbf{T}_{\text{OBS}}) = \phi_{\text{nF}}(\mathbf{t}, \mathbf{T}_{\text{OBS}}) - \phi_{\text{nF}}(\mathbf{t} - \boldsymbol{\tau}, \mathbf{T}_{\text{OBS}}) \quad (4.20)$$

A simulation is conducted to investigate the flicker FN in TD and the following features were confirmed:

- 1- $\overline{\Delta\phi_{\text{nF}}^2(\mathbf{t}, \boldsymbol{\tau}, \mathbf{T}_{\text{OBS}})}$ changes depending on the time instant at which the test is conducted, or at $\mathbf{t} = \mathbf{t}_0$ for a given seed (sample function \mathbf{U}), however, $E\{\overline{\Delta\phi_{\text{nF}}^2(\mathbf{t}, \boldsymbol{\tau}, \mathbf{T}_{\text{OBS}})}\}$ is independent of \mathbf{t}_0 , and \mathbf{U} , where $E\{\ \}$ is the expectation of any given random variable (**RV**).
- 2- In every run we obtain different frequency shifts $\overline{\Delta\phi_{\text{nF}}(\mathbf{t}, \boldsymbol{\tau}, \mathbf{T}_{\text{OBS}})}$ at the end of \mathbf{T}_{OBS} , which also \mathbf{U} and \mathbf{t}_0 dependence. However, this offset can be ignored.
- 3- The ACF of laser's field due to flicker FN only, is exactly equal $\exp(-\sigma_{\Delta\phi_{\text{nF}}}^2(\boldsymbol{\tau}, \mathbf{T}_{\text{OBS}})/2)$, which can fit (to some extent) a Gaussian profile [96].
- 4- The PSD shape is independent of \mathbf{U} or \mathbf{t}_0 , except that a different frequency shift is observed as discussed in Point 2.
- 5- $\mathbf{H}_{\text{OBS}}(\mathbf{f})$ can only be applied at the flicker FN term. This is true since the PSD of this term depends on \mathbf{T}_{OBS} .

Now from the variance definition [48],

$$\overline{\Delta\phi_{\text{nF}}^2(\mathbf{t}, \boldsymbol{\tau}, \mathbf{T}_{\text{OBS}})} = \sigma_{\Delta\phi_{\text{nF}}}^2(\boldsymbol{\tau}, \mathbf{T}_{\text{OBS}}) + \overline{\{\Delta\phi_{\text{nF}}(\mathbf{t}, \boldsymbol{\tau}, \mathbf{T}_{\text{OBS}})\}^2},$$

and since in Appendix-A3 we have assumed that $\overline{\Delta\phi_{nF}(t, \tau, T_{OBS})} = 0$, then by using (4.3), (4.5), (4.20), and (B2.2) in Appendix-A2 yields

$$\begin{aligned} \sigma_{\Delta\phi_{nF}}^2(\tau, T_{OBS}) &= \int_0^{\infty} 4 \sin^2(\pi f \tau) \cdot S_{\phi_{nF}}(f, T_{OBS}) \cdot H_{OBS}(f) df = \\ 4\pi\delta f \cdot f_C \tau^2 \cdot &\left\{ T_{OBS} \cdot \int_0^{(1/T_{OBS})} \text{sinc}^2(f\tau) df + \int_{(1/T_{OBS})}^{\infty} \frac{\text{sinc}^2(f\tau)}{f} df \right\}, \text{ which results} \\ \sigma_{\Delta\phi_{nF}}^2(\tau, T_{OBS}) &= 4\pi\delta f \cdot f_C \tau^2 \cdot Z(\tau_n) \end{aligned} \quad (4.21)$$

where $Z(\tau_n) = \text{sinc}(2\tau_n) - \frac{1}{2} \text{sinc}^2(\tau_n) + \frac{1}{\pi\tau_n} Si(2\pi\tau_n) - Ci(2\pi\tau_n)$, and

$$\tau_n = |\tau|/T_{OBS}.$$

Here Si , and Ci are sine and cosine integral [81]. In order to avoid the use of Si and Ci functions which are cumbersome functions, we resort to an approximated formula as

$$Z(\tau_n) \approx -\ln(\tau_n) + 0.0849 \quad (4.22)$$

which is applied for $[0 \leq \tau_n \leq 0.01]$, with an error $\leq \pm 10^{-6}$. Therefore the normalized BB-ACF due to flicker FN only is given by

$$R_{EN,F}(\tau) = \exp(-2\pi\delta f \cdot f_C \tau^2 \cdot Z(\tau_n)) \quad (4.23)$$

By using (4.22) without the **0.0849** factor, then the BB-DS-PSD due to flicker FN only is

$$\mathcal{L}_F(\mathbf{f}) = \mathcal{F}\mathcal{T}\{R_{EN,F}(\tau)\} = \mathcal{F}\mathcal{T}\{e^{-2\pi\delta f \cdot f_C \tau^2 \cdot Z(\tau_n)}\} \approx \mathcal{F}\mathcal{T}\{(\tau_n)^{2\pi\delta f \cdot f_C \tau^2}\} \quad (4.24)$$

Again, (4.24) does not have a simple $\mathcal{F}\mathcal{T}$ expression. The exact analytical solution is only obtained by series expansion which will not show clearly the effect of f_C , and T_{OBS} on linewidth estimation. From (4.14-b), and (4.23), the total normalized BB-ACF is

$$R_{EN}(\tau) = R_{EN,W}(\tau) \cdot R_{EN,F}(\tau) = \exp(-\pi\delta f |\tau| - 2\pi\delta f \cdot f_C \tau^2 \cdot Z(\tau_n)) \quad (4.25)$$

Therefore $\mathbf{S}_{EN}(\mathbf{f})$ is expressed as

$$\mathbf{S}_{EN}(\mathbf{f}) = \mathcal{F}\mathcal{T}\{R_{EN}(\tau)\} = \mathcal{L}_F(\mathbf{f}) * \mathcal{L}_W(\mathbf{f}) \quad (4.26)$$

Since an analytical solution is not possible, a fast Fourier transform ($\mathcal{F}\mathcal{F}\mathcal{T}$) can be used for $\mathbf{S}_{EN}(\mathbf{f})$ calculations with a sampling frequency (\mathbf{F}_S), and $\mathcal{F}\mathcal{F}\mathcal{T}$ length \mathbf{N}_F , are chosen for best accuracy. Usually the flicker FN is expressed by \mathbf{h}_F , which is independent of the white part; however, from (4.5), $\mathbf{h}_F = \delta f \cdot f_C / \pi$ and when δf changes (by driving current

for instant), \mathbf{f}_C also changes keeping \mathbf{h}_F constant. An approximate formula is obtained for the FWHM and the 6dB-down linewidth based on curve fittings with < 5% error as

$$\frac{\delta f_{\text{total}}}{\delta f} \approx 1 + \ell n(1 + f_{\text{CN}}\{\sqrt{\pi}\ell n(T_{\text{OBS}}) + \pi^3\}) + \left(\frac{\ell n(T_{\text{OBS}})}{2\pi} + \sqrt{2\pi}\right) f_{\text{CN}} \quad (4.27-a)$$

$$\begin{aligned} \frac{\delta f_{\text{total-6dB}}}{\delta f} \approx & \sqrt{3} + \ell n(1 + f_{\text{CN}}(2\sqrt{2}\ell n(T_{\text{OBS}}) + 4\pi^2)) \\ & + \left(\frac{\ell n\{T_{\text{OBS}}\}}{2\sqrt{3}} + 3\sqrt{3}\right) f_{\text{CN}} \end{aligned} \quad (4.27-b)$$

where $\mathbf{f}_{\text{CN}} = f_C/\delta f$, is the normalized corner frequency.

Equation (4.27-a) slightly overestimates the linewidth value compared with (4.17). We expected earlier that when both equations in (4.27) are solved simultaneously, then the unknowns can be obtained (δf , and \mathbf{f}_C) and no need for separate FN measurement. However, the slight error in (4.27) results an effective error in the simultaneous solution, and hence separate FN measurement is still required.

4.2.3.2.1 Numerical calculations

A single-mode SCL is examined here by calculating its line-shape in OD, its ACF, and the dependency of its linewidth value on \mathbf{T}_{OBS} , δf , and \mathbf{f}_C . Assuming $\delta f = 5\text{MHz}$, and $\mathbf{F}_S = 320\text{MHz}$ as constants while \mathbf{f}_{CN} , and \mathbf{N}_F are changed. In the first calculations, the ACF is demonstrated due to the flicker term first or $\mathbf{R}_{\text{EN,F}}(\tau)$ with, $\mathbf{f}_{\text{CN}} = [0.002, 0.005, 0.01, 0.05, 0.1]$, and $\mathbf{T}_{\text{OBS}} = 2^{19} / \mathbf{F}_S = 1.6\text{ms}$, which as shown in Fig. 4.3a, can fit a Gaussian profile. Next the ACFs due to white, flicker, and overall are calculated with $\mathbf{f}_{\text{CN}} = 0.2$, and $\mathbf{T}_{\text{OBS}} = 1.6\text{ms}$ as shown in Fig. 4.3b. Note that \mathbf{T}_{OBS} could be considered as the sweep time of spectrum analyzer (SA) used in the measurement or, $\{\mathbf{T}_{\text{OBS}} = \mathbf{F}_S/\mathbf{N}_F = 1/\text{RBW}\}$, where \mathbf{RBW} is the resolution bandwidth (BW). In the next example, the DS-PSD is calculated for different \mathbf{f}_{CN} with fixed \mathbf{T}_{OBS} . We assume $\mathbf{T}_{\text{OBS}} = 1.6\text{ms}$, and $\mathbf{f}_{\text{CN}} = [0.01, 0.09, 0.2]$ as shown in Fig. 4.4a, 4.4b, and 4.4c. The last example demonstrates δf_{total} as a function of \mathbf{f}_{CN} for different \mathbf{T}_{OBS} , and δf_{total} as a function of $\ell n(\mathbf{T}_{\text{OBS}})$ for different \mathbf{f}_{CN} . The \mathcal{FFF} size is chosen to be $\mathbf{N}_F = [2^{12}, 2^{13}, 2^{14}, 2^{15}, 2^{16}, 2^{17}, 2^{18}, 2^{19}, 2^{20}, 2^{21}, 2^{22}]$ corresponding to $\mathbf{T}_{\text{OBS}} = [12.8\mu\text{s} - 13.1\text{ms}]$, and $\mathbf{f}_{\text{CN}} = [0.0004 - 1]$ corresponding to $\mathbf{h}_F = [0.64 \times 10^9 - 8 \times 10^{12}] \text{Hz}^2$ as shown in Fig. 4.5.

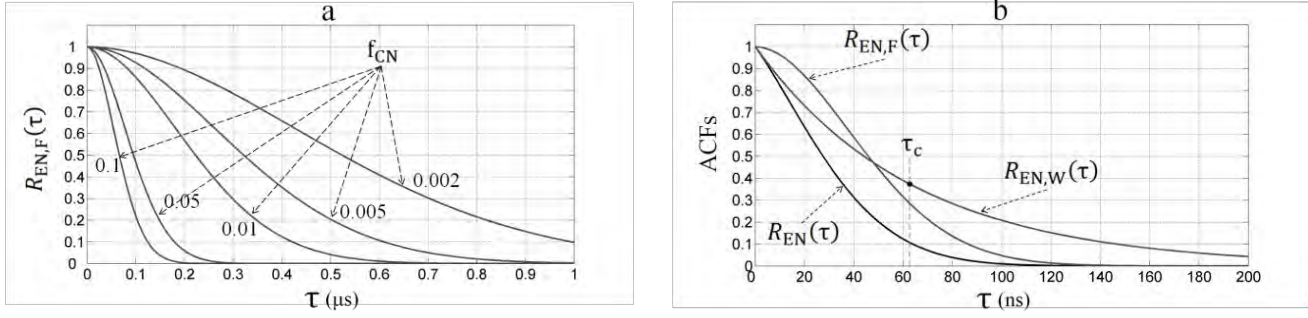


Fig. 4.3: Calculated ACF of SCL field. ACF due to the flicker FN only for different f_{CN} is shown in (a), while in (b), ACF of the flicker, white, and overall, with $f_{CN} = 0.2$. $T_{OBS} = 1.6\text{ms}$. $\tau_c = 1/(\pi\delta f)$ is coherence time of the white FN.

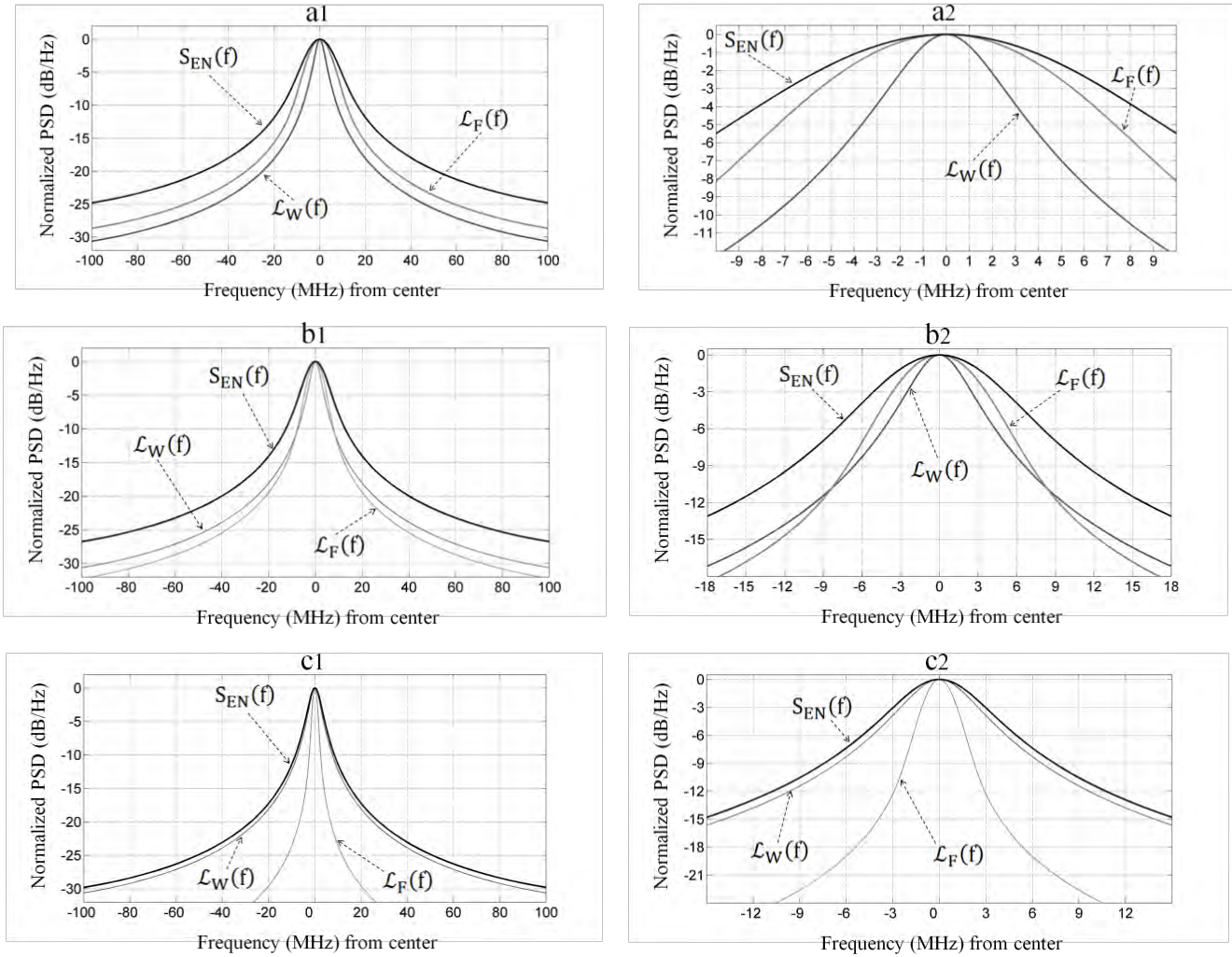


Fig. 4.4: Normalized calculated PSD due to white FN component $L_W(f)$, due to flicker FN component $L_F(f)$, and the overall $S_{EN}(f)$ for different values of f_{CN} . In (a1) and (a2), $f_{CN} = 0.2$ ($h_F \approx 1.6 \times 10^{12}$) showing the flicker effect is dominant. In (b1) and (b2), $f_{CN} = 0.09$ ($h_F \approx 7 \times 10^{11}$). In (c1) and (c2), $f_{CN} = 0.01$ ($h_F \approx 8 \times 10^{10}$), where the white is dominant. Here $F_s = 100\text{MHz}$, and $T_{OBS} \approx 42\text{ms}$.

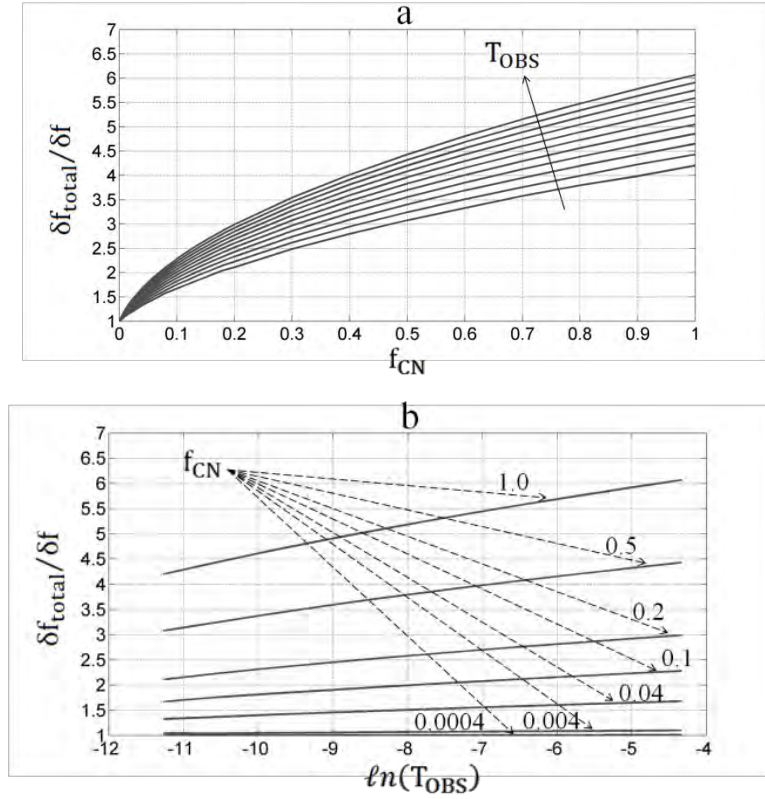


Fig. 4.5: Calculated FWHM linewidth normalized to the natural linewidth (due to white FN only) as a function of f_{CN} and T_{OBS} . In (a), $T_{\text{OBS}} = 12.8\mu\text{s} - 13.1\text{ms}$. In (b), almost linear relationship between δf_{total} and $\ln(T_{\text{OBS}})$.

Some observations from these calculations are listed below.

- The normalized ACF due to the flicker FN or $R_{\text{EN},F}(\tau)$ can fit Gaussian profile provided that $R_{\text{EN},F}(\tau = T_{\text{OBS}}) \rightarrow 0$, which results a Gaussian $\mathcal{L}_F(f)$.
- The calculated total linewidth is significantly wider than the natural one especially at large f_{CN} , and T_{OBS} values, which indicates large PN variance.

4.2.3.2.2 Mixed-field linewidth

When two SCLs are mixed in a photo diode (PD), then the net FN-SS-PSD is the sum of their individual FN-SS-PSDs assuming their FNs are zero-mean GRVs [100]. Therefore from (4.5),

$$S_{\text{fn}}(f) = \frac{\delta f_1}{\pi} \left(1 + \frac{f_{\text{C1}}}{|f|}\right) + \frac{\delta f_2}{\pi} \left(1 + \frac{f_{\text{C2}}}{|f|}\right) = \frac{\delta f_1 + \delta f_2}{\pi} \left(1 + \frac{\delta f_1 f_{\text{C1}}}{|f|(\delta f_1 + \delta f_2)} + \frac{\delta f_2 f_{\text{C2}}}{|f|(\delta f_1 + \delta f_2)}\right)$$

Hence

$$S_{\text{fn}}(f) = \frac{\delta f_{\text{eq.}}}{\pi} \left(1 + \frac{f_{\text{Ceq.}}}{|f|}\right) \quad (4.28)$$

where $\delta f_{eq} = \delta f_1 + \delta f_2$, and

$$f_{ceq} = \delta f_1 f_{c1} / (\delta f_1 + \delta f_2) + \delta f_2 f_{c2} / (\delta f_1 + \delta f_2).$$

Here $[\delta f_1, f_{c1}]$, and $[\delta f_2, f_{c2}]$ correspond to the first and the second SCL respectively.

Thus (4.27-a) can again be used to estimate the total linewidth when both SCLs have identical characteristics. It was estimated that $\delta f_{total-mixed}$ is bounded between $\sqrt{2}$ and 2 [96], which is confirmed here with $T_{OBS} = 0.2ms - 13.1ms$ as shown in Fig. 4.6.

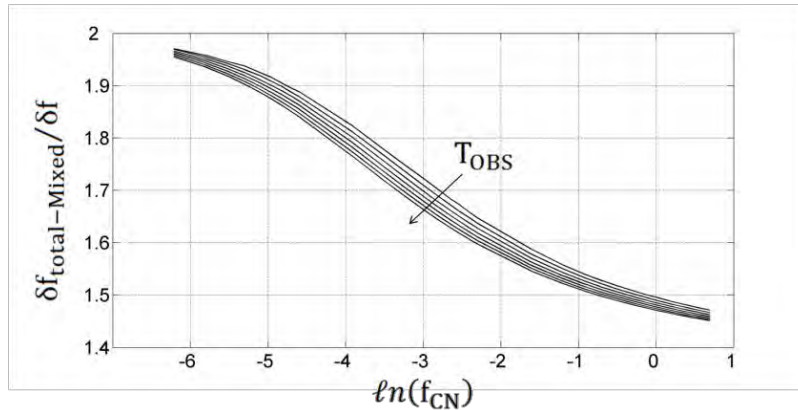


Fig. 4.6: Ratio of the mixed-field linewidth to unmixed one versus $\ln(f_{CN})$. This curve also shows the transition from Lorentzian to Gaussian characteristics. The arrow direction is towards the increase of T_{OBS} . Here both SCLs are assumed to be identical, and $T_{OBS} = 0.2ms - 13.1ms$.

4.2.3.3 PSD in OD when all parameters are counted

When all SCL's parameters are counted, then either (4.13) is solved numerically, or the following very useful features of SCL's noise are used in the approximation of (4.13)

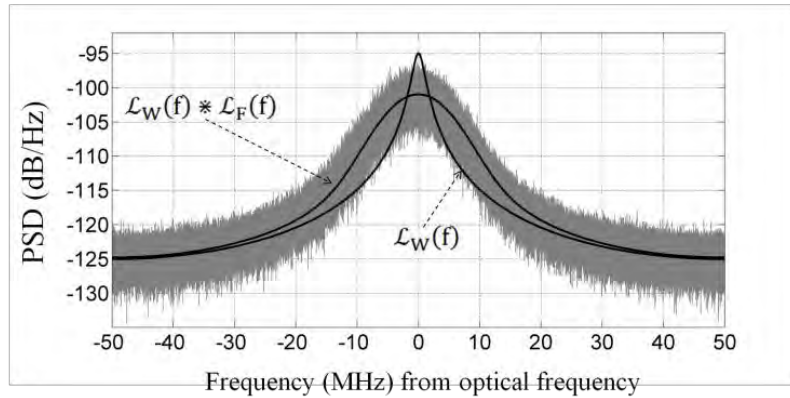
$$|H_c(f)|^2 \approx 1, \text{ and } |A_c(f)|^2 \approx 1 \dots\dots\dots f \ll F_R \tag{4.29-a}$$

$$\mathcal{L}_W(f) \approx S_{\phi_n}(f) \dots\dots\dots f \gg \delta f \tag{4.29-b}$$

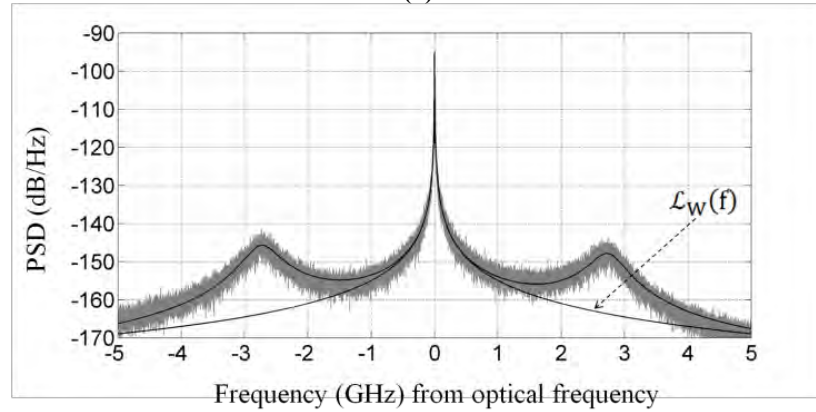
For instance, the PSD of a SCL with parameters given below is simulated using the SCL building-block introduced in Chapter 5, and calculated using (4.13) with low F_S to resolve low frequency spectral shape as shown in Fig. 4.7a, and high F_S for the relaxation oscillation monitoring as shown in Fig. 4.7b.

The SCL's parameters in the first example are $h_W \approx 0.64MHz$ ($\delta f = 2MHz$), $h_F \approx 1.27 \times 10^{12}$ ($f_C = 2MHz$), $F_R = 2.75GHz$, $\Gamma = 250MHz$, $P_O = 1mW$, $\alpha = 5$, $K_z \approx 575MHz$, $T_{obs} \approx 42ms$, and $RIN_L(0) = -140dB/Hz$. All these parameters change as the driving current changes, except h_F which is power independent [90]. The large signal is examined in the next example which is shown in Fig. 4.8 with the following

parameters $h_W \approx 32\text{MHz}$ ($\delta f = 100\text{MHz}$), $F_R = 6\text{GHz}$, $\Gamma = 500\text{MHz}$, $P_O = 1\text{mW}$, $\alpha = 5$, $K_z \approx 1.15\text{GHz}$, $T_{\text{obs}} \approx 5\mu\text{s}$, and $\text{RIN}_L(0) = -130\text{dB/Hz}$.



(a)



(b)

Fig. 4.7: Simulated and calculated DS-PSD in OD of a SCL (parameters are given in the text) showing the significance of the flicker FN when large h_F and T_{obs} values are used, with $F_S = 100\text{MHz}$ and $N_F = 2^{16}$ in (a), and $F_S = 20\text{GHz}$ and $N_F = 2^{16}$ in (b). Here $L_W(f)$ is the DS-PSD due to the white FN only.

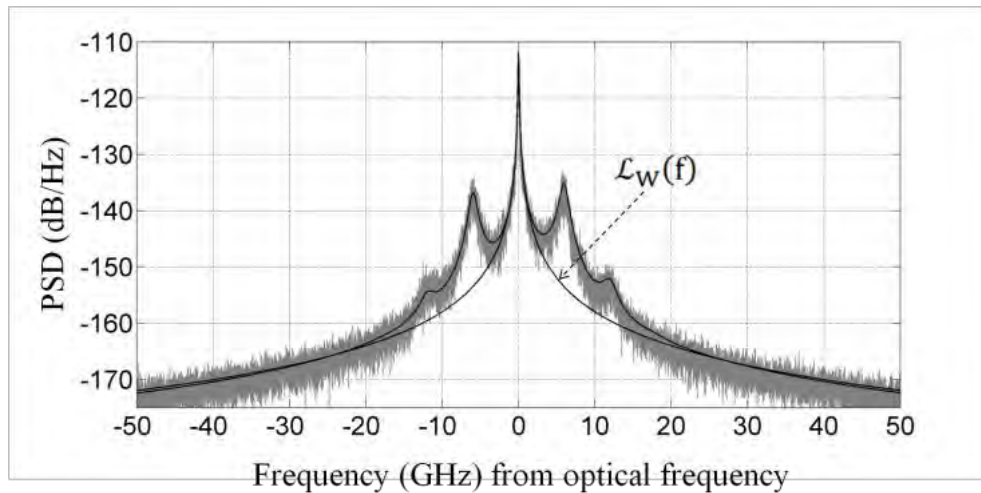


Fig. 4.8: Simulated and calculated DS-PSD in OD of a SCL with large PN and IN (parameters are given above). Here $F_S = 200\text{GHz}$ and $N_F = 2^{16}$.

Note that $\mathbf{S}_{\text{EN}}(\mathbf{f})$ exhibits a significantly broader linewidth than the natural one when \mathbf{h}_{F} and \mathbf{T}_{obs} are relatively large due to the flicker FN. A slight asymmetry can be observed in the relaxation oscillation peaks due to the cross PSD which is an odd function [101]. This asymmetry is a phenomenon that thoroughly studied in the literature [93], [101].

4.3 Measurement methods for SCLs

The common measurement methods of SCLs are demonstrated here, focusing on RIN, FN, line-shape, and time domain measurements. These measurement methods are important in validating the Simulink[®] model of the SCL in Chapter 5, and in OFDM system design in Chapter 8.

4.3.1 RIN Measurements

RIN is usually measured by direct detection of SCL field using PD setup shown in Fig. 4.9 [86], [91], [102], [103]. From (4.7), the SS-PSD in (W/Hz) of photo current after discarding the DC and $\alpha_n^2(\mathbf{t})$ terms is expressed as

$$S_{\text{PC}}(\mathbf{f}) = 4\mathcal{R}^2 P_0^2 R_L S_{\alpha_n, \text{SS}}(\mathbf{f}) + S_{\text{sh}}(\mathbf{f}) + S_{\text{th}}(\mathbf{f}) \quad (4.30)$$

where $S_{\text{sh}}(\mathbf{f}) = 2q_e I_{\text{DC}} R_L$, is SS-PSD of the shot noise,

$S_{\text{th}}(\mathbf{f}) = \mathcal{K} T^\circ n_f$, is the thermal noise SS-PSD normalized to the amplifier's gain,

R_L is load impedance (usually 50Ω),

$S_{\alpha_n, \text{SS}}(\mathbf{f})$ is the SS version of $S_{\alpha_n}(\mathbf{f})$,

q_e is electron charge (1.602×10^{-19} A·s),

\mathcal{K} is Boltzmann constant (1.38×10^{-23} W·s/K), and

n_f is noise figure of the trans-impedance amplifier's (TIA) in linear scale.

The electrical power meter is calibrated to read $I_{\text{DC}} = \mathcal{R} P_0$ as the mean current, and electrical power of $P_E = I_{\text{DC}}^2 R_L = \mathcal{R}^2 P_0^2 R_L$. From (4.30), the total RIN is expressed as

$$\begin{aligned} \text{RIN}_T(\mathbf{f}) &= S_{\text{PC}}(\mathbf{f})/P_E = \text{RIN}_L(\mathbf{f}) + \text{RIN}_{\text{sh}}(\mathbf{f}) + \text{RIN}_{\text{th}}(\mathbf{f}) \\ &= 4S_{\alpha_n, \text{SS}}(\mathbf{f}) + \frac{2q_e}{I_{\text{DC}}} + \frac{\mathcal{K} T^\circ n_f}{I_{\text{DC}}^2 R_L} \end{aligned} \quad (4.31)$$

where $\text{RIN}_L(\mathbf{f})$ is the SCL's RIN, $\text{RIN}_{\text{sh}}(\mathbf{f})$, and $\text{RIN}_{\text{th}}(\mathbf{f})$ are shot noise, and thermal noise RINs respectively. $S_{\text{th}}(\mathbf{f})$ is directly measured by terminating the amplifier's input

(I/P) to 50Ω (no signal) via an RF switch, while $\mathbf{S}_{sh}(\mathbf{f})$ is estimated from $\mathbf{S}_{sh}(\mathbf{f}) = \{2q_e I_{DC} R_L\}$, and hence $\mathbf{RIN}_L(\mathbf{f})$ is obtained, assuming a flat frequency response of the TIA and PD within the measurement band. In order to fit (4.9) with the measured spectrum, we first notice that frequency of the peak \mathbf{F}_p has a negligible difference to \mathbf{F}_R . The peak point is found from (4.9), as

$\frac{\partial}{\partial f} \mathbf{RIN}_L(\mathbf{f}) = 0$, which yields $\mathbf{F}_p = \mathbf{F}_R \cdot \sqrt{-y + \sqrt{(1+y)^2 - 4xy}}$, where $y = (K_z/\mathbf{F}_R)^2$, and $x = (\Gamma/\mathbf{F}_R)^2$. However, since $\Gamma \ll \mathbf{F}_R$ in a typical SCL [89], we assume $\mathbf{F}_p \approx \mathbf{F}_R$, and hence three points are adequate for fitting. The simplest measured points are at $\mathbf{f} = [0, \mathbf{F}_p/2, \mathbf{F}_p]$, at which the corresponding RINs and their equations are given in Table 4.1.

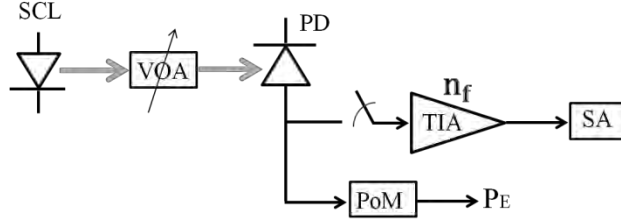


Fig. 4.9: Functional diagram of direct RIN measurement of SCL. VOA is variable optical attenuator, SA is spectrum analyzer, and PoM is an electrical power meter.

Table 4.1: Fitting (4.9) with the measured RIN.

f	0	$\mathbf{F}_p/2$	\mathbf{F}_p
$\mathbf{RIN}_{L,M}(\mathbf{f})$ (measured)	$\mathbf{RIN}_{L,M}(0)$	$\mathbf{RIN}_{L,M}(\mathbf{F}_p/2)$	$\mathbf{RIN}_{L,M}(\mathbf{F}_p)$
$\mathbf{RIN}_L(\mathbf{f})$ (Equation 4.9)	$K_o \cdot \frac{K_z^2}{\mathbf{F}_R^4}$	$K_o \cdot \frac{\mathbf{F}_R^2/4 + K_z^2}{9\mathbf{F}_R^4/16 + \Gamma^2\mathbf{F}_R^2}$	$K_o \cdot \frac{\mathbf{F}_R^2 + K_z^2}{4\Gamma^2\mathbf{F}_R^2}$
$\Delta = \frac{\mathbf{RIN}_{L,M}(\mathbf{f})}{\mathbf{RIN}_{L,M}(0)}$	$\Delta_0 = 1$	$\Delta_1 = \frac{4(1+4y)}{y(9+16x)}$	$\Delta_2 = \frac{(1+y)}{4xy}$

By solving Δ_1 with Δ_2 and then substituting $\mathbf{RIN}_L(0)$ yields

$$K_z \approx 2\mathbf{F}_R \cdot \sqrt{\frac{\Delta_2 - \Delta_1}{9\Delta_1\Delta_2 + 4\Delta_1 - 16\Delta_2}} \quad (4.32-a)$$

$$\Gamma \approx \frac{\mathbf{F}_R}{4} \cdot \sqrt{\frac{9\Delta_1 - 12}{\Delta_2 - \Delta_1}} \quad (4.32-b)$$

$$K_o = \mathbf{RIN}_L(0) \cdot \mathbf{F}_R^4 / K_z^2 \quad (4.32-c)$$

Therefore to extract \mathbf{F}_R , Γ , \mathbf{K}_z , and \mathbf{K}_o , then the required measurements are \mathbf{F}_p , \mathbf{RIN}_L at low frequencies or $\mathbf{RIN}_L(\mathbf{0})$, Δ_1 , and Δ_2 as in the example shown in Fig. 4.10.

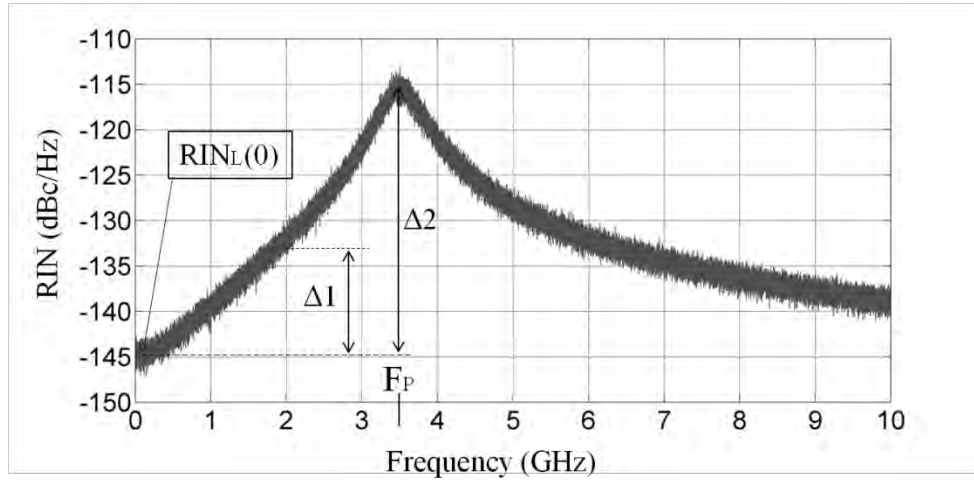


Fig. 4.10: An example of RIN simulated by SCL building-block (Chapter 5). Here $\mathbf{RIN}_L(\mathbf{0}) = -145 \text{ dBc/Hz}$ ($10^{-14.5}$), $\Delta_1 \approx 11.2 \text{ dB}$ (13.18), and $\Delta_2 \approx 29.5 \text{ dB}$ (891.25). Using (4.32), the fitting data are: $\mathbf{K}_z = 0.686 \text{ GHz}$, $\Gamma = 0.305 \text{ GHz}$, $\mathbf{F}_R \approx \mathbf{F}_p = 3.5 \text{ GHz}$, and $\mathbf{K}_o \approx 10^6$. $\mathbf{RBW} \approx 152 \text{ kHz}$.

4.3.2 FN Measurements

From (4.2), the FN can be measured by differentiating the envelope with respect to \mathbf{v}_O or with respect to beat-note frequency using a frequency discriminator either in optical or RF domain. The discriminator's (demodulator's) O/P SS-PSD or $\mathbf{S}_d(\mathbf{f})$ in either case is

$$\mathbf{S}_d(\mathbf{f}) = \eta \cdot \mathbf{S}_{\text{FT}}(\mathbf{f}) + \widetilde{\mathbf{S}}_{\text{IN}}(\mathbf{f}) \quad (4.33)$$

where: η is constant, $\mathbf{S}_{\text{FT}}(\mathbf{f})$ is total FN SS-PSD, which equals $\mathbf{S}_{\text{fn}}(\mathbf{f})$ of laser under test (LUT) if no other mixing field is used in the setup, and $\widetilde{\mathbf{S}}_{\text{IN}}(\mathbf{f})$ is the unwanted IN term. Any frequency discrimination device must have a reference frequency, which can be implemented by one of the methods given next.

4.3.2.1 FN measurements using direct method

In this method, Fabry-Perot optical resonator or the side of atomic absorption resonance are employed in the measurement with \mathbf{v}_O is tuned at the highest-slope frequency [104], [105]. The laser's FN is converted into IN and detected by a PD, and then the photocurrent is amplified and monitored by a SA as shown in Fig. 4.11.

This method is widely used in earlier work for the following reasons [90], [104]:

1) the optical discriminator usually has a wide dynamic range,

- 2) only the FN of LUT is produced without interfering with other FN sources,
- 3) T_{OBS} can very long, and
- 4) it does not require polarization controller (**PC**).

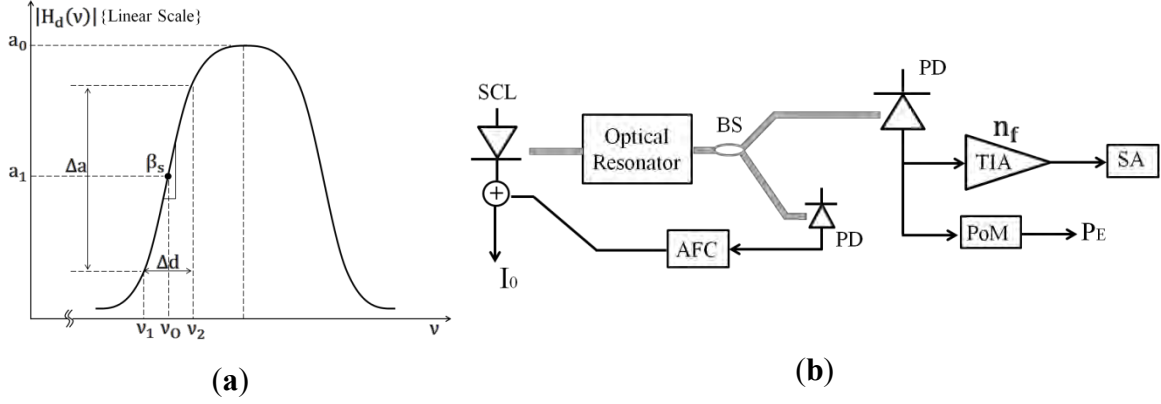


Fig. 4.11: Direct FN measurement of SCLs. In (a), resonator's TF and the optimum position of laser's frequency ν_0 is shown, while in (b), test setup with automatic frequency correction (AFC) to adjust ν_0 either by current injection or thermally [90]. Here **BS** is beam splitter.

However, $\widetilde{S}_{IN}(f)$ impairs the accuracy, besides, continuous frequency correction using an automatic frequency correction (AFC) is required to keep ν_0 at maximum slope point. Referring to Appendix-A4, the measured SS-PSD of photo current after scaling is

$$S_{fn}(f)_m \approx S_{fn}(f) + \left(\frac{a_1}{\beta_s}\right)^2 S_{\alpha_n, SS}(f) + \left(\frac{a_1}{\beta_s}\right) \sqrt{\left(\frac{\delta f}{\pi}\right) RIN_L(0) \left(\frac{\alpha^2}{1 + \alpha^2}\right) \cdot |H_c(f)|^2} + \frac{S_{sh}(t) + S_{th}(t)}{(2\mathcal{R}P_0 a_1 \beta_s)^2} \quad (4.34)$$

where $\beta_s = (\Delta a / \Delta d)$ is the slope of the discriminator at $\nu = \nu_0$ as shown in Fig. 4.11a, a_1 is the normalized amplitude at $\nu = \nu_0$. Here a_1 is calculated as, $a_1 = 10^{-\{\text{att}(\nu_0)_{dB}/20\}}$, where $\text{att}(\nu_0)_{dB}$ is attenuation at $\nu = \nu_0$. Equation (4.34) is valid assuming the measurement BW is much narrower than the discriminator's effective BW Δd .

4.3.2.2 FN measurements using heterodyne setup

In this method, LUT is mixed with a frequency-shifted auxiliary field which can be a highly stable reference laser or a SCL identical to LUT, or a delayed version of LUT as in the DSH test as illustrated in Fig. 4.6. FN is resolved by demodulating the beat-note and

the BB signal is then monitored by a SA [88]. The common frequency demodulators are slope discriminator (balanced), Phase-locked loop (**PLL**), and delay line discriminator.

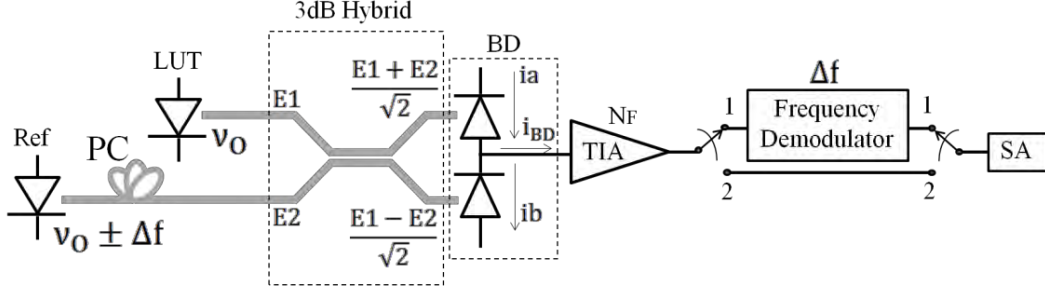


Fig. 4.12: Heterodyne FN measurement of SCLs with BD and external reference laser (Ref). FN is measured when the switch is at position (1) and spectrum shape is measured at position (2). Here **PC** is polarization controller, **BD** is balanced detector.

From Fig. 4.12, the photo-current in the balanced detector (**BD**) setup is $i_{BD}(t) = \{i_a(t) - i_b(t)\}$ which has an advantage of removing BB IN term, while if a single PD is used, then $i_{PD}(t) = i_a(t)$. Where

$$i_a(t) = \mathcal{R} \left\{ \frac{E1(t) + E2(t)}{\sqrt{2}} \right\} \left\{ \frac{E1(t) + E2(t)}{\sqrt{2}} \right\}^* + i_{sh1}(t) + i_{th}(t) \quad , \text{ and}$$

$$i_b(t) = \mathcal{R} \left\{ \frac{E1(t) - E2(t)}{\sqrt{2}} \right\} \left\{ \frac{E1(t) - E2(t)}{\sqrt{2}} \right\}^* + i_{sh2}(t) + i_{th}(t) \quad .$$

Although $i_{sh1}(t)$ and $i_{sh2}(t)$ have the same variance, they are uncorrelated. From (4.2), the field's strength of LUT and the auxiliary field are,

$$E1(t) \approx \sqrt{P_{O1}} \cdot (1 + \alpha_{n1}(t)) \cdot \exp(j2\pi\nu_{O1}t + j\phi_{n1}(t)) \quad , \text{ and}$$

$$E2(t) \approx \sqrt{P_{O2}} \cdot (1 + \alpha_{n2}(t)) \cdot \exp(j2\pi(\nu_{O1} \pm \Delta f)t + j\phi_{n2}(t)) \quad \text{respectively.}$$

where Δf here is the frequency shift between the two beams, P_{O1} , P_{O2} are optical power of LUT and the auxiliary laser respectively. Thus if the DC component and noise×noise terms are discarded, then photo-current of both setups are

$$(BD) \quad i_{PC}(t) \approx 2\mathcal{R}\sqrt{P_{O1}P_{O2}} \cdot (1 + \alpha_{n1}(t) + \alpha_{n2}(t)) \cdot \cos(2\pi\Delta ft + \Delta\phi_n(t)) + (i_{sh1}(t) - i_{sh2}(t)) + i_{th}(t) \quad (4.35-a)$$

$$(PD) \quad i_{PC}(t) \approx \mathcal{R}\sqrt{P_{O1}P_{O2}} \cdot (1 + \alpha_{n1}(t) + \alpha_{n2}(t)) \cdot \cos(2\pi\Delta ft + \Delta\phi_n(t)) + \mathcal{R}(P_{O1}\alpha_{n1}(t) + P_{O2}\alpha_{n2}(t)) + i_{sh1}(t) + i_{th}(t) \quad (4.35-b)$$

where $\Delta\boldsymbol{\phi}_n(\mathbf{t}) = \phi_{n1}(\mathbf{t}) - \phi_{n2}(\mathbf{t})$. Here $\boldsymbol{\phi}_{n1}(\mathbf{t})$ and $\boldsymbol{\phi}_{n2}(\mathbf{t})$ are assumed to be stationary RVs with zero-mean and finite variances for a finite \mathbf{T}_{OBS} . Statistically, variance of the sum or the subtraction of independent Gaussian RVs is the sum of their variances [100]. Two heterodyne discrimination techniques are discussed here.

4.3.2.2.1 RF frequency discriminator

Suppose a balanced RF frequency discriminator is employed to extract the FN. This discriminator is a bulky element and not easily tuned without losing its linearity and hence it is rarely used in the recent systems since a PLL is by far more efficient solution. Nevertheless such a discriminator is still necessary in UWB applications where PLL does not function anymore. Referring to the derivation in Appendix-A5, the measured SS-PSD of photo current after scaling is given by

$$\begin{aligned} \mathbf{S}_{\text{fn}}(\mathbf{f})_{\text{m}} \approx & S_{\text{fT}}(\mathbf{f}) + \left(\frac{B_d}{2}\right)^2 \left(S_{1\alpha_n, \text{SS}}(\mathbf{f}) + S_{2\alpha_n, \text{SS}}(\mathbf{f})\right) \\ & - B_d \left(\Re\{S_{1\alpha \times \mathbf{f}, \text{SS}}(\mathbf{f})\} + \Re\{S_{2\alpha \times \mathbf{f}, \text{SS}}(\mathbf{f})\}\right) \\ & + \left(\frac{B_d}{2}\right)^2 \frac{q_e(P_{O1} + P_{O2})}{2\mathcal{R}P_{O1}P_{O2}} + \left(\frac{B_d}{4}\right)^2 \frac{\mathcal{K}T^\circ N_f}{R_L(\mathcal{R}P_{O1}P_{O2})^2} \end{aligned} \quad (4.36)$$

where B_d is the effective discrimination BW, $S_{1\alpha_n, \text{SS}}(\mathbf{f})$, $\Re\{S_{1\alpha \times \mathbf{f}, \text{SS}}(\mathbf{f})\}$, $S_{2\alpha_n, \text{SS}}(\mathbf{f})$, and $\Re\{S_{2\alpha \times \mathbf{f}, \text{SS}}(\mathbf{f})\}$ are the SS-PSD of the IN and cross noise of LUT and the auxiliary laser respectively. The total FN is the sum of the individual FNs, or $\mathbf{S}_{\text{fT}}(\mathbf{f}) = S_{\text{fn1}}(\mathbf{f}) + S_{\text{fn2}}(\mathbf{f})$, however, $\mathbf{S}_{\text{fT}}(\mathbf{f}) \approx S_{\text{fn1}}(\mathbf{f})$ when $S_{\text{fn1}}(\mathbf{f}) \gg S_{\text{fn2}}(\mathbf{f})$ which is the case when the auxiliary laser is highly stable reference source, while $\mathbf{S}_{\text{fT}}(\mathbf{f}) \approx 2S_{\text{fn1}}(\mathbf{f})$ when the auxiliary laser is identical to the LUT. In brief, this method is more flexible than the direct one because the spectrum shape can be measured using the same setup. However the drawbacks are: frequency adjustment of either laser has to be sustained to keep $\Delta\mathbf{f}$ fixed at center frequency of the discriminator; an auxiliary laser (usually an expensive reference laser) is essential; besides the state of polarization (SOP) has to be maintained throughout \mathbf{T}_{OBS} .

4.3.2.2.2 Phase-locked loop (PLL)

A PLL is usually used as a frequency demodulator and functions more efficiently than the static discriminator in FN measurement for the following reasons:

- I. its parameters are easily adjusted via loop filter (**LF**),
- II. commercially available integrated circuits (**ICs**) are used in the design, and
- III. the BW in FN measurement is usually in the range of [1Hz-10MHz], hence wideband devices are not required.

A PLL locks on a tone, such as a narrowband modulated carrier such as in FN measurement or a wideband modulated signal with separate pilot. The loop BW is designed to be much higher (about **3.5** times the I/P signal's BW for Gaussian FM signal) than the beat-note BW to allow the PLL to track the fastest transitions of the signals with minimal delay [106]. In Fig. 4.13, a typical PLL configuration is shown. It consists of frequency tracking loop, and AFC. The PLL is designed to track the whole spectrum of a band-limited beat-note signal, and hence the LF must have a wide BW (fast). While the LF of the AFC circuit is designed to compensate frequency drift of both lasers via current driving circuit of the auxiliary laser, and hence AFC's LF must have a very narrow BW (slow). However, the compensated FN cannot be measured, which then requires a trade-off in the AFC design, which depends on LUT specifications and environmental condition and hence some trials (cut and try) are usually done.

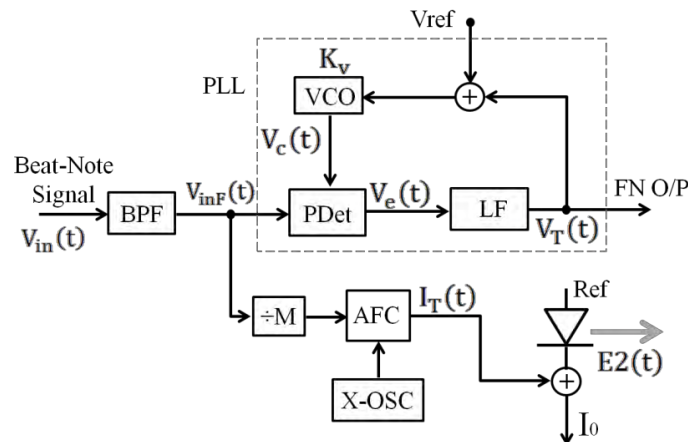


Fig. 4.13: A possible PLL configuration for FN measurement. **BPF** is a band-pass filter, **PDet** is phase detector, **VCO** is voltage controlled oscillator, **X-OSC** is crystal oscillator, **-M** is prescaler frequency divider, **LF** is loop filter, and K_v is the VCO constant (MHz/v).

The PLL (which actually functions as frequency-locked loop) holds lock to the I/P within its **Hold-in** range, however, long-term laser drift can be much higher than the VCO tuning range, and hence the AFC is essential for long **T_{Obs}**. The reference voltage **V_{ref}**, which is supplied from a high precision voltage reference, is tuned to put the VCO

frequency as close as Δf . The phase detector (**PDet**) in Fig. 4.13 is assumed to be of sinusoidal type i.e. a double-balanced mixer (**DBM**) followed by a low-pass filter (**LPF**) with IF port covers the frequency range $[DC, f \gg B_d]$. The beat-note signal after the TIA is filtered by a low-pass filter (**BPF**) with BW of B_d , to limit FN spectra as well as the IN as shown in Fig. 4.13. The design goal of the LF is to make the frequency error $f_e(t)$ between the beat-note instantaneous frequency $f_{BN}(t)$, and the VCO instantaneous frequency $f_{VCO}(t)$ always zero with time and throughout T_{OBS} . This is expressed as $\lim_{t \rightarrow \infty} \{f_e(t)\} = \lim_{t \rightarrow \infty} \{f_{VCO}(t) - f_{BN}(t)\} = 0$.

4.3.3 Delayed self-heterodyne (DSH) test

The DSH setup is widely used in spectrum shape and FN measurement since no reference laser is needed, and no frequency calibration is required as shown in Fig. 4.14 [88].

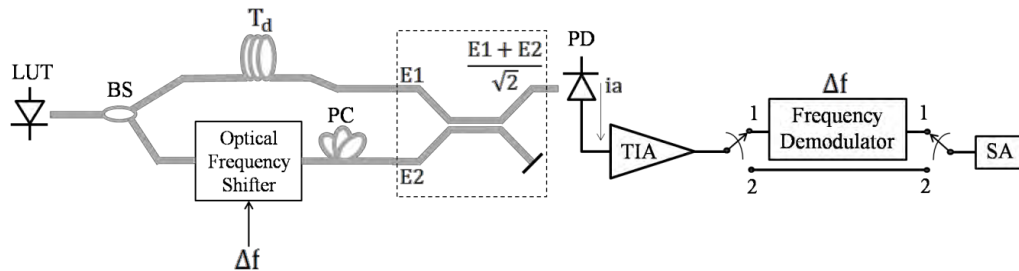


Fig. 4.14: DSH setup for line shape and FN measurement.

However, polarization alignment has to be maintained, and the time delay (T_d) cannot practically be very long due to fiber loss. Although an optical amplifier may be used to expand time delay range, the amplified spontaneous emission (**ASE**) noise reduces the measured signal to noise ratio (**SNR**) of the beat note, and increases the noise floor. An Acoustic Optical Modulator (**AOM**) is usually employed as an optical frequency shifter (**OFS**) to shift ν_0 by Δf with an RF synthesized signal generator as the reference IF frequency. However, the maximum modulation frequency is about 1GHz, which does not allow measurement of all line shape features, such as relaxation oscillation peaks unless recirculating loop is employed [107]. An optical IQ modulator can also be used as an alternative OFS with much wider BW when both Mach-Zehnder modulators (**MZM**)s are driven at the null point and the phase shifter at $\pi/2$ [50]. However, the biasing

condition has to be maintained throughout the experiment, and the LUT's power is highly attenuated as discussed in Section 3.4.1.

From (4.2) and referring to Fig. 4.14,

$$\mathbf{E1} = \sqrt{P_1} \cdot e^{j2\pi\nu_0(t-T_d)+\alpha_n(t-T_d)+j\phi_n(t-T_d)}, \text{ and}$$

$$\mathbf{E2} = \sqrt{P_2} \cdot e^{j2\pi(\nu_0+\Delta f)t+\alpha_n(t)+j\phi_n(t)},$$

where P_1 , and P_2 are the optical power corresponds to $\mathbf{E1}$ and $\mathbf{E2}$ fields respectively. As the 3-dB hybrid halves the received power of both beams, then the photo-current is

$$\begin{aligned} i_{PC}(t) &= (\mathcal{R}/2) \cdot \{E1 + E2\} \cdot \{E1 + E2\}^* \\ &= i_{BB}(t) + i_{BN}^+(t) + i_{BN}^-(t) + i_{sh}(t) + i_{th}(t) \end{aligned} \quad (4.37)$$

where $i_{BB}(t) = (\mathcal{R}/2) \cdot (P_1 \exp(2\alpha_n(t)) + P_2 \exp(2\alpha_n(t - T_d)))$,

$$i_{BN}^+(t) = (\mathcal{R}\sqrt{P_1 P_2}/2) \cdot \exp(j2\pi\Delta f t + \sum\alpha_n(t, T_d) + j\Delta\phi_n(t, T_d)),$$

$$i_{BN}^-(t) = (\mathcal{R}\sqrt{P_1 P_2}/2) \cdot \exp(-j2\pi\Delta f t + \sum\alpha_n(t, T_d) - j\Delta\phi_n(t, T_d)),$$

$$\sum\alpha_n(t, T_d) = \alpha_n(t) + \alpha_n(t - T_d), \text{ and}$$

$$\Delta\phi_n(t, T_d) = \phi_n(t) - \phi_n(t - T_d).$$

The ACF of $i_{PC}(t)$ after removing all zero-terms is

$$\begin{aligned} \mathbf{R}_{i_{PC}}(\tau) &= \langle i_{BB}(t) \cdot i_{BB}^*(t - \tau) \rangle + \langle i_{BN}^+(t) \cdot i_{BN}^{+*}(t - \tau) \rangle + \langle i_{BN}^-(t) \cdot i_{BN}^{-*}(t - \tau) \rangle \\ &\quad + \langle i_{sh}(t) \cdot i_{sh}^*(t - \tau) \rangle + \langle i_{th}(t) \cdot i_{th}^*(t - \tau) \rangle. \end{aligned}$$

Obviously the PSD of $i_{BN}^-(t)$ is the mirror-image of $i_{BN}^+(t)$, and hence only $\mathcal{S}\{i_{BN}^+(t)\}$ is calculated, besides, the SS-PSD (as measured by SA), is $2\mathcal{S}\{i_{BN}^+(t)\} + \mathcal{S}\{i_{BB}(t)\} + \mathcal{S}\{i_{sh}(t)\} + \mathcal{S}\{i_{th}(t)\}$. Note also that when a balanced-detector (**BD**) is used rather than a PD, then $i_{PC}(t) = 2i_{BN}^+(t) + 2i_{BN}^-(t) + \sqrt{2}i_{sh}(t) + i_{th}(t)$, since $i_{BB}(t)$ is vanished. Although shot noise is doubled in the BD setup, however, the SNR is improved. Focusing on (4.37), then the SS-PSD of the photo current can be written as

$$S_{PC}(f) = \mathcal{S}\{i_{BB}(t)\} + 2\mathcal{S}\{i_{BN}^+(t)\} + \mathcal{S}\{i_{sh}(t)\} + \mathcal{S}\{i_{th}(t)\} \quad (4.38)$$

Thus $\mathcal{S}\{i_{BB}(t)\}$, and $\mathcal{S}\{i_{BN}^+(t)\}$ are required to be derived. By recalling (4.37) this yields

$$\begin{aligned} \mathbf{R}_{i_{BB}}(\tau) &= \langle i_{BB}(t) \cdot i_{BB}^*(t - \tau) \rangle = (P_1 \mathcal{R}/2)^2 \cdot \\ &\quad \langle \exp(2\alpha_n(t) + 2\alpha_n(t - \tau)) + \beta^2 \exp(2\alpha_n(t - T_d) + 2\alpha_n(t - T_d - \tau)) \\ &\quad + \beta \exp(2\alpha_n(t) + 2\alpha_n(t - T_d - \tau)) \\ &\quad + \beta \exp(2\alpha_n(t - T_d) + 2\alpha_n(t - \tau)) \rangle \end{aligned}$$

where $\beta = P_2/P_1$.

Let $\mathbf{x}(t)$ be any zero-mean GRV then, $\mathcal{FT}\{x(t) + x(t - \Delta T)\} = x(f) + x(f)e^{-j2\pi f\Delta T} = 2x(f)e^{-j\pi f\Delta T}\cos(\pi f\Delta T)$, ΔT is any arbitrary delay. Therefore, $\langle (x(t) + x(t - \Delta T))^2 \rangle = \int_{-\infty}^{\infty} 4\cos^2(\pi f\Delta T)\mathcal{S}\{x(t)\}df$. Hence from (4.11) and after some arrangements yields

$$R_{i_{BB}}(\tau) = (P_1\mathcal{R}/2)^2 \cdot \left\{ (1 + \beta^2) \cdot \exp\left(16 \int_0^{\infty} S_{\alpha_n}(f)\cos^2(\pi f\tau) df\right) + \beta \left\{ \exp\left(16 \int_0^{\infty} S_{\alpha_n}(f)\cos^2(\pi f(T_d + \tau)) df\right) + \exp\left(16 \int_0^{\infty} S_{\alpha_n}(f)\cos^2(\pi f(T_d - \tau)) df\right) \right\} \right\} \quad (4.39-a)$$

$$\mathcal{S}\{i_{BB}(t)\} = 2\mathcal{FT}\{R_{i_{BB}}(\tau)\} \quad \dots\dots\dots f \geq 0 \quad (4.39-b)$$

Note that (4.39-b) contains DC term as well as BB IN-term simultaneously, and can be efficiently approximated when $\mathbf{i}_{BB}(t)$ in (4.37) is written as

$$\begin{aligned} \mathbf{i}_{BB}(t) &\approx (\mathcal{R}/2) \cdot \{P_1(1 + 2\alpha_n(t)) + P_2(1 + 2\alpha_n(t - T_d))\} \\ &= (\mathcal{R}/2)(P_1 + P_2) + \mathcal{R}\{P_1\alpha_n(t) + P_2\alpha_n(t - T_d)\} = i_{DC} + i_{IN}(t), \text{ hence} \end{aligned}$$

$$\begin{aligned} \mathcal{S}\{i_{BB}(t)\} &\approx \mathcal{S}\{i_{DC}\} + \mathcal{S}\{i_{IN}(t)\} \\ &= (\mathcal{R}(P_1 + P_2)/2)^2\delta(f) + 2(\mathcal{R}P_1)^2\{1 + 2\beta\cos(2\pi fT_d) + \beta^2\}S_{\alpha_n}(f) \end{aligned} \quad (4.40)$$

where from (4.8), $\mathbf{S}_{\alpha_n}(f) = \mathbf{RIN}_L(f)/8$. Although (4.39) results the exact BB IN PSD, however, the unwanted DC term is implicit in the calculation. Thus (4.40) can be used instead even for extreme values of δf , and $\mathbf{RIN}_L(\mathbf{0})$.

Next we derive the exact expression for $\mathcal{S}\{i_{BN}^+(t)\}$. From (4.37), the ACF of $\mathbf{i}_{BN}^+(t)$ is

$$\begin{aligned} R_{i_{BN}^+}(\tau) &= \langle i_{BN}^+(t)i_{BN}^{+*}(t - \tau) \rangle = (\mathcal{R}^2P_1P_2/4)e^{j2\pi\Delta f\tau} \cdot \\ &\quad \langle \exp(\alpha_n(t) + \alpha_n(t - \tau) + \alpha_n(t - T_d) + \alpha_n(t - T_d - \tau)) \\ &\quad \cdot \exp(j\phi_n(t) - j\phi_n(t - \tau) - j\phi_n(t - T_d) + j\phi_n(t - T_d - \tau)) \rangle \end{aligned}$$

By assuming the following variables,

$$\mathbf{x}_1(t) = \alpha_n(t) + \alpha_n(t - \tau) + \alpha_n(t - T_d) + \alpha_n(t - T_d - \tau), \text{ and}$$

$$\mathbf{x}_2(t) = \phi_n(t) - \phi_n(t - \tau) - \phi_n(t - T_d) + \phi_n(t - T_d - \tau), \text{ then from (4.11) yields}$$

$$\begin{aligned} R_{i_{BN}^+}(\tau) &= (\mathcal{R}^2P_1P_2/4)e^{j2\pi\Delta f\tau} \\ &\quad \cdot \exp(\langle |x_1(t)|^2 \rangle/2 - \langle |x_2(t)|^2 \rangle/2 + j\langle x_1(t)x_2^*(t) \rangle) \end{aligned} \quad (4.41)$$

Then by substituting of $\mathbf{x}_1(t)$, and $\mathbf{x}_2(t)$ in (4.12) and then in (4.41) yields

$$\begin{aligned}
R_{i_{\text{BN}}}^+(\boldsymbol{\tau}) &= (\mathcal{R}^2 P_1 P_2 / 4) \cdot \exp(j2\pi\Delta f\boldsymbol{\tau}) \\
&\cdot \left\{ \exp \left(4 \int_0^\infty \left(\{1 + \cos(\omega T_d) + \cos(\omega\tau) + \cos(\omega T_d) \cdot \cos(\omega\tau)\} S_{\alpha_n}(f) \right. \right. \right. \\
&\quad \left. \left. \left. + \{-1 + \cos(\omega T_d) + \cos(\omega\tau) - \cos(\omega T_d) \cdot \cos(\omega\tau)\} S_{\phi_n}(f) \right. \right. \right. \\
&\quad \left. \left. \left. - j2 \cdot \sin(\omega T_d) \cdot \sin(\omega\tau) \cdot S_{X_r}(f) \right) df \right) \right\} \quad (4.42\text{-a})
\end{aligned}$$

$$\mathcal{S}\{\mathbf{i}_{\text{BN}}^+(\mathbf{t})\} = (\mathcal{R}^2 P_1 P_2 / 4) \cdot \mathcal{FT}\{\exp(j2\pi\Delta f\boldsymbol{\tau}) \cdot R_{i_{\text{BN}}}^+(\boldsymbol{\tau})\} \quad (4.42\text{-b})$$

where $\boldsymbol{\omega} = 2\pi f$. Therefore the SS-PSD (as monitored by a SA) of photo current of the DSH test with PD setup in (4.38) is obtained by numerical calculation of $\mathcal{S}\{\mathbf{i}_{\text{BB}}(\mathbf{t})\}$ from (4.39), and $2\mathcal{S}\{\mathbf{i}_{\text{BN}}^+(\mathbf{t})\}$ from (4.42).

4.3.3.1 Beat-note PSD when only white FN is counted and $|\mathbf{H}_c(\mathbf{f})|^2 = 1$

An important special case is when only the white FN is counted with $|\mathbf{H}_c(\mathbf{f})|^2 = 1$, and all other parameters are ignored then from (4.42-a), or from (A6.7) in Appendix-A6, yields

$$\begin{aligned}
R_{i_{\text{BN}}}^+(\boldsymbol{\tau}) &= (\mathcal{R}^2 P_1 P_2 / 4) \cdot \exp(j2\pi\Delta f\boldsymbol{\tau}) \\
&\cdot \exp(-\pi\delta f \cdot \{2T_d + 2|\tau| - |T_d + \tau| - |T_d - \tau|\}) \quad (4.43)
\end{aligned}$$

Let $\mathcal{S}\{\mathbf{i}_{\text{BN}}(\mathbf{t})\} = 2\mathcal{S}\{\mathbf{i}_{\text{BN}}^+(\mathbf{t})\}$ be the beat-note component of $\mathbf{i}_{\text{PC}}(\mathbf{t})$ and as monitored by the SA. In Appendix-A7, $\mathcal{FT}\{\exp(-\pi\delta f \cdot \{2T_d + 2|\tau| - |T_d + \tau| - |T_d - \tau|\})\}$ is derived and yields the DS-PSD of the normalized-BB version of (4.43). Thus from (A7.1), the definition of $\mathcal{S}\{\mathbf{i}_{\text{BN}}(\mathbf{t})\}$, and frequency shift property of \mathcal{FT} yields

$$\begin{aligned}
\mathcal{S}\{\mathbf{i}_{\text{BN}}(\mathbf{t})\} &= (\mathcal{R}^2 P_1 P_2 / 2) \left\{ e^{-\Gamma_w} \cdot \delta(f - \Delta f) + \mathcal{L}_{w2}(f - \Delta f) \right. \\
&\quad \left. \cdot \{1 - e^{-\Gamma_w} \cdot (\cos(2\pi(f - \Delta f)T_d) + \Gamma_w \cdot \text{sinc}(2(f - \Delta f)T_d))\} \right\} \quad (4.44)
\end{aligned}$$

where $\mathcal{L}_{w2}(f) = \frac{\delta f}{\pi} \cdot \frac{1}{(\delta f)^2 + f^2}$, and $\Gamma_w = 2\pi\delta f T_d$.

This equation describes the beat-note SS-PSD when only white FN is counted and $|\mathbf{H}_c(\mathbf{f})|^2 = 1$ which was first derived and verified experimentally by Richter *et al.* [108].

4.3.3.2 Flicker FN contribution on the beat-note PSD

Effect of the flicker FN on $\mathcal{S}\{\mathbf{i}_{\text{BN}}(\mathbf{t})\}$ can be derived by calculating flicker's PN variance assuming that it has zero-mean, and as follows.

$\sigma_F^2(\tau, \mathbf{T}_d) = \overline{\Delta\phi_{nF}(t)^2} + \overline{\Delta\phi_{nF}(t-\tau)^2} - 2\overline{\Delta\phi_{nF}(t)\Delta\phi_{nF}(t-\tau)}$, where $\Delta\phi_{nF}(t) = \phi_{nF}(t) - \phi_{nF}(t - T_d)$. Thus from (4.21) and following the same procedure of the white part, then flicker's PN variance, and the normalized BB-DS-PSD are expressed as

$$\sigma_F^2(\tau, \mathbf{T}_d) = 4\pi\delta f \cdot f_C T_d^2 \cdot \left\{ 2Z(T_d/T_{OBS}) + 2\tau_n^2 \cdot Z(T_d/T_{OBS} \cdot |\tau_n|) - (1 - \tau_n)^2 \cdot Z(T_d/T_{OBS} \cdot |1 - \tau_n|) - (1 + \tau_n)^2 \cdot Z(T_d/T_{OBS} \cdot |1 + \tau_n|) \right\} \quad (4.45-a)$$

$$\mathcal{S}\{exp(j\Delta\phi_{nF}(t))\} = \mathcal{F}\mathcal{T}\{exp(-\sigma_F^2(\tau, T_d)/2)\} \quad (4.45-b)$$

4.3.3.3 Numerical computations

For convenience, let us use the following notations

$R_W(\tau, \mathbf{T}_d) = exp(-\pi\delta f \cdot \{2T_d + 2|\tau| - |T_d + \tau| - |T_d - \tau|\})$, as the ACF due to white FN only,

$R_F(\tau, \mathbf{T}_d) = exp(-\sigma_F^2(\tau, T_d)/2)$, as the ACF due to flicker FN only,

$R_T(\tau, \mathbf{T}_d) = R_W(\tau, T_d) \cdot R_F(\tau, T_d)$, as the overall ACF,

$S_W(f) = \mathcal{F}\mathcal{T}\{R_W(\tau, T_d)\}$, as the normalized BB-DS-PSD due to white FN only,

$S_F(f) = \mathcal{F}\mathcal{T}\{R_F(\tau, T_d)\}$, as the normalized BB-DS-PSD due to flicker FN only, and

$S(f) = \mathcal{F}\mathcal{T}\{R_T(\tau, T_d)\}$, as the overall normalized BB-DS-PSD. Now by using the following discrete vectors; $\mathbf{n} = [0, 1, \dots, N_F - 1]$ corresponds to τ ,

$\mathbf{k} = [(-N_F/2), (-N_F/2 + 1), \dots, (-1), (0), (1), \dots, (N_F/2 - 1)]$ corresponds to f ,

N_d is number of samples corresponds to \mathbf{T}_d , and N_F corresponds to \mathbf{T}_{OBS} .

Then the following scalable calculations of ACFs and PSDs are conducted.

In the first example, the ACFs are calculated in relatively short and long \mathbf{T}_d , showing that $R_F(\tau, \mathbf{T}_d)$ can fit Gaussian profile only when $R_F(\tau, \mathbf{T}_d) \rightarrow 0$ as $\tau \rightarrow \mathbf{T}_{OBS}$ as shown in Fig. 4.15. Note that when $R_F(\tau, \mathbf{T}_d) \rightarrow \rho_F$, and/or $R_W(\tau, \mathbf{T}_d) \rightarrow \rho_W$, then both $S_W(f)$, and $S_F(f)$ have $\delta(f)$ component and oscillating PSD. Where ρ_F and ρ_W are any arbitrary small numbers that bounded in (0, 1) interval. In the second example, we investigate $S_F(f)$ with three different values of \mathbf{T}_d versus different values of f_{CN} , using $f_S = 100\text{MHz}$, and $N_F = 4096$ as shown in Fig. 4.16. The normalized PSD is calculated as

$$\mathbf{PSD}(f)|_{normalized} = \mathbf{PSD}(f)/\mathbf{PSD}(0)$$

In the third example, we investigate the effect of \mathbf{T}_d on linewidth value due to the flicker component as shown in Fig. 4.17a and due to the white-flicker convolved effect as in Fig.

4.17b, with $F_S = 10\text{MHz}$, and $N_F = 4096$. The last three examples are accomplished to compare the differences between $S_W(f)$, $S_F(f)$, and $S(f)$ under different normal and extreme conditions of f_{CN} values, with $F_S = 100\text{MHz}$, and $N_F = 4096$, as shown in Fig. 18-20. In all the aforementioned examples, the missing parameters are listed at the upper right-hand side corner of each figure.

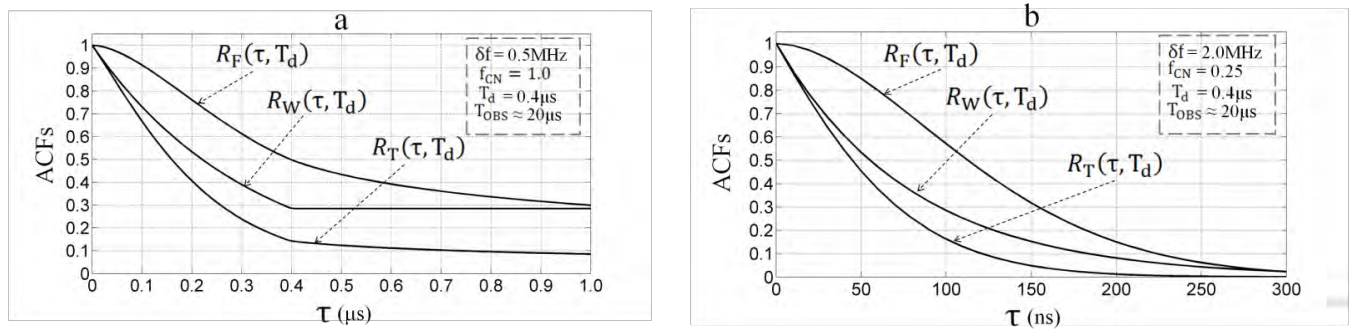
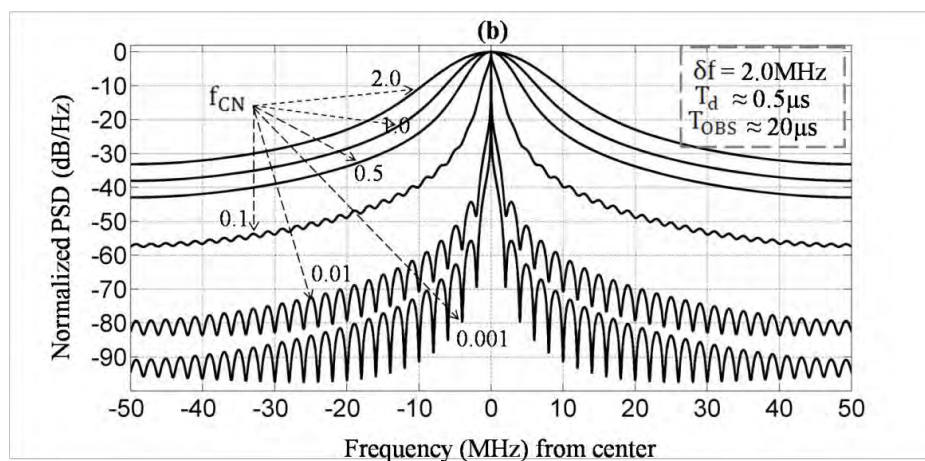
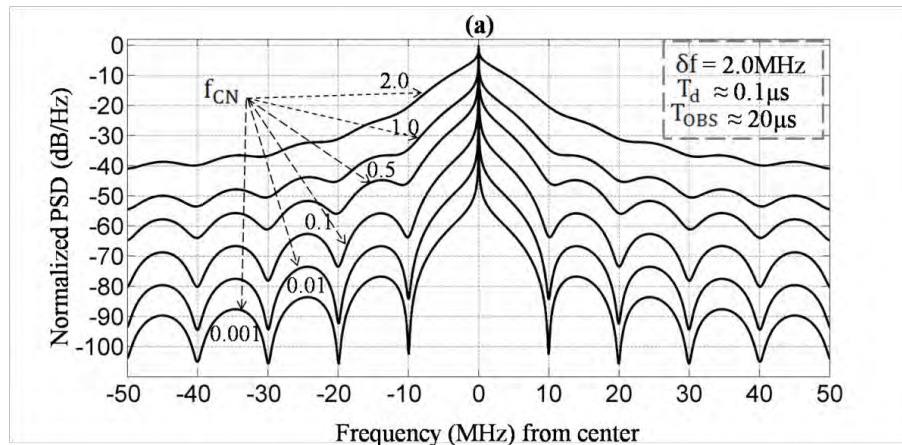


Fig. 4.15: ACF due to white FN, flicker FN, and the convolved effect. In (a), the ACFs are settled to a constant values ρ_F , ρ_W , and $\rho_F \times \rho_W$. In (b) all ACFs are settled to zero, and the flicker's ACF can be approximated to Gaussian profile.



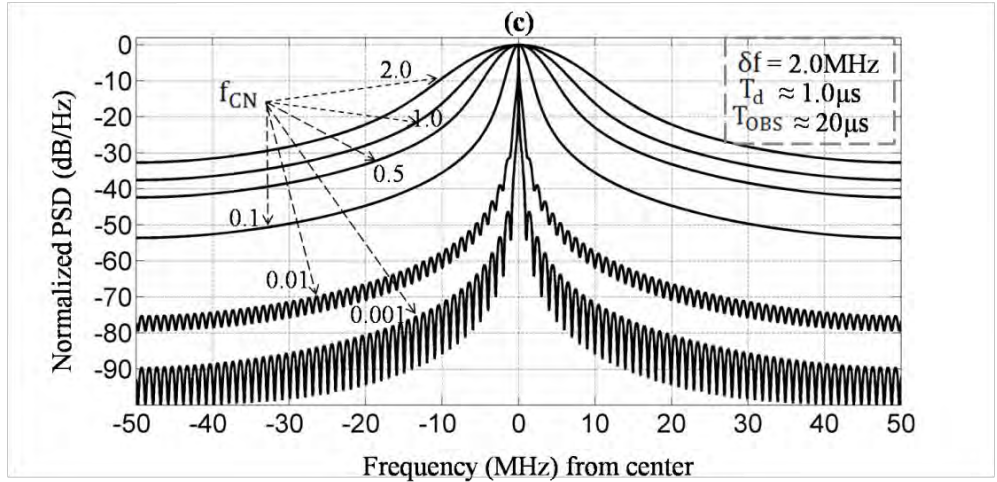


Fig. 4.16: Normalized $S_F(f)$ in the DSH test showing the evolution from oscillating line shape to a complete Gaussian line shape as a function of T_d , f_{CN} .

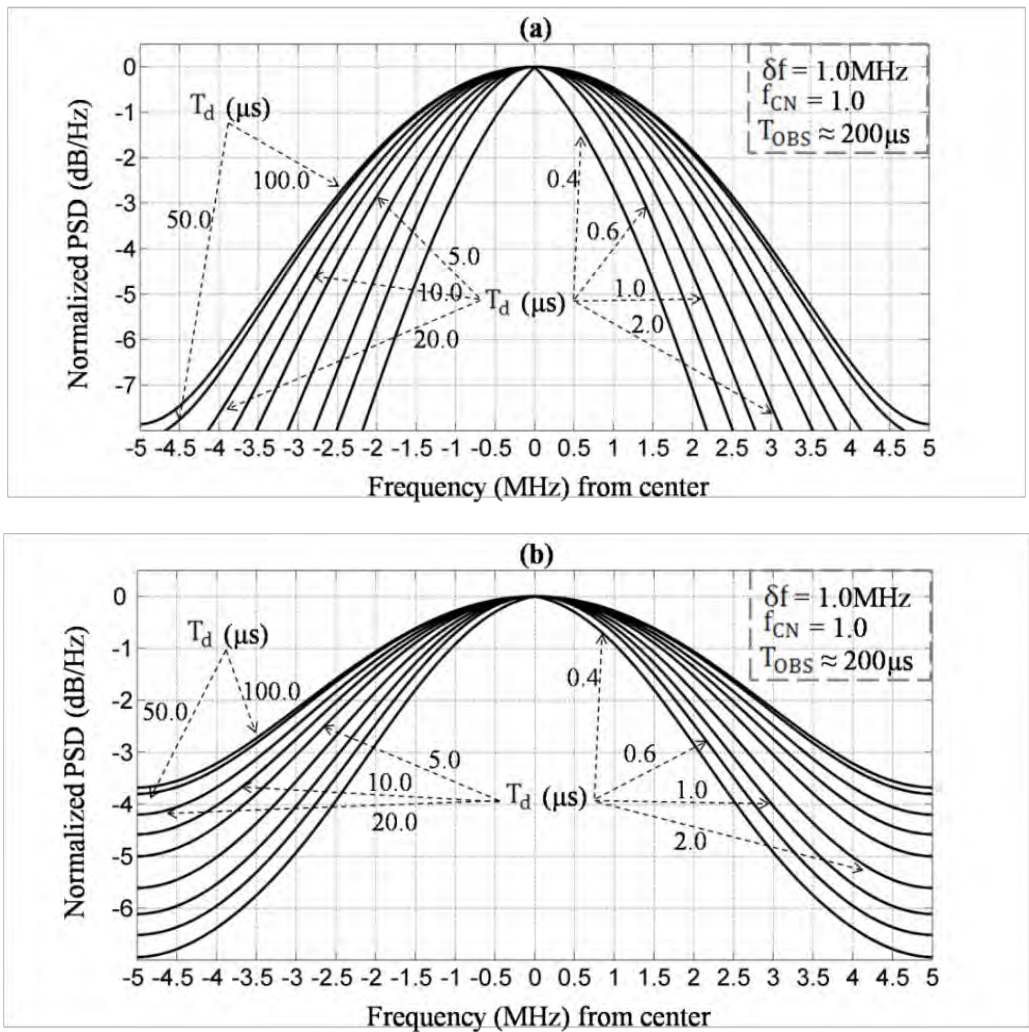


Fig. 4.17: Normalized $S_F(f)$ in (a), and $S(f)$ in (b) as a function of T_d showing linewidth broadening.

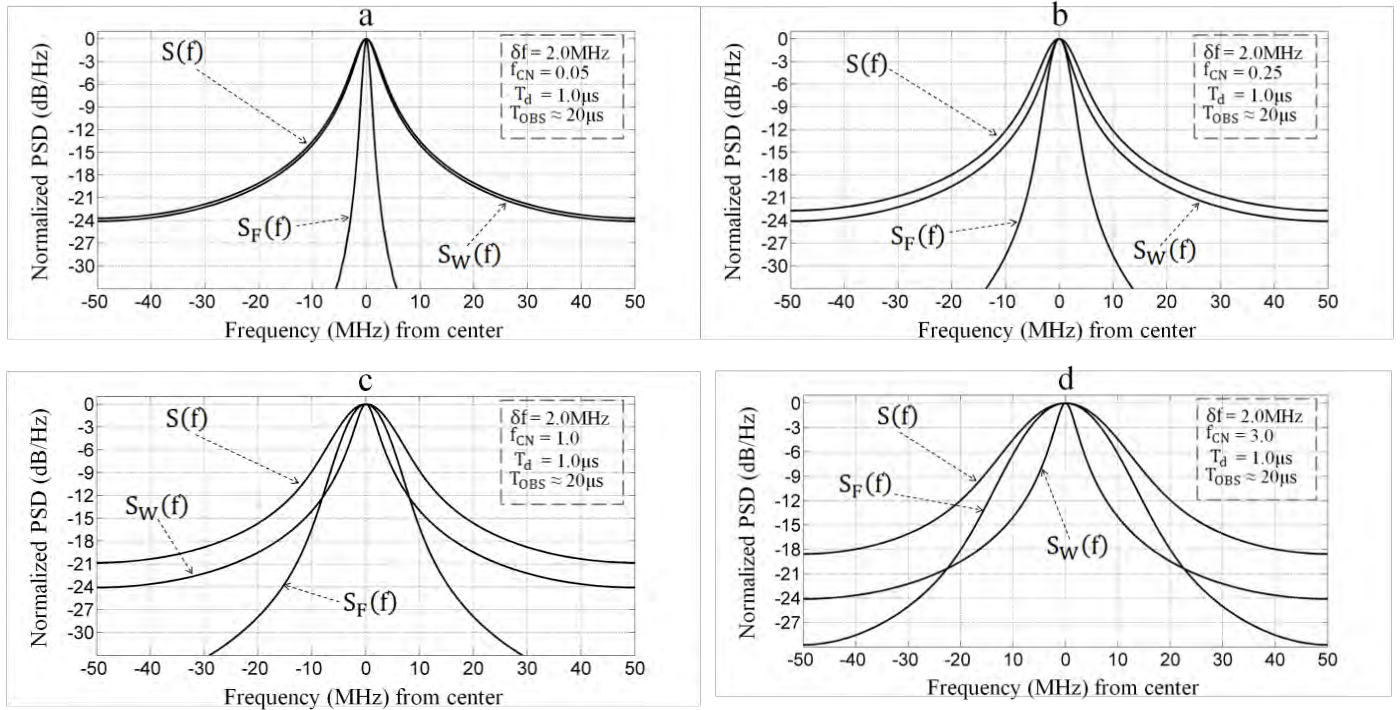


Fig. 4.18: Normalized $S_F(f)$, $S_W(f)$, and $S(f)$ showing the Lorentzian, Gaussian and Voigt lines shape respectively. T_d is chosen such that all functions have no oscillating spectra, and hence no $\delta(f)$ component.

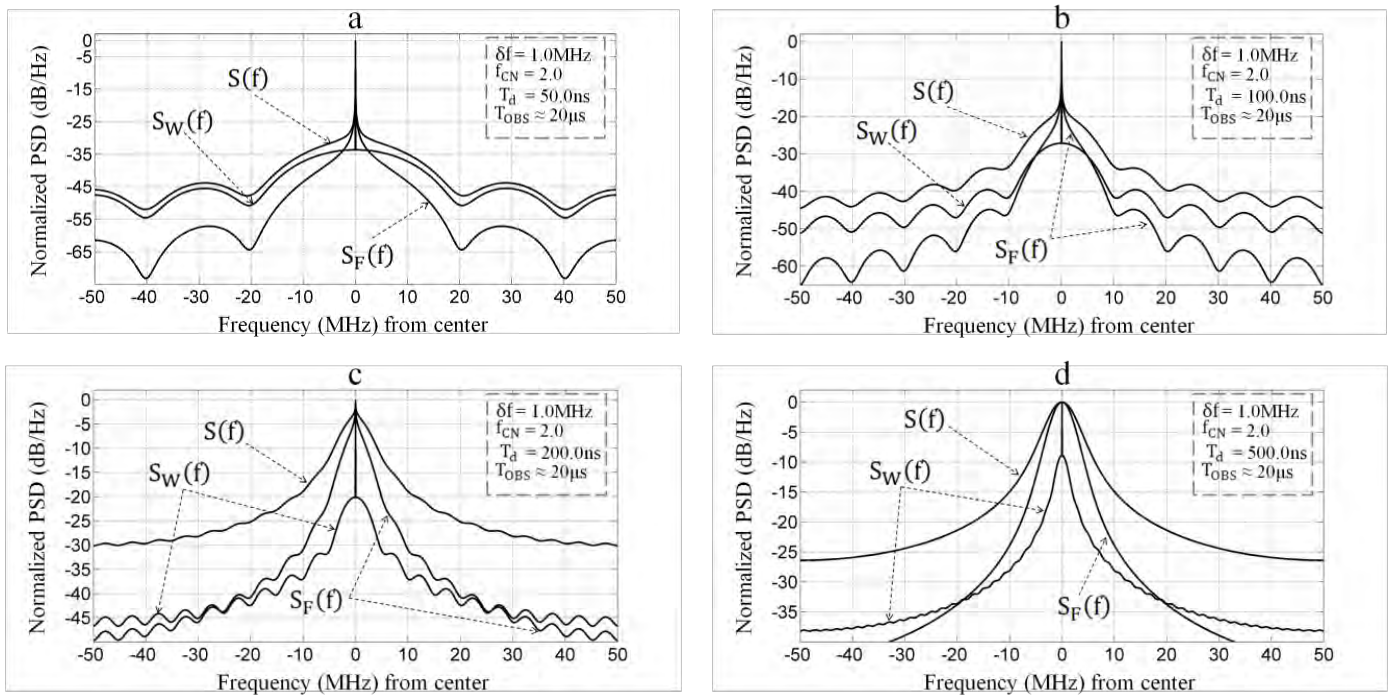


Fig. 4.19: Normalized $S_F(f)$, $S_W(f)$, and $S(f)$ in relatively short delay, showing the domination of the flicker component.

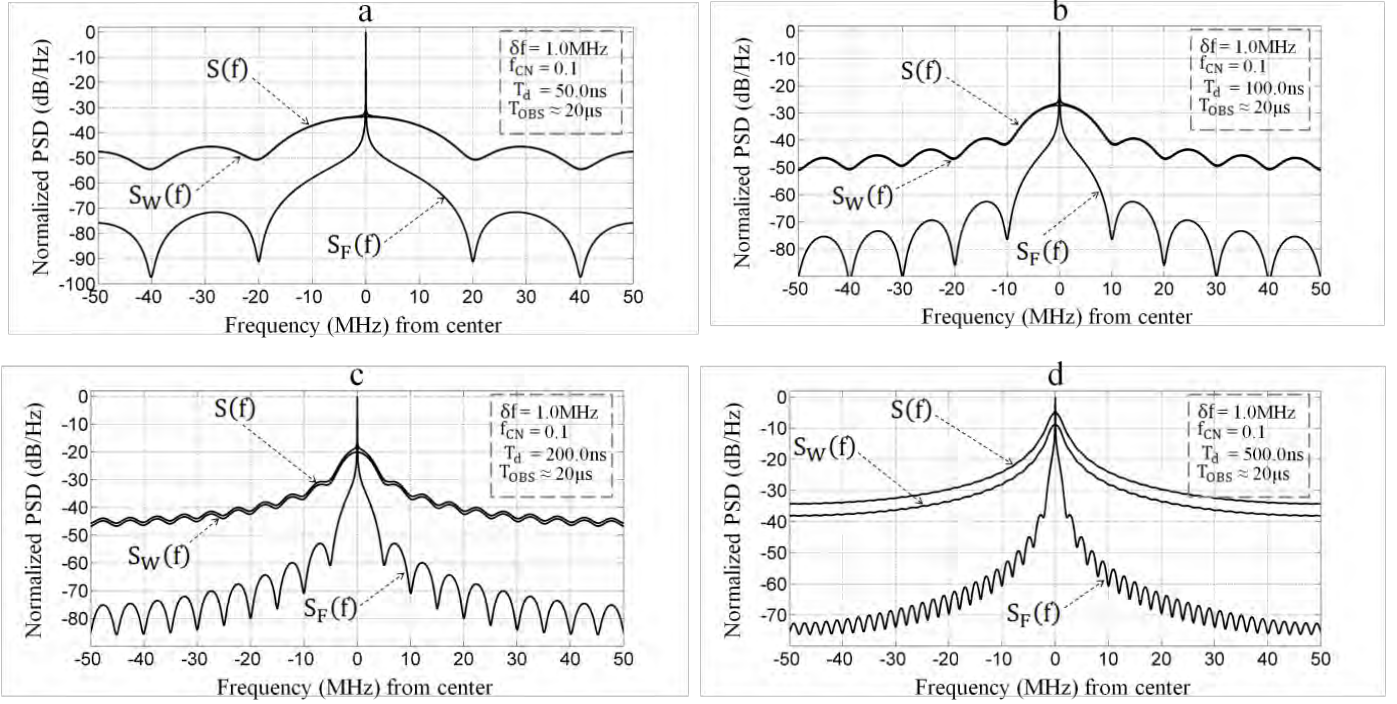


Fig. 4.20: Normalized $S_F(f)$, $S_W(f)$, and $S(f)$ in relatively short delay, showing the domination of the white component.

4.3.3.4 Main calculation results

We summarize the main results obtained from these calculations as follows:

1- $\delta(f)$ component of the flicker, white, and beat-note PSD approaches an arbitrarily small value $\{\epsilon_P\}$ at a specific minimal value of T_d or ($T_{d,min}$). For the white part and from (4.44), $\{e^{-\Gamma_w} = e^{-2\pi\delta f \cdot T_d} = \epsilon_P\}$, which yields $\{T_{d,min} = -\ln(\epsilon_P)/(2\pi\delta f)\}$. Hence if $\{\epsilon_P \approx 10^{-4}\}$ for instance, then $\{T_{d,min} \approx 9/(2\pi\delta f)\}$. While for the flicker component, then the final τ value is investigated by substituting, $\{\tau = T_{OBS}\}$ in (4.45-a) at different T_{OBS} . Now by approximating (4.45-a) for this specific case ($\tau = T_{OBS}$) then, $\{\sigma_F^2(\tau = T_{OBS}, T_d) \approx 8\pi\delta f \cdot f_C T_d^2 \cdot \ln(T_{OBS}/T_d)\}$, which is valid if $\{T_d \leq T_{OBS}/10\}$. Thus from (4.45-a) we obtain, $\{\exp(-4\pi\delta f \cdot f_C T_d^2 \cdot \ln(T_{OBS}/T_d)) = \epsilon_P\}$, and yields $\{T_d^2 \cdot \ln\{T_{OBS}/T_d\} = \ln\{\epsilon_P\}/(4\pi\delta f \cdot f_C)\}$, which can be solved numerically to obtain $T_{d,min}$ corresponds to the flicker component. The $\delta(f)$ component of $S(f)$, approaches ϵ_P depending on which component (white or the flicker) approaches ϵ_P first. Hence

$$\text{White} \quad T_{d,min,W} = \frac{-\ln\{\epsilon_P\}}{2\pi\delta f} \quad (4.46-a)$$

$$\text{Flicker} \quad (T_{d,\min,F})^2 \cdot \ln\left\{\frac{T_{d,\min,F}}{T_{OBS}}\right\} \approx \frac{-\ln\{\epsilon_P\}}{4\pi\delta f \cdot f_C} = \frac{-\ln\{\epsilon_P\}}{4\pi^2 h_F} \quad (4.46-b)$$

For example if a LUT with $\delta f = 2\text{MHz}$, $f_C = 0.5\text{Mhz}$ ($h_F \approx 3.2 \times 10^{11}$) and $\epsilon_P \approx 10^{-4}$, then from (4.46-a), $T_{d,\min,W} \approx 730\text{ns}$ which corresponds to fiber length of 146m (light speed in SSMF $\approx 200,000\text{km/s}$), while numerical solution of (4.46-b) yields $T_{d,\min,F} \approx 437\text{ns}$ which corresponds to fiber length of 87m. It is important to calculate $T_{d,\min}$ before investigating linewidth broadening due to time delay.

2- The flicker PSD follows a similar form of (4.44) as shown in Fig. 4.16, however, the exact expression cannot be derived analytically.

3- From Fig. 4.15, the ACF of flicker component cannot be approximated to Gaussian profile when $T_d < T_{d,\min,F}$ ($\epsilon_P > 0.1$), however, the ACF and its corresponding PSD can fit Gaussian profile when the $\delta(f)$ component approaches zero.

4- When $T_d \geq \text{lower}\{T_{d,\min,F}, T_{d,\min,W}\}$, then the measured linewidth is wider by $\sqrt{2}$ to 2 the optical domain linewidth as shown in Fig. 4.6.

5- From (4.27-a) if δf_{total} is replaced by $\delta f_{\text{total}}/2$, f_{CN} by $f_C/(2\delta f)$, T_{OBS} by T_d , and $T_d \geq \text{lower}\{T_{d,\min,F}, T_{d,\min,W}\}$, then $S(f)$ linewidth in the DSH test can be estimated efficiently. The results presented by the previously given computations, linewidth estimation, and curve fitting have good agreement with the references [96]-[98].

6- $S_F(f)$ predominantly depends on T_d assuming $T_{OBS} \geq T_d$, or $N_F \geq N_d$ regardless how much N_F is larger than N_d .

7- The linewidth is T_d -dependent, and it can be much wider than δf . Therefore either T_d is mentioned with linewidth's value, or a more feasible definition is introduced.

8- The common f_{CN} values of commercially available SCLs, flicker FN has a marginal effect in the DSH test especially at short T_d as illustrated in Fig. 20. That is for commercially available SCL with an active cooling and a tight electrical filtering in the active biasing circuit, the flicker FN has usually low f_{CN} value since it is to some extent environmentally controlled [109].

4.3.4 Time-Domain Frequency Stability Measurements

Two-sample variance or Allan variance is widely used to characterize frequency stability of any oscillator in time domain [110]. It describes frequency deviation during a specific time interval ΔT which is independent of the deviation from the center frequency. That is when the average frequency is known at a specific time instant t_0 , then it can be estimated at $t_0 + \Delta T$. The unnormalized Allan variance version is given by [88]

$$\text{By definition} \quad \sigma_f^2(\Delta T) \triangleq \frac{1}{2} \langle \{\bar{f}_{r+1} - \bar{f}_r\}^2 \rangle \quad (4.47-a)$$

$$\text{In practice} \quad \sigma_f^2(\Delta T) \approx \frac{1}{2(M-1)} \sum_{r=1}^{M-1} \{f_{r+1} - f_r\}^2 \quad (4.47-b)$$

where again ΔT is the sampling time (interval time),

$$\bar{f}_r = \left\{ \frac{1}{\Delta T} \int_{t_0}^{t_0 + \Delta T} f(t) dt \right\}$$

is the average frequency in the r -th interval, and M is number of successive measured samples. From frequency domain analysis, (4.47-a) can be rewritten as [111],

$\sigma_f^2(\Delta T) = \{2 \int_0^\infty S_{fn}(f) \cdot \sin^2(\pi f \cdot \Delta T) \cdot \text{sinc}^2(f \cdot \Delta T) df\}$, and when DSH setup is used then the beat-note FN SS-PSD is $S_{F,DSH}(f) = 4 \sin^2(\pi f \cdot T_d) \cdot S_{fn}(f)$, and hence

$$\sigma_f^2(\Delta T) = 8 \int_0^\infty \sin^2(\pi f \cdot \Delta T) \cdot \text{sinc}^2(f \cdot \Delta T) \cdot \sin^2(\pi f \cdot T_d) \cdot S_{fn}(f) df \quad (4.48)$$

Then by adding the random-walk frequency noise component and ignoring the relaxation oscillation, then the FN-SS-PSD in (Hz^2/Hz) of (4.5) can be rewritten as

$$S_{fn}(f) = h_W + \frac{h_F}{f} + \frac{h_R}{f^2} \quad (4.49)$$

where $h_W = \delta f / \pi$, $h_F = (\delta f \cdot f_C) / \pi$, and $h_R = (\delta f \cdot f_C \cdot f_{rw}) / \pi$.

Here f_{rw} is the corner frequency of the flicker and the random-walk terms. By substituting (4.49) in (4.48) yields

White FN	$\sigma_{f,W}^2(\Delta T) = \frac{h_W}{\Delta T} \cdot \begin{cases} 1 & \Delta T < T_d/2 \\ 2 \left(1 - \frac{\tau_d}{4}\right) & T_d/2 \leq \Delta T < T_d \\ 3 \frac{\tau_d}{2} & \Delta T \geq T_d \end{cases} \quad (4.50-a)$
-------------	--

Flicker FN	$\sigma_{f,F}^2(\Delta T) = h_F \cdot \left\{ 4\ell n\{2\} + 2(1 - \tau_d)^2 \ell n\{ 1 - \tau_d \} \right.$ $+ 2(1 + \tau_d)^2 \ell n\{1 + \tau_d\}$ $- \frac{1}{2}(2 - \tau_d)^2 \ell n\{ 2 - \tau_d \}$ $\left. - \frac{1}{2}(2 + \tau_d)^2 \ell n\{ 2 + \tau_d \} - 3\tau_d^2 \ell n\{\tau_d\} \right\} \quad (4.50-b)$ $\sigma_{f,F}^2(\Delta T = T_d) = 3.3740 \cdot h_F$ $\sigma_{f,F}^2\left(\Delta T = \frac{T_d}{2}\right) = 3.1394 \cdot h_F$
Random- Walk FN	$\sigma_{f,R}^2(\Delta T) = \frac{\pi^2 h_R \Delta T}{3} \cdot \begin{cases} 4 & \Delta T < T_d/2 \\ \tau_d^3 - 6\tau_d^2 + 12\tau_d - 4 & T_d/2 \leq \Delta T < T_d \\ 3\tau_d^2(2 - \tau_d) & \Delta T \geq T_d \end{cases} \quad (4.50-c)$

where $\tau_d = T_d/\Delta T$, and the $\{\sim\}$ sign indicates the DSH setup is adopted. Either the sweep time of an RF-SA is set to ΔT , and the average center frequency during this interval is chosen to be the spectral average, or by sampling the beat-note signal and the long time-samples record is divided into M segments, and the \mathcal{FFT} is applied in an offline mode (software based), and then the average frequency per segment is extracted [111]. In both ways, after M successive readings of center frequency then $\sigma_f(\Delta T)$ is obtained. Usually overlapped Allan variance is used to improve measurement confidence [111]; however, we only consider classical Allan variance here [110]. Obviously (4.50) is not the true two-sample variance of LUT due to the participation of the DSH TF, and hence some modifications are required. If the heterodyne FN measurement setup in Fig. 4.12 is reused again with high stability reference source, then $S_{fn}(f)$ is only limited by T_{OBS} which can be as long as required. Then (4.48) is rewritten as

$$\sigma_f^2(\Delta T) = 2 \int_0^{\infty} \sin^2(\pi f \Delta T) \cdot \text{sinc}^2(f \Delta T) \cdot S_{fn}(f) df$$

Now by substituting (4.49) in $\sigma_f^2(\Delta T)$ expression and solving the integration, then the true Allan variance of all individual FN components are obtained and given by

$$\text{White FN} \quad \sigma_{f,W}^2(\Delta T) = \frac{1}{2\Delta T} \cdot h_W \quad (4.51-a)$$

$$\text{Flicker FN} \quad \sigma_{f,F}^2(\Delta T) = 2\ell n\{2\} \cdot h_F \quad (4.51-b)$$

$$\text{Random-Walk FN} \quad \sigma_{f,R}^2(\Delta T) = \frac{2\pi^2}{3} \Delta T \cdot h_R \quad (4.51-c)$$

The relationship between the individual components of (4.50) and (4.51) is illustrated in Fig. 4.21, which depends only on $\tau_d = T_d/\Delta T$.

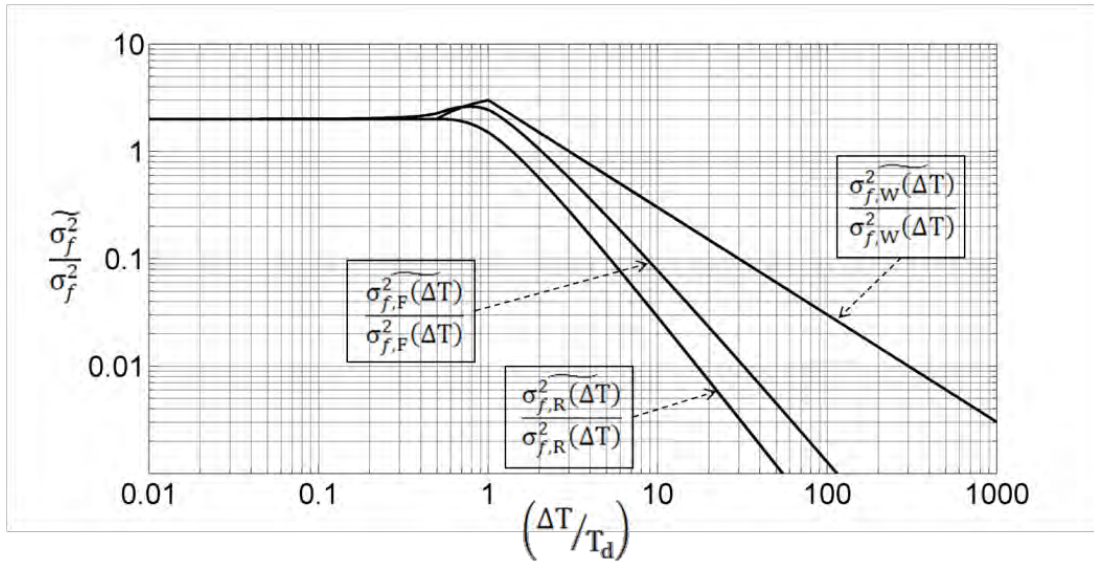


Fig. 4.21: Allan variance of the individual components in the DSH setup scaled to the individual components of direct FN measurement setup as a function of $1/\tau_d$.

It is possible to extract h_W , h_F , and h_R of the LUT by measuring Allan variance using three different T_d values and setting $\Delta T = T_d$ or $\tau_d = 1$ in every measurement. Then a set of three equations is solved simultaneously. As no knowledge is assumed about LUT, then the first delay may be chosen to be $T_{d1} = T_{d,min}$ as discussed in the previous section. The other two values (T_{d2} , and T_{d3}) have to be separated in a logarithmic scale to get a sensible effect of both the flicker and random-walk components. Now since

$$\sigma_f^2(\Delta T) = \sigma_{f,W}^2(\Delta T) + \sigma_{f,F}^2(\Delta T) + \sigma_{f,R}^2(\Delta T), \text{ and when } \tau_d = 1, \text{ then from (4.50),}$$

$$\sigma_f^2(T_d) = 3 h_W / (2T_d) + 3.374 h_F + \pi^2 h_R T_d.$$

$$\text{Let } \mathbf{X1} = 3h_W/2, \mathbf{X2} = 3.374h_F, \text{ and } \mathbf{X3} = \pi^2 h_R,$$

Let $\mathbf{U1}$, $\mathbf{U2}$, and $\mathbf{U3}$ equals to $\sigma_f^2(T_{d1})$, $\sigma_f^2(T_{d2})$, and $\sigma_f^2(T_{d3})$ respectively, then

$$U1 = \frac{X1}{T_{d1}} + X2 + X3 \cdot T_{d1} \quad (4.52-a)$$

$$U2 = \frac{X1}{T_{d2}} + X2 + X3 \cdot T_{d2} \quad (4.52-b)$$

$$U3 = \frac{X1}{T_{d3}} + X2 + X3 \cdot T_{d3} \quad (4.52-c)$$

Now let $\Delta U1 = U1 - U2$, and $\Delta U2 = U2 - U3$, then by solving (4.52) yields

$$\Delta U1 = X1 \cdot dT1 + X3 \cdot dT2 \quad (4.53-d)$$

$$\Delta U2 = X1 \cdot dT3 + X3 \cdot dT4 \quad (4.53-e)$$

where

$dT1 = (T_{d2} - T_{d1})/(T_{d1} \cdot T_{d2})$, $dT2 = (T_{d1} - T_{d2})$, $dT3 = (T_{d3} - T_{d2})/(T_{d3} \cdot T_{d3})$,
and $dT4 = (T_{d2} - T_{d3})$. Now by solving (4.53-a) with (4.53-b) yields

$$X1 = \frac{\Delta U1 \cdot dT4 - \Delta U2 \cdot dT2}{dT1 \cdot dT4 - dT2 \cdot dT3} \quad (4.54-a)$$

$$X3 = \frac{\Delta U2 \cdot dT1 - \Delta U1 \cdot dT3}{dT1 \cdot dT4 - dT2 \cdot dT3} \quad (4.54-b)$$

Then by substituting of $X1$ and $X3$ in (4.52-a), and by rearranging the equations yields

$$h_W = \frac{2}{3} \cdot \frac{T_{d1} T_{d2} T_{d3}}{(T_{d3} - T_{d1})} \cdot \left\{ \frac{\Delta U1}{T_{d2} - T_{d1}} - \frac{\Delta U2}{T_{d3} - T_{d2}} \right\} = \frac{\delta f}{\pi} \quad (4.55-a)$$

$$h_F = \frac{1}{3.374} \cdot \left(\sigma_f^2(T_{d1}) - \frac{1}{(T_{d3} - T_{d1})} \cdot \left\{ \frac{\Delta U1 \cdot (T_{d1}^2 + T_{d2} T_{d3})}{T_{d2} - T_{d1}} - \frac{\Delta U2 \cdot T_{d3} (T_{d1} + T_{d2})}{T_{d3} - T_{d2}} \right\} \right) = \frac{\delta f \cdot f_C}{\pi} \quad (4.55-b)$$

$$h_R = \frac{1}{\pi^2} \cdot \frac{1}{(T_{d3} - T_{d1})} \cdot \left\{ \frac{\Delta U1 \cdot T_{d1}}{T_{d2} - T_{d1}} - \frac{\Delta U2 \cdot T_{d3}}{T_{d3} - T_{d2}} \right\} = \frac{\delta f \cdot f_C \cdot f_{rw}}{\pi} \quad (4.55-c)$$

For example, suppose the fiber length corresponds to $T_{d,\min}$ is measured to be between 40m and 80m, or $\{200\text{ns} \leq T_{d,\min} \leq 400\text{ns}\}$, then we choose $T_{d,\min} = T_{d1} = 400\text{ns}$, and for sensible results we choose $T_{d2} \approx 10\mu\text{s}$ (2km), and $T_{d3} \approx 500\mu\text{s}$ (100km). If M is large enough such that the measurement uncertainty of center frequency deviation is **1%**, then **2%** error in the measured Allan variance is roughly expected. Suppose the measurements

are $\sigma_f(\overline{T_{d1}}) \approx 2.62\text{MHz}$, $\sigma_f(\overline{T_{d2}}) \approx 1.53\text{MHz}$, and $\sigma_f(\overline{T_{d3}}) \approx 1.6\text{MHz}$ with **1%** error, hence $\sigma_f^2(\overline{T_{d1}}) = 6.86 \times 10^{12}\text{Hz}^2$, $\sigma_f^2(\overline{T_{d2}}) = 2.34 \times 10^{12}\text{Hz}^2$, and $\sigma_f^2(\overline{T_{d3}}) = 2.56 \times 10^{12}\text{Hz}^2$ with **2%**, and $\Delta\mathbf{U1} \approx 4.52 \times 10^{12}\text{Hz}^2$ with 4% and $\Delta\mathbf{U2} \approx -0.22 \times 10^{12}\text{Hz}^2$ with about **40%** error. The LUT parameters are obtained by applying (4.55) and as listed in Table 4.2. The example shows clearly how $\mathbf{h_R}$ is sensitive to the measurement uncertainty, however, the estimation of $\delta\mathbf{f}$, and $\mathbf{f_C}$ is quite efficient. Besides, if the measurement is repeated many times, the estimated range of all parameters converges to a very accurate single point.

Table 4.2: Estimated parameters of LUT of the given example obtained using the suggested method.

Parameter	Estimated (Minimum)	Estimated (Maximum)	Exact Value	Percentage Error	Unit
h_W	1.224×10^6	1.329×10^6	1.273×10^6	$\approx 4.125\%$	Hz
h_F	6.2×10^{11}	6.53×10^{11}	6.366×10^{11}	$\approx 2.6\%$	Hz^2
h_R	6.0×10^{13}	10.3×10^{13}	8.34×10^{13}	$\approx 25\%$	Hz^3
δf	3.845	4.175	4.0	$\approx 4.125\%$	MHz
f_C	466	533	500	$\approx 6.7\%$	kHz
f_{rw}	84	180	131	$\approx 36\%$	Hz

We are now in a position to state the following assumption:

The SCL field can be resolved into two spectral components as

- i –**Time-independent** component which forms the minimal-linewidth-spectral-shape and defined from the DSH test with $\mathbf{T_d} = \mathbf{T_{d,min}}$.
- ii –**Time-dependent** component which fluctuates the center frequency $\mathbf{v_0}$ and defined from the two-sample test with $\Delta\mathbf{T} \gg \mathbf{T_{d,min}}$.

In general, the **1st** component is due to the white FN, while the **2nd** one is mainly due to the flicker FN [96]. In this assumption the laser field is assumed to be phase modulated by a source which is usually has a white PSD, and frequency modulated by a source which is usually has $1/f$ PSD such that those fields could be treated separately despite the fact that they are convolved. This assumption will be used in the feedforward loop analysis in Chapter 8.

4.4 Conclusions

In this chapter, some important characteristics of SCL have been demonstrated by analysis and calculation focusing particularly on PN. The significant effect of flicker FN on linewidth broadening is confirmed; however, in commercially available SCLs with tight active driving circuit and active cooling, this effect becomes marginal in the DSH setup with short T_d regardless of T_{OBS} . A new approximated formula for the FWHM linewidth in presence of flicker FN has been introduced and tested successfully based on comparison with experimental results in the literature. A derivation of the SCL's PSD when all parameters are counted has been achieved in both the free-running field in optical domain, and the beat-note signal in the DSH test. The numerical calculations involved in these generalized equations can be avoided benefiting from (4.29) or when some practical assumptions are used such as ignoring the IN term with $|\mathbf{H}_c(\mathbf{f})|^2 = 1$, which results in compact equations. In the measurement section, two new methods have been presented, which are concerning extraction of the parameters from the RIN measurements, and from time-domain stability measurements. By using these methods, \mathbf{F}_R , Γ , \mathbf{K}_Z , $\delta\mathbf{f}$, \mathbf{f}_C , \mathbf{f}_{rw} can be extracted accurately and repeatedly (except the case of \mathbf{f}_{rw}) and the only left unknown is α .

Chapter 5

Semiconductor Laser Simulator Model

5.1 Introduction

In this chapter, Simulink[®] functional model of a semiconductor laser (SCL) is constructed based on the theoretical study of Chapter 4 and measurements in the literature. The model is then validated using series of tests aiming to employ it as a reliable building block in the simulations throughout this work. Simulink[®] modeling is chosen to facilitate complex system simulation with different sampling frequencies, linear and nonlinear transfer functions, feedback and feedforward loops. The main aims of this chapter are to construct the functional model of SCL, and to validate the constructed building block.

5.2 Construction of SCL functional model

5.2.1 Design constraints

Simulink[®] is suitable for modeling and modification of systems with complex time-varying variables (dynamic simulation). However, the functional model of a device is certainly not the physical one, and hence the following constraints have been proposed for a successful building block:

1. The model has to exactly simulate all known SCL characteristics without any adjustment or manipulation, and assuming well above threshold current operating condition [31].
2. When the model is measured by all known measurement setups, exact results are always obtained compared to reliable measurements in the literature.
3. When a discrepancy is observed between the model results and recently developed derivations of a specific test, then a mistake has to have happened in the derivation and not in the model depending on point 1, and 2.
4. The model has to be independent of sampling frequency, a specific sample in the ensemble, and the selected seeds of random noise sources. The sampling frequency can be changed from Hz range up to THz range without change in the model specifications.

Apart from the SCL model presented here, a large library of different building blocks, which represent different optical and radio frequency (**RF**) components used in the simulations of different systems and measurement setups, has been constructed during this study using Simulink[®]. All these blocks fulfill point 2 and 3 in the aforementioned conditions, however, the SCL is the most crucial element, and hence this chapter is entirely dedicated to the SCL.

5.2.2 Model analysis

Referring to Section 4.2.2, the complex envelope of an un-modulated single-mode SCL can be characterized by its output (**O/P**) power (**P_O**) in (mW), natural linewidth (**δf**) (MHz) which results from the white part of frequency noise (**FN**), low frequency part of the relative intensity noise (**RIN_L(0)**) (dBc/Hz), relaxation oscillation frequency and damping factor (**F_R**) and (**Γ**) (GHz) and (MHz) respectively, corner frequency (**f_C**) (MHz) of the flicker part of FN, random-walk FN corner frequency (**f_{rw}**) (Hz), RIN fitting coefficient (**K_Z**) (MHz), and linewidth enhancement factor (**α**). These parameters are the essential inputs (**I/P**)s to the proposed Simulink[®] building block of SCLs. Additional parameters, such as the driving current to frequency coefficient (**β_I**) (GHz/mA), temperature to frequency coefficient (**β_{T°}**) (GHz/K), driving circuit transfer function (**TF**) or (**H_I(f)**), driving current ripple, and the state of polarization (**SOP**), are added whenever it is required [88]. This functional model is valid only when the driving current is constant and is higher than the threshold current which is the condition of practical operation in externally modulated OFDM systems. The optical center frequency (**ν_O**) (≈ 193.5 THz) of the SCL is used as a reference, and only frequency differences between different optical signals within the **1.55μm** optical window are considered in the simulation. Simulink[®] version 6.0 in conjunction with MATLAB[®] version 7.0 is used in all simulations and for constructions building blocks in this work. The first essential parameter is the sampling frequency (**F_S**) (GHz), which is set as the default when the SCL is used in complex system simulations, and chosen arbitrarily when a measurement of SCL itself is required. The second less critical parameter is the observation time (**T_{OBS}**) (s), which identifies simulation's run-time. The total number of samples per run-time is calculated as $N_{sa} = T_{OBS}/T_{sa} = T_{OBS} \cdot F_S$, where **T_{sa}** is the sampling time. When any

variable is required to be processed (plotting, variance calculation, etc.) outside Simulink[®] platform, then the common method is to export the variable in a file to the MATLAB[®] workspace, and then process off-line [112]. The discrete time and frequency vectors are expressed as, $\mathbf{n} = [1, 2, \dots, N_{\text{sa}}]$, and $\mathbf{k} = [(-N_{\mathcal{F}}/2), (-N_{\mathcal{F}}/2 + 1), \dots, (-1), (0), (1), \dots, (N_{\mathcal{F}}/2 - 1)]$ corresponding to the fast Fourier transform (\mathcal{FFT}) used in the power spectral density (**PSD**) measurement, where ($N_{\mathcal{F}}$) is the \mathcal{FFT} vector size. Hence in this case, \mathbf{n} is partitioned into \mathbf{M} segments, each with length of $N_{\mathcal{F}}$, provided that $N_{\mathcal{F}} \ll N_{\text{sa}}$ for an efficient PSD averaging [90]. The model implementation is discussed step-by-steps as follows.

- The normalized intensity noise (**IN**) term $\alpha_{\mathbf{n}}(\mathbf{t})$, is fully characterized using (4.8), and (4.9). This noise is driven by a real Gaussian random variable (**GRV**) $\mathbf{N}_i(\mathbf{t})$ with zero-mean and finite variance. Thus the double-sided (**DS**) PSD of $\mathbf{N}_i(\mathbf{t})$ is white, or by using the notation used in Section 4.2.2, $\mathcal{S}\{\mathbf{N}_i(\mathbf{t})\}$ is white.

Let $\mathbf{N}_i(\mathbf{t}) = y_1(\mathbf{t}) \cdot g_2$, where $y_1(\mathbf{t})$ is the normalized version of $\mathbf{N}_i(\mathbf{t})$ with $\sigma_{y_1}^2 = 1$. By applying the RIN TF $\mathbf{A}_c(\mathbf{f})$ in (4.9), then $\alpha_{\mathbf{n}}(\mathbf{f})$ is expressed as $\alpha_{\mathbf{n}}(\mathbf{f}) = y_1(\mathbf{f}) \cdot \sqrt{\text{RIN}_L(0)/8} \cdot \mathbf{A}_c(\mathbf{f})$. The $\mathbf{A}_c(\mathbf{f})$ vector is generated either by MATLAB[®] code, and then imported from the workspace as an external variable, or using finite impulse response (**FIR**) filter design [90]. The latter is definitely preferred since the block becomes standalone, and MATLAB[®] code is not required. In order to realize $\mathbf{A}_c(\mathbf{f})$ using the former method, a frequency vector \mathbf{k} has to be generated with \mathbf{F}_S , and $N_{\mathcal{F}}$ are selected such that the following condition is satisfied

$$\text{RBW} \ll \delta f \quad , \text{ where } \{\mathbf{RBW} = F_S/N_{\mathcal{F}}\} \text{ is the resolution bandwidth.}$$

$$\text{RBW} \ll 1/T_{\mathbf{d},\max} \quad , \text{ where } \mathbf{T}_{\mathbf{d},\max} \text{ is the maximum time delay in the complex system that the SCL is assumed to be part of it.}$$

$$F_S \gg 1/T_{\mathbf{d},\min} \quad , \text{ where } \mathbf{T}_{\mathbf{d},\min} \text{ is minimum time delay in the complex system that the SCL is assumed to be part of it. However this condition is not essential.}$$

From (4.9), the discrete version of $\mathbf{A}_c(\mathbf{f})$ is expressed as

$$\mathbf{A}_c[\mathbf{k}] \approx \frac{F_R^2}{K_z} \cdot \frac{-jk + \text{round}\{K_z/\text{RBW}\}}{(\text{round}\{F_R/\text{RBW}\})^2 - k^2 - j2k \cdot \text{round}\{\Gamma/\text{RBW}\}}$$

where $\text{round}\{\cdot\}$ is the round function. Accordingly $\alpha_n[\mathbf{n}]$ is calculated as

$\alpha_n[\mathbf{n}]|_{N_f} = g_2 \cdot \mathcal{I}\mathcal{F}\mathcal{F}\mathcal{T}\{A_c[k] \cdot \mathcal{F}\mathcal{F}\mathcal{T}\{y_1[n]\}\}$, where $\mathcal{I}\mathcal{F}\mathcal{F}\mathcal{T}$ is inverse fast Fourier transform. Window function is recommended to be applied to reject the very short spikes occurs between the successive frames [113].

- The white FN term $\omega_{nw}(\mathbf{t})$, is fully characterized using (4.4), (4.5), and (4.6). This noise is driven by two GRVs $\mathbf{N}_f(\mathbf{t})$, and $\mathbf{N}_i(\mathbf{t})$ as in (4.4).

- Let $\mathbf{y}_2(\mathbf{t})$ be the normalized version of $\mathbf{N}_f(\mathbf{t})$ with $\sigma_{y_1}^2 = \mathbf{1}$. Thus by introducing the cavity TF $\mathbf{H}_c(\mathbf{f})$, linewidth enhancement factor α , the discrete time and frequency vectors \mathbf{n} and \mathbf{k} respectively, and by following the same procedure of IN realization yields

$$\omega_{nw}[\mathbf{n}]|_{N_f} = -g_1 \cdot \gamma_1 \cdot \mathcal{I}\mathcal{F}\mathcal{F}\mathcal{T}\{H_c[k] \cdot \mathcal{F}\mathcal{F}\mathcal{T}\{y_1[n]\}\} + g_1 \cdot \gamma_2 \cdot y_2[n]$$

Where, $g_1 = \sqrt{2\pi\delta f}$, $\gamma_1 = \sqrt{\alpha^2/(1 + \alpha^2)}$, $\gamma_2 = \sqrt{1/(1 + \alpha^2)}$, and

$$\mathbf{H}_c[\mathbf{k}] \approx \frac{F_R^2}{(\text{round}\{F_R/\text{RBW}\})^2 - k^2 - j2k \cdot \text{round}\{\Gamma/\text{RBW}\}}$$

- The flicker FN term $\omega_{nf}(\mathbf{t})$ is characterized using (4.5) and the analysis in Section 4.2.3.2. This noise is generated from a white source $\mathbf{y}_3(\mathbf{t})$ with logarithmic-time memory [99]. Many techniques have been proposed to simulate this noise based on FIR filtering design; however, they are rather static, which cannot efficiently be adapted in this design [114]-[115]. Therefore, a new realization technique is proposed here based on employing the zero-order hold (**ZOH**) block as a memory element. In this technique, 31 ZOHs blocks are used with power of 2 multiples of the default sampling time per different block. Here $\{31\}$ is the maximum possible number before fractional sampling frequencies is introduced regarding to Simulink[®] V6.0. This technique is simple, fast, and results perfect fitting with the theory. The design equation is given in Table 5.1.

- The random-walk FN term $\omega_{nrw}(\mathbf{t})$ is also characterized using (4.5). This noise is generated from the integration process of a white source $\mathbf{y}_4(\mathbf{t})$, which is easy to be modeled in discrete time as

$$\omega_{nrw}[\mathbf{n}] = \sum_{m=1}^n y_4[m] \cdot g_4 \quad , \quad \text{Where} \quad g_4 = \sqrt{4\pi^3 \cdot \delta f \cdot f_c \cdot f_{rw}}$$

- The overall FN is $\omega_n[\mathbf{n}] = \omega_{nw}[\mathbf{n}] + \omega_{nf}[\mathbf{n}] + \omega_{nrw}[\mathbf{n}]$, and hence the O/P phase noise (**PN**) is calculated as

$$\Phi_n[n] = \sum_{m=1}^n \omega_n[m]$$

- The current-controlled oscillator (CCO) shifts center frequency of the SCL depending on the driving current-signal $i_d(t)$ when it is applied at the input (I/P) port (tuning port). This frequency shift is calculated as

$$f_d[n] = \beta_I \cdot i_d[n]$$

Assuming β_I is flat over $i_d(t)$'s bandwidth (BW).

5.2.3 Model implementation

From the aforementioned discussions, and referring to Fig. 5.1, a summary of all design parameters and equations are given in Table 5.1.

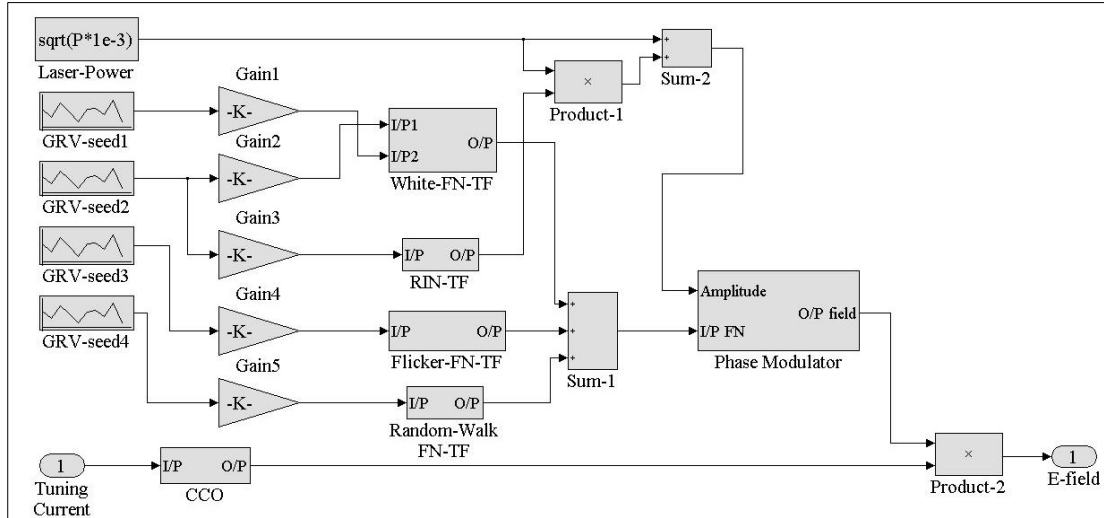


Fig. 5.1: Under mask (block's details) block diagram of the Simulink[®] V6.0 SCL building block.

Table 5.1 describes the basic SCL realization equations in the linear operating region, and hence the regions below the threshold and saturation are not considered. The SOP is assumed to be fixed. Furthermore, measured data might be required to describe some functions that cannot be generalized, such as the driving circuit TF. In this case, measured data is converted into a lookup table, or fitted by an FIR low pass filter (LPF) [113]. However, this is particularly important in wideband frequency sweeper, and in optical phase-locked loop designs which are not considered in this work [34]. In Table 5.2, a summary of all I/P variables and functional blocks used in Fig. 5.1, are connected to the variables and equations given in Table 5.1.

Table 5.1: Summary of SCL model design parameters and equations

Parameter	Equation	No.
$\alpha_n[n]$	$\alpha_n[n] _{N_F} = g2 \cdot \mathcal{I}\mathcal{F}\mathcal{F}\mathcal{T}\{A_c[k] \cdot \mathcal{F}\mathcal{F}\mathcal{T}\{y_1[n]\}\}$	(5.1)
	$A_c[k] \approx \frac{F_R^2}{K_z} \cdot \frac{-jk + \text{round}\{K_z/\text{RBW}\}}{(\text{round}\{F_R/\text{RBW}\})^2 - k^2 - j2k \cdot \text{round}\{\Gamma/\text{RBW}\}}$	(5.2)
	$g2 = \sqrt{F_S \cdot 10^9 \cdot 10^{\{\text{RIN}_L(0)/10\}}/8}$	(5.3)
	$y_1(\mathbf{t})$ is a GRV with zero-mean and $\sigma_{y_1}^2 = 1$	
$\omega_{nw}[n]$	$\omega_{nw}[n] _{N_F} = -g1\gamma1\mathcal{I}\mathcal{F}\mathcal{F}\mathcal{T}\{H_c[k] \cdot \mathcal{F}\mathcal{F}\mathcal{T}\{y_1[n]\}\} + g1\gamma2y_2[n]$	(5.4)
	$H_c[k] \approx \frac{F_R^2}{(\text{round}\{F_R/\text{RBW}\})^2 - k^2 - j2k \cdot \text{round}\{\Gamma/\text{RBW}\}}$	(5.5)
	$g1 = \sqrt{2\pi\delta f \cdot F_S \cdot 10^{15}}$	(5.6)
	$\gamma1 = \sqrt{\alpha^2/(1 + \alpha^2)}$	(5.7)
	$\gamma2 = \sqrt{1/(1 + \alpha^2)}$	(5.8)
	$y_2(\mathbf{t})$ is a GRV with zero-mean and $\sigma_{y_2}^2 = 1$	
$\omega_{nF}[n]$	$\omega_{nF}[n] = \sum_{h=0}^{30} A_h \cdot \text{ZOH}\{(y_3[n] \cdot g3), T_{Sr}\}$	(5.9)
	$T_{Sr} = 10^{-9} \cdot 2^h/F_S$	(5.10)
	$A_0 = 3/2, A_1 = 6/5, A_2 = 24/23, A_{3-30} \approx 1$	(5.11)
	$g3 = \sqrt{\pi \cdot \delta f \cdot f_c \cdot 10^{12}}$	(5.12)
	$y_3(\mathbf{t})$ is a GRV with zero-mean and $\sigma_{y_3}^2 = 1$	
$\omega_{nrw}[n]$	$\omega_{nrw}[n] = \sum_{m=1}^n y_4[m] \cdot g4 \cdot \frac{10^{-9}}{F_S}$	(5.13)
	$g4 = \sqrt{4\pi^3 \cdot \delta f \cdot f_c \cdot f_{rw} \cdot F_S \cdot 10^{21}}$	(5.14)
	$y_4(\mathbf{t})$ is a GRV with zero-mean and $\sigma_{y_4}^2 = 1$	

$\omega_n[n]$	$\omega_n[n] = \omega_{nW}[n] + \omega_{nF}[n] + \omega_{nrw}[n]$	(5.15)
$\phi_n[n]$	$\phi_n[n] = \sum_{m=1}^n \omega_n[m] \cdot \frac{10^{-9}}{F_S}$	(5.16)
E_1	$E_1 = \sqrt{P_0 \cdot 10^{-3}}$	(5.17)
$E_2[n]$	$E_2[n] = E_1 \cdot (1 + \alpha_n(n)) \cdot \exp(j\phi_n[n])$	(5.18)
$E_3[n]$	$E_3[n] = \exp(j2\pi f_d[n] \cdot n)$	(5.19)
	$f_d[n] = \beta_I \cdot 10^{12} \cdot i_d[n]$	(5.20)
	$i_d[n]$ is deriving current signal applied at the CCO I/P port	
$E_{O/P}[n]$	$E_{O/P}[n] = E_2[n] \cdot E_3[n]$	(5.21)

Table 5.2: Summary of input variables and functional blocks

Block name	Equation No.	Variables	I/P variables	Units of I/P variables	Reference Figure	Supporting Figure
Laser-Power	(5.17)	P	P_0	mW	5.1	-
GRV-seed1	(5.4)	$y_2[n]$	-	-	5.1	-
GRV-seed2	(5.1), (5.4)	$y_1[n]$	-	-	5.1	-
GRV-seed3	(5.9)	$y_3[n]$	Seed	-	5.1	-
GRV-seed4	(5.13)	$y_4[n]$	-	-	5.1	-
Gain1	(5.6)	g1	δf F_S	MHz GHz	5.1	-
Gain2	(5.6)	g1	δf F_S	MHz GHz	5.1	-
Gain3	(5.3)	g2	$RIN_L(0)$ F_S	dBc/Hz GHz	5.1	-
Gain4	(5.12)	g3	δf f_c	MHz MHz	5.1	-

Block name	Equation No.	Variables	I/P variables	Units of I/P variables	Reference Figure	Supporting Figure
Gain5	(5.14)	g_4	δf f_c f_{rw} F_S	MHz MHz Hz GHz	5.1	-
CCO	(5.19), (5.20)	$E_3[n]$, $f_d[n]$	β_I	GHz/mA	5.1	5.6
White-FN-TF	(5.4), (5.5), (5.7), (5.8)	$\omega_{nW}[n] _{N_F}$	F_S α F_R Γ N_F	GHz - GHz MHz -	5.1	5.2
RIN-TF	(5.1), (5.2)	$\alpha_n[n] _{N_F}$	F_S F_R Γ K_z N_F	GHz GHz MHz MHz -	5.1	5.3
Flicker-FN-TF	(5.9), (5.10), (5.11)	$\omega_{nF}[n]$	F_S Seed	GHz -	5.1	5.4
Random-Walk-FN-TF	(5.13)	$\omega_{nrw}[n]$	F_S	GHz	5.1	-
Phase Modulator	(5.16), (5.18)	$\phi_n[n]$, $E_2[n]$	F_S	GHz	5.1	5.5

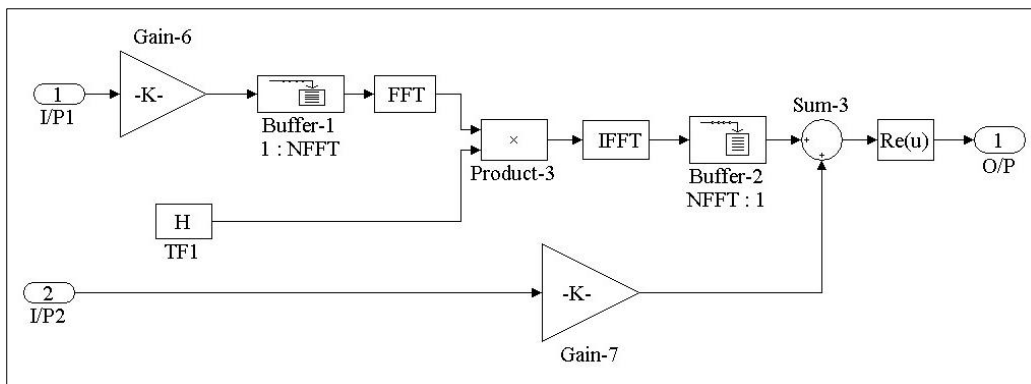


Fig. 5.2: Simplified under mask block diagram of the White-FN-TF block. Where \mathbf{H} corresponds to $\mathbf{H}_c[\mathbf{k}]$, **Gain6**, and **Gain7** correspond to γ_1 in (5.7) and γ_2 in (5.8) respectively. Note that the smoothing window is not shown, and the $\mathbf{Re}(\mathbf{u})$ block is used to reject the 150dB down imaginary component which causes signal error due to the data type attribute in Simulink®.

The GRVs $y_1[n]$, $y_2[n]$, $y_3[n]$, and $y_4[n]$ are independent GRVs (uncorrelated). Since the flicker FN causes an initial frequency shift as discussed in Section 4.2.3.2, selection of $y_3[n]$ seed is effective especially in short T_{OBS} . When the seed of $y_3[n]$ is set to be $\{410\}$, then the initial frequency shift is very small.

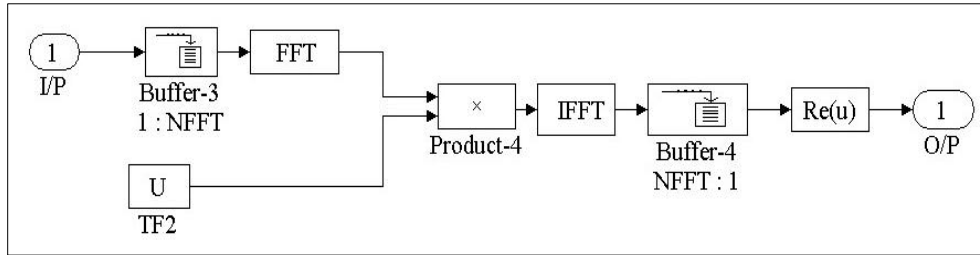


Fig. 5.3: Simplified under mask block diagram of RIN-TF block. Where U corresponds to $A_c[k]$.

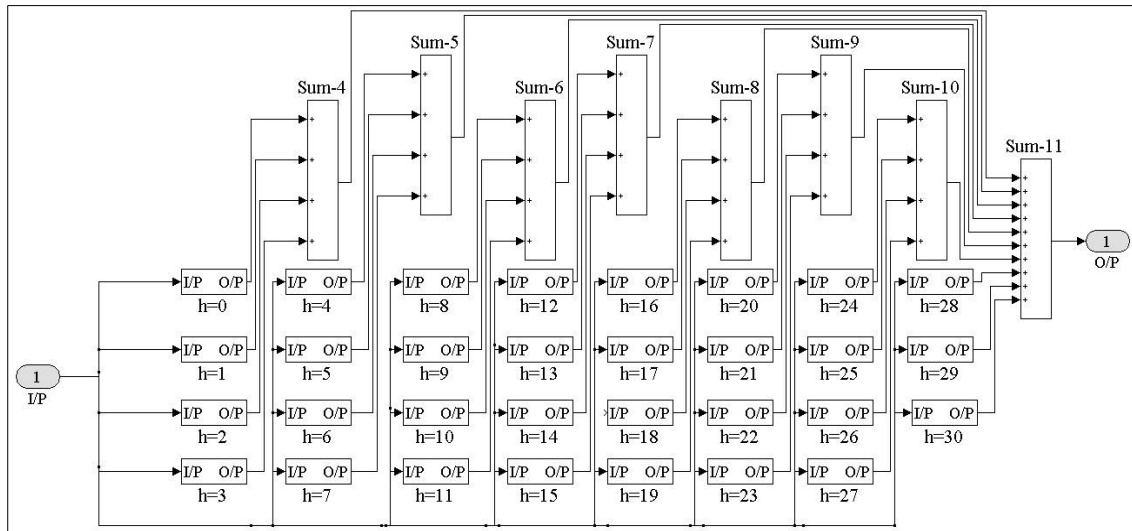


Fig. 5.4: Under mask of the flicker-FN-TF block. It consists of 31 ZOH blocks with logarithmic sampling time per block as given in (5.9)-(5.12).

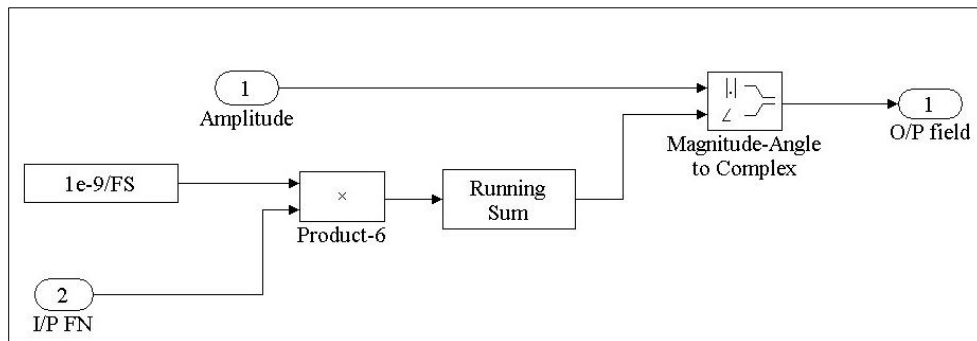


Fig. 5.5: Under mask of the Phase Modulator block.

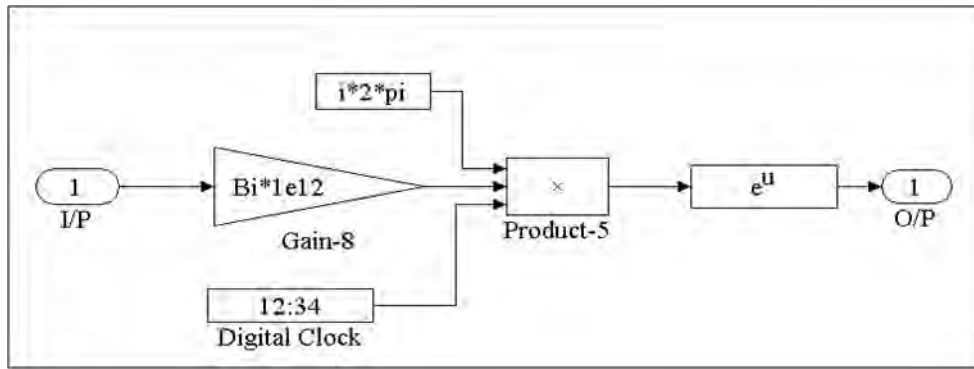


Fig. 5.6: Under mask of the CCO block.

5.3 Model validation

The building block is tested to examine its matching with well known SCL characteristics by simulating the measurement methods discussed in Chapter 4. The FN single-sided (SS) PSD is examined first, then FN and phase noise (PN) of the white and flicker components in time domain (TD) are examined and compared to reliable references in the literature. Finally the DSH test is used to simulate the beat-note SS-PSD. Note that PSD of the SCL in optical domain and RIN have been tested earlier in Chapter 4, and hence to avoid duplication, these tests are omitted here.

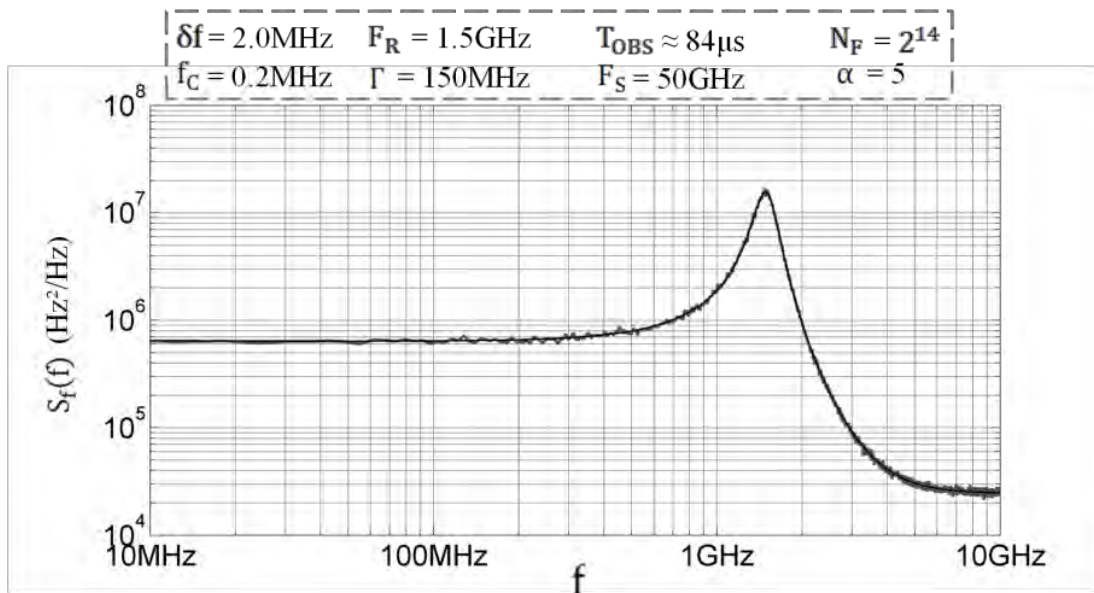


Fig. 5.7: Wide band FN-SS-PSD monitoring in relatively short T_{OBS} , and large F_S .

5.3.1 FN monitoring

The FN simulation is conducted in five different tests with different resolution to investigate if sampling frequency, laser parameters, and observation time might affect the result. All the five tests are successful since no discrepancy is observed in any test. The black solid line shown in Fig. 5.7-5.11 is the calculated SS-PSD of the FN as given by (4.5). All parameters and test conditions are attached with the figures for convenience.

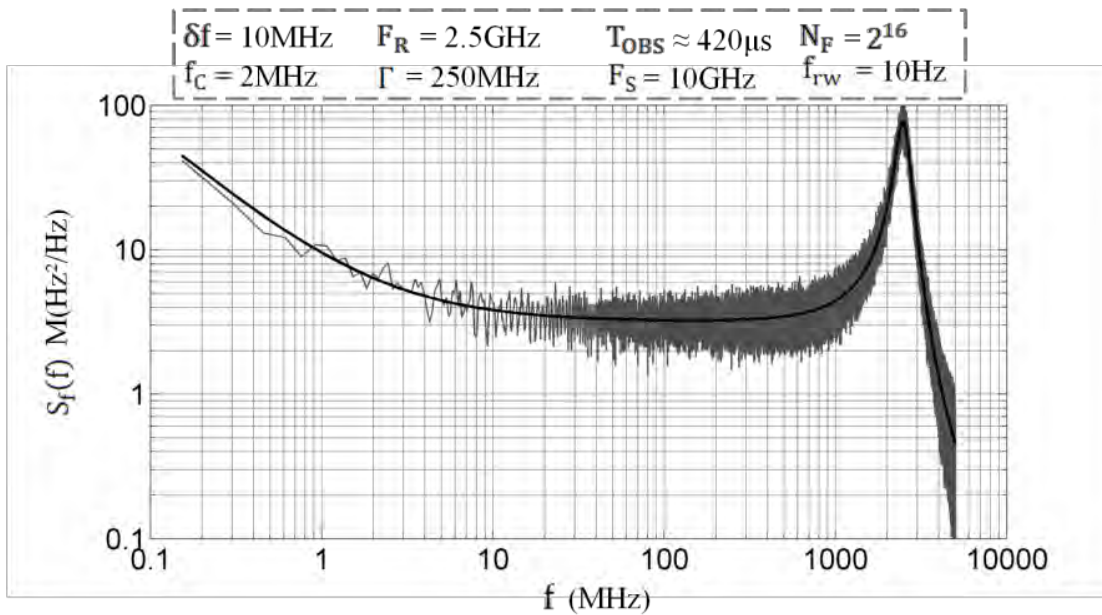


Fig. 5.8: FN-SS-PSD monitoring in relatively large linewidth.

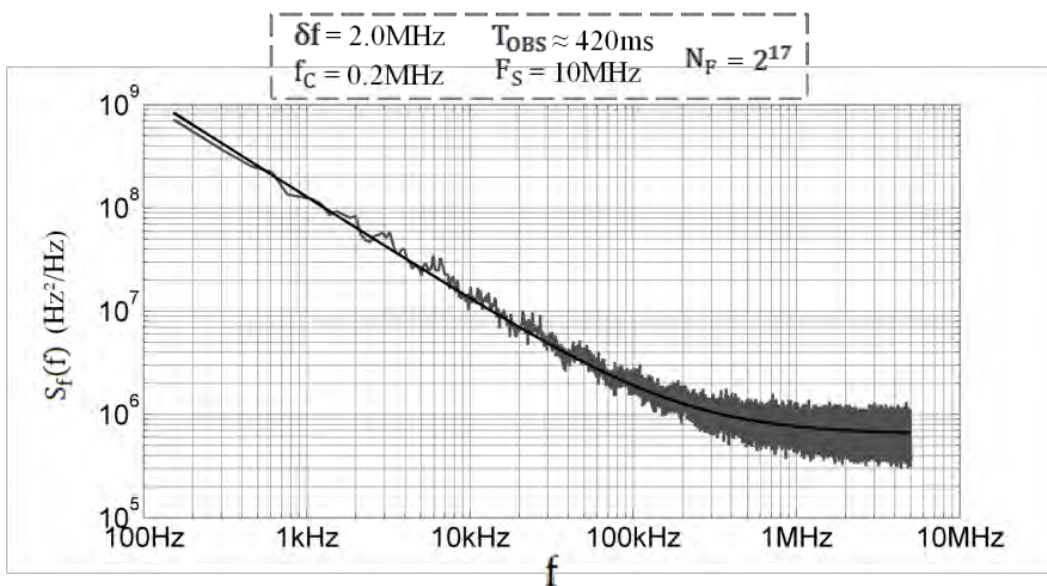


Fig. 5.9: FN-SS-PSD monitoring in relatively long T_{OBS} , and low F_S .

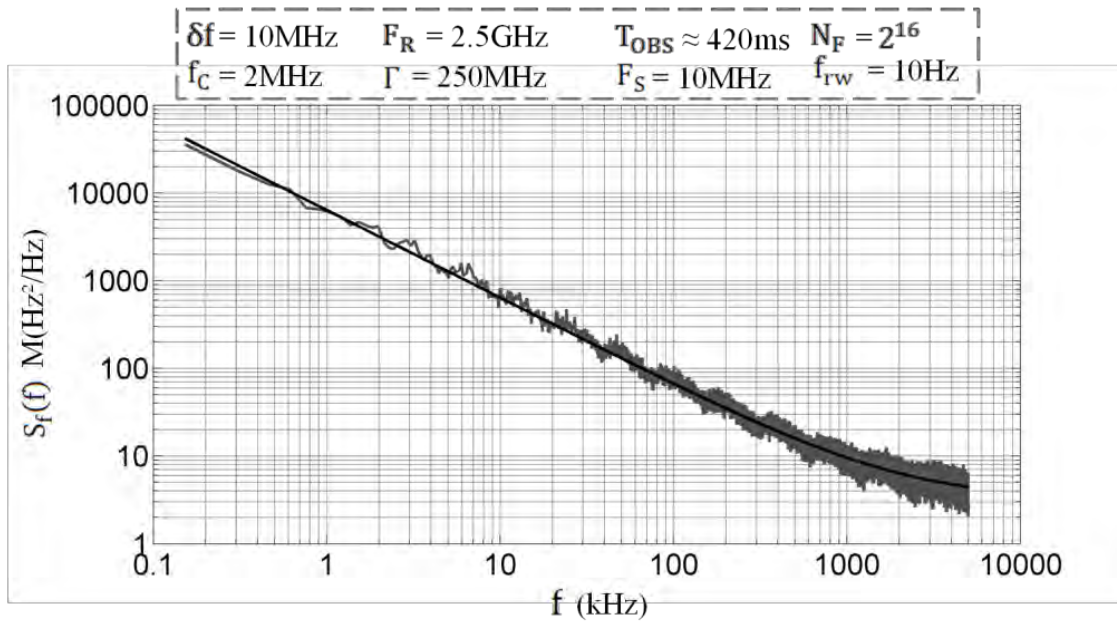


Fig. 5.10: FN-SS-PSD monitoring in relatively large linewidth, long T_{OBS} , and low F_S .

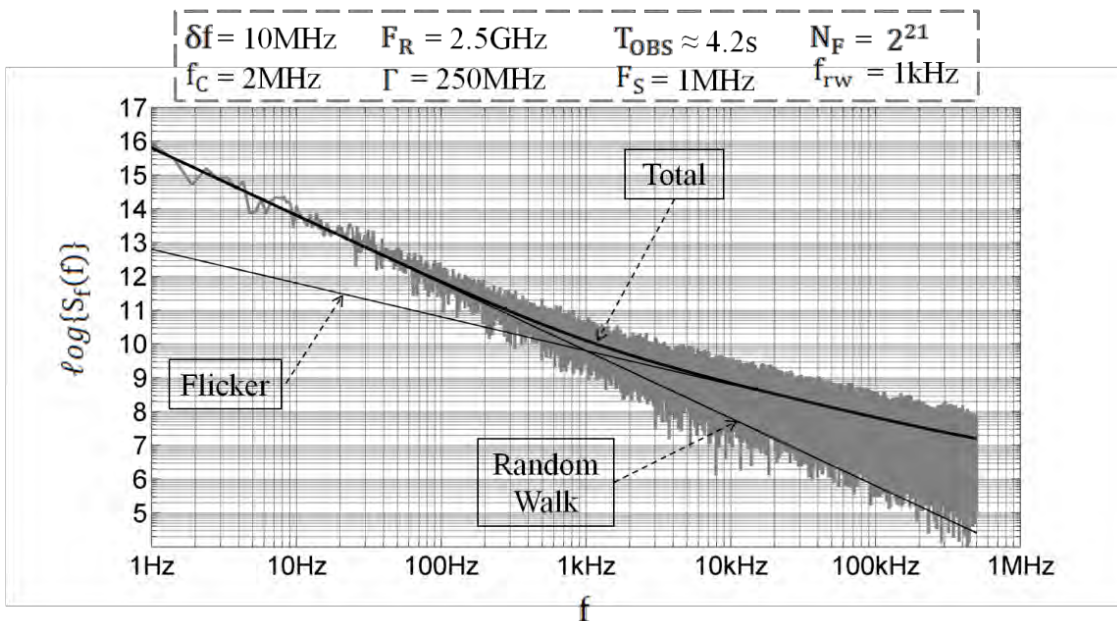
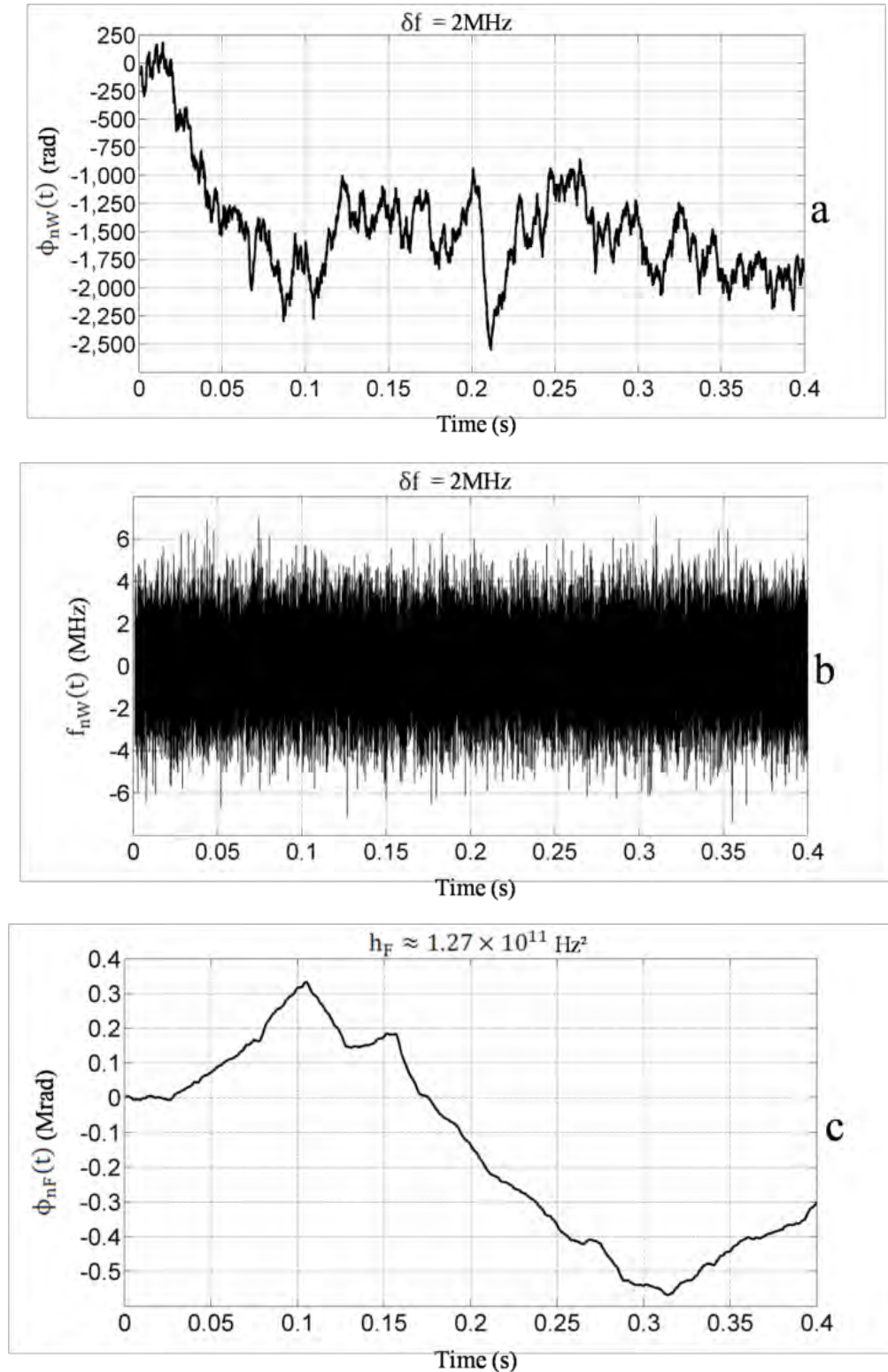


Fig. 5.11: FN-SS-PSD monitoring in logarithm of logarithmic scale focusing on random-walk component. Here relatively high f_{rw} is chosen for demonstration purposes.

5.3.2 Time domain monitoring

The FN and PN of both the flicker and the white components are demonstrated in the time domain with relatively long T_{OBS} for more in depth understanding of the behavior of the two components. A good agreement is observed between the simulation results and

the references [114], [115], [116], [31] (Chapter 6, Sections 6.4.3, and 6.6.2), [88], [96], which indicates the validity of this SCL model. In Fig. 5.12, h_W , h_F are white and flicker FN coefficients defined by (4.5).



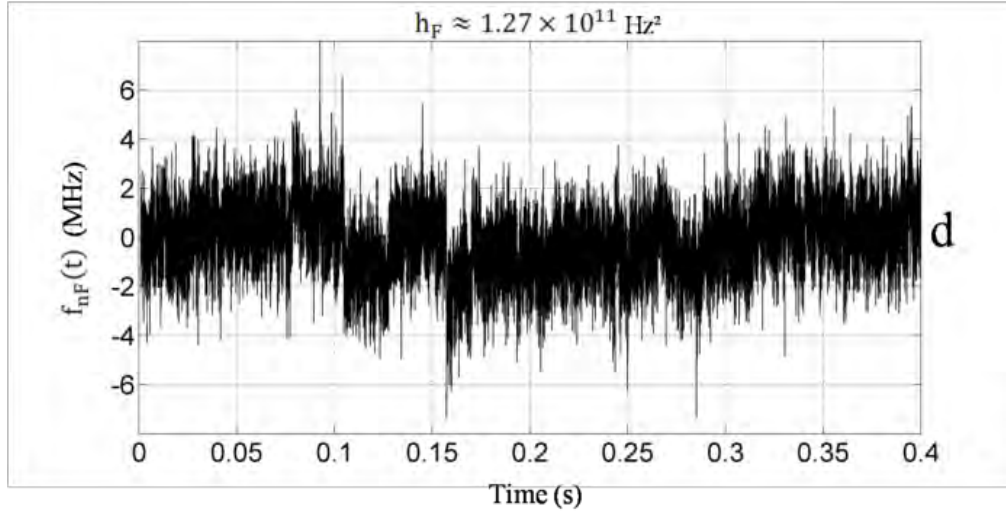


Fig. 5.12: Monitoring of SCL noise in time domain for a given seed. PN and FN of the white component are shown in (a) and (b) respectively, and PN and FN of the flicker component in (c) and (d) respectively.

5.3.3 Simulation results of DSH test

The DSH test setup shown in Fig. 4.14 is employed here with three distinct simulations. In the first test, the white, flicker, and the convolved beat-note SS-PSDs are monitored together with either the amplitude or the center frequency shifted to distinguish between them as shown in Fig. 5.13, and 5.14. In the second test, effect of differential time (T_d) is monitored in separate figures for each component as shown in Fig. 5.15.

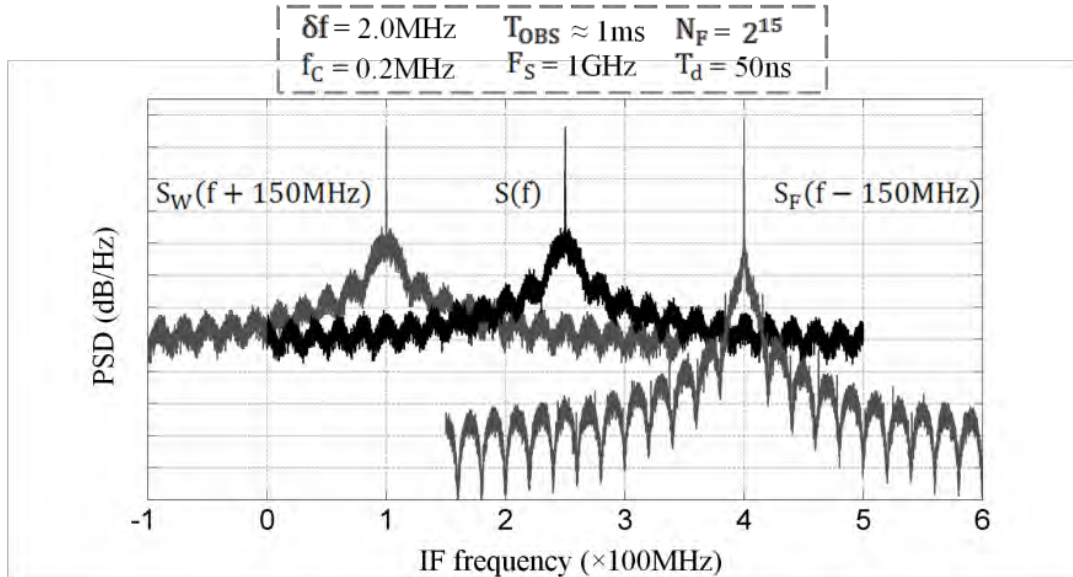


Fig. 5.13: Comparison of SS-PSD in DSH test of white $S_W(f)$, flicker $S_F(f)$, and beat-note $S(f)$, showing the dominant component. Here IF stands for “intermediate frequency”. Note that $S_F(f)$ decays much faster than $S_W(f)$, since it follows a Gaussian envelope [96].

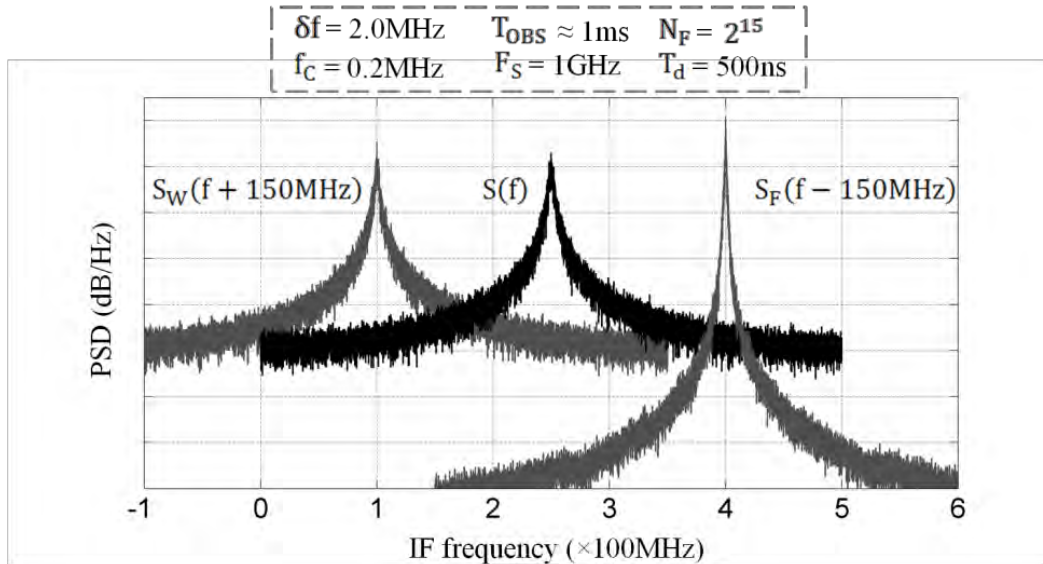
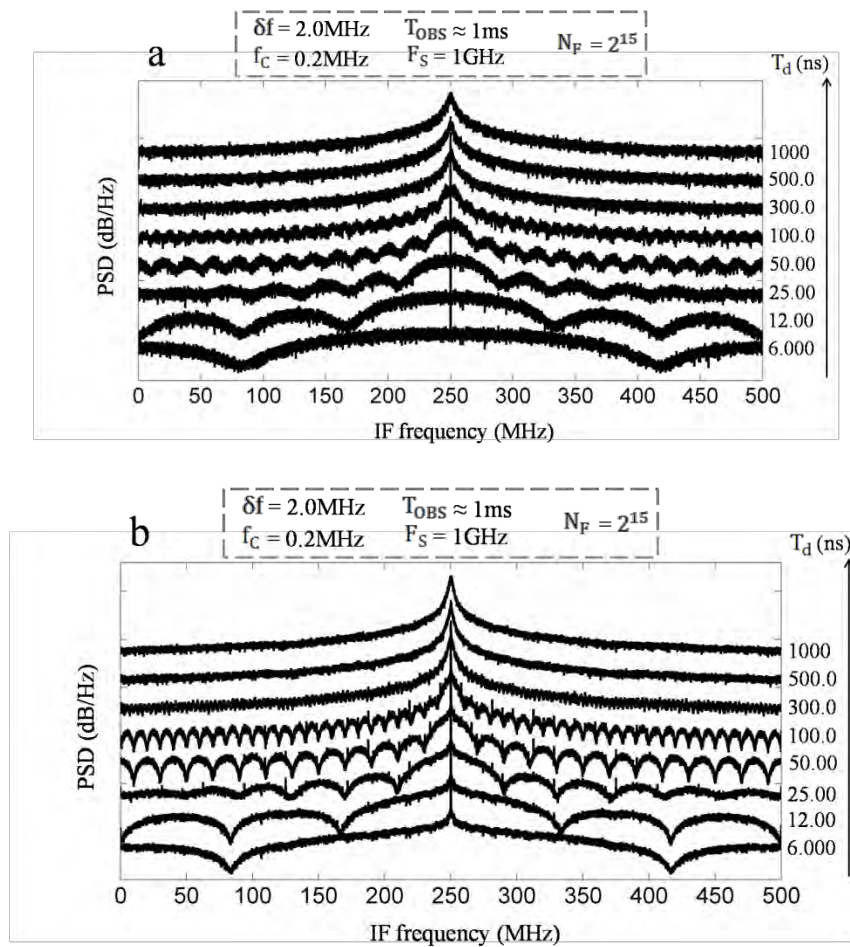


Fig. 5.14: Comparison of SS-PSD in DSH test of white $S_W(f)$, flicker $S_F(f)$, and beat-note $S(f)$, with 10 times higher T_d than the previous test. Note that $\delta(f)$ of $S_F(f)$ is higher by 6dB the $\delta(f)$ of $S_W(f)$, while $\delta(f)$ of $S(f)$ is almost vanished.



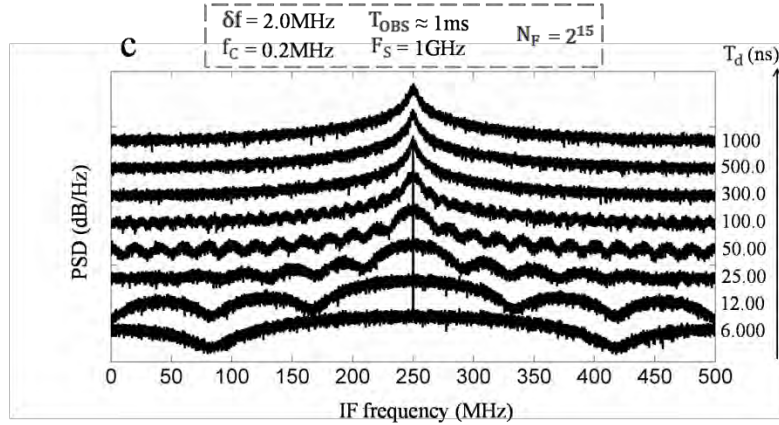
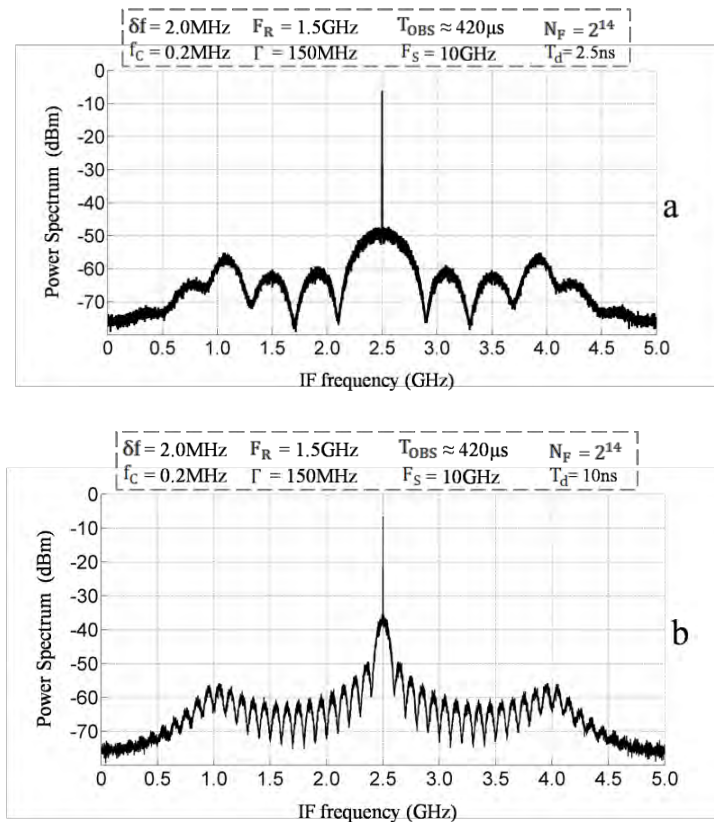


Fig. 5.15: Comparison of SS-PSD in DSH test of white $S_W(f)$ in (a), flicker $S_F(f)$ in (b), and beat-note $S(f)$ in (c) as a function of T_d for a given seed of the flicker component. The white and the beat-note PSDs are shifted by 20dB, while the flicker PSDs by 30dB for illustration.

In the previous tests, Fig. 5.13, 5.14, 5.15, the relaxation oscillation is ignored. While in the last test, Fig. 5.16, only the beat-note SS-PSD is shown taking into account the relaxation oscillation as in Fig. 5.16. In all the tests, perfect matching is observed between equation (4.38) and simulation results.



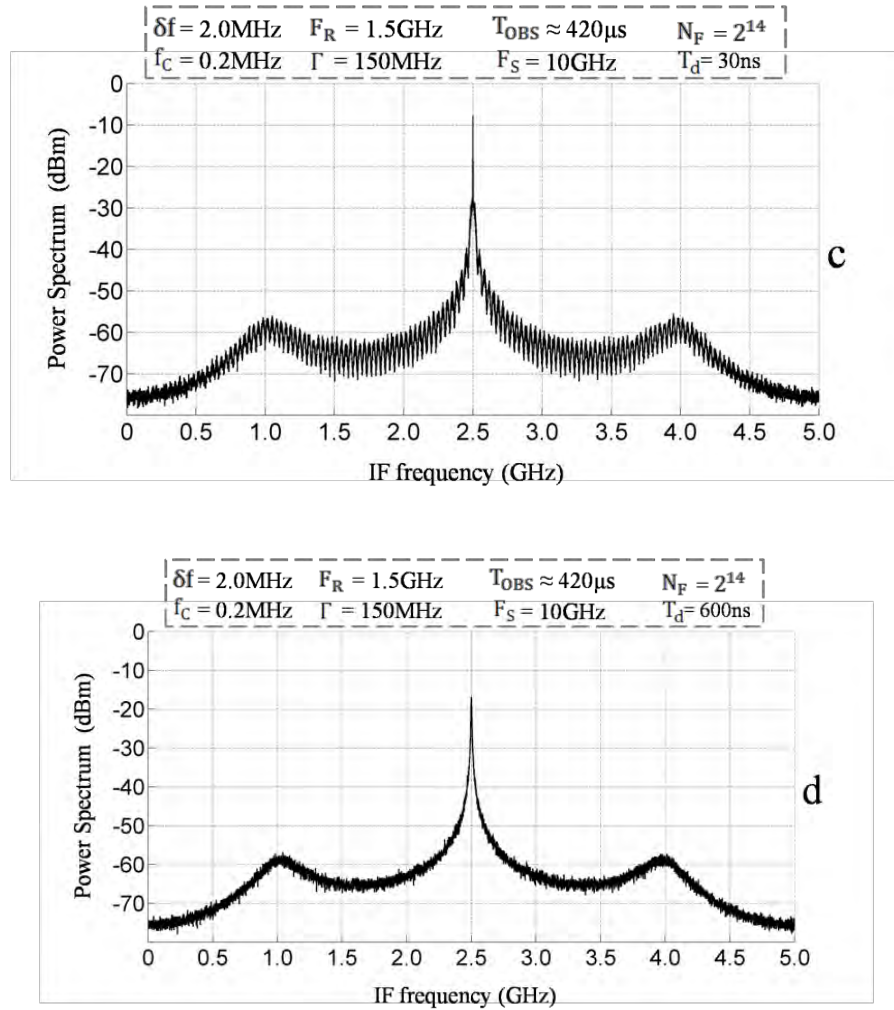


Fig. 5.16: Expected beat-note power spectrum in (dBm) in the DSH test with balanced-detector setup showing the evolution from heavily-nulled spectrum in (a) to a smoother spectrum in (d) as a function of T_d . Assuming IF amplifier's power gain of 13dB is used, $P_0 = 1\text{mW}$, $P_1 = P_2 = P_0/2$, and $\mathcal{R} = 1$.

5.4 Conclusions

In this chapter, a valid and reliable Simulink[®] functional model of the SCL has been constructed and tested. The model matches theoretical results given in Chapter 4, as well as experimental results from reliable references without any discrepancies. A new simple and yet efficient technique of flicker FN generation is demonstrated and employed in the model. Although this functional model is not a physical one, however, it simulates SCL's dynamics and noise satisfactorily. Accordingly the constructed model is considered to be valid and hence it will be used throughout this work.

Chapter 6

Exact Analysis of Semiconductor Laser Field along an Optical Fiber

6.1 Introduction

In this chapter, an analysis of semiconductor laser (SCL) field along the optical channel is accomplished to facilitate exact penalty estimation for coherent optical OFDM (CO-OFDM) systems in the next chapter. It is well known that optical channel (Standard Single-Mode Fiber) is highly dispersive in the 1.55 μm optical window, and hence SCLs' parameters must be measured or estimated well before using it in a specific system to be able to estimate the penalties and decide the required signal to noise ratio (SNR) margins. Chromatic dispersion (CD) is one of the challenging impairments of an optical channel since it produces a time distortion that has significant impact on the performance of a long-haul optical link. This time-distortion impairs not only the modulated signal, but also the optical carrier itself and phenomenon like phase noise (PN) to intensity noise (IN) conversion occur [45]. In CO-OFDM systems, the CD distorts the spectral components of every subcarrier with an identical transfer function (TF) over all subcarriers, and introduces a differential time delay (T_d) between the subcarriers, which is proportional to the frequency separation between them [55], [41]. Therefore an exact calculation of channel response is required especially when a pilot-aided feedforward loop (PA-FFL) is used in the receiver [36], [40]. The delayed self-heterodyne (DSH) test can be employed to simulate pilot-subcarrier beat-note power spectral density (PSD) with a setup similar to that shown in Fig. 6.1. This setup is useful to simulate heterodyne pilot-subcarrier beat-note PSD, self beat (direct detection by photo diode) PSD of both the pilot and the subcarrier, and homodyne pilot-subcarrier cross PSD. The main aims of this chapter are to:

- derive the exact pilot-subcarrier beat-note's PSD,
- isolate the PN and IN PSDs,
- make the results adaptable for the discrete calculation in the next chapter.

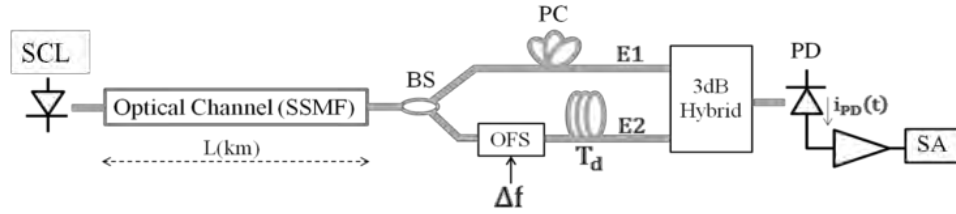


Fig. 6.1: DSH setup for dispersive field measurement. **BS** is beam splitter, **PC** is polarization controller, and **SA** is spectrum analyzer.

6.2 PSD of dispersive field components

PN to IN conversion of a SCL field was first analyzed by Yamamoto *et al.* while measuring SCL's RIN in a dispersive channel [45]. In their analysis, they expanded the laser's field using a Fourier-Bessel expansion assuming only white FN with $|\mathbf{H}_c(\mathbf{f})|^2 = 1$ (Section 4.2.2). They obtained a complicated and yet approximate solution for the dispersive field's RIN or $\mathbf{RIN}_D(\mathbf{f})$ which can be written as

$$\mathbf{RIN}_D(\mathbf{f}) \approx 8 \left\{ \sum_{n=0}^{\infty} J_x \left(\frac{1}{f} \sqrt{\frac{2\delta f}{\pi}} \right) J_{x+1} \left(\frac{1}{f} \sqrt{\frac{2\delta f}{\pi}} \right) \sin\{(2x+1)\pi f^2 \beta_D(L)\} \right\}^2 \quad (6.1)$$

where \mathbf{f} is the baseband (**BB**) frequency in (Hz), $J_x(\)$ is Bessel function of the first kind and order x [81], and $\beta_D(L)$ is the total group-velocity dispersion (**GVD**) over the channel in (s/Hz), and $\beta_D(L = 1\text{km}) \approx 1.4 \times 10^{-22}$ (s/Hz) for SSMF at the $1.55\mu\text{m}$ optical window as given in (3.10). Further analyses of $\mathbf{RIN}_D(\mathbf{f})$ have been done since Yamamoto's publication by obtaining more exact formulas and when all relevant SCL's parameters are included [46]-[47]. However, exact analytical solutions of $\mathbf{RIN}_D(\mathbf{f})$ when all SCL's parameters are counted are not possible in general, and hence it has to be solved numerically. For instance, in [46], although IN is included in the calculation, the result is valid only for short observation time (\mathbf{T}_{OBS}), and when the PN standard deviation is much lower than unity. While in [47], an exact solution is introduced when only white FN is counted and $|\mathbf{H}_c(\mathbf{f})|^2 = 1$; however, the derivation is not given in detail but the final result is accurate. Accordingly, in this chapter a further step in describing the dispersive field as well as the received PN and IN components before detection is performed is required to facilitate the beat-note PSD analysis of different detection

structures. In general, when the amplified spontaneous emission (**ASE**) noise is ignored, then from (4.2), and Section (3.2.3), the received field is exactly expressed as

$$E_r(f) = E(f) \cdot H_{ch}(f) \quad (6.2-a)$$

$$E_r(t) = \sqrt{P_O} \cdot \mathcal{JFT} \left\{ H_{ch}(f) \cdot \mathcal{FT} \left\{ \exp(j2\pi\nu_O t + j\phi_n(t) + \alpha_n(t)) \right\} \right\} \quad (6.2-b)$$

where: P_O is the transmitted output power, ν_O is the optical frequency (≈ 193.5 THz), $\phi_n(t)$ is PN in time domain (**TD**), $\alpha_n(t)$ is normalized IN in TD, \mathcal{FT} , and \mathcal{JFT} are the Fourier transform and inverse Fourier transform respectively. Although the channel response $H_{ch}(f)$ is covered in Section 3.2.3, it is required to be rewritten here after removing all constant terms to become

$$H_{ch}(f, L) = g_{ch}(L) \cdot \exp(-j\pi f^2 \beta_D(L)) \quad (6.3)$$

where, $g_{ch}(L)$ is the net gain/attenuation of the whole link. Now, by assuming that the received field contains also PN and IN terms (similar to (4.2)) even when $\alpha_n(t)$ is ignored, then (6.2-b) can be expressed as

$$E_r(t) = \sqrt{P_r} \cdot \exp(j2\pi\nu_O t + \alpha_{rn}(t) + j\phi_{rn}(t)) \quad (6.4)$$

where, P_r is the received optical power, $\phi_{rn}(t)$ and $\alpha_{rn}(t)$ are PN and normalized-IN terms after the dispersive channel respectively.

When the transmitted field is examined over a short T_{OBS} , and the PN standard deviation is much smaller than unity, then an approximation is possible and the baseband (**BB**) version of (4.2) can be written in time domain (**TD**) and in frequency domain (**FD**) as

$$E(t) \approx \sqrt{P_O} \cdot \{1 + \alpha_n(t) + j\phi_n(t)\} \quad (6.5-a)$$

$$E(f) \approx \sqrt{P_O} \cdot \{\delta(f) + \alpha_n(f) + j\phi_n(f)\} \quad (6.5-b)$$

Hence from (6.2-a), and (6.3), the BB version of the received field in FD is given by

$$\begin{aligned} E_r(f) &\approx \sqrt{P_r} \cdot \{\delta(f) + \alpha_n(f) + j\phi_n(f)\} \cdot \exp(-j\pi f^2 \beta_D(L)) \\ &= \sqrt{P_r} \cdot \{\delta(f) + \alpha_n(f) + j\phi_n(f)\} \cdot \{\cos(\pi f^2 \beta_D(L)) - j \sin(\pi f^2 \beta_D(L))\} \end{aligned} \quad (6.6)$$

Therefore by substituting of (4.12), then $E_r(t)$ is approximated as

$$\begin{aligned} E_r(t) &\approx \sqrt{P_r} \cdot \left\{ 1 + \int_0^\infty \left\{ \cos(\Psi) (\alpha_n(f) e^{j2\pi f t} + \alpha_n^*(f) e^{-j2\pi f t}) \right. \right. \\ &\quad \left. \left. + \sin(\Psi) (\phi_n(f) e^{j2\pi f t} + \phi_n^*(f) e^{-j2\pi f t}) \right\} df \right. \\ &\quad \left. + j \int_0^\infty \left\{ \cos(\Psi) (\phi_n(f) e^{j2\pi f t} + \phi_n^*(f) e^{-j2\pi f t}) \right. \right. \\ &\quad \left. \left. - \sin(\Psi) (\alpha_n(f) e^{j2\pi f t} + \alpha_n^*(f) e^{-j2\pi f t}) \right\} df \right\} \end{aligned} \quad (6.7)$$

where $\Psi = \pi\beta_D(L)f^2$, and * symbol is used for complex conjugation.

By comparing (6.7) with the approximate version of (6.4), then

$$\alpha_{rn}(t) \approx \int_0^{\infty} \left\{ \cos(\Psi) (\alpha_n(f)e^{j2\pi ft} + \alpha_n^*(f)e^{-j2\pi ft}) + \sin(\Psi) (\phi_n(f)e^{j2\pi ft} + \phi_n^*(f)e^{-j2\pi ft}) \right\} df \quad (6.8-a)$$

$$\phi_{rn}(t) \approx \int_0^{\infty} \left\{ \cos(\Psi) (\phi_n(f)e^{j2\pi ft} + \phi_n^*(f)e^{-j2\pi ft}) - \sin(\Psi) (\alpha_n(f)e^{j2\pi ft} + \alpha_n^*(f)e^{-j2\pi ft}) \right\} df \quad (6.8-b)$$

Hence from (6.4), the auto-correlation (ACF) of $\mathbf{E}_r(t)$ is,

$$\begin{aligned} R_{E_r}(\tau) &= \langle E_r(t) \cdot E_r^*(t - \tau) \rangle \\ &= P_r \cdot \exp(j2\pi\nu_0\tau) \cdot \langle \exp(\alpha_{rn}(t) + \alpha_{rn}(t - \tau) + j\phi_{rn}(t) - j\phi_{rn}(t - \tau)) \rangle \end{aligned} \quad (6.9)$$

Let

$\mathbf{x}_1(t) = \alpha_{rn}(t) + \alpha_{rn}(t - \tau)$, and $\mathbf{x}_2(t) = \phi_{rn}(t) - \phi_{rn}(t - \tau)$. Then from (6.8), and by assuming $\mathbf{x}_1(t)$, and $\mathbf{x}_2(t)$ are zero-mean Gaussian random variables (GRV) then

$$\frac{\langle |\mathbf{x}_1(t)|^2 \rangle}{2} = 4 \int_0^{\infty} \left\{ \cos^2(\pi f\tau) \cdot (S_{\alpha_n}(f)\cos^2(\Psi) + S_{\phi_n}(f)\sin^2(\Psi) + S_{X_r}(f)\sin(2\Psi)) \right\} df \quad (6.10-a)$$

$$\frac{\langle |\mathbf{x}_2(t)|^2 \rangle}{2} = 4 \int_0^{\infty} \left\{ \sin^2(\pi f\tau) \cdot (S_{\alpha_n}(f)\sin^2(\Psi) + S_{\phi_n}(f)\cos^2(\Psi) - S_{X_r}(f)\sin(2\Psi)) \right\} df \quad (6.10-b)$$

$$j\langle \mathbf{x}_1(t)\mathbf{x}_2^*(t) \rangle = 4 \int_0^{\infty} \sin(2\pi f\tau) \cdot S_{X_g}(f) df \quad (6.10-c)$$

where $S_{\alpha_n}(f)$, $S_{\phi_n}(f)$, $S_{X_r}(f)$, and $S_{X_g}(f)$ are the SCL's normalized-IN, PN, real and imaginary parts of cross noise double-sided (DS) PSD respectively. These PSDs can be calculated from (4.3), (4.5), (4.6), (4.8), (4.9), Appendix-A1, and the analysis in Section 4.2.3.2. Now by recalling (4.5), and (4.11), and by applying Wiener-Khintchin theorem, then the overall DS-PSD of $\mathbf{E}_r(t)$ in optical domain (OD) is

$$\begin{aligned} S_{E_r}(f) &= \mathcal{FT}\{R_{E_r}(\tau)\} = P_r \cdot \{ \exp(j2\pi\nu_0\tau) \} \\ &* \mathcal{FT} \left\{ \exp \left(\frac{\langle |\mathbf{x}_1(t)|^2 \rangle}{2} - \frac{\langle |\mathbf{x}_2(t)|^2 \rangle}{2} - \frac{\langle |\mathbf{x}_2(t)|^2 \rangle}{2} + j\langle \mathbf{x}_1(t)\mathbf{x}_2^*(t) \rangle \right) \right\} \\ &= P_r \cdot \delta(\nu - \nu_0) * S_{E_{rPN}}(f) * S_{E_{rIN}}(f) * S_X(f) * \mathcal{L}_F(f) \end{aligned} \quad (6.11)$$

Where $*$ stands for convolution, $\delta(\cdot)$ is the delta function, $\mathbf{x}_{2W}(\mathbf{t})$ is PN variances due to white FN, $\mathbf{x}_{2F}(\mathbf{t})$ is PN variances due to flicker FN, $\mathcal{L}_F(\mathbf{f}) = \mathcal{FT}\{e^{-\langle|\mathbf{x}_{2F}(\mathbf{t})|^2\rangle/2}\}$, is the DS-PSD of SCL's component due to flicker FN, $\mathbf{S}_{E_{rPN}}(\mathbf{f}) = \mathcal{FT}\{e^{-\langle|\mathbf{x}_{2W}(\mathbf{t})|^2\rangle/2}\}$, is the DS-PSD of SCL's component due to the dispersive white FN, $\mathbf{S}_{E_{rIN}}(\mathbf{f}) = \mathcal{FT}\{e^{\langle|\mathbf{x}_1(\mathbf{t})|^2\rangle/2}\}$, is the DS-PSD of the SCL field's component due to the dispersive IN, and $\mathbf{S}_X(\mathbf{f}) = \mathcal{FT}\{e^{j\langle\mathbf{x}_1(\mathbf{t})\mathbf{x}_2^*(\mathbf{t})\rangle}\}$, is the DS-PSD of the SCL field's component due to the cross dispersive IN and PN. Note that the random-walk in this derivation has been ignored since it has negligible effect in a short \mathbf{T}_{OBS} , and the flicker FN is assumed to be dispersion-independent since $\langle|\mathbf{x}_{2F}(\mathbf{t})|^2\rangle$ is marginal for short differential delay as discussed in section 4.3.3. Besides, $\mathbf{x}_{2W}(\mathbf{t})$, and $\mathbf{x}_{2F}(\mathbf{t})$ can be separated since they are completely uncorrelated [96]. From (6.11), the following notes have been observed:

- The cross noise $\mathbf{S}_X(\mathbf{f})$ term is independent on channel's dispersion. This can be easily proven by comparing (6.10-c) with (4.13).
- $\mathbf{S}_{E_r}(\mathbf{f})$ is identical to the non-dispersive one or $\mathbf{S}_E(\mathbf{f})$ whatever the fiber length is. This can easily be proven by comparing $\mathbf{R}_{E_r}(\boldsymbol{\tau})$ in (6.11) with (4.13).

Since no analytical solution is possible for (6.11), an important special case is considered here which is when only the white FN is counted and $\{|\mathbf{H}_c(\mathbf{f})|^2 = 1\}$, and all other SCL's parameters are ignored, then the individual components in (6.11) become,

$$\mathbf{S}_X(\mathbf{f}) = \delta(\mathbf{f}), \quad \mathcal{L}_F(\mathbf{f}) = \delta(\mathbf{f}),$$

$$\mathbf{S}_{E_{rPN}}(\mathbf{f}) = \mathcal{FT}\{exp(-4 \int_0^\infty S_{\phi_n}(f) \sin^2(\pi f \tau) \cos^2(\Psi) df)\}, \text{ and}$$

$$\mathbf{S}_{E_{rIN}}(\mathbf{f}) = \mathcal{FT}\{exp(4 \int_0^\infty S_{\phi_n}(f) \cos^2(\pi f \tau) \sin^2(\Psi) df)\}.$$

Solutions of these integrals involve Fresnel sine and cosine integrals [81] and other functions which do not show the hidden analytical expression. However, an extensive calculation leads to a semi-exact dispersive field model that describes $\mathbf{S}_{E_{rPN}}(\mathbf{f})$, and $\mathbf{S}_{E_{rIN}}(\mathbf{f})$ separately as

$$\mathbf{S}_{E_{rPN}}(\mathbf{f}) = \mathcal{L}_W(\mathbf{f}) \cdot \left(\frac{1 + exp(-\gamma) \cdot (\cos(2\Psi) + \gamma \cdot \text{sinc}(2\Psi/\pi))}{2} \right) \quad (6.12-a)$$

$$\mathbf{S}_{E_{rIN}}(\mathbf{f}) = \delta(\mathbf{f}) + \mathcal{L}_W(\mathbf{f}) \cdot \left(\frac{1 - exp(-\gamma) \cdot (\cos(2\Psi) + \gamma \cdot \text{sinc}(2\Psi/\pi))}{2} \right) \quad (6.12-b)$$

where $\boldsymbol{\gamma} = 2\pi\delta\mathbf{f} \cdot |\beta_D(\mathbf{L}) \cdot \mathbf{f}|$, and $\mathcal{L}_W(\mathbf{f})$ is defined in (4.14-b).

While when all parameters are taken into consideration, then (6.10), and (6.11) have to be solved numerically. However, the following useful features might be employed

$$|H_c(\mathbf{f})|^2 \approx 1, \text{ and } |A_c(\mathbf{f})|^2 \approx 1 \quad \dots\dots\dots f \ll F_R \quad (6.13-a)$$

$$\mathcal{L}_W(\mathbf{f}) \approx S_{\phi_n}(\mathbf{f}) \quad \dots\dots\dots f \gg \delta\mathbf{f} \quad (6.13-b)$$

Accordingly, the individual components of (6.11) can be written as

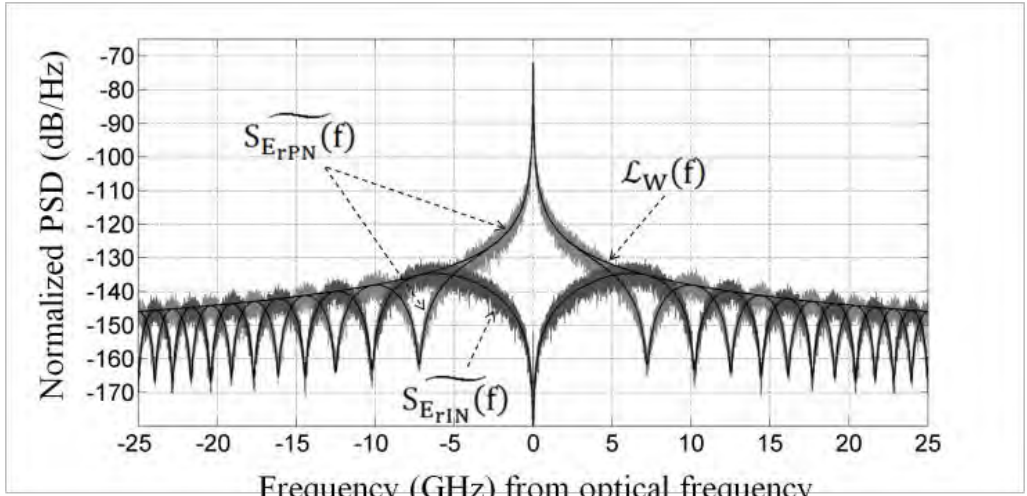
$$S_{E_{rPN}}(\mathbf{f}) \approx \mathcal{L}_F(\mathbf{f}) * \left\{ \widetilde{S_{E_{rPN}}}(\mathbf{f}) \cdot \frac{1 + \alpha^2 |H_c(\mathbf{f})|^2}{1 + \alpha^2} \right\} \\ + S_{\alpha_n}(\mathbf{f}) \cdot \sin^2(\Psi) - S_{Xr}(\mathbf{f}) \cdot \sin(2\Psi) \quad (6.14-a)$$

$$S_{E_{rIN}}(\mathbf{f}) \approx \mathcal{L}_F(\mathbf{f}) * \left\{ \widetilde{S_{E_{rIN}}}(\mathbf{f}) \cdot \frac{1 + \alpha^2 |H_c(\mathbf{f})|^2}{1 + \alpha^2} \right\} \\ + S_{\alpha_n}(\mathbf{f}) \cdot \cos^2(\Psi) + S_{Xr}(\mathbf{f}) \cdot \sin(2\Psi) \quad (6.14-b)$$

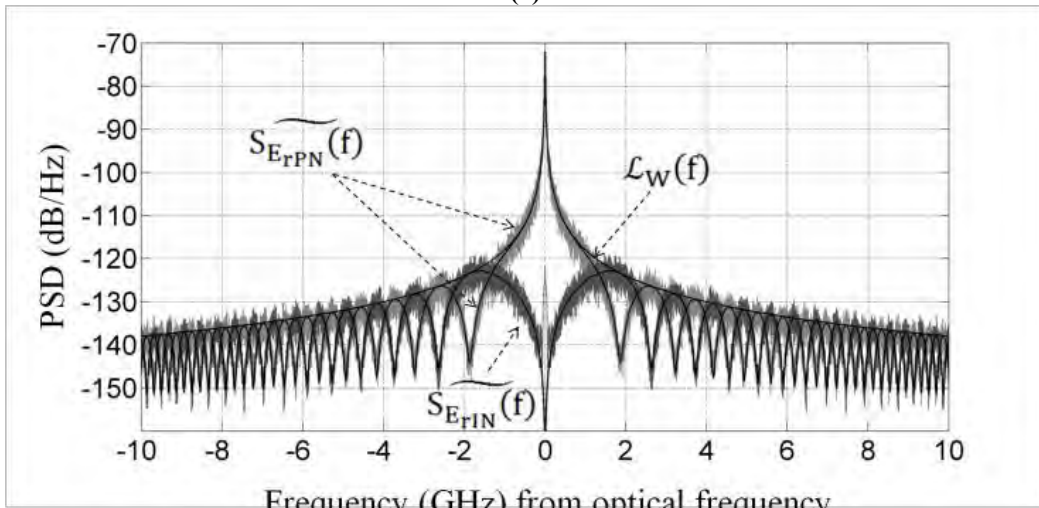
$$S_X(\mathbf{f}) \approx \begin{cases} -|S_{Xg}(\mathbf{f})| & \dots\dots\dots f \geq 0 \\ +|S_{Xg}(\mathbf{f})| & \dots\dots\dots f < 0 \end{cases} \quad (6.14-c)$$

Where $\widetilde{S_{E_{rPN}}}(\mathbf{f})$ is obtained from (6.12-a), $\widetilde{S_{E_{rIN}}}(\mathbf{f})$ from (6.12-b) after removing the $\boldsymbol{\delta}(\mathbf{f})$ term, and $\mathcal{L}_F(\mathbf{f})$ is defined in (4.24). Thus either (6.10), and (6.11) are calculated to obtain the exact PSDs, or by accepting the approximation of (6.14).

For example, the IN and PN components of SCL's dispersive field with $\delta\mathbf{f} = 10\text{MHz}$, and all other parameters are ignored, are extracted from the received field in real-time simulation, and calculated using (6.12) with $\mathbf{L} = 68.5\text{km}$, and $\mathbf{L} \approx 1027\text{km}$ by noticing that the $\boldsymbol{\delta}(\mathbf{f})$ term in (6.12-b) is removed in both cases as shown in Fig. 6.2. The simulation setup uses the SCL building block introduced in Chapter 5. In the second example, $\mathbf{L} = 68.5\text{km}$, is assumed, and a SCL with the following parameters; $\delta\mathbf{f} = 2\text{MHz}$, $\mathbf{f}_C = 2\text{MHz}$, $\mathbf{F}_R = 2.75\text{GHz}$, $\mathbf{\Gamma} = 250\text{MHz}$, $\mathbf{P}_r = 1\text{mW}$, $\alpha = 5$, $\mathbf{RIN}_L(\mathbf{0}) = -140\text{dB/Hz}$, $\mathbf{T}_{obs} \approx 42\text{ms}$, and $\mathbf{K}_z \approx 575\text{MHz}$. Note that the SCL's parameters given here are identical to that given in the example of Fig. 4.7. Both numerical calculation in (6.11), and the approximation of (6.14) lead to identical results which are shown in Fig. 6.3. The Sampling frequency (\mathbf{F}_S) in the two examples is 200GHz , and the fast Fourier transform (\mathcal{FFT}) vector size (\mathbf{N}_F) is 2^{19} in the first example, and $\mathbf{N}_F = 2^{16}$ in the second one.

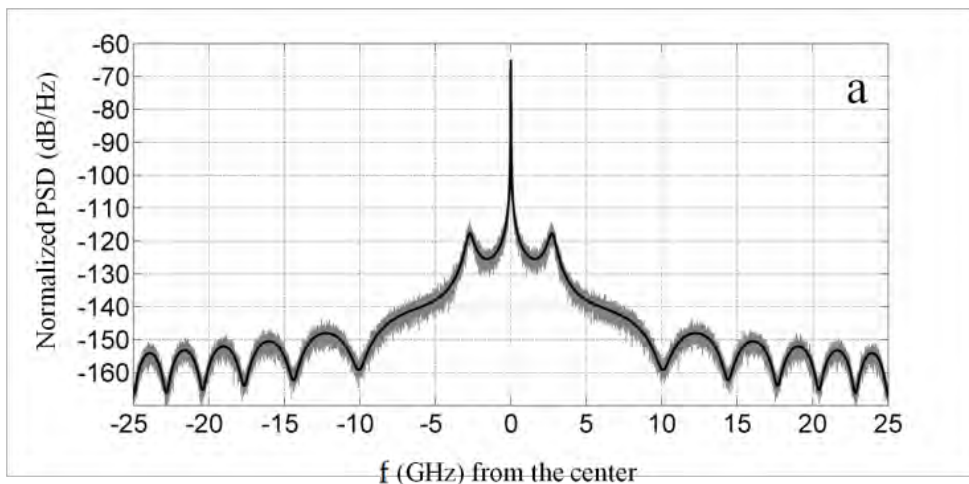


(a)



(b)

Fig. 6.2: Normalized BB-DS-PSD of dispersive field components when only white FN is counted and $|H_c(f)|^2 = 1$. In (a), $L = 68.5\text{km}$. In (b), $L \approx 1027\text{km}$. In both, $\delta f = 10\text{MHz}$, $F_s = 200\text{GHz}$ and $N_F = 2^{19}$.



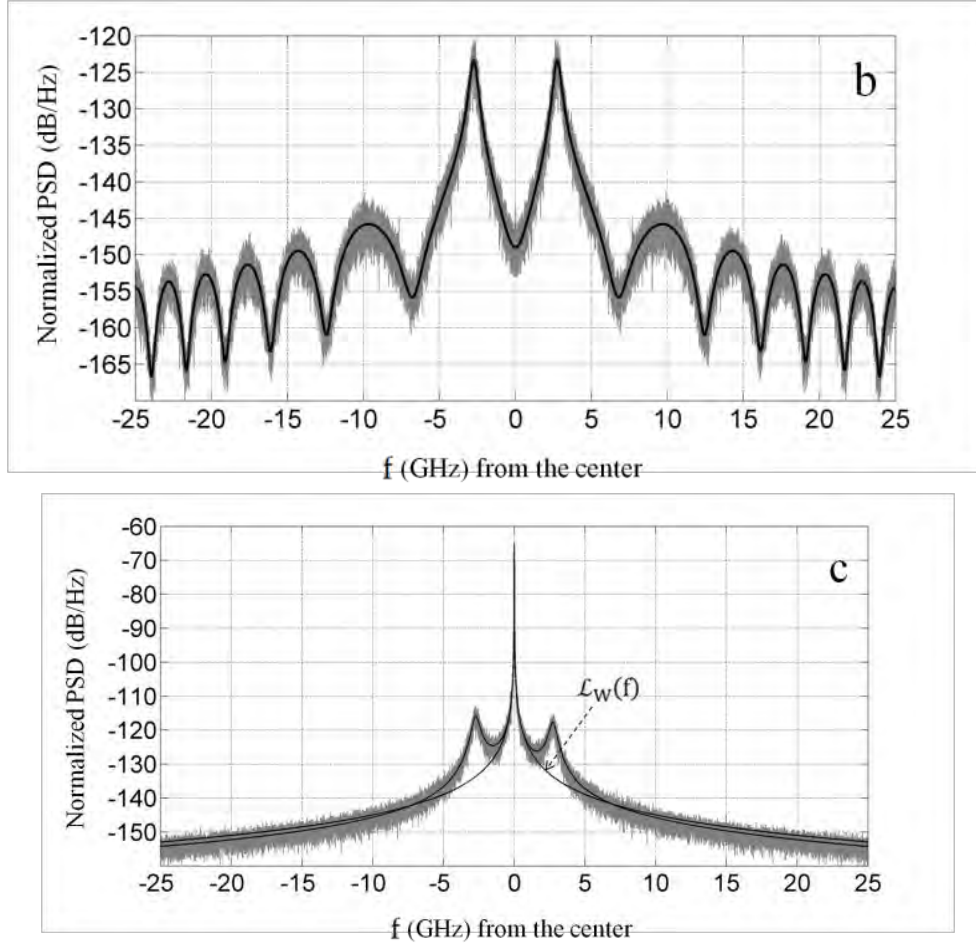


Fig. 6.3: PSD of SCL dispersive field in OD normalized to the received optical power P_r showing $S_{E_{rPN}}(f)$ in (a), $S_{E_{rIN}}(f)$ in (b), and $S_{E_r}(f)$ in (c). (Parameters are given in the text). $L = 68.5\text{km}$, $F_S = 200\text{GHz}$ and $N_F = 2^{16}$.

Note that Fig. 6.3c is identical to Fig. 4.7b, which is the DS-PSD of the transmitted field (normalization factor of $P_r = 1\text{mW}$ must be used with Fig. 4.7b), since the overall PSD is dispersion-independent as discussed earlier, and hence the optical and radio frequency (RF) spectrum analyzers (SA)s cannot detect the effect of dispersion in this case.

6.3 Analysis of DSH test of SCL's field along dispersive fiber

In this section, an approximate and an exact derivation of the beat-note PSD in the DSH test is conducted. From (6.2) and referring to Fig. 6.1,

$$\mathbf{E1} = \sqrt{P_1} \cdot e^{j2\pi\nu_0 t + \alpha_{rn}(t) + j\phi_{rn}(t)}, \text{ and}$$

$$\mathbf{E2} = \sqrt{P_2} \cdot e^{j2\pi(\nu_0 + \Delta f)(t - T_d) + \alpha_{rn}(t - T_d) + j\phi_{rn}(t - T_d)},$$

where \mathbf{P}_1 , and \mathbf{P}_2 are optical power corresponds to \mathbf{E}_1 and \mathbf{E}_2 fields respectively. As the 3-dB hybrid halves the received power of both beams, then the photo-current is

$$\begin{aligned} i_{PC}(t) &= (\mathcal{R}/2)\{E_1 + E_2\}\{E_1 + E_2\}^* \\ &= i_{BB}(t) + i_{BN}^+(t) + i_{BN}^-(t) + i_{sh}(t) + i_{th}(t) \end{aligned} \quad (6.15)$$

where $i_{BB}(t) = (\mathcal{R}/2) \cdot (P_1 \exp(2\alpha_{rn}(t)) + P_2 \exp(2\alpha_{rn}(t - T_d)))$,

$$i_{BN}^+(t) = (\mathcal{R}\sqrt{P_1 P_2}/2) \cdot \exp(j2\pi\Delta f t + \sum\alpha_{rn}(t, T_d) - j\Delta\phi_{rn}(t, T_d)),$$

$$i_{BN}^-(t) = (\mathcal{R}\sqrt{P_1 P_2}/2) \cdot \exp(-j2\pi\Delta f t + \sum\alpha_{rn}(t, T_d) + j\Delta\phi_{rn}(t, T_d)),$$

\mathcal{R} is the photo diode (PD) responsivity in (mA/mW),

$i_{sh}(t)$, and $i_{th}(t)$ are shot and thermal currents respectively.

6.3.1 Approximate analysis of the beat-frequency PSD in the DSH test

The normalized-BB version of $i_{BN}^+(t)$ or $i_{BN, BB}^+(t)$ is examined first in a short T_d and when PN standard deviation is much smaller than unity. Then from (6.8) yields

$$\begin{aligned} i_{BN, BB}^+(t) &= \{1 + \sum\alpha_{rn}(t, T_d) - j\Delta\phi_{rn}(t, T_d)\} \\ &\approx 1 + 2 \int_0^\infty \left\{ \{\cos(\Psi + \Phi) \alpha_n(f) + \sin(\Psi + \Phi) \phi_n(f)\} e^{j2\pi f(t - T_d/2)} \right. \\ &\quad \left. + \{\cos(\Psi - \Phi) \alpha_n^*(f) + \sin(\Psi - \Phi) \phi_n(f)^*\} e^{-j2\pi f(t - T_d/2)} \right\} df \end{aligned}$$

where $\Phi = \pi f T_d$, $\sum\alpha_{rn}(t, T_d) = \alpha_{rn}(t) + \alpha_{rn}(t - T_d)$, and

$$\Delta\phi_{rn}(t, T_d) = \phi_{rn}(t) - \phi_{rn}(t - T_d).$$

Therefore the approximated PSD of $i_{BN}^+(t)$ is

$$\begin{aligned} S_{BN}^+(f) &\approx (\mathcal{R}^2 P_1 P_2 / 4) \cdot \left\{ \delta(f - \Delta f) + 4\mathcal{F}\mathcal{T} \left\{ e^{+j2\pi\Delta f \tau} \cdot \int_0^\infty \left([\cos^2(\Psi + \Phi) \langle |\alpha_n(f)|^2 \rangle \right. \right. \right. \\ &\quad \left. \left. + \sin^2(\Psi + \Phi) \langle |\phi_n(f)|^2 \rangle + \sin(2(\Psi + \Phi)) \langle \alpha_n(f) \phi_n^*(f) + \alpha_n^*(f) \phi_n(f) \rangle / 2 \right] \cdot e^{j2\pi f \tau} \right. \right. \\ &\quad \left. \left. + [\cos^2(\Psi - \Phi) \langle |\alpha_n(f)|^2 \rangle + \sin^2(\Psi - \Phi) \langle |\phi_n(f)|^2 \rangle + \sin(2(\Psi - \Phi)) \right. \right. \\ &\quad \left. \left. \langle \alpha_n(f) \phi_n^*(f) + \alpha_n^*(f) \phi_n(f) \rangle / 2 \right] \cdot e^{-j2\pi f \tau} \right\} df \end{aligned}$$

By defining the following variable,

$$\Omega(f) = (\Psi + \Phi) = \pi f \cdot (T_d + f \cdot \beta_D(L))$$

The DS-PSD of $i_{BN}^+(t)$ is given by

$$\mathbf{S}_{\text{BN}}^+(\mathbf{f}) \approx (\mathcal{R}^2 P_1 P_2 / 4) \left\{ \delta(f - \Delta f) + 4 \{ S_{\alpha_n}(f - \Delta f) \cos^2(\Omega(f - \Delta f)) + S_{\phi_n}(f - \Delta f) \sin^2(\Omega(f - \Delta f)) + S_{X_r}(f - \Delta f) \sin(2\Omega(f - \Delta f)) \} \right\} \quad (6.16)$$

It is important to note that $\mathbf{S}_{\text{BN}}^+(\mathbf{f})$ exhibits asymmetric spectrum due to the high correlation between $\alpha_{rn}(\mathbf{t})$ and $\phi_{rn}(\mathbf{t})$ as illustrated in Fig. 6.4. In this example, the BB version of $\mathbf{S}_{\text{BN}}^+(\mathbf{f})$ is used with $\delta f = 10\text{MHz}$, $L = 1000\text{km}$, $T_d = 0.5\text{ns}$, and all other SCL's parameters are ignored. Many PSD patterns can be produced, which predominantly depend on the T_d value. PSD's asymmetric shape is a phenomenon that occurs in many other optical systems [70], [117], [118]. It results from the cross-PSD of a two highly-correlated noise components when detected in the passband frequency. For instance, in the dispersive channel, and when the SCL's IN is assumed to be negligible, the induced IN due to CD is highly correlated to the dispersive PN component, and hence this phenomenon occurs.

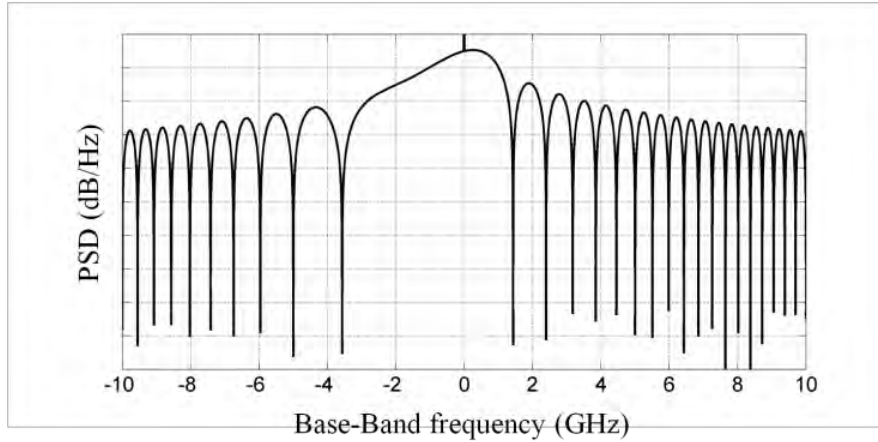


Fig. 6.4: Normalized BB-version PSD of the positive-frequency component of the photo-current $\mathbf{S}_{\text{BN}}^+(\mathbf{f})$ in the DSH test exhibiting asymmetrical nature.

6.3.2 Exact analysis of the beat-note PSD in the DSH test

From (6.15), the ACF of $\mathbf{i}_{\text{PC}}(\mathbf{t})$ after removing all zero-terms is given by

$$\mathbf{R}_{\mathbf{i}_{\text{PC}}}(\boldsymbol{\tau}) = \langle \mathbf{i}_{\text{BB}}(\mathbf{t}) \mathbf{i}_{\text{BB}}^*(\mathbf{t} - \boldsymbol{\tau}) \rangle + \langle \mathbf{i}_{\text{BN}}^+(\mathbf{t}) \mathbf{i}_{\text{BN}}^{+*}(\mathbf{t} - \boldsymbol{\tau}) \rangle + \langle \mathbf{i}_{\text{BN}}^-(\mathbf{t}) \mathbf{i}_{\text{BN}}^{-*}(\mathbf{t} - \boldsymbol{\tau}) \rangle + \langle \mathbf{i}_{\text{sh}}(\mathbf{t}) \mathbf{i}_{\text{sh}}^*(\mathbf{t} - \boldsymbol{\tau}) \rangle + \langle \mathbf{i}_{\text{th}}(\mathbf{t}) \mathbf{i}_{\text{th}}^*(\mathbf{t} - \boldsymbol{\tau}) \rangle$$

Obviously the PSD of $\mathbf{i}_{\text{BN}}^-(\mathbf{t})$ is the mirror-image of $\mathbf{i}_{\text{BN}}^+(\mathbf{t})$, and hence only $\mathbf{S}_{\text{BN}}^+(\mathbf{f})$ is calculated. Thus the single sided (SS) PSD (as measured by SA) of $\mathbf{i}_{\text{PC}}(\mathbf{t})$ is written as

$$\mathbf{S}_{\text{PC}}(\mathbf{f}) = S_{\text{BB}}(\mathbf{f}) + S_{\text{BN}}(\mathbf{f}) + S_{\text{sh}}(\mathbf{f}) + S_{\text{th}}(\mathbf{f}) \quad (6.17)$$

where the SS-PSDs of the individual terms given in (6.17) are calculated as follows,

$$\mathbf{S}_{\text{BB}}(\mathbf{f}) = \mathcal{F}\mathcal{T}\{i_{\text{BB}}(t)i_{\text{BB}}^*(t-\tau)\} \quad (6.18\text{-a})$$

$$\mathbf{S}_{\text{BN}}(\mathbf{f}) = 2 \cdot S_{\text{BN}}^+(\mathbf{f}) = 2 \cdot \mathcal{F}\mathcal{T}\{i_{\text{BN}}^+(t)i_{\text{BN}}^{+\ast}(t-\tau)\} \quad (6.18\text{-b})$$

$$\mathbf{S}_{\text{sh}}(\mathbf{f}) = 2 \cdot q \cdot i_{\text{DC}} = q \cdot \mathcal{R}(P_1 + P_2) \quad (6.18\text{-c})$$

$$\mathbf{S}_{\text{th}}(\mathbf{f}) = \mathcal{K} \cdot T^\circ \cdot N_f \quad (6.18\text{-d})$$

where q is electron charge (1.6×10^{-19} A·s), \mathcal{K} is Boltzmann constant (1.38×10^{-23} W·s/K), T° is temperature in (K), N_f is the trans-impedance amplifier's (TIA)'s noise figure in linear scale, and $\mathbf{S}_{\text{th}}(\mathbf{f})$ is normalized to TIA's gain. Exact expressions of $\mathbf{S}_{\text{BB}}(\mathbf{f})$, and $\mathbf{S}_{\text{BN}}^+(\mathbf{f})$ in (6.18-a), and (6.18-b) will be derived next. From the definition of $i_{\text{BB}}(t)$ in (6.15) yields

$$\begin{aligned} \mathbf{R}_{i_{\text{BB}}}(\tau) &= \langle i_{\text{BB}}(t) \cdot i_{\text{BB}}^*(t-\tau) \rangle = (P_1 \mathcal{R}/2)^2 \\ &\quad \cdot \left(e^{2\alpha_{\text{rn}}(t)+2\alpha_{\text{rn}}(t-\tau)} + \beta^2 \cdot e^{2\alpha_{\text{rn}}(t-T_d)+2\alpha_{\text{rn}}(t-T_d-\tau)} \right. \\ &\quad \left. + \beta \cdot e^{2\alpha_{\text{rn}}(t)+2\alpha_{\text{rn}}(t-T_d-\tau)} + \beta \cdot e^{2\alpha_{\text{rn}}(t-T_d)+2\alpha_{\text{rn}}(t-\tau)} \right) \end{aligned}$$

where $\beta = P_2/P_1$.

Let $\mathbf{x}(t)$ be any zero-mean GRV then,

$$\mathcal{F}\mathcal{T}\{\mathbf{x}(t) + \mathbf{x}(t - \Delta T)\} = \mathbf{x}(f) + \mathbf{x}(f)e^{-j2\pi f\Delta T} = 2\mathbf{x}(f) \cdot e^{-j\pi f\Delta T} \cos(\pi f\Delta T),$$

where ΔT is any arbitrary delay. Therefore,

$$\langle \{\mathbf{x}(t) + \mathbf{x}(t - \Delta T)\}^2 \rangle = \int_{-\infty}^{\infty} 4 \cos^2(\pi f\Delta T) \mathcal{S}\{\mathbf{x}(t)\} df$$

Hence from (4.11) and after some arrangements yields

$$\begin{aligned} \mathbf{R}_{i_{\text{BB}}}(\tau) &= (P_1 \mathcal{R}/2)^2 \\ &\quad \cdot \left\{ (1 + \beta^2) \cdot \exp \left(16 \int_0^{\infty} S_{\alpha r}(f) \cos^2(\pi f\tau) df \right) \right. \\ &\quad \left. + \beta \left\{ \exp \left(16 \int_0^{\infty} S_{\alpha r}(f) \cos^2(\pi f(T_d + \tau)) df \right) \right. \right. \\ &\quad \left. \left. + \exp \left(16 \int_0^{\infty} S_{\alpha r}(f) \cos^2(\pi f(T_d - \tau)) df \right) \right\} \right\} \quad (6.19\text{-a}) \end{aligned}$$

$$\mathbf{S}_{\text{BB}}(\mathbf{f}) = 2\mathcal{F}\mathcal{T}\{R_{i_{\text{BB}}}(\tau)\} \dots\dots\dots f \geq 0 \quad (6.19\text{-b})$$

where $\mathbf{S}_{\alpha r}(\mathbf{f}) = S_{\alpha_n}(f)\cos^2(\Psi) + S_{\phi_n}(f)\sin^2(\Psi) + S_{X_r}(f)\sin(2\Psi)$, is the DS-PSD of the received IN term (in small signal condition) which is derived from (6.8), and also used in (6.10). Here $\mathbf{S}_{\alpha r}(\mathbf{f})$ is identical to Yamamoto's RIN given in (6.1) when it

multiplied by 8 and $\alpha_n(\mathbf{t})$ is ignored. Note that (6.18-a) contains DC term as well as BB IN-term, and it can be efficiently approximated when $\mathbf{i}_{\text{BB}}(\mathbf{t})$ in (6.15) is written as

$$\begin{aligned}\mathbf{i}_{\text{BB}}(\mathbf{t}) &\approx (\mathcal{R}/2)\{P_1(1 + 2\alpha_{\text{rn}}(\mathbf{t})) + P_2(1 + 2\alpha_{\text{rn}}(\mathbf{t} - T_d))\} \\ &= (\mathcal{R}/2)(P_1 + P_2) + \mathcal{R}\{P_1\alpha_{\text{rn}}(\mathbf{t}) + P_2\alpha_{\text{rn}}(\mathbf{t} - T_d)\} = i_{\text{DC}} + i_{\text{IN}}(\mathbf{t}).\end{aligned}$$

Hence from (6.14-b), and (6.19) yields

$$\begin{aligned}\mathbf{S}_{\text{BB}}(\mathbf{f}) &\approx \mathbf{S}_{\text{DC}} + \mathbf{S}_{\text{IN}}(\mathbf{f}) = (\mathcal{R}(P_1 + P_2)/2)^2\delta(\mathbf{f}) \\ &\quad + 2(\mathcal{R}P_1)^2\{1 + 2\beta\cos(2\pi fT_d) + \beta^2\}S_{\text{E}_{\text{rIN}}}(\mathbf{f})\end{aligned}\quad (6.20)$$

Although (6.19) results the exact BB IN SS-PSD, it is time consuming and the unwanted DC term is implicit in the calculation. Thus (6.20) can be used instead even for extreme values of $\delta\mathbf{f}$, and $\mathbf{RIN}_{\text{L}}(\mathbf{0})$. The next step is to derive the exact expression for $\mathbf{S}_{\text{BN}}^+(\mathbf{f})$ as (6.16) is only an approximation. From the definition of $\mathbf{i}_{\text{BN}}^+(\mathbf{t})$ in (6.15) yields

$$\begin{aligned}\mathbf{R}_{\text{BN}}^+(\boldsymbol{\tau}) &= \langle i_{\text{BN}}^+(\mathbf{t}) \cdot i_{\text{BN}}^{+\ast}(\mathbf{t} - \boldsymbol{\tau}) \rangle = (\mathcal{R}^2 P_1 P_2 / 4) \cdot e^{j2\pi\Delta f\boldsymbol{\tau}} \cdot \\ &\quad \langle e^{\alpha_{\text{rn}}(\mathbf{t}) + \alpha_{\text{rn}}(\mathbf{t} - \boldsymbol{\tau}) + \alpha_{\text{rn}}(\mathbf{t} - T_d) + \alpha_{\text{rn}}(\mathbf{t} - T_d - \boldsymbol{\tau})} \cdot e^{-j\phi_{\text{rn}}(\mathbf{t}) + j\phi_{\text{rn}}(\mathbf{t} - \boldsymbol{\tau}) + j\phi_{\text{rn}}(\mathbf{t} - T_d) - j\phi_{\text{rn}}(\mathbf{t} - T_d - \boldsymbol{\tau})} \rangle\end{aligned}$$

By assuming the following variables,

$$\mathbf{x}_1(\mathbf{t}) = (\alpha_{\text{rn}}(\mathbf{t}) + \alpha_{\text{rn}}(\mathbf{t} - \boldsymbol{\tau}) + \alpha_{\text{rn}}(\mathbf{t} - T_d) + \alpha_{\text{rn}}(\mathbf{t} - T_d - \boldsymbol{\tau})), \text{ and}$$

$$\mathbf{x}_2(\mathbf{t}) = (\phi_{\text{rn}}(\mathbf{t}) - \phi_{\text{rn}}(\mathbf{t} - \boldsymbol{\tau}) - \phi_{\text{rn}}(\mathbf{t} - T_d) + \phi_{\text{rn}}(\mathbf{t} - T_d - \boldsymbol{\tau})),$$

then from (6.8), and (4.11) and after long simplifications, then

$$\begin{aligned}\mathbf{R}_{\text{BN}}^+(\boldsymbol{\tau}) &= (\mathcal{R}^2 P_1 P_2 / 4) \cdot \exp(j2\pi\Delta f\boldsymbol{\tau}) \\ &\quad \cdot \left\{ \exp\left(4 \int_0^\infty (\mathcal{A}_\alpha S_{\alpha_n}(\mathbf{f}) + \mathcal{A}_\phi S_{\phi_n}(\mathbf{f}) + 2\mathcal{A}_X S_{X_r}(\mathbf{f})) d\mathbf{f}\right) \right\}\end{aligned}\quad (6.21-a)$$

$$\mathbf{S}_{\text{BN}}^+(\mathbf{f}) = \mathcal{FT}\{\mathbf{R}_{\text{BN}}^+(\boldsymbol{\tau})\} \quad (6.21-b)$$

$$\begin{aligned}\text{where } \mathcal{A}_\alpha &= \cos(\omega T_d) + \cos(\omega\boldsymbol{\tau}) + \\ &\quad \cos(2\Psi) \cdot (1 + \cos(\omega T_d) \cdot \cos(\omega\boldsymbol{\tau})) \\ &\quad - j \cdot \sin(2\Psi) \cdot \sin(\omega T_d) \cdot \sin(\omega\boldsymbol{\tau}),\end{aligned}$$

$$\begin{aligned}\mathcal{A}_\phi &= \cos(\omega T_d) + \cos(\omega\boldsymbol{\tau}) \\ &\quad - \cos(2\Psi) \cdot (1 + \cos(\omega T_d) \cdot \cos(\omega\boldsymbol{\tau})) \\ &\quad + j \cdot \sin(2\Psi) \cdot \sin(\omega T_d) \cdot \sin(\omega\boldsymbol{\tau}), \text{ and}\end{aligned}$$

$$\begin{aligned}\mathcal{A}_X &= \sin(2\Psi) \cdot (1 + \cos(\omega T_d) \cdot \cos(\omega\boldsymbol{\tau})) \\ &\quad + j \cdot \cos(2\Psi) \cdot \sin(\omega T_d) \cdot \sin(\omega\boldsymbol{\tau}).\end{aligned}$$

Again, if only the white FN is considered assuming $\{|\mathbf{H}_c(\mathbf{f})|^2 = 1\}$, and all other parameters are ignored then,

$$\mathbf{S}_{\text{BN}}^+(\mathbf{f}) = (\mathcal{R}^2 P_1 P_2 / 4) \cdot \mathcal{FT}\{ \exp(j2\pi\Delta f\tau) \cdot \exp(4 \int_0^\infty S_{\phi_n}(f) \cdot \mathcal{A}_\phi df) \}.$$

If we focus on solving the integration in (6.21-a) then

$$\begin{aligned} 4 \int_0^\infty S_{\phi_n}(f) V_\phi df &= 4 \int_0^\infty (\delta f / (2\pi f^2)) \mathcal{A}_\phi df \\ &= -2\pi\delta f \cdot (T_d + |\tau| - |T_d + \tau|/2 - |T_d - \tau|/2) \\ &\quad - \frac{4\delta f}{\pi} \int_0^\infty \left(2\sin^2(\Psi)(1 + \cos(\omega T_d)\cos(\omega\tau)) + j \cdot \sin(2\Psi)\sin(\omega T_d)\sin(\omega\tau) \right) \frac{df}{f^2} \\ &= -\mathfrak{S} - \mathfrak{D} \end{aligned}$$

Therefore

$$\mathbf{S}_{\text{BN}}^+(\mathbf{f}) = (\mathcal{R}^2 P_1 P_2 / 4) \cdot \mathcal{FT}\{ \exp(j2\pi\Delta f\tau) \cdot \exp(-\mathfrak{S} - \mathfrak{D}) \}, \text{ where}$$

$$\mathfrak{S} = 2\pi\delta f \cdot (T_d + |\tau| - |T_d + \tau|/2 - |T_d - \tau|/2),$$

$$\mathfrak{D} = \frac{4\delta f}{\pi} \int_0^\infty \left(2\sin^2(\Psi)(1 + \cos(\omega T_d)\cos(\omega\tau)) + j \cdot \sin(2\Psi)\sin(\omega T_d) \cdot \sin(\omega\tau) \right) \frac{df}{f^2}$$

When the SCL output is directly measured (i.e. no dispersion), then $\mathfrak{D} = 0$ and hence

$\mathbf{S}_{\text{BN}}^+(\mathbf{f}) = (\mathcal{R}^2 P_1 P_2 / 4) \cdot \mathcal{FT}\{ \exp(j2\pi\Delta f\tau) \cdot \exp(-\mathfrak{S}) \}$, which was derived first by Richter *et al.* and covered in Section 4.3.3 [108]. However, when $\mathfrak{D} \neq 0$, then after extensive simplifications, yields

$$\boldsymbol{\eta}_{\mathbf{W}}(\mathbf{f}) = \mathcal{FT}\{ \exp(-\mathfrak{S} - \mathfrak{D}) \} = \exp(-2\pi\delta f T_d) \cdot \delta(f) + \mathcal{L}_{\mathbf{W}_2}(f) \cdot (1 - \mathcal{W}_{\mathbf{T}}(f)) \quad (6.22)$$

$$\text{where } \mathcal{L}_{\mathbf{W}_2}(\mathbf{f}) = \frac{\delta f}{\pi} \cdot \frac{1}{(\delta f)^2 + f^2},$$

$$\mathcal{W}_{\mathbf{T}}(\mathbf{f}) = \exp(-\gamma_{\mathbf{T}}(f)) \left(\cos(2\Omega(f)) + \gamma_{\mathbf{T}}(f) \cdot \text{sinc}(2\Omega(f)/\pi) \right), \text{ and}$$

$$\gamma_{\mathbf{T}}(\mathbf{f}) = 2\pi\delta f \cdot |\beta_{\mathbf{D}}(L)f + T_d|.$$

Thus in this special case yields

$$\mathbf{S}_{\text{BN}}^+(\mathbf{f}) = (\mathcal{R}^2 P_1 P_2 / 4) \cdot \boldsymbol{\eta}_{\mathbf{W}}(f - \Delta f) \quad (6.23)$$

6.3.3 Comparison with previous work

Richter *et al.* demonstrated analytically and experimentally the PSD of SCL field in DSH test without the dispersion effect [108]. In the following example, a comparison is held between the dispersive $\mathbf{S}_{\text{BN}}(\mathbf{f}) = 2\mathbf{S}_{\text{BN}}^+(\mathbf{f})$, which is denoted as $\mathbf{S}_{\text{BN}}(\mathbf{f})_{\mathbf{D}}$ with the non-

dispersive $\mathbf{S}_{\text{BN}}(\mathbf{f})$ which is denoted as $\mathbf{S}_{\text{BN}}(\mathbf{f})_{\text{ND}}$. The following parameters are used, $\delta\mathbf{f} = 10\text{MHz}$, a frequency shift of $\Delta\mathbf{f} = 15\text{GHz}$, and using a balanced detector (BD) rather than a PD to remove $\mathbf{i}_{\text{BB}}(\mathbf{t})$ term from (6.15), noting that in the BD setup, 6dB is added compared to the PD setup [50]. Assuming $L = 68.5\text{km}$, and $L \approx 205\text{km}$, and $\mathbf{S}_{\text{BN}}(\mathbf{f})$ is normalized to $(\mathcal{R}^2\mathbf{P}_1\mathbf{P}_2/2)$ as shown in Fig. 6.5. In the second example, the effect of different $\delta\mathbf{f}$ for a given L and for different L for a given $\delta\mathbf{f}$ with a frequency shift of $\Delta\mathbf{f} = 10\text{GHz}$ are shown in Fig. 6.6. Here T_d is calculated from (2.9) to be equal the differential time delay introduced by the channel and given by

$$T_d = \beta_D(L) \cdot \Delta\mathbf{f} \quad (6.24)$$

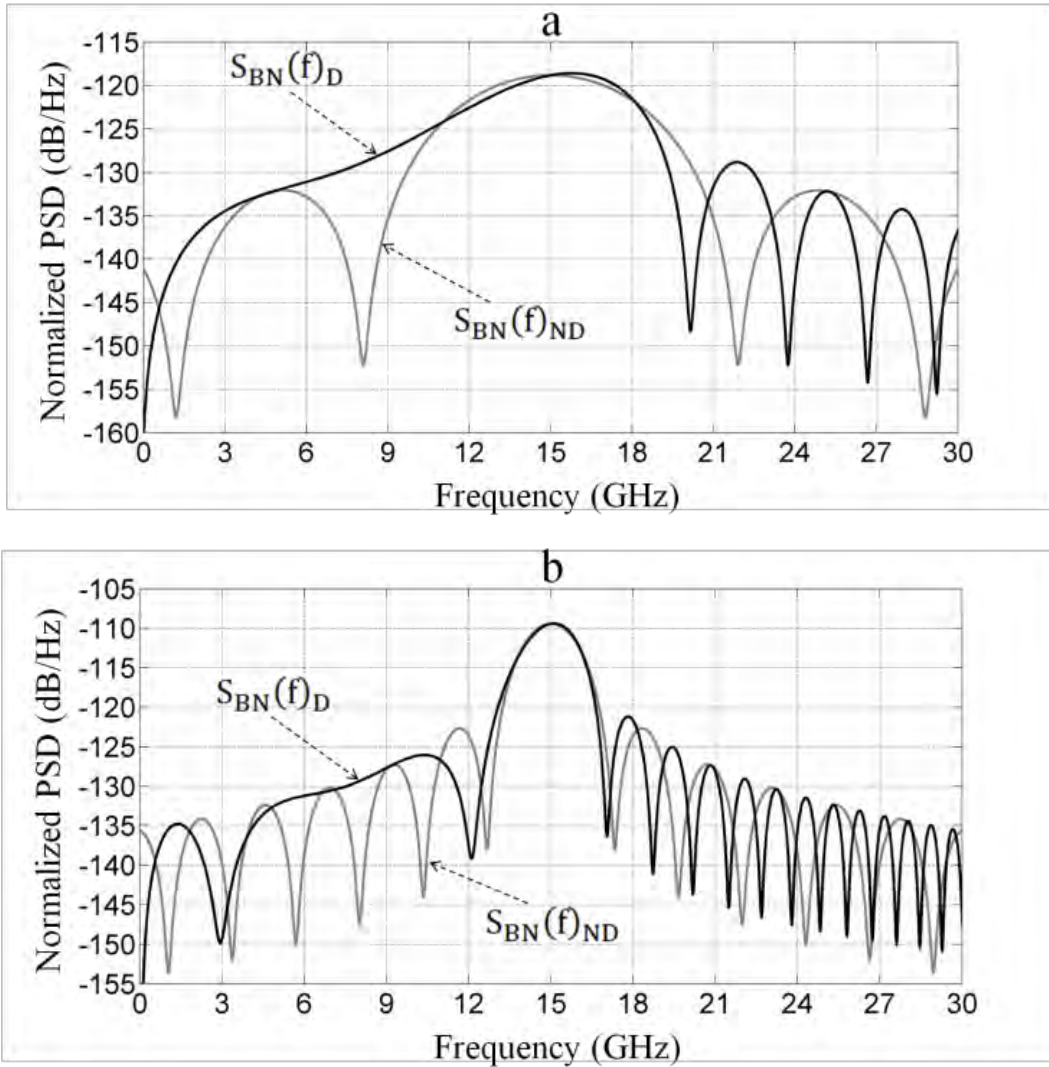


Fig. 6.5: Comparison of ground floor of dispersive $\mathbf{S}_{\text{BN}}(\mathbf{f})$ denoted as $\mathbf{S}_{\text{BN}}(\mathbf{f})_{\text{D}}$, and the non-dispersive one as $\mathbf{S}_{\text{BN}}(\mathbf{f})_{\text{ND}}$ normalized to $\mathcal{R}^2\mathbf{P}_1\mathbf{P}_2/2$. In (a), $L = 68.5\text{km}$, and in (b), $L \approx 205\text{km}$.

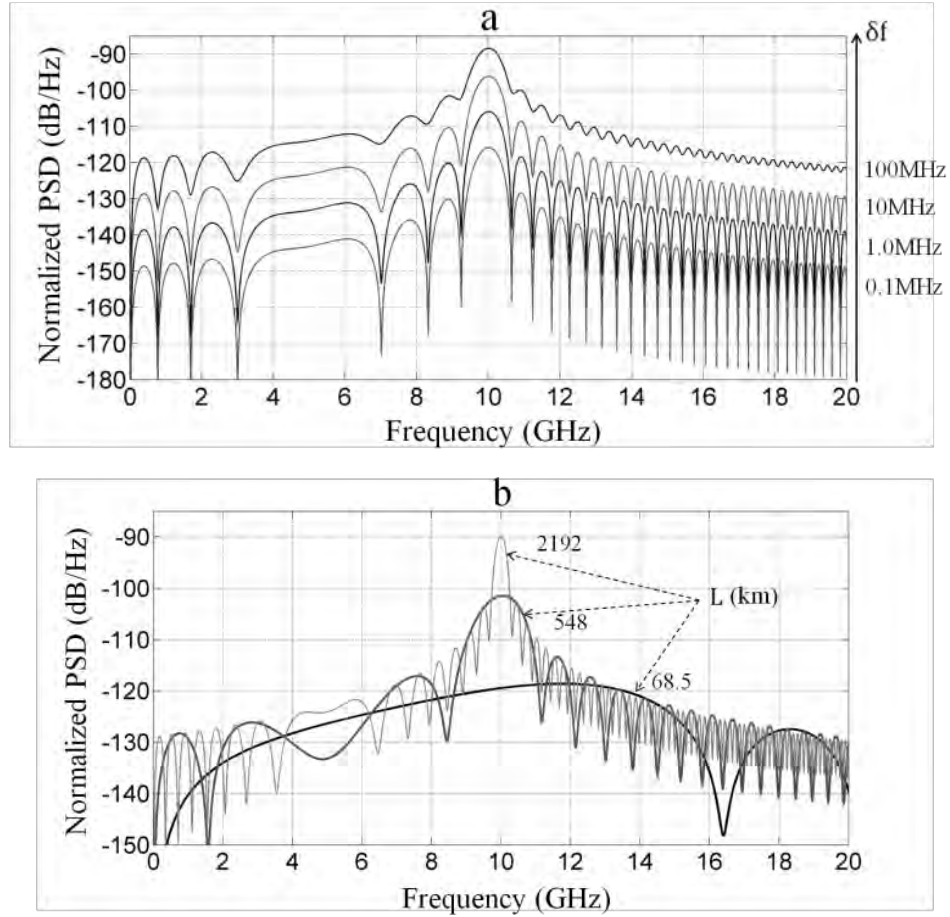


Fig. 6.6: Normalized ground floor of $\mathbf{S}_{\text{BN}}(\mathbf{f})_{\text{D}}$ showing the effect of different $\delta \mathbf{f}$ when $\mathbf{L} \approx 1027$ km in (a), and the effect of different \mathbf{L} when $\delta \mathbf{f} = 10$ MHz in (b).

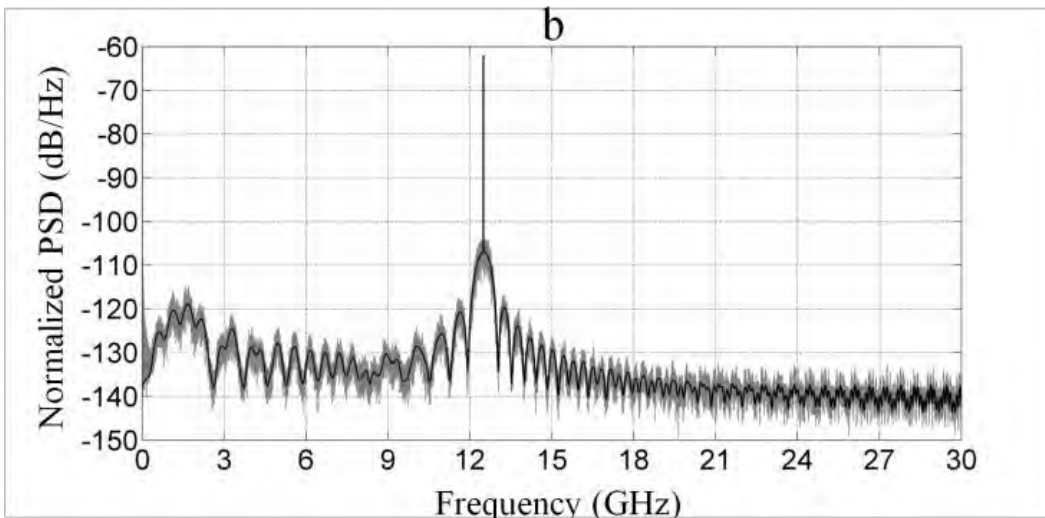
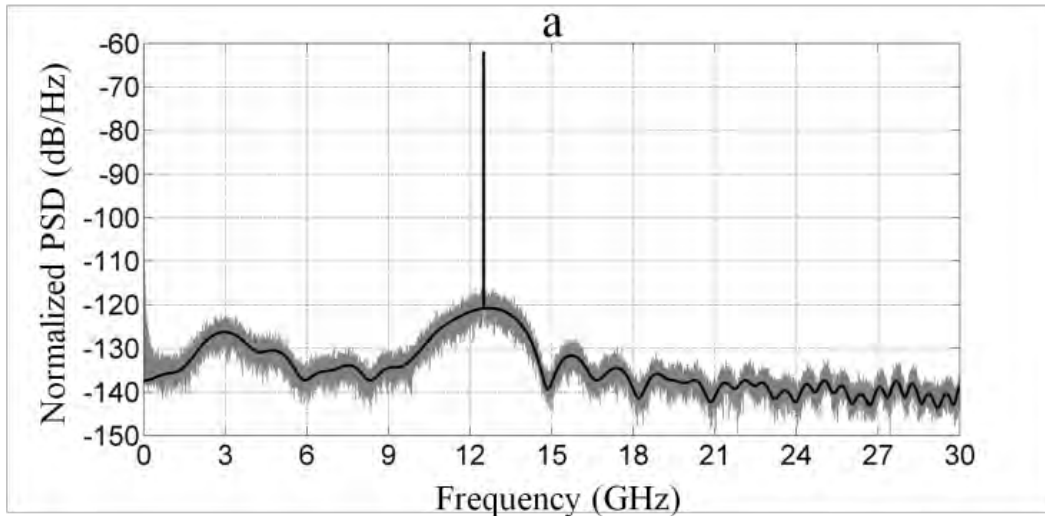
6.3.4 Semi-exact analytical solution

Benefiting from (6.13) and when all parameters are counted, then $\mathcal{FT}\{\exp(-\mathfrak{S} - \mathfrak{D})\}$, and $\mathbf{S}_{\text{BN}}(\mathbf{f})$ can be approximated, and hence from (6.22), (6.23), and (4.45) yields

$$\mathbf{S}_{\text{BN}}(\mathbf{f}) \approx (\mathcal{R}^2 P_1 P_2 / 2) \cdot \left\{ \eta_{\text{F}}(\mathbf{f} - \Delta \mathbf{f}) * \left(\eta_{\text{W}}(\mathbf{f} - \Delta \mathbf{f}) \frac{1 + \alpha^2 |\text{H}_c(\mathbf{f} - \Delta \mathbf{f})|^2}{1 + \alpha^2} \right) \right. \\ \left. + 4S_{\alpha_n}(\mathbf{f} - \Delta \mathbf{f}) \cos^2(\Omega(\mathbf{f} - \Delta \mathbf{f})) + 4S_{\text{Xr}}(\mathbf{f} - \Delta \mathbf{f}) \sin(2\Omega(\mathbf{f} - \Delta \mathbf{f})) \right\} \quad (6.25)$$

$$\text{where } \eta_{\text{F}}(\mathbf{f} - \Delta \mathbf{f}) \approx \mathcal{FT} \left\{ \exp(j2\pi \mathbf{f} \tau) \cdot \exp \left(2\pi \delta \mathbf{f} \tau_{\text{d}}^2 \mathbf{f}_{\text{c}} \cdot \left\{ -2Z \left(\frac{\tau_{\text{d}}}{\tau_{\text{obs}}} \right) \right. \right. \right. \\ \left. \left. \left. - 2\tau_{\text{n}}^2 Z \left(\frac{\tau_{\text{d}} |\tau_{\text{n}}|}{\tau_{\text{obs}}} \right) + (1 - \tau_{\text{n}})^2 Z \left(\frac{\tau_{\text{d}} |1 - \tau_{\text{n}}|}{\tau_{\text{obs}}} \right) + (1 + \tau_{\text{n}})^2 Z \left(\frac{\tau_{\text{d}} |1 + \tau_{\text{n}}|}{\tau_{\text{obs}}} \right) \right\} \right\}$$

Here $\eta_F(\mathbf{f})$ is the PSD part due to the contribution of flicker FN which is written as dispersion-independent term because the dispersion has a marginal effect on the flicker FN. Without loss of generalization and without proof (but supported by the simulation), $\eta_F(\mathbf{f} - \Delta\mathbf{f})$ in (6.25) can be ignored in most long-haul applications. Assuming all of the SCL's parameters are counted, then the following two examples are given to prove the matching between simulation and calculation of (6.17). In the first example, we use a SCL with parameters similar to that used in Fig. 4.7, with $L \approx 205\text{km}$, $L \approx 1027\text{km}$, and $\Delta\mathbf{f} = 12.5\text{GHz}$. The OFS is assumed to have 6-dB insertion loss and laser's power is 3dBm. A simulation is conducted and compared with calculations. First the relaxation oscillation is ignored as illustrated in Fig. 6.7a and 6.7b. Then all parameters are involved as shown in Fig. 6.7c and 6.7d. The black solid curve is the calculation of (6.17).



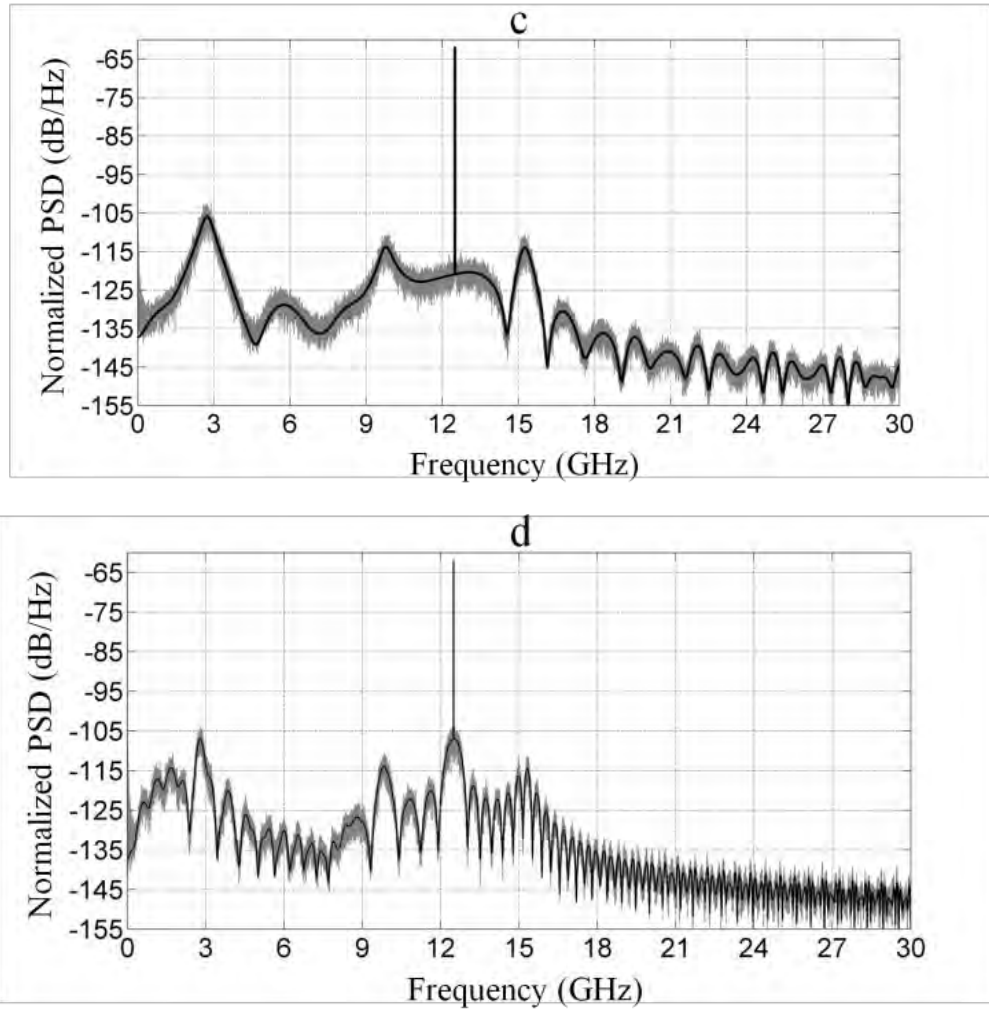
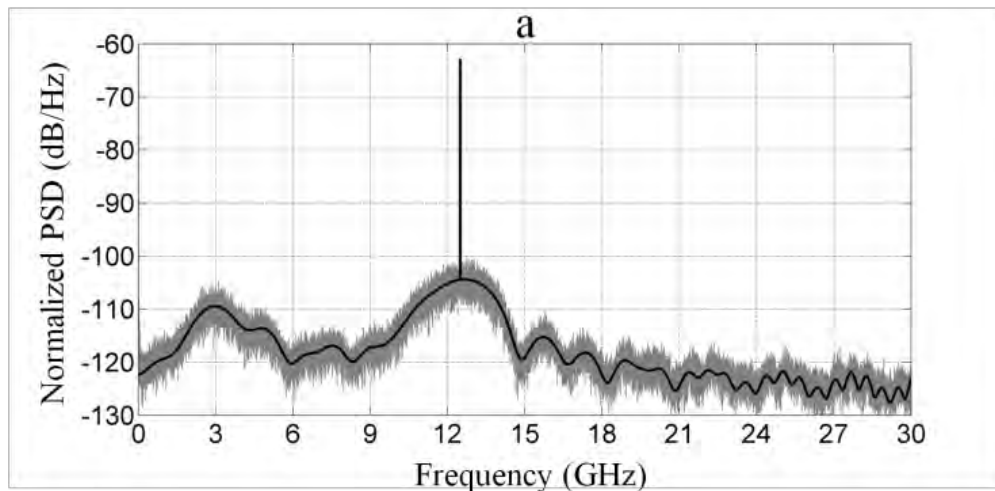


Fig. 6.7: Normalized $S_{PC}(f)$ in the DSH test with PD setup with SCL's parameters similar to that used in Fig. 4.7. In (a) and (c), $L \approx 205\text{km}$ and in (b) and (d), $L \approx 1027\text{km}$. The relaxation oscillation is ignored in (a) and (b). Normalization factor is $\mathcal{R}^2 P_1 P_2 / 2$, $F_S = 200\text{GHz}$ and $N_F = 2^{18}$.



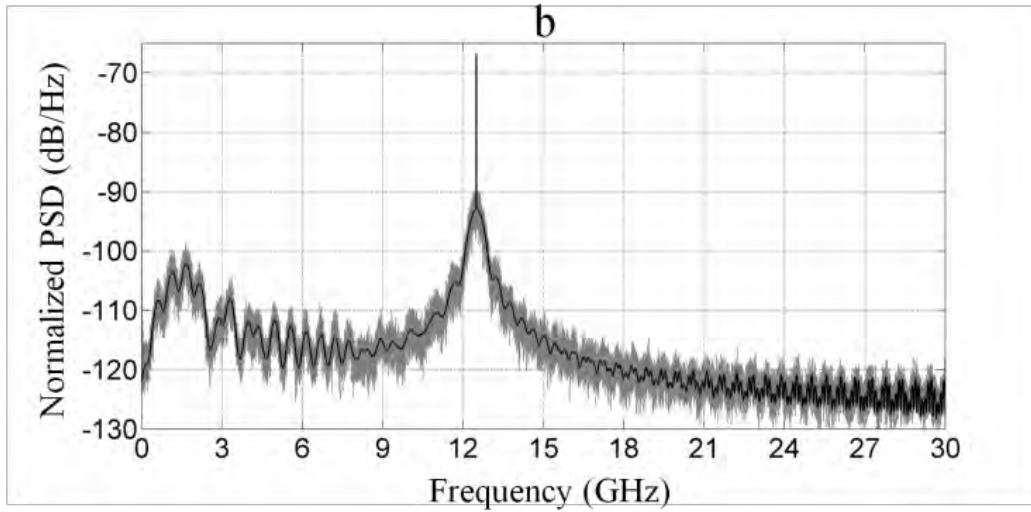


Fig. 6.8: Normalized $S_{PC}(f)$ in DSH test with PD setup with $L \approx 205\text{km}$ in (a), and $L \approx 1027\text{km}$ and in (b). Relaxation oscillation is ignored, $\delta f = 100\text{MHz}$, $RIN_L(0) = -125\text{dB/Hz}$, $F_S = 200\text{GHz}$ and $N_F = 2^{18}$.

In the second example, large signal is used with $\delta f = 100\text{MHz}$, $RIN_L(0) = -125\text{dB/Hz}$, relaxation oscillation effect is ignored, and $\Delta f = 12.5\text{GHz}$ as shown in Fig. 6.8.

Some observations from these figures are listed below.

- The beat-note main lobe increases as linewidth increases, which is predominantly due to the differential PN term of (6.25).
- As linewidth increases as the sharp nulls disappear and approaching a non-oscillating spectra at very broad linewidth.
- Many spectral patterns can be produced depending on L or T_d .
- As L or T_d increases, the spectral shape becomes more symmetrical.
- The low frequency noise floor, which is due to PN-to-IN of the self-beat components of the two beams, is significant, especially when relaxation oscillation is taken into account. However, this component can be suppressed using balanced-detector setup instead of a single PD setup.

Finally, $S_{PC}(f)$ in (6.17) is calculated exactly by using (6.18), (6.19) and (6.21), or efficiently approximated by using (6.18), (6.20), and (6.25) which is the main analytical result of this chapter.

6.4 PN and IN PSDs and variances

The PSDs of the PN and IN and variances of $\mathbf{i}_{PC}(\mathbf{t})$ in (6.15) are required to be extracted to facilitate penalty analysis in the next chapter. First from the aforementioned discussions, the BB version of $\mathbf{i}_{BN}^+(\mathbf{t})$ is given by

$\mathbf{i}_{BN, BB}^+(\mathbf{t}) = \exp(\sum \alpha_{rn}(t, T_d) - j\Delta\phi_{rn}(t, T_d))$, then from (6.8) yields

$$\mathbf{S}_{\sum \alpha_{rn}}(f) \approx 4\cos^2(\pi f T_d) \left(S_{\alpha_n}(f)\cos^2(\Psi) + S_{\phi_n}(f)\sin^2(\Psi) + S_{Xr}(f)\sin(2\Psi) \right) \quad (6.26-a)$$

$$\mathbf{S}_{\Delta\phi_{rn}}(f) \approx 4\sin^2(\pi f T_d) \left(S_{\alpha_n}(f)\sin^2(\Psi) + S_{\phi_n}(f)\cos^2(\Psi) - S_{Xr}(f)\sin(2\Psi) \right) \quad (6.26-b)$$

where $\mathbf{S}_{\sum \alpha_{rn}}(f)$ is the DS-PSD corresponds to $\sum \alpha_{rn}(\mathbf{t}, \mathbf{T}_d)$, and $\mathbf{S}_{\Delta\phi_{rn}}(f)$ is the DS-PSD corresponds to $\Delta\phi_{rn}(\mathbf{t}, \mathbf{T}_d)$. The theoretical free-running noise variance is calculated by integrating the DS-PSD from $-\infty$ to $+\infty$ assuming $t \rightarrow \infty$. However, neither $f \rightarrow \pm\infty$, nor $t \rightarrow \infty$ is realistic, hence an observation TF or $\mathbf{H}_{OBZ}(\mathbf{f})$ must be introduced, and band-limited integration or $f \rightarrow \pm f_M$ must be performed. Where \mathbf{f}_M is maximum SS frequency of the receiver. Again a special case is applied on (6.26), which is when only white FN component is counted, and $\{|\mathbf{H}_c(\mathbf{f})|^2 = 1\}$, then the free running variances are

$$\sigma_{\Delta\phi, FR}^2(\mathbf{T}_d) = 4\pi\delta f T_d^2 \cdot \int_0^{f_M} \text{sinc}^2(f T_d) \cdot \cos^2(\Psi) \cdot H_{OBZ}(f) df \quad (6.27-a)$$

$$\sigma_{\sum \alpha, FR}^2(\mathbf{T}_d) = \frac{4\delta f}{\pi} \cdot \int_0^{f_M} \frac{\cos^2(\pi f T_d)}{f^2} \cdot \sin^2(\Psi) \cdot H_{OBZ}(f) df \quad (6.27-b)$$

If \mathbf{T}_{OBS} is long enough, then $\mathbf{H}_{OBZ}(\mathbf{f})$ can be approximated to unity, and hence the ratio between dispersive and non-dispersive PN variances is given by

$$\{\sigma_{\Delta\phi, FR}^2(\mathbf{T}_d)\}_D / \{\sigma_{\Delta\phi, FR}^2(\mathbf{T}_d)\}_{ND} \approx 2T_d \int_0^{f_M} \text{sinc}^2(f T_d) \cdot \cos^2(\pi\beta_D(L)f^2) df \quad (6.28)$$

Here by substituting of $\Psi = 0$ in (42-a), then $\{\sigma_{\Delta\phi, FR}^2(\mathbf{T}_d)\}_{ND} \approx 2\pi\delta f T_d$ assuming $\mathbf{f}_M \gg \delta\mathbf{f}$, which is identical to (A2.5) in Appendix-A2. Equation (6.28) is calculated numerically assuming the 50GHz optical grid, and hence $\mathbf{f}_M = 25\text{GHz}$, and by using $\mathbf{N}_F = 2^{18}$ as shown in Fig. 6.9. The frequency separation $\Delta\mathbf{f}$ is indirectly changes (6.28) by changing \mathbf{T}_d as given in (6.24).

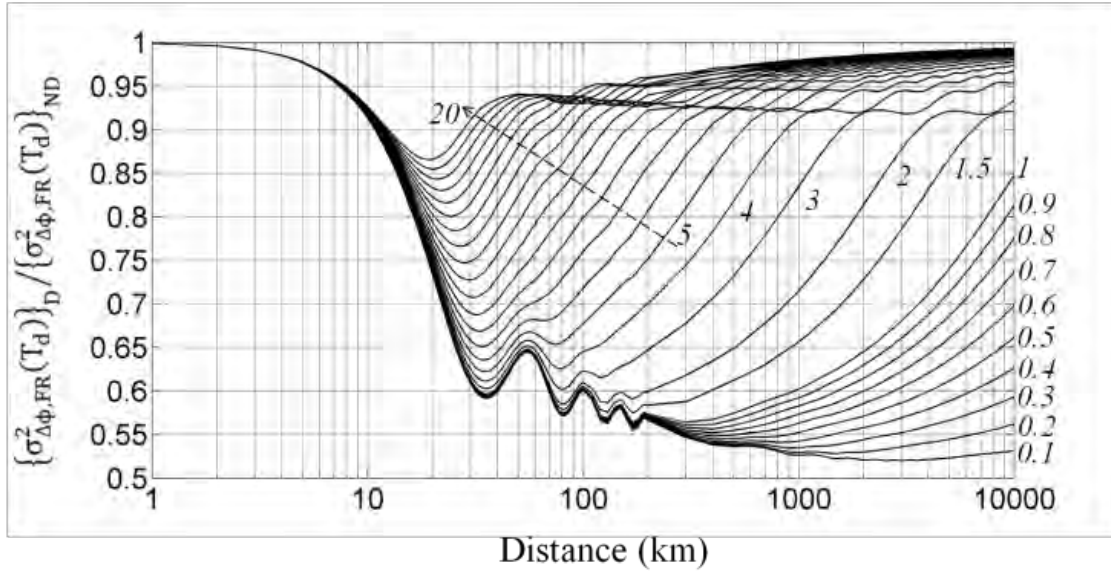


Fig. 6.9: Ratio of dispersive to non-dispersive free-running (50GHz grid-BW is assumed) PN variances of SCL field versus distance. The Italic-style written numbers are of Δf in (GHz), and the arrow indicates an increase of Δf in 1GHz steps from 5GHz to 20GHz.

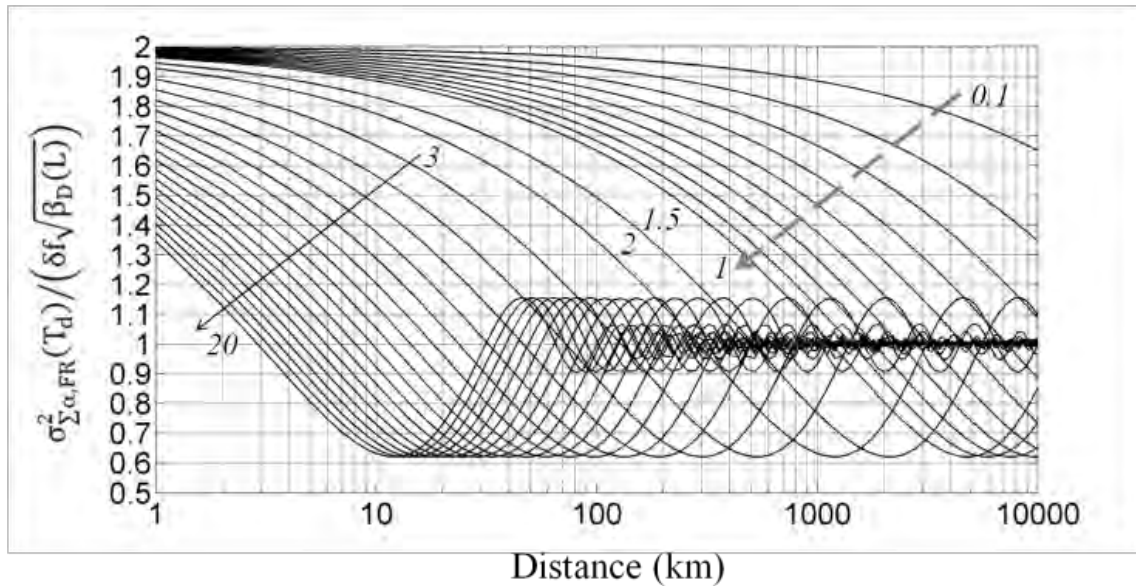


Fig. 6.10: Free-running (50GHz grid-BW is assumed) $\sigma_{\Sigma\alpha,FR}^2(T_d)$ normalized to $\delta f \sqrt{\beta_D(L)}$ of a dispersive SCL field. The Italic-style written numbers are of Δf in (GHz). The dashed-gray arrow indicates an increase of Δf in 0.1GHz step from 0.1GHz to 1GHz, and the solid-black arrow indicates an increase of Δf in 1GHz steps from 3GHz to 20GHz.

Although a numerical expressions for (6.27-a) and (6.27-b) do exist only when $\mathbf{f}_M \rightarrow \infty$, however, only that of (6.27-b) is mentioned here since that of (6.27-a) is complicated. Thus the following numerical solution can be used to calculate (6.27-b)

$$\sigma_{\Sigma\alpha,FR}^2(T_d) = \delta f \sqrt{\beta_D(L)} \cdot \left(1 + \sqrt{2} \cos\left(\frac{\pi}{2}x^2 + \frac{\pi}{4}\right) + \pi x \cdot \{FS(x) + FC(x) - 1\} \right) \quad (6.29)$$

where $\mathbf{x} = \{T_d/\sqrt{\beta_D(L)}\}$, $\mathbf{FS}(\mathbf{x}) \triangleq \int_0^x \sin(\pi\lambda^2/2)d\lambda$, $\mathbf{FC}(\mathbf{x}) \triangleq \int_0^x \cos(\pi\lambda^2/2)d\lambda$.

Here $\mathbf{FS}(\mathbf{x})$, and $\mathbf{FC}(\mathbf{x})$ Fresnel sine and cosine integrals [81]. The normalized version of (6.29) is calculated with normalization factor of $\delta f \sqrt{\beta_D(L)}$ as shown in Fig. 6.10. In a pilot-aided complex detection system (discussed in the next chapter), the PN and IN variances are much smaller than the free-running ones due to the correlation detection TF which acts as a band-limiter as in the configuration shown in Fig. 6.11.

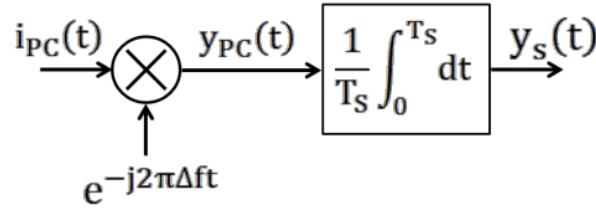


Fig. 6.11: Complex detection of beat-note signal.

For instance, the integrate-and-dump in single-carrier transmission system and the \mathcal{FFT} with large N_F value in OFDM receiver have identical TFs, which is based on signal averaging over symbol's time duration (T_S), and given by [69]

$$H_{RX}(f) = y_s(f)/y_{PC}(f) = \text{sinc}(f \cdot T_S) \quad (6.30)$$

where $\mathbf{y}_s(\mathbf{f}) = \mathcal{FT}\{y_s(t)\}$, and $\mathbf{y}_{PC}(\mathbf{f}) = \mathcal{FT}\{y_{PC}(t)\}$, as shown in Fig. 6.11.

For instance if $\delta f = 2\text{MHz}$, $\Delta f = 15\text{GHz}$, and $L \approx 1027\text{km}$, then from real-time simulation, and calculation of (6.27), and (6.28), then $\{\sigma_{\Delta\phi,FR}^2\}_D \approx 0.0265$, $\{\sigma_{\Sigma\alpha,FR}^2\}_D \approx 7.3 \times 10^{-4}$, while $\{\sigma_{\Delta\phi,FR}^2\}_{ND} \approx 0.0273$, and $\{\sigma_{\Sigma\alpha,FR}^2\}_{ND} \approx 1 \times 10^{-5}$ (theoretically zero when $\mathbf{f}_M \rightarrow \infty$) which indicates a slight reduction in $\{\sigma_{\Delta\phi,FR}^2\}_D$ compared to $\{\sigma_{\Delta\phi,FR}^2\}_{ND}$ as expected from (6.28); however, this reduction is at the expense of an increase in $\{\sigma_{\Sigma\alpha,FR}^2\}$ as shown in Fig. 6.12-a. While when modulation is applied to one of the two beams in the

above given example with $T_S = 5.12\text{ns}$ (about 200Msymbol/s), then the correlation detector's output for the dispersive and non-dispersive cases are almost identical as shown in Fig. 6.12-b. The complex signal and noise are convolved and have to be separated mathematically before calculating the noise variance.

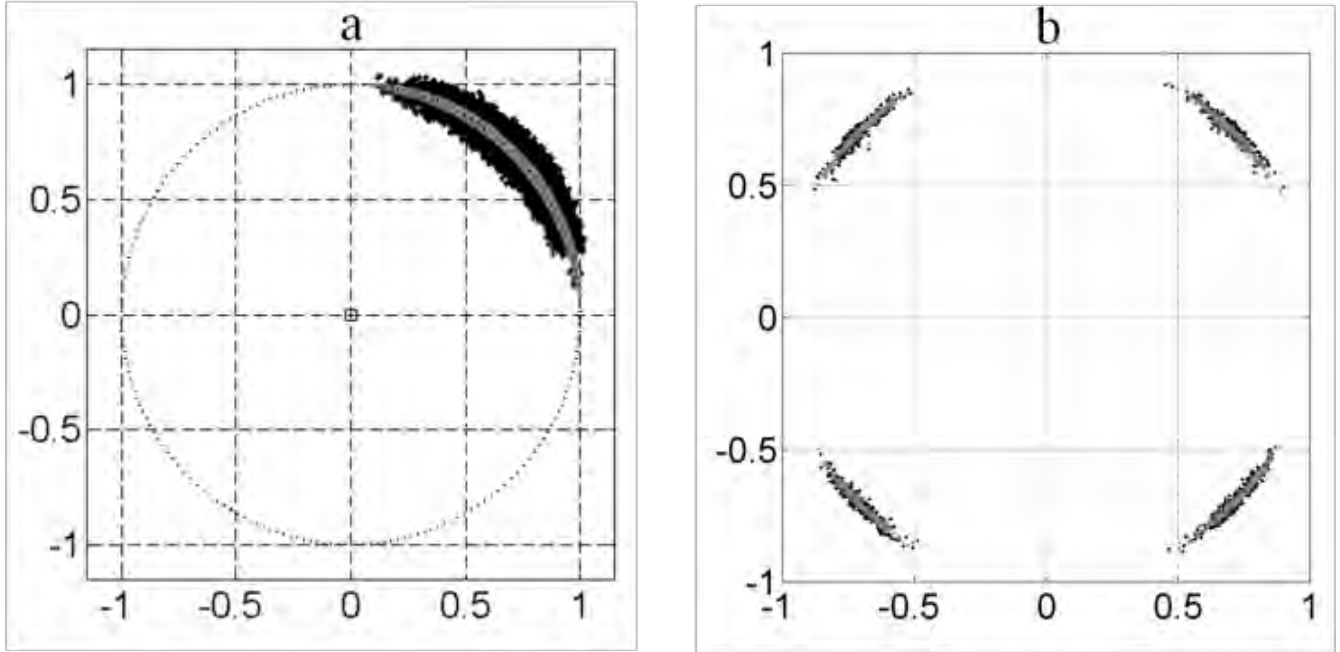


Fig. 6.12: $i_{\text{BN,BB}}^+(\mathbf{t})$ without correlation detection in (a), and QPSK-modulated $i_{\text{BN,BB}}^+(\mathbf{t})$ with correlation detection in (b). The gray color is for non-dispersive field and the black one is for dispersive field.

Thus, whenever noise-signal separation is possible, then the correlation detector's output noise variance is expressed by

$$\sigma_{Y,\text{Det}}^2(T_S)|_{O/P} = \int_{-f_M}^{f_M} S_Y(f) \cdot H_{\text{OBZ}}(f) \cdot \text{sinc}^2(fT_S) df \quad (6.31)$$

where $S_Y(\mathbf{f})$ is the DS-PSD of any noise signal $\mathbf{Y}(\mathbf{t})$ with zero-mean. Here $\sigma_{Y,\text{Det}}^2(T_S)$ is an absolute-time variance which is measured over the whole \mathbf{T}_{OBS} . The DSH test in this chapter is used as an analogy to the case of pilot-aided pre-detection noise-compensation which is particularly useful in OFDM system design [6], [8]. In this case, as all subcarriers are assumed to be uncorrelated, then every subcarrier has its own convolved PN and IN terms obtained from (6.26), and (6.31), and additional IN term (only when PD is used in the detection) resulting from $S_{\text{IN}}(\mathbf{f})$ in (6.20) or Yamamoto noise term [45]. The correlator's rejected-noise interfere the adjacent channels, which is known as inter-

carrier interference (**ICI**) [119]. The ICI is considered as complex additive white Gaussian noise (**AWGN**) since no correlation between the subcarriers is assumed, and it can be estimated by (6.17). Thus, if $\mathbf{T}_S \ll \mathbf{T}_{OBS}$, and from (6.20), (6.25), (6.26), and (6.30) yields

$$\sigma_{\Delta\phi,Det}^2(\mathbf{T}_d, \mathbf{T}_S) \approx \int_{-f_M}^{f_M} S_{\Delta\phi_{rn}}(f) \text{sinc}^2(fT_S) df \quad (6.32-a)$$

$$\sigma_{\Sigma\alpha,Det}^2(\mathbf{T}_d, \mathbf{T}_S) \approx \int_{-f_M}^{f_M} \left\{ S_{\Sigma\alpha_{rn}}(f) \text{sinc}^2(fT_S) + \frac{S_{IN}(f)}{2} \text{sinc}^2((f - m\tilde{\Delta}f)T_S) \right\} df \quad (6.32-b)$$

$$\sigma_{ICI}^2(\mathbf{T}_d, \mathbf{T}_S) \approx \sum_{\substack{k=-\frac{N}{2} \\ k \neq m}}^{\frac{N}{2}-1} \int_{-f_M}^{f_M} \widetilde{S}_{PC}(f - k\tilde{\Delta}f) \text{sinc}^2((f - m\tilde{\Delta}f)T_S) df \quad (6.32-c)$$

where $\widetilde{S}_{PC}(f)$ is $S_{PC}(f)$ from (6.17) without the $\delta(f)$ term, k is the frequency index of subcarriers, $\tilde{\Delta}f$ is the minimum frequency-separation between subcarriers, N is number of modulated subcarriers, and m is frequency index of the subcarrier under test. Note that $\sigma_{\Sigma\alpha,Det}^2(\mathbf{T}_d, \mathbf{T}_S)$, and $\sigma_{ICI}^2(\mathbf{T}_d, \mathbf{T}_S)$ are normalized to the subcarrier average power which is assumed to be constant here for all subcarriers. Note also that \mathbf{T}_d value used in (6.32) is function of $m - m_p$, where m_p is pilot's frequency index. Thus in this case,

$$T_d(m) = \beta_D(L) \cdot (m - m_p) \cdot \tilde{\Delta}f \quad (6.33)$$

Finally, the following are observed:

- 1- Whenever complex optical detection is performed (using a quadrature receiver for instance), and due to the BD basic feature, then $\mathbf{S}_{IN}(f)$ in (6-20) vanishes. However, when the ASE noise is high, then this **SNR** improvement is marginal.
- 2- $\sigma_{\Delta\phi,Det}^2(\mathbf{T}_d, \mathbf{T}_S)$ in dispersive and non-dispersive systems are almost identical when the symbol's time duration is much larger than the differential delay introduced by the channel response, or $\mathbf{T}_S \gg \mathbf{T}_d$, which is the case in most long-haul OFDM proposals.
- 3- There is a slight difference between the ICI with dispersion and ICI in the back-to-back test (without dispersion) due to the difference between (6.25) and Richter result [108] as shown in Fig. 6.5 and 6.6.

6.5 Conclusions

In this chapter, an analysis of SCL dispersive field has been presented paving the way to the next chapter. First components of the SCL's field in dispersive channel are extracted yielding a semi-exact analytical solution of the IN-DS-PSD given by (6.14-b), which is used in the analytical expression of the beat-note PSD given by (6.20). Furthermore, it is found that the dispersive field's PSD in the OD is identical to the non-dispersive field for any fiber distance. The second contribution is a determination of the exact PSD of the beat-note signal in the DSH test, which simulates the case of pilot-subcarrier beat-note PSD in the pilot-aided feedforward loop (**PA-FFL**), which will be discussed in the next chapter. The beat-note PSD of (6.17) exhibits asymmetrical PSD due to the high correlation between the received PN and the induced IN. This asymmetric spectrum results almost identical PN variance to that in back-to-back test (no dispersion but the differential time delay is assumed) in multi-carrier system like CO-OFDM due to the correlator's TF, however, the ICI term is expected to be different. It is also found that the free-running PN variance in the dispersive field is lower than that without dispersion but at the expense of an increase of free-running IN variance due to PN-to-IN phenomenon. In brief, four distinct noise sources affect the performance of any proposal of pre-demodulation / multiplexing PA-FFL CO-OFDM or in direct detection optical OFDM (**DDO-OFDM**) due to the channel's response and the SCL's parameters, these are:

- 1- Differential PN due to the differential time delay between the pilot and the subcarriers which is estimated using (6.32-a).
- 2- Total convolved (heterodyne) IN, which is estimated using the first part of (6.32-b).
- 3- Total convolved (homodyne and only when PD is used in the detection setup) IN which is estimated using the second part of (6.32-b).
- 4- The uncorrelated term which is approximately considered as AWGN (ICI) due to the adjacent channel interference, and can be estimated using (6.32-c).

Chapter 7

Effect of SCL Noise on CO-OFDM System Performance with/without PA-FFL

7.1 Introduction

In this chapter, effect of the transmitter's (TX)'s and receiver's (RX)'s semiconductor laser (SCL) noise on the coherent optical OFDM (CO-OFDM) system with and without a pilot-aided feed-forward loop (PA-FFL) is presented. First, an analysis and modeling of the CO-OFDM link without PA-FFL is demonstrated aiming to yield overall penalty due to the SCLs noise. Although the uncompensated noise model has been extensively studied in the literature especially in RF systems, however, a generalized model is discussed here taking the channel response and all the SCL parameters into account. Second the CO-OFDM system with PA-FFL is modeled and analyzed benefiting from the results of Chapter 6. Finally pilot-insertion optimization whether it is one of the subcarriers (SC)s or externally inserted is discussed thoroughly. The main aims of this chapter are to:

- estimate the conventional CO-OFDM's performance versus the SCLs' parameters,
- estimate the performance of the CO-OFDM with PA-FFL as a function of the SCLs' parameters, and the compensated bandwidth (BW),
- derive the optimal compensated BW, and optimal pilot-to-signal power ratio, and
- yield optimal pilot insertion conditions.

7.2 Effect of SCL noise on CO-OFDM performance

7.2.1 Modeling

Assuming perfect synchronization and polarization control is achieved, then the time-sample index ($\hat{\mathbf{n}}$) is identical for both the TX and RX. Similar to the analysis in Section 3.3.5, $\hat{\mathbf{n}} = [-N_{\mathcal{CP}}, \dots, -1, 0, 1, \dots, N_{\mathcal{F}} - N_{\mathcal{CP}}, \dots, N_{\mathcal{F}} - 1]$, and the frequency-sample index is $\mathbf{k} = [-N/2, \dots, -1, 1, \dots, N/2]$, where \mathbf{N} , $\mathbf{N}_{\mathcal{CP}}$, and $\mathbf{N}_{\mathcal{F}}$ are number of modulated-SCs, length of the cyclic prefix (CP), and the \mathcal{FFT} size respectively. Besides, when the timing-window is determined and the CP is removed, then the time-sample index

becomes $\mathbf{n} = [0, 1, \dots, N_{\mathcal{F}} - 1]$ as shown in Fig. 7.1. The discrete version of the transmitted signal is given by

$$\mathbf{V}[\hat{\mathbf{n}}, \ell] = \sum_{\ell} \sum_{\substack{k=-N/2 \\ k \neq 0}}^{N/2} c[k, \ell] \cdot \exp\left(j2\pi \frac{k}{N_{\mathcal{F}}} \hat{\mathbf{n}}\right), \text{ where } \ell \text{ is OFDM symbol's index.}$$

For notation simplicity, we will remove the first Sigma and the domain of \mathbf{k} , and hence

$$\mathbf{V}[\hat{\mathbf{n}}, \ell] = \sum_{\mathbf{k}} c[\mathbf{k}, \ell] \cdot \exp\left(j2\pi \frac{\mathbf{k}}{N_{\mathcal{F}}} \hat{\mathbf{n}}\right)$$

where $\mathbf{c}[\mathbf{k}, \ell]$ is the mapping state of the \mathbf{k} -th cell in the frequency vector ($\mathbf{F}\mathbf{r}\mathbf{V}$) in the ℓ -th OFDM symbol as discussed in Chapter 3. In Fig. 7.1, the TX carrier and RX local oscillator (LO), which will be denoted as **TX-LO-SCL**, and **RX-LO-SCL** are expressed respectively in their baseband (**BB**) discrete model as

$$\mathbf{E}_1[\hat{\mathbf{n}}, \ell] = \exp(\alpha_1[\hat{\mathbf{n}}, \ell] + j\phi_1[\hat{\mathbf{n}}, \ell]) \quad , \text{ and } \quad \mathbf{E}_2[\hat{\mathbf{n}}, \ell] = \exp(\alpha_2[\hat{\mathbf{n}}, \ell] + j\phi_2[\hat{\mathbf{n}}, \ell])$$

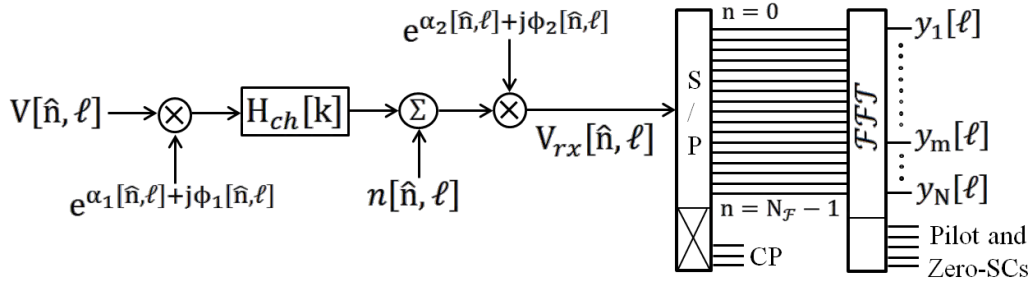


Fig. 7.1: Discrete model of the Conventional CO-OFDM link focusing on the SCLs noise.

where the subscripts “1”, and “2” are for the TX-LO-SCL and RX-LO-SCL respectively, $\alpha[\hat{\mathbf{n}}, \ell]$, and $\phi[\hat{\mathbf{n}}, \ell]$ are the relative intensity noise (**IN**) and PN terms respectively. From (3.14), the received signal can be expressed as

$$V_{rx}[\hat{\mathbf{n}}, \ell] = A \sum_{\mathbf{k}} \left\{ c[\mathbf{k}, \ell] \cdot \exp(j2\pi \hat{\mathbf{n}} \mathbf{k} / N_{\mathcal{F}} - j\pi \mathbf{Y}_L \mathbf{k}^2) \cdot \exp(j\tilde{\phi}_1[\hat{\mathbf{n}} - \varepsilon[\mathbf{k}], \ell] + j\phi_2[\hat{\mathbf{n}}, \ell]) \cdot \exp(\tilde{\alpha}_1[\hat{\mathbf{n}} - \varepsilon[\mathbf{k}], \ell] + \alpha_2[\hat{\mathbf{n}}, \ell]) \right\} + n[\hat{\mathbf{n}}, \ell] \quad (7.1)$$

where $\mathbf{Y}_L = \beta_D(L) \cdot (F_S / N_{\mathcal{F}})^2$, $\varepsilon[\mathbf{k}] = \mathbf{Y}_L \cdot N_{\mathcal{F}} \cdot \mathbf{k}$, $\mathbf{n}[\hat{\mathbf{n}}, \ell]$ is channel noise term,

F_S is the sampling frequency, \mathbf{A} is a constant,

$\beta_D(L)$ in (s/Hz) is the group velocity dispersion (**GVD**) as a function of total distance L in (km), which is calculated from (3.10), and

the “ \sim ” sign indicates the distorted version (due to channel response) of PN and IN functions are used.

Therefore the m -th output (**O/P**) from the \mathcal{FFT} computation is given by

$$\begin{aligned} \mathbf{y}_m[\ell] = & \frac{A}{N_{\mathcal{F}}} \sum_{n=0}^{N_{\mathcal{F}}-1} \sum_{\mathbf{k}} \left\{ c[\mathbf{k}, \ell] \cdot \exp(j2\pi n \cdot (\mathbf{k} - m)/N_{\mathcal{F}}) \cdot \exp(-j\pi \Upsilon_L k^2) \right. \\ & \left. \cdot \exp(j\widetilde{\phi}_1[n - \varepsilon[\mathbf{k}], \ell] + j\phi_2[n, \ell]) \cdot \exp(\widetilde{\alpha}_1[n - \varepsilon[\mathbf{k}], \ell] + \alpha_2[n, \ell]) \right\} \\ & + \frac{1}{N_{\mathcal{F}}} \sum_{n=0}^{N_{\mathcal{F}}-1} n[n, \ell] \cdot \exp(-j2\pi n \cdot m/N_{\mathcal{F}}) \end{aligned} \quad (7.2)$$

Note that the channel noise is a complex circular Gaussian random variable (**GRV**) with zero-mean, and hence no difference occurs when it multiplied by the RX-LO-SCL. Besides, since the channel noise is additive white Gaussian noise (**AWGN**), then its variance is equal for all SCs. Therefore (7.2) can be rewritten as follows

$$\mathbf{y}_m[\ell] = \mathbf{y}_{m,s}[\ell] + \mathbf{y}_{m,ICI}[\ell] + \mathbf{y}_{m,n}[\ell] \quad (7.3)$$

where $\mathbf{y}_{m,s}[\ell]$, $\mathbf{y}_{m,ICI}[\ell]$, and $\mathbf{y}_{m,n}[\ell]$ are respectively the signal term, the inter-carrier interference term (**ICI**), and the channel noise term. A distinct expression for each of (7.3) terms will be derived next.

7.2.2 Analysis of $\mathbf{y}_m[\ell]$ terms

7.2.2.1 The channel noise term $\mathbf{y}_{m,n}[\ell]$

The variance of the 1st term in (7.3) is calculated from Section 3.3.5 as follows

$$\sigma_n^2[m] = \sigma_n^2 = \langle \mathbf{y}_{m,n}[\ell] \mathbf{y}_{m,n}^*[\ell] \rangle_{\ell} = \langle |n[\mathbf{n}_x, \ell]|^2 \rangle_{\ell} / N_{\mathcal{F}} \quad (7.4)$$

where \mathbf{n}_x is any selected index of noise samples in time domain (**TD**), since the time average equals the ensemble average in the AWGN. Thus AWGN variance per SC equals the total received channel-noise power within a BW equals \mathbf{F}_S divided by the \mathcal{FFT} size.

7.2.2.2 The useful term $\mathbf{y}_{m,s}[\ell]$

The 2nd term in (7.3) is $\mathbf{y}_{m,s}[\ell]$, which is calculated from (7.2) by retaining the term with $\mathbf{k} = \mathbf{m}$ in the summation

$$\mathbf{y}_{m,s}[\ell] \cong A \cdot \{c[\mathbf{m}, \ell] e^{j\psi_a[\mathbf{m}]}\} \cdot \{\eta_{\phi,m}[\ell] + \eta_{\alpha,m}[\ell]\} \quad (7.5)$$

$$\text{where } \boldsymbol{\eta}_{\phi, \mathbf{m}}[\boldsymbol{\ell}] = \sum_{n=0}^{N_{\mathcal{F}}-1} \exp(j\widetilde{\phi}_1[n - \varepsilon[\mathbf{m}], \boldsymbol{\ell}] + j\phi_2[n, \boldsymbol{\ell}]) / N_{\mathcal{F}},$$

$$\boldsymbol{\eta}_{\alpha, \mathbf{m}}[\boldsymbol{\ell}] = \sum_{n=0}^{N_{\mathcal{F}}-1} (\widetilde{\alpha}_1[n - \varepsilon[\mathbf{m}], \boldsymbol{\ell}] + \alpha_2[n, \boldsymbol{\ell}]) / N_{\mathcal{F}}, \text{ and } \boldsymbol{\psi}_d[\mathbf{k}] = -\pi\gamma_L k^2.$$

7.2.2.2.1 Phase shift due to channel response

The first parameter in (7.5) is $\boldsymbol{\psi}_d[\mathbf{k}]$, which is irrelevant to the SCL's noise. This parameter is predictable since CD is a quasi-static effect, and hence it can be corrected by the aid of a training symbol (**TrS**) in the channel estimation and correction unit [4], [23]. For example, if $F_S = 10\text{GSps}$, $N_{\mathcal{F}} = 256$, $\mathbf{L} = [100, 300, 1000, 3000]\text{km}$ and $\mathbf{N} = 200$, then from (7.1), and (3.10), the unwrapped $\boldsymbol{\psi}_d[\mathbf{k}]$ is calculated and yields a parabolic phase curve as shown in Fig. 7.2 [27], [120], [121].

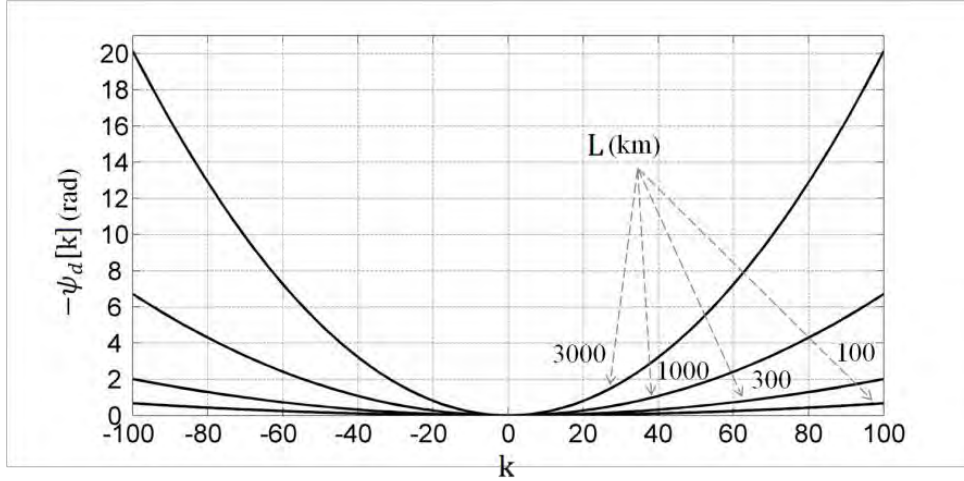


Fig. 7.2: Phase shift due to CD as a function of SC's frequency index. Here $F_S = 10\text{GSps}$, and $N_{\mathcal{F}} = 256$.

Note that when only the polarization-mode dispersion (**PMD**) is not counted, then from (3.14), a more exact expression of $\boldsymbol{\psi}_d[\mathbf{k}]$ is obtained as

$$\boldsymbol{\psi}_d[\mathbf{k}] = -\left\{ \phi_o + 2\pi T_o \left(\frac{F_S}{N_{\mathcal{F}}} \right) k + \pi\beta_D(L) \left(\frac{F_S}{N_{\mathcal{F}}} \right)^2 k^2 \right\} \quad (7.6)$$

where T_o is the mean propagation delay, and ϕ_o is an arbitrary phase.

7.2.2.2.2 $\boldsymbol{\eta}_{\phi, \mathbf{m}}[\boldsymbol{\ell}]$

The second important parameter in (7.5) is $\boldsymbol{\eta}_{\phi, \mathbf{m}}[\boldsymbol{\ell}]$, which describe the variation of the amplitude and phase of the **m-th** SC at different OFDM symbols due to SCL's PN.

7.2.2.2.1 Statistical description of $|\eta_{\phi,m}[\ell]|$

From (7.5), the amplitude of $\eta_{\phi,m}[\ell]$ parameter is given by

$$|\eta_{\phi,m}[\ell]| = \frac{|\sum_{n=0}^{N_{\mathcal{F}}-1} \exp(j\widetilde{\Phi}_1[n - \varepsilon[m], \ell] + j\Phi_2[n, \ell])|}{N_{\mathcal{F}}} \leq 1 \quad (7.7)$$

$|\eta_{\phi,m}[\ell]|$ has a statistical nature, which is similar to some extent the wireless fading channel. In the following example the statistics of $|\eta_{\phi,m}[\ell]|$ of a single SCL is demonstrated by simulating it versus ℓ with $\mathbf{F}_S = 10\text{GSps}$, $\mathbf{N}_{\mathcal{F}} = 256$, total number of OFDM symbols is 4000, only the white frequency noise (FN) is taken into account, and natural linewidth of $\delta\mathbf{f} = 1\text{MHz}$, and 10MHz as shown in Fig. 7.3.

In the second test, an OFDM signal consisting of 199 zero-SCs, one modulated-SC with QPSK mapping at $\mathbf{k} = 101$, and one pilot-SC at $\mathbf{k} = -100$, is examined. The other test parameters are $\mathbf{F}_S = 10\text{GSps}$, $\mathbf{N}_{\mathcal{F}} = 256$, and $\delta\mathbf{f} = 10\text{MHz}$. This setting ensures negligible ICI, and the pilot-SC can be used for phase equalization. First the modulated-SC is demodulated without phase error correction as shown in Fig. 7.4a. Then the pilot-SC is used to correct phase error in the demodulated-SC as shown in Fig. 7.4b.

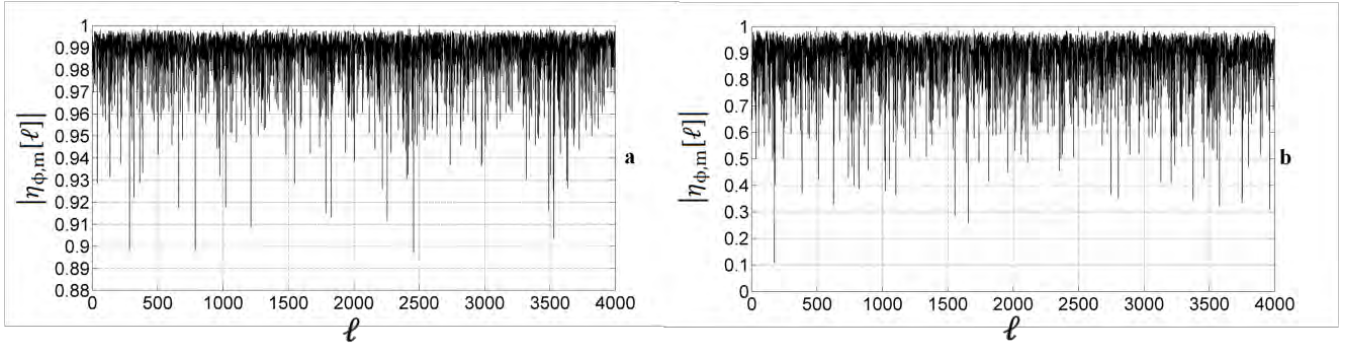


Fig. 7.3: Amplitude of the m -th SC as a function of OFDM's symbol index ℓ with $\delta\mathbf{f}_N = 0.0256$ ($\delta\mathbf{f} = 1\text{MHz}$) in (a), and $\delta\mathbf{f}_N = 0.256$ ($\delta\mathbf{f} = 10\text{MHz}$) in (b). Here $\mathbf{F}_S = 10\text{GSps}$, $\mathbf{N}_{\mathcal{F}} = 256$, and \mathbf{f}_{CN} is ignored.

The probability density function (PDF) is then calculated by dividing the domain of $[0, 1]$ into 10000 steps, and number of occurrence per step is counted and divided by the total number of OFDM symbols, which in this case equals 32,768 symbols. Two PDFs are calculated in this example; the first one is to investigate the effect of white FN only with $\delta\mathbf{f} = [1, 2, 5, 10, 20]\text{MHz}$ as shown in Fig. 7.5a, and the second one is to investigate the flicker FN effect with $\delta\mathbf{f} = 1\text{MHz}$, and the flicker corner frequency of $\mathbf{f}_C = [0.1, 0.2, 0.5, 1.0, 2.0]\text{MHz}$ as shown in Fig. 7.5b. It is more convenient to measure PN effect with

respect to the $\mathcal{FF}\mathcal{T}$ time-period $\mathbf{T}_{\mathcal{F}}$, where $\mathbf{T}_{\mathcal{F}} = N_{\mathcal{F}}/F_S$. Thus the normalized $\delta\mathbf{f}$ and $\mathbf{f}_{\mathcal{C}}$ are $\delta\mathbf{f}_{\mathcal{N}} = (\delta f \cdot N_{\mathcal{F}}/F_S)$, and $\mathbf{f}_{\mathcal{CN}} = (\delta f \cdot N_{\mathcal{F}}/F_S)$.

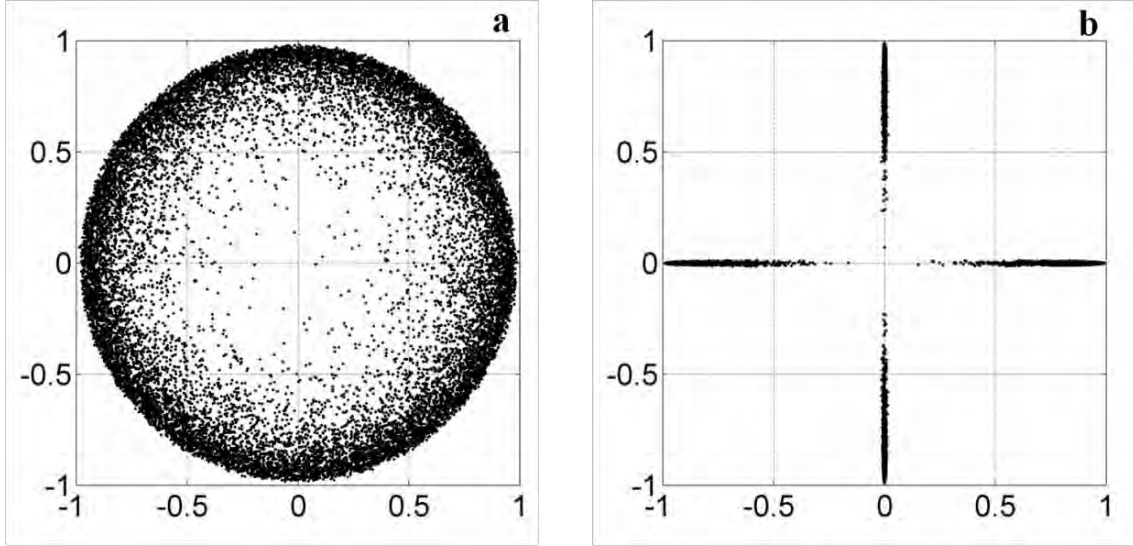


Fig. 7.4: Effect of SCL's PN on the m -th SC amplitude showing the non-equalized symbol in (a), and the equalized one in (b). Here $\delta\mathbf{f}_{\mathcal{N}} = 0.256$ ($\delta\mathbf{f} = 10\text{MHz}$), $F_S = 10\text{GSps}$, $N_{\mathcal{F}} = 256$, and QPSK mapping.

As expected, the flicker effect is marginal since $\mathbf{T}_{\mathcal{F}}$ is relatively small and the flicker PN variance is proportional to the square of $\mathbf{T}_{\mathcal{F}}$ as discussed in Section 4.3.3.2. This amplitude fluctuation results from PN-to-IN conversion due to filtering (averaging in OFDM), which occurs in many other applications such as filtering of phase-modulated signal, and filtering of SCL field in RF or optical domain [43]-[44]. From Fig. 7.4 it is obvious that even when the phase error is corrected via a free-of-noise pilot-SC, the modulated-SC is highly degraded despite the fact that the mean value is close to unity. Although some attempts were conducted by the author to formulate the PDF of $|\eta_{\phi,m}[\ell]|$, however, no fruitful results were obtained. As far as we know, the statistical effect of $|\eta_{\phi,m}[\ell]|$ has not been covered adequately in literature, and it is common to use the average value instead, which is in turn assumed to be unity [40]. Usually $\eta_{\phi,m}[\ell]$ of one of PN sources is linearized as $\eta_{\phi,m}[\ell] \approx 1 + j \sum_{n=0}^{N_{\mathcal{F}}-1} \phi[n, \ell]/N_{\mathcal{F}}$, and hence the common phase error (CPE) is obtained as $\mathbf{CPE}[\ell] = j \sum_{n=0}^{N_{\mathcal{F}}-1} \phi[n, \ell]/N_{\mathcal{F}}$ which is identical on all SCs at a given ℓ [122]. However, in optical OFDM and due to CD, this phase error is not common but a function of SC's frequency index. Besides, the linearization of the exponential function in (7.7) is only accurate for $\delta\mathbf{f}_{\mathcal{N}} \ll 0.1$.

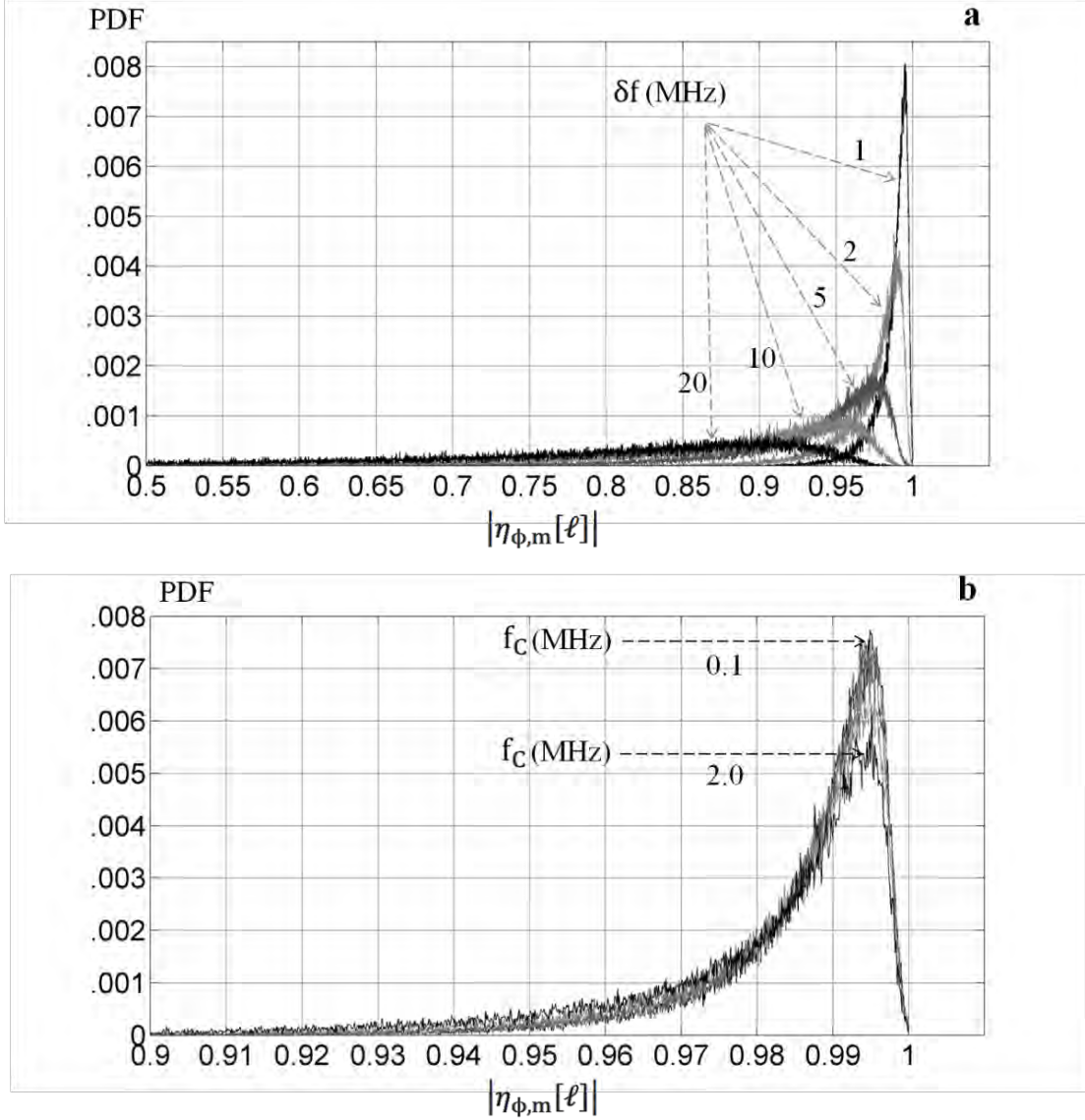


Fig. 7.5: PDF of the m -th SC amplitude with $\delta f_N = [0.0256, 0.0512, 0.128, 0.256, 0.512]$ and f_{CN} is ignored in (a), and $f_{CN} = [0.00256, 0.00512, 0.0128, 0.0256, 0.0512]$, and $\delta f_N = 0.0256$ in (b). Here $F_S = 10$ GSps, and $N_F = 256$.

From the continuous model in Section 3.3.1, which is equivalent to the discrete model with large N_F [69], the mean value of $|\eta_{\phi,m}[\ell]|$ can be estimated as

$$\langle |\eta_{\phi,m}[\ell]|^2 \rangle + \sigma_{|\eta_{\phi,m}|}^2 \cong \int_{-f_m}^{f_m} \text{sinc}^2(fT_F) \cdot (\widetilde{S_{EN1}}(f) * S_{EN2}(f)) \cdot df \quad (7.8)$$

where $\sigma_{|\eta_{\phi,m}|}^2$ is the IN variance corresponds to the statistics mentioned previously,

f_m is maximum single-sided (SS) frequency of the ADC, which equals $F_S/2$, and $*$ sign stands for convolution, $\widetilde{S_{EN1}}(f)$, and $S_{EN2}(f)$ are the normalized double-sided (DS) power spectral density (PSD) of the received TX-LO-SCL and RX-LO-SCL respectively.

When only the white FN is counted, and $\mathbf{H}_c[\mathbf{k}] = 1$, then from (4.14-b), (4.28) and by assuming $\mathbf{f}_m \rightarrow \infty$, (7.8) becomes

$$\langle |\eta_{\phi,m}[\ell]|^2 \rangle + \sigma_{|\eta_{\phi,m}|}^2 \cong 2 \left(\frac{\rho - 1 + e^{-\rho}}{\rho^2} \right) \quad (7.9)$$

Where $\rho = \pi \cdot (\delta f_{N1} + \delta f_{N2})$, $\delta \mathbf{f}_{N1}$, and $\delta \mathbf{f}_{N2}$ are the normalized natural linewidths of TX-LO-SCL and RX-LO-SCL respectively. Since the PDF of $|\eta_{\phi,m}[\ell]|$ is unknown yet, then it is not possible in this analysis to separate $\langle |\eta_{\phi,m}[\ell]|^2 \rangle$ and $\sigma_{|\eta_{\phi,m}|}^2$, and hence $\langle |\eta_{\phi,m}[\ell]|^2 \rangle$ is assumed to be equal the right-hand side of (7.9), which is valid for $\delta \mathbf{f}_N \leq 0.01$. Besides, $\langle |\eta_{\phi,m}[\ell]|^2 \rangle$ is the same for all SCs, and hence $\langle |\eta_{\phi,m}[\ell]|^2 \rangle = \langle |\eta_{\phi}[\ell]|^2 \rangle$. In brief, large SCL PN ($\delta \mathbf{f}_N \geq 0.1$) can cause loss of symbols at some ℓ values, which cannot be easily corrected after the \mathcal{FFT} process is performed, however, the average symbol's power is close to unity even for large linewidth, and hence an interleaver at the TX might be used to overcome the loss of entire symbols [48].

7.2.2.2.2 Statistical description of $\arg\{\eta_{\phi,m}[\ell]\}$

The unwrapped version of $\theta_m[\ell] = \arg\{\eta_{\phi,m}[\ell]\}$ has a random-walk phase statistics, which is similar to $\phi[\mathbf{n}, \ell]$ waveform as illustrated in Fig. 7.6a. However, the differential phase $\Delta\theta_m[\ell] = \arg\{\eta_{\phi,m}[\ell]\} - \arg\{\eta_{\phi,m}[\ell - 1]\}$ has a white phase statistics, and hence it can be modeled as a GRV [48] as illustrated in Fig. 7.6b. In the following simulation, $\theta_m[\ell]$, and $\Delta\theta_m[\ell]$ are demonstrated versus ℓ with $\mathbf{F}_S = 10\text{GSps}$, $\mathbf{N}_F = 256$, $\delta \mathbf{f} = 10\text{MHz}$, and total number of OFDM symbols is 15000. Note that the CP results small phase discontinuities between the successive OFDM symbols, however, this effect is ignored in this simulation. Again from the continuous model, (3.16), (4.28), and since $\langle \Delta\theta_m[\ell] \rangle_{\ell} = 0$, then the differential PN variance in (rad^2) can be estimated as

$$\langle |\Delta\theta_m[\ell]|^2 \rangle_{\ell} \cong 4 \int_{-f_m}^{f_m} \text{sinc}^2(fT_F) \sin^2(\pi fT_F) \cdot (\widetilde{S_{\phi_{n1}}}(f) + S_{\phi_{n2}}(f)) \cdot df \quad (7.10)$$

where $\widetilde{S_{\phi_{n1}}}(f)$, and $S_{\phi_{n2}}(f)$ are the PN-DS-PSD in (rad^2/Hz) of the received TX-LO-SCL and RX-LO-SCL respectively. Here (7.10) estimates phase shift between successive OFDM symbols, which is independent of \mathbf{k} . When only the white FN is counted, and $\mathbf{H}_c[\mathbf{k}] = 1$, then from (4.3), (4.5), (4.14-b) and by assuming $\mathbf{f}_m \rightarrow \infty$, (7.10) becomes

$$\langle |\Delta\theta_m[\ell]|^2 \rangle_\ell = \langle |\Delta\theta[\ell]|^2 \rangle_\ell \cong \frac{4\pi}{3} (\delta f_{N_1} + \delta f_{N_2}) \quad (\text{rad}^2) \quad (7.11)$$

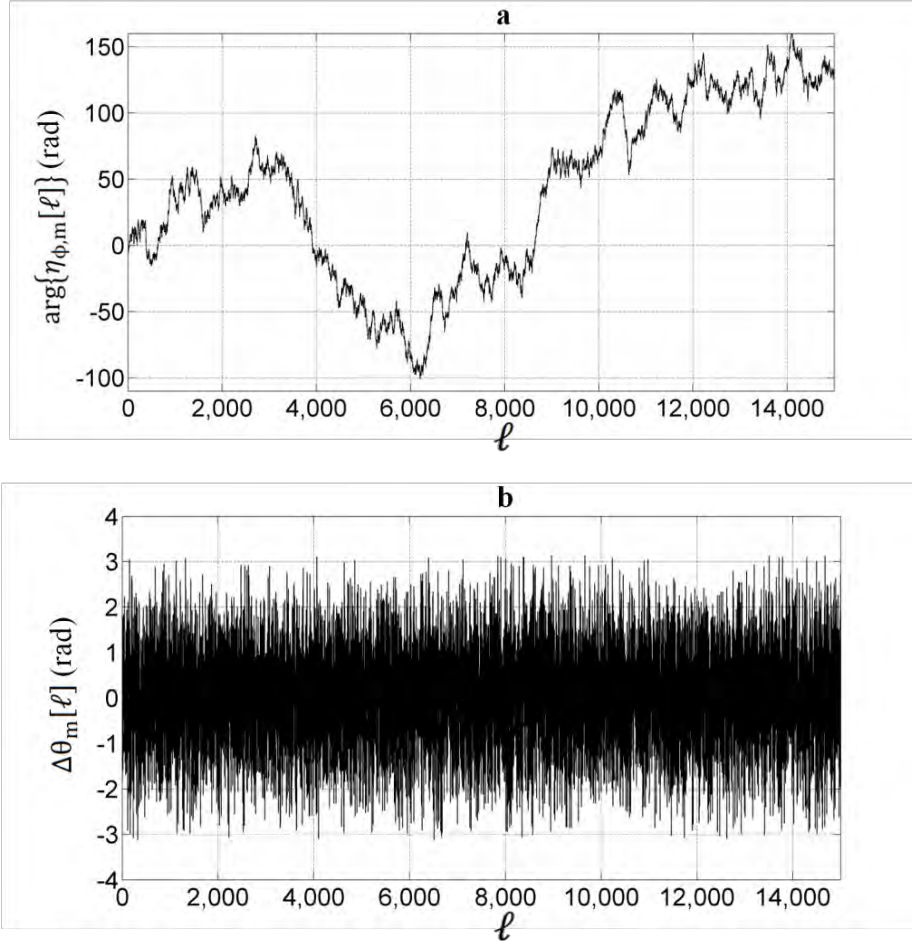


Fig. 7.6: Absolute phase shift of the m -th SC due to SCL's PN $\theta_m[\ell]$ as a function of ℓ is shown in (a), and the differential one $\Delta\theta_m[\ell]$ in (b). Here $F_S = 10\text{GSps}$, and $N_F = 256$, and $\delta f = 10\text{MHz}$.

7.2.2.2.3 $\eta_{\alpha,m}[\ell]$

The third parameter in (7.5) is $\eta_{\alpha,m}[\ell]$, which result from the IN terms of both SCLs. It has the same statistics of $\alpha[\mathbf{n}, \ell]$, and has a quite small contribution in the total penalty due to the SCL's noise. This is true since each SC shares approximately $1/N_F$ of total IN variance, and the relaxation peak, which could be higher by 20-dB or more than the average relative IN (**RIN**), is rejected in the **FFT** averaging process. Thus for an average **RIN** of up to -120dBc/Hz, this effect is negligible as long as the relaxation oscillation frequency F_R is much higher than the frequency separation between the subcarriers $\Delta f = F_S/N_F$, which is very common, and hence sum of all $\eta_{\alpha,k-m}[\ell]$ is added to the ICI term since $\eta_{\alpha,m}[\ell]$ is negligible.

7.2.2.3 The ICI term $\mathbf{y}_{m,ICI}[\ell]$

The 3rd term in (7.3) is the ICI component $\mathbf{y}_{m,ICI}[\ell]$, which is calculated from (7.3) when $\mathbf{k} \neq \mathbf{m}$ and hence

$$y_{m,ICI}[\ell] = \frac{A}{N_{\mathcal{F}}} \sum_{n=0}^{N_{\mathcal{F}}-1} \sum_{\substack{k \\ k \neq m}} c[k, \ell] e^{j2\pi n(k-m)/N_{\mathcal{F}} - \psi_d[k]} e^{j\tilde{\phi}_1[n-\varepsilon[k], \ell] + j\phi_2[n, \ell]} e^{\tilde{\alpha}_1[n-\varepsilon[k], \ell] + \alpha_2[n, \ell]} \quad (7.12)$$

This noise is usually modeled as a zero-mean complex AWGN for large value of \mathbf{N} , and hence its variance can directly be added to channel noise variance [119].

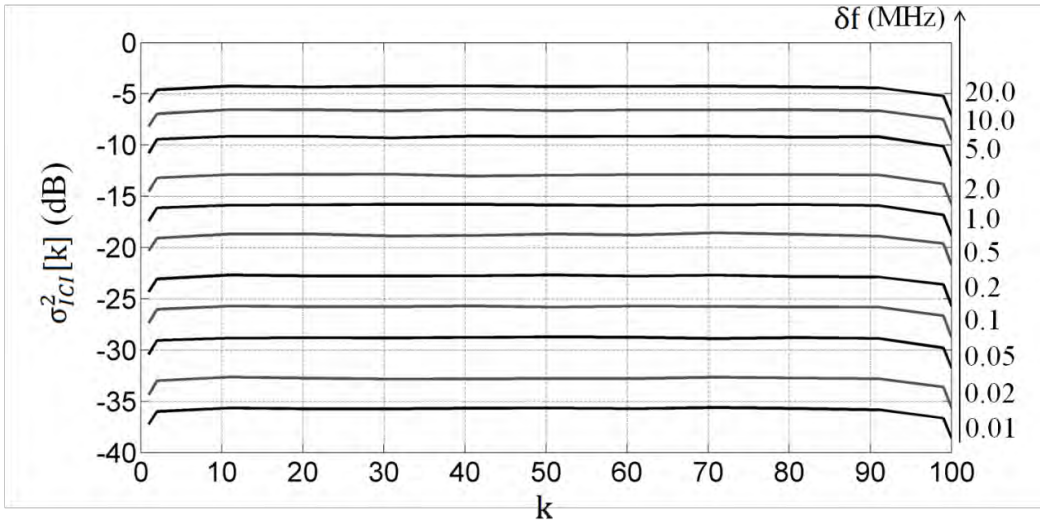


Fig. 7.7: Simulated $\sigma_{ICI}^2[\mathbf{k}]$ normalized to the SC power showing only the positive SCs when only the white FN is counted and $\mathbf{H}_c[\mathbf{k}] = 1$, and all the SCs have equal powers with $\delta\mathbf{f}_N$ values are as given in the text. Here $\mathbf{F}_S = 10\text{GSps}$, and $\mathbf{N}_{\mathcal{F}} = 256$.

Here $\sigma_{ICI}^2[\mathbf{m}]$ is derived as $\sigma_{ICI}^2[\mathbf{m}] = \langle y_{m,ICI}[\ell] y_{m,ICI}^*[\ell] \rangle_{\ell}$, which is presented in Appendix-A8. In (A8.1), channel response and all SCLs' parameters are counted in $\sigma_{ICI}^2[\mathbf{m}]$ estimation. While in (A8.2), only the white FN is counted, $\mathbf{H}_c[\mathbf{k}] = 1$, and all SCs are assumed to have equal powers. In the following calculations, $\mathbf{F}_S = 10\text{GSps}$, $\mathbf{N}_{\mathcal{F}} = 256$, $\mathbf{N} = 200$, $\delta\mathbf{f}_N = [0.000256, 0.000512, 0.00128, 0.00256, 0.00512, 0.0128, 0.0256, 0.0512, 0.128, 0.256, 0.5120]$, total number of OFDM symbols is 8192, $\langle |c[\mathbf{k}, \ell]|^2 \rangle_{\ell} = 1$, and only RX-LO-SCL effect is considered as shown in Fig. 7.7. In this simulation, the ICI variance is obtained by setting the SCs under test as zero-SC, noting that only one SC is tested per simulation-run per linewidth value. Note also that since the DC-SC is a zero-SC, a slight reduction in the $\sigma_{ICI}^2[\mathbf{m}]$ value at the first SC is observed.

From the continuous model in Section 3.3.1, the normalized $\sigma_{ICI}^2[\mathbf{m}]$ can be estimated as

$$\sigma_{ICI}^2[\mathbf{m}] \approx \sum_{\substack{k=-N/2 \\ k \neq m}}^{N/2} \int_{-f_m}^{f_m} \text{sinc}^2((f - m\Delta f)T_{\mathcal{F}}) \{ \widetilde{S_{EN1}}(f - k\Delta f) * S_{EN2}(f - k\Delta f) \} df \quad (7.13)$$

where $\Delta f = F_S/N_{\mathcal{F}} = 1/T_{\mathcal{F}}$, is the frequency spacing between the SCs.

Again when only the white FN is counted, $\mathbf{H}_c[\mathbf{k}] = 1$, and all SCs are assumed to have equal powers, then (7.13) can be solved easily assuming $\mathbf{f}_m \rightarrow \infty$ and expressed as

$$\sigma_{ICI}^2[\mathbf{m}] \approx \sum_{\substack{k=-N/2 \\ k \neq m}}^{N/2} \left\{ \frac{(1 - e^{-\rho}) \left\{ |k - m|^2 - \left(\frac{\rho}{2\pi}\right)^2 \right\}}{2\pi^2 \left\{ |k - m|^2 + \left(\frac{\rho}{2\pi}\right)^2 \right\}^2} + \frac{\left(\frac{\rho}{2\pi}\right)}{\pi \left\{ |k - m|^2 + \left(\frac{\rho}{2\pi}\right)^2 \right\}} \right\} \quad (7.14)$$

When $\rho \leq 2\pi/3$, or $(\delta f_{N1} + \delta f_{N2}) \leq 2/3$, then (7.14) can be approximated as

$$\sigma_{ICI}^2[\mathbf{m}] \approx \sum_{\substack{k=-N/2 \\ k \neq m}}^{N/2} \left\{ \frac{\rho + 1 - e^{-\rho}}{2\pi^2} \right\} \frac{1}{|k - m|^2} = \left\{ \frac{\rho + 1 - e^{-\rho}}{2\pi^2} \right\} \sum_{\substack{k=-N/2 \\ k \neq m}}^{N/2} \frac{1}{|k - m|^2} \quad (7.15)$$

Now for large \mathbf{N} , the following identity can be used [81]

$$\sum_{\substack{U=-\infty \\ U \neq 0}}^{\infty} \frac{1}{U^2} = \pi^2/3$$

Thus by considering the SCs which are close to the DC-SC, the worst case of (7.15) is

$$\sigma_{ICI}^2|_{maximum} \approx \frac{\rho + 1 - e^{-\rho}}{6} = \frac{1 + \pi(\delta f_{N1} + \delta f_{N2}) - e^{-\pi(\delta f_{N1} + \delta f_{N2})}}{6} \quad (7.16)$$

These results agree with the discrete calculations in Fig. 7.7, and with results in the literatures of RF-OFDM when PN is modeled as a Wiener process [119]-[123].

7.2.3 Performance estimation

7.2.3.1 Preliminary Analysis

The delivered signal-to-noise ratio per bit (\mathbf{SNR}_b) and the corresponding optical signal-to-noise ratio (\mathbf{OSNR}), which are discussed in Chapter 3, are considered as the independent variables in the following analyses. The mean signal power per SC is directly obtained from (7.5) as

$$P_{SC}[\mathbf{m}] \approx A^2 \langle |c[\mathbf{m}, \ell]|^2 \rangle_{\ell} \cdot \langle |\eta_{\phi, \mathbf{m}}[\ell]|^2 \rangle_{\ell} \quad (7.17)$$

This is true since there is no correlation between $\mathbf{c}[\mathbf{m}, \ell]$, and $\boldsymbol{\eta}_{\phi, \mathbf{m}}[\ell]$. On the other hand the AWGN term consists of the channel noise (amplified spontaneous emission (**ASE**) noise) and the ICI. Thus from (7.4), the added noise per SC is expressed as

$$\sigma_{nSC}^2[\mathbf{m}] = \sigma_n^2[\mathbf{m}] + \sigma_{ICI}^2[\mathbf{m}] = \sigma_n^2 + \sigma_{ICI}^2[\mathbf{m}] \quad (7.18)$$

where $\sigma_{ICI}^2[\mathbf{m}]$ is the true value of the ICI variance, while $\sigma_{ICIIN}^2[\mathbf{m}]$ is the normalized one. Since $\langle |\boldsymbol{\eta}_{\phi, \mathbf{m}}[\ell]|^2 \rangle_{\ell} = \langle |\boldsymbol{\eta}_{\phi}[\ell]|^2 \rangle_{\ell}$, then from (3.22), \mathbf{SNR}_b per SC can be written as

$$\mathbf{SNR}_b[\mathbf{m}] \approx \left(\frac{P_{SC}[\mathbf{m}]}{\sigma_{nSC}^2[\mathbf{m}]} \right) / m = \frac{A^2 \langle |c[\mathbf{m}, \ell]|^2 \rangle_{\ell} \cdot \langle |\boldsymbol{\eta}_{\phi}[\ell]|^2 \rangle_{\ell} / m}{\sigma_n^2 + \sigma_{ICI}^2[\mathbf{m}]}$$

where \mathbf{m} is number of bits per mapped symbol in the input (**I/P**) frequency vector (**FrV**). The analysis is highly simplified if all SCs have equal powers, since in this case, $\sigma_{ICIIN}^2[\mathbf{m}]$ can be used. Hence,

$$\mathbf{SNR}_b[\mathbf{m}] \approx \frac{A^2 \langle |c[\mathbf{m}, \ell]|^2 \rangle_{\ell} \cdot \langle |\boldsymbol{\eta}_{\phi}[\ell]|^2 \rangle_{\ell} / m}{\sigma_n^2 + A^2 \langle |c[\mathbf{m}, \ell]|^2 \rangle_{\ell} \sigma_{ICIIN}^2[\mathbf{m}]} = \frac{\langle |\boldsymbol{\eta}_{\phi}[\ell]|^2 \rangle_{\ell} / m}{\sigma_n^2[\mathbf{m}] / \{A^2 \langle |c[\mathbf{m}, \ell]|^2 \rangle_{\ell}\} + \sigma_{ICIIN}^2[\mathbf{m}]}$$

Now by defining the ideal signal-to-noise ratio as $\mathbf{SNR} = A^2 \langle |c[\mathbf{m}, \ell]|^2 \rangle_{\ell} / \sigma_n^2$, then

$$\mathbf{SNR}_b[\mathbf{m}] = \frac{\mathbf{SNR} / m}{1 + \mathbf{SNR} \cdot \sigma_{ICIIN}^2[\mathbf{m}]} \cdot \langle |\boldsymbol{\eta}_{\phi}[\ell]|^2 \rangle_{\ell} = \frac{\mathbf{SNR}_{bd} \cdot \langle |\boldsymbol{\eta}_{\phi}[\ell]|^2 \rangle_{\ell}}{1 + m \cdot \mathbf{SNR}_{bd} \cdot \sigma_{ICIIN}^2[\mathbf{m}]} \quad (7.19)$$

where \mathbf{SNR}_{bd} is the average delivered \mathbf{SNR}_b . Here $\sigma_{ICI}^2[\mathbf{m}]$, and $\langle |\boldsymbol{\eta}_{\phi}[\ell]|^2 \rangle_{\ell}$ are calculated exactly from (A8.1) in Appendix-A8, and (7.7) respectively. However, $\sigma_{ICI}^2[\mathbf{m}]$, and $\langle |\boldsymbol{\eta}_{\phi}[\ell]|^2 \rangle_{\ell}$ can also be characterized using (7.13) and (7.8) benefiting from the continuous model. The bit-error rate (**BER**) can be estimated for QPSK and 16-QAM for instance from (3.36). Besides, **BER** can be expressed with respect to the delivered **OSNR** (\mathbf{OSNR}_d) by assuming the overhead penalties are calculated separately, and the total received signal power equals the aggregative power of the modulated-SCs as discussed in Section 3.4.3. Thus from the analysis in Section 3.4.3, (7.19) can be rewritten with respect to the \mathbf{OSNR}_d as follows

$$\mathbf{SNR}_b[\mathbf{m}] = \frac{\left\{ \mathbf{OSNR}_d \cdot \left(\frac{B_{ref}}{BW_{nT}} \right) \cdot \delta_{pol} \right\} / m}{1 + \left\{ \mathbf{OSNR}_d \cdot \left(\frac{B_{ref}}{BW_{nT}} \right) \cdot \delta_{pol} \right\} \cdot \sigma_{ICI}^2[\mathbf{m}]} \cdot \langle |\boldsymbol{\eta}_{\phi}[\ell]|^2 \rangle_{\ell} \quad (7.20)$$

where $\mathbf{BW}_{nT} = N/T_{\mathcal{F}} = N \cdot \Delta f = N \cdot F_S/N_{\mathcal{F}}$, is the effective noise BW,

\mathbf{B}_{ref} is a reference noise BW (0.1nm or 12.5GHz at 1.55 μm), and

$$\delta_{pol} = \begin{cases} 1, & \text{in polarization multiplexing (**Pol-Mux**),} \\ 2, & \text{in single polarization transmission, and tight polarization control.} \end{cases}$$

Assuming $\mathbf{arg}\{\eta_{\phi,m}[\ell]\}$ error is corrected in every OFDM symbol.

7.2.3.2 Simulation results and calculation

In this example, a conventional QPSK-OFDM system with $\mathbf{F}_S = 10\text{GSps}$, $\mathbf{N}_{\mathcal{F}} = 256$, $\mathbf{N} = 200$, and CP is ignored is simulated and calculated assuming only the RX-LO-SCL is effective. Again the white FN is only considered with $\mathbf{H}_c[\mathbf{k}] = 1$, and all SCs are assumed to have equal powers. This special case is important since the flicker FN has a marginal effect when $\mathbf{f}_c \ll \delta f$, which is common in the recent commercially available SCL technologies, due to the low PN contribution during every OFDM symbol as discussed in Section 4.3.3.2. Besides, this special case is commonly used in RF-OFDM when PN is modelled as Wiener process, and hence it is useful for comparison purposes [119], [123]. In this simulation $\delta\mathbf{f}_{\mathbf{N}} = [0.000256, 0.00256, 0.0256, 0.0512, 0.256]$, which corresponds to $\delta\mathbf{f} = [0.01, 0.1, 1.0, 2.0, 10]\text{MHz}$, and also corresponds to the free-running variance obtained from (A2.5) in Appendix-A2 as,

$\sigma_W^2(\mathbf{T}_{\mathcal{F}}) = [1.6 \times 10^{-3}, 1.6 \times 10^{-2}, 0.161, 0.3217, 1.6]\text{rad}^2$. Total number of OFDM symbols is about 1.5Msymbols, and this large number was necessary to ensure accurate **BER** estimation at values above or equal 10^{-5} . The phase rotation (due to PN) is corrected in every OFDM symbol using an ideal technique, in which a free-of-AWGN and free of ICI pilot is conjugated and multiplied by the **FFT** O/P vector. This ideal technique is useful to demonstrate the effect of SCL's PN on the performance without considering the adopted phase-error correction technique. It hence shows the performance limits due to the SCL's PN when no pre-**FFT** PN compensation is used. The **BER** is analytically calculated using (7.9), (7.15), (7.19), and (3.36-a) as a function of \mathbf{SNR}_{bd} . The **50-th** SC is chosen in both the simulation and calculation, and the result is shown in Fig. 7.8.

From Fig. 7.8, and the previous discussion, some important notes are summarized below

- The simulation results (circular-marker) and calculation results (square marker) are not identical especially in the case of relatively large linewidth. The first justification is that the AWGN and the ICI are not the only sources of additive noise. The second justification for this discrepancy is by noting that $\sigma_{|\eta_{\phi,m}|}^2$ in (7.9) was ignored and this results in $\langle |\eta_{\phi,m}[\ell]|^2 \rangle + \sigma_{|\eta_{\phi,m}|}^2 \approx \langle |\eta_{\phi,m}[\ell]|^2 \rangle$. However, both justifications are wrong, since $\sigma_{|\eta_{\phi,m}|}^2$ (PN-to-IN term) is indeed a negligible noise term, and hence there is no other effective noise source as it has also been proven by the extensive simulation done by the author. The only possible justification for this divergence is that the ICI is essentially not a GRV.

In order to prove this assumption, two random variables (**RV**)s are generated with exactly equal variances. The first RV is obtained from the ICI simulation of the **50-th** SC with QPSK and 16-QAM mapping, while the other one is a zero-mean complex GRV. Exactly similar parameters of the previous simulation are used in this simulation with $\delta\mathbf{f} = 1\text{MHz}$, and the results are shown in Fig. 7.9. The scattering plots of both RVs are depicted in Fig. 7.9a, where the gray-colored plot is for the GRV, and the black one is for the ICI RV. In Fig. 7.9b, the calculated PDF (from simulation) of both RVs is shown (the PDF of the GRV is deleted and replaced by the analytical one for convenience). The results of Fig. 7.9, which is identical for the QPSK and 16-QAM mapping, indicates that the ICI cannot be considered as a complex GRV except when a very large number of SCs is used with a very small values of $\delta\mathbf{f}_N$.

- At relatively small $\delta\mathbf{f}_N$, the penalty is dominated by the ICI effect. It can be shown that if $\{\sigma_{\mathbf{W}}^2(\mathbf{T}_{\mathcal{F}}) = 2\pi\delta\mathbf{f}\mathbf{T}_{\mathcal{F}}\} \leq 0.1\text{rad}^2$, penalty of less than 1dB at $\mathbf{BER} = 10^{-3}$ is obtained. For instance, in the given system, $\mathbf{T}_{\mathcal{F}} = N_{\mathcal{F}}/F_S = 25.6\text{ns}$, hence $\delta\mathbf{f}|_{1\text{dB-pen}} \leq 0.6\text{MHz}$.
- As phase-error correction used here is an ideal one, then a higher penalty is expected in any other correction technique. For instance, when a noisy pilot-SC is used directly to correct phase-error in every OFDM symbol, then from (7.3), (7.4), and (7.5) the **m-th** modulated-SC and an arbitrarily chosen pilot-SC can be expressed as

$$\mathbf{y}_m[\ell] = c_m[\ell]e^{j\varphi[\ell]} + n_m[\ell], \text{ and } \mathbf{y}_p[\ell] = c_p e^{j\varphi[\ell]} + n_p[\ell].$$

where $\mathbf{n}_m[\ell]$, and $\mathbf{n}_p[\ell]$ are the AWGN terms of the \mathbf{m} -th modulated-SC and the pilot-SC respectively, which includes also the ICI, and $\boldsymbol{\varphi}[\ell]$ is the net phase-error due to the PN only. Therefore the \mathbf{m} -th O/P after direct multiplication is

$$\widetilde{\mathbf{y}}_m[\ell] = y_m[\ell] \cdot y_p^*[\ell] = c_m[\ell]c_p^* + \{c_m[\ell]n_p^*[\ell] + c_p^*n_m[\ell] + n_m[\ell]n_p^*[\ell]\}$$

Since c_p is constant (real or complex), then the useful O/P term is

$$\widetilde{\mathbf{y}}_{m,s}[\ell] = c_m[\ell]c_p^*, \text{ which is fully corrected. However, the noise term is}$$

$$\widetilde{\mathbf{y}}_{m,n}[\ell] = \{c_m[\ell]n_p^*[\ell] + c_p^*n_m[\ell] + n_m[\ell]n_p^*[\ell]\}. \text{ For simplicity, if } \langle |\mathbf{n}_m[\ell]|^2 \rangle_\ell = \langle |n_p[\ell]|^2 \rangle_\ell = \sigma_n^2, \text{ which implies that both SCs have the same ICI variance, then } \langle |\widetilde{\mathbf{y}}_{m,n}[\ell]|^2 \rangle_\ell \approx \langle |c_m[\ell]|^2 \rangle_\ell \cdot \sigma_n^2 + |c_p|^2 \cdot \sigma_n^2, \text{ and when } \langle |c_m[\ell]|^2 \rangle_\ell = |c_p|^2, \text{ then the noise power is doubled (note that noise} \times \text{noise term is ignored).}$$

Therefore 3dB more penalty is expected when direct multiplication of the pilot-conjugate is used, which is too much and unacceptable. The detected SC is simulated in four possible conditions, which are when no PN and only AWGN, no AWGN and only PN, PN and AWGN with ideal phase-error correction, and PN and AWGN with multiplication of pilot-conjugate, as shown in Fig. 7.10. In this simulation $\text{SNR}_{\text{bd}} \approx 10\text{dB}$, $\delta\mathbf{f} = 1\text{MHz}$, $\mathbf{F}_S = 10\text{GSps}$, $\mathbf{N}_{\mathcal{F}} = 256$, and 8192 OFDM symbols are used.

- When the TX-LO-SCL's PN effect is counted, then the **BER** is more degraded since the overall linewidth increases as discussed in Section 4.2.3.2.2. For instance when identical SCLs are used in the TX and RX, then the net normalized linewidth is $\delta\mathbf{f}_{\text{Neq.}} = 2\delta\mathbf{f}_N$ when only the white FN is counted.

Thus, in QPSK CO-OFDM, PN of both SCLs are required to be compensated before the **FFT** process is performed when $\delta\mathbf{f}_{\text{Neq.}} > 0.05$, or $\sigma_{\mathbf{W}}^2(\mathbf{T}_{\mathcal{F}}) < 0.3\text{rad}^2$. However, for higher constellation densities, more stringent linewidth requirements must be fulfilled.

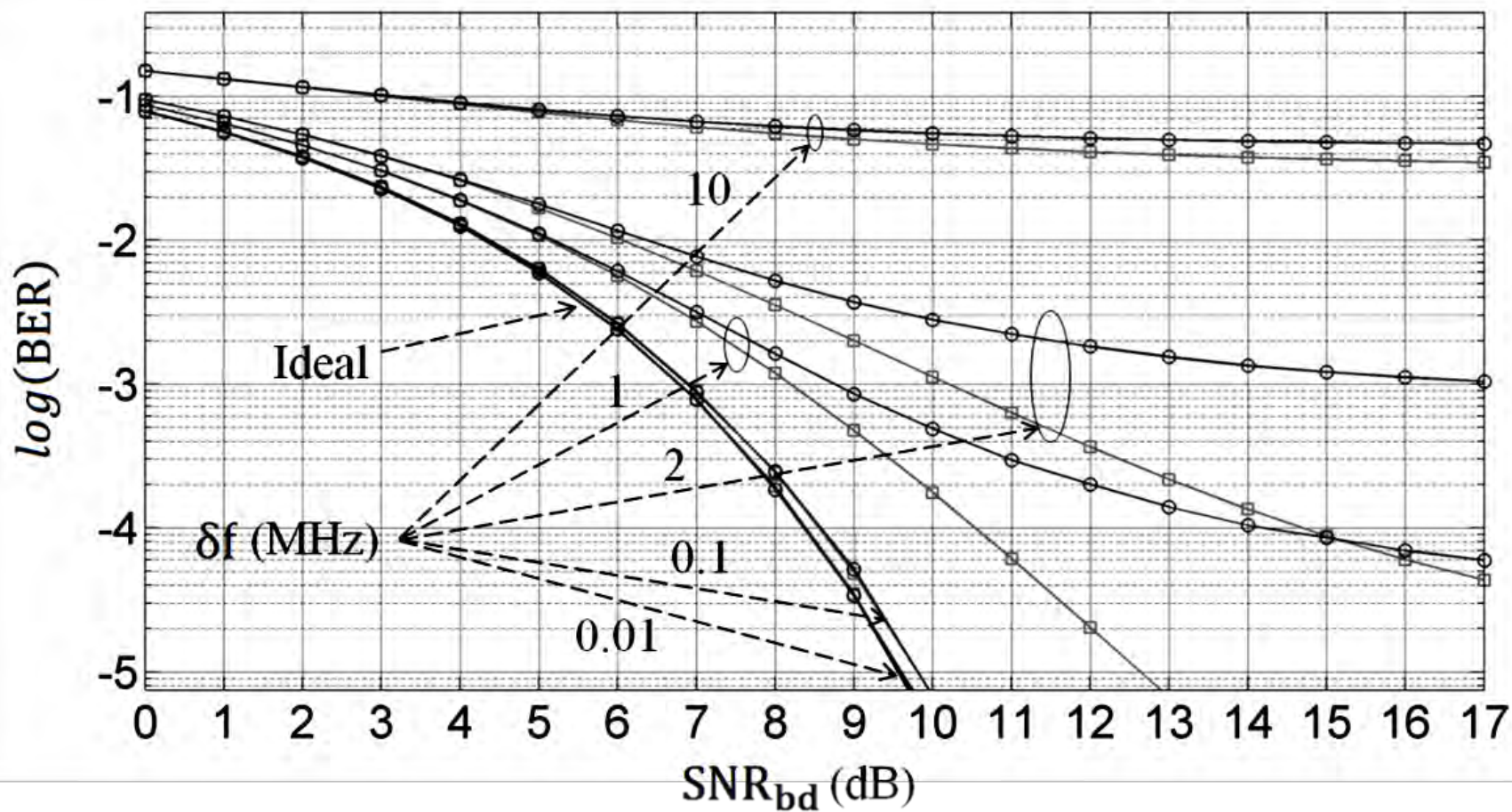


Fig. 7.8: BER as a function of the delivered SNR_b in the conventional OFDM when only PN of the RX-LO-SCL is the source of impairment. The circular-marker is for the simulated result, while the square one is for analytical calculation. Here $F_S = 10\text{GSps}$, $N_F = 256$, $N = 200$, and total number of OFDM symbols is about 1.5Msymbols.

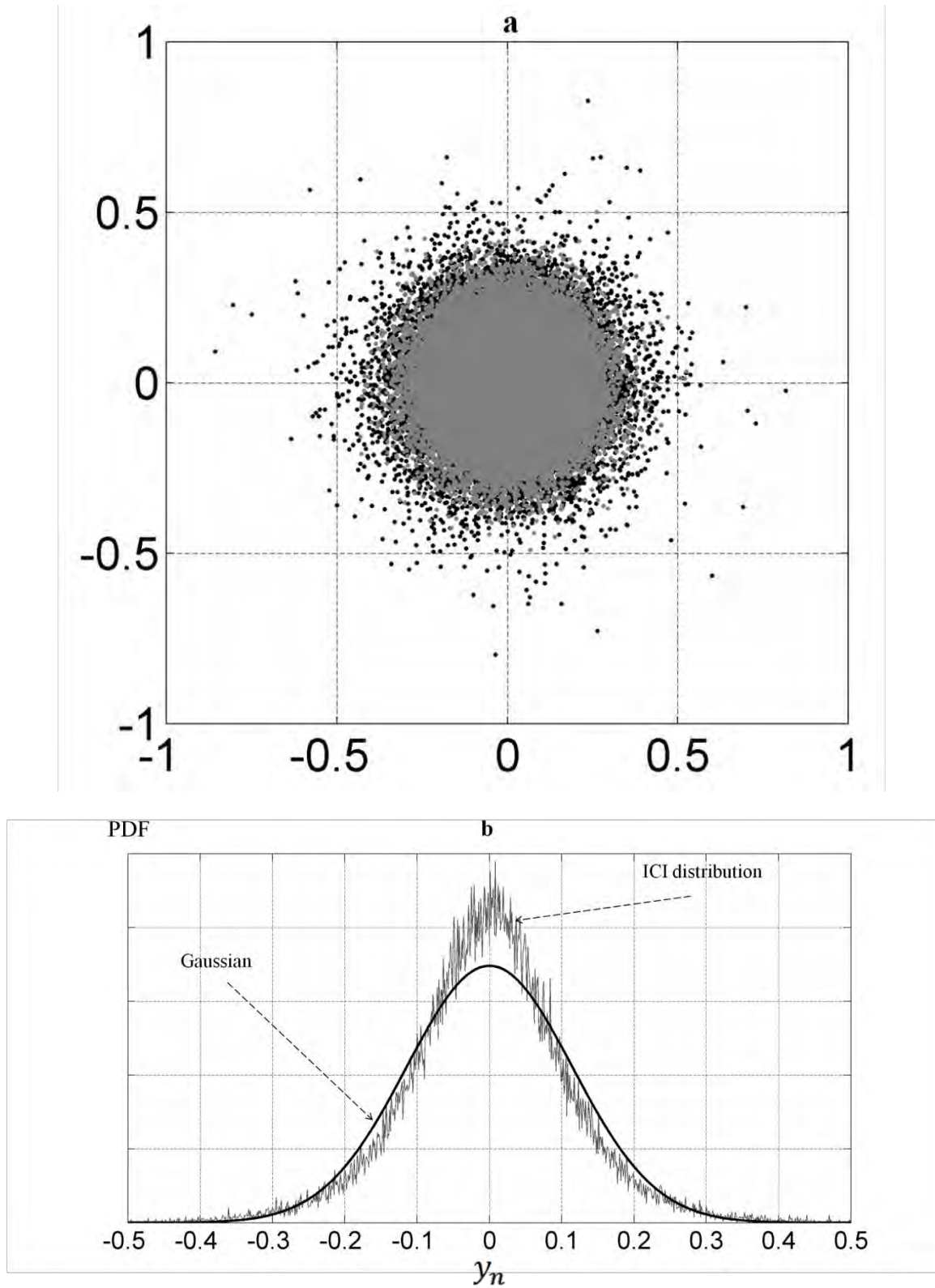


Fig. 7.9: Exact distribution of the ICI of the **50-th** SC with $F_S = 10\text{GSps}$, $N_F = 256$, $N = 200$, $\delta f = 1\text{MHz}$, and 49,182 OFDM symbols. In (a), the scattering plot of the ICI RV (black-colored) and a complex GRV (gray colored) with exactly same variance is shown. While the PDF (from simulation) of the ICI RV, and the analytical PDF of the GRV are shown in (b).

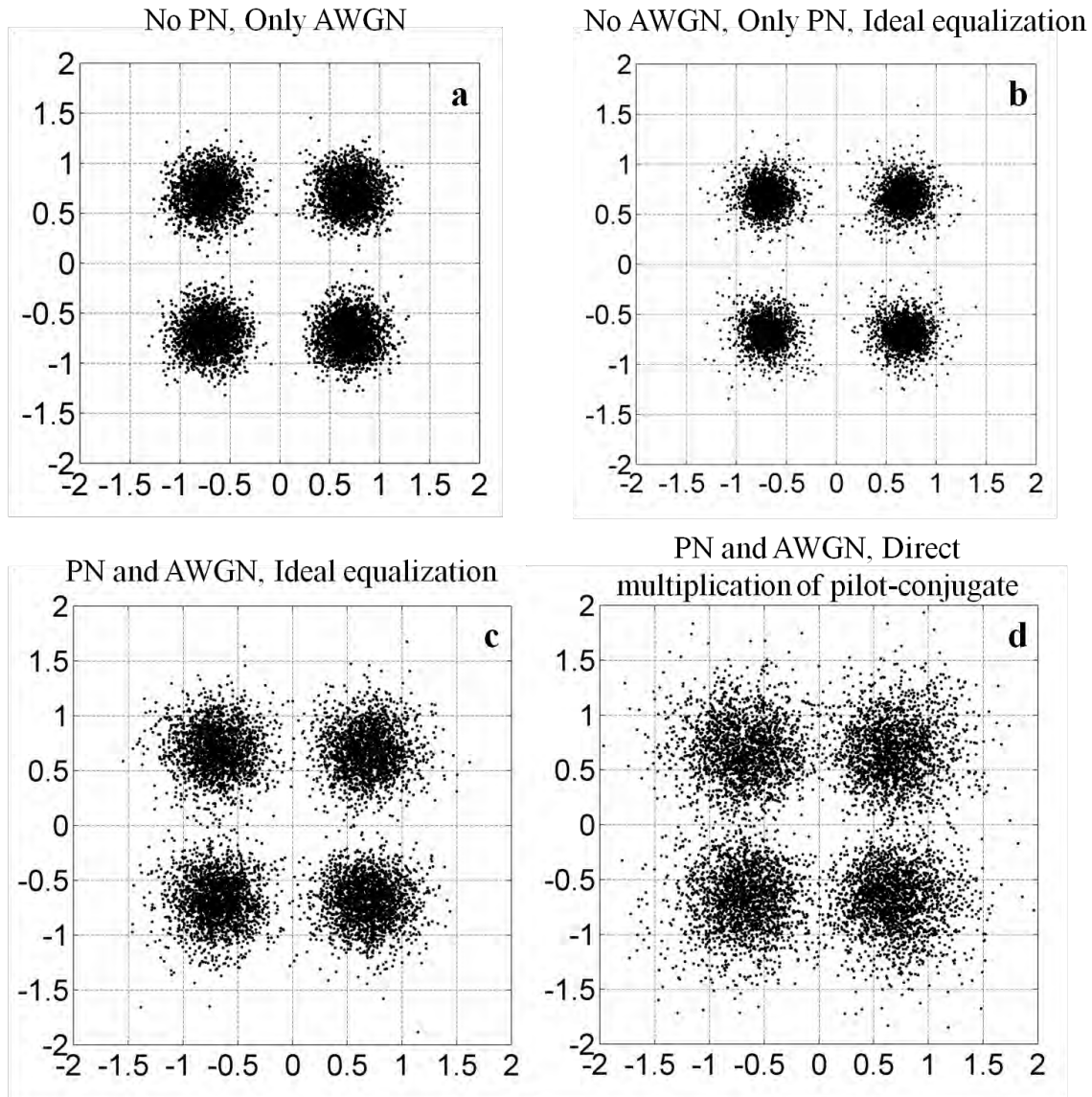


Fig. 7.10: The 50-th modulated-SC O/P in four possible conditions. No PN and only AWGN, no AWGN and only PN with an ideal phase-error correction, PN and AWGN with an ideal phase-error correction, and PN and AWGN with direct multiplication of pilot-conjugate are shown in (a), (b), (c), and (d) respectively.

Here $\text{SNR}_{\text{bd}} \approx 10\text{dB}$, $\delta f = 1\text{MHz}$, $F_S = 10\text{GSps}$, and $N_F = 256$.

7.3 OFDM system with pilot-aided feedforward loop

7.3.1 Modeling of OFDM link with PA-FFL

The functional model of an OFDM link with PA-FFL is shown in Fig. 7.11. In this model a pilot-tone is added (whether it is one of the SCs, or externally inserted via analog circuits) to the OFDM signal aiming to extract this pilot at the RX for pre-*FFT* PN compensation purposes.

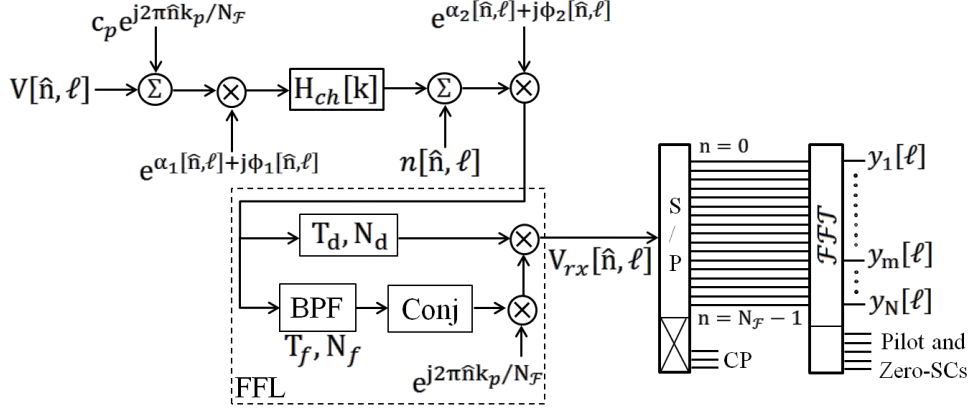


Fig. 7.11: Coherent OFDM link with functional PA-FFL model.

The pilot-tone is corrupted by SCLs' noises and experiences approximately identical channel effects just as the modulated-SCs, hence pre- \mathcal{FFT} compensation becomes useful. The main functions of the FFL block are extracting the pilot-tone using a band-pass filter (**BPF**) or a low-pass filter (**LPF**) depending on the adopted configuration [6], reversing the extracted pilot's phase, and multiplying the reversed-phase pilot by the received signal. Note that the $e^{j2\pi\hat{n}k_p/N_f}$ phasor in the FFL block is not essential, and it is introduced here to correct the modulated-signal's center-frequency. Side-pilot insertion, rather than center pilot [6], is proposed in this work to overcome pilot's extraction difficulty in CO-OFDM RX, and to halve the required frequency-gap between the modulated-SCs and the pilot tone. In the side-pilot insertion technique, a pilot-tone is inserted close to one of the modulated-signal's edges to relieve the BPF requirements (especially for a narrow-band BPF) as illustrated in Fig. 7.12. The BPF is generally characterized by its center frequency f_p , its effective BW (\mathbf{B}_C), and its group-delay (\mathbf{T}_f), which corresponds to (\mathbf{N}_f) time samples.

The chosen filter should have a flat group-delay over a BW that is much wider than \mathbf{B}_C to avoid phase distortion [124], and it is assumed for instance that it is tuned exactly at pilot's frequency. \mathbf{B}_C together with the pilot's power are design variables that will be discussed soon. A delay-line is required to equalize the time-delay introduced by the BPF's group-delay; however, for more generalization, this parameter is defined as (\mathbf{T}_d), which corresponds to (\mathbf{N}_d) time samples.

In general, the pilot-tone should be inserted as close to the OFDM's main lobe as possible to ensure as high a \mathbf{BW}_{eff} as possible as discussed in Section 3.3.1. However, the

allocated band-gap (\mathbf{BW}_G), shown in Fig. 7.12, is a design parameter that cannot be chosen arbitrarily. In the next analysis, the pilot's frequency index (\mathbf{k}_p) is assumed to be less than $\mathbf{N}_F/2$ or generated as one of the SCs for generalization purposes.

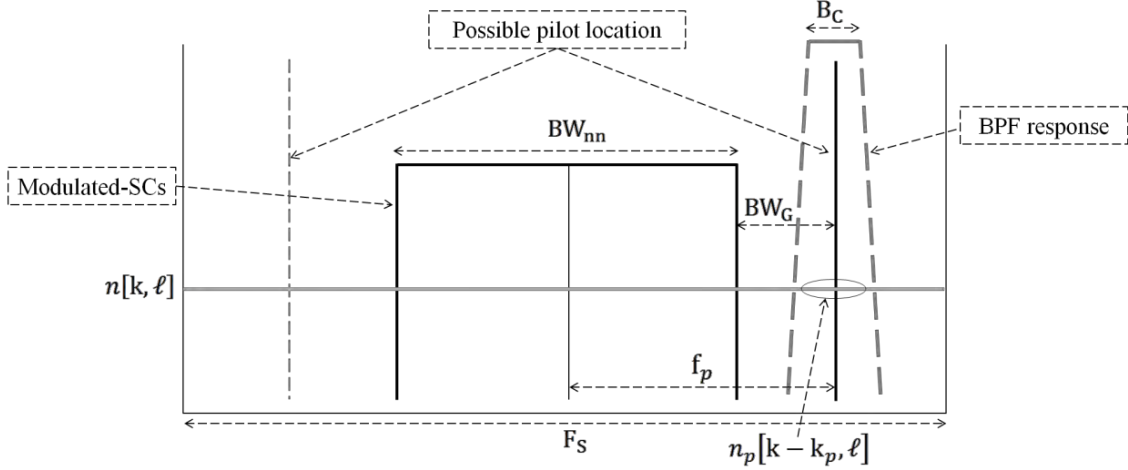


Fig. 7.12: Coherent OFDM link with functional PA-FFL model.

7.3.2 Analysis of OFDM link with PA-FFL

7.3.2.1 Preliminary Analysis

By following a similar treatment of that in Section 7.2.1, perfect synchronization is assumed, and hence the time-sample index ($\hat{\mathbf{n}}$) is identical for both TX and RX. Therefore, after analyzing the signal's route in Fig. 7.11, the received signal before the \mathcal{FFT} processor can be written as

$$\mathbf{V}_{rx}[\hat{\mathbf{n}}, \ell] = \mathbf{V}_s[\hat{\mathbf{n}}, \ell] + \mathbf{V}_p[\hat{\mathbf{n}}, \ell] + \mathbf{V}_n[\hat{\mathbf{n}}, \ell] \quad (7.21)$$

where $\mathbf{V}_s[\hat{\mathbf{n}}, \ell]$ is the modified useful-signal term, $\mathbf{V}_p[\hat{\mathbf{n}}, \ell]$ is the modified pilot-tone term, and $\mathbf{V}_n[\hat{\mathbf{n}}, \ell]$ is the modified noise term. At TX, the pilot-tone can be expressed as, $\mathbf{v}_p[\hat{\mathbf{n}}, \ell] = c_p e^{j2\pi\hat{\mathbf{n}}k_p/N_F}$, while at the RX, the BB version of the received ASE noise and side-lobes spectra that are encompassed by the FFL BPF is denoted as $\mathbf{n}_p[\hat{\mathbf{n}}, \ell]$ as shown in Fig. 7.11, and 7.12. Then the terms in (7.21) are derived and simplified using (7.1), (7.2), (7.6), and the same notation that is used in Section 7.2.1, and hence expressed as

$$\mathbf{V}_s[\hat{\mathbf{n}}, \ell] = \sum_{\mathbf{k}} c[\mathbf{k}, \ell] c_p^* \rho_{\mathbf{k}} \cdot \exp(j2\pi\hat{\mathbf{n}}\mathbf{k}/N_F) \cdot \exp(\alpha_{\mathbf{k}}[\hat{\mathbf{n}}, \ell] + j\phi_{\mathbf{k}}[\hat{\mathbf{n}}, \ell]) \quad (7.22)$$

$$V_p[\hat{n}, \ell] \approx \rho_p |c_p|^2 \cdot \exp(j2\pi\hat{n} k_p / N_F) \cdot \exp(\alpha_p[\hat{n}, \ell] + j\phi_p[\hat{n}, \ell]) \quad (7.23)$$

$$V_n[\hat{n}, \ell] \approx c_p^* n[\hat{n}, \ell] + c_p n_p^*[\hat{n}, \ell] e^{j2\pi\hat{n} k_p / N_F} + n_p^*[\hat{n}, \ell] \sum_k c[k, \ell] e^{j2\pi\hat{n} k / N_F} \quad (7.24)$$

Here the noise×noise term in (7.24) was ignored. It is more suitable to define the unknown variables by separate equations and as follows

$$\begin{aligned} \rho_k &= \exp(j\psi_d[k] - j\psi_d[k_p] - j2\pi N_d k / N_F + j2\pi N_f k_p / N_F) \\ &= \exp\left(-j \frac{2\pi}{N_F} \cdot \left\{ F_S T_o (k - k_p) + \frac{\beta_D(L) F_S^2}{2N_F} (k^2 - k_p^2) + (k N_d - k_p N_f) \right\}\right) \end{aligned} \quad (7.25-a)$$

$$\rho_p = \exp(-j2\pi N_d k_p / N_F + j2\pi N_f k_p / N_F) = \exp\left(-j \frac{2\pi k_p}{N_F} \cdot \Delta_N\right) \quad (7.25-b)$$

$$\alpha_k[\hat{n}, \ell] = \widetilde{\alpha}_1[\hat{n}, \ell] + \widetilde{\alpha}_{1F}[\hat{n} - \Delta_N - \delta_{kp}, \ell] + \alpha_2[\hat{n}, \ell] + \alpha_{2F}[\hat{n} - \Delta_N, \ell] \quad (7.25-c)$$

$$\phi_k[\hat{n}, \ell] = \widetilde{\phi}_1[\hat{n}, \ell] - \widetilde{\phi}_{1F}[\hat{n} - \Delta_N - \delta_{kp}, \ell] + \phi_2[\hat{n}, \ell] - \phi_{2F}[\hat{n} - \Delta_N, \ell] \quad (7.25-d)$$

$$\alpha_p[\hat{n}, \ell] = \widetilde{\alpha}_1[\hat{n}, \ell] + \widetilde{\alpha}_{1F}[\hat{n} - \Delta_N, \ell] + \alpha_2[\hat{n}, \ell] + \alpha_{2F}[\hat{n} - \Delta_N, \ell] \quad (7.25-e)$$

$$\phi_p[\hat{n}, \ell] = \widetilde{\phi}_1[\hat{n}, \ell] - \widetilde{\phi}_{1F}[\hat{n} - \Delta_N, \ell] + \phi_2[\hat{n}, \ell] - \phi_{2F}[\hat{n} - \Delta_N, \ell] \quad (7.25-f)$$

$$\Delta_N = N_f - N_d = F_S \cdot (T_f - T_d) \quad (7.25-g)$$

$$\delta_{kp} = \beta_D(L) \cdot \frac{F_S^2}{N_F} \cdot (k - k_p) \quad (7.25-h)$$

where the subscript “F” indicates that the filtered version of the PN and normalized IN is used (after the FFL-BPF). The preliminary notes which are obtained from (7.21)-(7.25) are as follows

- The parameter in (7.25-a) is a slow phase shift that can be corrected using a TrS, and hence it is less significant.
- The parameter in (7.25-d) is the important one since it determines the FFL block feasibility by reducing PN effect within a limited frequency band \mathbf{B}_C , which is the compensation BW.
- From (7.25-c) and (7.25-e), the IN increases in the modified OFDM signal and pilot.
- From (7.24), the noise floor is increased as a result of multiplication process.

Now by applying the \mathcal{FFT} on $\mathbf{V}_{rx}[\hat{\mathbf{n}}, \ell]$ given by (7.21), and by ignoring the pilot's term since it is not useful anymore, then the \mathbf{m} -th O/P expression is given by

$$\dot{y}_m[\ell] = \dot{y}_{m,s}[\ell] + \dot{y}_{m,ICI}[\ell] + \dot{y}_{m,n}[\ell] \quad (7.26)$$

where the $\{ \cdot \}$ sign indicates the modified O/Ps which are defined just as that in (7.3).

7.3.2.2 The modified noise term $\dot{y}_{m,n}[\ell]$

From (7.24), it is obvious that only two noise terms corrupt the useful signal, and hence the pilot's noise term will be discarded. Therefore the modified noise in (7.26) is

$$\begin{aligned} \dot{y}_{m,n}[\ell] = & \frac{c_p^*}{N_{\mathcal{F}}} \sum_{n=0}^{N_{\mathcal{F}}-1} n[n, \ell] e^{-j2\pi n m / N_{\mathcal{F}}} \\ & + \frac{1}{N_{\mathcal{F}}} \sum_{n=0}^{N_{\mathcal{F}}-1} n_p^*[n, \ell] \sum_{\mathbf{k}} c[\mathbf{k}, \ell] e^{j2\pi n(\mathbf{k}-m) / N_{\mathcal{F}}} \end{aligned} \quad (7.27)$$

where $n_p^*[n, \ell]$ is a band-limited noise consisting of the ASE noise and spectrum leakage of the OFDM signal around the pilot-tone and within \mathbf{B}_C as mentioned before. The first term in the right-hand side of (7.27) is the conventional ASE noise discussed in Section 7.2.2.1, and 2.3.6. However, the second term is introduced due to the multiplication process of the OFDM signal with a band-limited ASE noise in the FFL block. In order to analyze this cross-noise term, let \mathbf{B}_C be expressed by a number of frequency samples \mathbf{N}_C such that, $\mathbf{B}_C = N_C \cdot \Delta f = N_C \cdot F_S / N_{\mathcal{F}}$. Suppose also that $\mathbf{k} = [1, 2, \dots, N]$, and the cross-noise sample power is defined as σ_o^2 . For instance if \mathbf{N}_C is an odd number, and when all SCs have equal powers, then the following results of variance calculation of the cross-noise term are correct:

- At $\mathbf{k} = 1$, and $\mathbf{k} = N$, then number of the cross-noise samples (χ) is, $\chi = (N_C + 1)/2$.
- At $\mathbf{k} = 2$, and $\mathbf{k} = N-1$, then $\chi = 1 + (N_C + 1)/2$.
- From $\mathbf{k} = (N_C + 1)/2$ to $\mathbf{k} = (2N - N_C + 1)/2$, then $\chi = N_C$.
- Total number of SCs which have $\chi = N_C$ is $(N - N_C + 1)$.
- Total number of the cross-noise samples is $\chi_T = N \cdot N_C$.
- Total number of the effective cross-noise samples is $\chi_{\text{eff}} = N \cdot N_C - (N_C^2 - 1)/4$.
- The average number of cross-noise samples is $\chi_{\text{avg}} = N_C - \{(N_C^2 - 1)/(4N)\}$.

Therefore if the frequency index is written in the adopted way again, or

$\mathbf{k} = [-N/2, -N/2 + 1, \dots, -1, 1, 2, \dots, N/2]$, then the cross-noise PSD expressed by χ and as a function of \mathbf{k} can be written as

$$\chi[\mathbf{k}] = \begin{cases} N_C & \dots k_i = [(N_C - N - 1)/2, (N - N_C - 1)/2] \\ k + (N_C + N + 1)/2 & \dots k_i = [-N/2, (N_C - N - 3)/2] \\ -k + (N_C + N + 1)/2 & \dots k_i = [(N - N_C + 1)/2, N/2] \end{cases} \quad (7.28)$$

where \mathbf{k}_i represents an interval of \mathbf{k} values. Therefore the cross-noise per SC is calculated as $\{\chi[\mathbf{k}] \cdot \sigma_o^2\}$. From (3.39), and (7.27), the aggregative cross-noise variance is

$$\sigma_{nXT}^2 = \left(\frac{N_{rx}|B_{ref}}{\delta_{pol} \cdot B_{ref}} \right) \left(\frac{F_S}{N_{\mathcal{F}}} \right) \cdot N_C \cdot P_s = \sigma_n^2 \cdot N_C \cdot P_s$$

where $N_{rx}|B_{ref}$ is the received accumulated ASE noise power measured within B_{ref} , and P_s is the total OFDM signal's power. Therefore

$$\sigma_o^2 = \frac{\sigma_{nXT}^2}{N \cdot N_C} = \sigma_n^2 \cdot \frac{P_s}{N} = \sigma_n^2 \cdot \langle |c[\mathbf{k}, \ell]|^2 \rangle_{\ell}$$

Therefore this noise has an uneven distribution over the OFDM SCs, and hence noise per SC depends on \mathbf{k} . The minimum cross-noise variance per SC is at the first and last SCs (signal's edges), which is equal to

$$\sigma_{nXmin}^2 = \sigma_o^2 \cdot \chi[k = \pm N/2] = \sigma_o^2 \cdot (N_C + 1)/2,$$

while the maximum is at the middle $(N - N_C + 1)$ SCs with variance per SC of

$$\sigma_{nXmax}^2 = \sigma_o^2 \cdot N_C, \text{ whereas the average cross-noise variance per SC is}$$

$$\sigma_{nXave}^2 = \sigma_o^2 \cdot \left\{ N_C - \frac{N_C^2 - 1}{4N} \right\} = \sigma_n^2 \cdot \frac{P_s}{N} \cdot \left\{ N_C - \frac{N_C^2 - 1}{4N} \right\} \quad (7.29)$$

The cross-noise normalized PSD is simulated separately in the following example with $F_S = 10\text{GSps}$, $N_{\mathcal{F}} = 256$, $N = 100$, and $N_C = [11, 101]$ as shown in Fig. 7.13. Note that maximum $\{\sigma_{nXmax}^2/\sigma_{nXmin}^2 \approx 2\}$ or 3-dB difference. By assuming all the SCs have equal powers, no inside-band zero-SCs (except the DC-SC as discussed in Section 3.3.2.1), the spectrum leakage of the OFDM signal is ignored, and the FFL-BPF is an ideal filter, then from (7.27), and (7.28), the modified noise variance per SC is given by

$$\dot{\sigma}_n^2[m] \approx \sigma_n^2 \cdot \left\{ P_p + \frac{P_s}{N} \cdot \chi[m] \right\} = \left(\frac{N_{rx}|B_{ref}}{\delta_{pol} \cdot B_{ref}} \right) \left(\frac{F_S}{N_{\mathcal{F}}} \right) \cdot \left\{ P_p + \frac{P_s}{N} \cdot \chi[m] \right\} \quad (7.30)$$

where P_p the pilot's power. While from (7.29), the average noise variance per SC is

$$\dot{\sigma}_n^2 \approx \sigma_n^2 \cdot \left\{ P_p + \frac{P_s}{N} \cdot \chi_{ave} \right\} = \sigma_n^2 \cdot \left\{ P_p + \frac{P_s}{N} \cdot \left(N_C - \frac{N_C^2 - 1}{4N} \right) \right\} \quad (7.31)$$

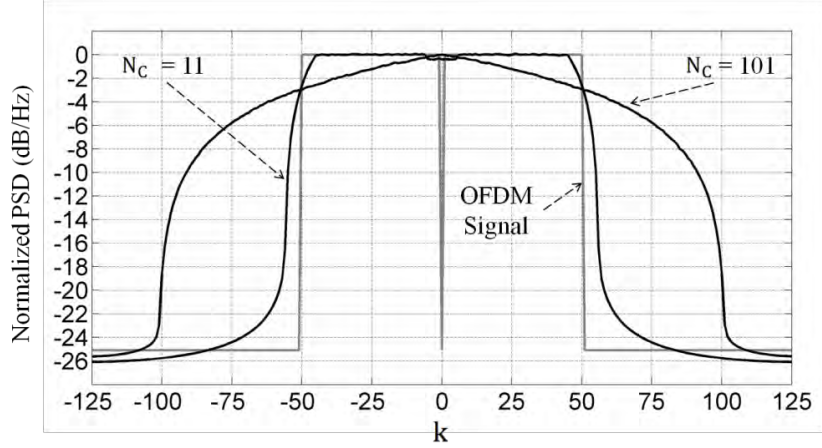


Fig. 7.13: Normalized cross-noise PSD (power per frequency sample) for two values of FFL-BPF expressed in number of frequency samples N_C .

7.3.2.3 The modified useful-signal term $\dot{y}_{m,s}[\ell]$

The modified useful term in (7.26) is obtained from the \mathcal{FFT} of (7.22) if $\mathbf{k} = \mathbf{m}$, hence

$$\dot{y}_{m,s}[\ell] \cong c[m, \ell] c_p^* \rho_m \cdot \mathcal{Z}_m[\ell] \quad (7.32)$$

$$\text{where } \mathcal{Z}_m[\ell] = \sum_{n=0}^{N_F-1} \exp(\alpha_m[n, \ell] + j\phi_m[n, \ell]) / N_F .$$

All the unknown parameters are calculated from (7.25-a), (7.25-c), and (7.25-d). Here $\mathcal{Z}_m[\ell]$ explains the usefulness of employing PA-FFL in the CO-OFDM systems, since it shows the elimination of high level low-frequency components of PN. From (7.25-d), (7.34), assuming an ideal FFL-BPF is used, the IN term is ignored, and since the Gaussian FN remains Gaussian FN when the FFL is employed [38], then

$$\Phi_m[\mathbf{n}, \ell] = \widetilde{\Phi}_1[\mathbf{n}, \ell] - \widetilde{\Phi}_{1F}[\mathbf{n} - \Delta_N - \delta_{mp}, \ell] + \phi_2[\mathbf{n}, \ell] - \phi_{2F}[\mathbf{n} - \Delta_N, \ell],$$

and hence when $\Delta_N = 0$ for instance, then

$$\begin{aligned} \mathcal{Z}_m[\ell] &= \sum_{n=0}^{N_F-1} \frac{\exp(j\{\widetilde{\Phi}_1[\mathbf{n}, \ell] - \widetilde{\Phi}_{1F}[\mathbf{n} - \delta_{mp}, \ell]\} + j\{\phi_2[\mathbf{n}, \ell] - \phi_{2F}[\mathbf{n}, \ell]\})}{N_F} \\ &\approx 1 + \frac{j}{N_F} \sum_{n=0}^{N_F-1} \left\{ \sum_{\mathbf{r}} \{\widetilde{\Phi}_1[\mathbf{r}, \ell] + \phi_2[\mathbf{r}, \ell]\} e^{-j2\pi \frac{\mathbf{r}}{N_F} n} \right. \\ &\quad \left. + \sum_{k=-N_C/2}^{N_C/2-1} j2\widetilde{\Phi}_1[k, \ell] e^{-j2\pi \frac{k}{N_F} (n - \delta_{mp}/2)} \sin\left(\pi \frac{k}{N_F} \delta_{mp}\right) \right\} \end{aligned} \quad (7.33)$$

where $\mathbf{r} = [-N_F/2, -N_F/2 + 1, \dots, -(1 + N_C/2), N_C/2, N_C/2 + 1, \dots, N_F/2 - 1]$.

This approximation of the exponential function is valid here unlike in Section 7.2.2.2, since the differential phase, which has typically a zero-mean and small variance, is

considered and not the absolute one. From (7.33) and referring to the domain of \mathbf{r} , the powerful frequency components of the PN (the low frequency components) vanish; however, it appears again when the $\delta_{mp} \neq 0$, or when the differential time-delay between the pilot-tone and the SCs is not zero. However, the re-emerging of these components is less significant as long as $\{\delta f \cdot \delta_{mp}/F_S\} \ll 1$, as it will be discussed in Section 7.3.7.2. Therefore the RX-LO-SCL effect is merely due to the weak high frequency components of the PN, which is similar to the first part of the TX-LO-SCL effect. Hence the compensated $\mathbf{CPE}[\ell]$ can be defined only for these parts by its mean value over ℓ since no attempt is made to equalize it on symbol-by-symbol bases after the \mathcal{FFT} is performed as in conventional OFDM. However, the second part of the TX-LO-SCL effect is due to the differential PN of the powerful components, which is proportional to the dispersive differential delay δ_{mp} . This part is one of the weak points of the PA-FFL especially when long-haul and ultra-wide BW (**UWB**) is considered. Here δ_{mp} changes depending on the frequency index of the modulated-SC \mathbf{m} , and hence from (7.25-h), as high as $|\mathbf{m} - \mathbf{k}_p|$ is, as more phase rotation is expected.

7.3.2.4 The modified ICI term $\dot{y}_{m,ICI}[\ell]$

The modified ICI term in (7.26) is obtained from the \mathcal{FFT} of (7.22) if $\mathbf{k} \neq \mathbf{m}$, and hence

$$\dot{y}_{m,ICI}[\ell] = \frac{1}{N_{\mathcal{F}}} \sum_{n=0}^{N_{\mathcal{F}}-1} \sum_{k \neq m} c[k, \ell] c_p^* \rho_k \cdot \exp(j2\pi n(k-m)/N_{\mathcal{F}}) \cdot \exp(\alpha_k[n, \ell] + j\phi_k[n, \ell]) \quad (7.34)$$

Linearization of $\phi_k[\mathbf{n}, \ell]$ is possible here due to the PN subtraction with the low long-term variance or $\sqrt{\langle |\phi_k[\mathbf{n}, \ell]|^2 \rangle_{\ell}} \ll 1$ rad. Therefore (7.34) becomes,

$$\dot{y}_{m,ICI}[\ell] \approx \frac{1}{N_{\mathcal{F}}} \sum_{n=0}^{N_{\mathcal{F}}-1} \sum_{k \neq m} c[k, \ell] c_p^* \rho_k \cdot e^{j2\pi n(k-m)/N_{\mathcal{F}}} \cdot \{1 + \alpha_k[n, \ell] + j\phi_k[n, \ell]\}$$

Hence $\dot{\sigma}_{ICI}^2[\mathbf{m}] = \langle \dot{y}_{m,ICI}[\ell] \cdot \dot{y}_{m,ICI}^*[\ell] \rangle_{\ell}$ is calculated in much easier way if all SCs have equal powers and as follows

$$\dot{\sigma}_{ICI}^2[\mathbf{m}] \approx \frac{|c_p|^2}{N_{\mathcal{F}}^2} \left\langle \sum_{n1=0}^{N_{\mathcal{F}}-1} \sum_{n2=0}^{N_{\mathcal{F}}-1} \sum_{k \neq m} |c[k, \ell]|^2 e^{j2\pi(k-m)(n1-n2)/N_{\mathcal{F}}} \cdot \{1 + \alpha_k[n1, \ell] + j\phi_k[n1, \ell]\} \cdot \{1 + \alpha_k[n2, \ell] - j\phi_k[n2, \ell]\} \right\rangle_{\ell}$$

Hence after simplifications, it can be written as

$$\sigma_{ICI}^2[m] \approx P_p P_{SC} \sum_{k \neq m} \{ \check{S}_\alpha[k, m] + \check{S}_\phi[k, m] + \check{S}_x[k, m] \} \quad (7.35)$$

$$\text{where } \check{S}_\alpha[\mathbf{k}, \mathbf{m}] = \frac{1}{N_{\mathcal{F}}} \left\langle \sum_{d=0}^{N_{\mathcal{F}}-1} \left\{ \left(\sum_{n=0}^{N_{\mathcal{F}}-1} \frac{\alpha_k[n, \ell] \alpha_k^*[n+d, \ell]}{N_{\mathcal{F}}} \right) e^{j2\pi \cdot k \cdot d / N_{\mathcal{F}}} \right\} e^{-j2\pi \cdot m \cdot d / N_{\mathcal{F}}} \right\rangle ,$$

$$\check{S}_\alpha[\mathbf{k}, \mathbf{m}] = \frac{1}{N_{\mathcal{F}}} \left\langle \sum_{d=0}^{N_{\mathcal{F}}-1} \left\{ \left(\sum_{n=0}^{N_{\mathcal{F}}-1} \frac{\phi_k[n, \ell] \phi_k^*[n+d, \ell]}{N_{\mathcal{F}}} \right) e^{j2\pi \cdot k \cdot d / N_{\mathcal{F}}} \right\} e^{-j2\pi \cdot m \cdot d / N_{\mathcal{F}}} \right\rangle , \text{ and}$$

$$\check{S}_x[\mathbf{k}, \mathbf{m}] = \frac{1}{N_{\mathcal{F}}} \left\langle \sum_{d=0}^{N_{\mathcal{F}}-1} \left\{ \left(\sum_{n=0}^{N_{\mathcal{F}}-1} \frac{j\phi_k[n, \ell] \alpha_k^*[n+d, \ell] - j\alpha_k[n, \ell] \phi_k^*[n+d, \ell]}{N_{\mathcal{F}}} \right) \cdot e^{j2\pi \cdot k \cdot d / N_{\mathcal{F}}} \right\} e^{-j2\pi \cdot m \cdot d / N_{\mathcal{F}}} \right\rangle$$

Here the terms between $\{ \}$ brackets are the short-time auto-correlation function (ACF) of noise terms multiplied by a frequency shifting phasor. Thus each $\check{S}[\mathbf{k}, \mathbf{m}]$ represents the ℓ -averaged \mathcal{FFT} of a short-time and frequency-shifted-ACF of the noise term, which according to Wiener-Khinchin theorem, corresponds to the power per frequency sample.

7.3.3 Effect of time-distorted SCL noise on an individual SC in PA-FFL

7.3.3.1 Long-term phase error

In the following simulations, the effect of TX-LO-SCL PN in PA-FFL OFDM system is examined. The effect of all additive noises has to be removed, and in order to do so, the ASE noise is cancelled, the pilot-tone is assumed to occupy the other orthogonal polarization to overcome the OFDM's spectrum leakage, and only one modulated-SC and one or two pilot-SCs are used per OFDM signal to ensure negligible ICI. The simulation parameters of the OFDM signal are $\mathbf{F}_S = 25\text{GSps}$, $N_{\mathcal{F}} = 256$, $\mathbf{N} = 200$, and CP is ignored. The DAC output is up-sampled to 200GSps to approach the continuous-time conditions, and then similar blocks of Fig. 7.11 are applied, with $\mathbf{L} \approx 205\text{km}$, only the White FN is counted with $\delta\mathbf{f}_N \approx [0.1, 0.4]$, and $\beta_C = N_C/N = [0.0512, 0.9]$. The pilot-tone's allocated index is $\mathbf{k}_p = -100$, and three OFDM signals are tested. The 1st one consists of one modulated-SC with $\mathbf{m} = -100$, and one pilot-SC at $\mathbf{k} = +100$, in the 2nd one $\mathbf{m} = +100$, and $\mathbf{k} = -100$, while in the 3rd one $\mathbf{m} = +1$, and two pilot-SCs are used

with $\mathbf{k1} = +100$, and $\mathbf{k2} = -100$. The simulation results are arranged such that the 1^{st} , 2^{nd} , and 3^{rd} columns correspond to the 1^{st} , 2^{nd} , and 3^{rd} OFDM settings respectively, while the 1^{st} , 2^{nd} , and 3^{rd} rows correspond to the PSDs before the TX-LO-SCL is mixed with the signal, after the FFL block (denoted as RX) with $\beta_{\mathbf{C}} = 0.9$, and $\delta\mathbf{f}_{\mathbf{N}} \approx 0.1$, and after the FFL block with $\beta_{\mathbf{C}} = 0.0512$, and $\delta\mathbf{f}_{\mathbf{N}} \approx 0.1$ respectively, as shown in Fig. 7.14. In the 2^{nd} row (which is the case when very large $B_{\mathbf{C}}$ is used), the PSD of the pilot-SCs (not the pilot-tone) exhibits perfect agreement with the beat-note and self-beat PSD derived in Chapter 6. For the 2^{nd} setting, the differential delay due to channel dispersion and the frequency shift between the pilot-tone and the pilot-SC is $\delta\mathbf{k}_{\mathbf{p}} = 0$ -samples, and $\Delta\mathbf{f}_{\mathbf{sh}} = 0$ Hz, and hence only the self-beat PSD within $B_{\mathbf{C}}$ is active, which is similar to detecting the SCL dispersive field by a photodiode.

While in 1^{st} setting, $\delta\mathbf{k}_{\mathbf{p}} = 14$ -samples $\equiv 0.56$ ns, $\Delta\mathbf{f}_{\mathbf{sh}} \approx 19.5$ GHz, and hence the beat-note PSD is produced, which is similar to detecting the SCL dispersive field using the delayed-self heterodyne (**DSH**) test. While in the 3^{rd} row (band-limited compensation), PSD of the pilot-SCs matches the results of Chapter 6 only within the compensation BW, whereas the rest of the spectrum (the tails) follows the same Lorentzian line-shape of the TX-LO-SCL (since only the white FN is considered here).

The modulated-SCs after the \mathcal{FFT} is performed of the three simulated settings are also examined to investigate the feasibility of the FFL in the CO-OFDM systems using 1024 OFDM symbols. Basically the 1^{st} setting shows a negligible phase rotation for both values of linewidth, while in the 3^{rd} setting, phase rotation which is proportional to $\delta\mathbf{f}_{\mathbf{N}}$ is obvious; however, maximum phase rotation occurs in the 2^{nd} setting since $\delta\mathbf{m}_{\mathbf{p}}$ is maximum, as shown in Fig. 7.15. In the large $\delta\mathbf{f}_{\mathbf{N}}$ value with limited $\beta_{\mathbf{C}}$, the mean amplitude is slightly less than unity, and an IN term is induced due to PN-to-IN due to filtering (averaging) as discussed in Section 7.2.2.2.1, and shown clearly for the 2^{nd} setting in Fig. 7.15. However, the most important feature here is that the average phase is constant for a large number of OFDM symbols due to the white nature of the compensated PN. Thus in long-haul and UWB CO-OFDM links with commercially available SCLs, the SCs which have large $|\mathbf{m} - \mathbf{k}_{\mathbf{p}}|$ values are experienced higher residual PN variances than those having small $|\mathbf{m} - \mathbf{k}_{\mathbf{p}}|$ values.

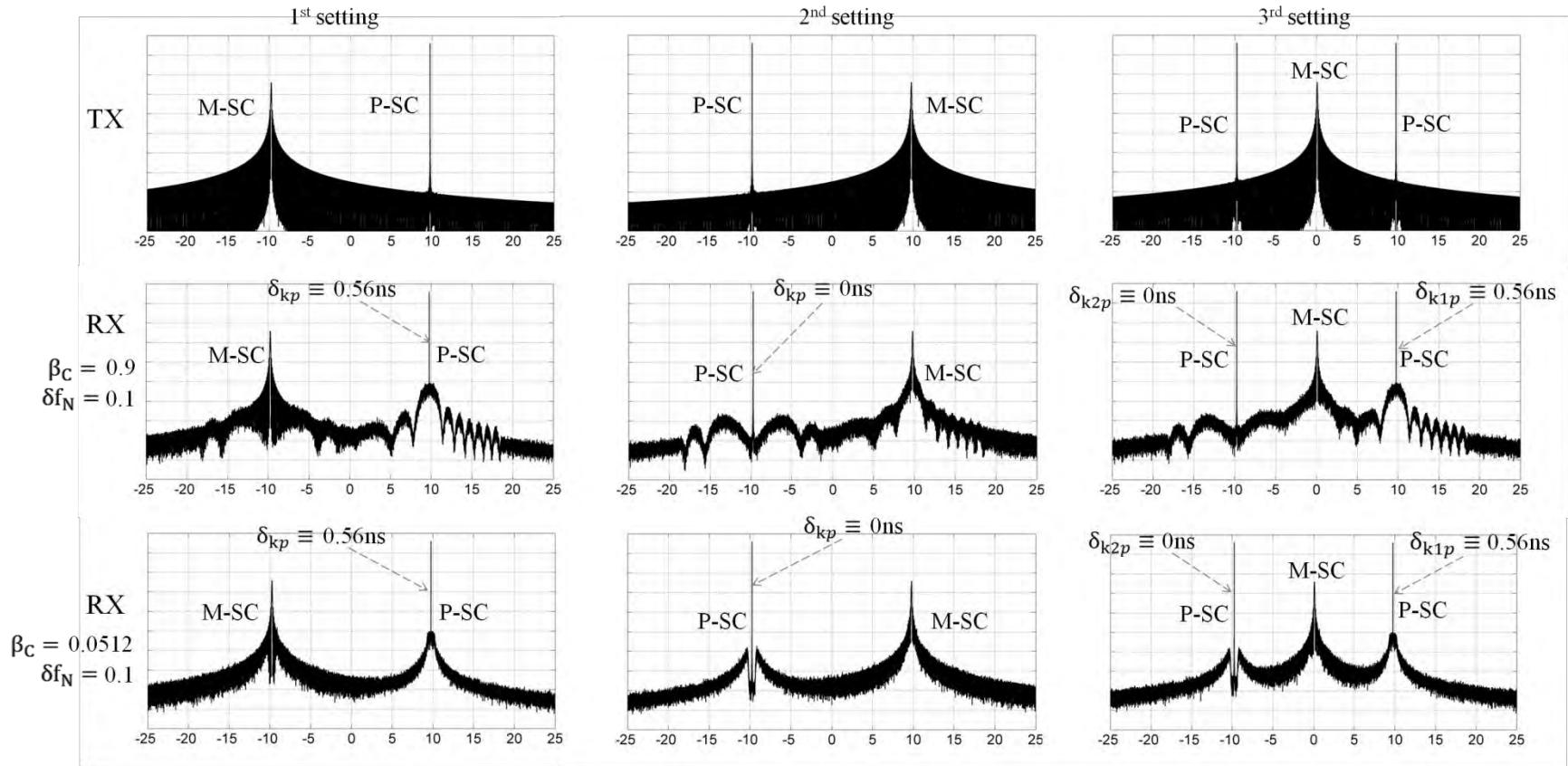


Fig. 7.14: Simulated PSDs at TX side (before mixing with TX-LO-SCL) in the first row, and after the FFL is performed (at RX and before the \mathcal{FFT} is applied which is denoted as RX) in the second and third rows of a three OFDM settings with parameters given in the text. The horizontal axes of all are the frequency axes in (GHz), while the vertical axes for all are in dB/Hz with 10dB/step. Here **M-SC** and **P-SC** stand for modulated-SC and pilot-SC (not the pilot-tone) respectively. The pilot-tone spectrum is at $\mathbf{k}_p = -100$ (≈ -10 GHz) and not shown for all settings.

Therefore either the constellation is chosen in a dynamic way, such that the worst affected SCs have a constellation with a better PN tolerance, or post- \mathcal{FFT} PN-correction is also employed to correct the residual PN error from symbol-to-symbol.

This example was chosen to demonstrate effect of the induced PN term due to the differential time-delay between the side pilot-tone and the SCs in an UWB CO-OFDM case, where a high frequency shift between the pilot and the SCs is assumed. The minimal possible value of the side pilot-tone's frequency index is $\mathbf{k}_p = |100|$, which can only be implemented by simulation since no guard-band is allocated. Simulation results agree with the derivations of the exact beat-note PSD presented in Chapter 6.

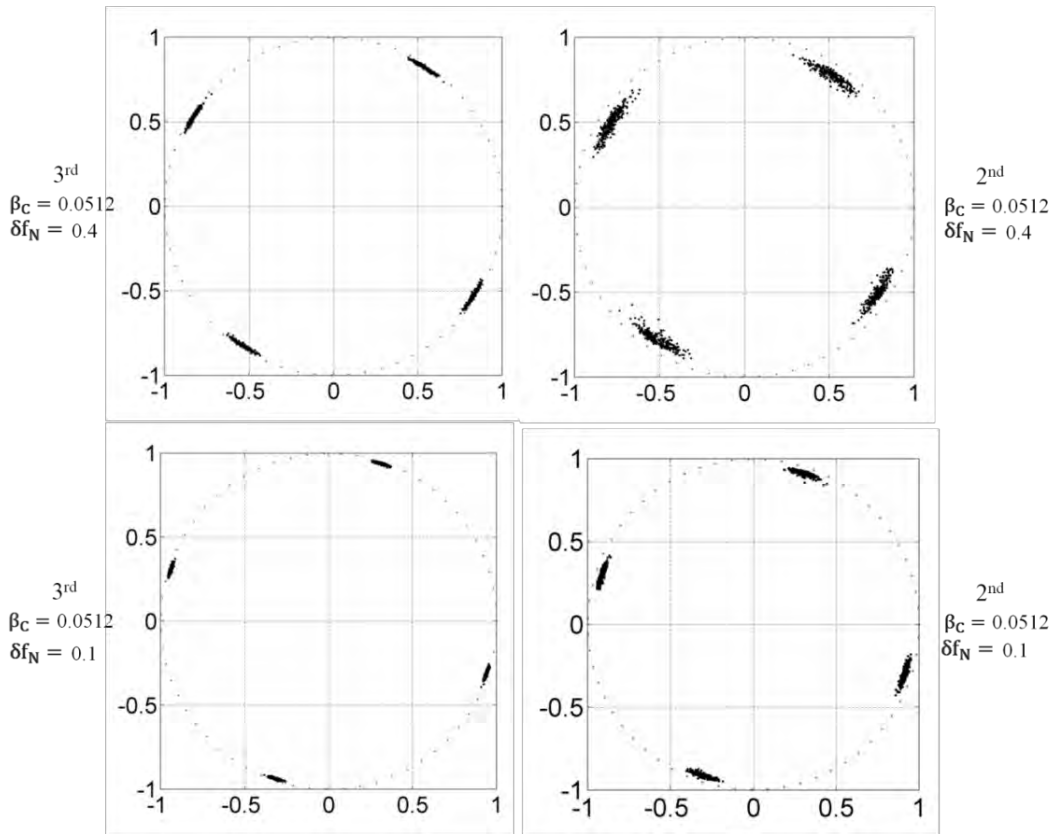


Fig. 7.15: Detected modulated-SCs (after the \mathcal{FFT} is applied) in the 2nd and 3rd settings showing the effect of differential time-delay due to CD between the pilot-tone and the modulated-SCs δ_{mp} and normalized linewidth δf_N on the residual phase error. In the 3rd setting, $\delta_{mp} \approx 7\text{samples} \equiv 283\text{ps}$, while in 2nd one $\delta_{mp} \approx 14\text{samples} \equiv 560\text{ps}$. Assuming only the white FN is counted. (The details are given in the text).

7.3.3.2 Analysis of spectral components of a pilot-SC in PA-FFL

7.3.3.2.1 BPF selection

The first condition of FFL BPF selection was to have a flat group-delay over a BW which is much higher than \mathbf{B}_C to avoid phase distortion. However, when analog filters are used

in the implementation, the maximally-flat group delay filters (Bessel filter) have usually poor steepness, and hence narrowband filtering becomes difficult [75].

In the following simulation, $F_S = 10\text{GHz}$, $B_C = 1.5\text{GHz}$ (corresponds to the 3-dB BW), assuming only the white FN is active with total linewidth of $\delta f = 10\text{MHz}$, the resolution BW is $\text{RBW} \approx 1.22\text{MHz}$, and four BPF prototypes are used as shown in Fig. 7.16. The 1st filter is approximately an ideal BPF, which is simulated using Hamming window with order of 4096, the 2nd one is 9th order Butterworth BPF, the 3rd one is 9th order Chebyshev type II BPF, while the 4th one is 9th order Bessel (Gaussian) BPF as shown in Fig.7.16a, 7.16b, 7.16c, and 7.16d respectively. This simulation shows that the Butterworth BPF is the best practical candidate for the FFL BPF selection, since its high steepness and marginal phase distortion within the passband result high PN rejection.

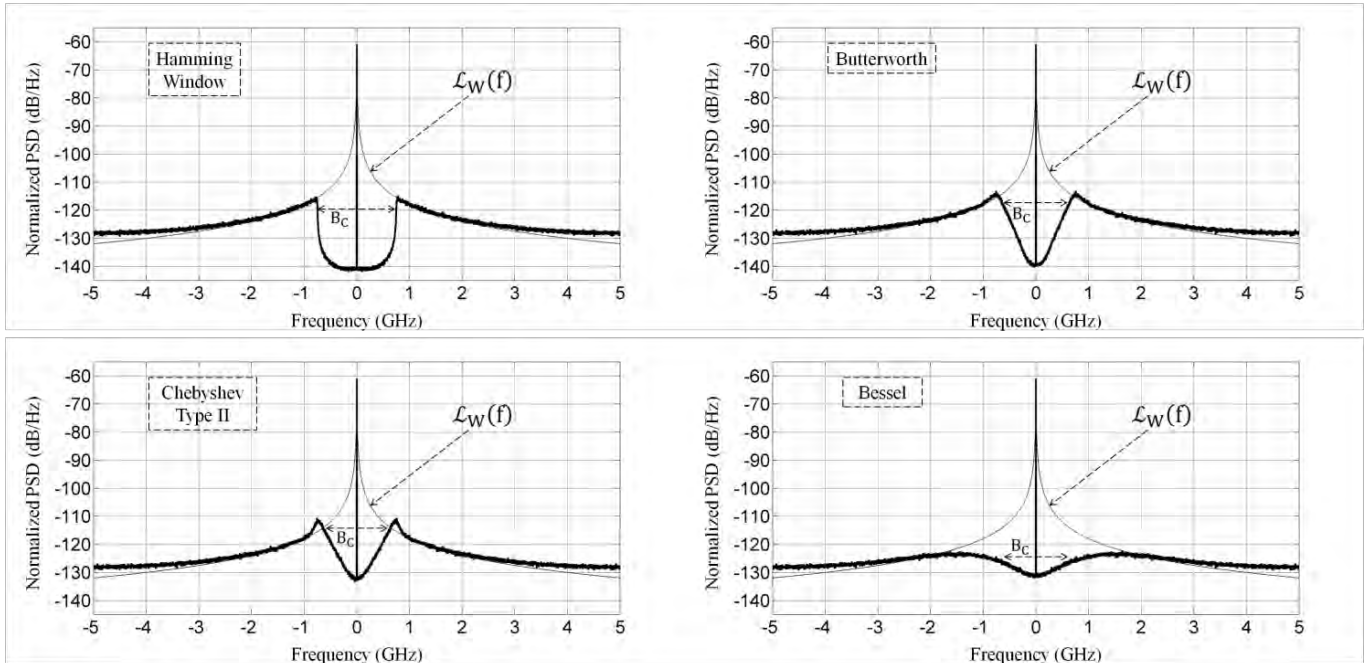


Fig. 7.16: Different BPF prototypes that can be used for PN compensation in the FFL block with $B_C = 1.5\text{GHz}$. The filter's prototypes are Hamming window with order of 4096 in (a), 9th order Butterworth BPF in (b), 9th order Chebyshev type II BPF in (c), and 9th order Bessel BPF in (d). Here $F_S = 10\text{GHz}$, $\delta f = 10\text{MHz}$, $\text{RBW} \approx 1.22\text{MHz}$, and $\mathcal{L}_W(f)$ is the SCLs' Lorentzian line-shape (calculated).

7.3.3.2.2 Effect of Δ_N when only the white FN is in effect

In the following simulation, effect of Δ_N or $\Delta T = T_f - T_d$ is examined using a Hamming window with order of 4096. The simulation parameters are $F_S = 10\text{GHz}$, $B_C = 1.5\text{GHz}$, $\delta f = 10\text{MHz}$, $\text{RBW} \approx 1.22\text{MHz}$, and the normalized ΔT of $\delta f \cdot \Delta T = [0, 0.001, 0.01, 0.1]$. As expected the beat-note PSD with differential time delay emerges only within B_C ,

while the Lorentzian line-shape still exists outside \mathbf{B}_C as shown in Fig. 7.17. This means that when the time delay of the time-equalization delay-line is not exactly equal the BPF's mean group delay (which results $\Delta\mathbf{T}$), then the SCs will be corrupted by a band-limited differential PN term that is fully characterized by the normalized version of (4.44). This effect causes an increase in the ICI as well as a long term differential PN variance that is common to all of the SCs.

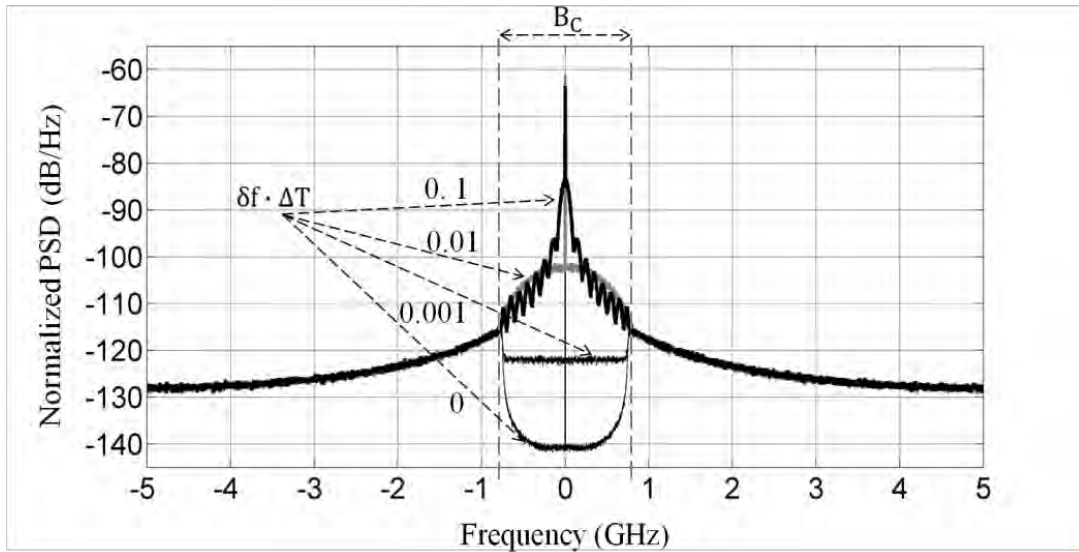


Fig. 7.17: Effect of $\Delta\mathbf{T}$ on the pre-ADC PSD of an arbitrary pilot-SC. The $\Delta\mathbf{T}$ is normalized with respect to the effective linewidth as $\delta\mathbf{f} \cdot \Delta\mathbf{T}$ with $\delta\mathbf{f} \cdot \Delta\mathbf{T} = [0, 0.001, 0.01, 0.1]$. Here $\mathbf{F}_S = 10\text{GHz}$, $\delta\mathbf{f} = 10\text{MHz}$, $\mathbf{RBW} \approx 1.22\text{MHz}$, and $\mathbf{B}_C = 1.5\text{GHz}$.

7.3.3.2.3 Effect of CD when only the white FN is effective

In the following simulation, effect of the CD is examined with pilot-tone to pilot-SC frequency separation of $\Delta\mathbf{f}_{sh} = |m - k_p| \cdot \Delta\mathbf{f} = 10\text{GHz}$, $\mathbf{F}_S = 200\text{GHz}$, $\delta\mathbf{f} = 10\text{MHz}$, $\mathbf{RBW} \approx 6.1\text{MHz}$, $\mathbf{L} = [0, 1, 4, 8] \times 68.5\text{km}$, $\beta_D(\mathbf{L}) \approx (1.4 \times 10^{-22}) \cdot \mathbf{L}$, $\mathbf{B}_C = 10\text{GHz}$ and Hamming window with order of 4096 is used as the FFL BPF as shown in Fig. 7.18.

The produced PSD consists of three parts, the 1st one is within \mathbf{B}_C , which is identical to the beat-note term of the DSH test of a dispersive SCL's field discussed in Chapter 6, the 2nd part is outside \mathbf{B}_C , which is merely the SCL's free-running PSD tails, while the 3rd part is a delta function. CD effect causes also an increase of the ICI and long term differential PN variance that is not common to all SC but depends on $|m - k_p|$.

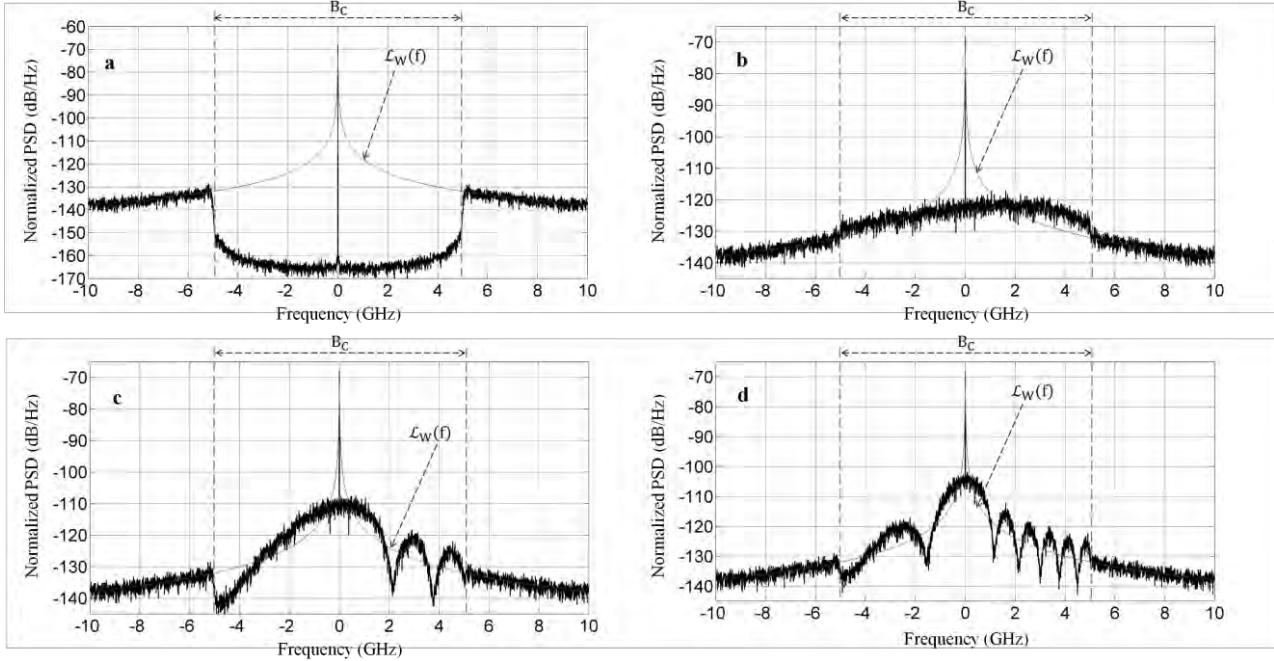


Fig. 7.18: Effect of CD on the pre-ADC PSD of an arbitrary pilot-SC with $\Delta f_{sh} = 10$ GHz and different link's distances. The PSD for $L = 0$ km, 68.5km, 68.5×4km, and 68.5×8km, are shown in (a), (b), (c), and (d) respectively. Here $F_S = 200$ GHz, $\delta f = 10$ MHz, $RBW \approx 6.1$ MHz, and $B_C = 10$ GHz. $\mathcal{L}_W(f)$ is the SCLs' Lorentzian line-shape (calculated)

7.3.3.2.4 Effect of CD when only the RIN is counted

In the following simulation, effect of the SCL's RIN is examined with pilot-tone to pilot-SC frequency separation of $\Delta f_{sh} = 10$ GHz, $F_S = 200$ GHz, $RBW \approx 6.1$ MHz, $B_C = 10$ GHz, $L = 8 \times 68.5$ km, Hamming window with order of 4096 is used as the FFL BPF, and a flat RIN is assumed with $RIN_L(0) = -140$ dBc/Hz as shown in Fig. 7.19a. While in Fig. 7.19b, the same parameters are used except $B_C = 7.8$ GHz and the relaxation oscillation is counted with $F_R = 8$ GHz, and $u = RIN_L(F_R)/RIN_L(0) = 15$ dB.

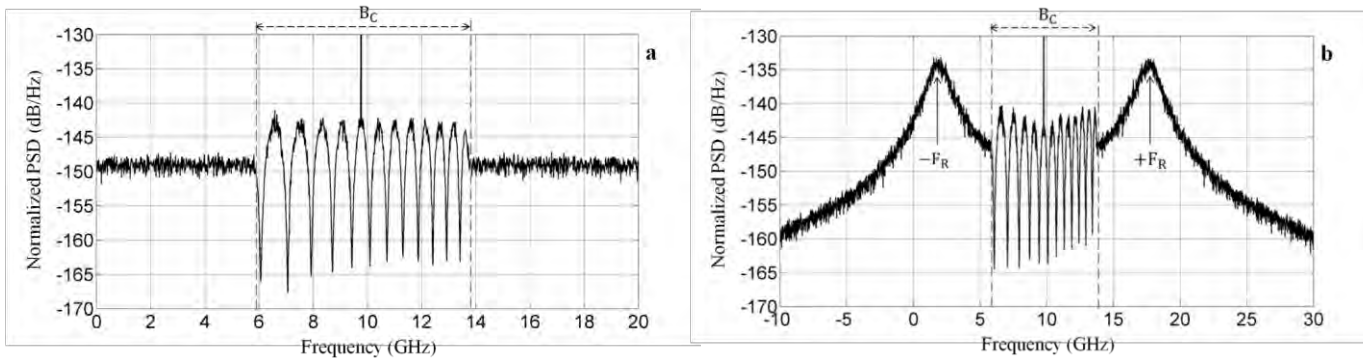


Fig. 7.19: Effect of CD on the pre-ADC PSD when only the SCL's RIN is active. In (a), flat RIN is assumed with $B_C = 10$ GHz is shown, while in (b), $B_C = 7.8$ GHz, $F_R = 8$ GHz, and $u = RIN_L(F_R)/RIN_L(0) = 15$ dB. The common parameters are $\Delta f_{sh} = 10$ GHz, $L = 68.5 \times 8$ km, and $RIN_L(0) = -140$ dBc/Hz.

7.3.3.2.5 PSD of a pilot-SC in PA-FFL when all parameters are counted

In the following simulation, the pre-ADC DS-PSD of a pilot SC in PA-FFL is examined as shown in Fig. 7.20 with $\Delta f_{sh} = 10\text{GHz}$, $F_S = 200\text{GHz}$, $\text{RBW} \approx 6.1\text{MHz}$, $B_C = 10\text{GHz}$, Hamming window with order of 4096 is used as the FFL BPF, $L = 4 \times 68.5\text{km}$ and identical SCLs are used in the TX and RX as before. The TX and RX SCL's parameters are $\delta f = 5\text{MHz}$, $f_c = 2\text{MHz}$, $F_R = 8\text{GHz}$, $\Gamma = 900\text{MHz}$, $K_z = 2.07\text{GHz}$, and $\text{RIN}_L(\mathbf{0}) = -145\text{dBc/Hz}$.

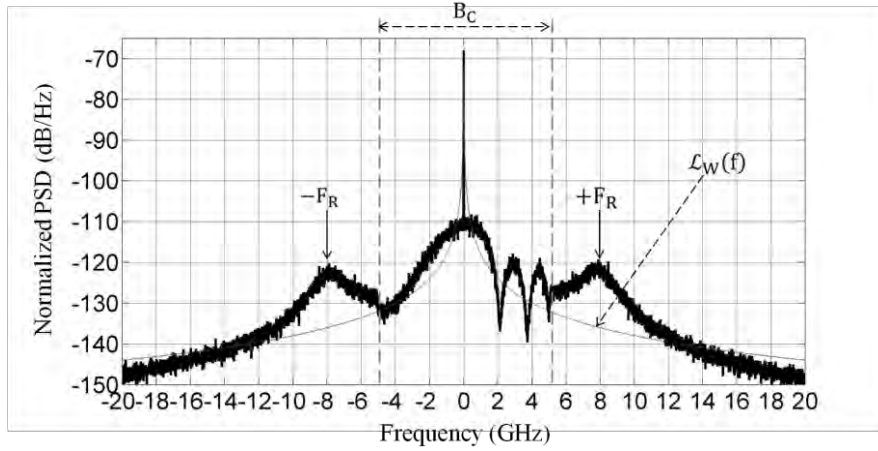


Fig. 7.20: Pre-ADC PSD of an arbitrary pilot-SC with $\Delta f_{sh} = -10\text{GHz}$, $L = 68.5 \times 4\text{km}$, total $\delta f = 10\text{MHz}$, $u = \text{RIN}_L(F_R)/\text{RIN}_L(0) = 25\text{dB}$, $B_C = 10\text{GHz}$, and other parameters are given in the text.

The results presented in this section confirm the FFL function by showing that the SCLs' noise, which are convolved with the SCs, are the delayed version of the pilot-tone's PN and IN signals. The results also show the domination of the white FN or the Lorentzian linewidth on the FFL performance even when high RIN is assumed.

7.3.4 Analytical equations of OFDM link with PA-FFL

The continuous model of OFDM link and results of Chapter 6 can be used to estimate the long term PN variance, IN variance, and ICI assuming large N value. Similar to the treatments of Section 6.3.2 focusing only on the beat-note term, then the DS-PSD of SCLs' noise after the FFL block and before demultiplexing ($\mathcal{F}\mathcal{F}\mathcal{T}$) is given by

$$S_k(f) \approx P_p P_{SC} \cdot \left\{ \left(\widetilde{S_{BN1}}(f - k\Delta f, \Delta T + \delta T_{kp}) * S_{BN2}(f - k\Delta f, \Delta T) \right) \cdot |H_{FFL}(f - k\Delta f)|^2 + \left(S_{EN1}(f - k\Delta f) * S_{EN2}(f - k\Delta f) \right) \cdot \{1 - |H_{FFL}(f - k\Delta f)|^2\} \right\} \quad (7.36)$$

where $\widetilde{\mathbf{S}}_{\text{BN1}}(f - k\Delta f, \Delta T + \delta T_{kp})$ is the normalized beat-note DS-PSD of a dispersive SCL field shifted in frequency by $\mathbf{k}\Delta f = k \cdot F_S/N_{\mathcal{F}}$, with differential delay between the pilot-tone and modulated-SC of $\Delta T + \delta T_{kp}$. This term is calculated exactly and analytically from the normalized version of (6.21) and (6.25) respectively. This term is for the TX-LO-SCL,

$\mathbf{S}_{\text{BN2}}(f - k\Delta f, \Delta T)$ is the normalized beat-note DS-PSD of a non-dispersive SCL field shifted in frequency by $\mathbf{k}\Delta f$, with differential delay ΔT . This term is calculated exactly from (4.44). This term is for the RX-LO-SCL,

$\mathbf{S}_{\text{EN1}}(f - k\Delta f)$, $\mathbf{S}_{\text{EN2}}(f - k\Delta f)$ are the normalized BB DS-PSD shifted in frequency by $\mathbf{k}\Delta f$ of the TX-LO-SCL and RX-LO-SCL fields in optical domain obtained generally from the numerical calculation of (4.13). Note that $\mathbf{S}_{\text{EN1}}(\mathbf{f})$ is directly used since the received DS-PSD of a dispersive SCL field is identical to transmitted one whatever the distance is, as it has been proven in Section 6.2,

$|\mathbf{H}_{\text{FFL}}(\mathbf{f})|$ is the BB amplitude response of the FFL-BPF,

$\Delta T = T_f - T_d = \Delta_N/F_S$ (s), is the error in the equalization delay-line, and

$\delta T_{kp} = \beta_D(L) \cdot (k - k_p) \cdot \Delta f = \delta_{kp}/F_S$, in (s).

Despite the compensation process, the mean SC's power is also affected by the residual PN and induced differential PN (due to CD) spectra. Hence by following a similar treatment to that in Section 7.2.2.2.1, the normalized SC power along with the induced IN term due to PN-to-IN due to filtering (averaging) is given by

$$\langle |\dot{\eta}_{\phi,m}[\ell]|^2 \rangle + \dot{\sigma}_{|\eta_{\phi,m}|}^2 \cong \int_{-f_m}^{f_m} \text{sinc}^2((f - m\Delta f)T_{\mathcal{F}}) \cdot \left(\frac{S_m(f)}{P_p P_{\text{SC}}} \right) \cdot df \quad (7.37)$$

where $\mathbf{S}_m(\mathbf{f})$ is obtained from (7.36) when $\mathbf{k} = \mathbf{m}$. Again we assume $\left\{ \langle |\dot{\eta}_{\phi,m}[\ell]|^2 \rangle \approx \langle |\dot{\eta}_{\phi,m}[\ell]|^2 \rangle + \dot{\sigma}_{|\eta_{\phi,m}|}^2 \right\}$ since $\dot{\sigma}_{|\eta_{\phi,m}|}^2$ is marginal. Now from (6.32-c), (7.13), and (7.36), then the ICI variance is calculated as

$$\dot{\sigma}_{ICI}^2[m] \approx \sum_{\substack{k=-N/2 \\ k \neq m}}^{N/2} \int_{-f_m}^{f_m} \text{sinc}^2((f - m\Delta f)T_{\mathcal{F}}) \cdot S_k(f) df \quad (7.38)$$

While the long-term variances of compensated-PN and IN are estimated next. From (7.25-d), $\Phi_{\mathbf{k}}[\hat{\mathbf{n}}, \ell]$ can be written in continuous form as

$\Phi_{\mathbf{k}}(\mathbf{t}) = \widetilde{\Phi}_1(\mathbf{t}) - \widetilde{\Phi}_{1F}(\mathbf{t} - \Delta T - \delta T_{kp}) + \Phi_2(\mathbf{t}) - \Phi_{2F}(\mathbf{t} - \Delta T)$, and

$\Phi_k(\mathbf{f}) = \widetilde{\Phi}_1(\mathbf{f})\{1 - |H_{\text{FFL}}(\mathbf{f})|e^{-j2\pi\mathbf{f}(\Delta T + \delta T_{kp})}\} + \Phi_2(\mathbf{f})\{1 - |H_{\text{FFL}}(\mathbf{f})|e^{-j2\pi\mathbf{f}\Delta T}\}$. Thus the DS-PSD in (rad^2/Hz) of the modified-PN term $\Phi_k(\mathbf{f})$ is given by

$$S_{\Phi_k}(\mathbf{f}) = \widetilde{S}_{\Phi_1}(\mathbf{f})\{1 + |H_{\text{FFL}}(\mathbf{f})|^2 - 2|H_{\text{FFL}}(\mathbf{f})|\cos(2\pi\mathbf{f}(\Delta T + \delta T_{kp}))\} + S_{\Phi_2}(\mathbf{f})\{1 + |H_{\text{FFL}}(\mathbf{f})|^2 - 2|H_{\text{FFL}}(\mathbf{f})|\cos(2\pi\mathbf{f}\Delta T)\} \quad (7.39)$$

where $\widetilde{S}_{\Phi_1}(\mathbf{f}) = S_{\alpha_n}(\mathbf{f})\sin^2(\Psi) + S_{\phi_n}(\mathbf{f})\cos^2(\Psi) - S_{X_r}(\mathbf{f})\sin(2\Psi)$, which is the PN DS-PSD of a dispersive field calculated from (6.8), the unknowns are covered in Chapter 4, and 6. This term is for the TX-LO-SCL and

$S_{\Phi_2}(\mathbf{f})$ is the PN DS-PSD of a SCL calculated from its SS version of (4.3). This term is for the RX-LO-SCL.

Therefore the modified PN variance is calculated as

$$\sigma_{\Phi}^2[k] = \int_{-f_m}^{f_m} \text{sinc}^2(fT_{\mathcal{F}}) \cdot S_{\Phi_k}(\mathbf{f}) \cdot df \quad (7.40)$$

Similarly and from (7.25-c), the IN DS-PSD and variance are respectively calculated as

$$S_{\alpha_k}(\mathbf{f}) = P_p P_{\text{SC}} \left\{ \widetilde{S}_{\alpha_1}(\mathbf{f}) \{1 + |H_{\text{FFL}}(\mathbf{f})|^2 + 2|H_{\text{FFL}}(\mathbf{f})|\cos(2\pi\mathbf{f}(\Delta T + \delta T_{kp}))\} + S_{\alpha_2}(\mathbf{f}) \{1 + |H_{\text{FFL}}(\mathbf{f})|^2 + 2|H_{\text{FFL}}(\mathbf{f})|\cos(2\pi\mathbf{f}\Delta T)\} \right\} \quad (7.41-a)$$

$$\sigma_{\alpha}^2[k] = \int_{-f_m}^{f_m} \text{sinc}^2(fT_{\mathcal{F}}) \cdot S_{\alpha_k}(\mathbf{f}) \cdot df \quad (7.41-b)$$

where $\widetilde{S}_{\alpha_1}(\mathbf{f}) = S_{\alpha_n}(\mathbf{f})\cos^2(\Psi) + S_{\phi_n}(\mathbf{f})\sin^2(\Psi) + S_{X_r}(\mathbf{f})\sin(2\Psi)$, which is the IN DS-PSD of a dispersive field calculated from (6.8). The unknowns are covered in Chapter 4, and 6. This term is for the TX-LO-SCL and

$S_{\alpha_2}(\mathbf{f})$ is the PN DS-PSD of a SCL calculated from (4.8). This term is for the RX-LO-SCL.

These analytical equations are indeed very accurate when relatively large number of SCs is used, and hence they are considered as a reliable characterized solution that can be used to describe the coloured noise in CO-OFDM with PA-FFL.

7.3.5 The modified colored noise variances estimation

In PA-FFL, three distinct noise terms have to be examined carefully before performance estimation is conducted, which are the modified noise term (ASE noise), the ICI term, and the phase error term. The 1st term has been covered in Section 7.3.2.2, while the 2nd and 3rd will be covered next.

7.3.5.1 The modified ICI variance

7.3.5.1.1 The modified ICI term in back-to-back setup for a special case

A common special case is considered here, which is when the back-to-back setup (**BBS**) is used to cancel CD effect or $\delta\mathbf{T}_{kp} = 0$, $\Delta\mathbf{T} = 0$, only the white FN is considered with $\mathbf{H}_c[\mathbf{k}] = 1$, and an ideal FFL-BPF is adopted. The results of this special case can be used when a Lorentzian SCLs' line-shape with low relaxation peaks is assumed, and in a short distance OFDM links, or a long-distance with narrowband OFDM signal. This special case is useful in the first estimation of optimal compensation BW ($\mathbf{B}_{C,opt}$). The exact solution given by (7.35) can show the effect of \mathbf{B}_C graphically, which is not useful for generalized $\mathbf{B}_{C,opt}$ estimation. While solution of (7.38) in conjugation with (4.14-b), and (4.28) is rather complicated since many numerical integrals are involved. However, when large number of SCs is used, and assuming $\delta\mathbf{f} = \delta f_1 + \delta f_2$ or $\delta\mathbf{f}_N = \delta f_{N1} + \delta f_{N2}$, then the normalized version of (7.38) can be efficiently approximated as

$$\hat{\sigma}_{ICIN}^2 \approx \delta f_N \cdot \left\{ 1 - \frac{2}{\pi} \tan^{-1}(N_C) \right\} \cdot \exp\left(-\frac{\pi}{2} \cdot N_C/N\right) \quad (7.42)$$

where $\hat{\sigma}_{ICIN}^2$ corresponds to the middle SCs. An error of less than 1% at $\delta\mathbf{f}_N \geq 1$ is noticed when comparing (7.42) and simulation results with about 5000 OFDM symbols. In the following calculations, $\mathbf{N}_F = 256$, $\mathbf{N} = 200$, $\mathbf{F}_S = 10\text{GSps}$, $\delta\mathbf{f}_N \approx [0.01, 0.1, 0.41, 1.0]$, and $\hat{\sigma}_{ICIN}^2[m = 50]$ is chosen as shown in Fig. 7.21. Obviously, the ICI can always be reduced by increasing \mathbf{N}_C and for very broad SCL's linewidth values, which is true but at the expense of an increase in the modified ASE noise term.

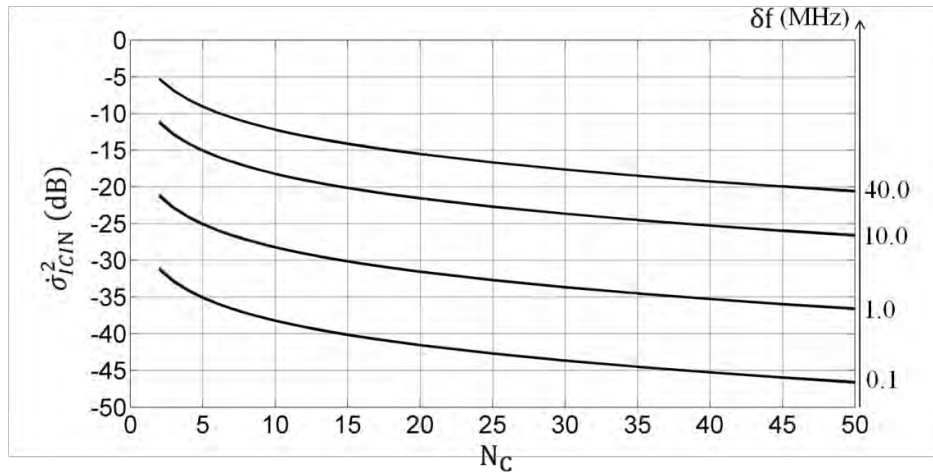


Fig. 7.21: The normalized modified ICI of $m = 50$ in BBS and when only the white FN is counted versus the compensation BW and total Lorentzian linewidth. Parameters are given in the text.

7.3.5.1.2 The modified ICI term when only the IN is ignored

First, when the IN is ignored and $\mathbf{H}_c[\mathbf{k}] = 1$, then (7.38) is used again to estimate the normalized modified ICI term in dispersive channel taking only the TX-LO-SCL effect into consideration, since the RX-LO-SCL effect can directly be obtained from (7.42). In the following 1st and 2nd calculations, the common parameters are $\mathbf{N}_F = 256$, $\mathbf{N} = 200$, $\mathbf{F}_S = 10\text{GSps}$, four values of \mathbf{N}_C are used which are $\mathbf{N}_C = [4, 8, 16, 32]$, the DC-SC is set to zero, and an ideal FFL BPF is used. The side pilot-tone's frequency-index \mathbf{k}_p in all the cases is set depending on the minimal possible index for a practical filtering as follows $|\mathbf{k}_p| \geq (\mathbf{N} + \mathbf{N}_C)/2$. The 1st calculation is aimed to demonstrate the channel response via the modified ICI term versus the SC index \mathbf{k} with TX-LO-SCL linewidth of $\delta\mathbf{f}_1 = 1\text{MHz}$, and the fiber distance $\mathbf{L} = 3000\text{km}$ as shown in Fig. 7.22. In the 2nd calculation, the modified ICI term versus \mathbf{k} is examined with $\delta\mathbf{f}_1 = 10\text{MHz}$, and $\mathbf{L} = 100\text{km}$, 300km , 1000km , and 3000km as shown in Fig. 7.23a, 7.23b, 7.23c, and 7.23d respectively. In the 3rd calculation, the modified ICI term versus \mathbf{N}_C is examined for the same OFDM setting with $\delta\mathbf{f}_1 = 1\text{MHz}$, $\mathbf{L} = [100, 300, 1000, 3000]\text{km}$, and still $\mathbf{H}_c[\mathbf{k}] = 1$ as shown in Fig. 7.24. Second, in the 4th calculation, the modified ICI term at $\mathbf{m} = 50$ versus \mathbf{N}_C is examined again taking $\mathbf{H}_c[\mathbf{k}]$ into account with same previous OFDM setting, $\delta\mathbf{f}_1 = 10\text{MHz}$, $\mathbf{L} = [100, 300, 1000, 3000]\text{km}$, $\mathbf{H}_c[\mathbf{k}] = 1$ as shown in Fig. 7.25a, $\mathbf{F}_R = 2\text{GHz}$, $\mathbf{\Gamma} = 200\text{MHz}$ as shown in Fig. 7.25b, and $\mathbf{F}_R = 2\text{GHz}$, $\mathbf{\Gamma} = 100\text{MHz}$ as shown in Fig. 7.25c. Third, in the 5th calculation, the modified ICI term versus \mathbf{L} is examined with same previous OFDM setting, $\delta\mathbf{f}_1 = [0.1, 1, 10, 40]\text{MHz}$, and $\mathbf{N}_C = 4, 8, 16, \text{ and } 32$ as shown in Fig. 7.26a, 7.26b, 6.26c, and 7.26d respectively.

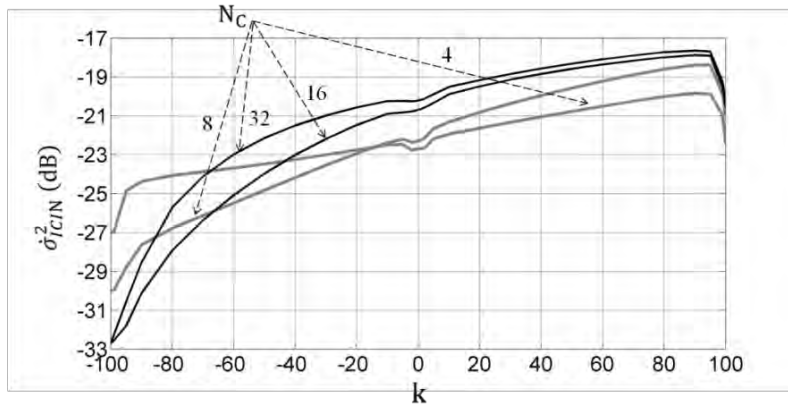


Fig. 7.22: The normalized modified ICI term versus \mathbf{k} and \mathbf{N}_C with $\delta\mathbf{f}_1 = 1\text{MHz}$, and $\mathbf{L} = 3000\text{km}$. The other parameters are in the text.

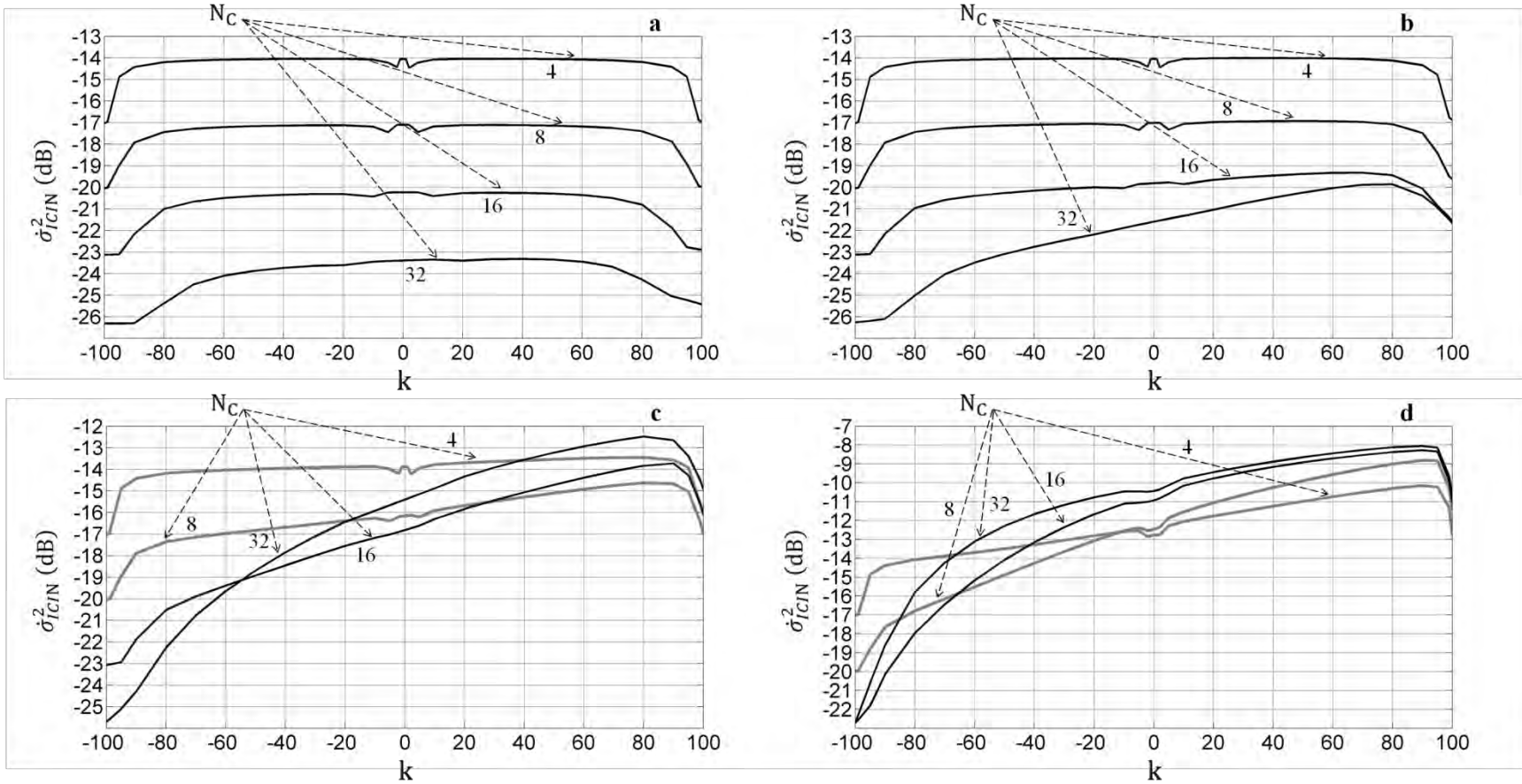


Fig. 7.23: The normalized modified ICI term versus k and N_C with $\delta f_1 = 10\text{MHz}$ and $L = 100\text{km}$, 300km , 1000km , and 3000km in (a), (b), (c), and (d) respectively. Here $F_S = 10\text{GSps}$, $N_F = 256$, $N = 200$, $N_C = [4, 8, 16, 32]$, the DC-SC is set to zero, only white FN of the TX-LO-SCL is counted and an ideal FFL BPF is used.

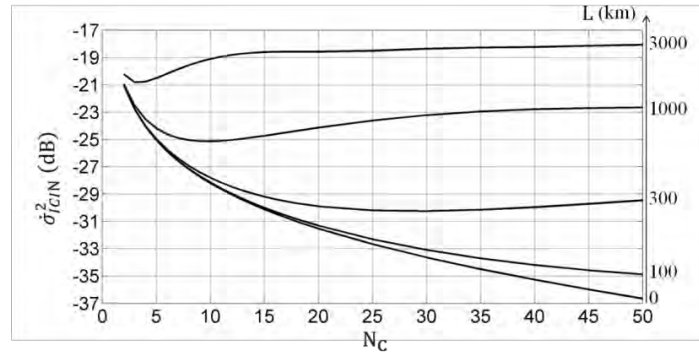


Fig. 7.24: The normalized modified ICI term versus N_C with $\delta f_1 = 1\text{MHz}$, and $L = 3000\text{km}$. The other parameters are in the text.

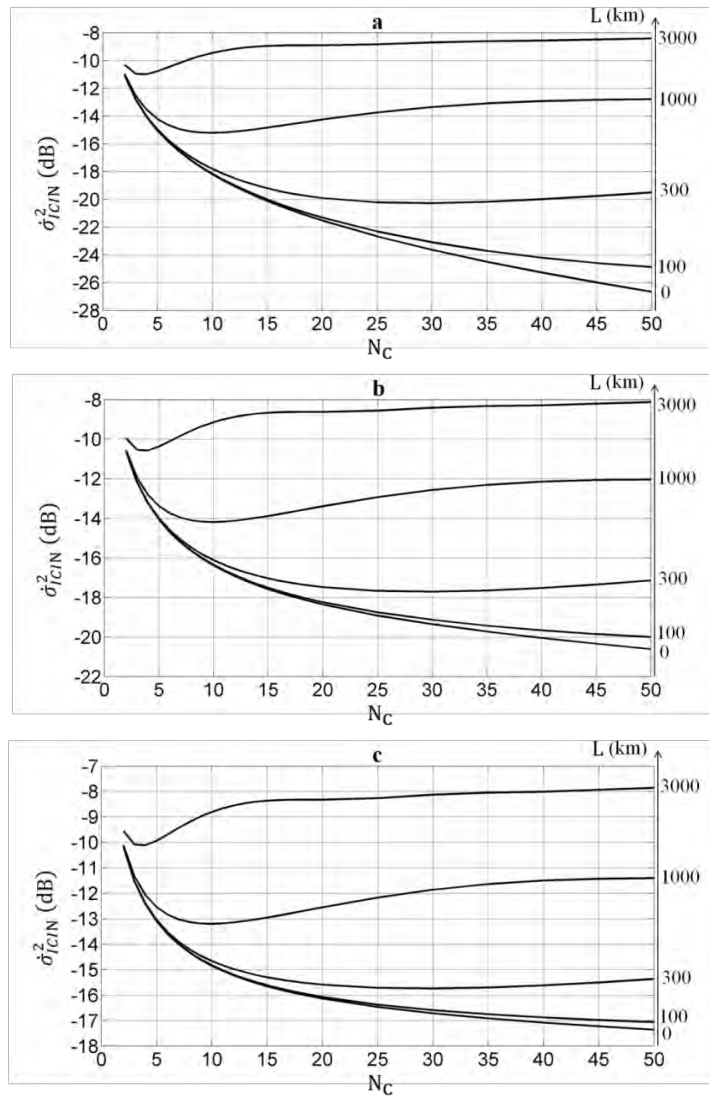


Fig. 7.25: The normalized modified ICI term of $m = 50$ versus N_C and L with $\delta f_1 = 10\text{MHz}$ taking the relaxation oscillation into account. Here $\mathbf{H}_c[\mathbf{k}] = 1$ in (a), $\mathbf{F}_R = 2\text{GHz}$, $\Gamma = 200\text{MHz}$ in (b), and $\mathbf{F}_R = 2\text{GHz}$, $\Gamma = 100\text{MHz}$ in (c). The other parameters are in the text.

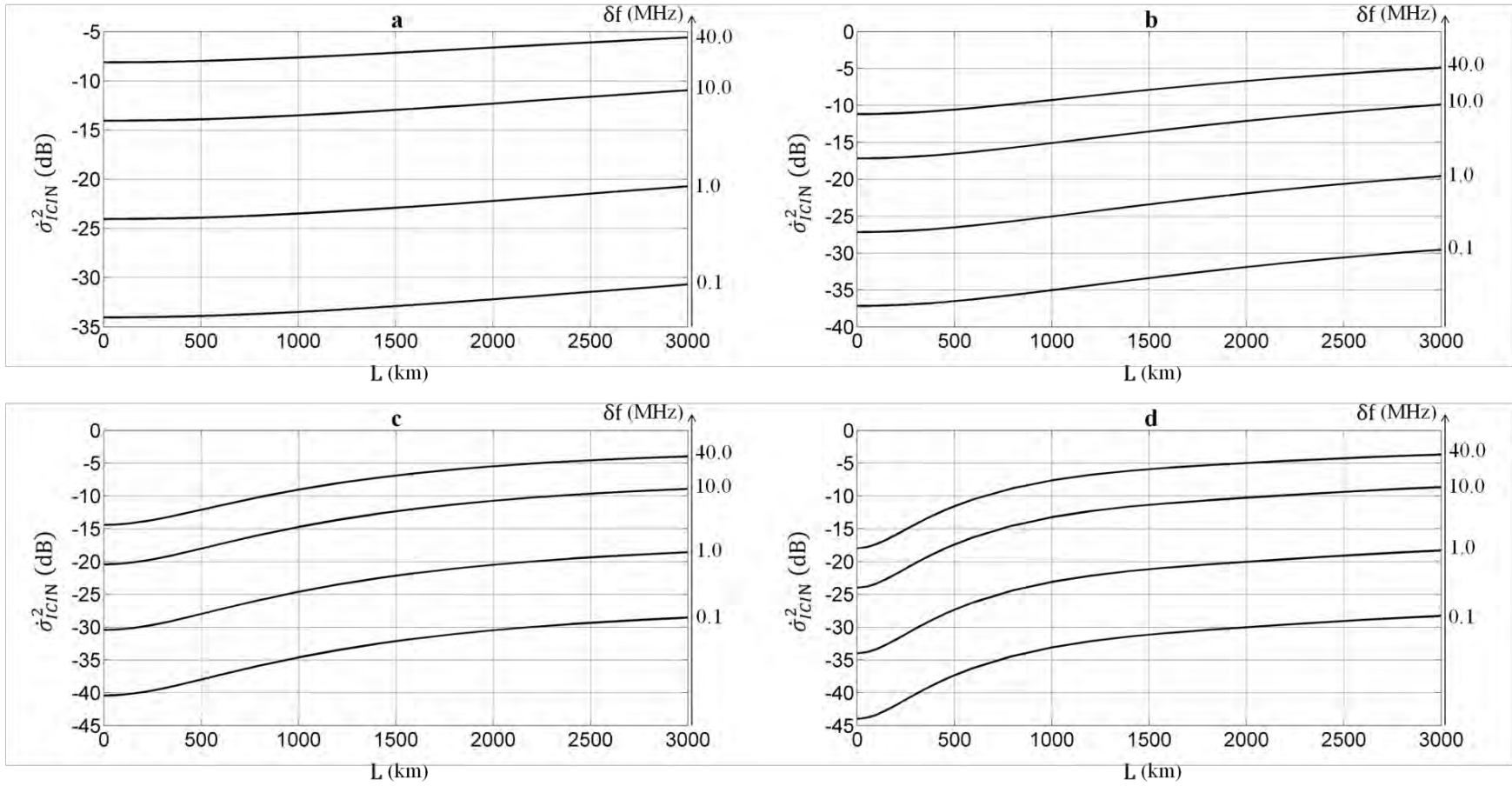


Fig. 7.26: The normalized modified ICI term versus L and δf_1 with $N_c = 4, 8, 16,$ and 32 in (a), (b), (c), and (d) respectively. Here $F_s = 10\text{GSps}$, $N_f = 256$, $N = 200$, $\delta f_1 = [0.1, 1, 10, 40]\text{MHz}$, the DC-SC is set to zero, only white FN of the TX-LO-SCL is counted and an ideal FFL BPF is used.

7.3.5.1.3 The modified ICI term when only the IN is counted

In the following calculations, the IN effect is examined with similar OFDM parameters given previously, when a flat RIN is assumed first, and second when $\mathbf{A}_c[\mathbf{k}]$ is counted. Hence in the 1st calculation, $\sigma_{ICIIN}^2[m = 50]$ due to RIN of both SCLs is checked versus N_C using BBS as shown in Fig. 7.27 with per SCL (TX-LO-SCL or RX-LO-SCL) $\mathbf{RIN}_L(\mathbf{0}) = [-150, -140, -130, -120]$ dBc/Hz. While in the 2nd calculation, $\mathbf{RIN}_L(\mathbf{0}) = -140$ dBc/Hz is assumed, and $\sigma_{ICIIN}^2[m = 50]$ due to the TX-LO-SCL only is checked versus N_C with $F_R = 1.5$ GHz, and $\mathbf{u} = \mathbf{RIN}_L(F_R)/\mathbf{RIN}_L(0) = 16.6$ dB as shown in Fig. 7.28a, $F_R = 1.5$ GHz, and $\mathbf{u} \approx 25.6$ dB as shown in Fig. 7.28b, and $F_R = 2$ GHz, $\Gamma = 100$ MHz, $K_z = 230$ MHz ($\mathbf{u} \approx 38.9$ dB) as shown in Fig. 7.28c.

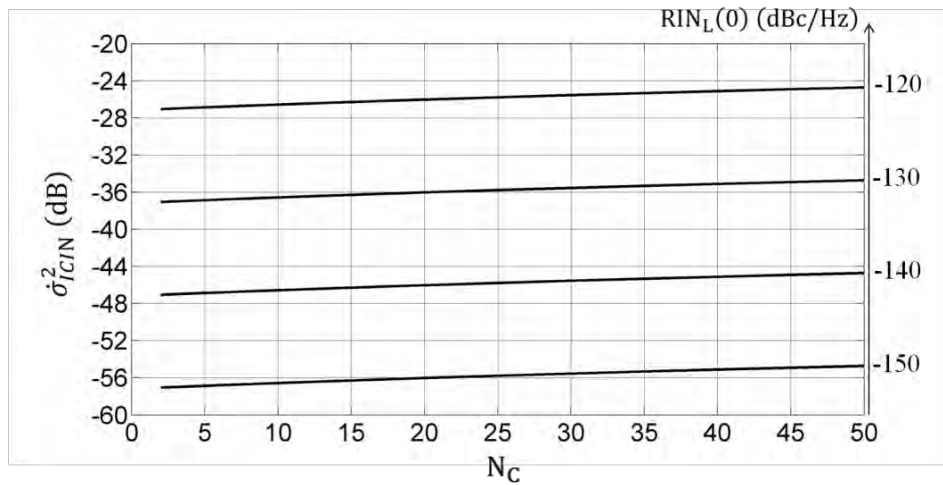
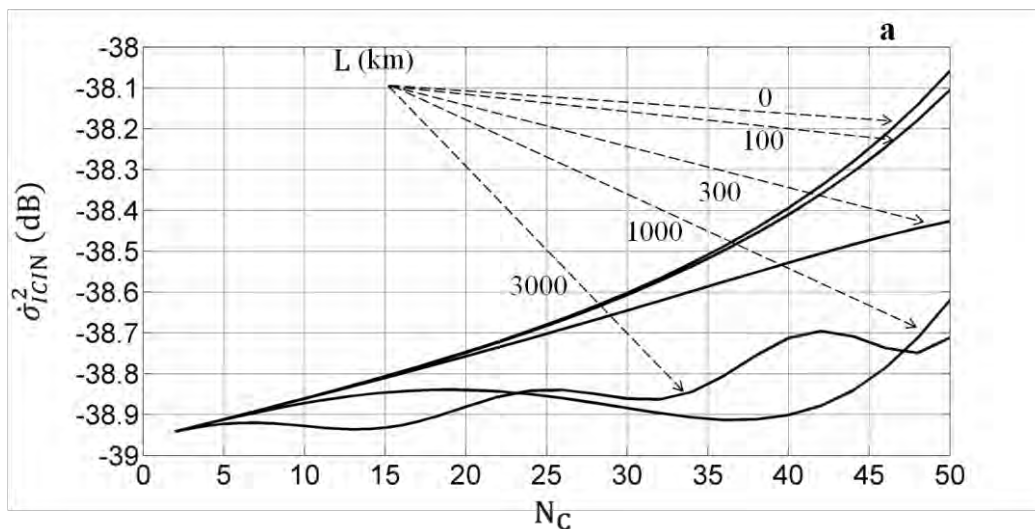


Fig. 7.27: The normalized modified ICI term due to the overall SCLs' RINs in BBS of $m = 50$ versus N_C and per SCL $\mathbf{RIN}_L(\mathbf{0})$. OFDM setting is given in the text.



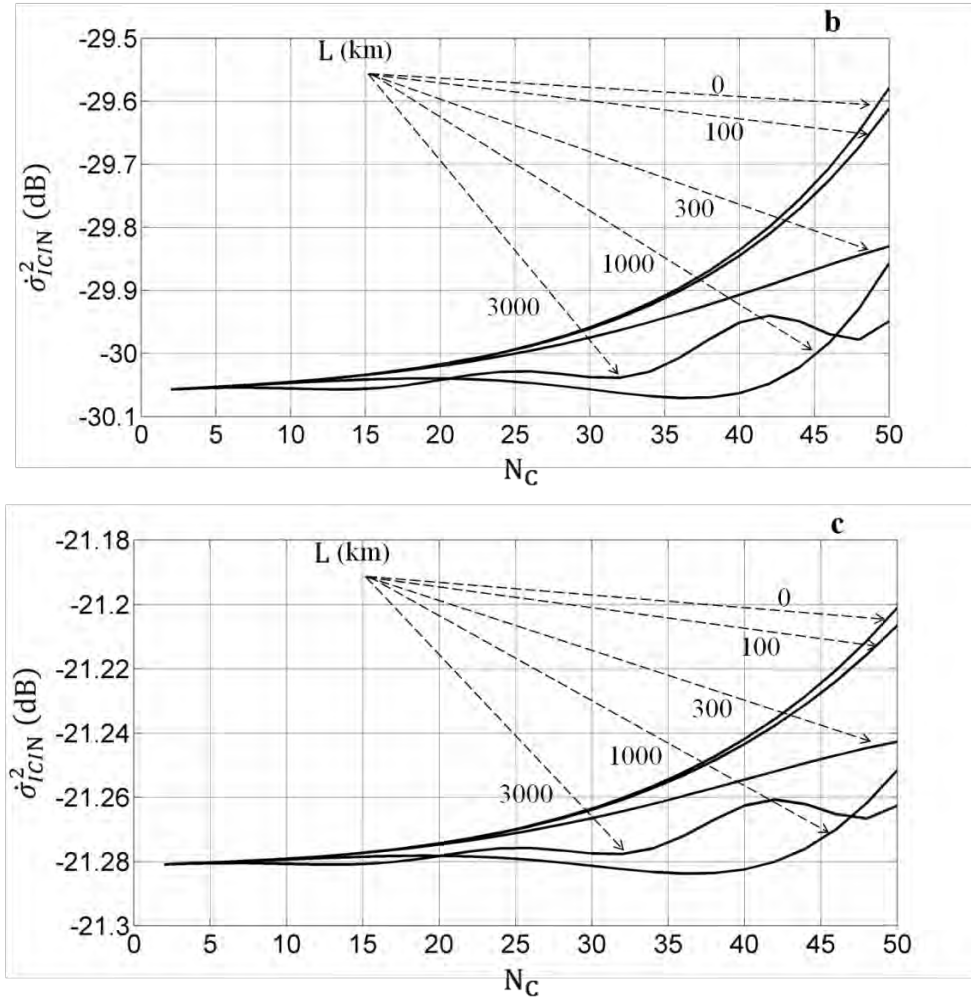


Fig. 7.28: The normalized modified ICI term due to the TX-LO-SCL's RIN only when $A_c[\mathbf{k}]$ of $\mathbf{m} = 50$ versus N_c and L with $RIN_L(\mathbf{0}) = -140\text{dBc/Hz}$. Here $F_R = 1.5\text{GHz}$, and $\mathbf{u} = RIN_L(F_R)/RIN_L(\mathbf{0}) = 16.6\text{dB}$ in (a), $F_R = 1.5\text{GHz}$, and $\mathbf{u} \approx 25.6\text{dB}$ in (b), and $F_R = 2\text{GHz}$, $\Gamma = 100\text{MHz}$, $K_z = 230\text{MHz}$ ($\mathbf{u} \approx 38.9\text{dB}$) in (c). The other parameters are in the text.

The results in this section show the following:

- there is always an optimal N_c versus L and $\delta\mathbf{f}_1$,
- the IN has an insignificant effect even with relatively high relaxation peak compared with $\delta\mathbf{f}_1$; however, its effect must be considered in high modulation density (mapping),
- there is a maximum value of $\delta\mathbf{f}_1$ for a given mapping and L that cannot be tolerated, while $\delta\mathbf{f}_2$ can have any value provided that $\Delta\mathbf{T} = 0$ as discussed in Section 7.3.3.2, and
- the worst-corrupted SCs' indices are within $+N/4 \rightarrow +N/2$ for negative side pilot-tone's index, and within $-N/4 \rightarrow -N/2$ for positive side pilot-tone's index. These SCs dominate the average **BER** of the system.

7.3.5.2 Long-term phase error variance

A long-term phase error term is produced due to the induced differential PN term, which emerges due to the mixing process of two time-shifted dispersive SCL's fields. Hence only the TX-LO-SCL characteristics (particularly $\delta\mathbf{f}_1$) determines the amount of this phase error, which can be estimated using (7.39) and (7.40), however, it can also be efficiently approximated when only the white FN is counted as follows

$$\sigma_\phi[\mathbf{m}]^\circ = \frac{180}{\pi} \sqrt{2\pi\delta\mathbf{f}_1 \cdot \Delta\mathbf{f} \cdot \beta_D(L)\Delta\mathbf{f} \cdot |\mathbf{m} - \mathbf{k}_p|} \quad (7.43)$$

where $\sigma_\phi[\mathbf{m}]^\circ$ is phase error standard deviation in (degrees). Note that we use \mathbf{k} and \mathbf{m} to indicate SCs' frequency index without prior notice. Note also that \mathbf{B}_C has a negligible effect provided that $\mathbf{B}_C \geq \Delta\mathbf{f}$. Using $\delta\mathbf{f}_1 = [1, 10]$ MHz with same OFDM setting given previously, the calculation results shown in Fig. 7.29 indicate that this residual PN can severely impair some of the OFDM's SCs especially when high density mapping is used. It is important to emphasize that the differential PN RV is a GRV, since the FFL process results no change in the original FN statistics [38].

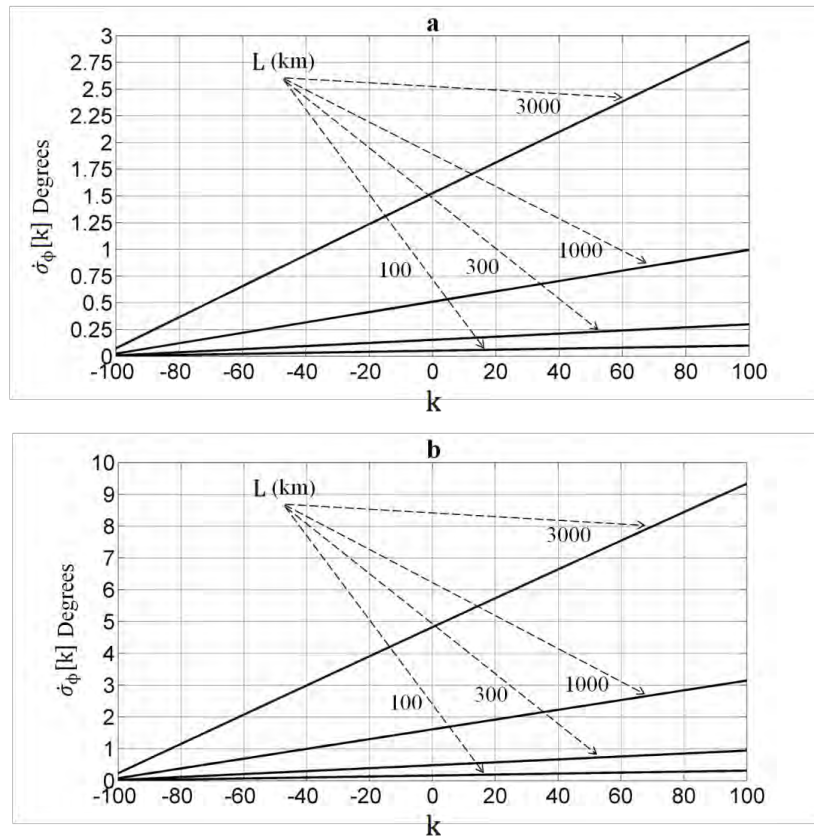


Fig. 7.29: Phase error standard deviation in (degrees) due to the TX-LO-SCL and when only the white FN is counted versus \mathbf{k} and L with $\delta\mathbf{f}_1 = 1$ MHz in (a), 10 MHz in (b).

7.3.5.3 Results discussion

- Performance of the OFDM system with PA-FFL is inhomogeneously distributed over the SCs. The SCs that have low $|\mathbf{m} - \mathbf{k}_p|$ values are less corrupted by all the induced effects due to TX-LO-SCL, while the SCs with high $|\mathbf{m} - \mathbf{k}_p|$ values are the worst.
- The long-term phase error has a linear relation versus \mathbf{k} , which its slope is a function of $\delta\mathbf{f}_1$, and \mathbf{L} . For instance, and as it will be shown soon, the QPSK mapping can tolerate $\dot{\sigma}_\phi[\mathbf{m}]^\circ \approx 7^\circ$ with only 1dB penalty at $\mathbf{BER}[\mathbf{m}] = 10^{-3}$, while for the 16-QAM, $\dot{\sigma}_\phi[\mathbf{m}]^\circ \approx 3.5^\circ$ for the same penalty at the given \mathbf{BER} .
- When a reference SCL is used at TX, then the performance is \mathbf{k} -independent except at the signal's edges as discussed in Section 7.3.2.2. Hence the PA-FFL technique becomes very efficient solution for long-haul CO-OFDM transmission when the TX-LO-SCL is a highly stable laser, and the RX-LO-SCL is a cheap SCL with $\delta\mathbf{f}_{N2} \leq 1$.
- IN contribution in the performance degradation is not significant for QPSK mapping provided that $\{\text{RIN}_L(0) + u \leq -120\text{dB}\}$. However, this term must be taken into in high level constellation. Besides, detection method (PD or BD) must also considered.
- The modulated-SCs between $+N/4 \rightarrow +N/2$ for a negative indexed pilot-tone are the worst-corrupted among all other SCs, and hence, only these indices might be considered in \mathbf{BER} analysis.

7.3.6 Performance Analysis

7.3.6.1 The modified \mathbf{SNR}_b equation

The effective \mathbf{SNR}_b along with $\dot{\sigma}_\phi[\mathbf{m}]^\circ$ lead to an estimation of the $\mathbf{BER}[\mathbf{m}]$ before a hard-decision is made for a given mapping. Let all the modulated-SCs be statistically independent and have equal power, which is usually the case in practical design. Then from (7.22), the effective power per SC is $\mathbf{P}_{SC} \approx P_s \cdot P_p/N$.

Here (7.26) shows that the overall modified noise consisting of a modified ASE and ICI noise terms, and since the ICI term is proportional to \mathbf{P}_{SC} as discussed in Section 7.2.2.3, then from (7.30), (3.40), (3.34-d), and assuming the ICI is a GRV, the effective \mathbf{SNR}_b is

$$\mathbf{SNR}_b[\mathbf{m}] = \frac{P_{SC}/m}{\dot{\sigma}_{nSC}^2[\mathbf{m}]} = \frac{P_{SC}/m}{\dot{\sigma}_n^2[\mathbf{m}] + P_{SC}\dot{\sigma}_{ICIN}^2[\mathbf{m}]} = \frac{P_s P_p / (N \cdot m)}{\sigma_n^2 \left\{ P_p + \frac{P_s}{N} \cdot \chi[\mathbf{m}] \right\} + \frac{P_s P_p}{N} \dot{\sigma}_{ICIN}^2[\mathbf{m}]}$$

Here σ_n^2 is the ASE noise power per frequency sample (within $\Delta f = F_s/N_F$), which depends on whether a homodyne or a heterodyne (with or without image rejection filter (**IRF**)) configuration is adopted [50]. In the current complex-model, an ideal detection is assumed, however, and for generalization purposes, σ_n^2 can be expressed as follows

$$\sigma_n^2 = \frac{N_{rx}|B_{ref}}{\delta_{pol} \cdot B_{ref}} \cdot \Delta f \cdot d \quad , \text{ where } d \approx \begin{cases} 1, & \text{homodyne, or heterodyne with IRF} \\ 2, & \text{heterodyne without IRF} \end{cases}$$

Now since the received power is $\mathbf{P}_{rx} = P_{sT} + P_p = P_{sT} \cdot (1 + \text{PSPR})$, where \mathbf{P}_{sT} is signal's total power including the overheads, **PSPR** is pilot-tone power to total OFDM signal power. Let **PSPR** is denoted by a dummy variable \mathbf{x} , therefore from (3.26), if pilot's overhead is excluded, then the useful signal's power is $\mathbf{P}_s = P_{sT}/\text{PEN}_{oh}$. Hence

$$\mathbf{P}_s = \frac{P_{rx}/\text{PEN}_{oh}}{(1 + \mathbf{x})} \quad , \text{ and } \quad \mathbf{P}_p = \frac{\mathbf{x}}{(1 + \mathbf{x})} P_{rx} \quad , \text{ therefore}$$

$$\text{SNR}_b[\mathbf{m}] = \frac{\mathbf{x} \cdot P_{rx}^2 / \{m \cdot (1 + \mathbf{x})^2 \cdot \text{PEN}_{oh}\}}{N_{rx}|B_{ref}} \cdot \frac{N \cdot \Delta f \cdot d}{\delta_{pol} B_{ref}} \cdot \left\{ \frac{\mathbf{x} P_{rx}}{(1 + \mathbf{x})} + \frac{P_{rx}}{\text{PEN}_{oh}(1 + \mathbf{x})} \cdot \frac{\chi[\mathbf{m}]}{N} \right\} + \frac{\mathbf{x} P_{rx}^2}{(1 + \mathbf{x})^2} \dot{\sigma}_{ICIN}^2[\mathbf{m}]$$

Then from (3.3) and after simplifications yields

$$\text{SNR}_b[\mathbf{m}] \approx \text{OSNR}_d \frac{\mathcal{W}_g}{m} \cdot \frac{1}{\left(\frac{1 + \mathbf{x}}{\mathbf{x}}\right) \left(\mathbf{x} + \frac{\chi[\mathbf{m}]/N}{\text{PEN}_{oh}}\right) + \mathcal{W}_g \text{OSNR}_d \cdot \dot{\sigma}_{ICIN}^2[\mathbf{m}]} \quad (7.44)$$

where $\mathcal{W}_g = \left(\frac{\delta_{pol}}{d \cdot \text{PEN}_{oh}}\right) \cdot \left(\frac{B_{ref}}{N \cdot \Delta f}\right) = \left(\frac{\delta_{pol}}{d \cdot \text{PEN}_{oh}}\right) \cdot \left(\frac{B_{ref}}{\text{BW}_{nT}}\right)$, and BW_{nT} is the total OFDM's noise BW defined by (3.34-d).

7.3.6.2 Optimal pilot-to-signal power ratio (PSPR)

From (7.44), and for any given $\chi[\mathbf{m}]$, there is an optimal value of \mathbf{x} which results maximum $\text{SNR}_b[\mathbf{m}]$, and can be determined by solving $\partial \text{SNR}_b[\mathbf{m}]/\partial \mathbf{x} = 0$. However, pilot-tone's power cannot be set for individual SCs, and hence averaging is necessary. Thus, let $\text{SNR}_b[\mathbf{m}]$ be denoted by $\text{SNR}_b, \dot{\sigma}_{ICIN}^2[\mathbf{m}]$ by $\langle \dot{\sigma}_{ICIN}^2 \rangle$, and $\chi[\mathbf{m}]$ by χ_{ave} , and hence, by making $\partial \text{SNR}_b/\partial \mathbf{x} = 0$ yields

$$(1 + \mathbf{x}) \left(\mathbf{x} + \frac{\chi_{ave}/N}{\text{PEN}_{oh}} \right) + \mathbf{x} \mathcal{W}_g \text{OSNR}_d \langle \dot{\sigma}_{ICIN}^2 \rangle$$

$$- \mathbf{x} \mathcal{W}_g \text{OSNR}_d \langle \dot{\sigma}_{ICIN}^2 \rangle - \mathbf{x} - 2\mathbf{x}^2 - \mathbf{x} \frac{\chi_{ave}/N}{\text{PEN}_{oh}} = 0$$

hence $\mathbf{x} = \sqrt{\frac{\chi_{ave}/N}{PEN_{oh}}}$, and by substituting of χ_{ave} or χ_{max} from Section 7.3.2.2 yields

$$PSPR_{opt} = \sqrt{\left(\beta_C - \frac{\beta_C^2}{4} + \frac{1}{4N^2}\right)/PEN_{oh}} \quad (\text{Average cross-noise}) \quad (7.45-a)$$

$$PSPR_{opt} = \sqrt{\beta_C/PEN_{oh}} \quad (\text{Worst case}) \quad (7.45-b)$$

where $\beta_C = N_C/N = B_C/BW_{nT}$. Note that only the CP and TrS overheads are counted in PEN_{oh} calculation using (3.26).

7.3.6.3 BER estimation when all the color noise components are GRVs.

In this analysis, the ICI component is assumed to be a GRV, which is valid when $\sigma_{ICIN}^2 \ll 1$, as it has been shown in Section 7.2.3.2. Therefore, $\mathbf{BER}[m]$ can be estimated versus \mathbf{OSNR}_d and for a given link's and SCLs' specifications using (7.44), and the results of Section 7.3.4. \mathbf{BER} of a different M-QAM mapping in presence of Gaussian PN are derived and discussed in Appendix-B. Therefore by recalling the exact \mathbf{BER} expressions of the QPSK and 16-QAM mapping from Appendix-B then

$$\text{QPSK,} \quad \mathbf{BER}[m] = \frac{1}{2} \int_{-\infty}^{\infty} \text{erfc}\left(\sqrt{\text{SNR}_b[m]}\right) \cdot \{\cos(\phi) - \sin(\phi)\} \cdot \mathcal{P}_\phi(\phi, m) d\phi \quad (7.46-a)$$

$$\begin{aligned} \text{16-QAM,} \quad \mathbf{BER}[m] = & \frac{1}{16} \int_{-\infty}^{\infty} \left\{ \text{erfc}\left(\sqrt{2\text{SNR}_b[m]}/5 \cdot \{\cos(\phi) + \sin(\phi)\}\right) \right. \\ & + \text{erfc}\left(\sqrt{8\text{SNR}_b[m]}/5 \cdot \{1 - (\cos(\phi) + \sin(\phi))/2\}\right) \\ & + \text{erfc}\left(\sqrt{8\text{SNR}_b[m]}/5 \cdot \{3(\cos(\phi) + \sin(\phi))/2 - 1\}\right) \\ & + \text{erfc}\left(\sqrt{8\text{SNR}_b[m]}/5 \cdot \{(3\cos(\phi) + \sin(\phi))/2 - 1\}\right) \\ & \left. + \text{erfc}\left(\sqrt{8\text{SNR}_b[m]}/5 \cdot \{1 - (\cos(\phi) + 3\sin(\phi))/2\}\right) \right. \\ & \left. + \text{erfc}\left(\sqrt{2\text{SNR}_b[m]}/5 \cdot \{\cos(\phi) + 3\sin(\phi)\}\right) \right\} \cdot \mathcal{P}_\phi(\phi, m) d\phi \end{aligned} \quad (7.46-b)$$

where $\mathcal{P}_\phi(\phi, m) = \frac{1}{\sqrt{2\pi \cdot \sigma_\phi^2[m]}} \cdot \exp\left(-\frac{\phi^2}{2\sigma_\phi^2[m]}\right)$, which is the PN PDF.

Although simple approximate analytical expressions of $\mathbf{BER}[\mathbf{m}]$ are also considered in Appendix-B, they can only be accurate for $\sigma_{\phi}[\mathbf{m}]^{\circ} \leq 3^{\circ}$.

The penalty due to the compensation process is computed with respect to the minimal required \mathbf{OSNR} at a specific \mathbf{BER} in an ideal link for a given mapping and OFDM signal's parameters. In the ideal link, both SCLs are ideal optical tones, $\mathbf{d} = 1$, and $\mathbf{PEN}_{\text{oh}} = 1$. Here the ideal $\mathbf{SNR}_{\mathbf{b}}$ is given by

$$\mathbf{SNR}_{\mathbf{b},\text{ideal}} = \mathbf{OSNR}_{\mathbf{d}} \cdot \left(\frac{\mathbf{B}_{\text{ref}}}{\mathbf{BW}_{nT}} \right) \cdot \left(\frac{\delta_{\text{pol}}}{m} \right) \quad (7.47)$$

From (7.47), it is possible then to obtain the minimal required \mathbf{OSNR} . For instance, the required $\mathbf{SNR}_{\mathbf{b},\text{ideal}}$ for QPSK and 16-QAM mapping are 7.77dB, and 10.49dB at $\mathbf{BER} = 10^{-3}$ respectively, which corresponds to $\mathbf{OSNR}_{\mathbf{d}}$ of 4.73dB and 11.46dB respectively. Obviously, when $\mathbf{d} = 2$, a 3dB detection method penalty is added.

7.3.7 Performance calculations

7.3.7.1 Calculation procedure

Based on the analyses of Sections 7.3.2.2, 7.3.4, 7.3.5, and 7.3.6, the following suggested procedure of $\mathbf{BER}[\mathbf{m}]$ calculation will result the optimal $\mathbf{B}_{\mathbf{C}}$ or $\mathbf{B}_{\mathbf{C},\text{opt}}$ as well as the required \mathbf{OSNR} at which the \mathbf{BER} reaches the targeted value, and as follows.

- The optical link power budget must be decided first by determining the available or maximum $\mathbf{OSNR}_{\mathbf{d}}$ for a given distance \mathbf{L} and launch power \mathbf{P}_{ch} . From Section 3.2.2.3 and assuming \mathbf{P}_{ch} is in the range of -10dBm to -3dBm, since the optimal \mathbf{P}_{ch} for optical OFDM is in this range [56], then maximum $\mathbf{OSNR}_{\mathbf{d}}$ is estimated.
- \mathbf{BER} of the worst-corrupted SC's indices is chosen to be a reference for $\mathbf{B}_{\mathbf{C}}$ selection. Based on the discussion of section 7.3.5.3, then under high $\delta\mathbf{f}_1$ values, the lowest $\mathbf{SNR}_{\mathbf{b}}[\mathbf{m}]$ is expected to be in the range of $+N/4 \rightarrow +N/2$, and hence by monitoring the $\mathbf{BER}[\mathbf{m}]$ at these values, optimal compensation BW ($\mathbf{B}_{\mathbf{C},\text{opt}}$) can be chosen.
- The detection method must be decided whether polarization control is employed or not, whether homodyne or heterodyne, and whether with or without IRF if the heterodyne detection is used, which determine \mathbf{d} , and δ_{pol} .
- The OFDM signal parameters must be known (referring to Section 3.3.2.1), which are the sampling frequency $\mathbf{F}_{\mathbf{S}}$, \mathcal{FFT} size $\mathbf{N}_{\mathcal{F}}$, number of modulated-SCs \mathbf{N} , number of

pilot-SCs \mathbf{N}_p , number of in-band zero-SCs \mathbf{N}_{ZI} , number of bits per symbol in the complex mapper \mathbf{m} , number of OFDM's data symbols per frame \mathbf{M}_{dt} , and number of OFDM's symbols per training symbol \mathbf{M}_{tr} (either 1 or 2). In this analysis, only one OFDM sub-channel per polarization is assumed.

- Length of the cyclic prefix \mathbf{N}_{CP} and the overhead penalty \mathbf{PEN}_{oh} are \mathbf{L} -dependence, hence either \mathbf{N}_{CP} and \mathbf{PEN}_{oh} equations or an average values are used in the calculation.
- In (7.44) $\chi[\mathbf{m}]$ is required, which is calculated from (7.28) for every selected \mathbf{m} .
- For any chosen compensation BW in number of frequency samples \mathbf{N}_C , $\mathbf{x} = \mathbf{PSPR}_{opt}$ expressed by (7.45-a), should always be used when substituting in (7.44).
- The side pilot-tone's frequency index must always satisfies the minimal-filtering required gap condition, which is $|\mathbf{k}_p| \geq (\mathbf{N} + \mathbf{N}_C)/2$.
- $\hat{\sigma}_{ICIN}^2[\mathbf{m}]$ is estimated from (7.36), and (7.38) for both SCLs. After this point, $\mathbf{SNR}_b[\mathbf{m}]$ is calculated and can be substituted in (7.46) if $\mathbf{m} = 2$ or 4.
- $\hat{\sigma}_\phi^2[\mathbf{m}]$ is estimated from (7.39), and (7.40), or (7.43) and then substituted in (7.46).
- For a given \mathbf{L} , OFDM's and SCLs' parameters, and for a range of \mathbf{N}_C , then $\mathbf{B}_{C,opt}$ that achieves the targeted \mathbf{BER} at the worst-SCs, and at a specific \mathbf{OSNR}_d can be decided.

The optimal compensation BW ($\mathbf{B}_{C,opt}$) selection is a critical issue, since it requires compromising between the optimal performance, and the highest BW-efficiency \mathbf{BW}_{eff} by making the guard-band \mathbf{BW}_G as small as possible. However, it also depends on the FFL realization structure, since the pilot-tone's frequency has to be maintained within the FFL-BPF's BW during the long-term transmission, and hence SCLs' frequency stability becomes an issue.

7.3.7.2 Calculation example

The OFDM signal parameters are $\mathbf{F}_S = 10\text{GSps}$, $\mathbf{N}_F = 256$, $\mathbf{N} = 200$, $\mathbf{N}_p = 0$, $\mathbf{N}_{ZI} = 1$ (DC-SC), $\mathbf{m} = 2$ (QPSK), $\mathbf{M}_{dt} = 32$, $\mathbf{M}_{tr} = 2$, \mathbf{N}_{CP} and \mathbf{PEN}_{oh} are \mathbf{L} -dependent, and hence they are assigned accordingly. Note that the pilot-tone is assumed to be externally inserted to expand the range of \mathbf{N}_C selection while maintaining $|\mathbf{k}_p| \geq (\mathbf{N} + \mathbf{N}_C)/2$ valid. Assuming all spans in the optical link are identical with span length of 60km, total span

loss of 15dB, the EDFA's gain equals the span loss with noise figure of 6dB, hence for the range of P_{ch} mentioned before, the available $OSNR_d$ versus L is shown in Fig. 7.30.

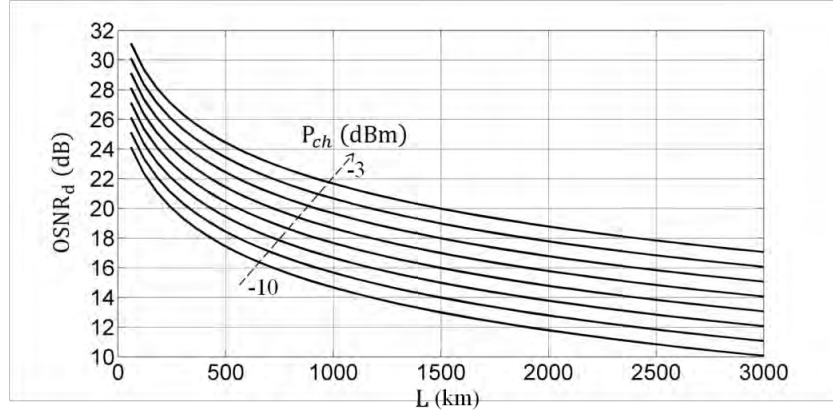


Fig. 7.30: Available $OSNR_d$ of the given example versus L with P_{ch} range of $[-10, -3]$ dBm. The optical link specifications are given in the text.

Now if N_{CP} is set to be just equal the accumulated dispersion, then for the given L range and OFDM signal's BW yields $N_{CP} \geq \{\beta_D(L) \cdot BW_{nn}\} \cdot F_S \approx \beta_D(L) \cdot F_S^2 \cdot N/N_F$, and the N_{CP} interval is given by $N_{CPi} \geq [0, 32]$. Hence from (3.26), the maximum overhead penalty is given by $PEN_{ohmax} = (1 + M_{tr}/M_{dt}) \cdot (1 + N_{CPmax}/N_F) \approx 1.2$ (0.775dB). For simplicity, $PEN_{oh} = 1.15$ (0.6dB) will be used for the whole L range. Therefore, from (7.44), \mathcal{W}_g can have the following values $\mathcal{W}_g \approx 2.783$ ($\delta_{pol} = 2$, and $d = 1$), which is chosen in the current calculation, $\mathcal{W}_g \approx 1.39$ ($\delta_{pol} = 2$, and $d = 2$, or $\delta_{pol} = 1$, and $d = 1$), and $\mathcal{W}_g \approx 0.7$ ($\delta_{pol} = 1$, and $d = 2$). The SCLs' parameters, N_C , and L are left as the independent variables for performance investigation. The remaining required variables in the $BER[m]$ estimation are $\chi[m]$, which is calculated from (7.28), $\dot{\sigma}_{ICIN}^2[m]$, which is estimated from (7.36), and (7.38), and $\dot{\sigma}_\phi[m]^\circ$, and $\dot{\sigma}_\phi^2[m]$, which are estimated from (7.39), and (7.40), or (7.43). In the 1st calculation, only the white FN is counted for both SCL's with $H_c[k] = 1$ and $\delta f_1 = \delta f_2 = 10$ MHz, and the preliminarily assigned distance L is from 100km to 3000km. The optimal N_C is calculated with respect to $m = 60-80$ since the noisier modulated-SCs are expected to be in this range. By following the aforementioned calculation procedure, all modulated SCs have to reach the targeted BER (before the hard-decision is accomplished) of 10^{-3} with minimal $OSNR_d$. The calculation is conducted with $k_p = -(N+N_C)/2 - 1$, and the results are shown in Fig. 7.31, and 7.32. The optimal compensation BW $B_{C,opt}$ is optimized with respect to

$m = 75$, and found to be a function of L , however, an average value of $B_{C,opt} \approx 12 \cdot \Delta f$, or $N_{C,opt} = 12$ is the best choice along the whole L range with $PSPR_{opt} = 0.227$ (-6.44dB). As shown in Fig. 7.31, the maximum range is also limited by the available OSNR for the given link; besides, the penalty involved in the compensation process is unacceptable compared with the ideal one, which is 4.73dB.

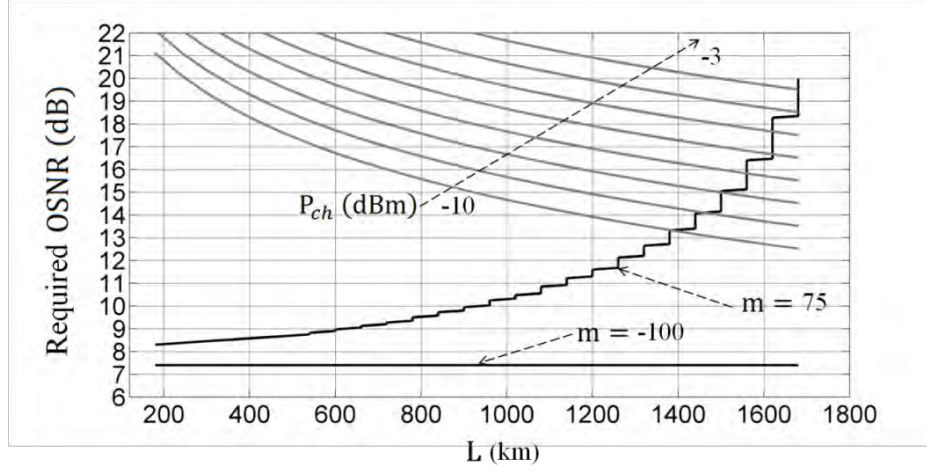


Fig. 7.31: Required OSNR for $m = 75$, and $m = -100$ with the available OSNR (gray colored curves) versus distance in PA-FFL CO-OFDM system with $\delta f_1 = \delta f_2 = 10\text{MHz}$, $N_{C,opt} = 12$, $PSPR_{opt} = 0.227$ (-6.44dB), and $k_p = -107$. The required OSNR increase is due to the increase of differential PN PSD due to dispersion (Chapter 6). The other details are in the text.

In fact, if $N_{C,opt} = 1$, and the ICI term is zero, then there is still a 1.2dB penalty due to PEN_{oh} , and the compensation process. Note that for a long-haul link with PA-FFL and relatively large TX-LO-SCL linewidth, the even power distribution of the OFDM's SCs is no more efficient and an adaptive power distribution highly recommended, however, uneven power distribution requires an adequate knowledge about the link's and SCL's parameters. The BER of the noisier modulated-SC, which is chosen carefully to be $m = 75$, is compared with lowest-noise modulated-SC, which definitely is $m = -100$ as shown in Fig. 7.32. In the 2nd calculation, a comparison is held between two cases which both have $\delta f_1 = \delta f_2 = 5\text{MHz}$, however, in the first one only the white FN with $H_c[k] = 1$ is counted, while in the second one, $RIN_L(0) = -140\text{dBc/Hz}$, $F_R = 2\text{GHz}$, $\Gamma = 200\text{MHz}$, $K_z = 460\text{MHz}$ are assumed. From the calculation results, a penalty of approximately 0.5dB to 1.0dB is observed due to the relaxation oscillation and the IN effects as shown in Fig. 7.33. In both cases, the average value of $B_{C,opt} \approx 7 \cdot \Delta f$, or $N_{C,opt} = 7$, which is optimized over the whole L range with $PSPR_{opt} = 0.174$ (-7.6dB), and $k_p = -105$.

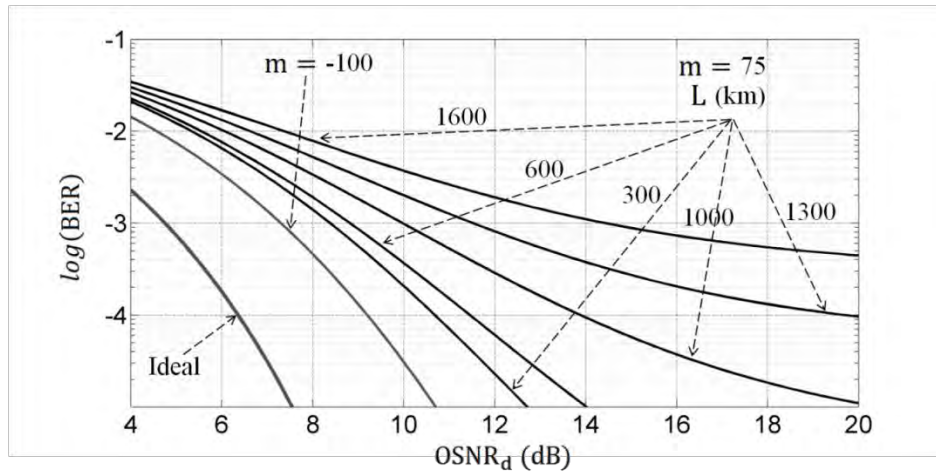


Fig. 7.32: BER of for $m = 75$, and $m = -100$ versus distance with $\delta f_1 = \delta f_2 = 10\text{MHz}$, $N_{c,opt} = 12$, $\text{PSPR}_{opt} = 0.227$ (-6.44dB), and $k_p = -107$. The other details are in the text.

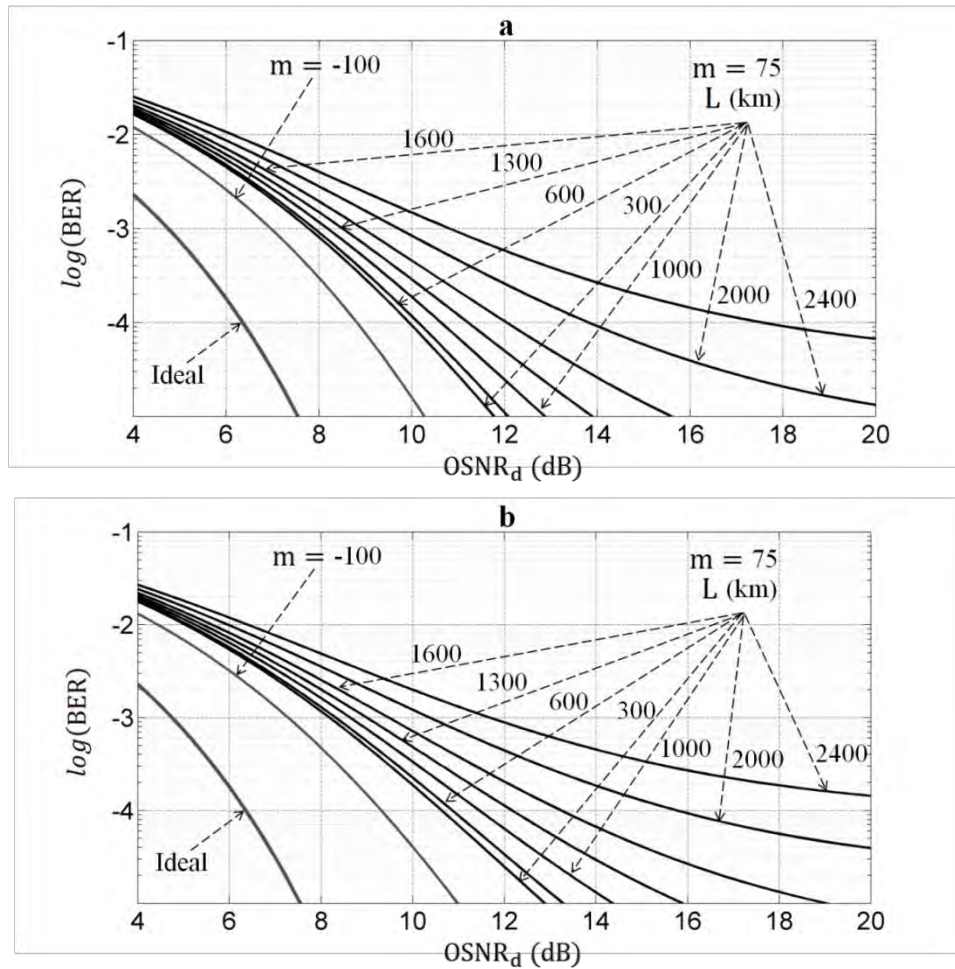


Fig. 7.33 BER of for $m = 75$, and $m = -100$ versus distance with $\delta f_1 = \delta f_2 = 5\text{MHz}$, $N_{c,opt} = 7$, $\text{PSPR}_{opt} = 0.174$ (-7.6dB), and $k_p = -105$. In (a), only the white FN is counted, while in (b), all the SCL's parameters are counted with $\text{RIN}_L(0) = -140\text{dBc/Hz}$, $F_R = 2\text{GHz}$, $\Gamma = 200\text{MHz}$, $K_Z = 460\text{MHz}$, and other details are in the text.

In the 3rd calculation, only the white FN is counted for both SCL's with $\mathbf{H}_c[\mathbf{k}] = 1$ and $\delta f_1 = \delta f_2 = 1\text{MHz}$ to investigate the distance expansion under relatively low PN. The performance curves show a significant improvement, and distance of 6000km becomes possible if the available OSNR can reach the required 8dB. Besides, the divergence between the $\text{BER}[m = 75]$, and $\text{BER}[m = -100]$ is about 0.25dB at $\text{BER} = 10^{-3}$ and $L = 300\text{km}$ as shown in Fig. 7.34. In this case, $N_{c,opt} = 3$, $\text{PSPR}_{opt} = 0.114$ (-9.4dB), and $k_p = -102$. In the last calculation, only the white FN is counted for both SCL's with $\mathbf{H}_c[\mathbf{k}] = 1$, however, the TX-LO-SCL's linewidth is set to be very small, $\delta f_1 = 100\text{kHz}$, and the RX-LO-SCL's linewidth is set to be relatively large, $\delta f_2 = 10\text{MHz}$. The design parameters are found to be similar to the 2nd test with $N_{c,opt} = 7$, $\text{PSPR}_{opt} = 0.174$ (-7.6dB), and $k_p = -105$. However, the interesting behavior, and as expected, is that the performance curve exhibits very low sensitivity versus fiber's distance with tolerable penalty as shown in Fig. 7.35. Hence it is expected that higher δf_2 can also be used with marginal changes in the performance curve, which in this specific condition, the PA-FFL becomes incomparable with any other detection proposals of CO-OFDM in presence of large PN. Note that at $m = -100$, the cross-noise itself is much lower (about 3dB) than that of $m = 75$, and this is why $\text{BER}[m = -100]$ is always better than $\text{BER}[m = 75]$ even when the strong dispersive components (PN and ICI) becomes weak due to low δf_2 .

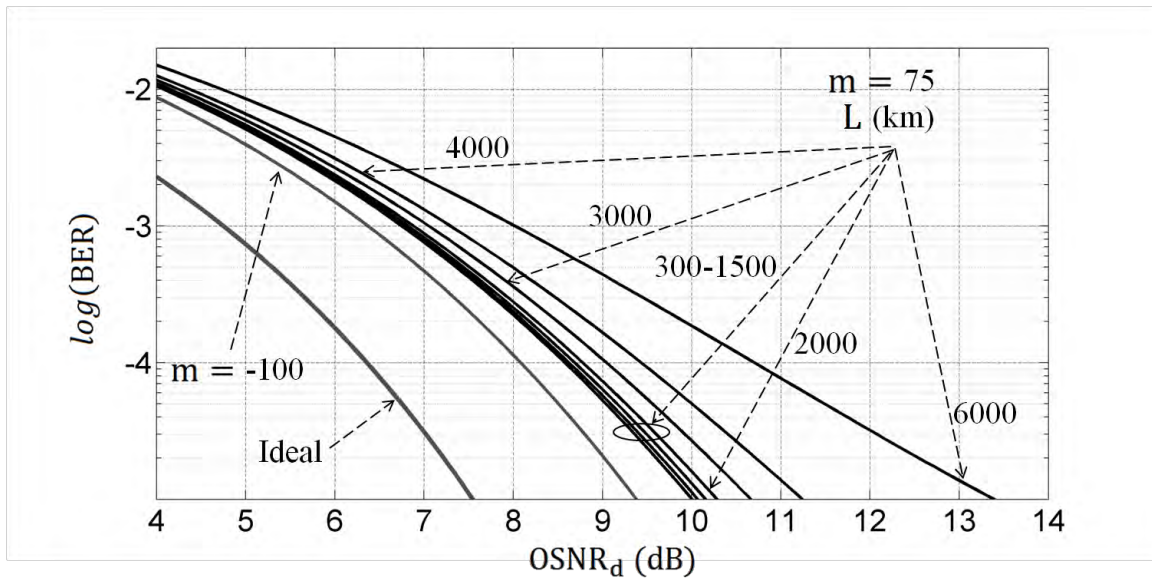


Fig. 7.34: BER of $m = 75$, and $m = -100$ versus distance with $\delta f_1 = \delta f_2 = 1\text{MHz}$, $N_{c,opt} = 3$, $\text{PSPR}_{opt} = 0.114$ (-9.4dB), and $k_p = -102$. Other details are in the text.

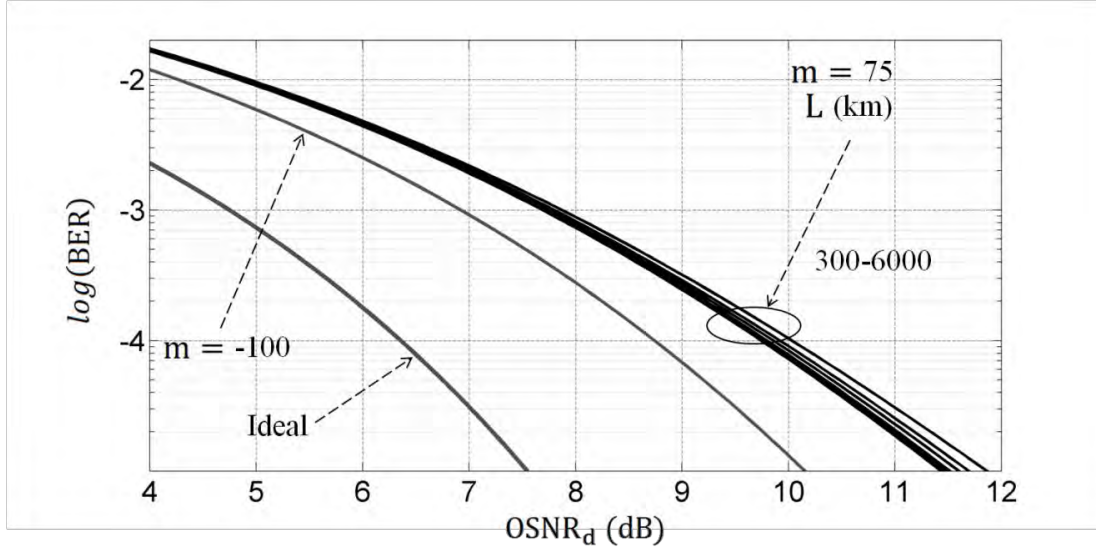


Fig. 7.35: BER of $m = 75$, and $m = -100$ versus distance with $\delta f_1 = 100\text{kHz}$, $\delta f_2 = 10\text{MHz}$, $N_{c,opt} = 7$, $\text{PSPR}_{opt} = 0.174$ (-7.6dB), and $k_p = -105$. Other details are in the text.

7.3.8 Linewidth tolerance

In the FFL block shown in Fig. 7.11, when time delay of the delay-line is set to be equal the BPF's group delay, then the less-corrupted SC is the pilot-tone itself as mentioned before. However, this setting might not be useful in long-haul UWB signal with relatively large TX-LO-SCL's linewidth since the worst-corrupted modulated-SC, which is a performance indicator of the whole signal, might not reach the targeted **BER**. Thus if the differential time delay between the delay-line and BPF's group delay is set in such a way that the less-corrupted SC is the DC-SC, then a much better results can be obtained, and the overall system's performance becomes less affected by the TX-LO-SCL's linewidth versus distance. Yet, not all commercially available SCLs can be used in CO-OFDM system with allowable penalties even when the PA-FFL is employed, and hence there is a maximum acceptable linewidth range for a given system, and for a given distance.

One of the major problems in optical OFDM's development is that there are no standard optical OFDM specifications, and hence the researcher has to investigate a wide range of possible OFDM parameters for generalization purposes. However, in this section, two OFDM system's settings are adopted;

- 1- in the 1st setting, $F_s = 6.4\text{GSps}$, $N_f = 256$, $N = 200$, $N_p = 0$, $N_{ZI} = 1$ (DC-SC), $m = 2$ or 4 (QPSK or 16-QAM), $\mathcal{W}_g = 5$ ($\delta_{pot} = 2$, and $d = 1$), and $\text{PEN}_{oh} = 1$, and

2- in the 2nd setting, $F_S = 12.8\text{GSps}$, $N_{\mathcal{F}} = 512$, $N = 400$, $N_p = 0$, $N_{ZI} = 1$ (DC-SC), $m = 2$ or 4 (QPSK or 16-QAM), $\mathcal{W}_g = 2.5$ ($\delta_{pot} = 2$, and $d = 1$), and $PEN_{oh} = 1$.

Both systems can be used as references for comparison purposes. The null-to-null BW of the first system is $BW_{nn} \approx 5\text{GHz}$, with maximum data-rate of 10Gbps (QPSK) and 20Gbps (16QAM), while for the second system, $BW_{nn} \approx 10\text{GHz}$, with maximum data-rate of 20Gbps (QPSK) and 40Gbps (16QAM). Besides two delay-line adjustments will be examined. In the 1st adjustment, the pilot-tone is the less-corrupted subcarrier, while in 2nd adjustment; the DC-SC is the less-corrupted SC. Since the average BER of the whole SCs is dominated by the worst-corrupted SCs, then these SCs are only considered.

In the 1st delay-line adjustment, the following parameters are used:

- 1- $OSNR_{\text{minimal}}$ at which $BER[m_{\text{worst-corrupted}}] = 10^{-3}$ is achieved,
- 2- $\delta f = \delta f_1 = \delta f_2$,
- 3- $N_{C,opt}$ is chosen versus δf , L , and m , and
- 4- $PSPR_{opt}$ is calculated versus $N_{C,opt}$.

In the 2nd delay-line adjustment, the following parameters are used:

- 1- $OSNR_{\text{minimal}}$ at which $BER[m_{\text{worst-corrupted}}] = 10^{-3}$ is achieved,
- 2- $\delta f = \delta f_1 = \delta f_2$,
- 3- $N_{C,opt}$ is chosen to be fixed versus L , and varies with δf , and m , as given in Table 7.1,
- 4- $PSPR_{opt}$ is calculated versus $N_{C,opt}$, and
- 5- Delay of the delay-line is adjusted in every different distance.

Table 6.1: $N_{C,opt}$ in the 2nd delay-line adjustment for the two OFDM settings versus δf , and m .

δf (MHz)	1 st Setting QPSK	2 nd Setting QPSK	1 st Setting 16-QAM	2 nd Setting 16-QAM
0.1	1	1	2	3
0.2	1	2	4	5
0.5	2	3	8	10
1.0	4	5	14	14
2.0	6	6	20	22
5.0	14	10	40	30
10.0	20	14	60	50

1st delay-line adjustment

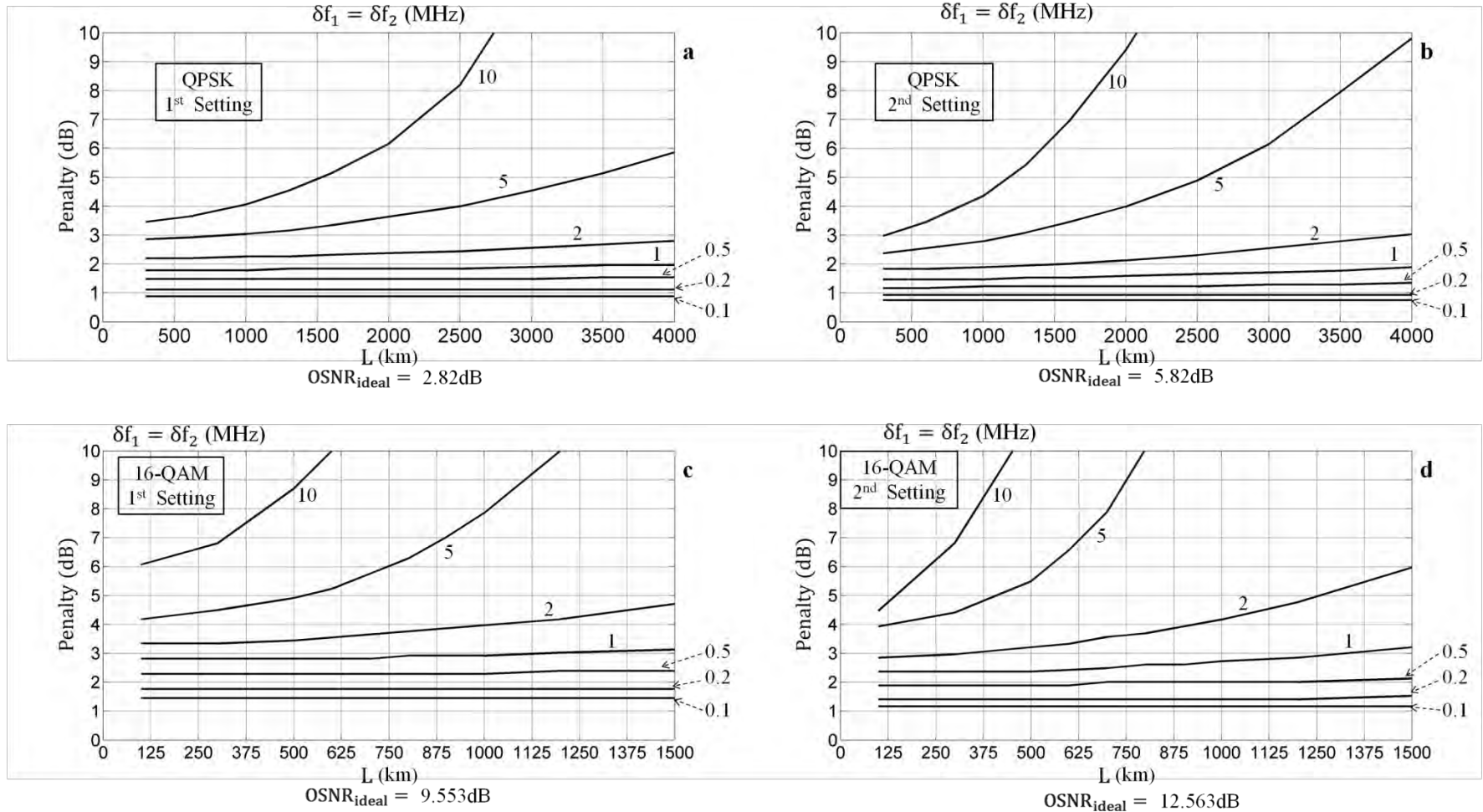


Fig. 7.36: OSNR penalty corresponds to SCLs linewidths versus distance of the 1st delay-line adjustment and the two suggested OFDM settings (given in the text). In (a), (b), (c), and (d), real-time simulation of the 1st setting with QPSK-mapping, 2nd setting with QPSK-mapping, 1st setting with 16-QAM mapping, and 2nd setting with 16-QAM respectively.

2nd delay-line adjustment

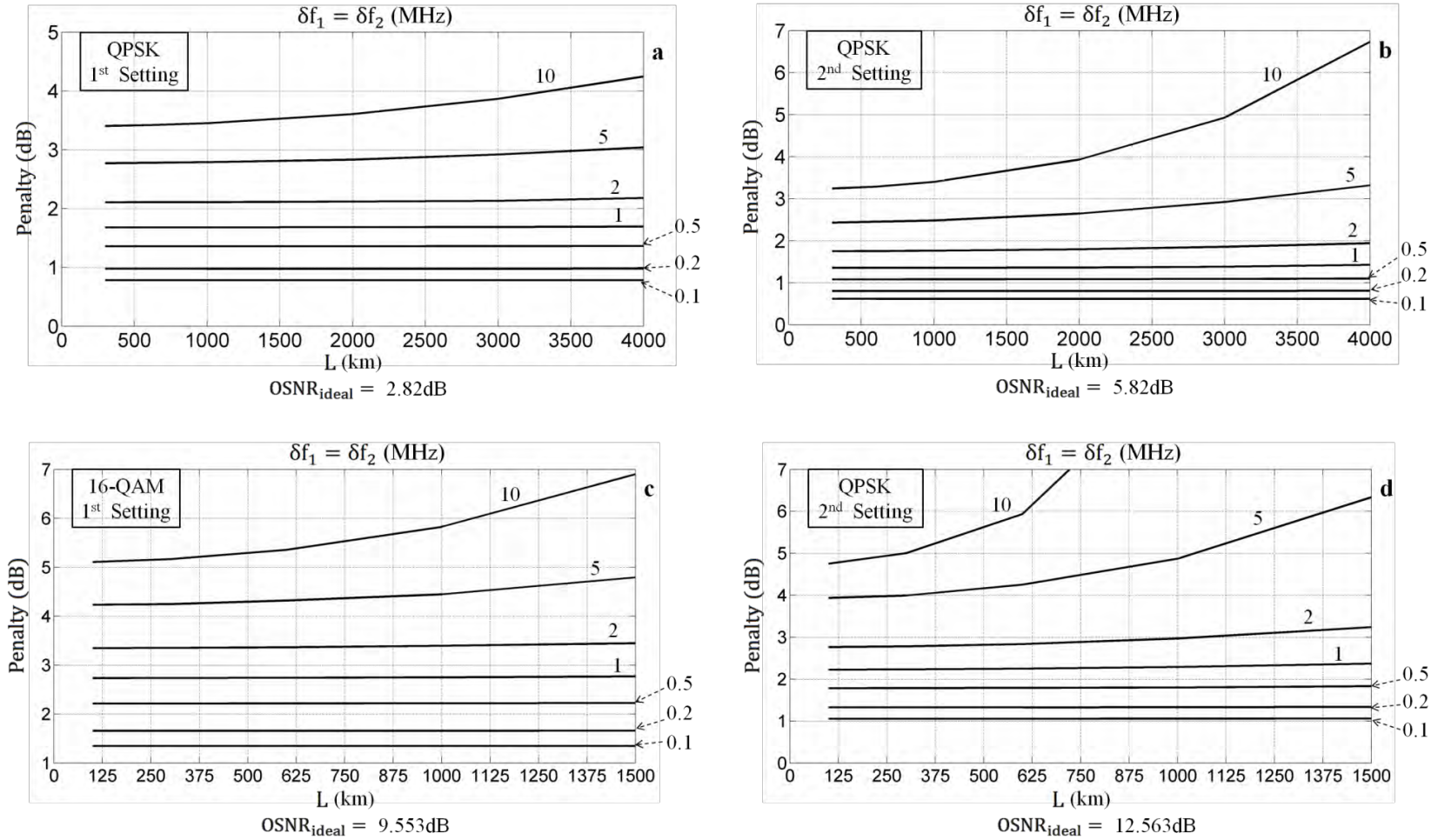


Fig. 7.37: OSNR penalty corresponds to SCLs linewidths versus distance of the 2nd delay-line adjustment and the two suggested OFDM settings (given in the text). In (a), (b), (c), and (d), 1st setting with QPSK-mapping, 2nd setting with QPSK-mapping, 1st setting with 16-QAM mapping, and 2nd setting with 16-QAM respectively.

For the 1st delay-line adjustment, the results shows that maximum SCLs linewidth of 2MHz can be used for QPSK mapping and for both system settings up to 4000km assuming **3dB** allowable **OSNR** penalty, and 1MHz for 16-QAM of both system settings up to 1500km with same **OSNR** penalty, as shown in Fig. 7.36. Higher values of δf might be used but at the expense of the allowable penalty and/or distance. For the 2nd delay-line adjustment, the results shows that, maximum SCLs linewidth of 5MHz can be used for QPSK mapping and for both system settings up to 4000km assuming **3dB** allowable **OSNR** penalty, and approximately 2MHz for 16-QAM of both systems and up to 1500km with same **OSNR** penalty, as shown in Fig. 7.37. Obviously linewidth of 10MHz for the TX-LO-SCL and the RX-LO-SCL can be used up to 4000km reach with QPSK mapping but with **4.25dB** penalty. Thus higher values of δf might be used but at the expense of the allowable penalty and/or distance. Many modulated SCs within the signal exhibit a better **BER**; however, the worst-corrupted ones dominate the overall performance.

Schmidt *et al.* have noticed first the uneven **BER** over the SCs in their experimental demonstration of DDO-OFDM [28], while Peng demonstrated this effect in more theoretical details focusing on the DDO-OFDM and the conventional CO-OFDM [41]. Although the analysis in this chapter can be compared with Peng's work, it is presented here for the first time focusing on CO-OFDM systems with PA-FFL.

7.3.9 Optimal side pilot-tone insertion conditions

The side pilot-tone can either be one of the SCs, or externally inserted, and in both cases, two conditions are required to be fulfilled for optimal performance, which are

$$|k_p| \geq (N + N_{C,opt})/2, \text{ and } \mathbf{PSPR} = \mathbf{PSPR}_{opt}.$$

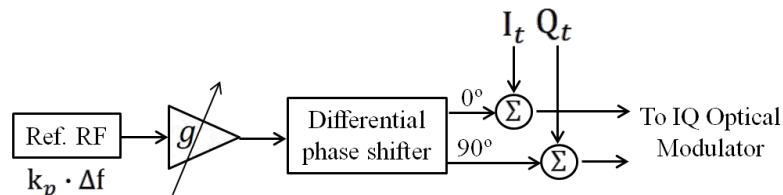


Fig. 7.38: Possible configuration for externally side pilot-tone insertion assuming an IQ optical modulator is employed in the TX front-end.

The externally-inserted side pilot-tone can be implemented using an RF IQ modulator with the configuration shown in Fig. 7.38 without restrictions [8].

In this setup, a synthesized reference RF source is required with frequency of $\mathbf{k}_p \cdot \Delta \mathbf{f}$, an RF amplifier with adjustable gain or with fixed gain followed by a variable RF attenuator, a 90deg narrowband differential phase shifter, and two power combiners (either resistive or transformers-based). The gain is adjusted with respect to the \mathbf{I}_t or \mathbf{Q}_t tributary power just after the AA-LPF such that the \mathbf{PSPR}_{opt} condition given by (7.45) is met. Note that the positive and negative \mathbf{k}_p sign can be easily set by connecting the 0° branch with \mathbf{I}_t or \mathbf{Q}_t and the 90° branch with \mathbf{Q}_t or \mathbf{I}_t respectively. While, when the side pilot-tone is one of the SCs, no additional hardware are required, and \mathbf{PSPR}_{opt} can easily be adjusted via DSP setting, however, a special attention must be paid to avoid the discontinuity that emerges due to the CP insertion. That is, every SC completes exactly an integer number of cycles in every symbol, however, when the CP is introduced then a discontinuity occurs between the last time sample of the current symbol, and first time sample of the new symbol, while continuity is maintained within the symbol itself. However, when a pilot-tone is considered, this discontinuity must be overcome since the pilot-tone would not be a pure sinusoid but a periodic signal with a frequency of $\mathbf{k}_p \cdot \Delta \mathbf{f}$, and a shape that depends on the amount of discontinuity (modulation depth), which can be expanded using Fourier series.

This discontinuity can be easily corrected by shifting the pilot-tone's phase periodically (every symbol). For instance let $\mathbf{F}_S = 10\text{GSps}$, $\mathbf{N}_F = 256$, $\mathbf{N} = 100$, $\mathbf{N}_p = 1$ (side pilot-tone), $\mathbf{N}_{ZI} = 1$ (DC-SC), $\mathbf{m} = 4$ (16-QAM), $\mathbf{N}_{CP} = 16$, and the required side pilot-tone's frequency index is $\mathbf{k}_p = 73$.

If no discontinuity correction is attempted, then the pilot-tone power is spread, and even no component at $\mathbf{k} = 73$ exists as shown in Fig. 7.39a. While when a periodic pilot-tone's phase shifting is done, then a pure sinusoid can always be obtained whatever \mathbf{k}_p is, as shown in Fig. 7.39b. The periodic pilot-tone's phase shift can be expressed as

$$\varphi_{sh}[\ell] = -2\pi \cdot \left(1 + \mathbf{k}_p \cdot \left(1 - \frac{\mathbf{N}_{CP}}{\mathbf{N}_F} \right) \right) \cdot (\ell - 1) \quad (7.48)$$

Accordingly, the frequency vector's input is $\exp(\mathbf{j} \cdot \varphi_{sh}[\ell])$ at the cell index of $\mathbf{k}_p + \mathbf{1}$ for positive pilot-tone, and $\mathbf{N}_F - |\mathbf{k}_p| + \mathbf{1}$ for negative pilot-tone noting that for negative indexes, then \mathbf{k}_p in (7.48) is substituted by $\mathbf{N}_F - |\mathbf{k}_p|$.

Therefore, whenever $\mathbf{N}_{C,opt} < 2(\mathbf{N}_{\mathcal{F}} - \mathbf{N})$, then it is much more efficient to insert the side pilot-tone as one of the SCs, since no additional analog components are required. However, the oversampling ratio γ_s and anti-aliasing filter's order discussed in Sections 3.3.2.1 and 3.3.4, have to be taken into account. In this case, (3.24) becomes

$$\gamma_s = \frac{\mathbf{N}_{\mathcal{F}}/2}{(1 + \mathbf{N}_{\mathbf{G}} + \mathbf{N}/2)} \quad (7.49)$$

where $\mathbf{N}_{\mathbf{G}}$ is the frequency gap measured in samples, or $\mathbf{BW}_{\mathbf{G}} = \mathbf{N}_{\mathbf{G}} \cdot \Delta f$.

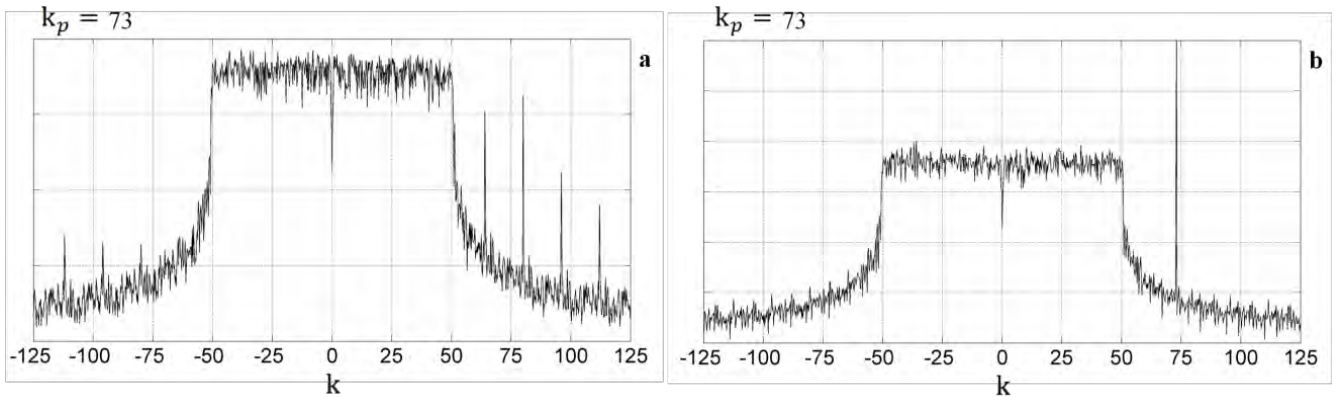


Fig. 7.39: Side pilot-tone as one of the SCs with unequalized CP's discontinuity in (a), and the equalized one in (b) assuming in both $\mathbf{k}_p = 73$. Here $\mathbf{F}_s = 10\text{GSps}$, $\mathbf{N}_{\mathcal{F}} = 256$, $\mathbf{N} = 100$, $\mathbf{N}_p = 1$ (side pilot-tone), $\mathbf{N}_{z1} = 1$ (DC-SC), $\mathbf{m} = 4$ (16-QAM), and $\mathbf{N}_{cp} = 16$.

7.4 Conclusions

In this chapter, performance of the CO-OFDM system with and without PA-FFL is discussed thoroughly. The first important result is that, in the conventional QPSK-CO-OFDM system (without PA-FFL), $\delta \mathbf{f}_{\text{Neq.}} = \delta f_{\mathbf{N}1} + \delta f_{\mathbf{N}1} < 0.05$, or $\sigma_{\mathbf{W}}^2(\mathbf{T}_{\mathcal{F}}) < 0.3\text{rad}^2$ can be tolerated, and the SCs can be recovered with a penalty of higher than 3dB at pre-hard-decision-BER of 10^{-3} . This is true provided that an ideal post- \mathbf{FFT} equalization technique is used, and without power margins, however, a much lower $\delta \mathbf{f}_{\text{Neq.}}$ must be used in a higher-order constellation. The second result is that, the ICI noise can only be modelled as GRV for low $\delta \mathbf{f}_{\text{Neq.}}$, otherwise the statistical nature of a relatively high $\delta \mathbf{f}_{\text{Neq.}}$ results a higher performance degradation than that if it is considered as a GRV, which requires further investigations. The PA-FFL has been proven here to be an

efficient practical candidate for combating the high SCLs' linewidth problem with two important delay-line adjustments.

First when the time-delay of the delay-line is adjusted to equalize the FFL BPF's group delay only once using back-to-back setup, then the PA-FFL technique is efficient in long-haul CO-OFDM when the TX-LO-SCL's linewidth δf_{N1} is relatively small, or as long as the induced powerful dispersive PN component is maintained to be small, otherwise the maximum reach is limited at relatively broad δf_{N1} . That is when the TX-LO-SCL's linewidth is narrow, the RX-LO-SCL's linewidth has a marginal influence in the performance degradation, and long-haul links of UWB OFDM becomes efficient.

The optimal compensation BW $\mathbf{B}_{C,opt}$ and \mathbf{PSPR}_{opt} have to be chosen to improve the transmission efficiency, and as discussed earlier, these two parameters are functions of the link parameters, SCLs' specifications, and the adopted mapping.

Second, if the time-delay of the delay-line is adjusted depending on the distance such that DC-SC (the centre SC) is always the less-corrupted SC, a better performance can be achieved, as in [127].

For instance for QPSK-CO-OFDM, $\delta f_{N1} = \delta f_{N2} = 2\text{MHz}$ in the 1st adjustment and $\delta f_{N1} = \delta f_{N2} = 5\text{MHz}$ in the 2nd one can be used with 3dB **OSNR** penalty at pre-hard-decision-**BER** of 10^{-3} up to 4000km. While for 16-QAM-CO-OFDM, $\delta f_{N1} = \delta f_{N2} = 1\text{MHz}$ in the 1st adjustment and $\delta f_{N1} = \delta f_{N2} = 2\text{MHz}$ in the 2nd one can be used with 3dB **OSNR** penalty at pre-hard-decision-**BER** of 10^{-3} up to 1500km. The 2nd adjustment can be even used for higher distances and linewidth with slightly higher penalties than the given one. It is also found that in broad TX-LO-SCL linewidth values, long distances, and UWB OFDM signals, the transmission efficiency can be improved when the power distribution over the OFDM's SCs is not even but depends on the pilot-tone's frequency index. Besides, it is not always recommended to choose the optimal parameters since other parameters should also be considered such as \mathbf{BW}_{eff} , the added margins, and SCLs' stability. The results of this chapter will be exploited in Chapter 8 to yield the optimal long-haul homodyne PA-FFL CO-OFDM design with 100Gbps data-rate.

Chapter 8

Design of an Optimal 100Gbps Homodyne CO-OFDM System

8.1 Introduction

In this chapter an optimal 100Gbps homodyne CO-OFDM design is presented assuming that a commercially available semiconductor laser (SCL) is used as the optical carrier in the transmitter (TX) and local oscillator (LO) in the receiver (RX). The TX and RX structures are modified benefiting from the results of Chapter 7 such that lowest penalty due to the SCLs' noise is attained, as well as all practical considerations for reliable long-term transmission are taken into account. In the proposed design, the pilot-aided feedforward loop (PA-FFL) for SCL phase noise (PN) reduction, polarization multiplexing (Pol-Mux) for doubling the data-rate, and polarization diversity structure to overcome state-of-polarization fluctuations are all employed. Although high digital-to-analog convertor (DAC) and analog-to digital convertor (ADC) requirements must still be fulfilled, this design is the promising candidate for the future CO-OFDM developments since no standard OFDM design has yet been adopted in the real optical network. The main goal of this chapter is to design a homodyne 100Gbps CO-OFDM system with an optimal performance, and best BW efficiency (BW_{eff}), using SCLs with arbitrary noise characteristics.

8.2 Optimal 100Gbps homodyne CO-OFDM design

8.2.1 Preliminary design parameters

In this proposed optical link, net data-rate of 100Gbps is assumed to be transmitted and received with minimal cost and optimal performance using homodyne CO-OFDM system and taking all the aforementioned consideration into account. A single compact OFDM signal is designed to meet this goal with 32-QAM mapping and Pol-Mux such that 50Gbps throughput per subchannel (per polarization) is assumed. As PA-FFL is adopted for PN compensation, an auxiliary RF circuit is introduced in the RX, which its function is similar to the discrete complex model discussed in Section 7.3.1. Although DSP techniques can be used for this purpose, however, analog solutions are better by far

regarding to the frequency resolution and cost. Besides, as the **APC** is avoided here, a polarization diversity structure is employed in the RX's main detection block, and the RX's auxiliary circuit as shown in Fig. 8.1.

Referring to the analysis in Section 3.3.2.1, the following parameters are initially set.

- RS(255, 239) is used as the FEC code with $\alpha_{\text{FEC}} = 0.9373$.
- The training symbol (**TrS**) consists of two OFDM symbols $\mathbf{M}_{\text{tr}} = 2$, and it is inserted after every 25 OFDM data symbols $\mathbf{M}_{\text{dt}} = 25$. This rate might not be the optimal one, however, the value used by Jansen *et al.* in their experimental work is adopted here [6].
- A new TrS developed by the author is adopted here for its superiority in the I/Q imbalance correction simplicity over the available TrSs, which will be discussed soon.
- Initial value of the cyclic prefix is set to be $\mathbf{N}_{\text{CP}} = 16$, which can be lower or higher depending on the distance **L**.
- Only one subchannel is set with the pilot-tone, which is one of the subcarriers (**SC**)s as discussed in Section 7.3.9. This ensures that the pilot-tone is extracted with a constant envelope and without a possibility of envelope fluctuations due to the channel response.
- The baseband (**BB**) OFDM design's common parameters of both subchannels are as follows: $\mathbf{N}_{\mathcal{F}} = 1024$, $\mathbf{N} = 808$, $\mathbf{N}_{\text{ZI}} = 1$ (DC-SC), $\mathbf{N}_{\text{CP}} = 16$, $\mathbf{M}_{\text{tr}} = 2$, $\mathbf{M}_{\text{dt}} = 25$, $\mathbf{m} = 5$ (32-QAM), $\alpha_{\text{FEC}} = 0.9373$, and from (2.25) yields, $\mathbf{F}_{\text{S}} = 15\text{GSps}$.
- The common overhead penalty of both subchannels is calculated from (6.26), assuming the pilot-tone is excluded, to be $\mathbf{PEN}_{\text{oh}} \approx 1.1$ (0.4dB).
- For the subchannel which is without a pilot-tone, The DAC and ADC requirements are $\mathbf{F}_{\text{S}} = 15\text{GSps}$, and $\mathbf{q}_b \geq 7\text{bits}$. Besides, $\mathbf{N}_{\text{ZO}} = \mathbf{N}_{\mathcal{F}} - \mathbf{N} - \mathbf{N}_{\text{ZI}} = 215$, and from (2.24), the oversampling ratio is $\mathbf{y}_s \approx 1.266$. Hence, minimal order of the anti-aliasing (**AA**) filter is **7** assuming Chebyshev type II is used as discussed in Section 3.3.4.
- For the subchannel with the side pilot-tone, \mathbf{N}_{ZO} , \mathbf{y}_s , and the AA-filter's order depends on the optimal compensation BW ($\mathbf{B}_{\text{C,opt}}$) of the FFL's bandpass filter (**BPF**), and hence these parameters will be decided next, however, the DAC and ADC requirements are identical to the previous one.

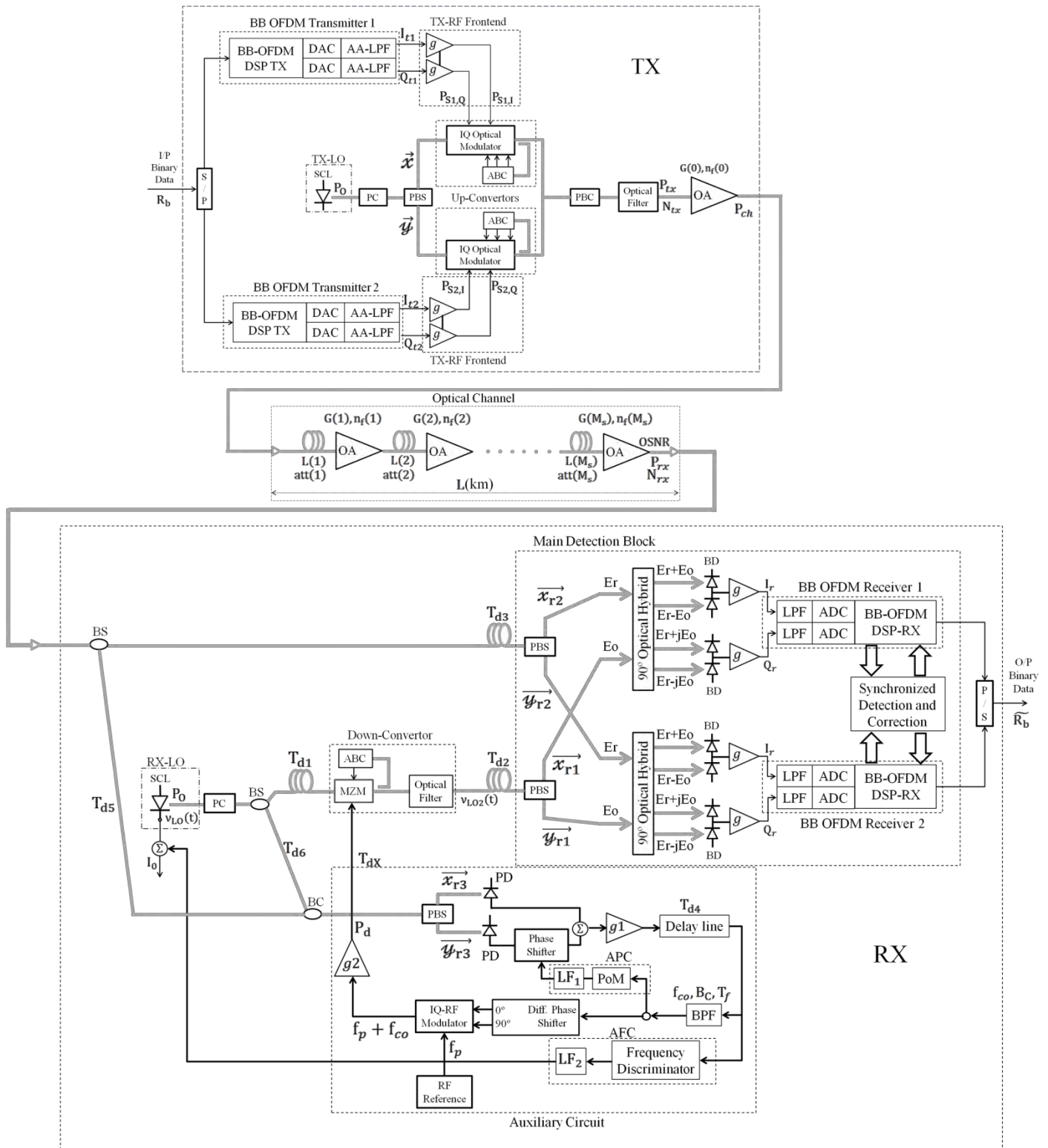


Fig. 8.1: Block diagram of the proposed 100Gbps homodyne CO-OFDM System. Here the gray-colored lines indicate optical fibers, while the black-colored ones are for electrical/RF signals. Parameters details and abbreviations are given in the text.

8.2.2 System Description

In order to fulfill the required data-rate, transmission distance, design considerations discussed in Section 2.5, and to ensure long term operation under different possible SCL specifications, the proposed system shown in Fig. 8.1 is designed as follows.

1- The input (**I/P**) data rate is divided into two tributaries each with 50Gbps data-rate using a two-bit serial-to-parallel (**S/P**) convertor. Each BB-OFDM transmitter produces two continuous-time signals, which are the real \mathbf{I}_t , and the imaginary \mathbf{Q}_t parts of the calculated time-vector (**TiV**) discussed in Section 3.3.6. These two branches are amplified using a wideband balance driver-amplifier (**DA**), which is assumed to have a high 1dB compression-point for a minimal nonlinearity contribution. The IQ optical modulator's driving levels $\mathbf{P}_{S,I}$, and $\mathbf{P}_{S,Q}$ are optimized for the minimal IQ optical modulator's nonlinearity contribution. From the other hand, the commercially available SCL are usually packaged with a polarization-maintained fiber (**PMF**), and hence the SOP is linear and can be easily known. It would be useful in this design if the SCL is equipped with a polarization beam-splitter (**PBS**), such that two linear SOPs are produced in a single package. However, it is also possible to rotate the SOP of the available SCL field by a 45° using a fixed polarization controller (**PC**), and then the two SOPs components are split using a PBS. Here the output (**O/P**) SOPs from the PBS are denoted by \vec{x} and \vec{y} , which are assumed to be the same SOP of the polarization beam-combiner (**PBC**) that is used to combine the two independent CO-OFDM signals. The combined signal is then filtered using either the wavelength division multiplexing (**WDM**) multiplexer or by an external optical BPF, and amplified using the front-end booster amplifier. As discussed in Section 3.4.1, each IQ optical modulator is biased at null for both Mach-Zehnder intensity modulators (**MZM**)s, and the optical phase shifter is biased at $\pi/2$ to form a single sideband modulator (**SSM**). The O/P optical signal is highly attenuated at this biasing condition, and hence the booster amplifier should be chosen to deliver a launch power \mathbf{P}_{ch} per WDM channel in the range of -10dBm to -3dBm, which is the optimal launch power with respect to fiber's nonlinearity [56]. An automatic biasing circuit (**ABC**) is essential for long-term operation due to the fluctuation of the switching voltage \mathbf{v}_π

with time. However, it is a real challenging problem to maintain the biasing voltages of the IQ modulator under low O/P optical power at the required biasing values.

- 2- After the optical link (discussed in Section 3.2.2) and the WDM demultiplexer (filter), the received signal is split into two branches using a beam splitter (**BS**). The **first** branch, which has a fiber length of \mathfrak{L}_1 corresponding to a time-delay of \mathbf{T}_{d5} , is mixed with the RX-LO-SCL's **1st** branch using a beam combiner (**BC**). While the **second** branch, which has a fiber length of \mathfrak{L}_2 corresponding to a time-delay of \mathbf{T}_{d3} , is connected to the main detection block. On the other hand, the RX-LO-SCL's field is split also into two arms using a BS. The **1st** arm, which has a fiber length of \mathfrak{L}_5 corresponding to a time-delay of \mathbf{T}_{d6} , is mixed with **first** branch of the received signal as mentioned before, and the **2nd** arm is connected to an optical down-conversion block with a fiber length of \mathfrak{L}_3 , which corresponds to a time-delay of \mathbf{T}_{d1} . The down-converted optical signal, which would have always (versus time) the same center frequency of the received signal, is connected to the main detection block via a fiber with length of \mathfrak{L}_4 , which corresponds to a time-delay of \mathbf{T}_{d2} . This selection of fiber lengths ensures minimal differential time-delay between the received signal and RX-LO-SCL. Similar to the TX arrangement, SOP of the RX-LO-SCL must be shifted by 45° using a PC directly after the RX-LO-SCL O/P connector, and the shifted SOP has to be maintained up to the two PBSs, which short lengths of fibers. This can be done using short lengths of PMFs for the fiber branches corresponding to \mathbf{T}_{d1} , \mathbf{T}_{d2} , and \mathbf{T}_{d5} .
- 3- In the main detection block, the **second** received signal's branch and the **2nd** RX-LO-SCL's branch after down conversion are analyzed into two linear SOPs using PBSs with reference SOPs of $\{\overrightarrow{x_{r2}}, \overrightarrow{y_{r2}}\}$, and $\{\overrightarrow{x_{r1}}, \overrightarrow{y_{r1}}\}$ respectively. The components of $\{\overrightarrow{x_{r1}}, \overrightarrow{x_{r2}}\}$, and $\{\overrightarrow{y_{r1}}, \overrightarrow{y_{r2}}\}$ are mixed separately using 90° optical hybrids, and then each BB signal is demodulated using an OFDM BB-RX as discussed in Section 3.3.2.2. In this polarization diversity structure, the sampling clock of both RXs has to be from the same reference clock, and clock synchronization is done simultaneously for both RXs, such that the two RXs are synchronized in frequency and time. Finally the O/P data streams of both RXs are combined via a two-bit parallel-to-serial convertor.

4- In the proposed auxiliary circuit, the 1st RX-LO-SCL's branch is mixed with **first** branch of the received signal using a PBC, and then the mixed field is analyzed into two linearly-polarized components using a PBS with a reference SOPs of $\{\vec{x}_{r3}, \vec{y}_{r3}\}$, and then each component is detected separately using a photo-diode (**PD**). Note that in this design, the RX-LO-SCL's power is preferred to be $\geq 5\text{dBm}$ to ensure it is much larger than the received signal's power even after the down conversion process, and to overcome the many power-splits involved in the system. Note also that, since the auxiliary circuit is designed to extract the side pilot-tone and re-mix it again with the RX-LO-SCL, then only narrowband components are required. The two photo-currents are then combined indirectly using a resistive summer. One of the photo-currents is phase-shifted using an automatic phase shifter (**APS**) to ensure a constant pilot-tone's envelope with time. An optional delay-line is placed after the amplified photo-current to adjust the auxiliary circuit's propagation delay T_{dx} , since it is much easier to change the time-delay in the RF domain than in optical domain. An FFL BPF with a center frequency of f_{co} and BW of B_C is used to extract the pilot-tone from the amplified photo-current, and then up-convert it using an RF IQ-modulator with a reference RF source's frequency of f_p . Then the signal is amplified using a driver amplifier with a driving O/P power of P_d . Two control loops are essential in the auxiliary circuit block, which are the APS loop, and automatic frequency control (**AFC**) loop. In the APS loop, the extracted pilot-tone's power is continuously measured to produce an error signal that is used to correct the second photo-current's phase via the APS's loop filter, (**LF₁**), which is designed based on peak-envelope tracking algorithm. While the AFC loop is used to maintain the pilot-tone's center frequency at the FFL BPF's center frequency f_{co} for long-term operation. In the AFC loop, a balanced frequency discriminator or a phase-locked loop (**PLL**) is used to generate the error signal corresponding to the difference between the beat-note frequency and f_{co} , and then a narrowband loop filter (**LF₂**) is used to correct frequency drift of the RX-LO-SCL continuously via current injection at the RX-LO-SCL's driving current port. The complexity of the auxiliary circuit block is considered to be low since it is proposed to be implemented in relatively low RF frequency (less than 1GHz) with narrowband components, which can be integrated in a single chip.

5- This design differs than Shieh's proposal [5] by employing a pre-**FFT** PN compensation, which allows commercially available SCLs to be used, and both proposals are similar to use the lowest requirements of both the DAC and the ADC. It differs than Jansen's proposal [6] by using an optical-FFL using cheap RF and optical components, which is an analog loop that is independent of the ADC requirements. A comparison is held between these three proposals in Section 8.3.

8.2.3 System Analysis

8.2.3.1 Frequency and phase analysis in the auxiliary circuit

The side pilot tone's frequency \mathbf{f}_p is calculated as $\mathbf{f}_p = k_p \cdot \Delta f = k_p \cdot F_S/N_F$,

where \mathbf{k}_p is the side pilot-tone's frequency index. The TX-LO-SCL's instantaneous phase can be written as

$$\phi_1(t) = \phi_{tx}(t) + \phi_x + 2\pi\nu_1 t + 2\pi \int_{-\infty}^t \epsilon_{f1}(t) dt \quad (8.1)$$

where $\phi_{tx}(t)$ is PN component due to the white frequency noise (FN), ν_1 is the TX-LO-SCL's mean optical frequency, ϕ_x is an arbitrary phase, and $\epsilon_{f1}(t)$ is the slow FN component which results from the flicker FN and the drift component as discussed in Section 4.3.4. Therefore, the pilot-tone's frequency in optical domain is given by

$$\nu_p(t) = \nu_1 + \mathbf{f}_p + \epsilon_{f1}(t) \quad (8.2)$$

While the received signal's center frequency is, $\nu_{rx}(t) = \nu_1 + \epsilon_{f1}(t)$. On the other hand, the RX-LO-SCL's instantaneous phase and frequency are respectively written as

$$\phi_2(t) = \phi_{LO}(t) + \phi_y + 2\pi\nu_2 t + 2\pi \int_{-\infty}^t \epsilon_{f2}(t) dt \quad (8.3-a)$$

$$\nu_{LO}(t) = \nu_2 + \epsilon_{f2}(t) - \Delta\epsilon_f(t) \quad (8.3-b)$$

where $\phi_{LO}(t)$ is PN component due to the white frequency noise (FN), ν_2 is the mean optical frequency, ϕ_y is an arbitrary phase, $\epsilon_{f2}(t)$ is the slow FN component, and $\Delta\epsilon_f(t)$ is the frequency component resulting from the AFC process. The FFL BPF's centre frequency is set to be \mathbf{f}_{co} , and hence frequency of the beat-note signal of the pilot-tone and the RX-LO-SCL must be adjusted to be equal to \mathbf{f}_{co} via scanning procedure of the RX-LO-SCL using current injection "capture phase", and then the AFC block is turned on "tracking phase". Therefore the initial tuning condition is

$$v_2 - (v_1 + f_p) = f_{co} \quad (8.4)$$

The instantaneous frequency (excluding the fast PN component) of the FFL BPF's O/P when the AFC is active is given by

$$\begin{aligned} f_F(t) &= v_{LO}(t) - v_p(t) = \{v_2 + \varepsilon_{f2}(t) - \Delta\varepsilon_f(t)\} - \{v_1 + f_p + \varepsilon_{f1}(t)\} \\ &= f_{co} + \varepsilon_{f2}(t) - \varepsilon_{f1}(t) - \Delta\varepsilon_f(t) \end{aligned} \quad (8.5)$$

Now since the RF IQ-modulator is used as an up-converter with a reference RF source's frequency of f_p , then the optical down-converter's instantaneous driving frequency is

$$\begin{aligned} f_d(t) &\approx f_p + f_F(t) = f_p + f_{co} + \varepsilon_{f2}(t) - \varepsilon_{f1}(t) - \Delta\varepsilon_f(t) \\ &= f_p + v_2 - (v_1 + f_p) + \varepsilon_{f2}(t) - \varepsilon_{f1}(t) - \Delta\varepsilon_f(t) \\ &= v_2 - v_1 + \varepsilon_{f2}(t) - \varepsilon_{f1}(t) - \Delta\varepsilon_f(t) \end{aligned} \quad (8.6)$$

Hence the down-converted RX-LO-SCL's instantaneous frequency is given by

$$\begin{aligned} v_{LO2}(t) &\approx v_{LO}(t) - f_d(t) \\ &= v_2 + \varepsilon_{f2}(t) - \Delta\varepsilon_f(t) - \{v_2 - v_1 + \varepsilon_{f2}(t) - \varepsilon_{f1}(t) - \Delta\varepsilon_f(t)\} = v_1 + \varepsilon_{f1}(t) \end{aligned} \quad (8.7)$$

Therefore, $v_{LO2}(t) = v_{rx}(t)$, which is the required goal. Here the optical BPF, in the optical down-conversion block, rejects the up-converted component, which can be implemented easily using the available commercial technologies only when f_p is large (more than 5GHz), which is the case in this design. Note that frequency component of the AFC's is vanished, which indicates that the auxiliary circuit's RF-loop can always correct frequency error provided that the beat-note frequency of the mixed pilot-tone and the RX-LO-SCL is encompassed by the FFL BPF' BW. However, due to the slow and powerful frequency drift of the TX-LO-SCL and RX-LO-SCL, this beat-note frequency can be far away from f_{co} , and hence the AFC loop is essential. On the other hand, the instantaneous fast PN component of the down-converted RX-LO-SCL is given by

$$\dot{\phi}_2(t) \approx \tilde{\phi}_{tx,F}(t) - \{\phi_{LO}(t) - \phi_{LO,F}(t)\} \quad (8.8)$$

where the $\{\tilde{\sim}\}$ indicates the distorted version due to channel dispersion is used, and the subscript **F** indicates the filtered version is used. Therefore the proposed auxiliary circuit functions exactly similar to the discrete complex model discussed in Section 7.3.1. All differential delays in this analysis are omitted assuming that time-delays of all optical branches are perfectly adjusted. Besides, the RF reference source in the RF up-converter block is assumed to have exactly same frequency of the pilot-tone $f_p = k_p \cdot \Delta f$, which is

not the case in practice and a slight frequency error is expected but this effect is marginal and can be tolerated. The AFC loop is designed based on time-domain stability analysis of both lasers as discussed in Section 4.3.4. Obviously, when the AFC block is inactive, the absolute frequency variance and not the differential one (Allan-variance) is required to be estimated, and the condition in this case is

$$\lim_{\Delta T \rightarrow \infty} \sqrt{\sigma_{f_1}^2(\Delta T) + \sigma_{f_2}^2(\Delta T)} \ll B_C \quad (8.9)$$

where $\sigma_{f_1}^2(\Delta T)$, and $\sigma_{f_2}^2(\Delta T)$ are respectively frequency noise variances of the TX-LO-SCL, and RX-LO-SCL with respect to the corresponding optical frequencies ν_1 and ν_2 . However, this ideal condition can only be fulfilled when very stable lasers are used, or relatively short time ΔT , and/or broad B_C . Hence the AFC block is essential, and in this case the differential frequency variance versus the time interval ΔT is required to be estimated to decide the required LF_2 's BW. In Section 4.3.4, the total Allan-variance of both SCLs can either be directly measured, or estimated if the total FN single-sided (SS) power spectral density (PSD) of both SCLs is known. For instance, if $\sqrt{\sigma_{f_1}^2(\Delta T) + \sigma_{f_2}^2(\Delta T)} < \rho_B \cdot B_C$, then the LF_2 's BW (B_{LF2}) must be chosen such that, $B_{LF2} \gg 1/\Delta T$ at that specific ΔT to ensure that LF_2 can correct the error, as discussed in Section 4.3.2.2.2, where $\rho_B < 1$. Thus, the design rule for the AFC loop is

$$\sqrt{\sigma_{f_1}^2(\Delta T) + \sigma_{f_2}^2(\Delta T)} < \rho_B \cdot B_C \quad , \quad B_{LF2} \gg 1/\Delta T \quad , \quad \text{and} \quad \rho_B < 1 \quad (8.10)$$

Design details of the AFC circuits will not be considered here since it is covered thoroughly in the literature [125], [126]. However, as far as this system is concerned, current to frequency coefficient (β_f) in (GHz/mA) of the RX-LO-SCL, and the frequency discriminator's constant must both known. Besides, since no RF spectrum analyzer (SA) is assumed to be used in the "capture phase", pilot-tone's power should be adequately higher than the OFDM signal within a finite BW, such that distinguishing using power monitoring is possible.

8.2.3.2 Propagation delay condition

In Fig. 8.1, when $T_{d5} = T_{d6}$ and all other delays are adjusted perfectly, then the pilot-tone-SC is the less-noisier SC, since the differential delay due to the channel response is

null, which is the case discussed in Chapter 7. However, the DC-SC can be set to have the best performance by careful adjustment of $\mathbf{T}_{d5} - \mathbf{T}_{d6}$. In general the following time-delay condition, which corresponds to fiber lengths of all branches, must be fulfilled

$$T_{d3} = T_{d1} + T_{d2} \quad , \text{ and} \quad T_{d1} = T_{dX} + (T_{d5} + T_{d6})/2 \quad (8.11)$$

This time delay can first be estimated from fibers' lengths, and then the back-to-back setup (**BBS**) is used for more accurate time-delay setting with only the TrS is used as the modulating signal. The reference SC is the pilot-tone SC itself after the **FFT** is performed assuming $\mathbf{T}_{d5} = \mathbf{T}_{d6}$. Hence as soon as minimal long-term phase error is observed in this SC, optimal timing condition is achieved. This represents the simplest way to estimate branches lengths since the precise determination of these lengths is complicated due to the involvement of the auxiliary circuit delay \mathbf{T}_{dX} . Time delay adjustment was exploited in other applications such as to improve the DDO-OFDM performance [127], and for RIN reduction [128].

8.2.3.3 Polarization diversity analysis

8.2.3.3.1 Polarization diversity analysis of the main detection block

Let the transmitted signal in continuous-time be expressed as

$$\vec{E}_{TX}(t) = \left((U_1(t) + c_p \cdot e^{j2\pi f_p t}) \cdot \vec{x} + U_2(t) \cdot \vec{y} \right) \cdot e^{j2\pi \nu_1 t} \quad (8.12)$$

where $\mathbf{U}_1(t) + \mathbf{c}_p \cdot \mathbf{e}^{j2\pi f_p t}$ is the 1st BB-OFDM signal with the side pilot-tone,

$\mathbf{U}_2(t)$ is the 2nd BB-OFDM signal.

Note that the I/Q imbalance as well as the TX-LO-SCL's noise are ignored for instance. Referring to Fig. 8.1 and the results of Section 3.2.3.2, the **m-th** O/P from the two BB-OFDM receivers (before the hard-decision is performed) can be expressed as

$$\begin{bmatrix} y_{1m,\ell} \\ y_{2m,\ell} \end{bmatrix} = \begin{bmatrix} Z_{m11} & Z_{m12} \\ Z_{m21} & Z_{m22} \end{bmatrix} \cdot \begin{bmatrix} c_{1m,\ell} \\ c_{2m,\ell} \end{bmatrix} + \begin{bmatrix} n_{1m,\ell} \\ n_{2m,\ell} \end{bmatrix} \quad (8.13)$$

where $\mathbf{c}_{1m,\ell}$, and $\mathbf{c}_{2m,\ell}$ are the **m-th** mapped symbols in the ℓ -th OFDM symbol of the 1st and the 2nd BB-OFDM transmitted signals respectively,

$\mathbf{n}_{1m,\ell}$, and $\mathbf{n}_{2m,\ell}$ are the **m-th** SC's ASE noise terms in the ℓ -th OFDM symbol of the 1st and the 2nd BB-OFDM RX respectively. Note that each noise term in (8.13) is resulted from a white-polarized ASE noise, and polarized cross-ASE noise described in Section 7.3.2.2, and hence the penalty calculations due to the compensation process would match that calculated in Section 7.3.6.1,

$$\begin{bmatrix} \mathcal{Z}_{m11} & \mathcal{Z}_{m12} \\ \mathcal{Z}_{m21} & \mathcal{Z}_{m22} \end{bmatrix} = \begin{bmatrix} \cos(\Psi_m)\cos(\Delta_{ph}) - j\sin(\Psi_m)\cos(\Sigma_{ph}) & \cos(\Psi_m)\sin(\Delta_{ph}) - j\sin(\Psi_m)\sin(\Sigma_{ph}) \\ -\cos(\Psi_m)\sin(\Delta_{ph}) - j\sin(\Psi_m)\sin(\Sigma_{ph}) & \cos(\Psi_m)\cos(\Delta_{ph}) + j\sin(\Psi_m)\cos(\Sigma_{ph}) \end{bmatrix},$$

$$\Psi_m = \pi \cdot m \cdot \overline{\tau_{\text{DGD}}}(\mathbf{L}) \cdot F_S/N_{\mathcal{F}}, \Delta_{ph} = \theta_i - (\psi + \epsilon_\theta), \Sigma_{ph} = \theta_i + (\psi + \epsilon_\theta),$$

θ_i is the polarization angle between the PBC's reference SOPs $\{\vec{x}, \vec{y}\}$, and the principal states of polarization (PSPs) $\{\vec{v}_{st}, \vec{v}_{ft}\}$ at TX as discussed in Section 3.2.3.2. Note that θ_i is assumed to be constant during at least one OFDM symbol,

ψ is the polarization angle between the reference SOPs $\{\vec{x}_{r2}, \vec{y}_{r2}\}$ of the 2nd PBS in the main detection block, and the PSPs as seen in the RX $\{\vec{v}_{sr}, \vec{v}_{fr}\}$,

ϵ_θ is the polarization angle between the reference SOPs $\{\vec{x}_{r2}, \vec{y}_{r2}\}$ of the 2nd PBS, and the reference SOPs $\{\vec{x}_{r1}, \vec{y}_{r1}\}$ of the 1st PBS in the main detection block, and

$\overline{\tau_{\text{DGD}}}(\mathbf{L})$ is the mean differential group-delay (DGD) between the two PSPs as discussed in Section 3.2.3.2.

Obviously, $\mathcal{Z}_{m22} = \mathcal{Z}_{m11}^*$, and $\mathcal{Z}_{m21} = -\mathcal{Z}_{m12}^*$ which facilitates extraction of the \mathcal{Z} -matrix coefficients. The important note here is that neither $\mathbf{y}_{1m,\ell}$, nor $\mathbf{y}_{2m,\ell}$ can simultaneously be null at any possible values of Ψ_m , θ_i , ψ , and ϵ_θ , and hence a steady detection is possible. However, an automatic gain-controllers (AGC)s before the \mathcal{FFT} blocks are necessary for a steady received level, which is common in the most communication systems [48]. A two-symbol TrS can be sent using the following setting, $\{c_{1m,\ell} \neq 0 \ \& \ c_{2m,\ell} = 0\}$, and $\{c_{1m,\ell+1} = 0 \ \& \ c_{2m,\ell+1} \neq 0 \ \& \ c_{1k_p,\ell+1} \neq 0\}$.

This setting facilitates the \mathcal{Z} -matrix extraction by mitigating the effect of noise contribution provided that the two BB-OFDM receivers are synchronized to each other. However, the I/Q imbalance and channel response cannot be isolated from the \mathcal{Z} -matrix, and hence all the convolved coefficients must simultaneously be extracted.

From the many efficient estimators proposed in literatures, the successful estimator is that which overcome the possible singularity of the \mathcal{Z} -matrix, uses the lowest number of computations, and results the lowest estimation penalty [78], [79], [51], [129], [130].

8.2.3.3.2 Polarization diversity analysis of the auxiliary circuit

Referring to Fig. 8.1, the adopted configuration of polarization splitting avoids the use of another PBS and ensures $\epsilon_\theta = 0$. Referring to Section 3.2.3.2 and after some simple derivations, the normalized O/P signal from the FFL BPF can be expressed as

$$\begin{aligned}
V_{NF}(t) \approx & \cos(\omega_{co}t + \varphi_0) \cdot \\
& (\cos(\psi_p)\cos(\ddot{\Delta}_{ph}) - \cos(\psi_p)\sin(\ddot{\Delta}_{ph})\cos(\zeta_p) - \sin(\psi_p)\sin(\ddot{\Sigma}_{ph})\sin(\zeta_p)) \\
& - \sin(\omega_{co}t + \varphi_0) \cdot \\
& (\sin(\psi_p)\cos(\ddot{\Sigma}_{ph}) + \sin(\psi_p)\sin(\ddot{\Sigma}_{ph})\cos(\zeta_p) - \cos(\psi_p)\sin(\ddot{\Delta}_{ph})\sin(\zeta_p))
\end{aligned} \tag{8.14}$$

where $\ddot{\Delta}_{ph} = \theta_i - \psi_2$, $\ddot{\Sigma}_{ph} = \theta_i + \psi_2$, $\omega_{co} = 2\pi f_{co}$, φ_0 is a constant phase,

$$\Psi_p = \pi \cdot (f - f_p) \cdot \overline{\tau_{DGD}}(L),$$

f is any frequency component with respect to f_p ,

ζ_p is the added phase due to the APS loop, and

ψ_2 is the polarization angle between the reference SOPs $\{\overline{\mathbf{x}}_{r3}, \overline{\mathbf{y}}_{r3}\}$ of the PBS in the auxiliary circuit, and the PSPs as seen in the RX $\{\overline{\mathbf{u}}_{sr}, \overline{\mathbf{v}}_{fr}\}$.

From (8.14), the O/P signal can always be corrected to be at the peak via ζ_p whatever the parameters $\ddot{\Delta}_{ph}$, $\ddot{\Sigma}_{ph}$, and Ψ_p are, and hence a steady envelope can be obtained. A simple APS based on envelope power measuring can be easily designed and optimized using few components since $f_{co} < 1\text{GHz}$, and the narrowband required response of the whole auxiliary circuit. As polarization's fluctuation rate in long-haul link is less than 1kHz, the LF₁'s BW (\mathbf{B}_{LF1}) should also be higher than this rate [106].

8.2.3.4 Overall channel response estimation

In UWB CO-OFDM systems the frequency-dependent I/Q imbalance, which is basically resulted from the AA-filters, driver amplifiers, and RX LPFs, is the critical one among the other sources of I/Q imbalance since it depends on the SC's index. Referring to the linear I/Q imbalance model described in Appendix-C1, and by considering only one of the two OFDM subchannel, the positive and negative **m-th** O/P at the **ℓ-th** OFDM's symbol when the channel noise is ignored can be expressed as

$$\begin{aligned}
y_{m,\ell}^+ &= \mathcal{K}_{m11} \cdot c_{m,\ell}^+ + \mathcal{K}_{m12} \cdot c_{m,\ell}^{-*} \\
y_{m,\ell}^- &= \mathcal{K}_{m21} \cdot c_{m,\ell}^{+*} + \mathcal{K}_{m22} \cdot c_{m,\ell}^-
\end{aligned} \tag{8.15}$$

where $c_{m,\ell}^+$, and $c_{m,\ell}^-$ are the (+**m**), and (-**m**) mapped symbols in the **ℓ**-th OFDM symbol respectively.

The \mathcal{K} -matrix, which combines the channel response (due to chromatic dispersion (**CD**) and PMD) and the TX and RX I/Q imbalance, is described in Appendix-C1. A pre-knowledge of the impairments' functions involved in this matrix might not necessary as long as the estimator can accomplish extraction of the coefficients efficiently [129].

The coefficients of the \mathcal{K} -matrix can be extracted much easier when a two-symbol TrS has the following feature, $\{c_{m,\ell}^+ \neq 0 \ \& \ c_{m,\ell}^- = 0\}$, and $\{c_{m,\ell+1}^+ = 0 \ \& \ c_{m,\ell+1}^- \neq 0\}$.

The author has developed a new TrS that has this feature as well as all other necessary features for OFDM synchronization. Although the new TrS is designed for $\mathbf{N}_{\mathcal{F}} = 1024$, as given in Appendix-C2, however, it can be designed for any $\mathbf{N}_{\mathcal{F}}$ size. Therefore by joining the polarization diversity with overall channel response yields

$$\begin{aligned}
y_{1m,\ell}^+ &= \mathcal{Z}_{m11}^+ (\mathcal{K}_{m11} \cdot c_{1m,\ell}^+ + \mathcal{K}_{m12} \cdot c_{1m,\ell}^{-*}) \\
&\quad + \mathcal{Z}_{m12}^+ (\mathcal{K}_{m11} \cdot c_{2m,\ell}^+ + \mathcal{K}_{m12} \cdot c_{2m,\ell}^{-*}) + n_{1m,\ell}^+ \\
y_{2m,\ell}^+ &= \mathcal{Z}_{m21}^+ (\mathcal{K}_{m11} \cdot c_{1m,\ell}^+ + \mathcal{K}_{m12} \cdot c_{1m,\ell}^{-*}) \\
&\quad + \mathcal{Z}_{m22}^+ (\mathcal{K}_{m11} \cdot c_{2m,\ell}^+ + \mathcal{K}_{m12} \cdot c_{2m,\ell}^{-*}) + n_{1m,\ell}^+ \\
y_{1m,\ell}^- &= \mathcal{Z}_{m11}^- (\mathcal{K}_{m21} \cdot c_{1m,\ell}^{+*} + \mathcal{K}_{m22} \cdot c_{1m,\ell}^-) \\
&\quad + \mathcal{Z}_{m12}^- (\mathcal{K}_{m21} \cdot c_{2m,\ell}^{+*} + \mathcal{K}_{m22} \cdot c_{2m,\ell}^-) + n_{1m,\ell}^- \\
y_{2m,\ell}^- &= \mathcal{Z}_{m21}^- (\mathcal{K}_{m21} \cdot c_{1m,\ell}^{+*} + \mathcal{K}_{m22} \cdot c_{1m,\ell}^-) \\
&\quad + \mathcal{Z}_{m22}^- (\mathcal{K}_{m21} \cdot c_{2m,\ell}^{+*} + \mathcal{K}_{m22} \cdot c_{2m,\ell}^-) + n_{2m,\ell}^-
\end{aligned} \tag{8.16}$$

Here all noise terms have equal variance. Note that (8.16) can also be written in a matrix form to result two SCs' O/P per OFDM subchannel. Usually the I/Q imbalance and the CD are quasi-static impairments, which varies slower than polarization's fluctuation rate, hence the \mathcal{Z} -matrix can be estimated while the \mathcal{K} -matrix is assumed to be constant. In this case, the TrS transmission condition is

$$\begin{aligned}
&\{c_{1m,\ell}^+ \neq 0 \ \& \ c_{1m,\ell}^- = 0\} \ \& \ \{c_{2m,\ell}^+ = 0 \ \& \ c_{2m,\ell}^- = 0\}, \\
&\{c_{1m,\ell+1}^+ = 0 \ \& \ c_{1m,\ell+1}^- = 0\} \ \& \ \{c_{2m,\ell+1}^+ = 0 \ \& \ c_{2m,\ell+1}^- \neq 0\}, \\
&\text{and in both cases } \{c_{1k_p,\ell+1} \neq 0\}
\end{aligned} \tag{8.17}$$

The adopted estimator must also use the following correlations between the coefficients

$$\begin{aligned}
\mathcal{Z}_{m22}^+ &= \mathcal{Z}_{m11}^{+*}, \text{ and } \mathcal{Z}_{m21}^+ = -\mathcal{Z}_{m12}^{+*} \\
\mathcal{Z}_{m22}^- &= \mathcal{Z}_{m11}^{-*}, \text{ and } \mathcal{Z}_{m21}^- = -\mathcal{Z}_{m12}^{-*}
\end{aligned} \tag{8.18}$$

8.2.3.5 Optimal operating conditions of the IQ optical modulators

8.2.3.5.1 Driver amplifiers' nonlinearity

Referring to Fig. 2.10, and 8.1, the AA-filters' O/Ps \mathbf{I}_t , and \mathbf{Q}_t are amplified using a wideband balanced driver amplifier (DA), and then the amplified tributaries with powers of $\mathbf{P}_{s,I}$, and $\mathbf{P}_{s,Q}$, derive the IQ optical modulator. As discussed in Section 3.3.2.1, a

transfer function can be used in the BB-OFDM DSP TX to equalize the DACs' and TX-RF frontend response, however, this transfer function cannot be used to equalize the I/Q imbalance. Hence a balanced amplifier is necessary to ensure minimal amplitude and phase frequency-dependant imbalance in the TX-RF frontend. It is also important to clip the OFDM signal before DACs for optimal sampling as discussed in Section 3.3.3. Besides, the DA has to have a high 1dB compression point to reduce its nonlinearity contribution as discussed in Appendix-D1. Among the many nonlinearity models proposed in the literature, the polynomial model can be adopted for the DA's case, however, this model is complicated since it requires to fit the transfer characteristic curve with a high order polynomial which is not an easy task [80], [131]. In Appendix-D1, the piece-wise model shown in Fig. D1.1 of the DA's transfer characteristic is adopted and developed to yield an approximated expression of the worst case DA's nonlinearity variance in the RX with an advantage of only few parameters are required. The DA's nonlinearity variance in the worst-case SC (DC-SC) can be expressed as

$$\sigma_{DA,nn}^2 = \langle |c_{m,\ell}|^2 \rangle_{\ell} \cdot \beta_g^2 \left\{ p_A \exp \left(-\sqrt{\frac{2}{\pi}} X_1 \right) + p_B \alpha_g (2 + \alpha_g) \exp \left(-\sqrt{\frac{2}{\pi}} X_2 + \{X_2 - X_1\} \left\{ \frac{\sqrt{2\pi}\beta_g}{1 + \sqrt{2\pi}\beta_g} \right\} \right) \right\} \quad (8.19)$$

where $\beta_g = (g_L - g_{NL})/g_L$, $\alpha_g = g_{NL}/(g_L - g_{NL})$,

$$p_A \approx \text{erfc}\{X_1/\sqrt{2}\}, \quad p_B = \text{erfc}\{X_2/\sqrt{2}\},$$

$$X_1 = \sqrt{P_{i1}/P_1} \quad , \quad X_2 = \sqrt{P_{is}/P_1} \quad , \quad g_L = \sqrt{G_L} \quad , \quad g_{NL} = \frac{\sqrt{P_{os}} - \sqrt{P_{o1}}}{\sqrt{P_{is}} - \sqrt{P_{i1}}} \quad ,$$

G_L is the DA's linear power gain in linear scale, $G_L = 10^{G_{L,dB}/10}$,

P_{o1} is O/P power at the 1dB compression point in linear scale,

P_{i1} is I/P power at the 1dB compression point in linear scale,

P_{os} is the saturated O/P (0.1dB) power in linear scale,

P_{is} is the saturated I/P power in linear scale, and

$P_I = P_Q$ is the DA's I/P power.

Note that in (8.19), the I/Q imbalance is ignored, and average transfer characteristic curve is assumed. While the exact DA's O/P power per I or Q tributary is given by

$$P_{s,I} = P_I G_L \cdot \left\{ 1 - \beta_o^2 \cdot \{p_A(C_1 - C_2 X_1^2) + p_B(1 - C_3 X_2^2) + \mathcal{H}_1 C_2 + \mathcal{H}_2 C_3\} \right\} \quad (8.20)$$

where $\beta_o = g_{NL}/g_L$, $\mathbf{c}_1 = (g_L^2 - g_{NL}^2)/g_{NL}^2$, $\mathbf{c}_2 = (g_L - g_{NL})^2/g_{NL}^2$,

$$\mathbf{c}_3 = 1 + 2 \frac{X_2}{X_1} \cdot \frac{g_L - g_{NL}}{g_{NL}},$$

$$\mathcal{H}_1 = \sqrt{\frac{2}{\pi}} \cdot X_1 \cdot \exp(-X_1^2/2) \quad , \text{ and } \quad \mathcal{H}_2 = \sqrt{\frac{2}{\pi}} \cdot X_2 \cdot \exp(-X_2^2/2) \quad .$$

Hence (8.19) is used to determine optimal DA's I/P power \mathbf{P}_I , or \mathbf{P}_Q for the minimal nonlinearity contribution for a given mapping, while (8.20) is used to calculate the IQ optical modulator's exact I/P powers.

8.2.3.5.2 Nonlinearity of the IQ optical modulator

The transfer characteristics of an MZM when it biased at the null point is a sine function described by (2.37). This transfer characteristic is usually expanded using Bessel-function [81], [132]; however, Taylor series can also be used and yields the same results as discussed thoroughly in Appendix-D2. When an IQ optical modulator is perfectly biased (no IQ imbalance), then the nonlinearity variance with respect to OFDM SC at RX as it is derived in Appendix-D2, can be approximated and yields the following expression

$$\sigma_{\text{OM,nn}}^2 \approx \frac{\langle |c_{m,\ell}|^2 \rangle_\ell}{\pi} \cdot \sin^4 \left(\frac{\pi}{2} X_3 \cdot \left\{ 1 + \frac{N/N_F}{\pi^3} \right\} \right) \quad (8.21)$$

where $X_3 = \sqrt{P_{s,I} \cdot R_L} / v_\pi$,

v_π is the MZM's switching voltage, and R_L is load impedance (usually 50Ω).

From Appendix-D2 again, optical O/P power from the IQ optical modulator under perfect biasing condition can be expressed respectively in linear scale and in dBm as follows

$$P_{tx} \approx \frac{P_O}{\text{att}_M} X_4 \cdot \left\{ 1 - X_4 + \frac{2}{3} X_4^2 - \frac{7}{24} X_4^3 + \frac{21}{320} X_4^4 \right\} \quad (8.21-a)$$

$$P_{tx,\text{dBm}} \approx P_{O,\text{dBm}} + P_{s,I,\text{dBm}} - 9.1 - \text{att}_{M,\text{dB}} - 20 \log(v_\pi) \\ + 10 \log \left(1 - X_4 + \frac{2}{3} X_4^2 - \frac{7}{24} X_4^3 + \frac{21}{320} X_4^4 \right) \quad (8.21-b)$$

where $X_4 = R_L \left(\frac{\pi}{2v_\pi} \right)^2 \cdot P_{s,I}$,

P_O is the TX-LO-SCL's power, and att_M is the modulator's optical loss.

Note that in (8.21-b), $R_L = 50\Omega$ is used.

8.2.3.5.3 Design calculation

Both \mathbf{P}_I , and $\mathbf{P}_{s,I}$ must be adjusted for the lowest nonlinearity contribution of both the DA, and the IQ optical modulator. The design steps are as follows.

- 1- The worst-case $\sigma_{\text{OM,nn}}^2$ must first be determined by defining the \mathbf{SNR}_b at the targeted **BER** for a given mapping, which results maximum $\mathbf{P}_{s,I}$. This is calculated as

$$\mathbf{SNR}_b = \frac{\mathbf{SNR}_{b,\text{ideal}}}{1 + m \cdot \mathbf{SNR}_{b,\text{ideal}} \cdot \sigma_{\text{OM,nn}}^2}$$

and hence $\sigma_{\text{OM,nn}}^2$ is estimated according to a given penalty criterion.

- 2- As maximum $\mathbf{P}_{s,I}$ is estimated, maximum \mathbf{P}_{tx} can be estimated for a given IQ optical modulator's specifications, and the required DA's specifications can be determined.
- 3- Since the selected DA can deliver maximum $\mathbf{P}_{s,I}$, however, its other specifications have to be examined using (8.19) to ensure $\sigma_{\text{DA,nn}}^2$ is lower than worst-case $\sigma_{\text{OM,nn}}^2$.

For instance, in the given homodyne CO-OFDM system, the ideal \mathbf{SNR}_b for **BER** = 10^{-3} is obtained from Appendix-D to be 12.6dB (18.2 in linear scale). If 0.5dB maximum penalty due to the IQ optical modulator is accepted, then $\sigma_{\text{OM,nn}}^2 \approx 1.34 \times 10^{-3}$ (-28.73dB). Suppose the IQ optical modulator has the following specifications; $\mathbf{att}_{M,\text{dB}} = 6\text{dB}$, $\mathbf{v}_\pi = 5\text{V}$, and $\mathbf{R}_L = 50\Omega$, then from (8.21), and by using $\mathbf{N} = 808$, and $\mathbf{N}_F = 1024$, the maximum $\mathbf{P}_{s,I} \approx 12.8\text{mW}$ (11dBm). Now by assuming the TX-LO-SCL's power $\mathbf{P}_O = 5\text{mW}$ (7dBm), then from (8.21), $\mathbf{P}_{tx} \approx 73.3\mu\text{W}$ (-11.35dBm). Additional optical loss might be introduced due to other frontend components such as the optical filter, and hence \mathbf{P}_{tx} decreases to be say -15dBm. However, \mathbf{P}_{tx} can be even lower if \mathbf{P}_O and/or the maximum allowable penalty is lower, and hence an optical booster is necessary to deliver the optimal \mathbf{P}_{ch} . Suppose the first selected commercially available DA's specifications are; $\mathbf{G}_{L,\text{dB}} = 20\text{dB}$, $\mathbf{P}_{o1,\text{dBm}} = 13\text{dBm}$, $\mathbf{P}_{os,\text{dBm}} = 15\text{dBm}$, and $\mathbf{G}_{\text{sat},\text{dB}} = 8\text{dB}$, which is the gain at saturation point. The required parameters for (8.19) are $\mathbf{P}_I = \mathbf{P}_{s,I}/\mathbf{G}_L \approx 0.126\text{mW}$ (-9dBm), $\mathbf{g}_L = 10$, $\mathbf{g}_{NL} \approx 2.45$, $\mathbf{X}_1 \approx 1.412$, $\mathbf{X}_2 \approx 5.62$, $\mathbf{p}_A \approx 0.158$, $\mathbf{p}_B \approx 1.91 \times 10^{-8}$ (ignored), and $\beta_g = 0.755$. Then from (8.19), $\sigma_{\text{DA,nn}}^2 \approx 0.029$ (-15.35dB) which is not acceptable.

The second selected commercially available DA's specifications are; $\mathbf{G}_{L,\text{dB}} = 20\text{dB}$, $\mathbf{P}_{o1,\text{dBm}} = 17\text{dBm}$, $\mathbf{P}_{os,\text{dBm}} = 20\text{dBm}$, and $\mathbf{G}_{\text{sat},\text{dB}} = 10\text{dB}$. By repeating the same steps

yields $\sigma_{DA,nn}^2 \approx 0.925 \times 10^{-3}$ (-30.34dB) which is a valid selection. Thus in DA's selection with minimal nonlinearity contribution, the effective parameter is X_1 , which its value depends roughly on $\{P_{o1,dBm} - P_{s1,dBm}\}$, and its valid value depends on m .

8.2.3.5.4 Automatic bias control (ABC) design

The ABC circuit, which is used to maintain biasing of the IQ optical modulator at optimal biasing condition, is available commercially for CO-QPSK systems with exactly same operating biasing condition of the CO-OFDM except that the driving voltage-swing should be $\pm v_\pi$. This driving level is much higher than the maximum allowable one for CO-OFDM. Thus under low power condition, the available ABC circuits are not useful, which impose new designs to be accomplished. The null points of both MZMs can be maintained via power monitoring using a PD followed by an electrical power meter, since a slight divergence from v_π causes significant increase in the optical carrier's power. However, phase-drift of the 90° phase shifter is the challenging issue since it cannot be distinguished easily via power monitoring. It is important to create an error signal that is used to correct the optical phase shifter's voltage continuously.

The author has noticed that this error signal can be extracted in RF domain when the OFDM signal is combined with a side pilot-tone. In the following ABC proposal, only a single PD is used without any additional optical components as shown in Fig. 8.2.

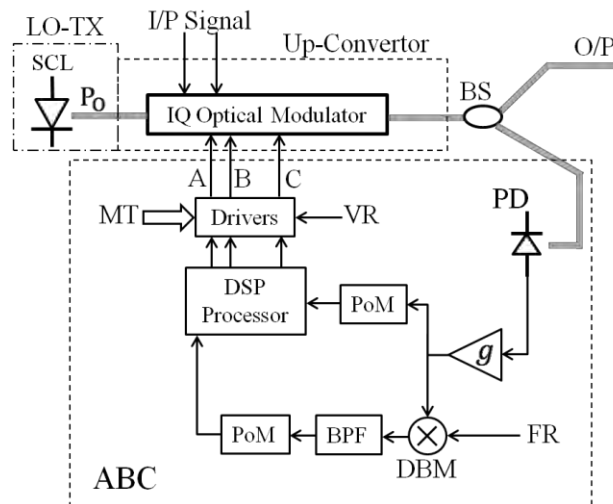


Fig. 8.2: The proposed ABC block used for IQ optical modulator's biasing. Here **DBM** is a double-balanced mixer, **PoM** is a power meter, **VR** is a reference voltage, **MT** stands for manual tuning, and **FR** is a reference RF source. More details are given in the text.

In Fig. 8.2, the BS splits O/P optical signal with an unequal ratio, say only 1:10 is detected by the PD. The photo-current is amplified and then its power is measured via an electrical power-meter (**PoM**). This PoM's O/P represents the first error signal, which is used to maintain the MZMs' biasing (**A** and **B**) at null points via a DSP processor. The DSP processor uses an algorithm based on minimal PoM's reading to correct the **A** and **B** voltage continuously. As the OFDM signal must be combined with a side pilot-tone, then an error signal for phase-error correction can be generated via the RF down-converter block. This block is a conventional block consisting of a reference RF source with a double-balanced mixer (**DBM**), a BPF, and another PoM. The second PoM's O/P represents the second error signal that is used by the DSP processor to correct the optical phase shifter's biasing (**C**) using an algorithm, which is also based on minimal power reading. The BPF's O/P is derived and can be expressed briefly as

$$\mathbf{V}_{\text{BPF}}(t) \approx \mathbf{A} \cdot \left\{ \cos(\omega_{\text{B}}t + \varphi_{\text{o}}) + 2\cos(\Theta) \cdot \cos(\omega_{\text{B}}t + \varphi_{\text{o}} - \theta_{\text{p}}) + \cos(\omega_{\text{B}}t + \varphi_{\text{o}} - 2\theta_{\text{p}}) \right\} \quad (8.22)$$

where **A** is constant, φ_{o} is an arbitrary phase,

$\omega_{\text{B}} = \omega_{\text{r}} - 2\omega_{\text{p}}$, is the BPF's angular center frequency,

ω_{r} is the RF angular reference frequency, ω_{p} is pilot-tone's angular frequency,

θ_{p} is differential phase between the real I, and imaginary Q tributaries with respect to the pilot-tone only. Ideally this phase is $\pm \pi/2$ but due to the I/Q imbalance, it can be different,

Θ is optical differential phase shift in the IQ optical modulator, which must be maintained to be $\pm \pi/2$.

Obviously $\mathbf{V}_{\text{BPF}}(t)$'s power tends to be zero when $\Theta = \pm \pi/2$, and $\theta_{\text{p}} = \pm \pi/2$. Thus θ_{p} has to be corrected before the I, and Q signals are connected to the IQ modulator, otherwise correction ambiguity occurs. Regarding to circuit complexity and cost, the RF reference source is the expensive device especially when ω_{p} is high, since ω_{r} has to be slightly higher than twice ω_{p} . While the other components are not critical and cheap since ω_{B} can be set to be in tens of MHz range, and the biasing drift is a slow process that does not require fast sampling and DSP processing. In this proposed ABC circuit, the side pilot-tone must be combined with the OFDM signal with an adequate power; otherwise phase shifter's biasing cannot be corrected.

8.2.4 Performance analysis and final design parameters

The performance of the proposed homodyne CO-OFDM system is calculated by examining the required **OSNR** at **BER** = 10^{-3} of the worst-corrupted SC, and whether it is less than **OSNR_d** or not for a given optical link, and SCLs' parameters, assuming **B_{C,opt}** and **PSPR_{opt}** are used. The AFC, APS, and ABCs are all assumed to operate perfectly, channel and polarization diversity equalizations' penalties are ignored, and no **OSNR** margin is included. Although this is not the case in practice, however, the main aim here is to investigate SCLs' effect and whether the system can be adopted or not. As discussed in Section 7.3.6, **B_{C,opt}** is a function of **L**, SCLs' parameters, and the used mapping, however, a fixed optimized value of **B_{C,opt}** is used for a given mapping and SCL's linewidth, and for all values of **L**. An exact **BER** expression of 32-QAM in presence of AWGN and Gaussian PN is derived in Appendix-B, which is necessary in **B_{C,opt}** estimation, and because it is a long expression, it will not be written here for convenience. As discussed earlier, the frequency index of the side pilot-tone should satisfy the condition of $|\mathbf{k}_p| \geq (N + N_{C,opt})/2$, however, due to OFDM's spectral leakage, which enhance the cross-noise term, an adequate frequency gap must be set. That is **BW_G** must be set by compromising between the optimal performance and BW efficiency (**BW_{eff}**) such that **BW_G** \geq **B_{C,opt}**/2 must always be applied. Note that either **B_{C,opt}** or **N_{C,opt}**, and either **BW_G** or **N_G** are used without prior notice, where **B_{C,opt}** = **N_{C,opt}** · Δf , and **BW_G** = **N_G** · Δf .

Referring to Fig. 8.1 and the discussion in Sections 8.2.2 and 8.2.3.2, two cases are considered here:

1. First when **T_{d5}** = **T_{d6}** and all other delays are adjusted perfectly, in which the pilot-tone is the less-noisier SC, and the worst-corrupted SC, which is used as a performance indicator, is located approximately at **m_{worst-case}** \approx $\lfloor 3N/4 \rfloor$. This case will be denoted as case-X.
2. Second when **T_{d5}** - **T_{d6}** is adjusted such that the differential delay between the pilot-tone and the DC-SC is null, which results **m_{worst-case}** \approx $\lfloor N/2 \rfloor$. This case will denoted as case-Y

By using the preliminary parameters given in Section 8.1.1, and from Section 7.3.6, $\mathbf{B}_{C,opt}$, and \mathbf{PSPR}_{opt} are calculated as it will be shown next assuming both SCLs are identical. Accordingly, the overall system's parameters are as follows.

- 1- Optical link parameters: span length = 50km, total span loss = 13dB, in-line amplifier's noise figure $\mathbf{n}_{F,dB} = 6\text{dB}$, in-line amplifier's gain is just equal the span loss, $\mathbf{P}_{ch,dBm} = [-10, -3]\text{dBm}$, and $\mathbf{L} = [50, 1000]\text{km}$.
- 2- OFDM signals common parameters: $\mathbf{F}_S = 15\text{GSps}$, $\mathbf{N}_F = 1024$, $\Delta\mathbf{f} \approx 14.65\text{MHz}$, $\mathbf{N} = 808$, $\mathbf{N}_{CP} = 16$, $\mathbf{M}_{tr} = 2$, $\mathbf{M}_{dt} = 25$, $\mathbf{m} = 5$, FEC RS(255, 239) with $\alpha_{FEC} = 0.9373$, $\mathbf{PEN}_{oh} \approx 1.1$ (0.4dB), and 7th order Chebyshev type II AA-filters.
- 3- The DAC and ADC requirements are $\mathbf{F}_S = 15\text{GSps}$, and $\mathbf{q}_b \geq 7\text{bits}$.
- 4- Both SCLs are identical with $\delta\mathbf{f}_1 = \delta\mathbf{f}_2$, $\mathbf{P}_O = 5\text{mW}$, $\mathbf{RIN}_L(\mathbf{0}) = -150\text{dBc/Hz}$, $\mathbf{F}_R = 2\text{GHz}$, $\mathbf{u} = \mathbf{RIN}_L(\mathbf{F}_R)/\mathbf{RIN}_L(\mathbf{0}) \approx 25\text{dB}$, and $\mathbf{f}_C = 100\text{kHz}$.
- 5- The IQ optical modulators' parameters are: $\mathbf{att}_{M,dB} = 6\text{dB}$, $\mathbf{v}_\pi = 5\text{V}$, and $\mathbf{R}_L = 50\Omega$, and maximum driving power is $\mathbf{P}_{s,I} \approx 12.8\text{mW}$ (11dBm).
- 6- The DA's specifications are: $\mathbf{G}_{L,dB} = 20\text{dB}$, $\mathbf{P}_{1dB,op} = 17\text{dBm}$, $\mathbf{P}_{sat,op} = 20\text{dBm}$, and $\mathbf{G}_{sat,dB} = 10\text{dB}$.
- 7- 9th order Butterworth BPF is used in the FFL block. Suggested values of center frequency \mathbf{f}_{co} are given in Table 8.1.
- 8- OFDM signal with the side pilot-tone: Optimized values of $\mathbf{N}_{C,opt}$ and other parameters are listed in Table 8.1 for the two given cases. The side pilot-tone is inserted as one of the SCs using the given technique in Section 7.3.9 provided that $\mathbf{N}_G \leq 22$ to ensure the oversampling ratio $\gamma_s \geq 1.2$ to relax the AA filtering design. Otherwise, when $\mathbf{N}_G > 22$, the pilot-tone should be externally inserted. DS-PSD of the computed time-vectors TiV of the two orthogonal OFDM subchannels (before DAC is applied) are shown in Fig. 8.3. While the DS-PSD of the optical transmitted signal just after the PBC and when $\mathbf{N}_G = 21$, is shown in Fig. 8.4.

A comparison is held between the required \mathbf{OSNR} and \mathbf{OSNR}_d versus \mathbf{L} and $\delta\mathbf{f}$ assuming the worst-corrupted SC is under investigation as shown in Fig. 8.5. Obviously when case-X is considered, performance degradation due to the dispersive PN (received dispersive field) component is quite significant especially for relatively

large linewidth values, due to the relatively large differential delay between the pilot-tone and the SC under test as shown in the simulation result of Fig. 8.5a. While when case-Y is investigated, then the performance is less sensitive to the dispersive PN component and approximately flat penalties versus L is obtained for up to $\delta f_1 = \delta f_2 = 2\text{MHz}$, and $L = 1000\text{km}$. When case-Y is employed, the system is approximately limited by the ASE noise and cross-noise as shown in Fig. 8.5b. These results are valid provided that the aforementioned assumptions, which concern with power margin, DSP equalizations, and automatic tracking circuits, are applied. Besides, 50km per span is adopted here with 13dB span's loss; however, if the distance per span is 80km, then maximum reach declines. In brief, when case-X is adopted (since it is much easier to set fiber branches corresponding to T_{d5} and T_{d6} to be equal) this system can work (based on performance of the worst-corrupted SC and limited P_{ch}) up to 300km when $\delta f_1 = \delta f_2 < 1\text{MHz}$. However, even this range might become challenging if a high DSP equalization penalty is involved, span's length is higher than 50km, the automatic circuits do not work properly, and when power margin is added. While when case-Y is used, $L = 250\text{km}$ for $\delta f_1 = \delta f_2 = 5\text{MHz}$, and $L = 400\text{km}$ for $\delta f_1 = \delta f_2 = 1\text{MHz}$, can be achieved, which is by far better than case-X provided that fiber lengths are adjusted for every different reach.

Table 8.1: Summary of the important design values corresponding to the case-X and case-Y.

$\delta f_1 = \delta f_2$ (MHz)	$N_{C,opt}$	$B_{C,opt}$ (MHz)	f_{co} (MHz)	$PSPR_{opt}$ (linear)	$PSPR_{opt}$ (dB)	N_G	BW_{eff} (bps/Hz) per polarization	Case
0.1	8	117.2	100	0.095	-11.2	5	4.193	X
0.5	14	205.1	150	0.125	-9	8	4.177	X
1.0	20	293.0	220	0.15	-8.24	11	4.162	X
2.0	40	586.0	400	0.211	-6.76	21	4.112	X
5.0	80	1172.0	800	0.3	-5.23	41	4.015	X
0.1	10	146.5	120	0.106	-9.75	6	4.188	Y
0.5	24	351.6	220	0.1637	-7.86	13	4.152	Y
1.0	40	586.0	400	0.211	-6.76	21	4.112	Y
2.0	60	879.0	600	0.257	-5.9	31	4.063	Y
5.0	120	1758.0	1200	0.36	-4.43	61	3.923	Y

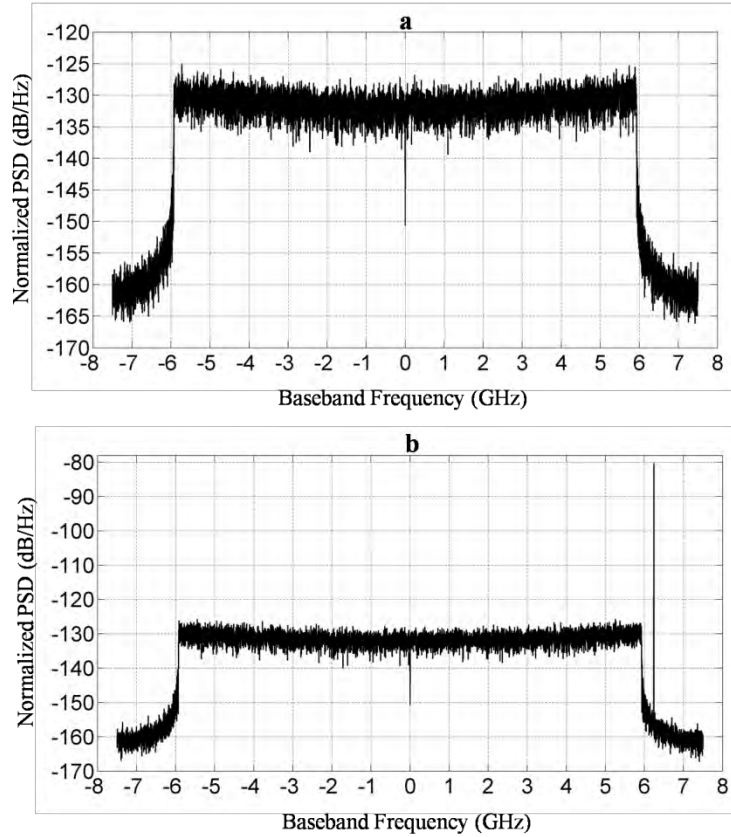


Fig. 8.3: Simulated DS-PSD of the BB OFDM signal (the computed time-vectors TiV before DAC’s function is applied) without and with the side pilot-tone in (a) and (b) respectively. A transfer function is applied at the frequency vector FrV to pre-equalize DACs’ response. Resolution BW is 1.53MHz.

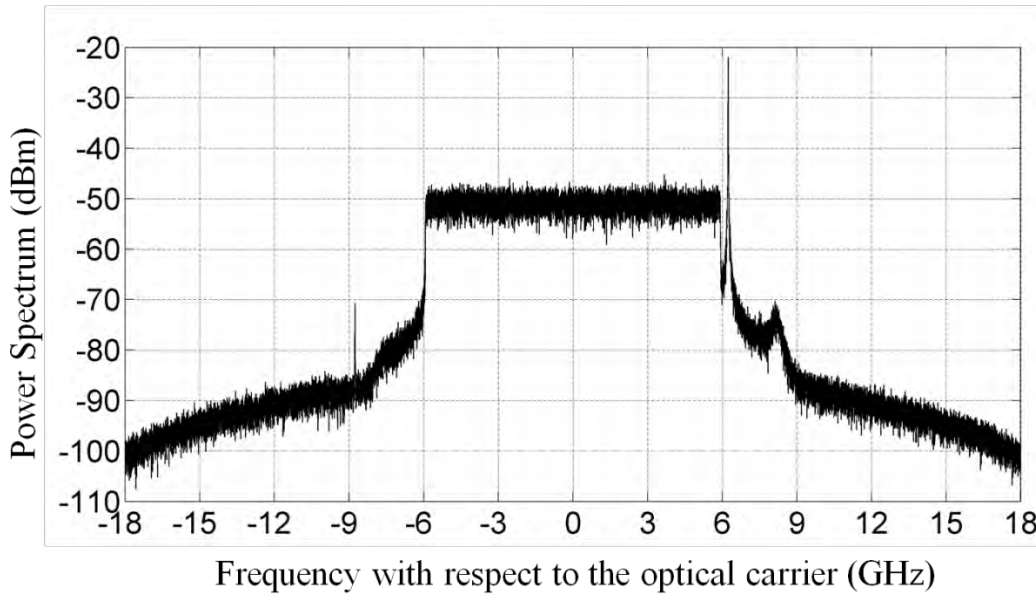


Fig. 8.4: Simulated power spectrum (dBm) in the optical domain of the transmitted OFDM signal just after the PBC in the TX. Two effects can be noticed here, the IQ nonlinearity contribution, which appears in the noise floor, and the relaxation oscillation of the pilot-tone. Resolution BW is 1.53MHz.

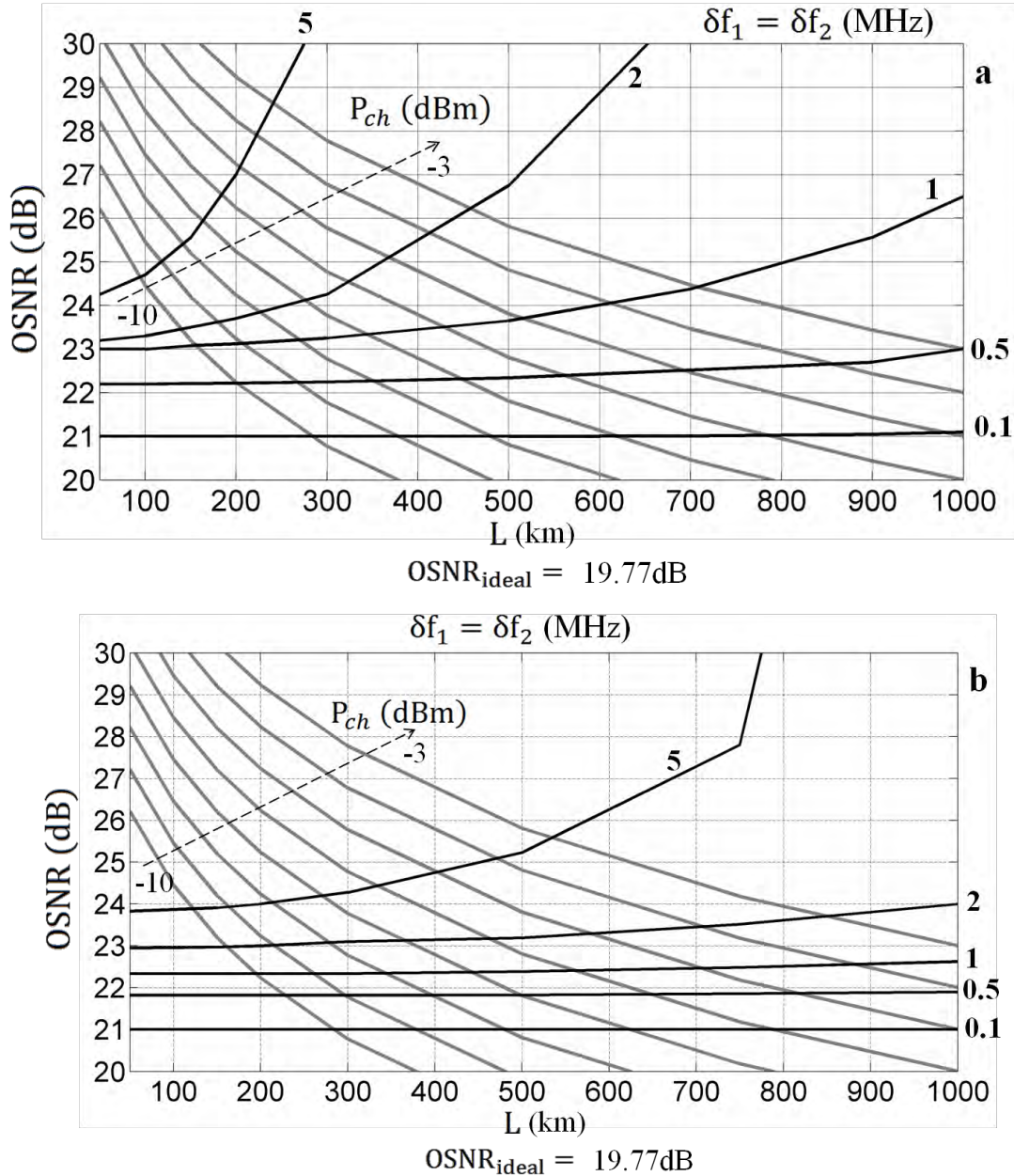


Fig. 8.5: Required OSNR (black-solid curves) and delivered OSNR (gray-solid curves) of the proposed homodyne CO-OFDM system versus L and δf showing the results when case-X is employed in (a), and when case-Y is employed in (b). Different launch powers P_{ch} are used since channel nonlinearity is not considered and hence optimal P_{ch} is unknown. The bold-written numbers corresponds to linewidth values.

8.3 Comparison with other CO-OFDM proposals

Comparison between different optical OFDM systems is not straightforward since no standard design has yet been accepted globally, or no real-time working system has yet been produced. Therefore, for a fair comparison, it is important to list all design

specifications regarding to the BB OFDM signal, DAC/ADC, SCLs, BW efficiency, data-rate, optical channel (fiber type, length per span, and amplifier's specifications) , and cost. Although average **BER** is usually considered, some SCs (the worst-corrupted ones) dominate this average, which is the case when pilot-tone is employed in the detection process as discussed previously. Two CO-OFDM proposals will be compared with our proposal focusing on the conceptual differences; the **1st** one was introduced by Jansen *et al.* [6], [10], and the **2nd** one by Shieh *et al.* [5], [23].

1. Jansen's proposal

- Pilot-aided heterodyne CO-OFDM system with/without Pol-Mux.
- QPSK up to 4160km (the longest experimental CO-OFDM distance), and 8-QAM up to 1000km using 100kHz SCL linewidth for the TX, and the RX.
- FDM can be used with pilot-tone in the middle of every subchannel.
- The pilot-tone is inserted via a slight biasing shift from the null point of the MZM or the IQ optical modulator. This technique was originally proposed by Schmidt [28].

Advantages:

- High reduction of SCL PN effect, and commercially available SCL can be used. However, no investigation about **BER** distribution over the SCs was given.

Disadvantages:

- The ADC sampling frequency F_s is at least four-times the minimal required one (their used setup) since the whole intermediate frequency (**IF**) spectrum is sampled.
- Although **PSPR_{opt}** was investigated in their work, method of pilot-tone insertion is a weak one, and cannot be controlled for long-term operation, since the **PSPR_{opt}** fluctuates due to parameters' fluctuation of the optical modulator.
- No image-rejection filter is used, and hence, the minimal **OSNR** penalty is 6dB. which represents the penalty floor.
- Manual polarization controller is essential (first experimental setups).
- High IF BW is necessary.

2. Shieh's proposal

- Conventional homodyne CO-OFDM with/without Pol-Mux.
- The 100Gbps proposal uses FDM with no guard band.

Advantages:

- Minimal required sampling frequency of DAC/ADC is used (first experiments).
- Lowest IF BW in (the first experiments).

Disadvantages:

- Stringent linewidth values are essential for practical post- \mathcal{FFT} PN equalization. For instance, in QPSK-CO-OFDM, they used $\Delta f \approx 70\text{MHz}$, and $\delta f = 100\text{kHz}$ for TX and RX, which corresponds 0.18rad^2 free-running PN variance.
- PN is enhanced due to the use of low sampling rate

Obviously the system proposed in this chapter is better than both Jansen's and Shieh's proposals, since it can be used with commercially available SCLs with relatively large PN, while using the minimal DAC/ADC requirements as well as minimal RF BW. Although this comparison is valid for relatively short distances, it can be held for long distance when the QPSK mapping is adopted instead of the 32-QAM. The system overcomes most of the design constraints of Section 2.5, and provides the best trade-off with fair cost.

8.4 Conclusions

In this chapter, a new 100Gbps homodyne CO-OFDM system with PA-FFL for PN reduction is introduced and examined. The system, as it proven here, can work properly with commercially available SCLs and becomes less PN sensitive with simple timing adjustment at the auxiliary circuit. All possible impairments of the used components and optical link (except fiber nonlinearity) in long-term operation are taken into account paving the way for practical design and implementation. Besides, worst-case performance estimation is adopted here to ensure that all SCs can reach the targeted **BER** and not only the less-corrupted ones. As long as the required **OSNR** is available, high SCLs' PN can be tolerated with acceptable penalties comparing with the conventional CO-OFDM, which is very sensitive to SCLs' PN. This system also exhibits **BW_{eff}** of roughly 4bps/Hz per polarization up to 500km assuming SCLs with 1MHz linewidth are used. All in all, the system is a promising design candidate for the future optical grid since the overall optical BW is about 12GHz for 100Gbps throughput.

Chapter 9

Conclusions and Future Work

9.1 Conclusions

This work is dedicated mainly for CO-OFDM system development focusing on the influence of SCLs' noise when PA-FFL is employed. Several important results and recommendations have been obtained from this study, which are summarized below.

1. PA-FFL is proven here to be an efficient technique for significantly improving the CO-OFDM's performance when SCLs with relatively large PN are used. For instance, in the conventional QPSK-CO-OFDM, $\delta f_{\text{Neq.}} = \delta f_{N1} + \delta f_{N2} \geq .03$, which is equivalent to free-running PN variance of $\sigma_{\mathbf{W}}^2(\mathbf{T}_{\mathcal{F}}) = 2\pi\delta f_{\text{eq.}}T_{\mathcal{F}} = 2\pi\delta f_{\text{Neq.}} \approx \underline{0.2\text{rad}^2}$ should be avoided since it represents the maximum tolerable linewidth condition with in **ideal** post-**FFT** PN equalizer. While when PA-FFL is used, $\delta f_{\text{Neq.}} = \underline{0.2}$ corresponding to $\sigma_{\mathbf{W}}^2(\mathbf{T}_{\mathcal{F}}) \approx \underline{1.26\text{rad}^2}$ without modifications and can be used up to 4000km with only 3dB penalty at pre-hard-decision-**BER** of 10^{-3} . Besides, higher $\delta f_{\text{Neq.}}$ can be tolerated with a slight increase in the penalty, while $\delta f_{\text{Neq.}} > \underline{.03}$ is not allowed in the conventional QPSK-CO-OFDM. In addition to that, when the TX-LO-SCL's linewidth δf_1 is relatively narrow, the CO-OFDM system with PA-FFL has almost a flat **OSNR** penalty versus distance, which is independent of how broad RX-LO-SCL's linewidth δf_2 is. Furthermore, in the conventional CO-OFDM with higher modulation density (constellation), more stringent $\delta f_{\text{Neq.}}$ than that given before must be fulfilled, while when 16-QAM mapping is employed with PA-FFL, $\delta f_{\text{Neq.}} = \underline{0.08}$ corresponding to $\sigma_{\mathbf{W}}^2(\mathbf{T}_{\mathcal{F}}) \approx \underline{0.5\text{rad}^2}$ can be used up to 1500km without modifications and with only 3dB penalty at pre-hard-decision-**BER** of 10^{-3} . The performance of the CO-OFDM with PA-FFL can be further improved when power distribution over the SCs is not even but depends on the pilot-tone's frequency index. Although in the CO-OFDM with PA-FFL, PN effect depends on the distance, by careful time delay adjustment of the delay-line in the FFL block, almost a flat penalty can be achieved.

2. The flicker noise has a marginal effect in the PA-FFL function; however, its effect is significant in frequency stability analysis, which is important in the AFC block design.
3. The relaxation oscillation's effect increases in the PA-FFL by increasing the modified ICI term. However, this effect is less critical in most of the available SCLs, and still the dominant parameter is the linewidth due to the white FN,
4. The new CO-OFDM design presented in Chapter 8 exhibits many advantages over the other proposals in the literature. The high \mathbf{BW}_{eff} of more than 4bps/Hz per polarization, the compact spectrum of about 12GHz per 100Gbps data-rate throughput, and commercially available SCLs can be used with $\delta\mathbf{f}_1 = \delta\mathbf{f}_2 = \underline{1\text{MHz}}$ up to 500km (noting that $\delta\mathbf{f}_2$ can be higher). Besides, polarization diversity matrix, I/Q imbalance matrix, and channel response matrix can be simultaneously estimated and corrected via DSP computation. The new proposed training symbol can facilitates extraction of the convolved matrix's coefficients as well as using it for OFDM synchronization. Commercially available components are required for RF circuits implementation, with minimal number of opto-electronic components. The main difficulty in this design is the DAC/ADC requirements, which are expected to be fulfilled in the near future.
5. The exact beat-note PSD expression derived in Chapter 6 was very useful in penalty analysis of CO-OFDM system with PA-FFL. This generalized and compact expression not only combines the works of Yamamoto *et al.* [45] and Richter *et al.* [108], but also takes all of the important SCL's parameters into account. Besides, the full description of the SCL's dispersive field can be used in many other applications such as DDO-OFDM's coloured noise variance estimation, SCM with pilot-aided detection, or RF-over-fiber systems.
6. It is found that distribution of the ICI noise in the conventional OFDM system cannot be considered as Gaussian when a SCL with relatively large linewidth is used. In general for QPSK-CO-OFDM, $\delta\mathbf{f}_{\text{Neq}} \leq \underline{0.02}$ corresponding to $\sigma_{\mathbf{W}}^2(\mathbf{T}_{\mathcal{F}}) \approx \underline{0.125\text{rad}^2}$, the ICI noise can be considered as a GRV if $\mathbf{BER} \geq 10^{-3}$ is considered. Otherwise the ICI distribution has a higher scattering rate than that of a GRV with the same variance, which causes more performance degradation compared with the Gaussian one.
7. The constructed SCL's functional model is a valid powerful tool for simulation of the optical systems despite it is not the exact physical model. This block along with a large

library of building blocks of different optical and RF components, can be used for real-time simulation of many linear and nonlinear optical system provided that no unknown phenomena exist. The sampling rate can be arbitrarily chosen with fast and slow loops, and linear and nonlinear blocks together in the system.

9.2 Future work

As in any other work, no perfection can be achieved without more patience, time, and further extensive efforts, and hence, many gaps are still required to be filled such as:

- 1- Using mathematical modeling to estimate the optimal power distribution over the OFDM' SCs for a given mapping when the PA-FFL is employed and a TX-LO-SCL with large PN is used. This step would considerably improve the performance by making the **BER** of the worst-corrupted SC equal to the less-corrupted one.
- 2- Deriving an expression for the exact launch power P_{ch} for the given homodyne CO-OFDM system, and for any other proposed CO-OFDM system with PA-FFL by introducing fiber nonlinearity, which has not been considered in this work.
- 3- Developing a new 100Gbps heterodyne QPSK-CO-OFDM system with PA-FFL, and as high BW_{eff} as possible. The new design is dedicated for ultra-long-haul transmission benefiting from the low required **OSNR** and the resilience of the QPSK modulation against all fiber and components impairments. Besides, in the new design, low DAC/ADC requirements are assumed by using FDM and Pol-Mux to achieve the required data-rate. Furthermore, it must also consider reducing the guard interval and the training symbol overhead since the penalty becomes intolerable. The key function here is the adopted multiplexing technique that can result high BW_{eff} with minimal number of optical components.
- 4- In-depth analysis of the ICI's PDF and second order statistics for an accurate **BER** estimation of the conventional CO-OFDM system when SCLs with large PN are used.
- 5- Improving the current SCL's model established in this work by introducing the cutoff and saturation region, power failure, environmental fluctuations, driving port's transfer function, and exact thermal transfer function. Besides, the building blocks library developed in this study can be expanded to cover many other opto-electronic devices, so that an optical communication blockset can be added to the Simulink[®] library.

Appendix-A: Derivation of Some Equations

Appendix-A1: Cross PSD derivation

In order to derive $\mathbf{S}_{Xg}(\mathbf{f})$, and $\mathbf{S}_{Xr}(\mathbf{f})$, we assume two noise sources $\mathbf{y}_1(\mathbf{t})$ and $\mathbf{y}_2(\mathbf{t})$, which are independent GRVs with zero-mean and $\{\sigma_{y_1}^2 = \sigma_{y_2}^2 = 1\}$. Therefore,

$$\alpha_n(\mathbf{f}) = y_1(\mathbf{f}) \cdot g_2 \cdot A_c(\mathbf{f}) \quad (\text{A1.1})$$

$$\phi_{nW}(\mathbf{f}) = \{y_1(\mathbf{f}) \cdot g_1 \cdot \gamma_1 \cdot H_c(\mathbf{f}) + y_2(\mathbf{f}) \cdot g_1 \cdot \gamma_2\} / (j2\pi f) \quad (\text{A1.2})$$

where $\mathbf{y}_1(\mathbf{f}) = \mathcal{FT}\{y_1(\mathbf{t})\}$, $\mathbf{y}_2(\mathbf{f}) = \mathcal{FT}\{y_2(\mathbf{t})\}$, $\phi_{nW}(\mathbf{f})$ is the PN component in FD due to the white FN only, and $\alpha_n(\mathbf{f})$ is normalized IN in FD. Then from (4.4) and the definition $\mathbf{RIN}_L(\mathbf{f})$ yields,

$$\mathbf{g1} = \sqrt{2\pi\delta f}, \mathbf{g2} = \sqrt{\mathbf{RIN}_L(0)/8}, \boldsymbol{\gamma1} = \sqrt{\alpha^2/(1 + \alpha^2)}, \text{ and } \boldsymbol{\gamma2} = \sqrt{1/(1 + \alpha^2)}.$$

From (4.13), $\mathbf{S}_{Xg}(\mathbf{f}) = \{\langle \alpha_n(\mathbf{f})\phi_n^*(\mathbf{f}) \rangle - \langle \alpha_n^*(\mathbf{f})\phi_n(\mathbf{f}) \rangle\} / 2$, and since $\mathbf{y}_2(\mathbf{t})$ is uncorrelated to $\alpha_n(\mathbf{t})$, then their cross-PSD is zero. Therefore

$$\langle \alpha_n(\mathbf{f})\phi_n^*(\mathbf{f}) \rangle = \frac{\langle |y_1(\mathbf{f})|^2 \rangle g_1 g_2 \gamma_1}{2\pi f} \cdot (jH_c^*(\mathbf{f})A_c(\mathbf{f})) \quad (\text{A1.3})$$

$$\langle \alpha_n^*(\mathbf{f})\phi_n(\mathbf{f}) \rangle = \frac{\langle |y_1(\mathbf{f})|^2 \rangle g_1 g_2 \gamma_1}{2\pi f} \cdot (jH_c(\mathbf{f})A_c^*(\mathbf{f})) \quad (\text{A1.4})$$

Let $\Re\{ \}$, and $\Im\{ \}$ denote respectively to the real and the imaginary part of any function. Therefore

$$(\langle \alpha_n(\mathbf{f})\phi_n^*(\mathbf{f}) \rangle - \langle \alpha_n^*(\mathbf{f})\phi_n(\mathbf{f}) \rangle) / 2 = j \frac{g_1 g_2 \gamma_1}{2\pi f} (\Re\{H_c(\mathbf{f})\}\Re\{A_c(\mathbf{f})\} + \Im\{H_c(\mathbf{f})\}\Im\{A_c(\mathbf{f})\})$$

Hence,
$$S_{Xg}(\mathbf{f}) = j \frac{g_1 g_2 \gamma_1}{2\pi f} \cdot (H_c(\mathbf{f})A_c^*(\mathbf{f}) + H_c^*(\mathbf{f})A_c(\mathbf{f})) / 2 \quad (\text{A1.5})$$

From (4.9), $\mathbf{A}_c(\mathbf{f})$ can be written as

$$\begin{aligned} A_c(\mathbf{f}) &= \frac{\sqrt{K_o}(-jf + K_z)}{F_R^2 - f^2 - j2\Gamma f} = \Re\{A_c(\mathbf{f})\} + j\Im\{A_c(\mathbf{f})\} \\ &= \sqrt{K_o} \frac{2\Gamma f^2 + K_z(F_R^2 - f^2)}{D} + j\sqrt{K_o} \frac{2\Gamma K_z f - f(F_R^2 - f^2)}{D} \end{aligned} \quad (\text{A1.6})$$

While from (4.6), $\mathbf{H}_c(\mathbf{f})$ can be written as

$$H_c(\mathbf{f}) = \frac{F_R^2}{F_R^2 - f^2 - j2\Gamma f} = \Re\{H_c(\mathbf{f})\} + j\Im\{H_c(\mathbf{f})\} = \frac{F_R^2(F_R^2 - f^2)}{D} + j \frac{2\Gamma F_R^2}{D} \quad (\text{A1.7})$$

where $\mathbf{D} = \{(F_R^2 - f^2)^2 + 4\Gamma^2 f^2\}$. Then after substituting of (A1.6) and (A1.7) in (A1.5), and after simplifications yields

$$S_{Xg}(f) = \sqrt{\frac{RIN_L(0) \cdot \delta f \cdot \alpha^2}{16\pi \cdot (1 + \alpha^2)}} \cdot \left(j \frac{|H_c(f)|^2}{f} \right) \quad (\text{A1.8})$$

Similar treatment is conducted for $\mathbf{S}_{Xr}(f)$, where

$$S_{Xr}(f) = (\langle \alpha_n(f) \phi_n^*(f) \rangle + \langle \alpha_n^*(f) \phi_n(f) \rangle) / 2 \quad (\text{A1.9})$$

Then by substituting of $\alpha_n(f)$, and $\phi_n(f)$ yields

$$\begin{aligned} S_{Xr}(f) &= \frac{g1g2\gamma1}{2\pi f} \cdot (-jH_c(f)A_c^*(f) + jH_c^*(f)A_c(f)) / 2 \\ &= \frac{g1g2\gamma1}{2\pi f} (\Im\{H_c(f)\}\Re\{A_c(f)\} - \Re\{H_c(f)\}\Im\{A_c(f)\}) \end{aligned} \quad (\text{A1.10})$$

Then after substituting of (A1.6) and (A1.7) in (A1.10), and after simplifications yields

$$\mathbf{S}_{Xr}(f) = \sqrt{\frac{RIN_L(0) \cdot \delta f \cdot \alpha^2}{16\pi \cdot (1 + \alpha^2)}} \cdot \left(\frac{|H_c(f)|^2}{K_z} \right) \quad (\text{A1.11})$$

Appendix-A2: Lorentzian Line-shape Derivation

From (4.10), if $\alpha_n(t) = 0$, then $\mathbf{R}_{EN}(\tau) = \langle \exp(j\Delta\phi_n(t)) \rangle$, and $\Delta\phi_n(t, \tau) = \phi_n(t) - \phi_n(t - \tau)$. By using (4.11) assuming $x_1(t) = \Delta\phi_n(t, \tau)$ then,

$$R_{EN}(\tau) = \langle \exp(j\Delta\phi_n(t)) \rangle = \exp(-\langle |x_2(t)|^2 \rangle / 2) \quad (\text{A2.1})$$

From time delay property of \mathcal{FT} [87], then

$\phi_n(t - \mathbf{T}_d) \equiv \phi_n(f)e^{-j2\pi f\mathbf{T}_d}$, then $\Delta\phi_n(f, \tau) = \phi_n(f) - \phi_n(f)e^{-j2\pi f\tau}$, or it can be written as $\Delta\phi_n(f, \tau) = j2e^{-j\pi f\tau} \sin\{\pi f\tau\} \phi_n(f)$, and hence

$$\mathcal{S}\{\Delta\phi_n(t, \tau)\} = S_{\Delta\phi_n}(f, \tau) = 4 \sin^2(\pi f\tau) \cdot S_{\phi_n}(f) \left(\frac{1}{1 + \alpha^2} + \frac{\alpha^2}{1 + \alpha^2} |H_c(f)|^2 \right) \quad (\text{A2.2})$$

From (4.3), and (4.5) we have

$$S_{\phi_n}(f) = \delta f / (2\pi f^2) \quad (\text{A2.3})$$

Then by substituting (A2.3) into (A2.2) yields

$$S_{\Delta\phi_n}(f, \tau) = \frac{2\pi\delta f\tau^2}{1 + \alpha^2} \text{sinc}^2(f\tau) + \frac{2\pi\delta f\tau^2\alpha^2}{1 + \alpha^2} \text{sinc}^2(f\tau)|H_c(f)|^2 \quad (\text{A2.4})$$

where $\text{sinc}(X) = \sin(\pi X) / (\pi X)$. Now since $|H_c(f)|^2 = 1$ is assumed, then

$$S_{\Delta\phi_n}(f, \tau) = 2\pi\delta f\tau^2 \cdot \text{sinc}^2(f\tau) \quad (\text{A2.4})$$

Therefore the differential PN variance is given by

$$\sigma_{\Delta\phi_n}^2(\tau) = 4\pi\delta f\tau^2 \cdot \int_0^\infty \text{sinc}^2(f\tau) df = 2\pi\delta f|\tau| \quad (\text{A2.5})$$

Accordingly, from (A2.1) yields

$$R_{\text{EN}}(\tau) = \exp(-\pi\delta f|\tau|) \quad (\text{A2.6})$$

By using **Wiener-Khintchin theorem** on (A2.6) assuming $\mathcal{L}_W(\mathbf{f}) = \mathcal{FT}\{R_{\text{EN}}(\tau)\}$, then

$$\mathcal{L}_W(\mathbf{f}) = \int_{-\infty}^\infty e^{-\pi\delta f|\tau|} e^{-j2\pi f\tau} d\tau = \frac{1}{(\pi\delta f + j2\pi f)} + \frac{1}{(\pi\delta f - j2\pi f)} = \frac{\delta f/(2\pi)}{(\delta f/2)^2 + f^2} \quad (\text{A2.7})$$

Appendix-A3: Limited T_{OBS} TF analysis

By choosing an arbitrary sample of $\mathbf{f}_{\text{nF}}(\mathbf{t})$, which is an arbitrary measurement of laser under test (**LUT**) assuming only flicker FN is counted. Then we assume this sample consists of a combination of sinusoids which is expressed as,

$\mathbf{f}_{\text{nF}}(\mathbf{t})|_\ell = \sum_i A_{i,\ell} \sin(2\pi f_i t + \theta_{i,\ell})$, where ℓ is the sample index in the ensemble, \mathbf{i} is frequency slot index, \mathbf{f}_i is the frequency of slot \mathbf{i} ($f_i = i$ when 1Hz frequency resolution is used), $\theta_{i,\ell}$ is the initial phase (at some time instant before the beginning of the test) of slot \mathbf{i} which is assumed to be uniformly distributed RV, and $A_{i,\ell}$ is amplitude. At $\mathbf{t} = \mathbf{t}_0$, the experiment is begun, then $\mathbf{f}_{\text{nF}}(\mathbf{t}_0)|_\ell = \sum_i A_{i,\ell} \sin(2\pi f_i t_0 + \theta_{i,\ell}) = \sum_i A_{i,\ell} \cdot \sin(\varphi_{i,\ell})$,

where $\varphi_{i,\ell} = 2\pi f_i t_0 + \theta_{i,\ell}$ as phase of the tone \mathbf{i} at \mathbf{t}_0 . Therefore, if $\mathbf{f}_{\text{nd}}(\mathbf{t})$ and $\mathbf{f}_{\text{nW}}(\mathbf{t})$ are ignored then from (4.18), $\mathbf{f}_{\text{ins},\ell}(\mathbf{t}_0) = \Delta f + \sum_i A_{i,\ell} \sin(\varphi_{i,\ell})$, which indicate that the beat-note frequency at \mathbf{t}_0 is high likely not to be exactly at Δf . Either we force $\mathbf{f}_{\text{ins}}(\mathbf{t}_0)$ to be at Δf , or we measure the line shape at $\{\Delta f + \text{offset}\}$. In both cases we may rewrite $\mathbf{f}_{\text{ins}}(\mathbf{t})$ as,

$\widehat{\mathbf{f}_{\text{ins}}}(\mathbf{t})|_\ell = \Delta f + \sum_i A_{i,\ell} \sin(2\pi f_i t + \theta_{i,\ell}) - \sum_i A_{i,\ell} \sin(\theta_{i,\ell})$, where $\widehat{\mathbf{f}_{\text{ins}}}(\mathbf{t})|_\ell$ is the instantaneous FN in time domain of an arbitrary sample that is forced to be measured at Δf assuming $\mathbf{t}_0 = 0$. Therefore the mean power per tone is,

$\langle \mathbf{P}_i \rangle = \frac{\langle A_i^2 \rangle}{T_{\text{OBS}}} \cdot \int_0^{T_{\text{OBS}}} \langle \sin^2(2\pi f_i t + \theta_i) + \sin^2(\theta_i) - 2\sin(\theta_i)\sin(2\pi f_i t + \theta_i) \rangle dt$, and since

$\langle \cos(2\theta_i) \rangle = 0$, $\langle \sin(2\theta_i) \rangle = 0$, and $\langle \sin^2(2\theta_i) \rangle = 1/2$, then

$\langle \mathbf{P}_i \rangle = \langle A_i^2 \rangle \cdot \{1 - \text{sinc}(f_i T_{\text{OBS}})\}$. Thus we define $\mathbf{H}_{\text{OBS}}(\mathbf{f}) = \{1 - \text{sinc}(f \cdot T_{\text{OBS}})\}$ as the

limited **T_{OBS}** TF which has a high-pass filter (**HPF**) response.

Appendix-A4: Optical frequency-discriminator analysis

O/P field from the discriminator shown in Fig. 4.11a is, $\mathbf{E}_O(\mathbf{t}) = \mathbf{E}(\mathbf{t}) * \mathbf{h}_d(\mathbf{t})$, where $\mathbf{h}_d(\mathbf{t})$ is the impulse response of the resonator whose TF is $\mathbf{H}_d(\mathbf{v})$. Suppose the active BW is $\Delta\mathbf{d}$, and let $\mathbf{H}_{d1}(\mathbf{v}) \approx j(a_1 + \beta_s \cdot (v - v_0)) \cdot \Pi\left(\frac{v-v_0}{\Delta\mathbf{d}}\right)$, as the TF in the active band $[v_1 \leq v \leq v_2]$, and $\mathbf{H}_{d2}(\mathbf{v}) = H_d(v) \cdot \left(1 - \Pi\left(\frac{v-v_0}{\Delta\mathbf{d}}\right)\right)$ as the TF in the band $[v < v_1] \cup [v > v_2]$ as shown in Fig. 4.11a, where β_s is the slope at \mathbf{v}_O .

Here $\beta_s = (\Delta a / \Delta d)$ in (s), $\Pi\left(\frac{v-v_0}{\Delta\mathbf{d}}\right)$ is a rectangular window function in optical frequency domain with frequency width of $\Delta\mathbf{d} = v_2 - v_1$, and \mathbf{a}_1 is the normalized amplitude at \mathbf{v}_O , where $\mathbf{a}_1 = 10^{-\{\text{att}(\mathbf{v}_O)_{\text{dB}}/20\}}$, and $\text{att}(\mathbf{v}_O)_{\text{dB}}$ is attenuation at \mathbf{v}_O . For instance, if $\Delta\mathbf{d} = 1\text{GHz}$, $\Delta a = 0.3$, then $\beta_s = 3 \times 10^{-10}$ (s). Now we may rewrite (4.2) in TD as $\mathbf{E}(\mathbf{t}) = E_s(\mathbf{t}) + E_n(\mathbf{t}) = \sqrt{P_0} \cdot e^{j2\pi v_0 t + j\phi_n(\mathbf{t})} + \sqrt{P_0} \alpha_n(\mathbf{t}) \cdot e^{j2\pi v_0 t + j\phi_n(\mathbf{t})}$, and $\mathbf{E}(\mathbf{v}) = E_s(\mathbf{v}) + E_n(\mathbf{v})$. Then the discriminator's O/P in optical FD is,

$$\begin{aligned} \mathbf{E}_O(\mathbf{v}) &= (E_s(\mathbf{v}) + E_n(\mathbf{v})) \cdot H_{d1}(\mathbf{v}) + (E_s(\mathbf{v}) + E_n(\mathbf{v})) \cdot H_{d2}(\mathbf{v}) \\ &= E_{s1}(\mathbf{v}) + E_{n1}(\mathbf{v}) + (E_s(\mathbf{v}) + E_n(\mathbf{v})) \cdot H_{d2}(\mathbf{v}), \text{ where} \end{aligned}$$

$$\mathbf{E}_{s1}(\mathbf{v}) = \mathcal{FT}\{\sqrt{P_0} e^{j2\pi v_0 t + j\phi_n(\mathbf{t})}\} \cdot H_{d1}(\mathbf{v}),$$

$$\mathbf{E}_{n1}(\mathbf{v}) = \mathcal{FT}\{\sqrt{P_0} \alpha_n(\mathbf{t}) e^{j2\pi v_0 t + j\phi_n(\mathbf{t})}\} \cdot H_{d1}(\mathbf{v}). \text{ Therefore}$$

$$\begin{aligned} \mathbf{E}_{s1}(\mathbf{v}) &= jE_s(\mathbf{v}) \cdot \{a_1 + \beta_s(v - v_0)\} \cdot \Pi\left(\frac{v-v_0}{\Delta\mathbf{d}}\right) \\ &= \left\{jE_s(\mathbf{v}) \cdot a_1 + (j2\pi v \cdot E_s(\mathbf{v})) \frac{\beta_s}{2\pi} - j2\pi v_0 E_s(\mathbf{v}) \cdot \frac{\beta_s}{2\pi}\right\} \cdot \Pi\left(\frac{v-v_0}{\Delta\mathbf{d}}\right). \end{aligned}$$

By using the differentiation property of \mathcal{FT} , and distributive property of convolution [87] then,

$$\begin{aligned} \mathbf{E}_{s1}(\mathbf{t}) &= j\sqrt{P_0} \cdot \left\{a_1 + \frac{\beta_s}{2\pi} \cdot \frac{d\phi_n(\mathbf{t})}{dt}\right\} \cdot e^{j2\pi v_0 t + j\phi_n(\mathbf{t})} * \Delta\mathbf{d} \cdot \text{sinc}(\Delta\mathbf{d} \cdot \mathbf{t}) e^{j2\pi v_0 t}, \text{ and } \mathbf{E}_{n1}(\mathbf{t}) = \\ &= \sqrt{P_0} \cdot \left\{\frac{\beta_s}{2\pi} \cdot \frac{d\alpha_n(\mathbf{t})}{dt} + j\alpha_n(\mathbf{t}) + j\alpha_n(\mathbf{t}) \frac{\beta_s}{2\pi} \cdot \frac{d\phi_n(\mathbf{t})}{dt}\right\} e^{j2\pi v_0 t + j\phi_n(\mathbf{t})} * \Delta\mathbf{d} \cdot \text{sinc}(\Delta\mathbf{d} \cdot \mathbf{t}) e^{j2\pi v_0 t}. \end{aligned}$$

Let $\mathbf{E}_{O1}(\mathbf{t}) = E_{s1}(\mathbf{t}) + E_{n1}(\mathbf{t})$, then

$$\begin{aligned} \mathbf{E}_{O1}(\mathbf{t}) &= \sqrt{P_0} \cdot \left\{\frac{\beta_s}{2\pi} \cdot \frac{d\alpha_n(\mathbf{t})}{dt} + j(1 + \alpha_n(\mathbf{t})) \cdot \left(a_1 + \frac{\beta_s}{2\pi} \cdot \frac{d\phi_n(\mathbf{t})}{dt}\right)\right\} \cdot e^{j2\pi v_0 t + j\phi_n(\mathbf{t})} * \Delta\mathbf{d} \\ &\quad \cdot \text{sinc}(\Delta\mathbf{d} \cdot \mathbf{t}) \cdot e^{j2\pi v_0 t} \end{aligned}$$

For instance when $\Delta\mathbf{d} \gg \delta\mathbf{f}$ and there is no sharp slopes in resonator's TF outside $\Delta\mathbf{d}$, then $\mathbf{E}_s(\mathbf{f}) \cdot \mathbf{H}_{d2}(\mathbf{f})$ could be ignored. According to this assumption, $\mathbf{E}_O(\mathbf{t}) \approx \mathbf{E}_{O1}(\mathbf{t})$, and

since $\Delta \mathbf{d}/2$ is much larger than measurement BW, then we can discard $\{\mathbf{sinc}(\Delta \cdot \mathbf{t})\}$ term. Hence the photo-current is, $\mathbf{i}_{PC}(\mathbf{t}) \approx \mathcal{R} \cdot E_{O1}(\mathbf{t}) \cdot E_{O1}^*(\mathbf{t})$ which after discarding all noise \times noise terms and the DC component becomes

$$i_{PC}(t) \approx 2\mathcal{R}P_0 a_1^2 \cdot \alpha_n(t) + 2\mathcal{R}P_0 a_1 \beta_s \cdot f_n(t) + i_{sh}(t) + i_{th}(t) \quad (\text{A4.1})$$

$$\text{where } \mathbf{f}_n(\mathbf{t}) = \left\{ \frac{1}{2\pi} \frac{d\phi_n(\mathbf{t})}{dt} \right\} .$$

Note that shot and thermal noise are uncorrelated with $\alpha_n(\mathbf{t})$ and $\mathbf{f}_n(\mathbf{t})$ and their PSDs are just added, while $\alpha_n(\mathbf{t})$ and $\mathbf{f}_n(\mathbf{t})$ are correlated since they are driven by same noise source $\mathbf{N}_i(\mathbf{t})$ as given in (4.4), hence their cross PSD has to be taken into account [90].

Let $\mathbf{K}_1 = 2\mathcal{R}P_0 a_1^2$, and $\mathbf{K}_2 = 2\mathcal{R}P_0 a_1 \beta_s$, then (A4.1) is written as $\mathbf{i}_{PC}(\mathbf{t}) \approx \mathbf{K}_1 \alpha_n(\mathbf{t}) + \mathbf{K}_2 \mathbf{f}_n(\mathbf{t}) + i_{sh}(t) + i_{th}(t)$. By calculating the ACF of $\mathbf{i}_{PC}(\mathbf{t})$ then,

$$\begin{aligned} \mathbf{R}_{i_{PC}}(\boldsymbol{\tau}) &= \langle i_{PC}(t) i_{PC}^*(t - \tau) \rangle = \mathbf{K}_1^2 \langle \alpha_n(t) \alpha_n^*(t - \tau) \rangle + \mathbf{K}_2^2 \langle f_n(t) f_n^*(t - \tau) \rangle \\ &\quad + \mathbf{K}_1 \mathbf{K}_2 \{ \langle \alpha_n(t) f_n^*(t - \tau) \rangle + \langle f_n(t) \alpha_n^*(t - \tau) \rangle \} + S_{sh}(t) + S_{th}(t) \end{aligned}$$

Since we are measuring the SS-PSD then $\mathcal{FT}\{\langle \alpha_n(t) \alpha_n^*(t - \tau) \rangle\} = \mathbf{S}_{\alpha_n, SS}(\mathbf{f})$, $\mathcal{FT}\{\langle f_n(t) f_n^*(t - \tau) \rangle\} = \mathbf{S}_{f_n}(\mathbf{f})$, while $\mathcal{FT}\{\langle \alpha_n(t) f_n^*(t - \tau) \rangle + \langle f_n(t) \alpha_n^*(t - \tau) \rangle\}$ is calculated in similar way given in appendix-A1, which yields $\mathcal{FT}\{\langle \alpha_n(t) f_n^*(t - \tau) \rangle + \langle f_n(t) \alpha_n^*(t - \tau) \rangle\} = \Re\{\mathbf{S}_{\alpha \times f, SS}(\mathbf{f})\}$, and

$$\Re\{\mathbf{S}_{\alpha \times f, SS}(\mathbf{f})\} = \sqrt{\left(\frac{\delta f}{\pi}\right) \cdot \text{RIN}_L(0) \cdot \left(\frac{\alpha^2}{1 + \alpha^2}\right) \cdot |H_c(f)|^2} \quad (\text{A4.2})$$

Therefore the photo current SS-PSD is

$$S_d(f) \approx \mathbf{K}_2^2 S_{f_n}(f) + \mathbf{K}_1^2 S_{\alpha_n, SS}(f) + \mathbf{K}_1 \mathbf{K}_2 \Re\{\mathbf{S}_{\alpha \times f, SS}(f)\} + S_{sh}(t) + S_{th}(t) \quad (\text{A4.3})$$

By comparing this equation with (4.33) we find that,

$$\boldsymbol{\eta} = \mathbf{K}_2^2, \text{ and } \widetilde{\mathbf{S}}_{IN}(\mathbf{f}) = \mathbf{K}_1^2 S_{\alpha_n, SS}(f) + \mathbf{K}_1 \mathbf{K}_2 \Re\{\mathbf{S}_{\alpha \times f, SS}(f)\} + S_{sh}(t) + S_{th}(t)$$

Finally (A4.3) is scaled to $\boldsymbol{\eta}$ and yields

$$\begin{aligned} S_{fn}(f)_m &\approx S_{fn}(f) + \left(\frac{\mathbf{K}_1}{\mathbf{K}_2}\right)^2 S_{\alpha_n, SS}(f) + \left(\frac{\mathbf{K}_1}{\mathbf{K}_2}\right) \Re\{\mathbf{S}_{\alpha \times f, SS}(f)\} + \frac{S_{sh}(t) + S_{th}(t)}{\mathbf{K}_2^2} \\ &\approx S_{fn}(f) + \left(\frac{a_1}{\beta_s}\right)^2 S_{\alpha_n, SS}(f) + \left(\frac{a_1}{\beta_s}\right) \sqrt{\left(\frac{\delta f}{\pi}\right) \cdot \text{RIN}_L(0) \cdot \left(\frac{\alpha^2}{1 + \alpha^2}\right) \cdot |H_c(f)|^2} \\ &\quad + \frac{S_{sh}(t) + S_{th}(t)}{(2\mathcal{R}P_0 a_1 \beta_s)^2} \end{aligned} \quad (\text{A4.4})$$

Appendix-A5: Analysis of heterodyne FN extraction using balanced discriminator

Let the TF of the frontend band-pass filter (**BPF**) is $\mathbf{H}_{\text{BPF}}(\mathbf{f})$ with impulse response $\mathbf{h}_{\text{BPF}}(\mathbf{t})$, and has the following optimum characteristics:

- 1) center frequency = $\Delta\mathbf{f}$,
- 2) flat response within the effective discrimination BW of \mathbf{B}_d in (Hz), and
- 3) constant group delay τ_g in (s) in the effective BW.

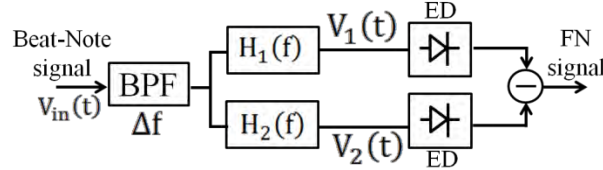


Fig. A5.1: Balanced frequency discriminator block diagram. **ED** is envelope detector.

From Fig. A5.1, we have

$$\mathbf{H}_1(\mathbf{f}) = j\beta_s \cdot \left\{ \mathbf{f} - \left(\Delta\mathbf{f} - \frac{\mathbf{B}_d}{2} \right) \right\} \quad (\text{A5.1-a})$$

$$\mathbf{H}_2(\mathbf{f}) = -j\beta_s \cdot \left\{ \mathbf{f} - \left(\Delta\mathbf{f} + \frac{\mathbf{B}_d}{2} \right) \right\} \quad (\text{A5.1-b})$$

where β_s is the normalized discriminator's slope. When perfect frequency alignment is achieved, i.e. when the optical frequency difference between the two lasers exactly equals the discriminator's center frequency $\Delta\mathbf{f}$ during every sweep of SA, then the following analysis is valid without distortion terms. Note that the low frequency components that will not be measured due to AFC function depends on the AFC tracking BW, which in turns depends on lasers' frequency shift during SA's sweep time. Assuming a BD setup is used as shown in Fig. 4.12, hence from (4.35-a) after introducing the TIA's gain of \mathbf{g} in (Ω), then the O/P voltage from the BPF is

$$\begin{aligned} \mathbf{V}_{\text{inF}}(\mathbf{t}) &= (\mathbf{g} \cdot i_{\text{PC}}(\mathbf{t})) * \mathbf{h}_{\text{BPF}}(\mathbf{t}) \\ &= \left(2\mathcal{R}g\sqrt{P_{O1}P_{O2}} \cdot (1 + \alpha_{n1}(\mathbf{t}) + \alpha_{n2}(\mathbf{t})) \cdot \cos(2\pi\Delta\mathbf{f}\mathbf{t} + \Delta\phi_n(\mathbf{t})) \right) \\ &\quad + \mathbf{g}(i_{\text{sh1}}(\mathbf{t}) - i_{\text{sh2}}(\mathbf{t})) + \mathbf{g}i_{\text{th}}(\mathbf{t}) * \mathbf{h}_{\text{BPF}}(\mathbf{t}) \end{aligned} \quad (\text{A5.2})$$

Hence from Fig. A5.1, $\mathbf{V}_1(\mathbf{f}) = \mathbf{H}_1(\mathbf{f})\mathbf{V}_{\text{inF}}(\mathbf{f}) = \{\mathbf{g} \cdot i_{\text{PC}}(\mathbf{f})\}\mathbf{H}_{\text{BPF}}(\mathbf{f})\mathbf{H}_1(\mathbf{f})$, and $\mathbf{V}_2(\mathbf{f}) = \mathbf{H}_2(\mathbf{f})\mathbf{V}_{\text{inF}}(\mathbf{f}) = \{\mathbf{g} \cdot i_{\text{PC}}(\mathbf{f})\}\mathbf{H}_{\text{BPF}}(\mathbf{f})\mathbf{H}_2(\mathbf{f})$. Therefore by substituting of (A5.1-a) yields

$$\begin{aligned} \mathbf{V}_1(\mathbf{f}) &= \left\{ \left(j2\pi\mathbf{f} \cdot (\mathbf{g} \cdot i_{\text{PC}}(\mathbf{f})) \right) \frac{\beta_s}{2\pi} - j\beta_s \cdot \left(\Delta\mathbf{f} - \frac{\mathbf{B}_d}{2} \right) \cdot (\mathbf{g} \cdot i_{\text{PC}}(\mathbf{f})) \right\} \cdot \mathbf{H}_{\text{BPF}}(\mathbf{f}) \\ &= -2\mathbf{g}\mathcal{R}\sqrt{P_{O1}P_{O2}}\beta_s \left\{ \frac{\mathbf{B}_d}{2} + \mathbf{f}_n(\mathbf{t}) \right\} \cdot \sin\{2\pi\Delta\mathbf{f}\mathbf{t} + \Delta\phi_n(\mathbf{t})\} * \mathbf{h}_{\text{BPF}}(\mathbf{t}) + \mathbf{v}_{n1}(\mathbf{t}) \end{aligned} \quad (\text{A5.3})$$

where $\mathbf{v}_{n1}(\mathbf{t})$ is the upper arm noise voltage. The envelope detector (**ED**) followed by a low-pass filter (**LPF**) functions as a frequency shifter that shifts the bandpass signal into the baseband with a conversion factor of ξ . Thus the O/P from the upper and lower arms of EDs are expressed as

$$\mathbf{V}_{O/P1}(\mathbf{t}) \approx -2g\mathcal{R}\sqrt{P_{O1}P_{O2}}\beta_s\xi \cdot \left\{ \frac{B_d}{2} + f_n(\mathbf{t}) \right\} + v_{nO/P1}(\mathbf{t}) \quad (\text{A5.4-a})$$

$$\mathbf{V}_{O/P2}(\mathbf{t}) \approx 2g\mathcal{R}\sqrt{P_{O1}P_{O2}}\beta_s\xi \cdot \left\{ -\frac{B_d}{2} + f_n(\mathbf{t}) \right\} + v_{nO/P2}(\mathbf{t}) \quad (\text{A5.4-b})$$

Then the net O/P voltage is $\mathbf{V}_{O/P}(\mathbf{t}) = \mathbf{V}_{O/P1}(\mathbf{t}) - \mathbf{V}_{O/P2}(\mathbf{t})$, which can be written as

$$\mathbf{V}_{O/P}(\mathbf{t}) \approx 4g\mathcal{R}\sqrt{P_{O1}P_{O2}}\beta_s\xi \cdot f_n(\mathbf{t}) + v_{nO/P}(\mathbf{t}) \quad (\text{A5.5})$$

Where the added noise term is

$$\begin{aligned} \mathbf{v}_{nO/P}(\mathbf{t}) \approx & g\beta_s B_d \xi \\ & \cdot \left(2\mathcal{R}\sqrt{P_{O1}P_{O2}}(\alpha_{n1}(\mathbf{t}) + \alpha_{n2}(\mathbf{t})) \cos\{2\pi\Delta f\mathbf{t} + \Delta\phi_n(\mathbf{t})\} \right. \\ & \left. + (i_{sh1}(\mathbf{t}) - i_{sh2}(\mathbf{t})) + i_{th}(\mathbf{t}) \right) \end{aligned} \quad (\text{A5.6})$$

Therefore the measured SS-PSD after scaling is

$$\begin{aligned} S_{fn}(f)_m \approx & S_{fT}(f) + \left(\frac{B_d}{2} \right)^2 \left(S_{1\alpha_n,SS}(f) + S_{2\alpha_n,SS}(f) \right) \\ & - B_d \left(\Re\{S_{1\alpha \times f,SS}(f)\} + \Re\{S_{2\alpha \times f,SS}(f)\} \right) + \left(\frac{B_d}{2} \right)^2 \frac{q_e(P_{O1} + P_{O2})}{2\mathcal{R}P_{O1}P_{O2}} \\ & + \left(\frac{B_d}{4} \right)^2 \frac{\mathcal{K}T^\circ N_f}{R_L(\mathcal{R}P_{O1}P_{O2})^2} \end{aligned} \quad (\text{A5.7})$$

Appendix-A6: Normalized-BB ACF due to the white FN in DSH test

Let $\mathbf{V} = \Delta\phi_T(\mathbf{t}) - \Delta\phi_T(\mathbf{t} - \tau)$, where $\Delta\phi_T(\mathbf{t}) = \phi_n(\mathbf{t}) - \phi_n(\mathbf{t} - T_d)$, assuming \mathbf{V} is Gaussian RV with zero mean, then

$$\sigma_V^2 = \overline{\Delta\phi_T(\mathbf{t})^2} + \overline{\Delta\phi_T(\mathbf{t} - \tau)^2} - 2\overline{\Delta\phi_T(\mathbf{t}) \cdot \Delta\phi_T(\mathbf{t} - \tau)} \quad (\text{A6.1})$$

From (4.18), the BB instantaneous FN is given in TD as

$\mathbf{f}_{ins}(\mathbf{t}) = f_{nrw}(\mathbf{t}) + f_{nF}(\mathbf{t}) + f_{nW}(\mathbf{t})$, and by ignoring $\mathbf{f}_{nrw}(\mathbf{t})$ for instant, then

$$\mathbf{f}_{ins}(\mathbf{t}) \approx f_{nF}(\mathbf{t}) + f_{nW}(\mathbf{t}) \quad (\text{A6.2})$$

Therefore $\phi_n(\mathbf{t}) \approx \phi_{nW}(\mathbf{t}) + \phi_{nF}(\mathbf{t})$, and $\Delta\phi_T(\mathbf{t}) \approx \Delta\phi_{TW}(\mathbf{t}) + \Delta\phi_{TF}(\mathbf{t})$. Now since $E\{\overline{\Delta\phi_T(\mathbf{t})^2}\}$ is time independent as it has been proven in section (4.2.3.1), then

$E\{\overline{\Delta\phi_T(\mathbf{t})^2}\} = E\{\overline{\Delta\phi_T(\mathbf{t} - \Delta T)^2}\}$, where ΔT is any time delay. For convenience, we might not use the expectation notation, then from (A6.1) yields

$$\begin{aligned}\sigma_V^2 &= 2\overline{\Delta\phi_T(t)^2} - 2\overline{\Delta\phi_T(t) \cdot \Delta\phi_T(t-\tau)} = \\ &2\overline{\{\phi_T(t) - \phi_T(t-T_d)\}^2} + 2\overline{\{\phi_T(t) - \phi_T(t-T_d)\} \cdot \{\phi_T(t-\tau) - \phi_T(t-T_d-\tau)\}}.\end{aligned}$$

Now since $\overline{\phi_{TW}(t) \cdot \phi_{TF}(t-\Delta T)} = 0$ since $\phi_{nW}(t)$ and $\phi_{nF}(t)$ are completely uncorrelated, then

$$\sigma_V^2 = \sigma_{VW}^2 + \sigma_{VF}^2 \quad (\text{A6.3})$$

where $\sigma_{VW}^2 = \overline{\Delta\phi_{TW}(t)^2} + \overline{\Delta\phi_{TW}(t-\tau)^2} - 2\overline{\Delta\phi_{TW}(t)\Delta\phi_{TW}(t-\tau)}$, and

$$\sigma_{VF}^2 = \overline{\Delta\phi_{TF}(t)^2} + \overline{\Delta\phi_{TF}(t-\tau)^2} - 2\overline{\Delta\phi_{TF}(t)\Delta\phi_{TF}(t-\tau)}.$$

For the white part,

$\sigma_{VW}^2 = \overline{\Delta\phi_{TW}(t)^2} + \overline{\Delta\phi_{TW}(t-\tau)^2} - 2\overline{\Delta\phi_{TW}(t)\Delta\phi_{TW}(t-\tau)}$, and from (A2.5) we have,

$$\overline{\Delta\phi_{TW}(t)^2} = 2\pi\delta f T_d, \text{ then } \sigma_{VW}^2 = 4\pi\delta f T_d - 2\overline{\Delta\phi_{TW}(t)\Delta\phi_{TW}(t-\tau)}$$

However, since $\overline{\Delta\phi_{TW}(t)^2} = \overline{\phi_{nW}(t)^2} + \overline{\phi_{nW}(t-T_d)^2} - 2\overline{\phi_{nW}(t)\phi_{nW}(t-T_d)}$, or

$$\overline{\Delta\phi_{TW}(t)^2} = 2\overline{\phi_{nW}(t)^2} - 2\overline{\phi_{nW}(t)\phi_{nW}(t-T_d)} = 2\pi\delta f T_d, \text{ then}$$

$\overline{\phi_{nW}(t)\phi_{nW}(t-T_d)} = \overline{\phi_{nW}(t)^2} - \pi\delta f T_d$, which can be written for any time delay ΔT as

$$\overline{\phi_{nW}(t)\phi_{nW}(t-\Delta T)} = \overline{\phi_{nW}(t)^2} - \pi\delta f \Delta T \quad (\text{A6.4})$$

Now since

$$\begin{aligned}\overline{\Delta\phi_{TW}(t)\Delta\phi_{TW}(t-\tau)} &= \overline{\{\phi_{nW}(t) - \phi_{nW}(t-T_d)\} \cdot \{\phi_{nW}(t-\tau) - \phi_{nW}(t-T_d-\tau)\}} \\ &= \overline{\phi_{nW}(t)\phi_{nW}(t-\tau)} + \overline{\phi_{nW}(t-T_d)\phi_{nW}(t-T_d-\tau)} - \overline{\phi_{nW}(t)\phi_{nW}(t-T_d-\tau)} - \\ &\overline{\phi_{nW}(t-T_d)\phi_{nW}(t-\tau)}, \text{ which has 3 different differential delays, } |\tau|, |T_d + \tau|, \text{ and } \\ &|T_d - \tau|. \text{ Then from (A6.4) yields}\end{aligned}$$

$$\begin{aligned}\overline{\Delta\phi_{TW}(t)\Delta\phi_{TW}(t-\tau)} &= 2\{\overline{\phi_{nW}(t)^2} - \pi\delta f |\tau|\} - \overline{\phi_{nW}(t)^2} + \pi\delta f |T_d + \tau| - \overline{\phi_{nW}(t)^2} + \pi\delta f |T_d - \tau| \\ &= -2\pi\delta f \cdot |\tau| + \pi\delta f \cdot |T_d + \tau| + \pi\delta f \cdot |T_d - \tau| \\ &= -\pi\delta f \cdot \{2|\tau| - |T_d + \tau| - |T_d - \tau|\}\end{aligned} \quad (\text{A6.5})$$

Accordingly from (A6.3) yields

$$\sigma_{VW}^2(\tau, T_d) = 2\pi\delta f \cdot \{2T_d + 2|\tau| - |T_d + \tau| - |T_d - \tau|\} \quad (\text{A6.6})$$

Therefore from (4.11), the normalized-BB ACF is calculated as

$$\begin{aligned}R_{N,BB}(\tau) &= \exp(-\sigma_{VW}^2(\tau, T_d)/2) \\ &= \exp(-\pi\delta f \cdot \{2T_d + 2|\tau| - |T_d + \tau| - |T_d - \tau|\})\end{aligned} \quad (\text{A6.7})$$

Appendix-A7: Normalized-BB version of Richter et al. equation

By applying Wiener-Khintchin theorem on the normalized-BB version of (4.43), then

$$\begin{aligned} \mathcal{S}\{\mathbf{i}_{\text{BN, BB}}^+(\mathbf{t})\} &= \int_{-\infty}^{\infty} R_{\text{BN, BB}}^+(\tau) e^{-j2\pi f\tau} d\tau = \int_{-\infty}^{-T_d} e^{-\pi\delta f\{2T_d-2\tau+(T_d+\tau)-(T_d-\tau)\}-j2\pi f\tau} d\tau + \\ &\int_{-T_d}^0 e^{-\pi\delta f\{2T_d-2\tau-(T_d+\tau)-(T_d-\tau)\}-j2\pi f\tau} d\tau + \int_0^{T_d} e^{-\pi\delta f\{2T_d+2\tau-(T_d+\tau)-(T_d-\tau)\}-j2\pi f\tau} d\tau + \\ &\int_{T_d}^{\infty} e^{-\pi\delta f\{2T_d+2\tau-(T_d+\tau)+(T_d-\tau)\}-j2\pi f\tau} d\tau = \int_{-\infty}^{-T_d} e^{-2\pi\delta f\Gamma_d-j2\pi f\tau} d\tau + \int_{-T_d}^0 e^{+2\pi(\delta f-jf)\tau} d\tau + \\ &\int_0^{T_d} e^{-2\pi(\delta f+jf)\tau} d\tau + \int_{T_d}^{\infty} e^{-2\pi\delta f\Gamma_d-j2\pi f\tau} d\tau = \mathbf{I}_1 + \mathbf{I}_2 + \mathbf{I}_3 + \mathbf{I}_4. \end{aligned}$$

$$\text{where, } \mathbf{I}_1 + \mathbf{I}_4 = \int_{-\infty}^{-T_d} e^{-2\pi\delta f\Gamma_d-j2\pi f\tau} d\tau + \int_{T_d}^{\infty} e^{-2\pi\delta f\Gamma_d-j2\pi f\tau} d\tau$$

$$= e^{-2\pi\delta f\Gamma_d} \int_{-\infty}^{\infty} \left\{1 - \Pi\left(\frac{\tau}{2T_d}\right)\right\} e^{-j2\pi f\tau} d\tau = e^{-2\pi\delta f\Gamma_d} \cdot \{\delta(f) - 2T_d \cdot \text{sinc}(2fT_d)\}$$

$$= e^{-2\pi\delta f\Gamma_d} \cdot \left\{\delta(f) - \frac{\sin(2\pi fT_d)}{\pi f}\right\},$$

$$\text{and } \mathbf{I}_2 + \mathbf{I}_3 = \int_{-T_d}^0 e^{+2\pi(\delta f-jf)\tau} d\tau + \int_0^{T_d} e^{-2\pi(\delta f+jf)\tau} d\tau$$

$$= \frac{1}{2\pi(\delta f-jf)} \cdot \{1 - e^{-2\pi(\delta f-jf)T_d}\} + \frac{1}{2\pi(\delta f+jf)} \cdot \{1 - e^{-2\pi(\delta f+jf)T_d}\} = \frac{1}{2\pi(\delta f-jf)} + \frac{1}{2\pi(\delta f+jf)}$$

$$- \frac{e^{-2\pi\delta fT_d} \cdot e^{j2\pi fT_d}}{2\pi(\delta f-jf)} - \frac{e^{-2\pi\delta fT_d} \cdot e^{-j2\pi fT_d}}{2\pi(\delta f+jf)} = \frac{\delta f}{\pi(\delta f^2+f^2)} - \frac{e^{-2\pi\delta fT_d}}{2\pi} \cdot \left\{\frac{e^{j2\pi fT_d}}{(\delta f-jf)} + \frac{e^{-j2\pi fT_d}}{(\delta f+jf)}\right\}$$

$$= \frac{\delta f}{\pi(\delta f^2+f^2)} - \frac{e^{-2\pi\delta fT_d}}{\pi} \cdot \frac{\delta f \cos(2\pi fT_d)}{\delta f^2+f^2} + \frac{e^{-2\pi\delta fT_d}}{\pi} \cdot \frac{f \sin(2\pi fT_d)}{\delta f^2+f^2}. \text{ Thus } \mathbf{I}_1 + \mathbf{I}_2 + \mathbf{I}_3 + \mathbf{I}_4 =$$

$$e^{-2\pi\delta fT_d} \cdot \delta(f) + \frac{\delta f}{\pi(\delta f^2+f^2)} - \frac{e^{-2\pi\delta fT_d}}{\pi} \cdot \frac{\delta f \cos(2\pi fT_d)}{\delta f^2+f^2} - \frac{e^{-2\pi\delta fT_d} \cdot \sin(2\pi fT_d)}{\pi} \left\{\frac{1}{f} - \frac{f}{\delta f^2+f^2}\right\} =$$

$$e^{-2\pi\delta fT_d} \cdot \delta(f) + \frac{\delta f}{\pi(\delta f^2+f^2)} \left\{1 - e^{-2\pi\delta fT_d} \left(\cos(2\pi fT_d) + \frac{\delta f}{f} \cdot \sin(2\pi fT_d)\right)\right\}. \text{ Therefore}$$

$$\begin{aligned} \mathcal{S}\{\mathbf{i}_{\text{BN, BB}}^+(\mathbf{t})\} &= e^{-\Gamma_W} \cdot \delta(f) + \mathcal{L}_{W2}(f) \\ &\cdot \left\{1 - e^{-\Gamma_W} \cdot (\cos(2\pi fT_d) + \Gamma_W \cdot \text{sinc}(2fT_d))\right\} \end{aligned} \quad (\text{A7.1})$$

where $\mathcal{L}_{W2}(f) = (\delta f/\pi)/\{(\delta f)^2 + f^2\}$, and $\Gamma_W = 2\pi\delta fT_d$.

Appendix-A8: ICI in the conventional OFDM system

For simplicity of notation, we assume only the RX-LO-SCL is effective, and hence (7.12)

can be written as

$$\begin{aligned} y_{m, \text{ICI}}[\ell] &= \frac{A}{N_{\mathcal{F}}} \sum_{n=0}^{N_{\mathcal{F}}-1} \sum_{\substack{k \\ k \neq m}} c[k, \ell] e^{j2\pi n(k-m)/N_{\mathcal{F}}-j\psi_d[k]} e^{\alpha_2[n, \ell]+j\phi_2[n, \ell]} \\ &\approx \frac{A}{N_{\mathcal{F}}} \sum_{n=0}^{N_{\mathcal{F}}-1} \sum_{\substack{k \\ k \neq m}} \{c[k, \ell] e^{-j\psi_d[k]}\} \cdot \{1 + \alpha_2[n, \ell]\} \cdot e^{j\phi_2[n, \ell]} \cdot e^{j2\pi n(k-m)/N_{\mathcal{F}}} \end{aligned}$$

Thus the ICI variance is directly calculated as follows

$$\begin{aligned} \sigma_{ICI}^2[\mathbf{m}] &= \langle y_{m,ICI}[\ell] y_{m,ICI}^*[\ell] \rangle_\ell \approx \\ &\left\langle \left(\frac{A}{N_{\mathcal{F}}} \right)^2 \sum_{n_1=0}^{N_{\mathcal{F}}-1} \sum_{n_2=0}^{N_{\mathcal{F}}-1} \sum_{\substack{k_1 \\ k_2 \\ k_1 \neq m \quad k_2 \neq m}} c[k_1, \ell] c^*[k_2, \ell] e^{-j\psi_d[k_1] + j\psi_d[k_2]} e^{j\frac{2\pi}{N_{\mathcal{F}}}(n_1(k_1-m) - n_2(k_2-m))} \right. \\ &\quad \left. \cdot \{ e^{j\phi_2[n_1, \ell] - j\phi_2[n_2, \ell]} + \alpha_2[n_1, \ell] \alpha_2[n_2, \ell] + e^{j\phi_2[n_1, \ell]} \alpha_2[n_2, \ell] + e^{-j\phi_2[n_2, \ell]} \alpha_2[n_1, \ell] \} \right\rangle \end{aligned}$$

Now since the non-zero averages of a large number of OFDM symbols are obtained only when $\mathbf{k}_1 = \mathbf{k}_2$. Therefore

$$\begin{aligned} \sigma_{ICI}^2[\mathbf{m}] &\approx \left\langle \left(\frac{A}{N_{\mathcal{F}}} \right)^2 \sum_{n_1=0}^{N_{\mathcal{F}}-1} \sum_{n_2=0}^{N_{\mathcal{F}}-1} \sum_{\substack{k \\ k \neq m}} |c[k, \ell]|^2 e^{j\frac{2\pi}{N_{\mathcal{F}}}(k-m) \cdot (n_1 - n_2)} \right. \\ &\quad \left. \cdot \{ e^{j\phi_2[n_1, \ell] - j\phi_2[n_2, \ell]} + \alpha_2[n_1, \ell] \alpha_2[n_2, \ell] + \{ e^{j\phi_2[n_1, \ell]} \alpha_2[n_2, \ell] + e^{-j\phi_2[n_2, \ell]} \alpha_2[n_1, \ell] \} \} \right\rangle \\ &\approx \left\langle \left(\frac{A}{N_{\mathcal{F}}} \right)^2 \sum_{n_1=0}^{N_{\mathcal{F}}-1} \sum_{n_2=0}^{N_{\mathcal{F}}-1} \sum_{\substack{k \\ k \neq m}} |c[k, \ell]|^2 e^{j\frac{2\pi}{N_{\mathcal{F}}}(k-m) \cdot (n_1 - n_2)} \cdot \mathcal{M}[n_1, n_2, \ell] \right\rangle \end{aligned}$$

$$\begin{aligned} \text{where } \mathcal{M}[\mathbf{n}_1, \mathbf{n}_2, \ell] &= \left\{ e^{j\phi_2[n_1, \ell] - j\phi_2[n_2, \ell]} + \alpha_2[n_1, \ell] \alpha_2[n_2, \ell] \right. \\ &\quad \left. + \{ e^{j\phi_2[n_1, \ell]} \alpha_2[n_2, \ell] + e^{-j\phi_2[n_2, \ell]} \alpha_2[n_1, \ell] \} \right\} . \end{aligned}$$

Now if the TX-LO-SCL noise and channel response are also introduced, then $\sigma_{ICI}^2[\mathbf{m}]$ after expansion can be rewritten as

$$\begin{aligned} \sigma_{ICI}^2[\mathbf{m}] &= \left(\frac{A}{N_{\mathcal{F}}} \right)^2 \left\langle \sum_{\substack{k \\ k \neq m}} |c[k, \ell]|^2 \right. \\ &\quad \left\{ \sum_{n=0}^{N_{\mathcal{F}}-1} \left(1 + |\alpha_2[n, \ell]|^2 + |\tilde{\alpha}_1[n - \varepsilon[k], \ell]|^2 + 2\alpha_2[n, \ell] \cdot \cos(\phi_2[n, \ell]) \right. \right. \\ &\quad \left. \left. + 2\tilde{\alpha}_1[n - \varepsilon[k], \ell] \cdot \cos(\tilde{\Phi}_1[n - \varepsilon[k], \ell]) \right) + 2 \sum_{r=1}^{N_{\mathcal{F}}-1} \sum_{d=0}^{N_{\mathcal{F}}-1-d} \right. \\ &\quad \cos(\omega_{km}r + \phi_2[d, \ell] - \phi_2[d+r, \ell] + \tilde{\Phi}_1[d - \varepsilon[k], \ell] - \tilde{\Phi}_1[d+r - \varepsilon[k], \ell]) \\ &\quad + \{ \alpha_2[d, \ell] \cdot \alpha_2[d+r, \ell] + \tilde{\alpha}_1[d - \varepsilon[k], \ell] \cdot \tilde{\alpha}_1[d+r - \varepsilon[k], \ell] \} \cos(\omega_{km}r) + \\ &\quad \left. \left. \{ \alpha_2[d+r, \ell] + \tilde{\alpha}_1[d+r - \varepsilon[k], \ell] \} \cos(\omega_{km}r - \phi_2[d, \ell] - \tilde{\Phi}_1[d - \varepsilon[k], \ell]) + \right. \right. \\ &\quad \left. \left. \{ \alpha_2[d, \ell] + \tilde{\alpha}_1[d - \varepsilon[k], \ell] \} \cos(\omega_{km}r + \phi_2[d+r, \ell] + \tilde{\Phi}_1[d+r - \varepsilon[k], \ell]) \right\} \right\rangle_\ell \end{aligned} \quad (\text{A8.1})$$

where $\omega_{km} = 2\pi(k-m)/N_{\mathcal{F}}$.

This expression is complicated since all the effective SCLs' parameters are counted and channel response is considered, therefore it is calculated numerically. However, when only the white FN is counted, $\mathbf{H}_c[\mathbf{k}] = 1$, all SCs have equal powers, and no pilot-SC is used, then (A8.1) can be approximated to the following form

$$\sigma_{ICI}^2[\text{m}] = \left(\frac{N \cdot P_{SC}}{N_{\mathcal{F}}} \right) \cdot \left(1 + \frac{2}{N \cdot N_{\mathcal{F}}} \left\langle \sum_{\substack{\mathbf{k} \\ \mathbf{k} \neq \mathbf{m}}}^{N_{\mathcal{F}}-1} \sum_{r=1}^{N_{\mathcal{F}}-1-d} \sum_{d=0}^{N_{\mathcal{F}}-1-d} \cos(\omega_{\mathbf{k}\mathbf{m}}r + \Delta\phi_2[\mathbf{d}, r, \ell] + \Delta\widetilde{\phi}_1[\mathbf{d}, r, \varepsilon[\mathbf{k}], \ell]) \right\rangle_{\ell} \right) \quad (\text{A8.2})$$

where $\mathbf{P}_{SC} = \langle |c[\mathbf{k}, \ell]|^2 \rangle_{\ell}$,

$$\Delta\phi_2[\mathbf{d}, \mathbf{r}, \ell] = \phi_2[\mathbf{d}, \ell] - \phi_2[\mathbf{d} + \mathbf{r}, \ell], \text{ and}$$

$$\Delta\widetilde{\phi}_1[\mathbf{d}, \mathbf{r}, \varepsilon[\mathbf{k}], \ell] = \widetilde{\phi}_1[\mathbf{d} - \varepsilon[\mathbf{k}], \ell] - \widetilde{\phi}_1[\mathbf{d} + \mathbf{r} - \varepsilon[\mathbf{k}], \ell].$$

Appendix-A9: Rate equations of the Semiconductor

The SCL's photon density $S_{Ph}(\mathbf{t})$ (photons/m³), charge carrier density $N_{cc}(\mathbf{t})$ (charge/m³), and phase $\phi_E(\mathbf{t})$ (rad) are governed by the following equations [31]

$$\frac{\partial S_{Ph}(\mathbf{t})}{\partial \mathbf{t}} = \Gamma_C G_C(\mathbf{t}) S_{Ph}(\mathbf{t}) - \frac{S_{Ph}(\mathbf{t})}{\tau_{Ph}} + \frac{C_S N_{cc}(\mathbf{t})}{\tau_{cc}} + F_S(\mathbf{t}) \quad (\text{A9.1})$$

$$\frac{\partial N_{cc}(\mathbf{t})}{\partial \mathbf{t}} = \frac{J(\mathbf{t})}{\delta h \cdot q_e} - \Gamma_C G_C(\mathbf{t}) S_{Ph}(\mathbf{t}) - \frac{N_{cc}(\mathbf{t})}{\tau_{cc}} + F_N(\mathbf{t}) \quad (\text{A9.2})$$

$$\frac{\partial \phi_E(\mathbf{t})}{\partial \mathbf{t}} = \frac{\alpha_S}{2} \left\{ \Gamma_C G_C(\mathbf{t}) - \frac{1}{\tau_{Ph}} \right\} + F_{\phi}(\mathbf{t}) \quad (\text{A9.3})$$

where $G_C(\mathbf{t})$ is the power gain of the active region,

τ_{cc} is the charge carrier's life time (s),

τ_{Ph} is the photon's life time (s),

δh is the thickness of the active region (m) (Fig. 4.1),

q_e is the electron charge (1.602×10^{-19} A·s),

$J(\mathbf{t})$ is the injected current density (A/m²),

Γ_C is the field's confinement factor in the active region [31],

α_S is the anti-guiding factor [31],

C_S is the ratio between number of photons belonging to the same mode of laser's oscillating mode, to number of spontaneous emission photons, and

$F_S(\mathbf{t})$, $F_N(\mathbf{t})$, and $F_\phi(\mathbf{t})$ are Langevin noise sources (uncorrelated GRVs) corresponding to photon density rate of change, charge carrier density rate of change, and field's phase rate of change (angular frequency) respectively.

Solutions of these equations result the following:

- steady state oscillation characteristics, which describe: the threshold current, output power, and spectrum of the longitudinal mode and inter-mode,
- modulation characteristics, which describe: small signal modulation response, step response, sinusoidal modulation and frequency response, frequency chirp, large signal transient response, and turn-on delay, and
- noise characteristics, which describe, intensity noise, frequency noise, back-reflection induced noise, mode-hopping noise, mode-partition noise, and spectrum linewidth.

Appendix-B: BER of Different M-QAM Mapping in Presence of Gaussian Phase Noise

BER analysis becomes straightforward by analyzing the color noise component into the two orthogonal axes **I**, and **Q** with respect to the selected point in the constellation, and hence error occurrence is decided depending on the decision boundaries [48]. As soon as an expression of symbol error-rate **SER** versus phase noise (**PN**) θ is derived, then the PN's probability density function (**PDF**) is applied afterward to obtain the **BER** expression. In PA-FFL, it is proven that the PN has a Gaussian distribution with variance determined from the compensation process itself as discussed in Section 7.3.5.2. The following parameters will be used in this analysis:

- \mathbf{d} is minimal Euclidean distance between the constellation points. For instance, $\mathbf{d} = 2$ is used in Fig. B1 only for illustration, and hence any value is expected.
- \mathbf{k}_{gray} is the ratio between **BER** of a given mapping, to **BER** when the Gray code is assumed to be achieved between all points of the same mapping.
- \mathbf{m} is number of bits per mapped symbol.
- $\rho_{\theta}(\theta)$ is PN's PDF, and Gaussian PDF is used here for a given σ_{θ}^2 .
- The horizontal axis is denoted as I, and the vertical one as Q.
- \mathbf{r}_i, ψ_i are the Euclidean distance of the \mathbf{i} -th point with respect to the coordinate center, and \mathbf{i} -th point's angle with respect to horizontal axis.
- The average power of a given mapping is calculated as

$$\mathbf{P}_{\mathbf{M}} = \sum_{i=1}^{\mathbf{M}} \mathbf{P}_i / \mathbf{M} = \sum_{i=1}^{\mathbf{M}} r_i^2 / \mathbf{M} \quad , \text{ where } \mathbf{M} = 2^m \text{ is total number of points,}$$

\mathbf{P}_i is power of the \mathbf{i} -th point. The average power can also be written as, $\mathbf{P}_{\mathbf{M}} = \mathbf{E}_s / \mathbf{T}_s$, where \mathbf{E}_s is average energy per symbol, and \mathbf{T}_s is symbol's time duration.

- χ_c is a factor used to connect \mathbf{d} with $\mathbf{P}_{\mathbf{M}}$ as, $\mathbf{P}_{\mathbf{M}} = \chi_c \cdot \mathbf{d}^2$. This factor is also important in comparison between the different constellations.

- \mathbf{u} which is defined as

$$\mathbf{u} = \left(\frac{\mathbf{d}/2}{\sigma_n} \right) = \sqrt{\frac{\mathbf{P}_{\mathbf{M}}/\chi_c}{4\sigma_n^2}} = \sqrt{\frac{\mathbf{E}_s/\mathbf{T}_s}{2\chi_c S_n/\mathbf{T}_s}} = \sqrt{\frac{\text{SNR}}{2\chi_c}} = \sqrt{\frac{\mathbf{m} \cdot \text{SNR}_b}{2\chi_c}} \quad (\text{B.1})$$

where σ_n is standard deviation of the complex additive white Gaussian noise (AWGN) in only one axis I, or Q (half the noise variance), S_n is the complex AWGN's single-sided (SS) power spectral density (PSD) in (W/Hz), SNR and SNR_b are the signal to noise ratio and SNR per bit respectively.

- The **BER** is calculated as

$$\mathbf{BER} = \frac{k_{gray}}{m} \cdot \int_{-\pi}^{\pi} \rho_{\theta}(\theta) \cdot \left\{ \sum_{i=1}^M P_{S,i}(\theta)/M \right\} \cdot d\theta \quad (\text{B.2})$$

where $P_{S,i}(\theta)$ is **SER** of the i -th point.

- The Q_e function and the complementary error function *erfc* are related as follows [81]

$$\mathbf{erfc}(\mathbf{X}) = \frac{1}{2} Q_e(\mathbf{X}/\sqrt{2}) \quad , \text{ where } \mathbf{X} \text{ is a dummy variable.}$$

A. QPSK

All points in the QPSK mapping are identical as shown in Fig. B.1a, and hence only one point is required to be investigated. Here $m = 2$, $r_i = d/\sqrt{2}$ and $\psi_i = 45^\circ$ ($\pi/4$) for all points, $P_M = r_i^2 = d^2/2$, $\chi_c = 1/2$, $\mathbf{u} = \sqrt{2SNR_b}$, and Gray code is achieved $k_{gray} = 1$.

For point “00”, $\mathbf{I} = r_i \cos(\theta + \pi/4) = r_i \cos(\pi/4) \cos(\theta) - r_i \sin(\pi/4) \sin(\theta)$,

Thus $\mathbf{I} = I_{00} \cos(\theta) - Q_{00} \sin(\theta) = I_{00} \{\cos(\theta) - \sin(\theta)\}$, where I_{00} , and Q_{00} are the coordinates of point “00”. The first error function is

$\mu_I = I_{00} - I = I_{00} \{1 - \cos(\theta) + \sin(\theta)\}$, and hence symbol's error occurs when $|\mu_I| > d/2$. Similar treatment for the error function in the Q axis which yields

$\mu_Q = I_{00} \{1 - \cos(\theta) - \sin(\theta)\}$. So far only the PN is considered, and hence by adding the AWGN components \mathbf{I}_n , and \mathbf{Q}_n yields

If $|\mu_I + \mathbf{I}_n| > d/2 \rightarrow \text{error}$, hence when $|\mathbf{I}_n| > \{\cos(\theta) - \sin(\theta)\} \cdot d/2 \rightarrow \text{error}$.

If $|\mu_Q + \mathbf{Q}_n| > d/2 \rightarrow \text{error}$, hence when $|\mathbf{Q}_n| > \{\cos(\theta) + \sin(\theta)\} \cdot d/2 \rightarrow \text{error}$.

Since both errors can occur at the same time, and since \mathbf{I}_n and \mathbf{Q}_n are mutually independent, it is more accurate to write the probability of correct detection of point “00” as $\mathcal{P}_{C,00} = (1 - \mathcal{P}_{eI,00}) \cdot (1 - \mathcal{P}_{eQ,00})$,

where $\mathcal{P}_{eI,00}$, and $\mathcal{P}_{eQ,00}$ are probability of error along the I, and Q coordinates of point “00”. Thus the overall probability of symbol's error of point “00” is given by

$\mathcal{P}_{e,00} = 1 - \mathcal{P}_{C,00} = 1 - (1 - \mathcal{P}_{eI,00}) \cdot (1 - \mathcal{P}_{eQ,00}) \approx \mathcal{P}_{eI,00} + \mathcal{P}_{eQ,00}$. Hence

$$\mathcal{P}_{eI,00} = \frac{1}{M} Q_e \left(\frac{d/2}{\sigma_n} \cdot \{\cos(\theta) - \sin(\theta)\} \right) = Q_e(u \cdot \{\cos(\theta) - \sin(\theta)\}) \quad , \text{ and}$$

$$\mathcal{P}_{eQ,00} = \frac{1}{M} Q_e \left(\frac{d/2}{\sigma_n} \cdot \{\cos(\theta) + \sin(\theta)\} \right) = Q_e(u \cdot \{\cos(\theta) + \sin(\theta)\}) \quad .$$

Now since $\{\cos(\theta) - \sin(\theta)\}$ has identical effect to $\{\cos(\theta) + \sin(\theta)\}$ in long-term then and from (B.2) yields

$$\text{QPSK:} \quad \mathbf{BER} = \int_{-\pi}^{\pi} \rho_{\theta}(\theta) \cdot \text{erfc}(\sqrt{\text{SNR}_b} \cdot \{\cos(\theta) - \sin(\theta)\}) \cdot d\theta \quad (\text{B.3})$$

An approximated analytical solution can be obtained assuming the PN effect is only occurs along an axis which is perpendicular to \mathbf{r}_i . In this case

$$\text{QPSK:} \quad \mathbf{BER} \approx \text{erfc} \left(\sqrt{\frac{\text{SNR}_b}{1 + m \cdot \text{SNR}_b \cdot \sigma_{\theta}^2}} \right) \quad \dots \quad \sigma_{\theta} \leq 3^{\circ} \quad (\text{B.4})$$

B. 32-QAM

Only five distinct points in the 32-QAM mapping are required to be investigated, which can be “00000”, “00010”, “10010”, “11000”, and “11010” as shown in Fig. B.1c. Here $m = 5$, $\mathbf{r}_i = [\sqrt{1}, \sqrt{5}, \sqrt{9}, \sqrt{13}, \sqrt{17}] d/\sqrt{2}$ and $\boldsymbol{\psi}_i = [45^{\circ}, 71.565^{\circ}, 45^{\circ}, 78.69^{\circ}, 59.036^{\circ}]$, $\mathbf{P}_M = 5d^2$, $\boldsymbol{\chi}_c = 5$, $\mathbf{u} = \sqrt{\text{SNR}_b}/2$, and Gray code is not possible for all points and hence $k_{gray} \approx (29/25 = 1.16)$.

Table B.1: Summary of the important design values corresponding to the case-X and case-Y.

Point	Change of I , and Q coordinates of due to PN	I , and Q correct detection conditions	N_{SP}
$\mathbf{a}_1(00000)$	$\mathbf{I} = \{\cos(\theta) - \sin(\theta)\} \cdot d/2$ $\mathbf{Q} = \{\cos(\theta) + \sin(\theta)\} \cdot d/2$	$\{0 < \mathbf{I} < d\} \& \{0 < \mathbf{Q} < d\}$	4
$\mathbf{a}_2(00010)$	$\mathbf{I} = \{\cos(\theta) - 3 \sin(\theta)\} \cdot d/2$ $\mathbf{Q} = \{3 \cos(\theta) + \sin(\theta)\} \cdot d/2$	$\{0 < \mathbf{I} < d\} \& \{d < \mathbf{Q} < 2d\}$	8
$\mathbf{a}_3(10010)$	$\mathbf{I} = 3\{\cos(\theta) - \sin(\theta)\} \cdot d/2$ $\mathbf{Q} = 3\{\cos(\theta) + \sin(\theta)\} \cdot d/2$	$\{d < \mathbf{I} < 2d\} \& \{d < \mathbf{Q} < 2d\}$	4
$\mathbf{a}_4(11000)$	$\mathbf{I} = \{\cos(\theta) - 5 \sin(\theta)\} \cdot d/2$ $\mathbf{Q} = \{5 \cos(\theta) + \sin(\theta)\} \cdot d/2$	$\{0 < \mathbf{I} < d\} \& \{\mathbf{Q} > 2d\}$	8
$\mathbf{a}_5(11010)$	$\mathbf{I} = \{3 \cos(\theta) - 5 \sin(\theta)\} \cdot d/2$ $\mathbf{Q} = \{5 \cos(\theta) + 3 \sin(\theta)\} \cdot d/2$	$(\{d < \mathbf{I} < 2d\} \& \{\mathbf{Q} > 2d\}) \cup (0.5\{\mathbf{I} > 2d\} \& \{\mathbf{Q} > 2d\})$	8

Table B.2: Summary of the important design values corresponding to the case-X and case-Y.

Point	Probability of symbol's error $\mathcal{P}_{e,ai}$ corresponding to point \mathbf{a}_i
$\mathbf{a}_1(00000)$	$\mathcal{P}_{e,a1} = \{1 - (1 - q1 - q2) \cdot (1 - q3 - q4)\}/M$ $\mathbf{q1} = Q_e(u \cdot \{\cos(\theta) - \sin(\theta)\})$ $\mathbf{q2} = Q_e(u \cdot \{2 - \{\cos(\theta) - \sin(\theta)\}\})$ $\mathbf{q3} = Q_e(u \cdot \{\cos(\theta) + \sin(\theta)\})$ $\mathbf{q4} = Q_e(u \cdot \{2 - \{\cos(\theta) + \sin(\theta)\}\})$
$\mathbf{a}_2(00010)$	$\mathcal{P}_{e,a2} = \{1 - (1 - q1 - q2) \cdot (1 - q3 - q4)\}/M$ $\mathbf{q1} = Q_e(u \cdot \{\cos(\theta) - 3 \sin(\theta)\})$ $\mathbf{q2} = Q_e(u \cdot \{2 - \{\cos(\theta) - 3 \sin(\theta)\}\})$ $\mathbf{q3} = Q_e(u \cdot \{3 \cos(\theta) + \sin(\theta) - 2\})$ $\mathbf{q4} = Q_e(u \cdot \{4 - \{3 \cos(\theta) + \sin(\theta)\}\})$
$\mathbf{a}_3(10010)$	$\mathcal{P}_{e,a3} = \{1 - (1 - q1 - q2) \cdot (1 - q3 - q4)\}/M$ $\mathbf{q1} = Q_e(u \cdot \{3 \cos(\theta) - 3 \sin(\theta) - 2\})$ $\mathbf{q2} = Q_e(u \cdot \{4 - 3\{\cos(\theta) - \sin(\theta)\}\})$ $\mathbf{q3} = Q_e(u \cdot \{3\{\cos(\theta) + \sin(\theta) - 2\}\})$ $\mathbf{q4} = Q_e(u \cdot \{4 - 3\{\cos(\theta) + \sin(\theta)\}\})$
$\mathbf{a}_4(11000)$	$\mathcal{P}_{e,a4} = \{1 - (1 - q1 - q2) \cdot (1 - q3)\}/M$ $\mathbf{q1} = Q_e(u \cdot \{\cos(\theta) - 5 \sin(\theta)\})$ $\mathbf{q2} = Q_e(u \cdot \{2 - \{\cos(\theta) - 5 \sin(\theta)\}\})$ $\mathbf{q3} = Q_e(u \cdot \{5 \cos(\theta) + \sin(\theta) - 4\})$
$\mathbf{a}_5(11010)$	$\mathcal{P}_{c,a5} \approx \{(1 - q1 - q2) \cdot (1 - q3) + q2 \cdot (1 - q3)/2\}/M$ $\approx \{(1 - q1 - q2/2) \cdot (1 - q3)\}/M$ $\mathcal{P}_{e,a5} \approx \{q1 + q3 + q2/2\}/M$ $\mathbf{q1} = Q_e(u \cdot \{3 \cos(\theta) - 5 \sin(\theta) - 2\})$ $\mathbf{q2} = Q_e(u \cdot \{4 - \{3 \cos(\theta) - 5 \sin(\theta)\}\})$ $\mathbf{q3} = Q_e(u \cdot \{5 \cos(\theta) + 3 \sin(\theta) - 4\})$

By following the same steps of QPSK analysis, Table B.1, and Table B.2 are yielded, where N_{SP} stands for number of similar points.

Thus from (B.2), the **BER** of 32-QAM is given by

$$\text{32-QAM BER} \approx \left(\frac{1.16}{40}\right) \int_{-\pi}^{\pi} \rho_{\theta}(\theta) \cdot \{\mathcal{P}_{e,a1} + 2\mathcal{P}_{e,a2} + \mathcal{P}_{e,a3} + 2\mathcal{P}_{e,a4} + 2\mathcal{P}_{e,a5}\} d\theta \quad (\text{B.5})$$

An approximated analytical solution can also be obtained for the 32-QAM assuming the PN effect is only occurs along an axis which is perpendicular to \mathbf{r}_i . In this case

$$\begin{aligned}
 \text{BER} \approx & \left(\frac{1.16}{8} \right) \left\{ \operatorname{erfc} \left(\sqrt{\frac{\text{SNR}_b/4}{1 + \text{SNR}_b \sigma_\theta^2/2}} \right) \right. \\
 & + \operatorname{erfc} \left(\sqrt{\frac{\text{SNR}_b/4}{1 + 9 \cdot \text{SNR}_b \sigma_\theta^2/2}} \right) \\
 & \left. + \frac{7}{10} \operatorname{erfc} \left(\sqrt{\frac{\text{SNR}_b/4}{1 + 25 \cdot \text{SNR}_b \sigma_\theta^2/2}} \right) \right\} \dots \sigma_\theta \leq 2^\circ \quad (\text{B.6})
 \end{aligned}$$

C. 16-QAM

Only three distinct points in the 16-QAM mapping are required to be investigated, which can be “0011”, “0001”, and “0000” as shown in Fig. B.1b. Here $\mathbf{m} = 4$, $\mathbf{r}_i = [\sqrt{1}, \sqrt{5}, \sqrt{9}]d/\sqrt{2}$ and $\boldsymbol{\psi}_i = [45^\circ, 71.565^\circ, 45^\circ]$, $\mathbf{P}_M = 5d^2/2$, $\boldsymbol{\chi}_c = 5/2$, $\mathbf{u} = \sqrt{4\text{SNR}_b/5}$, and Gray code is achieved $\mathbf{k}_{gray} = 1$.

By following the same previous analysis yields

$$\begin{aligned}
 \text{BER}[m] = & \frac{1}{16} \int_{-\infty}^{\infty} \left\{ \operatorname{erfc} \left(\sqrt{2\text{SNR}_b/5} \cdot \{\cos(\theta) + \sin(\theta)\} \right) \right. \\
 & + \operatorname{erfc} \left(\sqrt{8\text{SNR}_b/5} \cdot \{1 - (\cos(\theta) + \sin(\theta))/2\} \right) \\
 & + \operatorname{erfc} \left(\sqrt{8\text{SNR}_b/5} \cdot \{3(\cos(\theta) + \sin(\theta))/2 - 1\} \right) \\
 & + \operatorname{erfc} \left(\sqrt{8\text{SNR}_b/5} \cdot \{(3\cos(\theta) + \sin(\theta))/2 - 1\} \right) \\
 & + \operatorname{erfc} \left(\sqrt{8\text{SNR}_b/5} \cdot \{1 - (\cos(\theta) + 3\sin(\theta))/2\} \right) \\
 & \left. + \operatorname{erfc} \left(\sqrt{2\text{SNR}_b/5} \cdot \{\cos(\theta) + 3\sin(\theta)\} \right) \right\} \cdot \rho_\theta(\theta) d\theta
 \end{aligned} \quad (\text{B.7})$$

An approximated analytical solution can also be obtained for the 16-QAM as

$$\begin{aligned}
 \text{BER} \approx & \frac{3}{4} \left\{ \operatorname{erfc} \left(\sqrt{\frac{2\text{SNR}_b/5}{1 + 4\text{SNR}_b \sigma_\theta^2/5}} \right) \right. \\
 & \left. + \operatorname{erfc} \left(\sqrt{\frac{2\text{SNR}_b/5}{1 + 36\text{SNR}_b \sigma_\theta^2/5}} \right) \right\} \dots \sigma_\theta \leq 3^\circ \quad (\text{B.8})
 \end{aligned}$$

The results of (B.3), (B.5), and (B.7) are shown in Fig. B.2.

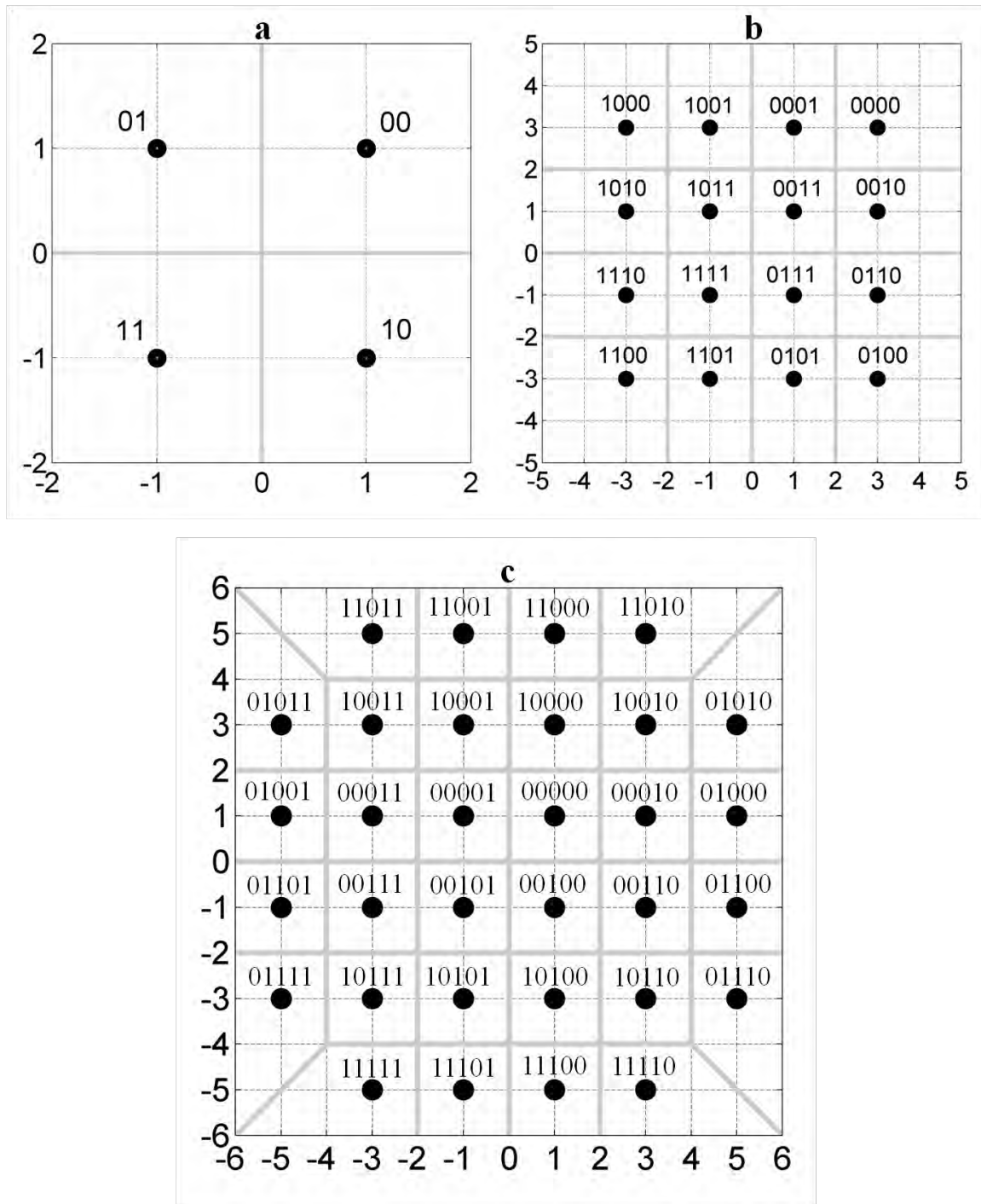


Fig. B.1: QPSK, 16-QAM, and 32-QAM constellations in (a), (b), and (c) respectively.

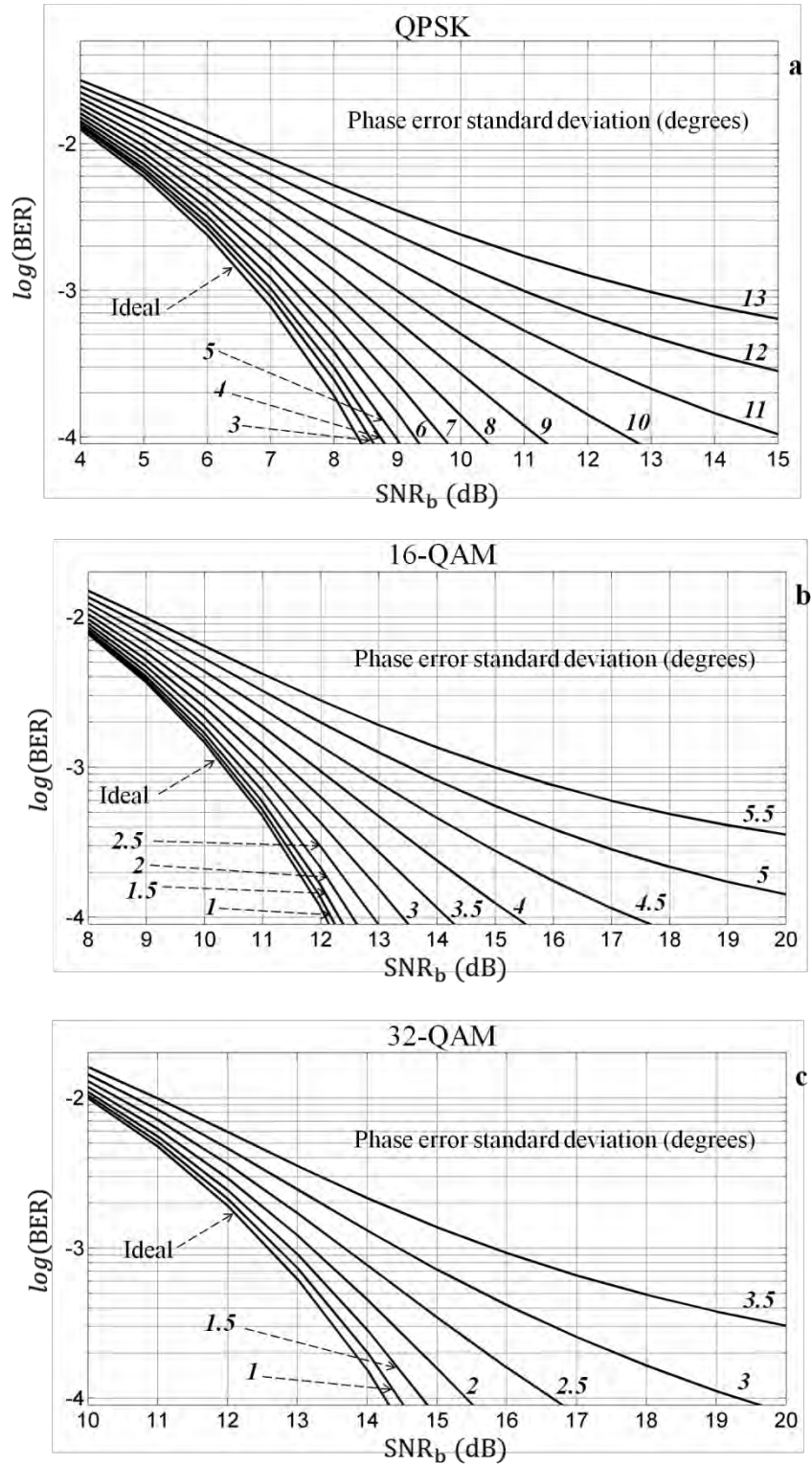


Fig. B.2: Calculation of (B.3), (B.5), and (B.7) corresponds to (a), (b), and (c) respectively. The Italic-style written numbers is for PN standard deviation (degrees).

Appendix-C: I/Q Imbalance Analysis and the Proposed Training Symbol

Appendix-C1: I/Q Imbalance Analysis

Asymmetrical I/Q imbalance model is adopted here for the complete link as shown in Fig. C1.1 [79]. As the differential effect matters; one of the two branches in the transmitter (TX), and receiver (RX) has a unity transfer function. Here $\mathbf{a}[\mathbf{k}] = \ddot{\mathbf{a}}[\mathbf{k}] \cdot \mathbf{a}_0$, and $\mathbf{b}[\mathbf{k}] = \ddot{\mathbf{b}}[\mathbf{k}] \cdot \mathbf{b}_0$, where $\ddot{\mathbf{a}}[\mathbf{k}]$, and $\ddot{\mathbf{b}}[\mathbf{k}]$ are the true differential gain in TX-RF block and RX-RF block respectively. Referring to Fig. C1.1 and after the fast Fourier transform (\mathcal{FFT}) is applied, output (O/P) of the + (\mathbf{m} -th) subcarrier (SC), and – (\mathbf{m} -th) SC can be expressed as

$$\begin{aligned} y_{\mathbf{m},\ell}^+ &= \mathcal{K}_{\mathbf{m}11} \cdot c_{\mathbf{m},\ell}^+ + \mathcal{K}_{\mathbf{m}12} \cdot c_{\mathbf{m},\ell}^-^* \\ y_{\mathbf{m},\ell}^- &= \mathcal{K}_{\mathbf{m}21} \cdot c_{\mathbf{m},\ell}^+^* + \mathcal{K}_{\mathbf{m}22} \cdot c_{\mathbf{m},\ell}^- \end{aligned} \quad (\text{C1.1})$$

$$\begin{aligned} \text{where } \mathcal{K}_{\mathbf{m}11} &= \frac{1}{4} \left(e^{j\mathcal{B}_1[\mathbf{m}]} (1 + a[\mathbf{m}]e^{j(\theta_t + \varphi[\mathbf{m}])}) (1 + b[\mathbf{m}]e^{j(\psi[\mathbf{m}] - \theta_r)}) \right. \\ &\quad \left. + e^{j\mathcal{B}_2[\mathbf{m}]} (1 - a[\mathbf{m}]e^{j(\theta_t - \varphi[\mathbf{m}])}) (1 - b[\mathbf{m}]e^{j(\psi[\mathbf{m}] + \theta_r)}) \right) , \\ \mathcal{K}_{\mathbf{m}12} &= \frac{1}{4} \left(e^{j\mathcal{B}_2[\mathbf{m}]} (1 - b[\mathbf{m}]e^{j(\psi[\mathbf{m}] + \theta_r)}) (1 + a[\mathbf{m}]e^{-j(\theta_t - \varphi[\mathbf{m}])}) \right. \\ &\quad \left. + e^{j\mathcal{B}_1[\mathbf{m}]} (1 + b[\mathbf{m}]e^{j(\psi[\mathbf{m}] - \theta_r)}) (1 - a[\mathbf{m}]e^{j(\theta_t + \varphi[\mathbf{m}])}) \right) , \\ \mathcal{K}_{\mathbf{m}21} &= \frac{1}{4} \left(e^{-j\mathcal{B}_1[\mathbf{m}]} (1 + a[\mathbf{m}]e^{j(\theta_t + \varphi[\mathbf{m}])}) (1 - b[\mathbf{m}]e^{-j(\psi[\mathbf{m}] - \theta_r)}) \right. \\ &\quad \left. + e^{-j\mathcal{B}_2[\mathbf{m}]} (1 - a[\mathbf{m}]e^{j(\theta_t - \varphi[\mathbf{m}])}) (1 + b[\mathbf{m}]e^{-j(\psi[\mathbf{m}] + \theta_r)}) \right) , \\ \mathcal{K}_{\mathbf{m}22} &= \frac{1}{4} \left(e^{-j\mathcal{B}_2[\mathbf{m}]} (1 + b[\mathbf{m}]e^{-j(\psi[\mathbf{m}] + \theta_r)}) (1 + a[\mathbf{m}]e^{j(\theta_t - \varphi[\mathbf{m}])}) \right. \\ &\quad \left. + e^{-j\mathcal{B}_1[\mathbf{m}]} (1 - b[\mathbf{m}]e^{-j(\psi[\mathbf{m}] - \theta_r)}) (1 - a[\mathbf{m}]e^{-j(\theta_t + \varphi[\mathbf{m}])}) \right) , \\ e^{j\mathcal{B}_1[\mathbf{m}]} &= \rho_{\mathbf{m}} , \\ e^{j\mathcal{B}_2[\mathbf{m}]} &= \rho_{-\mathbf{m}} , \\ \rho_{\mathbf{m}} \text{, and } \rho_{-\mathbf{m}} &\text{ are calculated by using (6.25), and} \end{aligned}$$

$c_{\mathbf{m},\ell}^+$, and $c_{\mathbf{m},\ell}^-$ are the (+ \mathbf{m}), and (– \mathbf{m}) mapped symbols in the ℓ -th OFDM symbol respectively.

Here $\mathbf{a}[\mathbf{m}]e^{j\varphi[\mathbf{m}]}$, and $\mathbf{b}[\mathbf{m}]e^{j\theta_r}$ matrices can be extracted from the scattering parameters measurement of the TX-RF and RX-RF units (Section 3.3.6) using a network analyzer. The I/Q imbalance parameters of the IQ optical modulator and the 90° optical hybrid cannot be directly measured, and hence they are considered to be unknowns, which can be estimated together with channel response parameters via a training symbol.

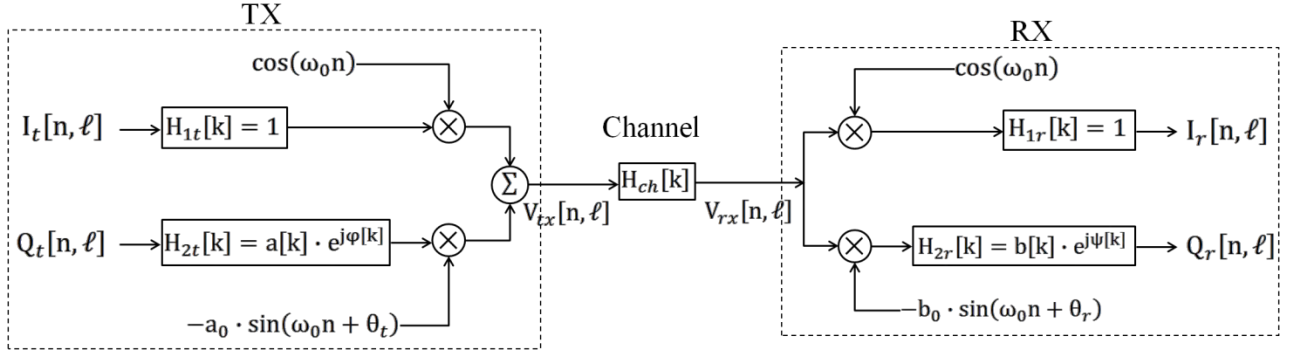


Fig. C1.1: Asymmetrical I/Q imbalance linear model for the CO-OFDM system.

Appendix-C2: The Proposed Training Symbol (TrS)

The TrS was first proposed for frequency and time synchronization of the OFDM signal, however, it is found that the TrS can further be used for channel and I/Q imbalance estimation and correction [22], [67], [71]. For instance, estimation of the I/Q imbalance's \mathcal{K} -matrix can be facilitated if the TrS is formed from a two successive OFDM symbols and has the following feature $\{c_{m,\ell}^+ \neq 0 \ \& \ c_{m,\ell}^- = 0\}$, and $\{c_{m,\ell+1}^+ = 0 \ \& \ c_{m,\ell+1}^- \neq 0\}$, which results only odd or even SCs can be corrected, while \mathcal{K} -matrix's coefficients of the of missing SCs are interpolated.

The new proposed TrS has this feature as well as all other required features for OFDM synchronization, and can be described as follows.

- The TrS is designed for $\mathcal{F}\mathcal{F}\mathcal{T}$ size of $\mathbf{N}_{\mathcal{F}} = 1024$, and can be easily configured for other values of $\mathbf{N}_{\mathcal{F}}$.
- The TrS is generated in the frequency domain by setting the frequency vector (\mathbf{FrV}) using a weighted polar signal ($\pm\mathbf{A}$). Where the \mathbf{A} value is selected such that power of the TrS equals the OFDM's average power.

- The TrS has to have a low peak-to-average power ratio **PAPR** to be less affected by the components' and channel's nonlinearities as recommended by Schmidl and Cox [22]. In this new proposal, **PAPR** = 5.185dB.
- The TrS can work efficiently under very low signal to noise ratio **SNR**, which is close to performance of the TrS proposed in [71].
- The TrS is formed from two successive OFDM's symbols, and hence it consists of two parts. The real-component of O/P time samples of the **1st** or **2nd** part has an even symmetry with the center, while the imaginary-component has an odd symmetry.
- The TrS is generated using three pseudo noise codes as follows

$$\mathbf{C}_1 = [111111010101100110111011010010011100010111100101000110000100000],$$

$$\mathbf{C}_2 = [1111100110100100001010111011000],$$
 and

$$\mathbf{C}_3 = [1110100].$$
Lengths of \mathbf{C}_1 , \mathbf{C}_2 , and \mathbf{C}_3 vectors are 63, 31, and 7 chips respectively.

- FrV setting of **1st** part of the TrS is as follows
Only 202 SCs are used in the FrV's setting and the rest are set to zero. The true (physical) frequency indices of the SCs that have non-zero values are

$$\mathbf{k}_{+t1} = [3, 7, 11, 15, 19, \dots, 403], \text{ and}$$

$$\mathbf{k}_{-t1} = [-1, -5, -9, -13, -17, \dots, -401].$$

This can be transformed into MATLAB[®] code indices as

$$\mathbf{k}_{+M1} = [4, 8, 12, 16, 20, \dots, 404], \text{ and}$$

$$\mathbf{k}_{-M1} = [N_{\mathcal{F}}, N_{\mathcal{F}} - 4, N_{\mathcal{F}} - 8, N_{\mathcal{F}} - 12, N_{\mathcal{F}} - 16, \dots, N_{\mathcal{F}} - 400].$$

Setting values corresponding to these positive and negative FrVs are,

$$\mathbf{V}_1[\mathbf{k}_{+M1}] = A \cdot [\mathbf{C}_1 \ \mathbf{C}_2 \ \mathbf{C}_3], \text{ and}$$

$$\mathbf{V}_1[\mathbf{k}_{-M1}] = A \cdot [-\mathbf{C}_1 \ \mathbf{C}_2 - \mathbf{C}_3].$$

Where $\mathbf{V}_1[\]$ is the FrV used in the **1st** part of the TrS.

- FrV setting of **2nd** part of the TrS is as follows

$$\mathbf{k}_{+t2} = [1, 5, 9, 13, 17, \dots, 401], \mathbf{k}_{-t2} = [-3, -7, -11, -15, -19, \dots, -403],$$

$$\mathbf{k}_{+M2} = [2, 6, 10, 14, 18, \dots, 402], \mathbf{k}_{-M2} = [N_{\mathcal{F}} - 2, N_{\mathcal{F}} - 6, N_{\mathcal{F}} - 10, N_{\mathcal{F}} - 14,$$

$$N_{\mathcal{F}} - 18, \dots, N_{\mathcal{F}} - 404]. \mathbf{V}_2[\mathbf{k}_{+M2}] = A \cdot [\mathbf{C}_1 \ \mathbf{C}_2 \ \mathbf{C}_3], \text{ and } \mathbf{V}_2[\mathbf{k}_{-M2}] = A \cdot$$

$$[-\mathbf{C}_1 \ \mathbf{C}_2 - \mathbf{C}_3].$$
 Hence only the frequency indices change in the **2nd** part.

- The optimal timing window of the \mathcal{FFT} 's block can be determined periodically via the DSP computations shown in Fig. C2.1. Correlation detection is performed benefiting from the fact that when the 1st or the 2nd part of the TrS is mixed with its delayed version with an optimal delay of $N_{\mathcal{F}}/4$ time samples, maximum correlation of either part is obtained. Besides, a shift register (SR) is used to perform a sliding correlator' structure with an optimal SR's size of $3(N_{\mathcal{F}} + N_{CP})/4$, where N_{CP} is the cyclic prefix length. Two time-shifted peaks with opposite signs are always obtained from the correlator corresponding to the 1st and 2nd parts of the TrS. The decision block's function is either to use peak-detection algorithm, averaging of the two successive peaks, or zero-crossing detection. All these decision techniques are examined and the results are; the peak-detection algorithm is the optimal one when the very low SNR is the case, but at the expense of timing error of ± 10 time samples. While zero-crossing detection is accurate when adequate SNR is available and almost no timing error is monitored.

This TrS is resilient in high phase noise links, and a frequency offset of up to 5 frequency samples can be tolerated. Mathematical derivations have not yet been completed, however, the \mathcal{FFT} 's timing window and I/Q imbalance correction accomplished by simulations, are very promising.

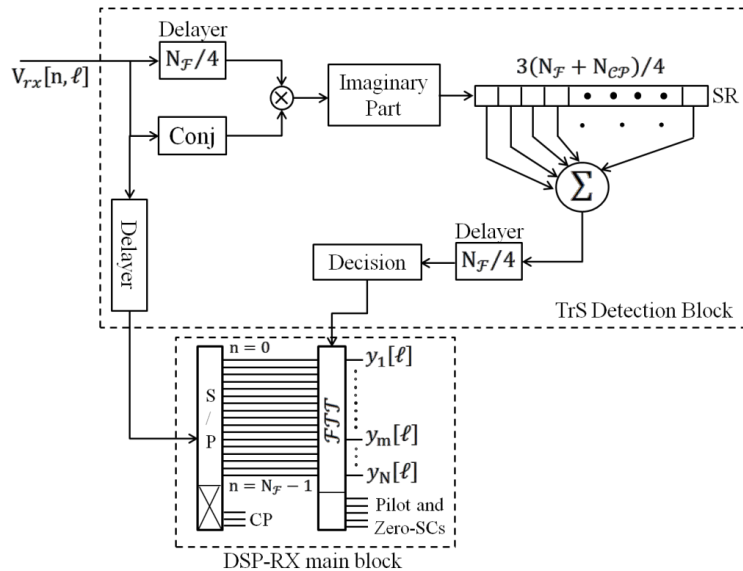


Fig. C2.1: Block diagram of the DSP computations used to determine the \mathcal{FFT} 's timing window using the proposed TrS. Details are given in the text.

Appendix-D: Nonlinearity Effect due to the Driver Amplifiers and the IQ Optical Modulators

Appendix-D1: Driver amplifiers' nonlinearity

Many models in the literatures describe class-C RF power amplifiers, while linear amplifiers are usually characterized by their 3rd order inter-modulation distortion using the two-tone test [133]-[134]. However, in ultra wideband (UWB) signals, such as optical OFDM's baseband (BB) real (I), and imaginary (Q) signals, the 3rd order intercept point becomes invalid. The polynomial model is usually employed for this purpose by fitting the driver amplifier's power transfer characteristics with a specific polynomial, which uses input (I/P) power as the independent variable [80], [131]. Although this model is accurate and widely used in amplifier's simulation, however, it is complicated since a high-order polynomial is usually required. Besides, the transfer characteristic itself is a frequency dependent, which imposes a Volterra series or similar expansions to be used. In the following analysis, a piece-wise voltage transfer characteristic of a driver amplifier with a memory-less nonlinearity is adopted as shown in Fig. D1.1. The aim of this simplified model is to yield the equations that govern the selection of the driver amplifier based on its specifications, and the tolerated worst-case nonlinearity-variance for a given OFDM's constellation.

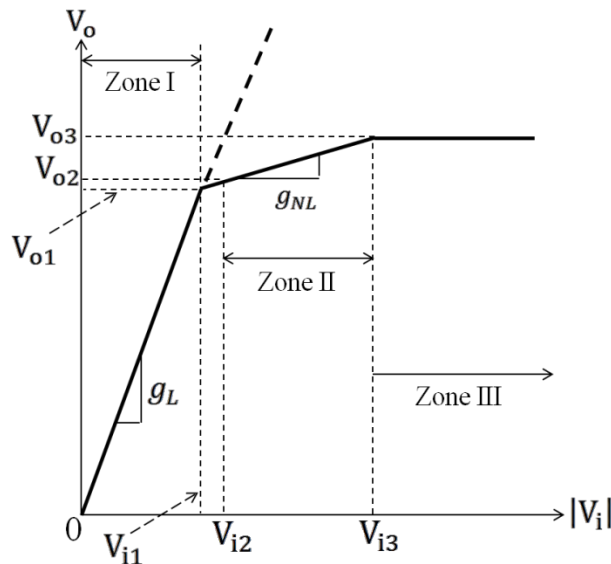


Fig. D1.1: Piece-wise transfer characteristics of the driver amplifier.

The BB-OFDM's tributaries I, and Q can be considered as Gaussian random variable (**GRV**)s when a large number of modulated subcarriers (**SC**)s (**N**) is used. Output (**O/P**) of the anti-aliasing filter's (Section 3.3.4) can be expressed as

$$P_I = P_Q = \alpha_c \cdot \left(\frac{N \cdot \langle |c[k, \ell]|^2 \rangle_\ell}{2N_{\mathcal{F}}^2} \right) \quad (\text{D1.1})$$

where α_c is constant, $N_{\mathcal{F}}$ is the **IFFT** size (Section 3.3.2), and $\langle |c[k, \ell]|^2 \rangle_\ell$ is the average power per SC. The values shown in Fig. D1.1 are calculated as follows.

$$g_L = \sqrt{G_L} = 10^{G_{L,\text{dB}}/20} \quad , \text{ and} \quad g_{NL} = \frac{V_{o3} - V_{o2}}{V_{i3} - V_{i2}} \quad (\text{D1.2-a})$$

$$V_{i1} = \frac{V_{o2} - g_{NL}V_{i2}}{g_L - g_{NL}} \quad , \text{ and} \quad V_{o1} = g_L V_{i1} \quad (\text{D1.2-b})$$

$$V_{o3} = 10^{(\text{PO}_{\text{sat,dBm}}/20)} \cdot \mathcal{r} \quad , \text{ and} \quad V_{i3} = 10^{(\text{PI}_{\text{sat,dBm}}/20)} \cdot \mathcal{r} \quad (\text{D1.2-c})$$

$$V_{o2} = 10^{(\text{PO}_{1\text{dB,dBm}}/20)} \cdot \mathcal{r} \quad , \text{ and} \quad V_{i2} = 10^{(\text{PI}_{1\text{dB,dBm}}/20)} \cdot \mathcal{r} \quad (\text{D1.2-d})$$

where $\mathcal{r} = \sqrt{R_L/1000}$, $\text{PO}_{1\text{dB,dBm}}$, $\text{PI}_{1\text{dB,dBm}}$, $\text{PO}_{\text{sat,dBm}}$, and $\text{PI}_{\text{sat,dBm}}$ are power in (dBm) of O/P at the 1dB compression point, of I/P at the 1dB compression point, of O/P at saturation, and of I/P at saturation respectively. Other variables might be introduced as

$$X_1 = V_{i1}/\sqrt{P_1} \quad , \quad X_2 = V_{i3}/\sqrt{P_1} \quad , \quad X_{\text{max}} = V_{\text{imax}}/\sqrt{P_1} = \sqrt{\text{PAPR}} \quad (\text{D1.3-a})$$

$$p_A = \text{erfc}\{X_1/\sqrt{2}\} - \text{erfc}\{X_{\text{max}}/\sqrt{2}\} \quad , \quad p_B = \text{erfc}\{X_2/\sqrt{2}\} - \text{erfc}\{X_{\text{max}}/\sqrt{2}\} \quad (\text{D1.3-b})$$

where **PAPR** stands for peak instantaneous power to average power of either I or Q expressed in linear scale, and V_{imax} is the maximum instantaneous I/P voltage of either I or Q. When clipping is used before DACs are performed, then X_{max} might be expected to be $X_{\text{max}} = V_{\text{clipping}}/\sqrt{P_1}$, which is true in the discrete model, however, this is not true in real-time domain when the anti-aliasing filter's response increases **PAPR** again unless a flat group-delay filter such as Bessel-prototype filter is used. Besides, X_{max} can be ignored here since **PAPR_{dB}** (no clipping) for the two tributaries is between 10-13dB [69].

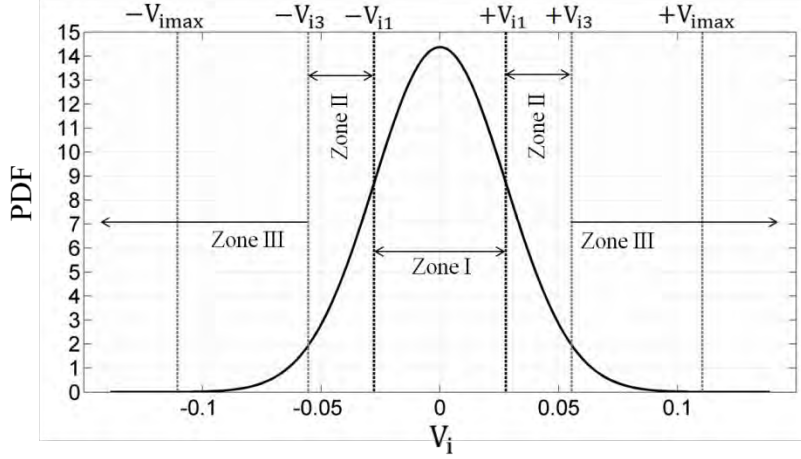


Fig. D1.2: PDF of either I or Q signals assuming $X_1 = 1$, $X_2 = 2$, and $\text{PAPR}_{\text{dB}} = 12\text{dB}$.

The probability density function (**PDF**) of the instantaneous I/P voltage of either I or Q is shown in Fig. D1.2, assuming large value of N is used, $X_1 = 1$, $X_2 = 2$, and $\text{PAPR}_{\text{dB}} = 12\text{dB}$. Referring to Fig. D1.1, and D1.2, then the amplifier's O/P voltage is given by

$$V_o[n, \ell] = g_L V_i[n, \ell] \cdot \rho_x[n, \ell] + \{g_L V_{i1} + g_{NL}\{|V_i[n, \ell]| - V_{i1}\}\} \cdot \text{Sg}[n, \ell] \cdot \rho_y[n, \ell] + \{V_{i1}\{g_L - g_{NL}\} + V_{i3} g_{NL}\} \cdot \text{Sg}[n, \ell] \cdot \rho_z[n, \ell] \quad (\text{D1.4})$$

where $\rho_x[n, \ell] = 1$, for $\{|V_i[n, \ell]| < V_{i1}\}$,

$\rho_y[n, \ell] = 1$, for $\{V_{i1} \leq |V_i[n, \ell]| < V_{i3}\}$,

$\rho_z[n, \ell] = 1$, for $\{|V_i[n, \ell]| \geq V_{i3}\}$, and

$\text{Sg}[n, \ell]$ is sign of the time sample (± 1).

Thus (D1.4) can be rewritten for I and Q branches as follows

$$I_o[n, \ell]/g_L = I_i[n, \ell] \cdot \{1 - \beta_1 \rho_1[n, \ell] - \beta_0 \rho_2[n, \ell]\} + \beta_1 \rho_1[n, \ell] \cdot \text{Sg}_1[n, \ell] \cdot V_{i1} + \beta_0 \rho_2[n, \ell] \cdot \text{Sg}_1[n, \ell] \cdot V_{i3} \quad (\text{D1.5-a})$$

$$Q_o[n, \ell]/g_L = Q_i[n, \ell] \cdot \{1 - \beta_1 \rho_{11}[n, \ell] - \beta_0 \rho_{22}[n, \ell]\} + \beta_1 \rho_{11}[n, \ell] \cdot \text{Sg}_2[n, \ell] \cdot V_{i1} + \beta_0 \rho_{22}[n, \ell] \cdot \text{Sg}_2[n, \ell] \cdot V_{i3} \quad (\text{D1.5-b})$$

where $\beta_0 = g_{NL}/g_L$, and $\beta_1 = 1 - \beta_0$.

$\rho_1[n, \ell] = U[n] - \rho_{x1}[n, \ell]$, $\rho_2[n, \ell] = \rho_{z1}[n, \ell]$,

$\rho_{11}[n, \ell] = U[n] - \rho_{x2}[n, \ell]$, $\rho_{22}[n, \ell] = \rho_{z2}[n, \ell]$, and

$U[n]$ is unity vector with length of $N_{\mathcal{F}}$.

These equations are valid assuming both I and Q amplifiers are exactly matched, the I/Q imbalance is ignored, and both I and Q signals are completely uncorrelated. Here

subscript “1” indicates the I-tributary and “2” for the Q-tributary. Although the statistics of ρ_1 and ρ_{11} is similar to the telegraph signal, however, an exact PDF is not easy to be described since it depends on the oversampling ratio as well as V_{i1} , and V_{i3} .

Accordingly, the O/P complex signal can be written as

$$V_t[n, \ell]/g_L = I_o[n, \ell]/g_L + j Q_o[n, \ell]/g_L \quad (D1.6)$$

Now the exact O/P power per I or Q amplifier can be obtained from (D1.5-a) assuming,

$$S_1 = \{1 - \beta_1 \rho_1[n, \ell] - \beta_0 \rho_2[n, \ell]\}, \text{ and}$$

$$S_2 = \{\beta_1 \rho_1[n, \ell] V_{i1} + \beta_0 \rho_2[n, \ell] V_{i3}\}, \text{ then}$$

$$I_o[n, \ell]/g_L = S_1 \cdot I_i[n, \ell] + S_2 \cdot S_{g1}[n, \ell], \text{ and hence}$$

$$P_{OI}/G_L = \langle \{S_1 I_i[n, \ell]\}^2 \rangle + \langle S_2^2 \rangle + 2 \langle S_{g1}[n, \ell] I_i[n, \ell] S_1 S_2 \rangle, \text{ where } P_{OI} = \langle I_o[n, \ell]^2 \rangle.$$

Now since $\{S_{g1}[n, \ell] I_i[n, \ell]\} = |I_i[n, \ell]|$, then

$$P_{OI}/G_L = \langle \{S_1 I_i[n, \ell]\}^2 \rangle + \langle S_2^2 \rangle + 2 \langle |I_i[n, \ell]| S_1 S_2 \rangle \quad (D1.7)$$

The 1st term is $\langle S_2^2 \rangle = \langle \{\beta_1 \rho_1[n, \ell] V_{i1} + \beta_0 \rho_2[n, \ell] V_{i3}\}^2 \rangle$

$$= \langle \beta_1^2 V_{i1}^2 \rho_1[n, \ell]^2 + \beta_0^2 V_{i3}^2 \rho_2[n, \ell]^2 + 2\beta_0 \beta_1 V_{i1} V_{i3} \rho_1[n, \ell] \rho_2[n, \ell] \rangle$$

However, $\rho_1[n, \ell]^2 = \rho_1[n, \ell]$, $\rho_2[n, \ell]^2 = \rho_2[n, \ell]$, and $\rho_1[n, \ell] \rho_2[n, \ell] = \rho_2[n, \ell]$,

Then $\langle S_2^2 \rangle = \beta_0^2 V_{i1}^2 \langle \alpha_1^2 \rho_1[n, \ell] + \alpha_2^2 \rho_2[n, \ell] \{1 + 2\alpha_3\} \rangle$.

Where $\alpha_1 = \beta_1/\beta_0 = (g_L - g_{NL})/g_{NL}$, $\alpha_2 = V_{i3}/V_{i1} = X_2/X_1$, and $\alpha_3 = \alpha_1/\alpha_2$.

Now since $\langle \rho_1[n, \ell] \rangle = p_A$, $\langle \rho_2[n, \ell] \rangle = p_B$, and $V_{i1}^2 = P_I \cdot X_1^2$ then

$$\frac{\langle S_2^2 \rangle}{P_I} = \beta_0^2 X_1^2 \cdot \{p_A \cdot \alpha_1^2 + p_B \cdot \alpha_2^2 (1 + 2\alpha_3)\}$$

The 2nd term in (D1.7) is

$$\begin{aligned} \langle \{S_1 I_i[n, \ell]\}^2 \rangle &= \langle I_i[n, \ell]^2 \cdot \{1 - \beta_1 \rho_1[n, \ell] - \beta_0 \rho_2[n, \ell]\}^2 \rangle \\ &= \langle I_i[n, \ell]^2 \rangle - \langle I_i[n, \ell] \rho_1[n, \ell] \rangle \{1 - \beta_0^2\} - \langle I_i[n, \ell] \rho_2[n, \ell] \rangle \beta_0^2 \end{aligned}$$

Now by benefiting from some statistical relationship of the Gaussian PDF, yields

$$\frac{\langle \{S_1 I_i[n, \ell]\}^2 \rangle}{P_I} = 1 - \{1 - \beta_0^2\} \left\{ p_A + \sqrt{\frac{2}{\pi}} X_1 e^{-(X_1^2/2)} \right\} - \beta_0^2 \left\{ p_B + \sqrt{\frac{2}{\pi}} X_2 e^{-(X_2^2/2)} \right\}$$

While the 3rd term in (D1.7) is $2\langle |I_i[n, \ell]| S_1 S_2 \rangle$, which is derived to be

$$\frac{2\langle |I_i[n, \ell]| S_1 S_2 \rangle}{P_I} = 2\beta_0\beta_1 \sqrt{\frac{2}{\pi}} X_1 \{e^{-(X_1^2/2)} - e^{-(X_2^2/2)}\}$$

Therefore the exact O/P power from either amplifier $\mathbf{P}_{s,I}$ or $\mathbf{P}_{s,Q}$ is given by

$$P_{s,I} = P_I G_L \cdot \left\{ 1 - \beta_o^2 \cdot \{p_A(C_1 - C_2 X_1^2) + p_B(1 - C_3 X_2^2) + \mathcal{H}_1 C_2 + \mathcal{H}_2 C_3\} \right\} \quad (D1.8)$$

where $\beta_o = g_{NL}/g_L$, $C_1 = (g_L^2 - g_{NL}^2)/g_{NL}^2$, $C_2 = (g_L - g_{NL})^2/g_{NL}^2$,

$$C_3 = 1 + 2 \frac{X_2}{X_1} \cdot \frac{g_L - g_{NL}}{g_{NL}} ,$$

$$\mathcal{H}_1 = \sqrt{\frac{2}{\pi}} \cdot X_1 \cdot \exp(-X_1^2/2) \quad , \text{ and } \quad \mathcal{H}_2 = \sqrt{\frac{2}{\pi}} \cdot X_2 \cdot \exp(-X_2^2/2)$$

• In order to calculate the driver amplifier's nonlinearity variance versus the SC's frequency index \mathbf{m} , then from the analysis in Section 3.3.5, and by expanding (D1.6), ignoring g_L since it is common for all terms, and by applying the \mathcal{FFT} yields

$$y[\mathbf{m}, \ell] = y_1[\mathbf{m}, \ell] + y_2[\mathbf{m}, \ell] + y_3[\mathbf{m}, \ell] + y_4[\mathbf{m}, \ell] \quad (D1.9)$$

$$\text{where } y_1[\mathbf{m}, \ell] = \frac{1}{N_{\mathcal{F}}} \sum_{n=0}^{N_{\mathcal{F}}-1} \sum_{k=-N/2}^{N/2} c[k, \ell] \cdot \exp\left(j2\pi \frac{k-m}{N_{\mathcal{F}}} n\right) = c[\mathbf{m}, \ell] ,$$

$$y_2[\mathbf{m}, \ell] = \sum_{n=0}^{N_{\mathcal{F}}-1} \rho_{zz}[n, \ell] \cdot \exp\left(-j2\pi \frac{m}{N_{\mathcal{F}}} n\right) ,$$

$$y_3[\mathbf{m}, \ell] = -\frac{1}{2N_{\mathcal{F}}} \sum_{n=0}^{N_{\mathcal{F}}-1} \sum_{k=-N/2}^{N/2} c[k, \ell] \rho_{xx}[n, \ell] \cdot \exp\left(j2\pi \frac{k-m}{N_{\mathcal{F}}} n\right) ,$$

$$y_4[\mathbf{m}, \ell] = -\frac{1}{2N_{\mathcal{F}}} \sum_{n=0}^{N_{\mathcal{F}}-1} \sum_{k=-N/2}^{N/2} c[k, \ell]^* \rho_{yy}[n, \ell] \cdot \exp\left(-j2\pi \frac{k+m}{N_{\mathcal{F}}} n\right) ,$$

$$\begin{aligned} \rho_{zz}[\mathbf{n}, \ell] = & A_1 \{ \rho_1[n, \ell] \text{Sg}_1[n, \ell] + j\rho_{11}[n, \ell] \text{Sg}_2[n, \ell] \} \\ & + A_0 \{ \rho_2[n, \ell] \text{Sg}_1[n, \ell] + j\rho_{22}[n, \ell] \text{Sg}_2[n, \ell] \} , \end{aligned}$$

$$\rho_{xx}[\mathbf{n}, \ell] = \beta_1\{\rho_1[\mathbf{n}, \ell] + \rho_{11}[\mathbf{n}, \ell]\} + \beta_0\{\rho_2[\mathbf{n}, \ell] + \rho_{22}[\mathbf{n}, \ell]\} \quad ,$$

$$\rho_{yy}[\mathbf{n}, \ell] = \beta_1\{\rho_1[\mathbf{n}, \ell] - \rho_{11}[\mathbf{n}, \ell]\} + \beta_0\{\rho_2[\mathbf{n}, \ell] - \rho_{22}[\mathbf{n}, \ell]\} \quad ,$$

$$\mathbf{A}_1 = \beta_1 \cdot \mathbf{V}_{i1}, \text{ and } \mathbf{A}_0 = \beta_0 \cdot \mathbf{V}_{i3}.$$

Therefore the nonlinearity noise variance is given by

$$\begin{aligned} \sigma_{\text{DA,nn}}^2[\mathbf{m}] &= \langle (y[\mathbf{m}, \ell] - c[\mathbf{m}, \ell]) \cdot (y[\mathbf{m}, \ell] - c[\mathbf{m}, \ell])^* \rangle_\ell \\ &= \langle |y_2[\mathbf{m}, \ell]|^2 \rangle_\ell + \langle |y_3[\mathbf{m}, \ell]|^2 \rangle_\ell + \langle |y_4[\mathbf{m}, \ell]|^2 \rangle_\ell \\ &\quad + 2\{\langle y_2[\mathbf{m}, \ell]y_3[\mathbf{m}, \ell]^* \rangle_\ell + \langle y_2[\mathbf{m}, \ell]y_4[\mathbf{m}, \ell]^* \rangle_\ell + \langle y_3[\mathbf{m}, \ell]y_4[\mathbf{m}, \ell]^* \rangle_\ell\} \end{aligned} \quad (\text{D1.10})$$

Although the accurate derivation of $\sigma_{\text{DA,nn}}^2[\mathbf{m}]$ is very complicated and time-consuming, however, the author has completed it successfully, and for convenience, only final results will be written here. Thus $\sigma_{\text{DA,nn}}^2[\mathbf{m}]$ can be expressed as

$$\begin{aligned} \sigma_{\text{DA,nn}}^2[\mathbf{m}] &= \langle |c[\mathbf{m}, \ell]|^2 \rangle_\ell \cdot \frac{N}{N_{\mathcal{F}}} \cdot \\ &\quad \left\{ \beta_1^2 \cdot \{p_A(1 + X_1^2) - \mathcal{H}_1\} \cdot \gamma_0 \cdot \sum_{r=0}^{N_{\mathcal{F}}-1} F_{11}[r] \cdot \cos\left(\frac{2\pi}{N_{\mathcal{F}}} \mathbf{m} \cdot \mathbf{r}\right) \right. \\ &\quad \left. 2\beta_0\beta_1 \cdot \{p_B(1 + X_1X_2) - \mathcal{H}_{12}\} \cdot \gamma_0 \cdot \sum_{r=0}^{N_{\mathcal{F}}-1} F_{12}[r] \cdot \cos\left(\frac{2\pi}{N_{\mathcal{F}}} \mathbf{m} \cdot \mathbf{r}\right) \right. \\ &\quad \left. \beta_0^2 \cdot \{p_B(1 + X_2^2) - \mathcal{H}_2\} \cdot \gamma_0 \cdot \sum_{r=0}^{N_{\mathcal{F}}-1} F_{22}[r] \cdot \cos\left(\frac{2\pi}{N_{\mathcal{F}}} \mathbf{m} \cdot \mathbf{r}\right) \right\} \end{aligned} \quad (\text{D1.11})$$

$$\text{where } \mathcal{H}_{12} = \sqrt{\frac{2}{\pi}} \cdot X_1 \cdot \exp(-X_2^2/2) \quad ,$$

$$\gamma_0 = \begin{cases} 1, & r = 0 \\ 2, & r \neq 0 \end{cases} \quad ,$$

$$\mathbf{F}_{11}[\mathbf{r}] = \frac{1}{p_A \cdot N_{\mathcal{F}}} \left\langle \sum_{u=0}^{N_{\mathcal{F}}-r-1} \rho_1[u, \ell] \text{Sg}_1[u, \ell] \rho_1[u+r, \ell] \text{Sg}_1[u+r, \ell] \right\rangle \quad ,$$

$$\mathbf{F}_{22}[\mathbf{r}] = \frac{1}{\mathfrak{p}_B \cdot N_{\mathcal{F}}} \left\langle \sum_{u=0}^{N_{\mathcal{F}}-r-1} \rho_2[u, \ell] \text{Sg}_2[u, \ell] \rho_2[u+r, \ell] \text{Sg}_2[u+r, \ell] \right\rangle, \text{ and}$$

$$\mathbf{F}_{12}[\mathbf{r}] = \frac{1}{\mathfrak{p}_B \cdot N_{\mathcal{F}}} \left\langle \sum_{u=0}^{N_{\mathcal{F}}-r-1} \rho_1[u, \ell] \text{Sg}_1[u, \ell] \rho_2[u+r, \ell] \text{Sg}_2[u+r, \ell] \right\rangle.$$

Here (D1.11) describes exactly the driver amplifier's nonlinearity variance in every SC. Here (**F**) functions are the autocorrelation functions which depend on the oversampling ratio. However, if the worst-case, or the DC-SC is considered, then $\sigma_{\text{DA,nn}}^2[\mathbf{m}] = \sigma_{\text{DA,nn}}^2$, and instead of using $\mathbf{V}_{\mathbf{o}1}$, and $\mathbf{V}_{\mathbf{i}1}$, the 1-dB compression point I/P and O/P values will be used since their values are usually very close to $\mathbf{V}_{\mathbf{o}1}$, and $\mathbf{V}_{\mathbf{i}1}$ and hence

$$\sigma_{\text{DA,nn}}^2 = \langle |c_{m,\ell}|^2 \rangle_{\ell} \cdot \beta_g^2 \left\{ \mathfrak{p}_A \exp\left(-\sqrt{\frac{2}{\pi}} X_1\right) + \mathfrak{p}_B \alpha_g (2 + \alpha_g) \exp\left(-\sqrt{\frac{2}{\pi}} X_2 + \{X_2 - X_1\} \left\{ \frac{\sqrt{2\pi}\beta_g}{1 + \sqrt{2\pi}\beta_g} \right\}\right) \right\} \quad (\text{D1.12})$$

where $\beta_g = (g_L - g_{NL})/g_L$, $\alpha_g = g_{NL}/(g_L - g_{NL})$,

$$\mathfrak{p}_A \approx \text{erfc}\{X_1/\sqrt{2}\}, \quad \mathfrak{p}_B = \text{erfc}\{X_2/\sqrt{2}\},$$

$$X_1 = \sqrt{P_{i1}/P_i} \quad , \quad X_2 = \sqrt{P_{is}/P_i} \quad ,$$

$$g_L = \sqrt{G_L} \quad , \quad g_{NL} = \frac{\sqrt{P_{os}} - \sqrt{P_{o1}}}{\sqrt{P_{is}} - \sqrt{P_{i1}}} \quad ,$$

G_L is the DA's linear power gain in linear scale, $G_L = 10^{G_{L,\text{dB}}/10}$,

P_{o1} is O/P power at the 1dB compression point in linear scale,

P_{i1} is I/P power at the 1dB compression point in linear scale,

P_{os} is the saturated O/P (0.1dB) power in linear scale,

P_{is} is the saturated I/P power in linear scale, and

$P_i = P_Q$ is the DA's I/P power.

For instance, In Fig. D1.3, the double-sided (**DS**) power spectral density (**PSD**) of an OFDM signal with $N = 50$, and $N_{\mathcal{F}} = 128$ after a driver amplifier with $X_1 = 1$, $X_2 = 2$, $g_L = 7$, and $g_{NL} = 1$ is shown.

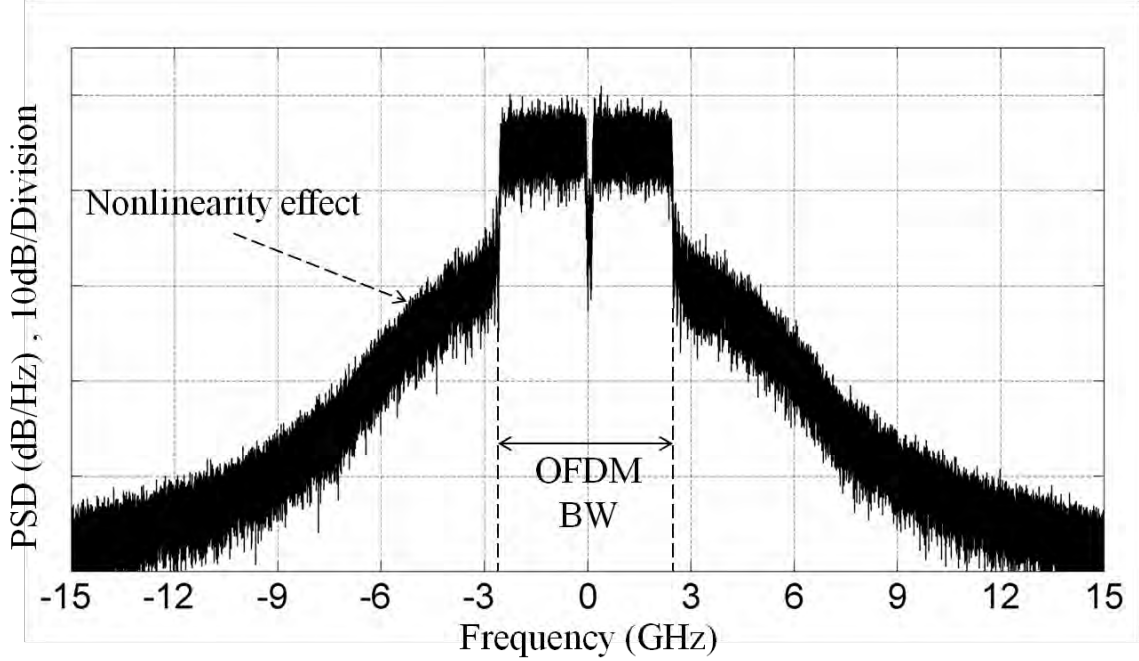


Fig. D1.3: DS-PSD of an OFDM signal with $N = 50$, and $N_F = 128$ after a driver amplifier with $X_1 = 1$, $X_2 = 2$, $g_L = 7$, and $g_{NL} = 1$.

Appendix-D2: IQ optical modulator's nonlinearity

It is found that optimal biasing point of the Mach-Zehnder intensity modulator (MZM) with lowest nonlinearity penalty is at the null point [50]. The MZM and IQ optical modulator are discussed in Section 3.4.1, hence only the nonlinearity contribution is considered for instance. From (3.38-a), and under perfect biasing conditions of the IQ optical modulator, the normalized-BB-discrete-version of the O/P optical field can be written benefiting from the sine function expansion as [81]

$$\begin{aligned}
 E[n, \ell] &= E_I[n, \ell] + jE_Q[n, \ell] = \sin\left(\frac{\pi}{2} \cdot \frac{I[n, \ell]}{v_\pi}\right) + j\sin\left(\frac{\pi}{2} \cdot \frac{Q[n, \ell]}{v_\pi}\right) \\
 &\approx \left(\frac{\pi}{2v_\pi}\right) I[n, \ell] - \frac{1}{3!} \left(\frac{\pi}{2v_\pi}\right)^3 I[n, \ell]^3 + \frac{1}{5!} \left(\frac{\pi}{2v_\pi}\right)^5 I[n, \ell]^5 \\
 &\quad j\left(\frac{\pi}{2v_\pi}\right) Q[n, \ell] - j\frac{1}{3!} \left(\frac{\pi}{2v_\pi}\right)^3 Q[n, \ell]^3 + j\frac{1}{5!} \left(\frac{\pi}{2v_\pi}\right)^5 Q[n, \ell]^5
 \end{aligned} \tag{D2.13}$$

Only the 3rd and the 5th orders of the expansion are considered here.

Let $\mathbf{Z}[n, \ell] = I[n, \ell] + jQ[n, \ell]$, which is the BB OFDM signal, and for notation simplicity, we will use $\mathbf{Z} = Z[n, \ell]$. Thus the received complex field can be written in more appropriate way as follows

$$E_r[n, \ell] = Z - \frac{\mathcal{A}^2}{3!} \left\{ \frac{3}{4} Z^2 (Z^*) + \frac{1}{4} (Z^*)^3 \right\} + \frac{\mathcal{A}^4}{5!} \left\{ \frac{5}{8} Z^3 (Z^*)^2 + \frac{5}{16} Z (Z^*)^4 + \frac{1}{16} Z^5 \right\} \quad (\text{D2.13})$$

Therefore when the $\mathcal{F}\mathcal{F}\mathcal{T}$ is applied, then the \mathbf{m} -th SC O/P is

$$y[m, \ell] = c[m, \ell] - \frac{\mathcal{A}^2}{3!} y_3[m, \ell] + \frac{\mathcal{A}^4}{5!} y_5[m, \ell] \quad (\text{D2.14})$$

where $\mathcal{A} = \frac{\pi}{2v_\pi}$,

$$\mathbf{y}_3[\mathbf{m}, \boldsymbol{\ell}] = \sum_{n=0}^{N_F-1} \left\{ \frac{3}{4} Z^2 (Z^*) + \frac{1}{4} (Z^*)^3 \right\} \cdot \exp\left(-j2\pi \frac{\mathbf{m}}{N_F} n\right) \quad , \text{ and}$$

$$\mathbf{y}_5[\mathbf{m}, \boldsymbol{\ell}] = \sum_{n=0}^{N_F-1} \left\{ \frac{5}{8} Z^3 (Z^*)^2 + \frac{5}{16} Z (Z^*)^4 + \frac{1}{16} Z^5 \right\} \cdot \exp\left(-j2\pi \frac{\mathbf{m}}{N_F} n\right) \quad .$$

Hence the nonlinearity variance is calculated as

$$\begin{aligned} \sigma_{\text{OM,nn}}^2[\mathbf{m}] &\approx \langle (y[m, \ell] - c[m, \ell]) \cdot (y[m, \ell] - c[m, \ell])^* \rangle_\ell, \\ &= \left(\frac{\mathcal{A}^2}{3!} \right)^2 \left\{ |y_3[m, \ell]|^2 - 2 \left(\mathcal{A}^2 \frac{3!}{5!} \right) \Re\{y_3[m, \ell] \cdot y_5[m, \ell]^*\} + \left(\mathcal{A}^2 \frac{3!}{5!} \right)^2 |y_5[m, \ell]|^2 \right\} \end{aligned}$$

The next step is very long since it implies expansions of $\mathbf{y}_3[\mathbf{m}, \boldsymbol{\ell}]$, and $\mathbf{y}_5[\mathbf{m}, \boldsymbol{\ell}]$ terms. However, after a long investigation, a simple and nice expression is obtained for the worst-corrupted SC (the DC-SC), which can be written as

$$\sigma_{\text{OM,nn}}^2 \approx \frac{\langle |c_{\mathbf{m},\ell}|^2 \rangle_\ell}{\pi} \cdot \sin^4 \left(\frac{\pi}{2} X_3 \cdot \left\{ 1 + \frac{N/N_F}{\pi^3} \right\} \right) \quad (\text{D2.15})$$

where $X_3 = \{\sqrt{P_{s,I}} \cdot R_L / v_\pi\}$,

v_π is the MZM's switching voltage, and R_L is load impedance (usually 50Ω).

Finally a semi-exact O/P power expression of the IQ optical modulator under optimal biasing condition is considered here. From (2.38-a), the O/P power is given as

$$\mathbf{P}_{\text{tx}} = \frac{P_O}{\text{att}_M} \cdot \left\langle \sin^2 \left(\frac{\pi}{2} \cdot \frac{I(t)}{v_\pi} \right) \right\rangle \quad ,$$

where \mathbf{P}_0 is the laser's power, \mathbf{att}_M is the modulator's loss. Thus by expanding the sine term up to the 5th power yields

$$\mathbf{P}_{tx} \approx \frac{P_0}{\mathbf{att}_M} \cdot \left\langle \left\{ \mathcal{A}I(t) - \frac{\mathcal{A}^3}{3!} I(t)^3 + \frac{\mathcal{A}^5}{5!} I(t)^5 \right\} \cdot \left\{ \mathcal{A}I(t) - \frac{\mathcal{A}^3}{3!} I(t)^3 + \frac{\mathcal{A}^5}{5!} I(t)^5 \right\} \right\rangle$$

Then after simplifying the terms between the brackets yields

$$\mathbf{P}_{tx} \approx \frac{P_0}{\mathbf{att}_M} \cdot \left\{ \mathcal{A}^2 \langle I(t)^2 \rangle - \frac{2}{3!} \mathcal{A}^4 \langle I(t)^4 \rangle + \left(\frac{2}{5!} + \frac{1}{3!^2} \right) \mathcal{A}^6 \langle I(t)^6 \rangle - \frac{2}{3!5!} \mathcal{A}^8 \langle I(t)^8 \rangle + \frac{2}{5!^2} \mathcal{A}^{10} \langle I(t)^{10} \rangle \right\}$$

Now by using the following important feature of the GRVs [100]

$$\langle \mathbf{I}(t)^{2x} \rangle = \langle I(t)^2 \rangle^x \cdot \prod_{r=1}^x 2(x-r) + 1 \quad , \text{ then after substitution we obtain,}$$

$$\mathbf{P}_{tx} \approx \frac{P_0}{\mathbf{att}_M} X_4 \cdot \left\{ 1 - X_4 + \frac{2}{3} X_4^2 - \frac{7}{24} X_4^3 + \frac{21}{320} X_4^4 \right\} \quad (\text{D.15})$$

where $X_4 = R_L \left(\frac{\pi}{2V_\pi} \right)^2 \cdot P_{s,I}$, and $P_{s,I}$ is the driving power of I or Q branch.

Bibliography

- [1] M. Nakazawa, *High Spectral Density Optical Communication Technologies*. Springer, 2010.
- [2] Lars Gruner-Nielsen, Marie Wandel, Poul Kristensen, Carsten Jørgensen, Lene Vilbrad Jørgensen, Bent Edvold, Bera Palsdottir, and Dan Jakobsen, "Dispersion-Compensating Fibers," *Journal of Lightwave Technol.*, vol. 23, pp. 3566-3579, 2005.
- [3] Jean Armstrong, "OFDM for Optical Communications," *Journal of Lightwave Technol.*, vol. 27, pp. 189-204, 2009.
- [4] Arthur James Lowery, Liang Bangyuan Du, and Jean Armstrong, "Performance of Optical OFDM in Ultralong-Haul WDM Lightwave Systems" *Journal of Lightwave Technol.*, vol. 25, pp. 131-138, 2007.
- [5] W. Shieh, H. Bao, and Y. Tang, "Coherent Optical OFDM: theory and design," *Optics Express*, Vol. 16 Issue 2, pp.841-859, 2008.
- [6] Sander L. Jansen, Itsuro Morita, Tim C. W. Schenk, Noriyuki Takeda, and Hideaki Tanaka, "Coherent Optical 25.8-Gb/s OFDM Transmission Over 4160-km SSMF," *Journal of Lightwave Technol.*, vol. 26, pp. 6-15, 2008.
- [7] Wei-Ren Peng, Xiaoxia Wu, Vahid R. Arbab, Kai-Ming Feng, Bishara Shamee, Louis C. Christen, Jeng-Yuan Yang, Alan E. Willner, Sien Chi, "Theoretical and Experimental Investigations of Direct-Detection RF-Tone-Assisted Optical OFDM Systems" *Journal Lightwave Technol.*, vol. 27, pp. 1332-1339, 2009.
- [8] Brendon J. C. Schmidt, Zuraidah Zan, Liang B. Du, and Arthur J. Lowery, "100Gbit/s Transmission using Single-Band Direct-Detection OFDM" in *Optical Fiber Conference (2009)*, paper PDPC3.
- [9] Qi Yang, Yan Tang, Yiran Ma, and William Shieh, "Experimental Demonstration and Numerical Simulation of 107-Gb/s High Spectral Efficiency Coherent Optical OFDM," *Journal of Lightwave Technol.*, vol. 27, pp. 168-176, 2009.
- [10] Sander L. Jansen, Itsuro Morita, and Hideaki Tanaka, "10×121.9 Gb/s PMD-OFDM Transmission with 2-b/s/Hz Spectral Efficiency over 1,000km of SSMF" in *Optical Fiber Conference (2008)*, paper PDP2.
- [11] D. Hillerkuss, R. Schmogrow, M. Meyer, S. Wolf, M. Jordan, P. Kleinow, N. Lindenmann, P. C. Schindler, A. Melikyan, X. Yang, S. Ben-Ezra, B. Nebendahl, M. Dreschmann, J. Meyer, F. Parmigiani, P. Petropoulos, B. Resan, A. Oehler, K. Weingarten, L. Altenhain, T. Ellermeyer, M. Moeller, M. Huebner, J. Becker, C. Koos, W. Freude, and J. Leuthold, "26 Tbit/s line-rate super-channel transmission utilizing all-optical fast Fourier transform processing," *Nature Photon.* 5(6), 364-471 (2011).
- [12] Cunyun Ye, *Tunable External Cavity Diode Lasers*. World Scientific, 2004.
- [13] K. C. Kao, G. A. Hockham, "Dielectric-fibre surface waveguide for optical frequencies," *proceeding of the Inst. of Elect. Eng.*, vol. 113, pp. 1151-1158, 1966.

- [14] Casimer Decusatis, *Fiber Optics Data Communication*. Academic Press, 2002.
- [15] D. Hillerkuss, R. Schmogrow, M. Meyer, S. Wolf, M. Jordan, P. Kleinow, N. Lindenmann, P. C. Schindler, A. Melikyan, X. Yang, S. Ben-Ezra, B. Nebendahl, M. Dreschmann, J. Meyer, F. Parmigiani, P. Petropoulos, B. Resan, A. Oehler, K. Weingarten, L. Altenhain, T. Ellermeyer, M. Moeller, M. Huebner, J. Becker, C. Koos, W. Freude, and J. Leuthold, "Single-laser 32.5 Tbit/s Nyquist WDM transmission," 2012arXiv1203.2516H.
- [16] A. Sano, H. Masuda, T. Kobayashi, M. Fujiwara, K. Horikoshi, E. Yoshida, Y. Matsui, M. Mizoguchi, H. Yamazaki, Y. Sakamaki, and H. Ishii, "69.1-Tb/s (432 × 171-Gb/s) C- and extended L-band transmission over 240km using PMD-16-QAM modulation and digital coherent detection," in *Optical fiber communication conference* (Optical Society of America, 2010), paper PDPB7.
- [17] Dayou Qian, Ming-Fang Huang, Ezra Ip, Yue-Kai Huang, Yin Shao, Junqiang Hu, and Ting Wang, "101.7-Tb/s (370 × 294-Gb/s) PMD-128QAM-OFDM Transmission over 3×55km SSMF using Pilot-based Phase Noise Mitigation," in *Optical fiber communication conference* (2011), paper PDPB5.
- [18] R. W. Chang, "High-Speed Multichannel Data Transmission with Bandlimited Orthogonal Signals," *Bell Sys. Tech. Journal*, vol. 45, Dec. 1966, pp. 1775-96.
- [19] S. B. Weinstein and P. M. Elbert, "Data Transmission for Frequency-Division Multiplexing Using the Discrete Fourier Transform," *IEEE Trans. Commun. Tech.*, vol. 19, pp. 628-634, 1971.
- [20] A. Peled and A. Ruiz, "Frequency domain data transmission using reduced computational complexity algorithms," *Acoustic, Speech, and Signal Processing, IEEE International Conference on ICASSP'80*, vol. 5, pp. 964-967, 1980.
- [21] L. J. Cimini, "Analysis and simulation of a digital mobile channel using orthogonal frequency division multiplexing," *IEEE Trans. Commun.*, vol. COM-33, pp. 665-675, 1985.
- [22] T. M. Schmidl and D. C. Cox, "Robust Frequency and Timing Synchronization for OFDM," *IEEE Trans. Commun.*, vol. 45, pp. 1613-1621, 1997.
- [23] William Shieh and Ivan Djordjevic, *Orthogonal Frequency Division Multiplexing for Optical Communications*. ELSEVIER, 2009.
- [24] Yannis Benlachar, Philip M. Watts, Rachid Bouziane, Peter Milder, Deepak Rangaraj, Anthony Cartolano, Robert Koutsoyannis, James C. Hoe, Markus Puschel, Madeleine Glick, and Robert I. Killey, "Generation of optical OFDM signal using 21.4GS/s real time digital signal processing," *Optics Express*, vol. 17, pp. 17658-17668, 2009.
- [25] R. Schmogrow, M. Winter, D. Hillerkuss, B. Nebendahl, S. Ben-Ezra, J. Mayer, M. Dreschmann, M. Huebner, J. Becker, C. Koos, W. Freude, and J. Leuthold, "Real-Time OFDM transmitter beyond 100Gbit/s," *Optics Express*, vol. 19, pp. 12740-12749, 2011.

- [26] Beril Inan, Susmita Adhikari, Ozgur Karakaya, Peter Kainzmaier, Micheal Mocker, Heinrich von Kirchbauer, Norbert Hanik, and Sander L. Jansen, "Real-Time 93.8-Gb/s polarization-multiplexed OFDM transmitter with 1024-point IFFT," *Optics Express*, vol. 19, No. 26, 2011.
- [27] A. J. Lowery and J. Armstrong, "Orthogonal frequency division multiplexing for dispersion compensation of long-haul optical systems," *Optics Express*, vol. 14, pp. 2079-2084, 2006.
- [28] B. J. Schmidt, A. J. Lowery, and J. Armstrong, "Experimental Demonstration of 20Gbit/s Direct-Detection Optical OFDM and 12Gbit/s with a colorless Transmitter," in *Optical Fiber Commun. Conference and Exposition and The National Fiber Optic Engineers Conference*, OSA Technical Digest Series (CD) (Optical Society of America, 2007), paper PDP18.
- [29] Andrew D. Ellis, Jian Zhao, and David Cotter, "Approaching the Non-Linear Shannon Limit," *Journal of Lightwave Technol.*, vol. 28, pp. 423-433, 2010.
- [30] A. J. Lowery, "Improving Sensitivity and Spectral Efficiency in Direct-Detection Optical OFDM Systems," in *Optical Fiber Commun./National Fiber Optic Engineers Conference*, OFC/NFOEC (2008), paper OMM4.
- [31] T. Suhara, *Semiconductor Laser Fundamentals*. CRC Press, 2004.
- [32] E. Ip, and J. M. Kahn, "Carrier Synchronization for 3- and 4-bit-per-Symbol Optical Transmission," *Journal of Lightwave Technol.*, vol. 23, pp. 4110-4124, 2005.
- [33] Naresh Satyan, Wei Liang, and Amnon Yariv, "Coherence Cloning Using Semiconductor Laser Optical Phase-Lock Loops," *IEEE Journal of Quantum Electronics*, vol. 45, pp. 755-761, 2009.
- [34] R. T. Ramos, and A. J. Seeds, "Delay, Linewidth and bandwidth limitations in optical phase-locked loop design," *Electron Lett.*, vol. 26, pp. 389-390, 1990.
- [35] M. Bagheri, F. Aflatouni, A. Imani, A. Goel, and H. Hashemi, "Semiconductor laser phase-noise cancellation using an electrical feed-forward scheme," *Opt. Lett.*, vol. 34, pp. 2979-2981, 2009.
- [36] Frederick H. Raab, Peter Asbeck, Steve Cripps, Peter B. Kenington, Zoya B. Popovic, Nick Potheary, John F. Sevic, and Nathan O. Sokal, "Power Amplifiers and Transmitter for RF and Microwave," *IEEE Trans. On microwave theory and tech.*, vol. 50, pp. 814-826, 2002.
- [37] Donald K. Belcher, Michael A Wohl, and Kent E. Bagwell, "Feed-Forward Correction Loop With Adaptive Predistortion Injection For Linearization Of RF Power Amplifier," USA Patent no. 5,760,646 (1998).
- [38] Ezra Ip and Joseph Kahn, "Feedforward Carrier Recovery for Coherent Optical Communications" *Journal Lightwave Technol.*, vol. 25, pp. 2675-2692, 2007.
- [39] T. Beukema, M. Sorna, K. Selander, S. Zier, B. L. Ji, P. Murfet, J. Mason, W. Rhee, H. Ainspan, and M. Beakes, "A 6.4-Gb/s CMOS SerDes Core With Feed-Forward and Decision-Feedback Equalization" *IEEE Journal of Solid-State Circuits*, vol. 40, pp. 2633-2645, 2005.

- [40] Patrick Robertson and Stefan Kaiser, "Analysis of the Effects of Phase-Noise in Orthogonal Frequency Division Multiplexing (OFDM) Systems," *IEEE International Conference on Communications*, Conference Records, pp. 1652-1657, 1995.
- [41] Wei-Ren Peng, "Analysis of Laser Phase Noise Effect in Direct-Detection Optical OFDM Transmission," *Journal of Lightwave Technol.*, vol. 28, pp. 2526-2536, 2010.
- [42] Irshaad Fatadin and Seb J. Savory, "Impact of Phase to amplitude noise conversion in coherent optical systems with digital dispersion compensation," *Opt. Express* 18, 16273-16278 (2010).
- [43] J. A. Armstrong, "Theory of Interferometric Analysis of Laser Phase Noise," *Journal of Optical Society of America*, vol. 56, pp. 1024-1031, 1966.
- [44] R. Centeno Neelen, D. M. Boersma, M. P. van Exter, G. Neinhuis, and J. P. Woerdman, "Spectral filtering within the Schawlow-Townes linewidth of a Semiconductor Laser," *Phys. Review Lett.*, vol. 69, Issue 4, pp. 593-596, 1992.
- [45] S. Yamamoto, N. Edagawa, H. Taga, Y. Yoshida, and H. Wakabayashi, "Analysis of Laser Phase Noise to Intensity Noise Conversion by Chromatic Dispersion in Intensity Modulation and Direct Detection Optical-Fiber Transmission," *Journal of Lightwave Technol.*, vol. 8, pp. 1716-1722, 1990.
- [46] K. Petermann, "FM-AM Noise Conversion in Dispersive Single-Mode Fiber Transmission Lines," *Electronic Lett.*, vol. 26, pp. 2097-2098, 1990.
- [47] W. K. Marshall, B. Crosignani, and A. Yariv, "Laser phase noise to intensity noise conversion by lowest-order group-velocity dispersion in optical fiber: exact theory," *Opt. Lett.*, vol. 25, pp. 165-167, 2000.
- [48] John G. Proakis, *Digital Communications*. (3rd ed.), McGraw-Hill, 1995.
- [49] Rene-Jean Essiambre, Gerhard Kramer, Peter J. Winzer, Gerard J. Foschini, and Bernhard Geobel, "Capacity Limits of Optical Fiber Networks," *Journal of Lightwave Technol.*, vol. 28, pp. 662-701, 2010.
- [50] Keang-Po Ho, *Phase-Modulated Optical Communication Systems*. Springer, 2005.
- [51] Seb J. Savory, "Digital Coherent Optical Receivers: Algorithms and Subsystems," *IEEE Journal of Selected Topics in Quantum Electronics*, vol. 16, pp. 1164-1179, 2010.
- [52] Ioannis Roudas, Athanasios Vgenis, Constantinos S. Petrou, Dimitris Toumpakaris, Jason Hurley, Michael Sauer, John Downie, Yihong Mauro, and Srikanth Raghavan, "Optimal Polarization Demultiplexing for Coherent Optical Communication Systems," *Journal of Lightwave Technol.*, vol. 28, pp. 1121-1134, 2010.
- [53] J. M. Tang and K. Alan Shore, "Maximizing the Transmission Performance of Adaptively Modulated Optical OFDM Signals in Multimode-Fiber Link by Optimizing Analog-to-Digital Convertors," *Journal of Lightwave Technol.*, vol. 25, pp. 787-798, 2007.

- [54] Kyunghwan Oh, Un-Chul Paek, *Silica Optical Fiber Technology for Devices and Components*. John Wiley & Sons, 2012.
- [55] Govind P. Agrawal, *Fiber-Optic Communication Systems*. (4th ed.) John Wiley & Sons, 2011.
- [56] Sander L. Jansen, Bernhard Spinnler, Itsuro Morita, Sebastian Randel, and Hideaki Tanaka, "100GbE: QPSK versus OFDM" *Opt. Fiber Technol.* Invited paper 2009.
- [57] D. M. Baney, P. Gallion, and R. S. Tucker, "Theory and measurement techniques for the noise figure of optical amplifiers," *Opt. Fiber Technol.*, vol. 6, 122-154 (2000).
- [58] IEC 61280-2-9 Fiber-optic communication subsystem test procedure-Part 2-9: Digital systems – Optical signal-to-noise ratio measurement for dense wavelength-division multiplexed systems.
- [59] Liang Du and Arthur Lowery, "Compensating XPM for 100 Gbit/s coherent channels with 10 Gbit/s direct-detection NRZ neighbors," in *Optical fiber communication conference* (2010), paper OTuE7.
- [60] Keang-Po Ho and Joseph M. Kahn, "Electronic Compensation Technique to Mitigate Nonlinear Phase Noise," *Journal of Lightwave Technol.*, vol. 22, pp. 779-783, 2004.
- [61] J. P. Gordan, H. Kogelnik, "PMD fundamentals: Polarization mode dispersion in optical fibers," *Proc. Nat. Acad. Sci.*, vol. 97, no. 9, 4541-4550 (2000).
- [62] C. D. Poole, R. E. Wagner, "Phenomenological Approach to Polarization Dispersion in Long Single-Mode Fibers," Delay, Linewidth and bandwidth limitations in optical phase-locked loop design," *Electron Lett.*, vol. 22, pp. 1029-1030, 1986.
- [63] Lianshan Yan, M. C. Hauer, Y. Shi, X. S. Yao, Y. Wang, Alan E. Willner, and W. L. Kath, "Polarization-Mode-Dispersion Emulator Using Variable Differential-Group-Delay (DGD) Elements and Its Use for Experimental Importance Sampling," *Journal of Lightwave Technol.*, vol. 22, pp. 1051-1058, 2007.
- [64] Biao Fu and Rongqing Hui, "Fiber Chromatic Dispersion and Polarization-Mode Dispersion Monitoring Using Coherent Detection," *IEEE Photonic Tech. Lett.*, vol. 17, pp. 1561-1563, 2005.
- [65] Michael Speth, Stefan Fechtel, Gunnar Fock, and Heinrich Meyr, "Optimum Receiver Design for Wireless Broad-Band Systems Using OFDM-Part I," *IEEE Trans. On Commun.*, vol. 47, pp. 1668-1677, 1999.
- [66] Michael Speth, Stefan Fechtel, Gunnar Fock, and Heinrich Meyr, "Optimum Receiver Design for OFDM-Based Broadband Transmission-Part II: A Case Study," *IEEE Trans. On Commun.*, vol. 49, pp. 571-578, 2001.
- [67] M. Morelli, C. -C. Jay Kuo, and Man-On Pun, "Synchronization Techniques for Orthogonal Frequency Division Multiple Access (OFDMA): A Tutorial Review," *proceeding of IEEE*, vol. 95, pp. 1394-1427, 2007.

- [68] Stephen B. Wicker and Vijay K. Bhargave, *Reed Solomon Codes and Their Applications*. IEEE Press, 1994.
- [69] Dr. Henrik Schulze, Christian Luders, *Theory and Applications of Ofdm and Cdma*. John Wiley, 2005.
- [70] Steven W. Smith, *The Scientist and Engineer's Guide to Digital Signal Processing*. California Technical Pub., 1997.
- [71] Byungjoon Park, Hyunsoo Cheon, Changeon Kang, and Daesik Hong, "A Novel Timing Estimation Method for OFDM Systems," *IEEE Commun. Lett.*, vol. 7, pp. 239-241, 2003.
- [72] Daniel J.F. Barros and Joseph Kahn, "Optimized Dispersion Compensation Using Orthogonal Frequency-Division Multiplexing," *Journal of Lightwave Technol.*, vol. 26, pp. 2889-2898, 2008.
- [73] Fred Buchali, Roman Dischler, Axel Klekamp, Michael Bernhard, and Daniel Efinger, "Realization of a real-time 12.1 Gb/s optical OFDM transmitter and its application in a 109 Gb/s transmission system with coherent reception," *Optical Commun. Conference, ECOC*, pp. 1-2, 2009.
- [74] Christian R. Berger, Yannis Benlachtar, and Robert I. Killey, "Optimum Clipping for Optical OFDM with Limited Resolution DAC/ADC," in *Signal Processing in Photonic Commun.*, OSA Tech. Digest (CD) (Optical Society of America, 2011), paper SPMB5.
- [75] L. D. Paarmann, *Design and Analysis of Analog Filters*. Springer, 2001.
- [76] Xuejun Zhang and Lawrence E. Larson, "Gain and Phase Error-Free LINC Transmitter," *IEEE Trans. On Vehicular Tech.*, vol. 49, pp. 1986-1994, 2000.
- [77] J. Lee, F. Breyer, S. Randel, O. Ziemann, H. P. van den Boom, and A. M. Koonen, "Low-Cost and Robust 1-Gbit/s Plastic Optical Fiber Based on Light-Emitting Diode Technology," in *Optical Fiber Commun. Conference and Exposition and the National Fiber Optic Engineers Conference*, OSA Tech. Digest (CD) (Optical Society of America, 2008), paper OWB3.
- [78] J. Tubbax, Boris Come, Liesbet Van der Perre, Luc Deneire, Stephane Donny, and Marc Engels, "Compensation of IQ imbalance in OFDM systems," in *IEEE International Commun. Conference*, vol. 5, pp. 3402-3407, 2003.
- [79] Deepaknath Tandur and Marc Moonen, "Joint Adaptive Compensation of Transmitter and Receiver IQ Imbalance Under Carrier Frequency Offset in OFDM-Based Systems," *IEEE Trans. On Signal Processing*, vol. 55, pp. 5246-5252, 2007.
- [80] V. A. Bohara and S. H. Ting, "Theoretical Analysis of OFDM signals in Nonlinear Polynomial Models" *Information, Commun. & Signal Process.*, 6th International Conference, pp. 1-5, 2007.
- [81] Larry C. Andrews, *Special Functions of Mathematics for Engineers*. (2nd ed.), SPIE Press, 1992.

- [82] Y. Tang, X. Yi, W. Shieh, and R. Evans, "Optimum Design of Coherent Optical OFDM Transmitter," *Optical Fiber Commun. and the National Fiber Optic Engineers Conference*, 2007, paper JThA47.
- [83] A. Yariv, *Optical Electronic in Modern Communications*. Oxford University Press, New York, (4th ed.), 1997.
- [84] Junji Ohtsubo, *Semiconductor Lasers: Stability, Instability and Chaos*. Springer, 2006.
- [85] K. Peterman, *Laser Diode Modulation and Noise*. Norwell, MA: Kluwer, 1988.
- [86] Kerry Vahala and Amnon Yariv, "Semiclassical Theory of Noise in Semiconductor Lasers-Part II," *IEEE J. Quantum Electron.*, vol. QE-19, pp. 1102-1109, 1983.
- [87] R. N. Bracewell, *The Fourier Transform and Its Applications*. (3rd ed.), Boston: McGraw-Hill, 2000.
- [88] O. Ishida, "Delayed-Self-Heterodyne Measurement of Laser Frequency Fluctuations," *Journal Lightwave Technol.*, vol. 9, pp. 1528-1533, 1991.
- [89] C. H. Henry, "Phase noise in semiconductor lasers," *Journal of Lightwave Technol.*, vol. LT-4, pp. 298-310, 1986.
- [90] K. Kikuchi and T. Okoshi, "Estimation of Linewidth Enhancement Factor of AlGaAs Lasers by Correlation Measurement Between FM and AM Noises," *IEEE Journal of Quantum Electron.*, vol. QE-21, pp. 669-673, 1985.
- [91] I. Joindoint, "Measurement of relative intensity noise (RIN) in semiconductor lasers," *J. Phys. III*, vol. 2, pp. 1591-1603, 1992.
- [92] Christopher J. O'Brien, Marian M. Majewski, and Aleksandar D. Rakic, "A comparison of small signal modulation parameter extraction techniques for vertical-cavity, surface emitting lasers" *Microwave, Radar & Wireless Commun. International Conference MIKON*, pp. 169-172, 2006.
- [93] K. Vahala, C. Harder, and A. Yariv, "Observation of relaxation resonance effects in the field spectrum of semiconductor laser" *Appl. Phys. Lett.*, vol. 42, pp. 211-213, 1983.
- [94] K. Kikuchi, "Effect of 1/f type FM noise on semiconductor laser linewidth residual in high power limit," *IEEE J. Quantum Electron.*, vol. QE-25, pp. 684-688, 1989.
- [95] M. J. O'Mahoney and I. D. Henning, "Semiconductor linewidth broadening due to 1/f carrier noise," *Electron Lett.*, vol. 19, pp. 1000-1001, 1983.
- [96] L. B. Mercer, "1/f Frequency Noise Effects on Self-Heterodyne Linewidth Measurements," *Journal of Lightwave Technol.*, vol. 9, pp. 485-493, 1991.
- [97] K. Kikuchi and T. Okoshi, "Dependence of semiconductor laser linewidth on measurement time: evidence of predominance of 1/f noise," *Electron Lett.*, vol. 21, pp. 1011-1012, 1985.
- [98] M. Nazarathy, W.V. Sorin, D.M. Baney, and S.A. Newton, "Spectral analysis of optical mixing measurements," *Journal of Lightwave Technol.*, vol.7, no.7, pp.1083-1096, Jul 1989.

- [99] M. S. Keshner, "1/f Noise," *proceeding of IEEE*, vol. 70, pp. 212-1018, 1982.
- [100] J. K. Patel, C. B. Read, *Handbook of Normal Distribution*. (2nd ed.), Marcel Dekker, 1996.
- [101] M. P. van Exter, W. A. Hamel, J. P. Woerdman, and B. R. P. Zeilmans, "Spectral Signature of Relaxation Oscillation in Semiconductor Laser," *Journal of Quantum Electronics*, vol. 28, pp. 1470-1478, 1992.
- [102] Asier Villafranca, Javier Lasobras, Jose A. Lazaro, and Ignacio Garces, "Characterization of the Main Semiconductor Laser Static and Dynamic Working Parameters From CW Optical Spectrum Measurements," *IEEE Journal of Quantum Electron.*, vol. 43, pp. 116-122, 2007.
- [103] "Digital Communication Analyzer (DCA), Measure Relative Intensity Noise (RIN)", Product Note 86100-7, Agilent Technologies.
- [104] E. Bava, G. Galzerano, and C. Svelto, "Fabry-Perot frequency discriminators: sensitivity, amplitude noise immunity and noise limits," *Instrumentation and Measurement Technol. Conference, Proceedings of the 17th IEEE*, pp. 169-172, 2006.
- [105] Paul K. J. Park, S. K. Shin, H. C. Ji, and Y. C. Chung, "Frequency stabilization of multiple semiconductor lasers using digital feedback loop," *Journal of Optics Commun.* , vol. 272, pp. 217-220, 2007.
- [106] F. M. Gardner, *Phaselock Techniques*. (3rd ed.), John Wiley & Sons, 2005.
- [107] H. Tsuchida, "Simple technique for improving the resolution of the delayed self-heterodyne method," *Opt. Lett.*, vol. (11), pp. 640-642, 1990.
- [108] L. G. Richter, H. I. Mandelburg, M. S. Kruger, and P. A. McGrath, "Linewidth determination from self-heterodyne measurements with subcoherence delay times," *IEEE Journal of Quantum Electron.*, vol. QE-22, pp. 2070-2074, 1986.
- [109] Pascal Correc, Oliver Girard, and Ildefonso F. de Faria, "On the Thermal Contribution to the FM Response of DFB: Theory and Experiment," *IEEE Journal of Quantum Electron.*, vol. 30, pp. 2485-2490, 1994.
- [110] D. W. Allan, "Statistics of Atomic Frequency Standards," *Proceedings of the IEEE*, vol. 54, pp. 221-230, 1966.
- [111] Cornell Drentea, *Modern Communications Receiver Design and Technology.*, Artech House, 2010.
- [112] Steven T. Karris, *Introduction to Simulink: With Engineering Applications*, Orchard Publications, 2008.
- [113] A. Zaknich, *Principles of Adaptive Filters and Self-Learning Systems*. Springer, 2005.
- [114] Jeremy Kasdin, "Discrete Simulation of Colored Noise and Stochastic Processes and $1/f^\alpha$ Power Law Noise Generation," *Proceedings of the IEEE*, vol. 83, pp. 802-827, 1995.

- [115] Edoardo Milotti, “ $1/f$ noise: a pedagogical review,” arXiv. Physics/0204033.
- [116] Christine Spiegelberg, Jihong Geng, Yongdan Hu, Yushi Kaneda, Shibin Jiang, and N Peyghambarian, “Low-Noise Narrow-Linewidth Fiber Laser at 1550 nm (June 2003),” *Journal of Lightwave Technol.*, vol. 22, pp. 57-62, 2004.
- [117] Guohua Qi, Jianping Yao, Joe Sereglyi, Stephane Raquet, Claude Belisle, Xiupu Zhang, Ke Wu, and Raman Kashyap, “Phase-Noise Analysis of Optically Generated Millimeter-Wave Signals With External Optical Modulation Techniques,” *Journal of Lightwave Technol.*, vol. 24, pp. 4861-4875, 2006
- [118] Xiaoke Yi and Robert. A. Minasian, “Dispersion Induced RF Distortion of Spectrum-Sliced Microwave-Photonic Filters,” *IEEE Trans. On microwave theory and tech.*, vol. 54, pp. 880-886, 2006.
- [119] Songping Wu and Yeheskel Bar-Ness, “A Phase Noise Suppression Algorithm for OFDM-Based WLANs,” *IEEE Commun. Lett.*, vol. 6, pp. 535-537, 2002.
- [120] Xingwen Yi, William Shieh, and Yiran Ma, “Phase Noise Effects on High Spectral Efficiency Coherent Optical OFDM Transmission,” *Journal of Lightwave Technol.*, vol. 26, pp. 1309-1316, 2008.
- [121] Xingwen Yi, William Shieh, and Yan Tang, “Phase Estimation for Coherent Optical OFDM,” *IEEE Photonic Tech. Lett.*, vol. 19, pp. 919-921, 2007.
- [122] Ana Garcia Armada, “Understanding the effects of Phase Noise in Orthogonal Frequency Division Multiplexing (OFDM),” *IEEE Trans. On Broadcasting*, vol. 47, pp. 153-159, 2001.
- [123] Thierry Pollet, Mark Van Bladel, and Marc Moeneclaey, “BER Sensitivity of OFDM Systems to Carrier Frequency Offset and Wiener Phase Noise,” *IEEE Trans. On Commun.*, vol. 43, pp. 191-193, 1995.
- [124] Xiang Liu, Linn F. Mollenauer, and Xing Wei, “Impact of Group-Delay Ripple in Transmission Systems Including Phase-Modulated Formats,” *IEEE Photonic Technol. Lett.*, vol. 16, pp. 305-307, 2004.
- [125] Francis D. Natali, “AFC Tracking Algorithms,” *IEEE Trans. On Commun*, vol. COM-32, pp. 935-947, 1984.
- [126] Wayne V. Sorin, Kok Wai Chang, Geraldine A. Conrad, and Paul R. Hernday, “Frequency Domain Analysis of an Optical FM Discriminator,” *Journal of Lightwave Technol.*, vol. 10, pp. 787-793, 1992.
- [127] Zuraidah Zan, Liang B. Du, and Arthur J. Lowery, “Experimental Demonstration on the Reduction of Linewidth Impact in a Self-Heterodyne Optical OFDM System” in *Optical Fiber Conference (2010)*, paper JThA8.
- [128] Lap-Shun Fock, Anthony Kwan, and Rodney S. Tucker, “Reduction of Semiconductor Laser Intensity Noise by Feedforward Compensation: Experiment and Theory,” *Journal of Lightwave Technol.*, vol. 10, pp. 1919-1925, 1992.

- [129] A. Schuchert and R. Hasholzner, "A Novel IQ Imbalance Compensation Scheme for the Reception of OFDM Signals," *IEEE Trans. On Consumer Electronics*, vol. 47, pp. 313-318, 2001.
- [130] W. Shieh, W. Chen, and R. S. Tucker, "Polarization mode dispersion mitigation in coherent optical orthogonal frequency division multiplexed systems," *Electron Lett.*, vol. 42. no. 17, 2006.
- [131] Tong Wang and Jacek Ilow, "Compensation of Nonlinear Distortion with Memory Effects in OFDM Transmitters," *Global Telecommun. Conference, 2004. GLOBECOM'04.IEEE.*, vol. 4, pp. 2398-2403, 2006.
- [132] Graham H. Smith, Dalma Novak, and Zaheer Ahmed, "Overcoming Chromatic-Dispersion Effect in Fiber-Wireless Systems Incorporating External Modulators," *IEEE Trans. On Microwave Theory and Tech.*, vol. 45, pp. 1410-1415, 1997.
- [133] Adel A. M. Saleh, "Frequency-Independent and Frequency-Dependent Nonlinear Models of TWT Amplifiers," *IEEE Trans. On Commun.*, vol. 29, pp. 1715-1720, 1981.
- [134] Christopher J. Clark, Christopher P. Silva, Andrew A. Moulthrop, and Michael S. Muha, "Power-Amplifier Characterization Using a Two-Tone Measurement Technique," *IEEE Trans. On Microwave Theory and Tech.*, vol. 50, pp. 1590-1602, 2002.